



Programme Area: Carbon Capture and Storage

Project: High Hydrogen

Title: Flammability, ignition, deflagration to detonation transition (DDT)
Potential for hydrogen based fuels.

Abstract:

This deliverable is part 3 of 5 in this project and provides the laboratory analysis of hydrogen based fuels with their reactions across different types of experiments. The report commences with an executive summary written by Hans J Michels, the CTO for this project. The initial reports were written by Imperial College and investigate the binary gas mixtures identified by WP1 of this project. This is aimed at building a chemical model to support a greater level of prediction for mixed gas systems. Using a variety of test equipment to ensure the experimental findings can be justified and repeated the auto ignition temperature, reaction strengths and DDT potential were all investigated. The primary finding was that H₂ mixed with CH₄ demonstrated a calming influence on the reaction where as H₂ CO reacted close to pure H₂ at even low mixtures concentrations and was nearly twice as reactive as the CH₄ mixtures.

Context:

Hydrogen is likely to be an increasingly important fuel component in the future. This £3.5m project was designed to advance the safe design and operation of gas turbines, reciprocating engines and combined heat and power systems using hydrogen-based fuels. Through new modelling and large-scale experimental work the project sought to identify the bounds of safe design and operation of high efficiency combined cycle gas turbine and combined heat and power systems operating on a range of fuels with high and variable concentrations of hydrogen. The goal of the project was to increase the range of fuels that can be safely used in power and heat generating plant. The project involved the Health and Safety Laboratory, an agency of the Health and Safety Executive, in collaboration with Imperial Consultants, the consulting arm of Imperial College London.

Disclaimer:

The Energy Technologies Institute is making this document available to use under the Energy Technologies Institute Open Licence for Materials. Please refer to the Energy Technologies Institute website for the terms and conditions of this licence. The Information is licensed 'as is' and the Energy Technologies Institute excludes all representations, warranties, obligations and liabilities in relation to the Information to the maximum extent permitted by law. The Energy Technologies Institute is not liable for any errors or omissions in the Information and shall not be liable for any loss, injury or damage of any kind caused by its use. This exclusion of liability includes, but is not limited to, any direct, indirect, special, incidental, consequential, punitive, or exemplary damages in each case such as loss of revenue, data, anticipated profits, and lost business. The Energy Technologies Institute does not guarantee the continued supply of the Information. Notwithstanding any statement to the contrary contained on the face of this document, the Energy Technologies Institute confirms that the authors of the document have consented to its publication by the Energy Technologies Institute.

Executive Summary & Report 1:
CTO's Overview of WP2.1
Hans J Michels, CTO

ETI Contract PE02062
“High Hydrogen”
Stage Gate 2 Report
6 February 2013

Executive Summary

These documents comprise in four reports the work that represents the Milestone 3 Deliverables of the ETI contract PE02062 “High Hydrogen Project”, as discussed at the Stage Gate 2 meetings at the ETI on 15 October and 28 November 2012.

Based on investigation of fundamental combustion characteristics of binary mixtures of H_2/CH_4 and H_2/CO , the technical Overview of Report 1 lists the main findings, conclusions, recommendations and gaps in current knowledge together with requirements for additional work.

The results reported in Report 2 from experiments at Imperial College and Stanford University on the ignition, turbulent deflagration and DDT potential of the above fuel systems give full credence to industry’s concerns about the explosive risks associated with flame-out scenarios from the use of “high-hydrogen” mixtures and 100% H_2 , which extend significantly to high- H_2/CO fuels. Such risks are found to be particularly relevant for conditions at the *entries to exhaust ducts and heat exchangers*.

For 100% H_2 and these simple binary mixtures the risks appear manageable at relatively low “CCGT” equivalence concentrations or at high inert dilution ratios. In this context the moderating influence of CH_4 on H_2 has been identified, which calls for additional study of high $H_2/CO/CH_4$ mixtures. For the much higher equivalence ratios of these binary fuels at “CCGE” concentrations, and without dilution, critical levels of detonation potential limit enrichment by H_2 appear to be less than $2/3^{rd}$ for CH_4 and $1/3^{rd}$ for CO . This adds to the need for a wider study and quantification of the potential benefits of dilution and of the potential hazards from reactive additives.

The results and their analysis provide clear recommendations for the 20 run test programme of Task 2, which is to concentrate on the explosive

behaviour along the binary boundaries at the “high-hydrogen” end of the H₂/CH₄/CO fuel system.

As reported in Report 3, Task 2 modelling was carried out by BAE Systems of blasts in the simplified hydrogen driven model of a power generation system. It concludes that for the Task 2 design the very high detonation transients and the longer duration expansion wave pressures are both acceptable.

Report 4 details predictions by IS&A Consultants of pressure development in the one-dimensional model arrangements for the flame acceleration and detonation of the same binary fuel systems, which are generally in line with the BAE Systems results. Unfortunately these were only performed for the Imperial College flame tube facility and fall short of the requirements for Task 2. The work needs to be updated to the Task 2 scenario as it requires to be validated in a 3-way comparison with BAE Systems and Task 2 experimental results, before the same methods can confidently be used to provide shock development and over-pressure prediction for the more vulnerable Task 3 design of a model turbine/gas engine exhaust duct.

At the Stage Gate meeting of 28 November 2012 it has been agreed that, subject to acceptance of this report, the work to date satisfies the deliverables of the project at this point.

Contents

- Report 1:** CTO's Overview of Work Package 2, Task 1. Prof H.J. Michels, Imperial College London.
- Report 2a:** Ignition, turbulent deflagration and DDT potential of hydrogen / methane and hydrogen / carbon monoxide mixtures with air. Prof P.R. Lindstedt, Imperial College London
- Report 2b:** Shock Tube Studies of the Ignition Delay Times of Syn-Gases. Prof. R. K. Hanson, Dr. D. F. Davidson, Stanford University.
- Report 3:** Modelling of blast in hydrogen power generation systems. Dr R.Rosario, BAE Systems.
- Report 4:** One-Dimesional model predictions of test rigs pressure distributions (deliverable One). Dr G. Munday, Information Search and Analysis Consultants.

Report 1. CTO's Overview of Work Package 2, Task 1

H J Michels.

*Department of Chemical Engineering
Imperial College London, Exhibition Road, London SW72AZ*

1.1. Introduction

This programme originally aimed to address the Schedule of Delivery (SoD) in the contract documents, Schedule 5, part 2. However, as result of four modifications, this report is of more limited scope than stipulated in the Schedule, to which the following changes have been agreed and made:

- (a) The first changes concerned with the fuel systems to be investigated. As a result of the discussions at the 1st Stage Gate Meeting on 15 February 2012, the fuel-diluent systems investigated are not those proposed in the Work Package 1 Report on the basis of its literature survey. Instead, the experimental work carried out under Task 1 of Work Package 2 has considered the combustion characteristics of binary systems of hydrogen with methane and carbon monoxide.
- (b) The second variation is that the work has focussed on detonation propensity, rather than detonative behaviour. As a result, no measurements of the latter have been considered for Task 1; such incidental tests may be included in Task 2 to determine critical boundaries.
- (c) The third change is that for issues concerned with flame detection, recording, progress evaluation and control, the deliverables (Work Package 3) have already been considered independently, submitted and assessed by ETI referees.
- (d) Finally we note that the ETI had approved an extension for submission of Task 2 Design and Build.

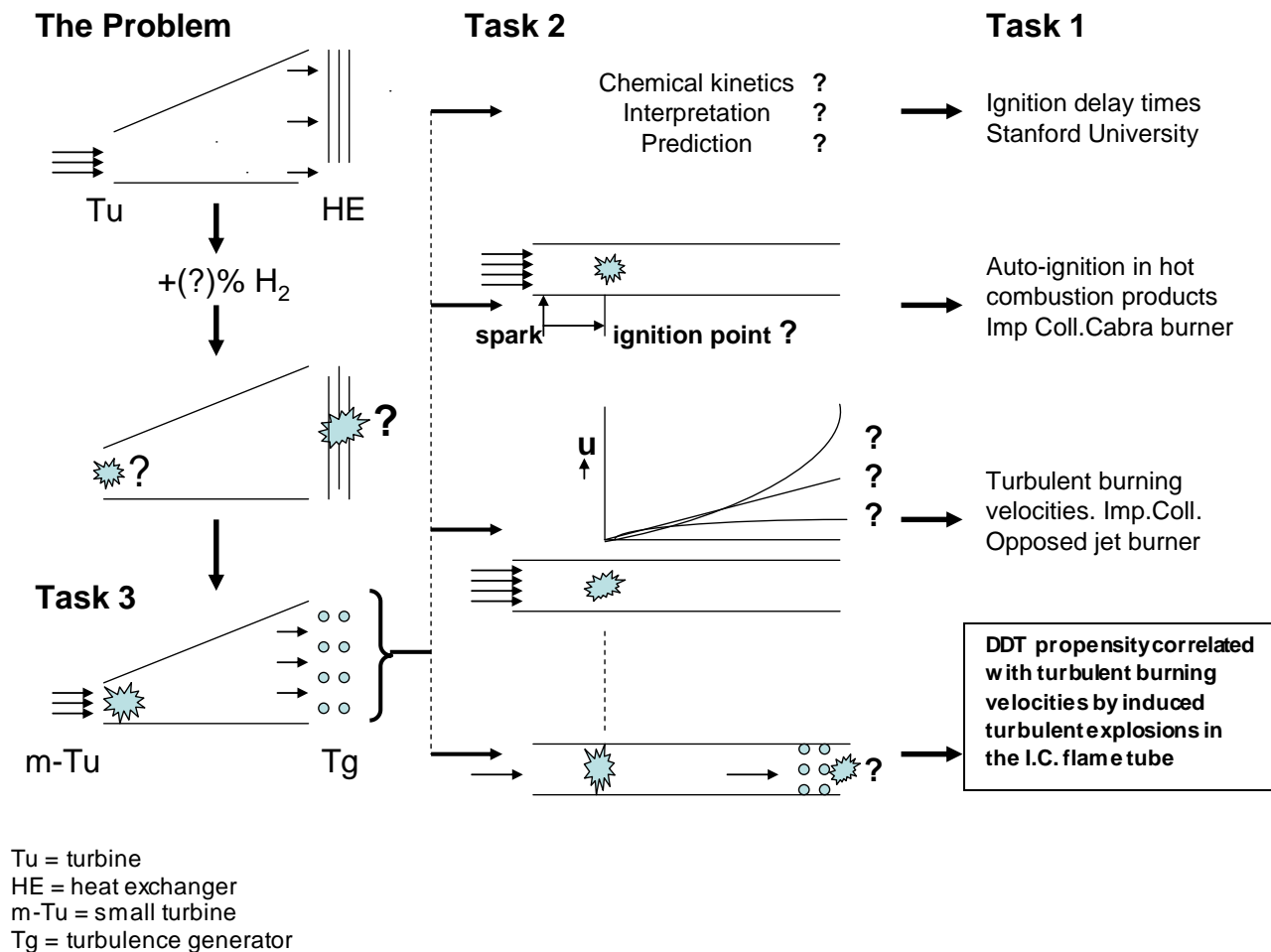
To provide the deliverables for Stage Gate 2, this report is therefore restricted to considering:

- (i) The modified experimental investigations of Work Package 2 Task 1 carried out at Imperial College, their evaluation and interpretation and the recommendations based on these results for the Work Package 2, Task 2 programme (Report 2a);
- (ii) The ignition-delay data provided by Stanford University (Report 2b);
- (iii) The Task 2 modelling work by BAE Systems (Report 3); and
- (iv) Modelling work (Deliverable One) by IS&AC (Report 4). Note: the modelling predictions from this work for Work Package 2, Task 3 (Deliverable Two) will in part depend on the outcome of the Task 2 investigation. Their discussion will therefore be deferred to the Work Package 2, Task 2 Report.

Structure of the Work Package 2 investigation

Work Package 2 aims to achieve the value objective of the project: to resolve questions about the proper balance between energy efficiency enhancement and hazard and safety issues from hydrogen addition and use of 100% hydrogen for CCGT and CCGE fuel streams.

To this end, a reduced size model of a CCGT installation will be built to study the ignition, flame development, pressure generation and detonation propensity of the test mixture scenarios of 1.1(a) above (Task 3). The focus will be on the dangers of explosive ignition in the inlets of the exhaust system and the heat exchanger. In preparation for this, a pilot study of these properties and behaviours is required. This will be investigated in a 12 m long, 0.6 m diameter tube, where critical operating conditions are to be evaluated in a specially designed, flexible and high strength test environment (Task 2). In preparation for this, Task 1 aimed to determine the fundamental chemical kinetics and the broader combustion behaviour of the selected binary fuel systems. The diagram below shows the sequential requirements of the Work Package 2 programme.



1.2. Investigation of Ignition, Turbulent Deflagration and DDT potential of Hydrogen Rich Mixtures (Imperial College - Report 2)

Within Task 1 in line with the objectives of the programme, the fuel mixtures investigated were those of relevance to the operation of combined cycle gas turbines (CCGT) and gas engines (CCGE).

As agreed at the 1st Stage Gate Meeting, the impact of fuel reactivity changes on key parameters of binary methane and carbon monoxide mixtures with increasing amounts of hydrogen was studied. The total fuel content was varied from an equivalence ratio of 0.3 to 0.8; addition of nitrogen to mitigate reactivity was also considered. The test matrix covered

11 H₂/CH₄ component ratios, including 100% of each; the H₂/CO matrix covered an additional 7 mixtures with up to 70% CO.

The approved programme involved four separate assessments of the influence of chemistry and flow on the combustion efficiency and explosivity of these fuel systems, specifically involving studies of:

- (a) Ignition-delay;
- (b) Auto-ignition in turbulent shear between a fuel jet and a stream of hot combustion products;
- (c) The strength of turbulent deflagrations as a function of fuel composition; and
- (d) Deflagration to detonation propensity in obstructed turbulent flow.

Critical information on chemical kinetics for the ignition-delay studies was obtained from Stanford University, reported in Report 2(b). Results for (b), (c) and (d) are reported in Report 2(a) of this report and complete the current experimental contributions by Imperial College to Work Package 2, Task 1.

The Report 2(a) fully details all aspects of the work. The objectives, methods and experimental facilities are described, the results analysed with the recognition of clear trends in the behaviour of characteristic flame development, intensity and propagation parameters for the fuel mixtures of interest. Modelling for turbulent burning velocity predictions and confirmation has been performed and the consequences of the findings for the testing and use of the fuel mixtures in large CCGT/CCGE model and practical systems have been identified.

Findings and Recommendations from Report 2 (a) & (b):

The purpose of Work Package 2, Task 1 was to obtain primary information for the execution of Tasks 2 and 3, and therefore the findings and recommendations from these Tasks may appropriately be discussed together. Report 2 highlights as the main observations:

- (a) The investigation found generally parallel trends for each of the four assessments, in particular between the auto-ignition results in hot turbulent flow conditions from Imperial College and the Stanford University data on laminar flow ignition-delay.

- (b) Comparison of these results cannot however be completed until the Stanford University results, obtained at enhanced pressure to reach the required lower temperature levels, have been extrapolated. Related chemical kinetics will need to be developed both for this and for prediction and analysis of future project results.
- (c) Enriching H₂/CH₄ mixtures with further H₂ proportionally enhances reactivity. For the use of relatively high CH₄ fuel systems in industrial scale installations, it is not recommended to use more than 40% H₂, unless the equivalence of the fuel mixture is reduced or accompanied by significant inert dilution.
- (d) The enhancement of the explosivity of CO by H₂ is more than twice that for comparable CH₄/H₂ mixtures. For practical systems with significant CO content, extreme caution over H₂-enrichment is therefore warranted.
- (e) Where the moderation by dilution with inert is employed, there is a high chance that any pre-mixed fuel mixture ejected unburned will ignite on the hot exhaust surfaces. Assurance must therefore be incorporated into designs that the flow will be fully mixed and/or combusted before it meets major turbulence-generating obstructions, such as upon entry into heat exchangers.
- (f) Levels of (normalised) turbulent burning velocity and overpressure are reliable quantitative indicators of increased/hazardous detonation propensity.
- (g) For the range of fuel mixture compositions proposed from the above work to be appropriate for large scale experimentation and/or practical use, in-house modelling based on the parameters obtained from this work supports the experimental findings and conclusions.

The forward feed from Task 1 to Task 2 is summarised in the following diagram.

Task 2

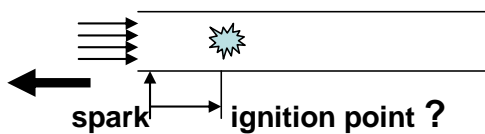
Ignition & reactivity data agree with IC results, but additional work on chemical kinetics essential for full agreement and future analysis.

Chemical kinetics ?
Interpretation ?
Prediction ?

Task 1

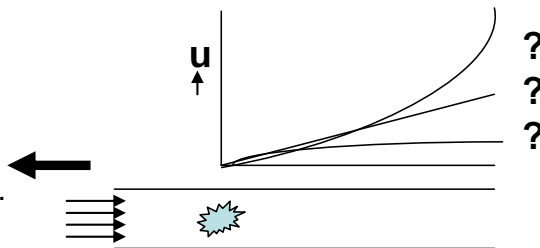
Ignition delay times obtained by Stanford University.

Duct temperature may be too low for self-ignition to occur. After adequate mixing spark & ignition points can be set to ensure combustion.



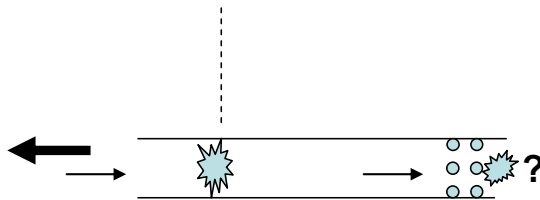
Auto-ignition in hot combustion products obtained by Imperial College (IC) using the Cabra burner.

Composition-, stoichiometry- and dilution limits to H_2 enrichment, have been quantified from turbulence and flame acceleration.



Turbulent burning velocities obtained in the IC opposed jet burner. A scaling relationship obtained.

Quantification of critical levels of turbulent flame velocity and overpressures to avoid risk of DDT have been made



DDT propensity shown to be correlated with turbulent burning velocities by induced turbulent explosions in the IC flame tube.

Recommendations for the Task 2 programme.

Within the constraints of currently agreed funding, the results of the Task 1 investigations at Imperial College and Stanford University lead to the following outline for a 20 test core programme that will concentrate on the major hazards of H_2 enrichment of both binary systems:

- High H_2 including 100% H_2 ;
- At high velocity, high temperature at the entry to the Task 2 rig;
- At low velocity at the entry to the turbulence generator, modelling a heat exchanger, with increasing depth of tubular arrangement.

Tentatively and subject to review in the light of ongoing experience, the detailed programme will be as follows:

For H₂/CH₄:

- 2 tests to verify high velocity entry conditions (incl. 100% H₂);
- 3 tests to verify free flame initiation, flame development and overpressure generation ahead of the turbulence generator;
- 6 tests to study flow, turbulence, combustion kernel development and overpressure generation within the turbulence generator.

For H₂/CO:

- 1 test to verify high velocity entry conditions;
- 6 tests to study flow, turbulence, combustion kernel development and overpressure generation within the turbulence generator.

Contingency:

- 2 tests, which may be used to test moderation of the high H₂/CO reactivity by CH₄.

1.3. Modelling of blast in hydrogen power generation systems (BAE Systems - Report 3)

The programme described in this report aim to simulate the “worst case” effects of a detonation wave on the structure of the Task 2 rig. Three different modelling approaches were used to predict the dynamic and static pressures generated along the centreline of the duct, at its wall and near the turbine exhaust by a detonating stoichiometric mixture of H₂ and CO contaminated air. Detonation ignition was considered close to the exhaust and half way down the tube. At the exhaust, peak pressure predictions were between 17 and 25 bar.a. For the latter, high detonation shock front overpressures were 35 - 100 bar.a; they did not occur at the tube wall and their existence was too brief to influence material strength considerations. Pressures at the tube wall peaked at 29 bar.a. Longer duration and more important “Static” pressures did not exceed 6 bar.a.

The work did not and would not have been able to consider the likelihood of a deflagration-to-detonation transition (DDT). With detonation propensity rather than detonative behaviour now a major focus of the programme, its main value lies in determining the maximum over-pressures and their locations in instances where, unintentionally, DDT would have occurred. The model chosen was also of an initial design, for which the exhaust-tube transfer will now be significantly different. Given that the tube design is

based on a static working pressure of 20 bar.a and a safety factor of 1.5, the results give confidence about the suitability of the design.

1.4. One dimensional model predictions of test rigs' pressure distributions (Deliverable One; IS&AC – Report 4)

The aim of this modelling was to study the detonative behaviour and detonation potential of the binary systems of H₂/CH₄ and H₂/CO agreed with the ETI. For these systems, the properties of alternative concentrations from the ranges investigated experimentally at Imperial College were used to predict overpressures from high temperature combustion of enriched turbine exhaust mixtures. Based on simplified assumptions for flame acceleration and pressure wave generation after ignition, transient overpressures were evaluated and described in Report 4.

Conclusions from this work are as follows:

- (a) Deliverable One produced two sets of results – detonative and flame acceleration data – obtained by two methods: Analytical and the Method of Characteristics (MOC).
- (b) The results for detonation are not very different from those of the BAE Systems' approach, giving a measure of confidence on detonative behaviour. As stated above, the BAE Systems' approach did not deal with flame acceleration.
- (c) Deliverable One does not directly address the Task 2 situation, but was based on a system similar to Task 1, namely Imperial College's flame tube. As such, it could be presented as a more general validation method for flame acceleration and detonative behaviour based on the Imperial College confinements.
- (d) However, the Imperial College rig was used to study flame acceleration up to detonation propensity, not detonation. The part of Deliverable One which provides predictions for detonative behaviour has no relevance to the Task 1 scenario, but its flame acceleration work might be compared with the Imperial College results. (Note: As the BAE Systems contract, the IS&AC contract had been based on the original, pre-Stage Gate 1 brief.)

- (e) The Imperial College investigation was not set up to test critical parameters for this validation. The agreement on pressure development was at best 'reasonable.'
- (f) To deliver predictions for the Task 2 tests, the configuration of the 600 mm diameter rig had to be known. In the crucial area for flame initiation, acceleration and critical overpressures from strong deflagrations and unintended detonations, the modified design will be appreciably different from the simple early single tube design. At the scheduled time for the production of Deliverable One, the design of the Task 2 rig had not been finalised. The HSL and involved other members of the Consortium were granted an extension to deliver on this.
- (g) Given the subsequent modifications of the original provisional Task 2 design, it is evident that the Deliverable One modelling would not only need further input, but its methods and software would need adapting to deal with new situations, especially in the exhaust entry area.
- (h) Given the evidence available to date, the expenditure made, the capability and required modifications to the IS&AC technology and the absence of comprehensive kinetic data, we recommend that the results to date are noted and used as appropriate, bearing in mind their limitations. We would also recommend further IS&AC-Deliverable One modelling. This will first of all make it possible to compare its predictions of pressure distributions for Task 2 with similar predictions from BAE Systems, as well as in due course with the results from Task 2 tests. More importantly it will contribute to the validation of and selection from both computational techniques for use in pressure distribution predictions for Task 3.
- (i) In due course IS&AC Deliverable Two, which is directed at the Task 3 configuration, may similarly also need to be reviewed when the results of Task 2 are available. At this stage, an application will be made only for additional funding to convert the Deliverable One model to the Task 2 configuration.

- (j) Meanwhile, alternative techniques should be considered to model fuel reactivity in turbulent flow and its influence on detonation propensity. However, these are unlikely to be readily available or affordable.

1.5 Gaps in current understanding and/or information

The following gaps have been identified from the Task 1 work at Imperial College and Stanford University:

- (a) Despite the similarity in trends between the Stanford University data and the auto-ignition results from Imperial College, we are currently unable to extrapolate confidently the 1.4-1.8 atm results from Stanford University to ambient pressure levels in order to achieve a more direct quantitative comparison. This will require chemical kinetic information.
- (b) The same lack of insight in reactivity prevents us from understanding the remarkable ability of even relatively low levels of H₂ to activate CO to such high reactivity that it responds almost as rapidly as H₂.
- (c) In contrast, CH₄ has a very moderating effect on H₂ reactivity. Whilst worthy of further investigation, the possibility that it will similarly limit reactivity of high-H₂/CO mixtures has potentially significant implications for the safe operation of CCGT and CCGE energy generating systems.
- (d) An additional benefit of more advanced chemical kinetics can arise because the work has additionally shown that to appreciate the critical role of the H₂/CO composition ratio a much better understanding is required of its influence on ignitability and subsequent explosion strength. These reflect differences between reactivity and energetics that have important implications for the design and local temperature control of different power generation applications.
- (e) The evidence of the Task 1 work also necessitates additional work on the moderating role of diluents, the representative role that N₂ for this category of mixture components and the influence of more reactive hydrocarbons, which may trigger reactivity of slower responding fuels.

- (f) Even with successful completion of the current ETI programme, outstanding questions will remain about the relevance of the findings and recommendations to realistic additives to the model mixtures investigated. Early identification and assessment of such additives (e.g. water) and basic amended mixture analysis, concurrent with Task 2 and Task 3 work would extend application of the results of the current study to future design and operational schedules.
- (g) One of the two most hazardous of the practical situations modelled in this programme is at the exhaust entry point of a turbine in flame-out conditions. A further, broader analysis of potential methods to model its conditions, including real or model fuel-injection procedures, would increase the reliability and relevance of test results.

1.6. Recommendations for additional Task 1 work.

The work proposed below would optimise the benefits of work already carried out and/or ensure that timely assessment of how the later sections of the programme can properly support the achievement of the Value Objective. Costing of such additional activities is not included here.

- (a) Sub-section 1.5 has provided justifications for investigating the chemical kinetics of H_2/CO and H_2/CH_4 interaction for enhanced benefit from the Imperial College work.
- (b) Subsequent to this, the Stanford University data should be extrapolated to ambient pressure conditions.
- (c) The moderation of H_2/CO interaction by CH_4 needs to be investigated experimentally for a number of high H_2 mixtures in advance of any extension in the Task 2 programme. A limited set of previous used techniques will suffice.
- (d) Similar compact experimental programmes are essential to identify more systematically the influence of dilution at various equivalence ratios and reactive hydrocarbons

- (e) For the IS&AC modelling: if confidence is required to complete and use Deliverable Two (not yet submitted) to assess explosion/detonation hazards in the Task 3 facility, the Deliverable One work needs to be adapted to fully represent the Task two scenario and validated against experimental evidence and predictions from the BAE Systems' submission.

58 Prince's Gate
Exhibition Road
London SW7 2PG
T: +44 (0)20 7594 6565
F: +44 (0)20 7594 6570
W: www.imperial-consultants.co.uk

**Ignition, Turbulent Deflagration
and DDT Potential of H₂/CH₄ and
H₂/CO mixtures with Air**

**Ignition, Turbulent Deflagration and DDT
Potential of H₂/CH₄ and H₂/CO mixtures
with Air**

**Prepared for Energy Technologies Institute
Project CC1018**

*F. Hampp, K.H.H. Goh, H.J. Michels and R.P. Lindstedt**

*Department of Mechanical Engineering
Imperial College, Exhibition Road, London SW7 2AZ, UK*

*Corresponding author. Email: p.lindstedt@imperial.ac.uk; Tel: +44-20-7594 7039; Fax: +44-20-7594 5696

Abstract

The current study investigates the impact of fuel reactivity changes on key parameters of relevance to the operation of combined cycle gas turbines (CCGT) and gas engines (CCGE) caused by the gradual enhancement of methane or carbon monoxide mixtures with hydrogen. The study covers premixed fuel lean (a stoichiometry of 0.80) binary blends of H_2/CH_4 and H_2/CO . The former represents mixtures of interest to the decarbonisation of installed power generating capacity and the latter is related to the use of biomass (waste gas) and some forms of syngas. The impact of nitrogen dilution is also considered. The H_2/CH_4 matrix covers the full range between the pure components and with intermediate steps of 90/10, 80/20, 70/30, 60/40, 50/50, 40/60 and 25/75. The H_2/CO blends cover mixtures of 90/10, 80/20, 70/30, 60/40, 50/50, 40/60 and 30/70. In some cases, additional and/or alternative mixtures were considered in order to further elucidate trends in light of obtained results.

The experimental configurations were chosen to investigate flammability, ignition characteristics, the influence of turbulence on the strength of deflagrations and the deflagration to detonation transition (DDT) potential. Four different configurations were used in order to provide a comprehensive assessment of the relative influence of chemistry and flow: (i) Ignition delay times were measured by Stanford University using a shock tube configuration in order to provide a purely chemical kinetic related measure of reactivity. (ii) Auto-ignition in a turbulent shear layer formed between a fuel jet and a stream of hot combustion products was investigated in order to explore the influence of turbulence under conditions that can be correlated with the Stanford experiments. The configuration is also related directly to the practical case where reactants are ejected into hot combustion products. (iii) Turbulent burning velocities were determined using fractal grid generated turbulence in an opposed jet configuration in order to determine the strength of turbulent deflagrations as a function of fuel composition. (iv) The DDT potential in a turbulent flow was assessed using an obstructed shock tube configuration with explosion over-pressures determined and related to the fuel reactivity and the strength of the turbulent deflagration phase. The study accordingly provides a comprehensive assessment of fuel reactivity in systems related to the use of hydrogen rich mixtures under CCGT and CCGE relevant conditions.

The results consistently show a notable difference between dilution with CO and CH_4 . Comparatively small amounts of added CH_4 is causing a noticeable decline in mixture reactivity while a CO content of up to 50% shows only a modest impact. The results obtained from the shock tube and auto-ignition studies suggest that under the current condition the reactivity of CH_4/H_2 blends becomes increasingly reduced by the CH_4 component beyond the 50/50 mixture. By contrast, CO mixtures remain much more reactive over the entire range of conditions. A strong impact of dilution has also been shown and the effect is consistent with a reduced ability of the H_2 component of the fuel blend to trigger auto-ignition of the carbon containing components. The latter conclusion is further supported by the appearance of twin reaction zones in the turbulent shear layer ignition studies with the effect more pronounced at lower temperatures.

The strength of turbulent deflagrations, as characterised by the turbulent burning velocity, suggests the same trend as outlined above for the chemical kinetic measurements with a somewhat less pronounced influence of the underlying chemistry as may be expected from theoretical considerations. The explosion over-pressure measure-

ments used as an indicator of DDT potential under turbulent flow conditions suggest that a 50% increase to around 150 kPa, as compared to 100 kPa for the pure methane case, is obtained for CH_4 mixtures with around 50% H_2 and CO mixtures with 20% H_2 . Hence, extreme caution is required for blends of the latter type while it can be expected that blends with CH_4 are less sensitive. The testing of hydrogen enriched mixtures in large scale practical systems should hence commence with CH_4/H_2 blends with low hydrogen contents subject to a gradual increase. The use of more than 40% hydrogen is not recommended even for such systems at the present time and the use of diluted mixtures is also recommended as an appropriate starting point. The ignition delay time trends are fully consistent with determined turbulent burning velocities and DDT studies. It is our expectation that further larger (or laboratory) scale experimentation will confirm these trends and permit a more delineated set of recommendations that differentiates between mixtures with CO and CH_4 . It may also be noted that to establish the potentially mitigating influence of CH_4 on H_2/CO mixtures would require an investigation of ternary blends. The strong impact of dilution suggests that significant care must be taken in designing large scale experimental rigs. In a practical scenario it is likely that a premixed unreacted mixture is ejected directly into a post-device (e.g. heat exchanger or duct) environment. Accordingly, any additional time scales associated with the mixing of a fuel blend with an oxidiser at the same time as it undergoes mixing with hot combustion products may unduly influence the observed results.

Modelling studies featuring ignition delay times and the determination of laminar burning properties have also been performed to support an evaluation of the accuracy of state of the art chemical kinetic models and theoretical correlations for the turbulent burning velocity. The results show that the latter can be correlated with reasonable success up to comparatively high ($\leq 60\%$) hydrogen contents and that uncertainties still prevail in the basic chemical kinetic parameters - particularly for the CO/H_2 system. The latter observation further emphasises the need for caution when using such systems in large scale experimentation or practical systems.

Overall, the current study has quantified the impact of increasing hydrogen content on the mixture reactivity under laboratory condition with key system differences identified. Given the apparent discrepancies between the two types of binary mixtures and likely ternary systems (e.g. COG and/or bio syngas) in practical applications, it is suggested that the latter should be investigated to establish any potential mitigation obtained via the introduction of methane. It is further noted that the chemistry behaviour of CO/H_2 blends merits further investigation in order to provide a predictive capability of ignition delay times and permit the subsequent investigation of secondary effects such as the use of different diluents.

Keywords: Hydrogen, carbon monoxide, methane, ignition delay times, auto-ignition, fuel reactivity, deflagration, DDT potential.

1 Introduction

The test strategy adopted for the laboratory studies forming part of ETI project PE02162 features the use of binary fuel blends of H_2/CH_4 and H_2/CO starting from the case of 100% H_2 and with the gradual addition of the second component. The small scale laboratory tests, used as basis for future work within the project, uniquely feature four complementary approaches covering a wide range of conditions: (i) A fuel reactivity assessment through the use of ignition delay times obtained from conventional laminar shock tube experiments, (ii) a fuel reactivity assessment via the study of auto-ignition in turbulent flow fields, (iii) the determination of the strength of turbulent deflagrations via the determination of turbulent burning velocities and (iv) the determination of the deflagration to detonation transition (DDT) potential in an obstructed shock tube with optical access.

It must be noted that the actual conditions experienced in a practical CCGT and CCGE devices present significant challenges in terms of deriving even a relative assessment of the reactivity of different fuel blends. For example, the exhaust temperatures encountered in a practical CCGT scenario will be strongly dependent on the design of a gas turbine and the degree of mixing of the unburnt fuel blend with pre-existing combustion products at the exit plane of the combustor. Hence, the problem is not well-defined and the sensitivity to the exhaust temperature is here considered as an additional parameter. The implications for the project from the increased workload of using a larger number of mixtures has to some extent been mitigated by moderate changes in the overall work programme, notably by emphasising the importance of detonability rather than detonation behaviour of mixtures and the focus on parameters such as over-pressure generation in obstructed tubes as part on an assessment of the DDT potential.

The fuel blends investigated as part of the current study focus on the more reactive end of the spectrum with mixtures ratios of hydrogen to carbon monoxide of 100/0, 90/10, 80/20, 70/30, 60/40, 50/50, 40/60 and 30/70 prior to dilution. The proposed range covers the majority of H_2/CO ratios identified as part of the Literature Review performed as part of Work Package 1 [1]. A narrower range of blends was originally proposed for the H_2/CH_4 blends encompassing 100/0, 90/10, 80/20, 70/30, 60/40 and 50/50 in line with the obtained mixture information. The latter set of mixtures was, however, subsequently extended on a best endeavours basis, to include 40/60, 25/75 (or 20/80) and 0/100. In addition, a combustion device dependent dilution factor was taken into account. For practical application, it can be assumed that overall lean premixed combustion will be used and/or that significant dilution of the fuel stream will take place prior to conditions of relevance to the current investigation. Hence, it is likely that the overall hydrogen concentration in the mixture prior to combustion will not exceed 25% by volume in a fully premixed mode and, perhaps, less than half of that in the context of a gas turbine combustor. With the further dilution

expected in a gas turbine engine, the proposed test matrix will therefore move the hydrogen content towards the lower flammability limit.

The practical temperature range is, as stated above, not well-established. However, it may be noted that auto-ignition has been found to be difficult (e.g. Choi and Chung [2]) even in the context of laminar lifted flames of methane and hydrogen at temperatures below 940 K. The temperature window explored in laminar experiments in the current study goes down to below 940 K for H_2/CO blends and to around 1000 K for the less reactive H_2/CH_4 blends. Practical conditions are most likely to be turbulent in nature, with a corresponding increase in the propensity to flame extinction, and the minimum temperature of the combustion products was accordingly increased to around 1040 K for these experiments in order to enable flames to be established.

The first sets of data to be considered refers to ignition delay times obtained in a Stanford shock tube facility. The determined data is directly related to the chemical kinetics of the system and hence provide a basis for the assessment of the accuracy of state-of-the-art models in the context of the current systems. The Stanford shock tube facility is generally regarded as world leading and ignition delay time data was produced for the following H_2/CH_4 mixtures: 100/0, 80/20, 60/40, 40/60 and 20/80. Data was also obtained for H_2/CO mixtures of 80/20, 60/40 and 40/60. These data sets provide a pure basis for an assessment of the changes in the chemical kinetics of the system. The data covers system dependent temperatures down to around 940 K with measurements performed around 1.7 atm to extend the temperature envelope while maintaining accuracy.

The second data sets features the determination of auto-ignition delay times in turbulent flow fields. The Cabra burner geometry [3, 4, 5, 6, 7] has been successfully used to study such flows using high velocity fuel streams injected at ambient temperatures in a co-flowing stream of dilute combustion products at temperatures down to 1045 K. Due to the nature of the shear layer driven mixing, the temperature at the point of ignition will be lower. In the current work, the geometry has been used at as low a temperature as can be achieved while still covering the fuel reactivity range of interest. Gkagkas and Lindstedt [8, 9] modelled the auto-ignition of CH_4 and H_2 mixtures using the transported probability density function approach [10, 11, 12, 13] and clarified the ignition events leading to flame stabilisation. Wang and Pope [14] showed that the auto-ignition chemistry has a direct and significant influence on computed extinction and re-ignition characteristics. The Cabra burner thus has a clear track record in terms of both experimental and computational studies of direct relevance to the current objectives and has been adopted with the intention of providing information pertinent to item (ii) above. The second section of the current report accordingly outlines experimental results aimed at clarifying changes in fuel reactivity caused by a reduction in hydrogen content and covers an assessment of the auto-ignition propensity of the selected fuel blends in turbulent flow fields. The latter is of fundamental importance in the context

of risks associated with the propensity of mixtures to form flame kernels that may grow into high-speed deflagrations or detonations. Past studies also suggest that state of the art computational methods can also be applied with confidence to elucidate the flow field structure further should the need arise. The study further permits a comparison with the Stanford data and an assessment of qualitative and quantitative correlations between the two methods.

The third data set reports the strength of turbulent deflagrations, as characterised by the turbulent burning velocity, for the selected mixtures. The opposed jet configuration, used in the current study, has a long track record that includes the work by Potter and co-workers [15, 16, 17] on diffusion flames formed between two opposing streams in an enclosed chamber. Pandya and Weinberg [18, 19] also used an opposed jet burner to investigate laminar diffusion flames and Tsuji and Yamaoka [20, 21, 22] stabilised a flame using flow from a porous cylinder. The pioneering work led to an extensive use of opposed jet configurations for the study of non-premixed and premixed flames in laminar and turbulent flow environments, including the work of Shepherd et al. [23], Rolon et al. [24], Mastorakos et al. [25], Kostiuik et al. [26, 27, 28], Mounaïm-Rousselle and Gökalp [29], Sardi et al. [30, 31, 32], Stan and Johnson [33] and Geyer et al. [34]. Due to its basic geometry and ideal optical access, the opposed jet geometry was characterised by Geipel et al. [35] as canonical configuration to evaluate the capabilities of numerical turbulent reactive flows models. It was applied by Lindstedt and Váos [36, 37] to investigate a modified dissipation rate equation presented by Yakhot et al. [38], coupled with a Reynolds Stress closure of Haworth and Pope [39, 40]. The opposed jet geometry was further used by Geyer et al. [41, 42] for the validation of Large Eddy Simulations (LES) simulations. Coppola et al. [43] used turbulence generators with a blockage ratio of 90% to enhance turbulence intensity levels. Independently, a parametric study on isothermal opposed jet flows was carried out by Geipel et al. [35] to investigate the benefit of cross fractal grids over conventional turbulence generating grids. The cross fractal grids were derived from the findings of Vassilicos and co-workers [44, 45, 46]. The substitution of conventional grids with fractal grids resulted in an increase of more than 100% in turbulence levels as shown by Geipel et al. [35]. The opposed jet configuration used in the current study corresponds to the latest development of Goh et al. [47] where premixed turbulent flames are stabilised against a stream of hot combustion products with the relevant information presented in Section 5.

The final data set reports the potential for turbulence enhanced deflagration to detonation transition for a wide range of different H_2/CH_4 and H_2/CO mixtures. The basic shock tube configuration and an evaluation of different obstacle configurations has been reported by Sakthitharan [48] and McCann [49]. Lindstedt and Sakthitharan [50] further reported time-resolved measurements of flow and turbulence velocities obtained using Laser Doppler Anemometry (LDA) for a single obstacle configuration. The latter study was used as a basis for the application of high-speed particle image velocimetry in the current work.

The experimental results obtained in the earlier studies have subsequently been used by Kuan et al. [51] as a basis for the evaluation of predictive methods applicable to the computation of explosion kernels in turbulent flow fields. The results obtained were encouraging, but the latter aspect does not form part of the current study. The current data sets were obtained in an obstructed shock tube facility featuring two obstacles placed in a manner to induce the transition of laminar flames to turbulent explosions with minimum over-pressures of 150 kPa and flame speeds in excess of 200 m/s for pure methane–air mixtures. The latter were used as a reference case as such mixtures are commonly used in the context of both CCGT and CCGE applications.

Overall, the current study provides a quantification of the impact of increasing hydrogen content on methane and carbon monoxide mixture reactivity under a uniquely wide range of laboratory condition with key system similarities and differences identified at each stage.

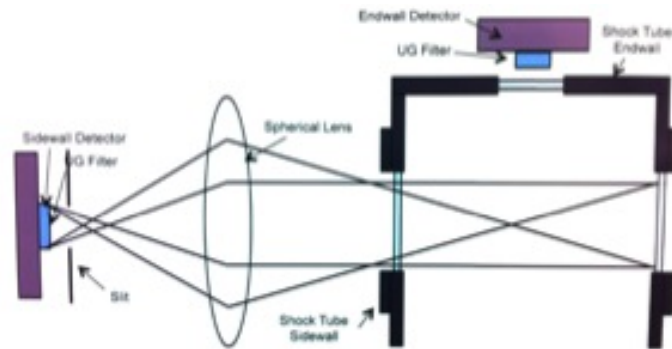


Fig. 1: Diagnostic setup for the Stanford shock tube facility

2 Ignition Delay Times for Hydrogen Rich Mixtures with Methane and Carbon Monoxide

The study below reports the chemical influence on ignition properties of fuel mixtures featuring hydrogen with methane and carbon monoxide. Ignition delay times (IDTs) were measured using shock tube methodologies at the Mechanical Engineering Department at Stanford University. The IDTs were measured behind reflected shock waves using endwall emission (OH^*) and sidewall pressure signals. The conditions feature a temperature range of 940 to 1200 K with fuel mixtures of H_2/CH_4 , (100/0, 80/20, 60/40, 40/60, 20/80) and H_2/CO (80/20, 60/40, 40/60) at a single stoichiometry of 0.8 for oxygen content up to 21%. The composition of air for all experiments performed at Imperial College was for the purposes of the current report assumed to be 21% O_2 and 79% N_2 resulting in a N_2/O_2 ratio of 3.76. In the experimental work performed at Stanford Univer-

sity, the N_2 was substituted by Ar , a common practice in shock tube studies of ignition delay times, leading to a Ar/O_2 ratio of 3.76. The use of Ar does not present any additional technical difficulties in comparing computational results as the collision efficiencies of both species are well established. The data discussed below is also available in tabular form in the final report submitted by Stanford University.

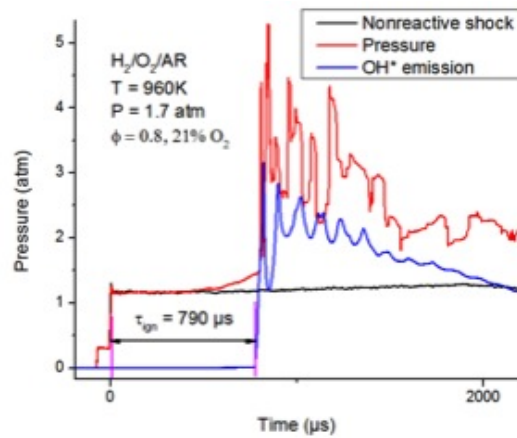


Fig. 2: Example shock tube emission and pressure data.

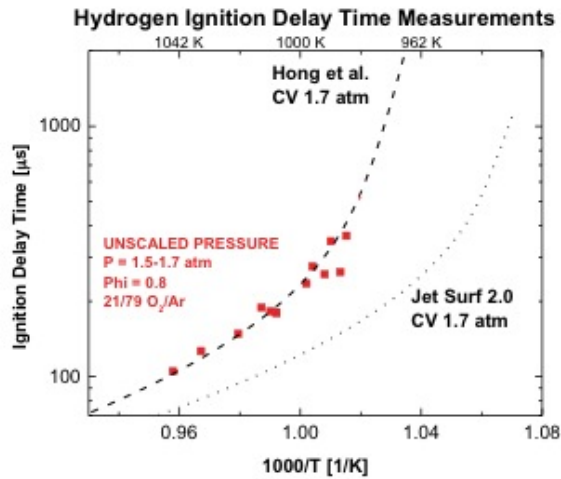


Fig. 3: Ignition delay time data obtained for the pure hydrogen system.

2.1 Experimental Conditions and Procedure

The IDTs were measured using OH* emissions at both sidewall (2 cm from end wall) and end wall locations from the OH-band near 306 nm with the side wall pressure obtained at the same location. Ignition delay times from all methods were nearly identical and end wall values are reported. The shock emission diagnostic setup is shown in Fig. 1 and further details have been reported by Davidson and Hanson [52]. The ignition delay time was defined as the time interval between the arrival of the reflected shock at the observation point and the extrapolation of the most rapid signal rise to the pre-ignition baseline. Representative data are shown in Fig. 2.

2.2 Results and Discussion

The ignition delay times are shown in final form in Figs. 3 to 5. Simulations of measurements were also performed using constant volume simulations and the hydrogen mechanism of Hong et al. [53] and the JetSurF 2.0 mechanism of Wang et al. [54]. Excellent agreement is obtained with results using the former mechanism for pure hydrogen cases and good agreement with the JetSurF 2.0 mechanism for the H_2/CO and H_2/CH_4 mixtures. However, it is also evident that the latter mechanism, which represents a substantial update upon earlier efforts such as the well known GRI Mechanisms, does not reproduce the pure hydrogen data with sufficient accuracy. Hence, some uncertainties remain regarding the cause of the level of agreement obtained for high hydrogen content mixtures and it is suggested that an effort is made as part of future work to derive a reconciled chemical kinetic mechanism that can represent both sets of data. Such work would also permit the accurate extrapolation to 1 atm pressure. It should be emphasised that this is a new finding and one of the recommendations of the report is that the extrapolation aspect is covered in further work. It should be emphasised that the current data was obtained at a pressure of around 1.7 atm in order to access lower temperatures. Hence, it would be desirable to relate the current IDT data quantitatively to the atmospheric pressure data obtained at Imperial College as reported in the following sections. Such an effort requires the derivation of an updated chemical kinetic mechanism applicable to all considered data sets. A further benefit would be that the derived mechanism could also be used at higher pressures of relevance to high-speed (supersonic) flames and their interactions with heat exchanger tubes.

The pure H_2 mixtures show an exceptionally strong increase in the time to ignition for temperatures below 960 K as illustrated in Fig. 3. The result is consistent with the study of Choi and Chung [2], who reported difficulties in stabilising laminar flames of methane and hydrogen at temperatures below 940 K. The ability of the chemical kinetic model by Hong et al. [53] to reproduce the trends both qualitatively and quantitatively is also very encouraging and suggests that extrapolations to lower temperatures can be performed with reasonable confidence. The data obtained for the H_2/CH_4 mixtures shown in

Fig. 4 highlight a strong influence of methane addition on the measured IDT. By contrast, the data obtained for the H_2/CO system suggests that systems with up to 60% CO behave essentially as pure hydrogen mixtures. Hence, from an ignition point of view, extreme caution is required when it comes to the use of such mixtures. These trends are explored further below in the context of the ignition behaviour, as well as, deflagration and explosion strengths in the presence of turbulence.

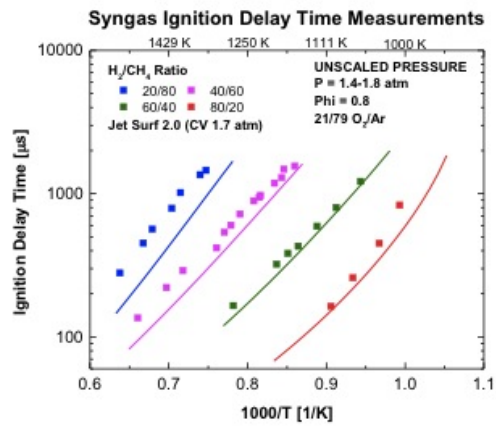


Fig. 4: Ignition delay time data obtained for the H_2/CH_4 system.

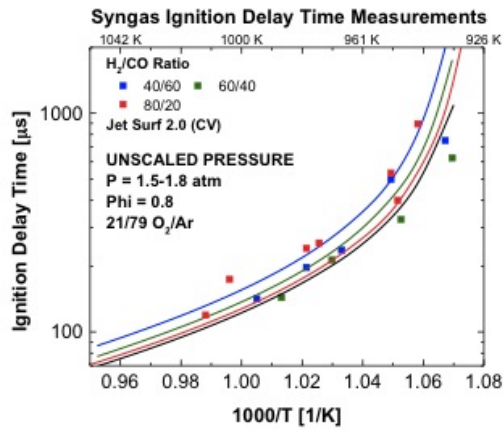


Fig. 5: Ignition delay time data obtained for the H_2/CO system.

3 Auto-Ignition of Hydrogen Rich Mixtures in Hot Combustion Products

3.1 Experimental Configuration

3.1.1 Burner Configuration

The design of the current vitiated coflow burner is based on the Cabra burner [3] and the current version is shown schematically in Fig. 6. Several modifications were implemented to fulfil the safety requirements for the current experiments and to ensure homogenised mixtures in the vitiated coflow and for the fuel-air mixture in the central jet nozzle. Furthermore, the burner was modified to permit a larger number of gas components used to create the hot combustion products in the coflow and in the central core jet. The mixing of the reactant streams used to create the combustion products was initially performed in a primary mixing chamber with the resulting gas mixture subsequently passed to a circumferential ring featuring 32 radial nozzles used to inject the gas mixture into a secondary mixing vessel.

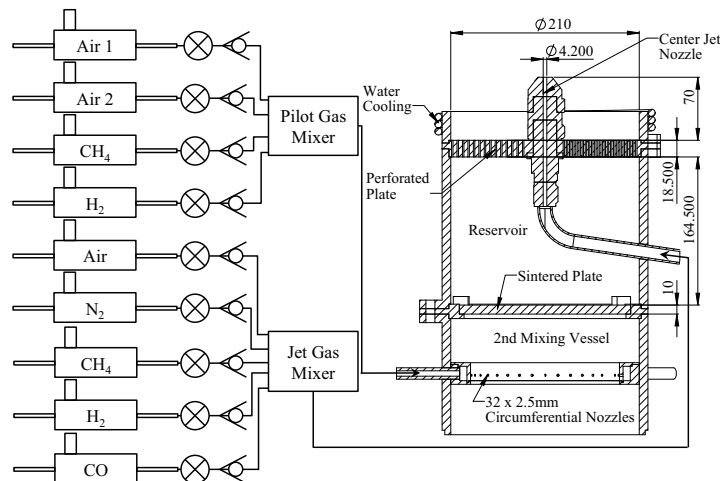


Fig. 6: Schematic of the lifted flame burner test facility

A sintered plate with a maximum pore size of $76 \mu\text{m}$ [55] was used as a flame arrestor and to separate the secondary mixing chamber from the reservoir leading up to the perforated disc used to stabilise the flames producing the hot combustion products. The reservoir vessel was sealed using a plate with a diameter of 210 mm perforated with 2200 holes of diameter 1.58 mm resulting in a blockage ratio of 87%. A lean premixed flame was stabilised on each of the

2200 holes providing a controlled combustion product stream that surrounded the centre nozzle. The gas mixture components for the central jet were also injected into a gas mixer. To improve the homogenisation, a sintered disk, with identical maximum pore size to that outlined above ($76\ \mu\text{m}$), was inserted just before the outlet of the gas mixer. Additionally, the sintered plate served as flame arrester should flash back occur in the central fuel jet. The homogenised gas mixtures were subsequently passed directly to a jet nozzle with an inner diameter $D = 4.2\ \text{mm}$. The central jet nozzle outlet is located 70 mm from the perforated pilot plate to ensure uniform properties of the coflowing combustion products. A photograph of the burner facility is shown in Fig. 7, while Fig. 8 depicts the inside of the burner by means of a computer assisted design illustration.



Fig. 7: Photograph of the lifted flame burner

3.1.2 Safety Precautions

The explosion (e.g. hydrogen) and toxicity (e.g. carbon monoxide) hazards associated with the reactant gases used in the current study demand a reliable safety control system that prohibits the injection of unburned reactants into the laboratory cell or the process exhaust extraction system. Thus, two Omega thermocouples [56] were installed to monitor and record the temperature of the combustion products in the vitiated coflowing stream. The first thermocouple was of an R-type that features a fast response time and provides highly accu-

rate temperature measurements while the second thermocouple was a shielded K-type that is robust and hence acted as backup safety system. If either one of the thermocouples detected a temperature lower than a defined safe temperature, a shut off signal is sent to the fuel mass flow controllers (MFC). The safe temperature was defined as high as feasible such that the response time for shut down was optimised (< 1 s) while allowing for minor temperature variations resulting from normal operation. The full set of operating procedures, safety assessments and the associated documentation is available upon request.

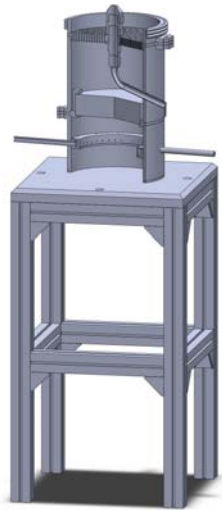


Fig. 8: Sectioned computer assisted design image of the burner

3.1.3 Measurement and Analysis Arrangements

The main objective of the current part of the experimental study was to investigate the influence of the hydrogen content of binary gas mixtures with methane and carbon monoxide upon the reactivity of the mixture as quantified by the flame lift-off height. The latter is a direct measure of the reactivity of the fuel blend and related to the ignition delay time through the Lagrangian history of a fluid element undergoing auto-ignition. The initial data obtained in the current study therefore amounts to the determination of the lift-off height as a function of the mixture composition and the temperature of the vitiated coflow of combustion products. For mixtures containing hydrocarbons (or fragments thereof) the natural choice is to image excited state CH^* light emissions. However, the current mixture matrix has a strong focus on the upper reactivity side of the H_2

fuel blends – including pure H_2 . Most mixtures are expected to offer a weak (or no) CH^* signal, but a strong OH^* signal that is invisible to the human eye and can not be analysed in such a manner. As consequence, OH^* chemiluminescence was used to detect the flame position using an interline-transfer CCD-camera (LaVision Intense Camera [57]) with an acquisition size of 1376×1040 pixels and a intensified relay optics (IRO) unit (intensifier type V7670U-70-P43, photocathode S20, phosphor P43) to capture the instantaneous OH radical distribution. The intensifier gain was adjusted from 70 to 85 to compensate for the weaker signal obtained with increasingly stretched reaction zones. The exposure time of the camera and intensifier was set to $50 \mu s$ and the image interrogation region was set to 250 mm.

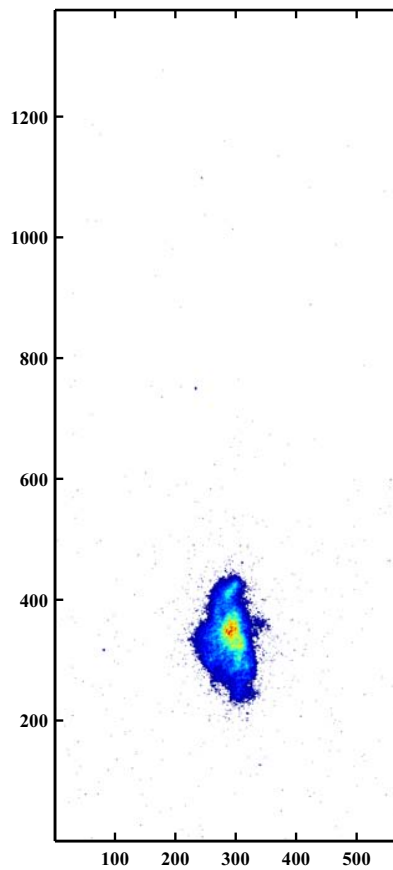


Fig. 9: Instantaneous OH^* signal with high signal to noise ratio

To achieve statistically independent data, 1000 images were captured for each set of conditions with repetition rates of 9 Hz or 15 Hz. To improve the signal to

noise ratio, a background subtraction of the raw images was performed to reduce noise. As the background noise is dependent on the intensifier gain, a set of 100 images was taken for each gain used. Following the actual measurements for a particular fuel mixture, the corresponding average background image was subtracted from the raw images. A sample image of an instantaneous OH^* signal with a high signal to noise ratio resulting from a concentrated reaction zone of a hydrogen/carbon monoxide mixture is shown in Fig. 9. By contrast, Fig. 10 depicts an OH^* signal with significantly lower signal to noise ratio resulting from a stretched reaction zone of a hydrogen/methane mixture. Subsequently, further calculations, i.e. determination of the average, root mean square, and instantaneous flame lift-off height, were performed on the basis of the corrected images.

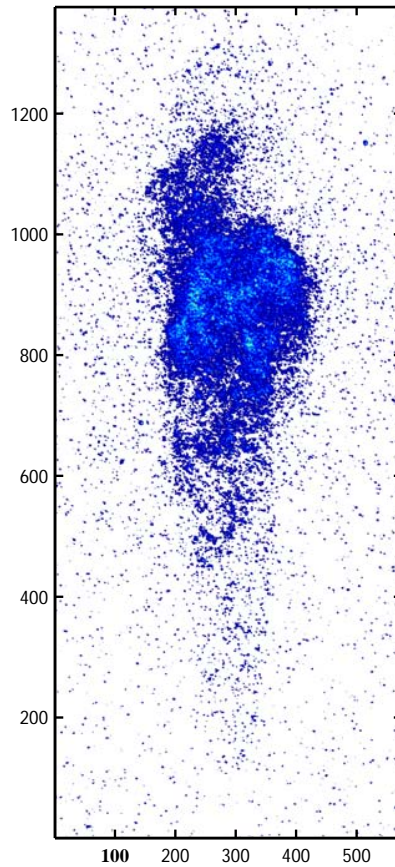


Fig. 10: Instantaneous OH^* signal with low signal to noise ratio

Finally, the temperature of the combustion products in the coflow were recorded

with a repetition rate of ~ 3 Hz throughout the whole experiment using an R-type thermocouple in order to determine any fluctuations or drift in the mean temperature. The latter measurements were used to provide an uncertainty estimate.

3.2 Experimental Conditions and Procedure

3.2.1 Jet Conditions and Syngas Mixtures

The current study investigates binary fuel blends of H_2/CH_4 and H_2/CO . The H_2/CH_4 mixtures cover the full range between the pure components and with intermediate steps of 90/10, 80/20, 70/30, 60/40, 50/50, 40/60 and 25/75. The H_2/CO blends cover mixtures of 90/10, 80/20, 70/30, 60/40, 50/50, 40/60 and 30/70. Furthermore, dilution of the fuel blend with nitrogen was also investigated. The wide spectrum of proposed gas mixtures results in considerable differences in gas properties, e.g. the unburned gas density (ρ_u), as well as reactivities. A detailed summary of all investigated gas mixtures is presented in Appendix A. The intrusion of a free jet into an essentially stagnant medium is primarily governed by the momentum ($M_j = \rho_u u_j^2$) of the jet, rather than the jet velocity u_j , and we have chosen to conserve the momentum of the jet. A further advantage is that the Reynolds number remains approximately constant. The value of the jet momentum was defined such that the jet velocity of the mixture that exhibits the highest reactivity has an exit jet velocity value $u_j \approx 100$ m/s. The resulting jet momentum is $M_j = 0.125$ N. The conservation of momentum results, due to the differences in mixture densities caused primarily by molecular weight changes through varying hydrogen concentrations, in a jet velocity which is calculated by:

$$u_j = \sqrt{\frac{M_j}{\rho_u}} \quad (1)$$

The jet velocity was accordingly varied from $u_j = 100.1$ m/s for the case of pure H_2 -air mixtures to $u_j = 89.13$ m/s for the corresponding pure CH_4 -air case. The equivalence ratio for all mixtures was maintained constant at $\Phi_j = 0.8$ and the required mole fractions in the fuel jet were calculated as shown in Eq. (2),

$$\begin{aligned} &\chi_{CH_4} \cdot CH_4 + \chi_{H_2} \cdot H_2 + \chi_{CO} \cdot CO + \beta_j \cdot O_2 + 3.76 \cdot \beta_j \cdot N_2 \rightarrow \\ &(\chi_{CH_4} + \chi_{CO}) \cdot CO_2 + (2 \cdot \chi_{CH_4} + \chi_{H_2}) \cdot H_2O + (\beta_j - \alpha_j) \cdot O_2 \\ &+ 3.76 \cdot \beta_j \cdot N_2 \end{aligned} \quad (2)$$

$$\chi_{Air} = 4.76 \cdot \beta_j, \text{ where } \beta_j = \frac{\alpha_j}{\Phi} \text{ and } \alpha_j = (2 \cdot \chi_{CH_4} + \frac{\chi_{H_2}}{2} + \frac{\chi_{CO}}{2})$$

Additionally, a further set of mixtures were diluted with N_2 by adding the same amount of N_2 as already introduced via the air stream. The additional N_2 mole fraction was calculated from:

$$\begin{aligned} d &= \frac{3.76}{4.76} \cdot \chi_{Air} \\ \chi_{N_2} &= \frac{d}{1+d} \end{aligned} \quad (3)$$

Accordingly, a total of 34 fuel blends were investigated which each covering a suitable temperature range. The conditions used for all mixtures are presented in Appendix A.

3.2.2 The Coflow of Hot Combustion Products

The wide range of fuel blends investigated leads to significant variation in mixture reactivity. As a consequence, the temperature of the coflowing combustion products must be adjusted in order to stabilise lifted flames for all of the proposed mixture conditions. In the current work, the pilot temperature was modified by adding small quantities of CH_4 into the pilot gas stream starting from a pure H_2 -air stream. The CH_4 addition has a strong effect on the pilot temperature with 2 slpm CH_4 , compared to a total flow rate of ~ 2075 slpm (standard litre per minute), increasing the temperature ~ 20 K. Detailed pilot conditions are presented in Appendix A for each of the mixtures investigated. The equivalence ratio of the pilot varies somewhat as it is utilised for temperature control as shown in Eq. (4),

$$\begin{aligned} a \cdot CH_4 + b \cdot H_2 + \beta_p \cdot O_2 + 3.76 \cdot \beta_p \cdot N_2 &\rightarrow \\ a \cdot CO_2 + (2a + b) \cdot H_2O + (\beta_p - \alpha_p) \cdot O_2 + 3.76 \cdot \beta_p \cdot N_2 &\quad (4) \\ \text{where } \alpha_p = (2a + \frac{b}{2}) \text{ and } \beta_p = \frac{\alpha_p}{\Phi}. & \end{aligned}$$

The difference of $(\beta_p - \alpha_p)$ represents an estimate for the residual O_2 concentration in the burned gas of the pilot stream.

3.2.3 Control of the Experiment

A purpose designed LabView [58] interface was programmed to control experimental parameters and to initiate shutdown procedures. The interface allows an accurate setting of operating conditions, monitoring of flow rates and temperatures and also writes essential parameters to a log file. The velocities, equivalence ratios, unburned gas densities and molecular weights (MW) of the reactant streams, as well as the estimated residual O_2 concentration in the hot coflow, are also calculated and displayed. All flow rates were accurately regulated using Bronkhorst EL-FLOW Select series flow controllers [59] with an error of less than $\pm 0.5\%$ of full scale.

3.2.4 Operational Boundaries

Prior to the actual experiments, the potential constraints of the test facilities were explored with respect to flow velocities, coflow temperatures and the range of possible reactant stream compositions.

The lower flow velocity limit for the coflow of hot combustion products was defined by the flashback of the pilot flames stabilised on the perforated plate discussed above. This limit was not exhausted as sufficiently low pilot velocities were achieved before flashback occurred. The upper pilot velocity was

bounded by the capacity limit of the mass flow controllers (MFCs). In total, four MFCs were connected to the pilot gas mixer. Two air lines were drawn from the Howden air compressor facility located in the Department of Mechanical Engineering and fitted with MFCs with a total flow rate of 2045 slpm ($4.405 * 10^{-2}$ kg/s), one MFC was allocated to CH_4 with a maximum flow rate of 140.1 slpm ($1.667 * 10^{-3}$ kg/s) and a fourth MFC regulated the H_2 flow rate up to 235.0 slpm ($3.500 * 10^{-4}$ kg/s).

The lower coflow temperature limit is restricted by the blow-off of the pilot flames used to generate the hot combustion products. The current study necessitated a comprehensive investigation and a lower temperature limit of $T_{p,low} = 1045$ K was established while maintaining stable combustion suitably insensitive to minor flow fluctuations. The resulting conditions, which are here defined as the base case, featured an air flow rate of 1850 slpm and a H_2 flow rate of 220 slpm. The corresponding equivalence ratio is $\Phi \approx 0.28$ and accordingly leads to highly diluted combustion products. The upper temperature limit of the coflow stream is restricted by the material properties of the nozzle. This limit was not exploited due to the focus on lower temperatures in the current study. The resulting temperature window is compatible with the shock tube data obtained from Stanford University, as outlined in Section 2, and the expected required increase as compared to laminar flame conditions [2].

The lower and upper limits of the core jet velocity are dependent on the reactivity of the mixture and restricted by flashback and blow-off respectively. The boundaries were explored indirectly by means of varying the coflow temperature. Raising the coflow temperature results in a higher reactivity of the mixture and stabilises the flame closer to the nozzle exit. The flashback limit and flame stabilisation on the actual nozzle were avoided. A reduction in the coflow temperature results in a reduced mixture reactivity eventually leading to flame extinction following blow-off. The latter limit was investigated thoroughly as the main objective implies the need to stabilise all mixtures at the lowest possible temperature.

Entrainment of ambient air into the hot pilot stream restricts the maximum lift-off height that can be determined reliably. The limit is defined as the height where the vitiated coflow stream becomes mixed with ambient air and thus does not provide a controlled environment. The upper limit for the flame lift-off height was found to be around $X/D \geq 50$, which is reflected in a significant increase in measurement uncertainties. Therefore, all data points with a flame lift-off height of $X/D \geq 50$ were excluded from further analysis.

3.3 Post-processing and Lift-off Height Definition

The large number of different mixtures and the use of an average of five temperatures per mixture resulted in a total of approximately 165,000 instantaneous flame images. The number of images necessitated the development of an auto-

matic flame location algorithm and a purpose written C++ algorithm was used to detect the flame lift-off height in each instantaneous image. The flame lift-off height is here detected by means of the steepest gradient in the average OH^* concentration which approximates the location of the strongest reaction zone. The IMX reader from LaVision [57] is implemented to import the instantaneous OH^* image. Subsequently, the following steps are performed to assess the flame lift-off height from the input data:

1. Integration over all pixels in vertical direction results in an average distribution locating horizontal position of the flame.
2. Pixels which are located far left or far right from the flame are excluded from the subsequent analysis.
3. Integration in the horizontal direction of the remaining pixels which leads to an average (potentially noisy) signal locating the flame in vertical direction.
4. A moving average filter was applied in combination with a gradient detection algorithm.
5. The overall steepest gradient is found iteratively, starting from a coarse filtering range over the whole signal and up to a fine filtering range over a small section locating the flame lift-off height precisely.
6. The respective steepest gradient is found iteratively by means of a central difference scheme.
7. The mean flame lift-off height and the root mean square value are subsequently calculated from the detected instantaneous flame lift-off heights.

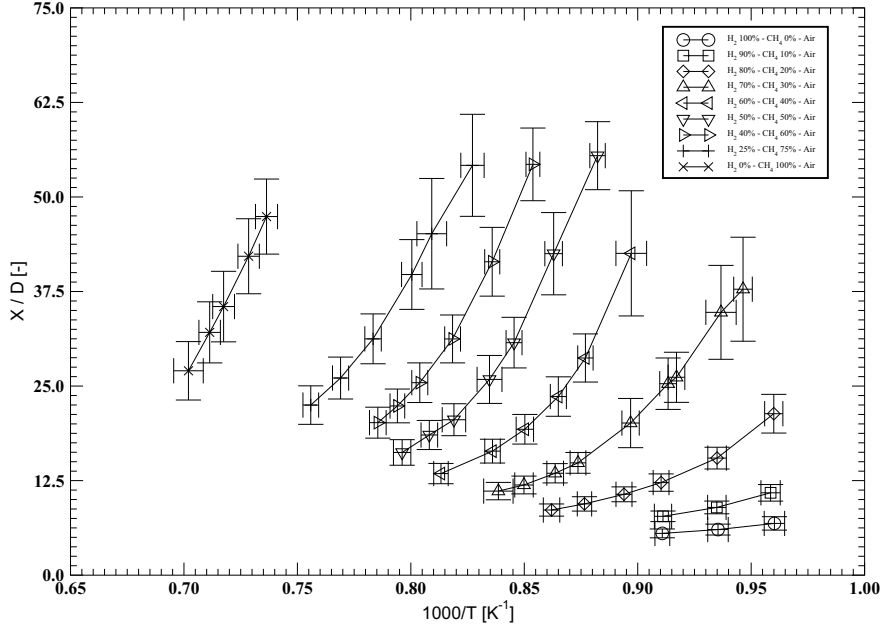
Subsequently, the mean flame lift-off height and root mean square value were stored along with the reciprocal temperature and auto-ignition delay time. The above operations allowed a sufficiently quick and reliable detection of the mean flame lift-off height for all cases.

3.4 Results and Discussion

A main objective of the current investigation is to determine the influence of CH_4 and CO on the reactivity of H_2 based fuel blends. Binary fuel mixtures of H_2/CH_4 have been studied by a significant number of researchers, though typically not under conditions of relevance to the current study [60, 61, 62, 63, 64]. The current systematic study leading to a consistent data base for the auto-ignition of such mixtures under turbulent flow conditions is unique.

Tab. 1: Fuel mixtures investigated for the case of H_2/CH_4 blending.

Mixture	u_j [m/s]	χ_{H_2}	χ_{CH_4}	χ_{CO}	χ_{N_2}	χ_{Air}
H_2 100% - Air	100.1	0.2516	0.0000	0.0000	0.0000	0.7484
H_2 90% - CH_4 10% - Air	96.82	0.1849	0.0205	0.0000	0.0000	0.7946
H_2 80% - CH_4 20% - Air	94.74	0.1389	0.0347	0.0000	0.0000	0.8264
H_2 70% - CH_4 30% - Air	93.29	0.1052	0.0451	0.0000	0.0000	0.8497
H_2 60% - CH_4 40% - Air	92.23	0.0795	0.0530	0.0000	0.0000	0.8675
H_2 50% - CH_4 50% - Air	91.42	0.0593	0.0593	0.0000	0.0000	0.8815
H_2 40% - CH_4 60% - Air	90.78	0.0429	0.0643	0.0000	0.0000	0.8928
H_2 25% - CH_4 75% - Air	90.08	0.0240	0.0710	0.0000	0.0000	0.9050
H_2 0% - CH_4 100% - Air	89.17	0.0000	0.0775	0.0000	0.0000	0.9225

Fig. 11: Dimensionless flame lift-off heights for H_2 based fuels with increased CH_4 blending.

Investigations covering fuel blends of H_2/CO , on the other hand, are uncommon and mainly related to research on syngas utilisation and fuel flexibility [65, 66, 67]. Lieuwen et al. [66] reports the auto-ignition delay times for various H_2/CH_4 and H_2/CO mixtures at $\Phi = 0.4$ and $P = 15$ atm obtained from numerical investigations. However, as pointed out in Section 2, uncertainties prevail in the relevant chemistry and experimental data remains essential. In the following sections, the impact of gradually substituting H_2 by either CH_4 or CO is reported while the equivalence ratio of the core jet was maintained

at $\Phi_j = 0.8$. Moreover, the jet momentum was kept constant which leads to a varying jet velocity due to changes in the unburned gas density as detailed above. The coflow temperature was utilised as further parameter and varied within the operating limits for each mixture. A summary of all investigated fuel blends and conditions is presented in Appendix A.

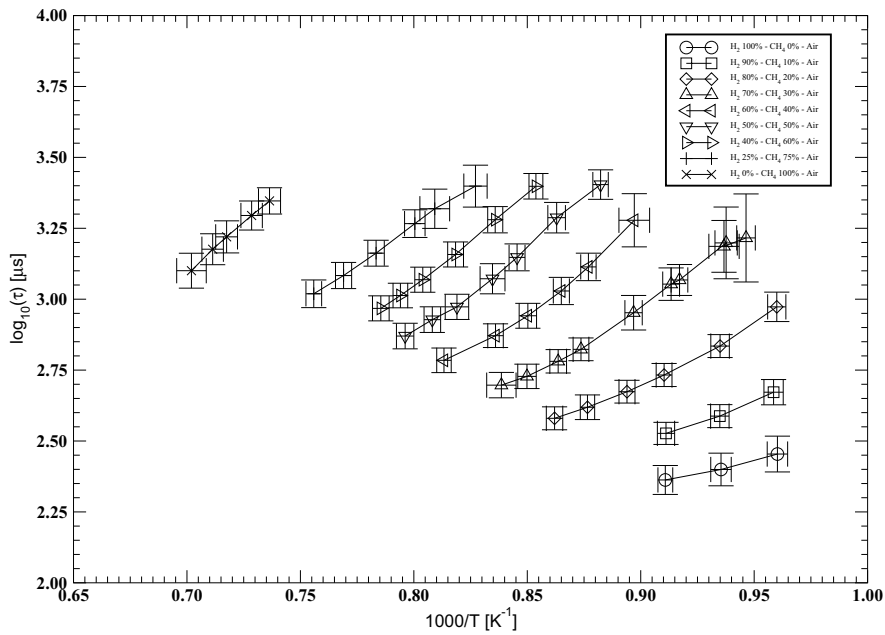


Fig. 12: Auto-ignition delay times for H_2 based fuels with increased CH_4 blending.

3.4.1 Mixtures of Hydrogen with Methane

The case of H_2 based fuel mixtures with CH_4 as the blending component were investigated starting with pure hydrogen. Methane was introduced incrementally until H_2 was completely substituted by CH_4 . The fuel mixture compositions for the investigated cases are listed in Table 1. The relative reactivity E_r was measured indirectly based on the flame lift-off height variation as a function of temperature as defined in Section 3.3. A standard Arrhenius diagram was found suitable for this purpose. However, it must be pointed out that E_r is not a conventional activation energy (e.g. E_A) as it is influenced by both chemistry and flow statistics. The conventional activation energies, free of such considerations, can readily be determined from the Stanford shock tube data as outlined in Section 2 and in the final report [1] for Work Package 1. In the current context, a low flame lift-off height indicates high reactivity and vice versa. The flame lift-off height, measured in mm , is subsequently related to the

nozzle diameter $D = 4.2 \text{ mm}$ leading to the dimensionless lift-off height X/D .

The most straightforward visualisation of the flame lift-off height is on the basis of the mean image which was calculated for each mixture and coflow temperature using a set of 1000 instantaneous images. Samples of the mean flame location are therefore shown in Fig. 74 to Fig. 82 in Appendix A for all investigated H_2/CH_4 fuel blends and for three of the coflow temperature. As discussed above, significant differences in the mixture reactivity necessitated adjustments of the coflow temperature range on a case to case basis. Detailed conditions for all mixtures and pilot temperatures are listed in Tables 44 to 52 in Appendix A.

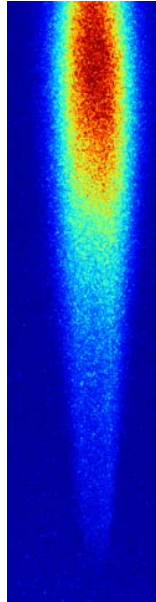


Fig. 13: Separation of the reaction zones in H_2/CH_4 mixtures

The measured dimensionless lift-off heights X/D are shown in Fig. 11 versus $1000/T [K^{-1}]$ for all mixtures listed in Table 1. The data clearly illustrates that the flame lift-off height increases significantly with successive H_2 substitutions by CH_4 . As discussed earlier, an increase in the flame lift-off height is directly related to a decrease in relative reactivity. The sharp impact of H_2 substitution with CH_4 was also reported by Lieuwen et al. [66]. Comparing the case of pure H_2 with mixtures of 10% and 20% CH_4 at the lower pilot temperature limit of $T_p \approx 1040 \text{ K}$ reveals an increase of X/D from 6.846, via 10.89 to 21.35 corresponding to increases of 59% and 96%, respectively. The cases featuring pure H_2 and with a 10% CH_4 substitution are restricted to a maximum coflow temperature of $T_p \approx 1095 \text{ K}$ due to the risk of flashback. The temperature

range for the 20% CH_4 fuel blend could be extended up to $T_p \approx 1160$ K.

The required increase in T_p is another indicator of a reduced mixture reactivity and suggests a significant decrease compared to the pure H_2 case and that with 10% CH_4 . The measurements show that mixtures with a further substitution of H_2 , leading to fuel blends with CH_4 fraction $> 30\%$, cannot be stabilised at the lower coflow temperature limit due to the reduced reactivity. For the case of 30% CH_4 a minimum temperature $T_p \approx 1090$ K is required and, as a further consequence of the lower reactivity, the upper temperature limit is raised to $T_p \approx 1190$ K. Furthermore, a strong increase in the temperature sensitivity, as compared to the mixtures with an increased H_2 content, is observed as indicated by the steeper gradient. Further substitution of H_2 with CH_4 continues the same trend with an increase in required minimum and possible maximum coflow temperatures.

Comparisons on a basis of X/D data is sufficient to illustrate the behaviour of the different mixtures. Interestingly, it may be noted that the lift-off height appears to consist of two slopes for the more methane rich mixtures. At higher temperatures, the initial slope appears related to the hydrogen content of the mixture, while at lower temperatures the slope approaches that of the pure methane case. The trend becomes more pronounced for H_2 contents $\leq 70\%$. An analysis of the corresponding OH^* images suggest that the H_2 content acts as an initiator of chemical reaction, but that the effect is not sufficiently strong to trigger a rapid ignition of CH_4 at lower temperatures and with reduced amounts of hydrogen. Hence, there is a tendency for reaction zones to separate in H_2/CH_4 mixtures. The separation of the reaction zones is illustrated in Fig. 13 by the signal tail caused by OH^* below the main reaction zone.

It is possible to translate the lift-off height to an approximate auto-ignition delay time on the basis of the flame lift-off height and jet bulk velocity as shown in Eq. (5).

$$\tau = \frac{X}{\sqrt{(M_j/\rho_{u,j})}} \quad (5)$$

The above expression does not correspond to a conventional definition as it is influenced by turbulence and mixture inhomogeneities in the shear layer formed between the core jet and the coflow of hot combustion products. However, the slope of the resulting curves in a conventional Arrhenius diagram suggest a near linear behaviour for a substantial number of the considered cases as shown in Fig. 12, where the auto-ignition delay times are plotted in the form of $\log_{10}(\tau)$ against $1000/T$. Furthermore, the spreading of the curves suggests a nearly linear dependency on the H_2 concentration. The latter finding is supported by other investigators [60, 61] who calculated the auto-ignition delay time using Eq. (6), where γ is the hydrogen mole fraction with τ_{mix} , τ_{CH_4} and τ_{H_2} the ignition delay times for the mixture, pure methane and pure hydrogen respectively. The relationship was suggested to be accurate for a H_2 blending range

from 0% CH_4 up to and including 40% CH_4 .

$$\tau_{mix} = \tau_{H_2}^\gamma \cdot \tau_{CH_4}^{(1-\gamma)} \quad (6)$$

A quantitative interpretation of the auto-ignition delay time requires an analytical fit to the experimental data. Comparing the slopes of the fitted functions with the logarithm of an Arrhenius form allows an estimate of the relative reactivity as shown in Eq. (7),

$$\begin{aligned} \tau &= A \cdot e^{E_r/(R \cdot T)} \\ \log_{10}(\tau) &= \log_{10}(A) + \log_{10}(e^{E_r/R \cdot T}) \\ \log_{10}(\tau) &= \log_{10}(A) + 0.4343 \cdot \frac{E_r}{R} \cdot \frac{1}{T} \\ m \cdot \frac{1}{T} &= 0.4343 \cdot \frac{E_r}{R} \cdot \frac{1}{T} \Rightarrow E_r = \frac{m \cdot R}{0.4343} \end{aligned} \quad (7)$$

where A a pre-exponential factor, R the universal gas constant and m is the slope of the fitted linear function. The inferred logarithmic Arrhenius functions are listed for all H_2/CH_4 fuel mixtures in Table 2. The listed fits reveal a progressive increase in the slope with a decreasing H_2 fraction for fuel blends up to a mixture ratio of 50/50 H_2/CH_4 . The relative reactivities determined using Eq. (7) are also shown.

Reductions in the H_2 content below 50% introduces some scatter in the results. Mixtures with a CH_4 fraction $\geq 50\%$ are stabilised at a significantly higher flame lift-off height, which increases the uncertainties in the current simplified analysis. Accordingly, a selective further analysis can be performed using transported probability density function methods (e.g. [8]) as part of future work. Nevertheless, it should also be pointed out that the mixture with 25% hydrogen is at the very limit of the range for the MFC used and that measurements were performed on a best-endeavours effort for this case. Hence, the uncertainties for the other mixtures should probably not be exaggerated. The relative reactivity can also be determined based on the highest temperatures for each data set by simply removing the lower temperature data from the analysis. Such a procedure is not recommended in the current context, but results in the linear relationship given in Eq. (6). Table 3 lists the relative reactivities (E_r) (see Table 2), the inferred values for the high temperature range ($E_{r,h}$) and the theoretical values ($E_{r,t}$) obtained using Eq. (6). It is evident that the values obtained by the linear relationship match the relative reactivity values at the higher temperature very well, with the exception of the case 25% $H_2/75\% CH_4$.

3.4.2 Hydrogen Blending with Carbon Monoxide

The second fuel blend component, carbon monoxide, was studied in a similar manner to that outlined above and the cases investigated are listed in Table 4. The corresponding flame lift-off heights, determined in the same way as for the

Tab. 2: Linear functions valid for the investigated temperature range fitted to the logarithm of the auto-ignition delay time (IDT) in μs and the calculated relative reactivity E_r for H_2/CH_4 fuel blends

Mixture	Arrhenius Fit [μs]	E_r [J/mol]
H_2 100% – Air	$\log_{10}(\tau) = \frac{1850}{T} + 0.6745$	$3.542E + 04$
H_2 90% – CH_4 10% – Air	$\log_{10}(\tau) = \frac{3062}{T} - 0.2668$	$5.861E + 04$
H_2 80% – CH_4 20% – Air	$\log_{10}(\tau) = \frac{3973}{T} - 0.8656$	$7.607E + 04$
H_2 70% – CH_4 30% – Air	$\log_{10}(\tau) = \frac{5168}{T} - 1.667$	$9.893E + 04$
H_2 60% – CH_4 40% – Air	$\log_{10}(\tau) = \frac{5862}{T} - 2.018$	$1.122E + 05$
H_2 50% – CH_4 50% – Air	$\log_{10}(\tau) = \frac{6366}{T} - 2.222$	$1.219E + 05$
H_2 40% – CH_4 60% – Air	$\log_{10}(\tau) = \frac{6360}{T} - 2.037$	$1.217E + 05$
H_2 25% – CH_4 75% – Air	$\log_{10}(\tau) = \frac{5669}{T} - 1.124$	$1.085E + 05$
H_2 0% – CH_4 100% – Air	$\log_{10}(\tau) = \frac{7104}{T} - 1.881$	$1.360E + 05$

Tab. 3: Linear functions valid for the investigated temperature range fitted to the logarithm of the auto-ignition delay time data and the calculated relative reactivity E_r for H_2/CH_4 fuel blends. The relative reactivity for the high temperature ignition branch ($E_{r,h}$) and the expression given by Eq. (6) ($E_{r,t}$) are also shown.

Mixture	E_r [J/mol]	$E_{r,h}$ [J/mol]	$E_{r,t}$ [J/mol]
H_2 100% – Air	$3.542E + 04$	$3.542E + 04$	$3.542E + 04$
H_2 90% – CH_4 10% – Air	$5.861E + 04$	$4.908E + 04$	$4.668E + 04$
H_2 80% – CH_4 20% – Air	$7.607E + 04$	$5.640E + 04$	$5.795E + 04$
H_2 70% – CH_4 30% – Air	$9.893E + 04$	$6.465E + 04$	$6.921E + 04$
H_2 60% – CH_4 40% – Air	$1.122E + 05$	$8.059E + 04$	$8.048E + 04$
H_2 50% – CH_4 50% – Air	$1.219E + 05$	$8.632E + 04$	$9.175E + 04$
H_2 40% – CH_4 60% – Air	$1.217E + 05$	$1.047E + 05$	$1.030E + 05$
H_2 25% – CH_4 75% – Air	$1.085E + 05$	$1.065E + 05$	$1.199E + 05$
H_2 0% – CH_4 100% – Air	$1.360E + 05$	$1.481E + 05$	$1.481E + 05$

Tab. 4: Fuel mixtures investigated in the scope of H_2/CO blending

Mixture	u_j [m/s]	χ_{H_2}	χ_{CH_4}	χ_{CO}	χ_{N_2}	χ_{Air}
H_2 100% – Air	100.1	0.2516	0.0000	0.0000	0.0000	0.7484
H_2 90% – CO 10% – Air	98.66	0.2264	0.0000	0.0252	0.0000	0.7484
H_2 80% – CO 20% – Air	97.28	0.2013	0.0000	0.0503	0.0000	0.7484
H_2 70% – CO 30% – Air	95.95	0.1761	0.0000	0.0755	0.0000	0.7484
H_2 60% – CO 40% – Air	94.68	0.1509	0.0000	0.1006	0.0000	0.7484
H_2 50% – CO 50% – Air	93.45	0.1258	0.0000	0.1258	0.0000	0.7484
H_2 40% – CO 60% – Air	92.28	0.1006	0.0000	0.1509	0.0000	0.7484
H_2 30% – CO 70% – Air	91.14	0.0755	0.0000	0.1761	0.0000	0.7484

H_2/CH_4 blends, are shown in Fig. 14. As shown for the CH_4 blends, the lift-off height increases with the introduction of CO . However, compared to the CH_4 mixtures, the trend is much less pronounced, as is particularly evident for mixtures with a CO content lower than 50%. The result corresponds qualitatively very well with the results reported by Lieuwen et al. [66] and can be directly related to the higher intrinsic reactivity of CO compared to CH_4 . In this context it may be noted that all investigated H_2/CO fuel blends could be stabilised at the lowest possible coflow temperature of $T_p \approx 1040$ K and that the reaction zone separation obtained for some H_2/CH_4 mixtures was not observed. The results suggest a comparatively low impact of H_2 substitution with CO . Furthermore, mixtures with a H_2 concentration down to 60% could only be investigated in the same narrow temperature range as the pure H_2 case due to the risk of flashback. Further substitution of H_2 with CO shows an increasingly strong effect on the relative mixture reactivity. This suggests that the auto-ignition affinity of H_2/CO mixtures is governed by H_2 up to a volumetric mixture fraction of 50/50. A further CO addition results in a more significant increase in flame lift-off height at a given temperature and a more pronounced non-linearity. Furthermore, the upper temperature limit could be extended and permitted the investigation of a wider temperature range.

A qualitatively similar behaviour was observed by Fotache et al. [67] for H_2/CO fuel blends in a study featuring ignition against a hot air stream in a counterflow (opposed jet) arrangement. Three ignition regimes were defined: (1) A hydrogen dominated regime for $100\% < \chi_{H_2} < 17\%$, (2) a transition regime spanning from $17\% < \chi_{H_2} < 7\%$ and (3) a hydrogen catalysed regime for $\chi_{H_2} < 7\%$. According to this classification, all mixtures investigated in the current study are within the hydrogen dominated ignition regime. However, a noticeable increase in the ignition temperature for volumetric hydrogen concentrations of $\chi_{H_2} < 12.58\%$ ($\chi_{H_2} = 12.58\%$ corresponds to the 50% $H_2/50\%$ CO mixture) was observed in the experimental data with the ignition temperature remaining constant for a $\chi_{H_2} > 12.58\%$ followed by an increase of approximately 20 K when $12.58\% > \chi_{H_2} > 7.55\%$. This latter agrees well with modelling approach by Sung et al. [65]. Such observations are consistent with results presented in Fig. 14, which show a significant influence on the flame lift-off height when the

Tab. 5: Linear functions valid for the investigated temperature range fitted to the logarithm of the IDT in μs and the calculated relative reactivity E_r for H_2/CO fuel blends

Mixture	Arrhenius Fit [μs]	E_r [J/mol]
H_2 100% – Air	$\log_{10}(\tau) = \frac{1850}{T} + 0.6745$	$3.542E + 04$
H_2 90% – CO 10% – Air	$\log_{10}(\tau) = \frac{2376}{T} + 0.2237$	$4.549E + 04$
H_2 80% – CO 20% – Air	$\log_{10}(\tau) = \frac{2384}{T} + 0.2695$	$4.562E + 04$
H_2 70% – CO 30% – Air	$\log_{10}(\tau) = \frac{2530}{T} + 0.1932$	$4.844E + 04$
H_2 60% – CO 40% – Air	$\log_{10}(\tau) = \frac{2835}{T} - 0.01727$	$5.427E + 04$
H_2 50% – CO 50% – Air	$\log_{10}(\tau) = \frac{3029}{T} - 0.1124$	$5.799E + 04$
H_2 40% – CO 60% – Air	$\log_{10}(\tau) = \frac{2986}{T} + 0.01974$	$5.716E + 04$
H_2 30% – CO 70% – Air	$\log_{10}(\tau) = \frac{3194}{T} - 0.06546$	$6.114E + 04$

CO blending fraction exceeds 50%. Therefore, the current findings suggest that the hydrogen dominated regime is narrower, with the transition regime starting with $\chi_{H_2} < 50\%$ as suggested by Sung et al. [65].

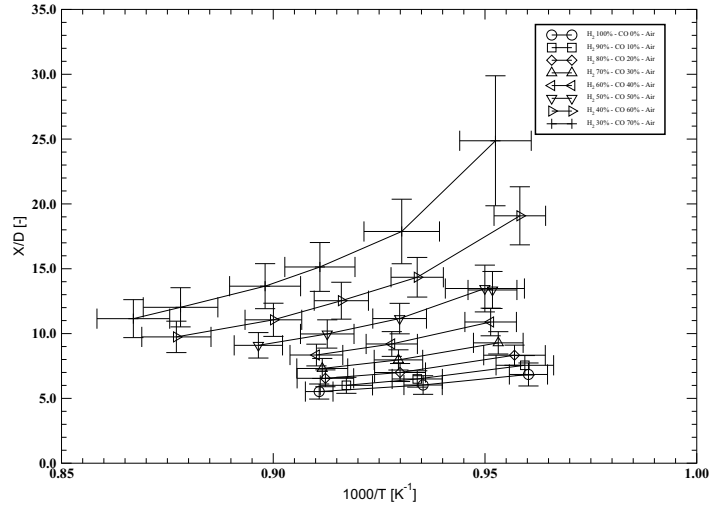


Fig. 14: Flame lift-off heights for H_2 based fuels with CO blending.

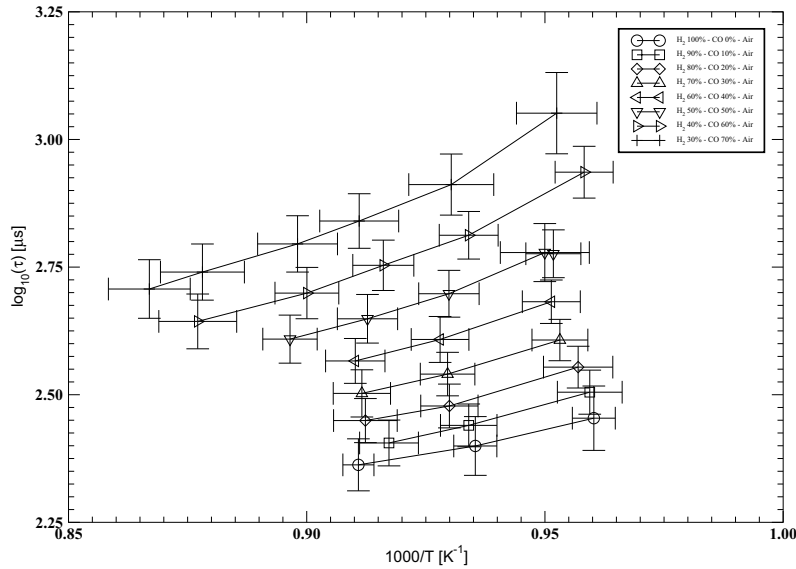


Fig. 15: Auto-ignition delay times for H_2 based fuels with CO blending

The corresponding auto-ignition delay times are shown in Fig. 15 and display the linearity between $\log_{10}(\tau)$ and the reciprocal of the temperature. The significantly lower maximum lift-off height of H_2/CO fuel blends, compared to the H_2/CH_4 mixtures discussed above, reduces the uncertainties associated with the current simplified analysis, though mixtures with a CO content exceeding 50% show some scatter. The fitting of an Arrhenius-like function to the ignition delay time data reveals that the slope steadily increases with the possible exception of the case with 40% H_2 . The corresponding Arrhenius fits are listed in Table 5 along with the calculated values for the relative reactivity.

3.4.3 Hydrogen Blending with a Constant CH_4 or CO Fraction

The different impacts of introducing CH_4 or CO in blends with H_2 is further analysed in the following sections in order to provide a direct comparison between mixtures with the same amount of substitution on a molar basis.

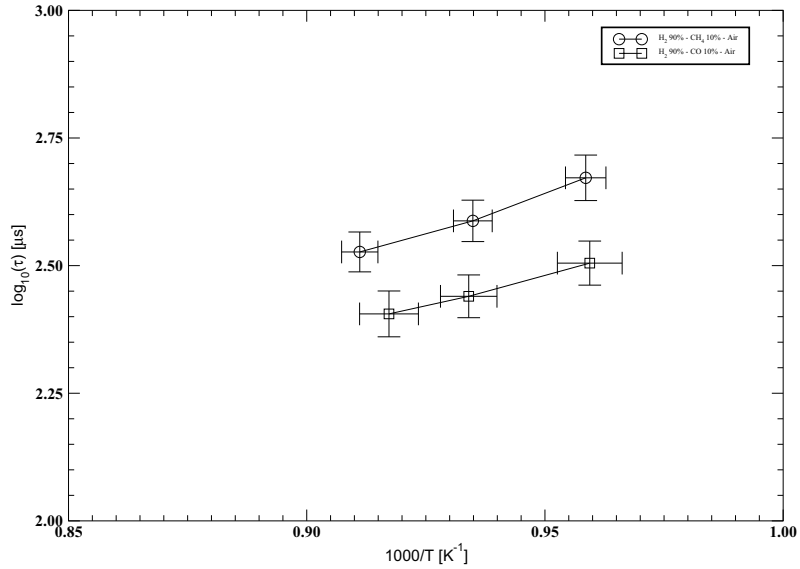
3.4.4 Mixtures with 90% Hydrogen

A comparison of mixtures with 90% H_2 blended with CH_4 or CO shows a clear difference in behaviour. It is evident, as shown in Fig. 16, that the addition of 10% CH_4 has a significant impact compared to the corresponding case with CO addition. Such differences caused by the addition of CH_4 and CO have also been reported in the context of laminar burning velocities [63] and for computed ignition delay times [66]. To quantify the actual differences between CH_4 and

Tab. 6: Auto-ignition delay time comparison for 90% H_2 based fuels.

Mixture	T_p [K]	τ [μ s]
H_2 100% – Air	1041	284.4
H_2 90% – CH_4 10% – Air	1043	469.9
H_2 90% – CO 10% – Air	1042	319.8

CO blending in the context of auto-ignition in a turbulent flow field, Table 6 lists the determined auto-ignition delay times for both mixtures. A comparison with pure H_2 at the lowest possible pilot temperature of $T_p \approx 1040$ K is also made. The addition of 10% CO results in an increase in τ of 12%, while an addition of 10% CH_4 leads to an increase of 65%. This finding suggests that the introduction of small quantities of CH_4 has a much more significant impact on the ignition characteristics of H_2 than the corresponding introduction of CO .

Fig. 16: Auto-ignition delay times with 90% H_2 blended with CH_4 or CO .

The fitted Arrhenius functions further illustrate the differences. As shown in Table 7, the inferred relative reactivities differ significantly for the two blending components. While the ratio of $E_{r,H_2/CH_4}/E_{r,H_2}$ increases to ~ 1.65 , the ratio of $E_{r,H_2/CO}/E_{r,H_2}$ remains at ~ 1.28 .

Tab. 7: Arrhenius fit for the IDT in μs and relative reactivity E_r comparison for 90% H_2 based fuels.

Mixture	Arrhenius Fit [μs]	E_r [J/mol]
H_2 100% – Air	$\log_{10}(\tau) = \frac{1850}{T} + 0.6745$	$3.542E + 04$
H_2 90% – CH_4 10% – Air	$\log_{10}(\tau) = \frac{3062}{T} - 0.2668$	$5.861E + 04$
H_2 90% – CO 10% – Air	$\log_{10}(\tau) = \frac{2376}{T} + 0.2237$	$4.549E + 04$

Tab. 8: Auto-ignition delay time comparison for 80% H_2 based fuels.

Mixture	T_p [K]	τ [μs]
H_2 100% – Air	1041	284.4
H_2 80% – CH_4 20% – Air	1041	939.7
H_2 80% – CO 20% – Air	1045	358.1

3.4.5 Mixtures with 80% Hydrogen

A further substitution of H_2 to produce mixtures with 80% H_2 amplifies the differences observed for the 90% H_2 case. While the H_2/CO mixture is barely affected by the additional replacement, the reactivity of the H_2/CH_4 mixture decreases radically. This finding agrees well, qualitatively, with the behaviour reported by Lieuwen et al. [66]. The actual changes in the auto-ignition delay times are shown in Table 8 and the addition of 20% CH_4 leads to an increase of auto-ignition delay time by a factor of ~ 3.3 at a pilot temperature of $T_p \approx 1040$ K. By contrast the addition of CO results in a raise of a factor ~ 1.3 .

To relate the behaviour over a range of temperatures, a more suitable comparison can be obtained via the inferred relative reactivity values listed in Table 9. The increase in blending fraction, regardless of CH_4 or CO , increases the value of E_r . For the current blending ratio, the impact of the introduction of CO on the ignition characteristic of the mixture appears straightforward since:

$$\frac{\tau_{H_2}}{\tau_{H_2/CO}} \approx \frac{E_{r,H_2}}{E_{r,H_2/CO}} \quad (8)$$

However, for the case of CH_4 the blending the ratio is not conserved and, instead, the following applies:

$$\frac{\tau_{H_2}}{\tau_{H_2/CH_4}} \geq \frac{E_{r,H_2}}{E_{r,H_2/CH_4}} \quad (9)$$

The effect suggests that the influence of CH_4 on the ignition characteristic of the mixture is more profound at lower temperatures. The finding is supported by

Tab. 9: Arrhenius fit the IDT in μs and relative reactivity E_r comparison for 80% H_2 based fuels.

Mixture	Arrhenius Fit [μs]	E_r [J/mol]
H_2 100% – Air	$\log_{10}(\tau) = \frac{1850}{T} + 0.6745$	$3.542E + 04$
H_2 80% – CH_4 20% – Air	$\log_{10}(\tau) = \frac{3973}{T} - 0.8656$	$7.607E + 04$
H_2 80% – CO 20% – Air	$\log_{10}(\tau) = \frac{2384}{T} + 0.2695$	$4.562E + 04$

Tab. 10: Auto-ignition delay time comparison for 70%, 60% and 50% H_2 based fuels.

Mixture	T_p [K]	τ [μs]
H_2 70% – CH_4 30% – Air	1095	1130
H_2 70% – CO 30% – Air	1097	318.1
H_2 70% – CO 30% – Air	1049	404.6
H_2 60% – CH_4 40% – Air	1115	1898
H_2 60% – CO 40% – Air	1099	368.3
H_2 60% – CO 40% – Air	1051	481.0
H_2 50% – CH_4 50% – Air	1133	2535
H_2 50% – CO 50% – Air	1115	406.3
H_2 50% – CO 50% – Air	1051	597.2

the slightly non-linear characteristics depicted in Fig. 17. Inferring the relative reactivity in a narrow temperature range around 1040 K leads to a much higher value of the reactivity barrier that sustains the ignition delay time ratio.

3.4.6 Mixtures with 70% to 50% Hydrogen

The tendencies discussed for the 90% and 80% H_2 mixtures are carried forward and further amplified with increasing blending factors. The relative reactivity of 50% H_2/CH_4 mixtures is reduced to a level where a comparison at similar temperatures is no longer possible due to the lack of overlapping measurements. The sample auto-ignition delay times and the respective coflow temperatures are listed in Table 10. The auto-ignition delay times for the lowest pilot temperature investigated for the H_2/CO mixtures are also listed in Table 10. The reported values clearly indicate significant discrepancies between the two blending components. While ignition delay times for the H_2/CO mixtures remain of the same order as for the pure H_2 case, those for H_2/CH_4 show much reduced reactivity. The Arrhenius fits as well as the relative reactivity values for the cases 70% to 50% hydrogen are shown in Table 11. The comparisons show that the CH_4 blending component introduces a much stronger temperature dependency.

Tab. 11: Arrhenius fit for the IDT in μs and relative reactivity E_r comparison for 70%, 60% and 50% H_2 based fuels.

Mixture	Arrhenius Fit [μs]	E_r [J/mol]
H_2 100% – Air	$\log_{10}(\tau) = \frac{1850}{T} + 0.6745$	$3.542E + 04$
H_2 70% – CH_4 30% – Air	$\log_{10}(\tau) = \frac{5168}{T} - 1.667$	$9.893E + 04$
H_2 70% – CO 30% – Air	$\log_{10}(\tau) = \frac{2530}{T} + 0.1932$	$4.844E + 04$
H_2 60% – CH_4 40% – Air	$\log_{10}(\tau) = \frac{5862}{T} - 2.018$	$1.122E + 05$
H_2 60% – CO 40% – Air	$\log_{10}(\tau) = \frac{2835}{T} - 0.01727$	$5.427E + 04$
H_2 50% – CH_4 50% – Air	$\log_{10}(\tau) = \frac{6366}{T} - 2.222$	$1.219E + 05$
H_2 50% – CO 50% – Air	$\log_{10}(\tau) = \frac{3029}{T} - 0.1124$	$5.799E + 04$

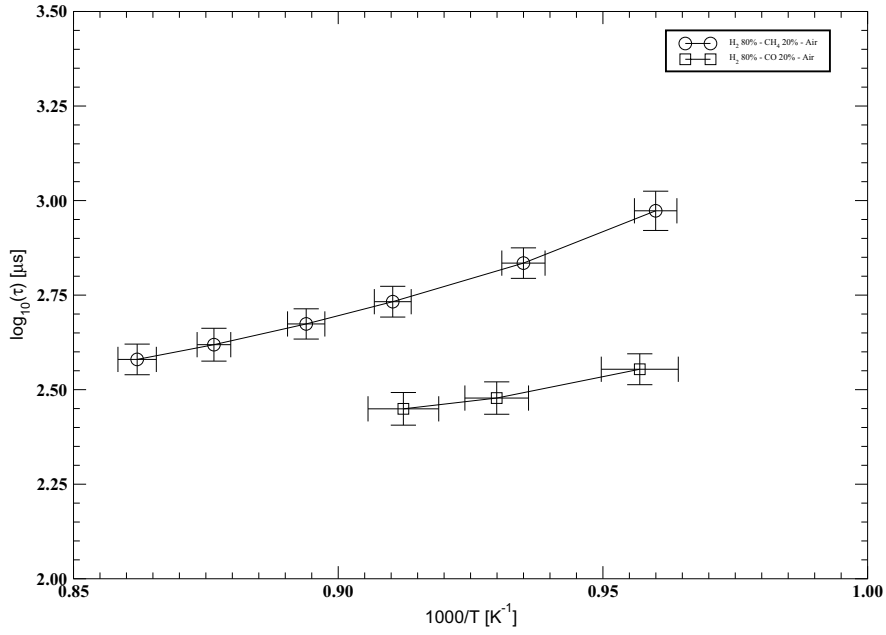


Fig. 17: Auto-ignition delay times for 80% H_2 mixtures with a comparison of the impact of CH_4 and CO blending.

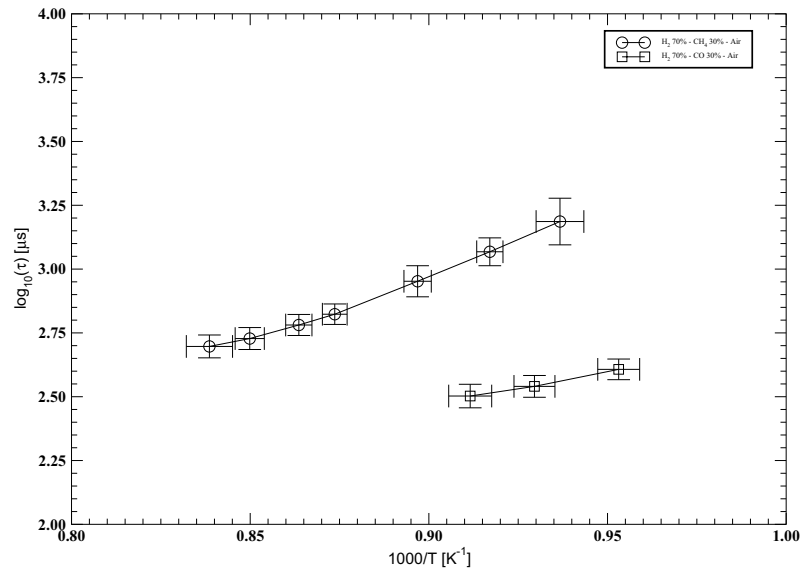


Fig. 18: Auto-ignition delay times for 70% H_2 mixtures with a comparison of the impact of CH_4 and CO blending.

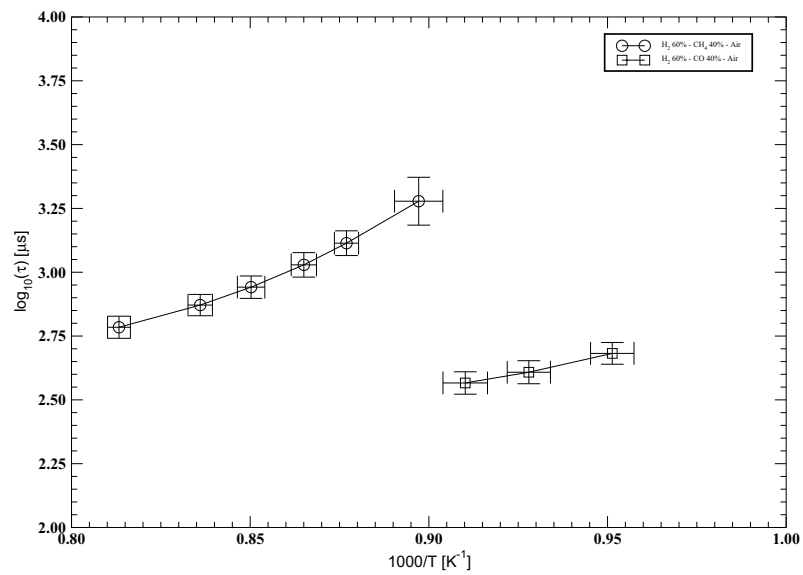


Fig. 19: Auto-ignition delay times of 60% H_2 mixtures with a comparison of the impact of CH_4 and CO blending.

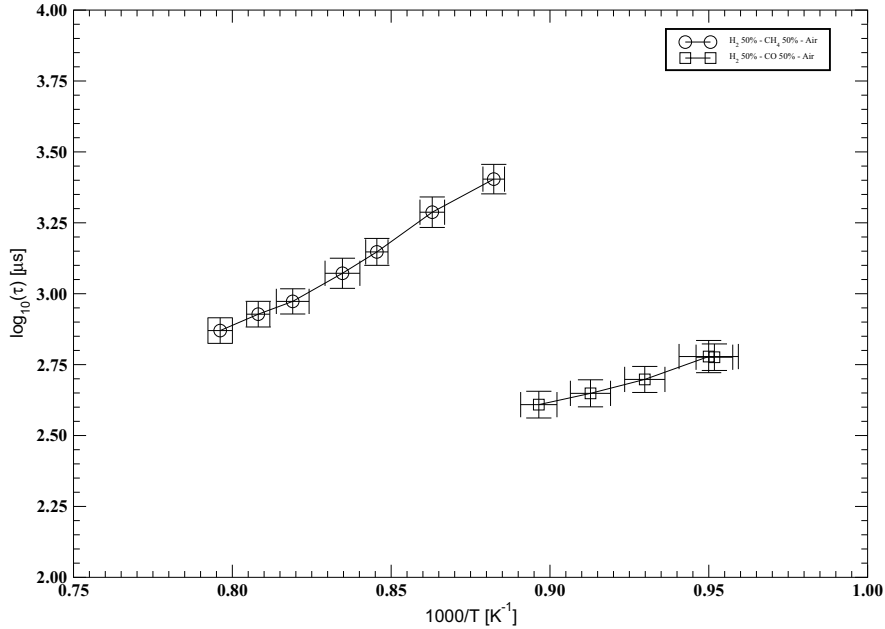


Fig. 20: Auto-ignition delay times of 50% H_2 mixtures with a comparison of the impact of CH_4 and CO blending.

The $\log_{10}(\tau)$ versus the reciprocal temperature is plotted for all three blending ratios in Figs. 18, 19 and 20 for decreasing values of the H_2 mole fraction. While the slope of the H_2/CO mixture, depicted in Fig. 18, is close to be perfectly linear, the gradient in the H_2/CH_4 line is a function of temperature. This suggests that the addition of 30% CH_4 introduces a temperature dependency on the ignition characteristics. The same behaviour is observed in Fig. 19, which shows the impact of a 40% blending factor. As shown in Fig. 20, the non-linearity of the H_2/CH_4 remains present for the 50/50 mixture. However, it is also evident that by then a slight non-linearity as a function of the coflow temperature is also introduced for the H_2/CO mixture. This suggests that the impact of CO blending is also gradually becoming dependent on the coflow temperature, but at much higher dilution levels as compared CH_4 . The finding suggests that the ignition characteristics of the mixture has moved into the transition regime for blending factors $> 50\%$ CO .

3.4.7 Mixtures with 40% Hydrogen

The mixtures consisting of 60% CH_4 and 60% CO continue the trend discussed above. Thus the effect of CH_4 addition remains significantly stronger than for CO . However, as compared to the 50% H_2 cases, the influence of CO on the mixture reactivity is amplified as shown in Table 12. It should also be noted

Tab. 12: Auto-ignition delay time comparison for 40% Hydrogen based fuels

Mixture	T_p [K]	τ [μ s]
H_2 40% – CH_4 60% – Air	1171	2501
H_2 40% – CO 60% – Air	1044	862.7

that at the higher coflow temperatures required to stabilise the CH_4 flames, the slope becomes essentially linear. The difference in reactivity is also evident from the values of the relative reactivity. The significantly larger gradient obtained for H_2/CH_4 is evident.

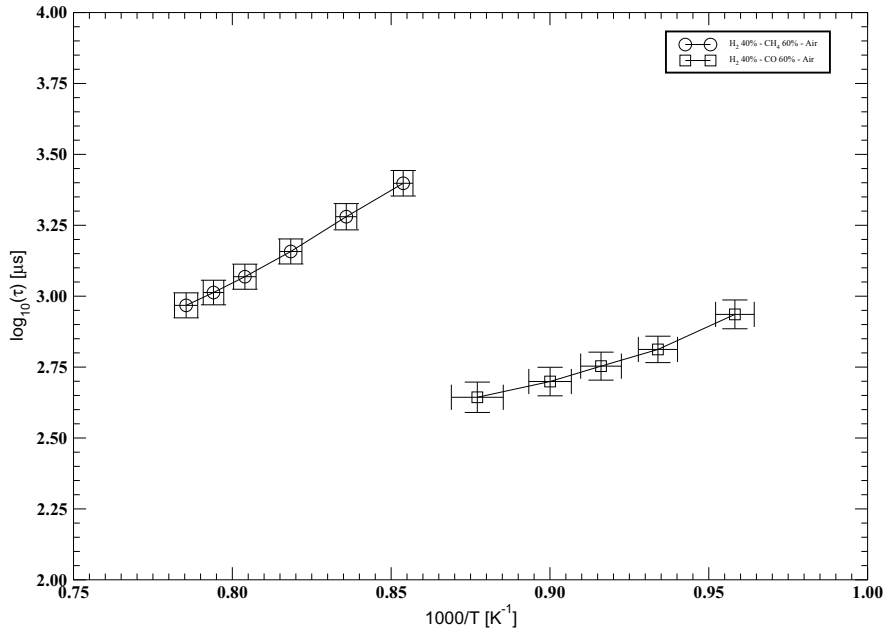


Fig. 21: Auto-ignition delay times for 40% H_2 mixtures with a comparison of the impact of CH_4 and CO blending.

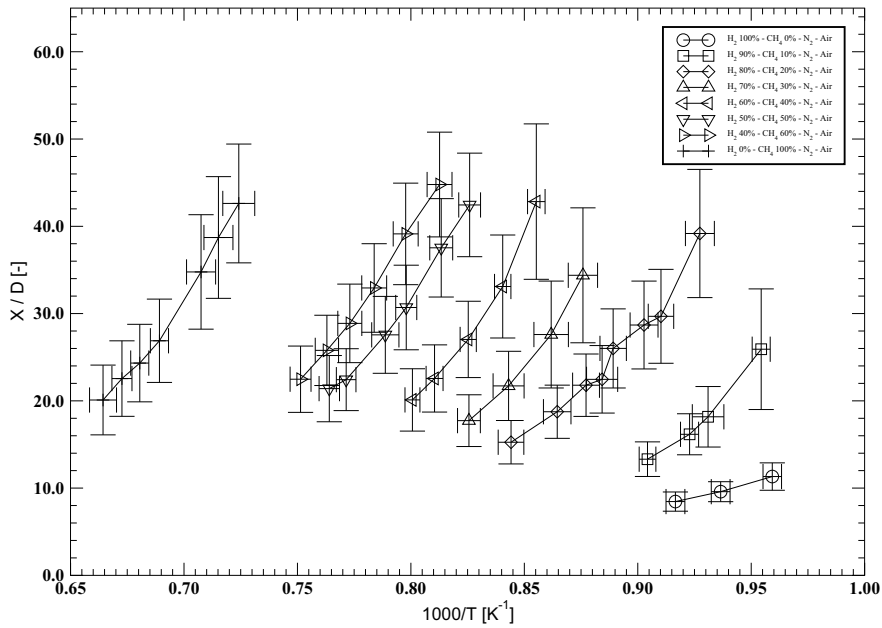
As suggested for the 50% H_2/CO mixture, the impact of CO on the ignition characteristic of the mixture becomes apparent exceeding 50% CO . This is supported by the slope of H_2/CO in Fig. 21. It is evident that the $\log_{10}(\tau)$ has a certain non-linearity with respect to reciprocal coflow temperature, which, once again, is an indicator that the ignition characteristics of CO manifests itself increasingly with decreasing temperature.

Tab. 13: Arrhenius fit for the IDT in μs and relative reactivity E_r comparison for 40% hydrogen based fuels

Mixture	Arrhenius Fit [μs]	E_r [J/mol]
H_2 40% – CH_4 60% – Air	$\log_{10}(\tau) = \frac{6360}{T} - 2.037$	$1.217E + 05$
H_2 40% – CO 60% – Air	$\log_{10}(\tau) = \frac{2986}{T} + 0.01974$	$5.716E + 04$

3.4.8 Hydrogen Blending with Methane and Nitrogen Dilution

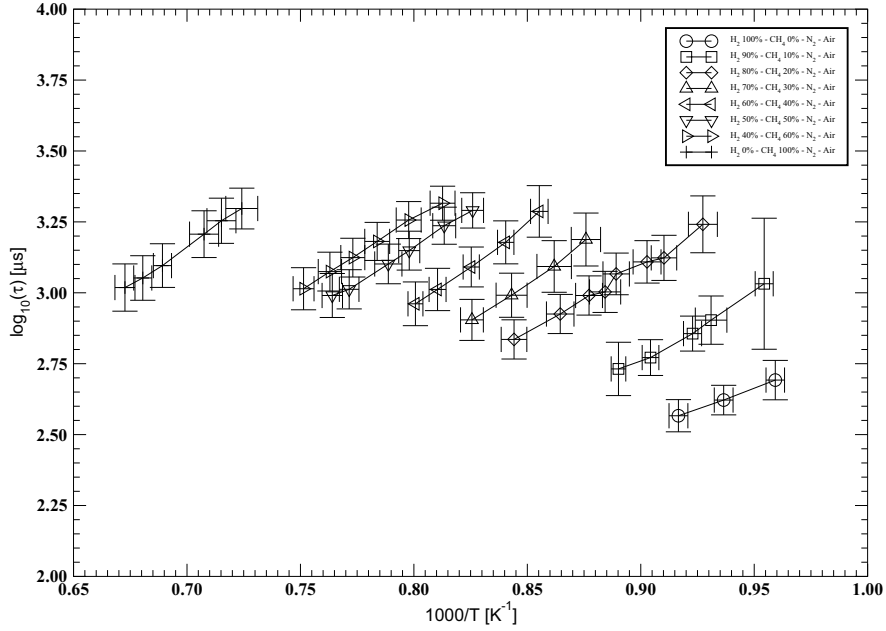
The composition of syngas is strongly dependent on the primary feedstock, i.e. coal, biomass, waste, but also on the process, e.g. gasifying agent. While oxyfuel gasification produces a rather clean gas, only traces of diluents are present in such a feedstock while gasification with air leads to a high N_2 content. The dilution introduces an inert mass which, compared to the non-diluted case, reduces the fuel concentrations, adds a heat sink into the mixtures, and affects third body reactions. A definition for the auto-ignition delay time which allows such effects is commonly used as discussed by Spadaccini [68].

Fig. 22: Flame lift-off heights for H_2 based fuel blends with N_2 dilution and increased CH_4 content.

Tab. 14: Fuel mixtures investigated for H_2/CH_4 blends with further N_2 dilution.

Mixture	u_j [m/s]	χ_{H_2}	χ_{CH_4}	χ_{CO}	χ_{N_2}	χ_{Air}
H_2 100% - N_2 - Air	95.54	0.1581	0.0000	0.0000	0.3715	0.4704
H_2 90% - CH_4 10% - N_2 - Air	93.60	0.1136	0.0126	0.0000	0.3856	0.4882
H_2 80% - CH_4 20% - N_2 - Air	92.37	0.0840	0.0210	0.0000	0.3950	0.5000
H_2 70% - CH_4 30% - N_2 - Air	91.52	0.0630	0.0270	0.0000	0.4016	0.5084
H_2 60% - CH_4 40% - N_2 - Air	90.90	0.0470	0.0315	0.0000	0.4066	0.5147
H_2 50% - CH_4 50% - N_2 - Air	90.43	0.0349	0.0349	0.0000	0.4105	0.5197
H_2 40% - CH_4 60% - N_2 - Air	90.06	0.0251	0.0377	0.0000	0.4136	0.5236
H_2 0% - CH_4 100% - N_2 - Air	89.13	0.0000	0.0448	0.0000	0.4215	0.5336

The frequent appearance of highly diluted syngas necessitates an investigation of the impact upon the reactivity of fuel blends. In the current work, the fuel mixtures discussed above were diluted with N_2 with the added mole fraction calculated via Eq. (3). The resulting mole fractions, along with the jet velocity, of the fuel mixtures $H_2/CH_4/N_2$ studied in this section are listed in Table 14. As shown here, the fuel mole fractions, and therefore concentrations, are considerably reduced compared to the non-diluted mixtures.

Fig. 23: Auto-ignition delay times for H_2 based fuel blends with N_2 dilution and increased CH_4 content.

Tab. 15: Linear functions fitted to the logarithm of the IDT in μs and calculated relative reactivity E_r for $H_2/CH_4/N_2$ fuel blends

Mixture	Arrhenius Fit [μs]	E_r [J/mol]
H_2 100% – N_2 – Air	$\log_{10}(\tau) = \frac{2947}{T} - 0.1358$	$5.641E + 04$
H_2 90% – CH_4 10% – N_2 – Air	$\log_{10}(\tau) = \frac{4740}{T} - 1.505$	$9.074E + 04$
H_2 80% – CH_4 20% – N_2 – Air	$\log_{10}(\tau) = \frac{4755}{T} - 1.183$	$9.102E + 04$
H_2 70% – CH_4 30% – N_2 – Air	$\log_{10}(\tau) = \frac{5596}{T} - 1.721$	$1.071E + 05$
H_2 60% – CH_4 40% – N_2 – Air	$\log_{10}(\tau) = \frac{5889}{T} - 1.761$	$1.127E + 05$
H_2 50% – CH_4 50% – N_2 – Air	$\log_{10}(\tau) = \frac{5012}{T} - 0.8478$	$9.596E + 04$
H_2 40% – CH_4 60% – N_2 – Air	$\log_{10}(\tau) = \frac{4999}{T} - 0.7394$	$9.570E + 04$
H_2 0% – CH_4 100% – N_2 – Air	$\log_{10}(\tau) = \frac{5577}{T} - 0.7401$	$1.068E + 05$

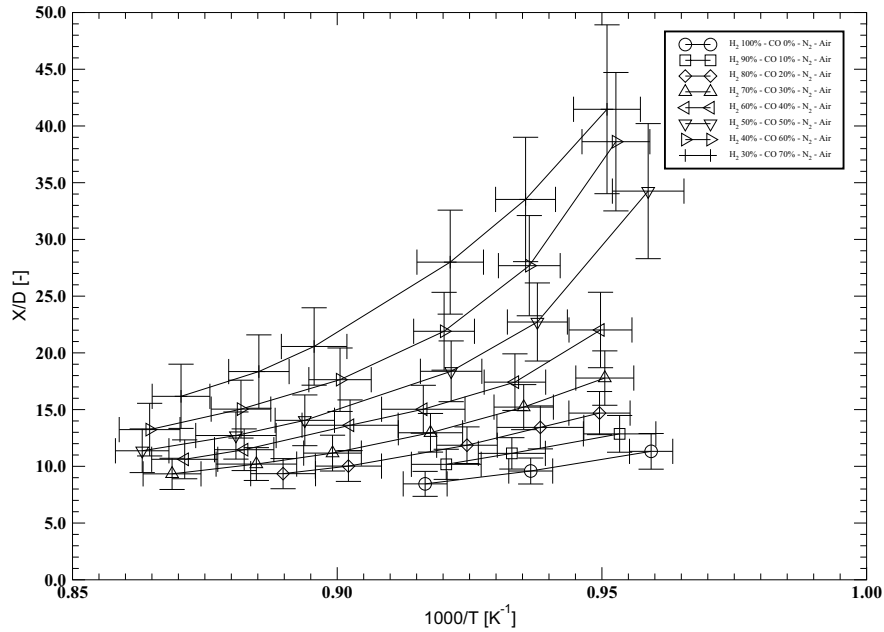
The measured flame lift-off heights are shown in Fig. 22 and it is evident that the substitution of H_2 with CH_4 has, similar to the non-diluted case, a strong impact on the mixture reactivity. It can also be observed that the impact of CH_4 blending is more pronounced for the N_2 diluted mixtures. Such an effect can be expected since dilution generally slows down the reaction progress resulting in a larger flame lift-off height. A comparison of the pure H_2/N_2 blend with a mixture containing 10% CH_4 shows a sharp increase of the flame lift-off height. The findings reported in Fig. 22 suggest that a blending factor of only 10% CH_4 has a strong influence on the mixture reactivity with the diluted mixture already located in the transition regime, while the non-diluted fuel blend remains in the H_2 dominated regime. For higher CH_4 blending factors, the influence of N_2 dilution is also evident from the need to use higher coflow temperatures to achieve similar flame lift-off heights as compared to the undiluted cases. This follows from the fact that the maximum feasible flame lift-off height is reached at much lower fuel blending factors than for the non-diluted cases. In the extreme example of 100% CH_4 , the investigated temperature range is $1355 \text{ K} < T_p < 1425 \text{ K}$ for the non-diluted mixture, while the diluted mixture required a temperature range of $1380 \text{ K} < T_p < 1480 \text{ K}$.

The auto-ignition delay times, determined as discussed above, are shown in Fig. 23. The linearity as a function of reciprocal temperature is maintained with N_2 dilution. However, the actual auto-ignition delay time, its slope, and therefore the relative reactivity E_r , is affected by the dilution. A more detailed comparison between the diluted and non-diluted mixtures can be found below. The fitted logarithmic Arrhenius functions are shown in Table 15 along with the determined relative reactivity. The functions indicate a continuous increase

Tab. 16: Fuel mixtures investigated in the scope of H_2/CO blending and further N_2 dilution

Mixture	u_j [m/s]	χ_{H_2}	χ_{CH_4}	χ_{CO}	χ_{N_2}	χ_{Air}
H_2 100% - N_2 - Air	95.54	0.1581	0.0000	0.0000	0.3715	0.4704
H_2 90% - CO 10% - N_2 - Air	94.75	0.1423	0.0000	0.0158	0.3715	0.4704
H_2 80% - CO 20% - N_2 - Air	93.97	0.1265	0.0000	0.0316	0.3715	0.4704
H_2 70% - CO 30% - N_2 - Air	93.21	0.1107	0.0000	0.0474	0.3715	0.4704
H_2 60% - CO 40% - N_2 - Air	92.47	0.0949	0.0000	0.0632	0.3715	0.4704
H_2 50% - CO 50% - N_2 - Air	91.74	0.0791	0.0000	0.0791	0.3715	0.4704
H_2 40% - CO 60% - N_2 - Air	91.04	0.0632	0.0000	0.0949	0.3715	0.4704
H_2 30% - CO 70% - N_2 - Air	90.35	0.0474	0.0000	0.1107	0.3715	0.4704

of the gradient, and therefore relative reactivity up to 40% CH_4 addition. The relative reactivity barriers (E_r) for mixtures of $H_2 \geq 60\%$ are consistently higher than the values for the non-diluted cases.

Fig. 24: Flame lift-off heights for H_2 based fuel blends with N_2 dilution and increased CO content.

3.4.9 Hydrogen Blending with Carbon Monoxide and Nitrogen Dilution

The impact of N_2 dilution on H_2/CO fuel blends was also investigated by applying the method shown in Eq. (3). The mixture compositions for all cases are listed in Table 16. The dimensionless flame lift-off heights for the listed mixtures

are shown in Fig. 24. The impact of CO addition to diluted H_2 mixtures suggests a slightly different behaviour compared to the non-diluted counterparts. It is evident that small quantities of CO (e.g. 10%) have noticeable impact on the mixture reactivity and, therefore, flame lift-off heights. The curves are also more spread out, i.e. an increasing CO fraction has a more distinct impact on the flame lift-off height than observed for the non-diluted counterpart. However, since the 100% H_2/N_2 mixture already features a significantly decreased reactivity it can be suggested that the dilution effect is rather strong in the current system where the dynamics between mixture reactivity and flow comes to the fore.

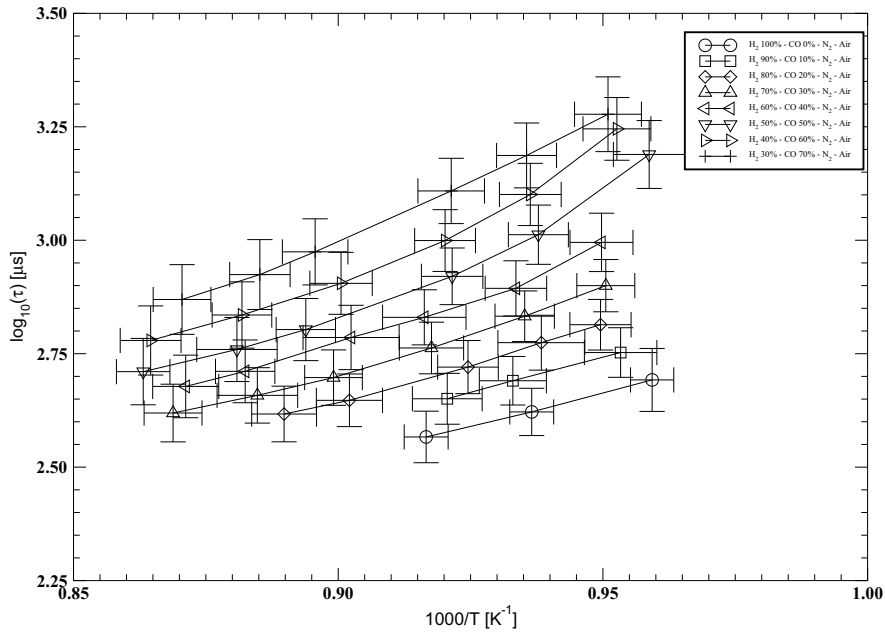


Fig. 25: Auto-ignition delay times for H_2 based fuel blends with N_2 dilution and increased CO content.

The auto-ignition delay times for the $H_2/CO/N_2$ mixtures are shown in Fig. 25. It is evident that, similar to the non-diluted mixtures, low CO fuel fractions have a very moderate impact on the mixture ignition characteristics. It is obvious that up to and including the 70% $H_2/30\%$ CO mixture, the reactivity of hydrogen dominates the mixture reactivity. Starting with the 60% $H_2/40\%$ CO mixture, the slopes of the auto-ignition delay time curves show a slight non-linearity which indicates the increasing influence of CO on the mixture reactivity. The fitted Arrhenius functions along with the determined values for the relative reactivity are shown in Table 17. The relative reactivity increases consistently with an increasing H_2 substitution. It is evident that at a fuel blending ratio of

Tab. 17: Linear functions fitted to the logarithm of the IDT in μs and calculated relative reactivity E_r for $H_2/CO/N_2$ fuel blends

Mixture	Arrhenius Fit [μs]	E_r [J/mol]
H_2 100% – N_2 – <i>Air</i>	$\log_{10}(\tau) = \frac{2947}{T} - 0.1358$	$5.641E + 04$
H_2 90% – CO 10% – N_2 – <i>Air</i>	$\log_{10}(\tau) = \frac{3105}{T} - 0.2077$	$5.945E + 04$
H_2 80% – CO 20% – N_2 – <i>Air</i>	$\log_{10}(\tau) = \frac{3335}{T} - 0.3564$	$6.384E + 04$
H_2 70% – CO 30% – N_2 – <i>Air</i>	$\log_{10}(\tau) = \frac{3449}{T} - 0.3909$	$6.602E + 04$
H_2 60% – CO 40% – N_2 – <i>Air</i>	$\log_{10}(\tau) = \frac{3483}{T} - 0.3592$	$6.668E + 04$
H_2 50% – CO 50% – N_2 – <i>Air</i>	$\log_{10}(\tau) = \frac{4050}{T} - 0.8018$	$7.754E + 04$
H_2 40% – CO 60% – N_2 – <i>Air</i>	$\log_{10}(\tau) = \frac{4436}{T} - 1.071$	$8.492E + 04$
H_2 30% – CO 70% – N_2 – <i>Air</i>	$\log_{10}(\tau) = \frac{4952}{T} - 1.452$	$9.479E + 04$

60% $H_2/40\%$ CO/N_2 a distinct shift is observed in the increase of the relative reactivity barrier. The relative reactivity of the mixtures are approximately governed by Eq. (10):

$$\begin{aligned}
 E_r &= m \cdot \chi_{H_2} + t \quad \text{for } H_2 \geq 60\% \\
 E_r &= 3.4 \cdot m \cdot \chi_{H_2} + 1.45 \cdot t \quad \text{for } H_2 \leq 60\%
 \end{aligned}
 \tag{10}$$

where m and t are the gradient and intercept, respectively, obtained via least squares linear fit to the data.

3.4.10 The Impact of Dilution on Mixture Reactivity

The N_2 dilution effects on the current fuel lean premixed flames of binary H_2 based fuel blends are analysed further in the current section. The influence of N_2 dilution on a pure H_2 premixed flame is considered first. At the lowest coflow temperature, the flame corresponding to the non-diluted case is stabilised at a lift-off height of $X/D = 6.846$ ($\tau = 284 \mu\text{s}$), while N_2 dilution results in stabilisation at $X/D = 11.32$ ($\tau = 492 \mu\text{s}$). The corresponding increase is $\sim 65\%$. The lower reactivity of the diluted cases is the result of a broadening of the reaction zone due to heat extraction by the inert gas. The effect of N_2 dilution on pure H_2 is illustrated in Fig. 26 in terms of the auto-ignition delay time. The results show that the N_2 diluted mixture exhibits a significantly lower reactivity and therefore a longer auto-ignition delay time at a constant coflow temperature.

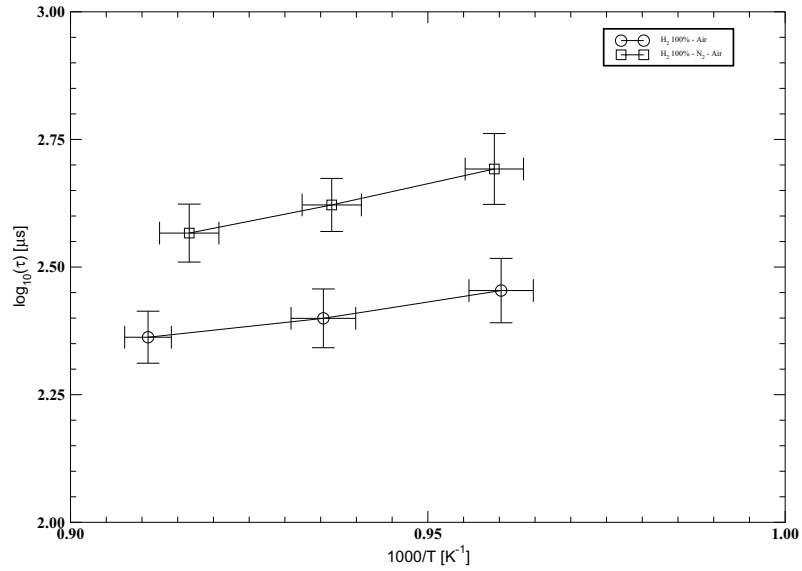


Fig. 26: Effect of N_2 dilution on auto-ignition delay times of 100% H_2 mixtures.

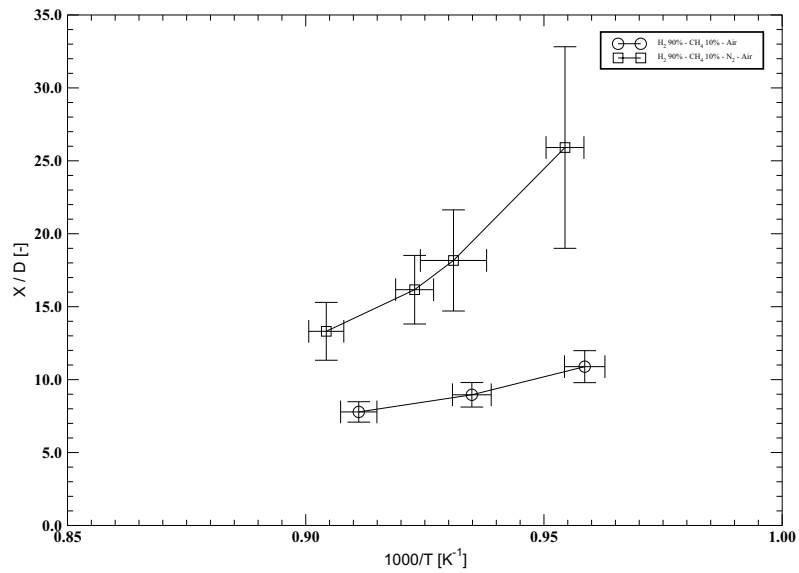


Fig. 27: Effect of N_2 dilution on auto-ignition delay times of fuel mixtures with 90% H_2 /10% CH_4 .

Tab. 18: Effect of N_2 dilution on the relative reactivity and auto-ignition delay time of fuel blends with 90% H_2 /10% CH_4

Mixture	T_p [K]	X/D	τ [μ s]
H_2 90% – CH_4 10% – Air	1043	10.87	469.9
H_2 90% – CH_4 10% – N_2 – Air	1048	25.98	1076

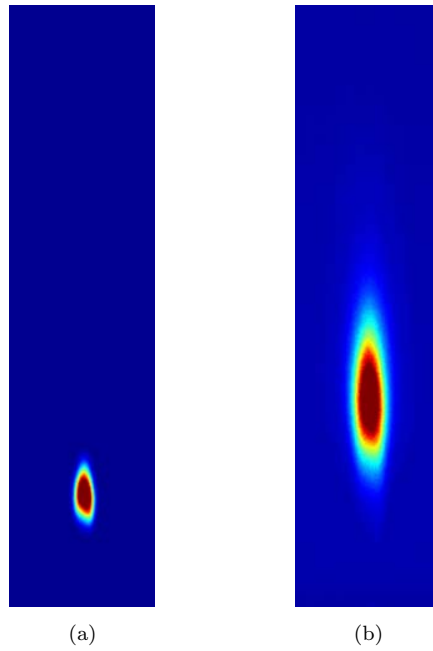


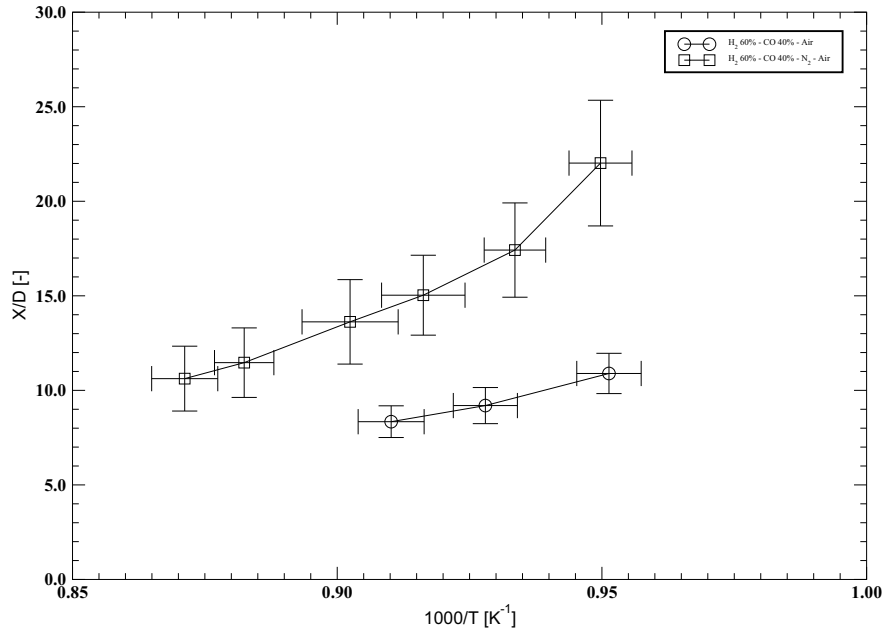
Fig. 28: OH^* Chemiluminescence: (a) H_2 90% – CH_4 10% at $T_p \approx 1075$ K; (b) H_2 90% – CH_4 10% – N_2 at $T_p \approx 1075$ K

A fuel blending fraction of 10% CH_4 had a modest effect on the ignition characteristics of non-diluted mixtures, while the diluted corresponding mixture showed a significant impact. The flame lift-off heights for the cases of 90% H_2 /10% CH_4 and 90% H_2 /10% CH_4/N_2 are shown in Fig. 27. The dimensionless lift-off height is chosen here as an illustration. A small amount of CH_4 blending introduces a significant shift for the non-diluted case. The effect is amplified with N_2 dilution as the fuel concentrations are significantly reduced which has a direct impact on the amount of heat release and the auto-ignition delay time. The earlier discussed effect of the separation of the reaction zones is more distinct for the N_2 diluted case. This finding and the stretching of the

Tab. 19: Effect of N_2 dilution on the relative reactivity and auto-ignition delay time of fuel blends with 60% H_2 /40% CO

Mixture	T_p [K]	X/D	τ [μ s]
H_2 60% – CO 40% – <i>Air</i>	1051	10.79	481.0
H_2 60% – CO 40% – N_2 – <i>Air</i>	1053	21.97	989.1

reaction zone is illustrated in Fig. 28. To quantify the difference in reactivity, Table 18 lists the dimensionless flame lift-off height and the determined auto-ignition delay time for both mixtures. An increase in the auto-ignition delay time by a factor of ~ 2.5 is observed for the N_2 diluted scenario.

Fig. 29: Effect of N_2 dilution on auto-ignition delay times for fuel mixtures with 60% H_2 /40% CO .

Results for the case with CO blending is shown in Fig. 29 shows the effect of N_2 dilution on a mixture of 60% H_2 /40% CO . As discussed previously, the ignition characteristics of CO becomes more predominant as indicated by the extended reaction zone. At higher temperatures, the evident linearity suggests a predominant H_2 ignition regime, while at lower temperatures the impact of CO becomes apparent and the mixture is transferred into the transition regime. A

reason for this behaviour might be the difference in auto-ignition temperatures of the separate components or a failure by the hydrogen component to release sufficient energy on a suitable time scale to trigger ignition of the carbon containing fuel mixture component. Such an observation is consistent with noted differences in behaviour between CO and CH_4 and should ideally be investigated further. The effect can be inferred from the emerging non-linearity at lower temperatures which indicates the increasing impact of CO blending on the ignition characteristics of the mixture. Therefore, dilution appears to have an indirect influence on the ignition characteristics of H_2/CO mixtures through a delayed auto-ignition. The actual auto-ignition delay times and dimensional flame lift-off heights are shown in Table 19. The auto-ignition delay time increases by a factor of ~ 2 for the N_2 diluted case. The OH^* chemiluminescence of the 60% $H_2/40\%$ CO is shown in Fig. 30 which supports the discussion of an extended reaction zone for the diluted case.

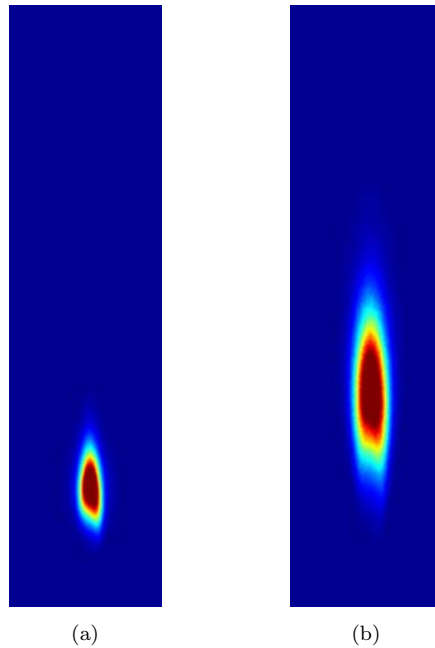


Fig. 30: OH^* Chemiluminescence: (a) H_2 60% – CO 40% at $T_p \approx 1051$ K; (b) H_2 60% – CO 40% – N_2 at $T_p \approx 1053$ K

As detailed in the discussion above, the N_2 dilution of turbulent lean premixed flames has a significant impact on the flame lift-off height. This is primarily due to the extraction of heat from the reaction zone by the diluent which, consequently, slows down the reaction progress and results in a broadening effect of the reaction zone. In terms of the auto-ignition delay time, the introduction of

a diluent reduces the concentration of fuel components which, in turn, affect the ignition delay. Overall, the current experimental series has served to emphasise the importance of dilution effects in the context of flowing systems.

4 Discussion of Ignition Delay Times and Auto-ignition in Turbulent Flows

The current study has investigated the impact on fuel reactivity of the gradual dilution of hydrogen with either methane or carbon monoxide. To this effect, ignition delay times and times to auto-ignition were obtained, respectively, in a shock tube and in a turbulent shear driven flow. The shock tube experiments were conducted at Stanford University under conditions corresponding to measurements normally used to determine chemical rate constant data as outlined in Section 2. The turbulent flow experiments were conducted using a Cabra burner geometry with auto-ignition occurring in a turbulent shear layer formed between a fuel jet and hot combustion products as outlined in Section 3. The results obtained under turbulent conditions suggest that the reactivity of CH_4/H_2 blends becomes dominated comparatively rapidly by the CH_4 component. By contrast, CO mixtures remain much more reactive over the entire range of conditions and a CO content of up to 50% has a modest impact on the time to ignition. The impact of nitrogen dilution was also studied and results suggest that dilution effects become particularly important in the context of triggering the heat release from carbon containing species.

Both studies show that the difference between dilution with CO and CH_4 is significant to the point where it becomes a primary parameter in any safety assessment associated with the risk of ignition - irrespective of the flow field conditions. It has also been shown that comparatively small amounts of added CH_4 cause a decline in mixture reactivity when mixed with hydrogen. As well as excellent qualitative agreement between the two studies, quantitative comparisons of the time to ignition in both configurations reveal a surprisingly good level of agreement. However, firm conclusions can only be made after extrapolation of the Stanford shock tube data from 1.7 atm to 1 atm as ignition delay times are pressure dependent and tend to reduce with an increase in pressure. Such an extrapolation should ideally be preceded by improvements to the arguably best available chemical reaction mechanisms as already applied. Irrespective of such concerns, the purely chemical kinetic data shows that hydrogen addition to CO mixtures essentially provides a synergetic effect with mixtures of up to 60% CO effectively providing the same ignition delay as pure hydrogen mixtures down to temperatures around 940 K. Furthermore, the studies of auto-ignition in the turbulent shear layer has revealed the case dependent presence of two reaction zones with the hydrogen content important in triggering the subsequent heat release associated with the methane component. By contrast, mixtures featuring carbon monoxide do not appear to exhibit such behaviour.

5 Turbulent Burning Velocities for Hydrogen Mixtures with Methane and Carbon monoxide

The propensity of fuel mixtures to ignite is a key aspect of any assessment of their reactivity. However, it is not sufficient in the current context where the strength of the subsequent deflagration and the propensity to cause a deflagration to detonation transition also needs to be assessed. The current part of the report investigates the strength of the resulting deflagrations as characterised by the turbulent burning velocity. The fuel mixtures investigated are nearly identical to the blends covered in Section 3. The H_2/CH_4 fuel blends cover the full range between the pure components and with intermediate steps of 90/10, 80/20, 70/30, 60/40, 50/50, 40/60 and 20/80. The H_2/CO blends cover mixtures of 90/10, 80/20, 70/30, 60/40, 50/50, 40/60 and 30/70. The impact of dilution with nitrogen on the reactivity of the fuel blends was also studied. The currently used opposed jet configuration [47] is arguably the ideal geometry to determine turbulent burning velocities, see Section 1, and the current report includes a summary of the experimental configuration along with the selected conditions. The post-processing techniques are also outlined along with a discussion of the experimental results and their relationship to the studies of ignition delay time and auto-ignition data discussed in Sections 2 and 3.

Given the extreme reactivity range covered, from pure hydrogen-air to pure methane-air mixtures, an effort is also made to generalise the experimental results by investigating comparatively simple normalisation factors derived from theoretical studies of turbulent flame propagation. To this effect, the corresponding laminar flame properties have also been computed.

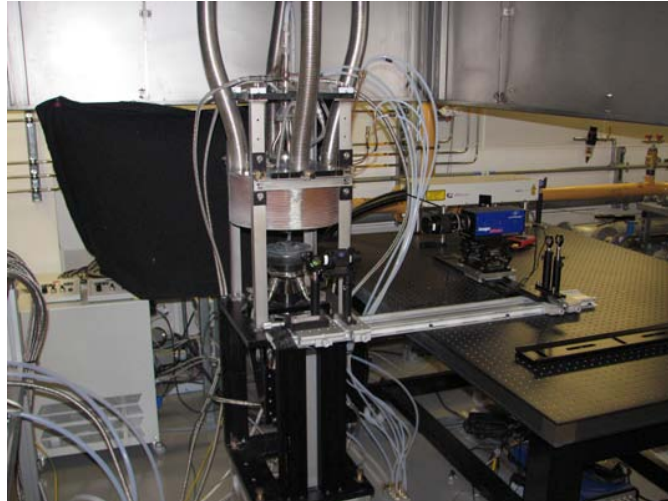


Fig. 31: The current opposed jet configuration.

5.1 Experimental configuration

5.1.1 Burner configuration

The opposed jet configuration is shown in Fig. 31 and a schematic given in Fig. 32. The current burner arrangement has previously been used by Geipel et al. [35] and Goh et al. [47, 69] and is a development of that used in preceding studies by Sardi et al. [30], Geyer et al. [41] and Lindstedt et al. [70, 71]. The burner configuration consists of two identical opposing nozzles with an inner diameter $D = 30$ mm and a length $L = 50$ mm. Both nozzles are water cooled to avoid preheating of the reactants and to prevent nozzle damage. The nozzle separation (H), the distance between the two nozzle exits, is set to one nozzle diameter following the parametric studies of Luff [72] in order to remove flow instabilities. Enhanced turbulence levels are generated by the introduction of grids located 50 mm upstream of the nozzle exit. The characteristics of the grids are discussed further below.

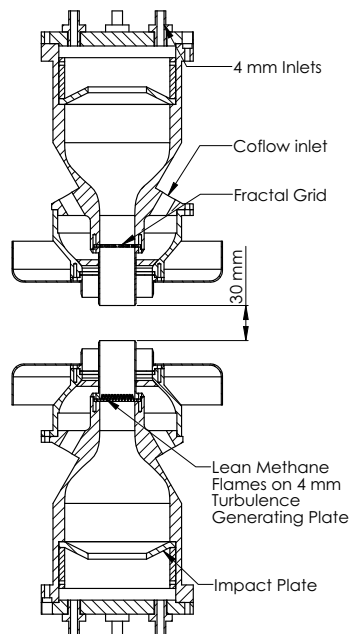


Fig. 32: Schematic opposed jet burner configuration.

The current part of the investigation seeks to clarify the impact of differences in fuel reactivity caused by increasing H_2 addition on the strength of turbulent deflagrations. Given the wide range of reactivities, it was found necessary

Tab. 20: Conditions in lower nozzle featuring hot combustion products

Parameter	Value	Unit
Blockage ratio TGP	0.45	–
Hole diameter TGP	4.00	mm
Blockage ratio FCG	0.65	–
Thickest fractal bar	2.00	mm
Thinnest fractal bar	0.50	mm

to carefully consider the applied configuration in order to provide a consistent comparison basis. A preheat configuration, previously performed by Geipel et al. [73] and Goh et al. [47] was chosen over the conventional twin flame configuration used by Geyer et al. [41] and Lindstedt et al. [70]. The configuration has been shown [47] to provide consistent turbulent burning velocities and offer some considerable advantages in the current context:

- Cases can be compared on a basis of identical flow conditions with a constant exit bulk velocity from the upper nozzle generating a narrow range of turbulent velocity fluctuations.
- Constant conditions of the hot combustion products emerging from the lower nozzle further enhances the comparability of results.
- The point of transition of a self-sustaining propagating turbulent flame to distributed reaction in the hot combustion products can be assessed as a function the mixture stoichiometry and hence provide a further indicator of mixture reactivity.
- All fuel gases injected from the upper nozzle are combusted which is a safety requirement when investigating mixtures with H_2 and CO .

The hot combustion products merging from the lower nozzle were generated using premixed $H_2 - CH_4$ flames stabilised on a turbulence generating (perforated) plate (TGP) fitted into the lower nozzle (LN). The composition of the combustion products, including the oxygen residual, has been shown not to exert a strong impact on the combustion behaviour [74] even for non-self-sustaining flames. The principal impact is hence to provide a source of heat to deliver the advantages discussed above. Furthermore, for self-sustaining flames propagating away from the hot combustion products, the case of greatest interest in the current study, the impact can be expected to be minimal [47].

A sintered plate with mean and maximum pore sizes of $37 \mu\text{m}$ and $155 \mu\text{m}$ was installed upstream of the perforated plate as an additional safety measurement and acts as flame arrestor should flashback occur. A fractal cross grid (FCG) with a blockage ratio of approximately 65%, based on a design of Hurst and Vassilicos [46], was installed in the upper nozzle (UN). Geipel et al. [35] have shown that fractal grids can provide a strong increase in turbulence intensity as compared to conventional perforated plates and hence provide a distinct

advantage in the current context. The perforated plate and the fractal grid are shown in Fig. 33 and details given in Table 20.

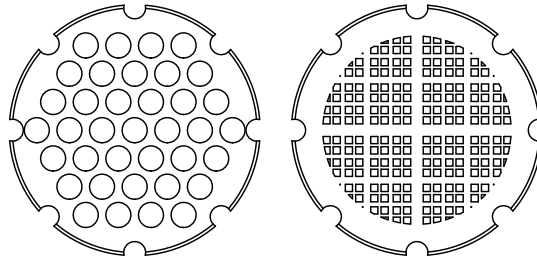


Fig. 33: Turbulence generating grids; Left: Conventional turbulence generating plate; Right: Fractal cross grid.

5.1.2 Flow control system

To control experimental parameters and perform shutdown, if required, a purpose designed LabView [58] interface was programmed in similar manner to that reported previously [75]. The interface allows an accurate setting of operating conditions, the monitoring of flow rates and temperatures and also writes essential parameters to a log file. The velocities, equivalence ratios, unburned gas densities and molecular weights (MW) of the reactant streams, as well as the estimated residual O_2 concentration in the hot combustion products, are also calculated during operation and are displayed for monitoring purposes. All flow rates were accurately regulated using nine mass flow controllers (MFCs) from the Bronkhorst EL-FLOW Select series [59] each with an error of less than $\pm 0.5\%$ of full scale. The communication between the MFCs and the LabView interface was established through a Readout/Control unit Type E-7000 that provides power and signal transfer to each MFC via a flow-bus system. All gases, including air delivered from Howden compressors, were supplied at a pressure of 4.0 bar(g).

All mass flow controllers, with the exception of the air supply for the upper nozzle, were directly connected to the gas mixing manifolds for the lower and upper nozzles to minimise the number of connections. Helium pressure tested stainless steel flexible tubing was used for all fuels (H_2 , CH_4 , and CO) while Polytetrafluoroethylene (PTFE) hoses were used for air and nitrogen. The MFC for the air supply to the upper nozzle was connected to a custom built fluidised bed solid particle seeder with an additional bypass control. The seeded flow was subsequently passed into the gas mixing manifold of the upper nozzle. The Al_2O_3 particles exhibit a diameter of $\sim 3 \mu m$ and the characteristics have been discussed by Goh et al. [47] among others. The purposed designed gas mixing manifolds allow for the injection of five separate gases along with a carrier gas. The inlet pipes into the gas mixer are equipped with non-return valves for each

inlet stream in order to eliminate back flow into the supply pipes. The non-return valves were obtained from Swagelok [76] and feature a cracking pressure of ~ 69 kPa or ~ 172 kPa depending on the stream. In the lower nozzle, the gas mixture is directed from the mixing manifold to the burner nozzle via the sintered and perforated plates. The perforated plate, used to stabilise the lean premixed flames in the lower nozzle, was mounted downstream of the sintered plate and 50 mm upstream of the nozzle exit. The upper nozzle is prepared with a similar gas mixing system with only a difference in pipe length due to the available space and the absence of the non-return valve of the air supply line. The latter is inevitable as the air of the upper nozzle carries aluminium oxide Al_2O_3 seeding particles for the turbulence measurements. However, for safety reasons a non-return valve for the air supply pipe is installed before the seeding of the flow. The use of solid particles in the upper stream also prevents the use of a sintered plate in the upper nozzle. Hence, the flow after the gas mixer is injected into the nozzle and exits directly through the fractal turbulence generating grid. A typical flame location for this experimental configuration is shown in Fig. 34.



Fig. 34: Typical flame position of the reactants injected from the upper nozzle stabilised against the hot combustion products emerging from the lower nozzle.

5.2 Experimental conditions and procedure

The primary objective of the current work package is to determine the turbulent burning velocity (S_T) for different binary H_2/CH_4 and H_2/CO fuel blends. Initial investigations were performed to define the boundary conditions for the

mixture with highest and lowest reactivity in order to specify appropriate operating conditions. The mixture with the lowest reactivity, pure CH_4 , limits the minimum temperature of the combustion products emerging from the lower nozzle. A further reduction in temperature results in non-self-propagating flames and a regime transition to flameless combustion. The point of transition is of interest as it provides additional information concerning the reactivity of the mixture, but does not constitute the main topic of the current investigation. The most reactive mixture, pure H_2 , determines the minimum outflow velocity required in the upper nozzle to avoid flashback. The determined conditions are listed in Table 21 and were applied for the whole mixture matrix. The operating procedure was defined as follows:

1. The air flow rates for the lower and upper nozzles were set to obtain unburnt gas velocities of 1 m/s and 4 m/s, respectively.
2. Ignite the mixture after injecting CH_4 into the lower nozzle to achieve an equivalence ratio of $\Phi = 0.80$ while scaling the flow rates to maintain an unburnt gas velocity of 1 m/s.
3. Increase the unburnt gas velocities in the lower and upper nozzles in a stepwise manner while gradually substituting CH_4 with H_2 in the lower nozzle with only air injected into the upper nozzle. To avoid flashback in the lower nozzle, the equivalence ratio is adjusted to achieve the operating conditions specified in Table 21.
4. Once the operating condition has been reached, the required fuel mixture is introduced in the upper nozzle. Initially, a very lean mixture with the correct fuel ratio (e.g. 50% H_2 /50% CH_4) is introduced using a significantly lower flow rate.
5. Subsequently, the equivalence ratio is gradually increased until a self-propagating flame is stabilised. This condition defines the first measurement point for each mixture.
6. The equivalence ratio is then increased until the flashback limit is reached, which defines the last measurement point for each mixture.

The above procedure was repeated for all mixtures.

5.3 Measurement and Analysis Arrangements

A particle image velocimetry (PIV) system (LaVision FlowMaster) [58] was applied to investigate the axial and radial velocity components of the flow. A Litron Nano LG 175-10 PIV Nd:YAG laser [77] was used to illuminate the central plane between the two nozzles. The near and far field of the laser beam was adjusted by means of two mirrors and subsequently parallelised using a set of convex and concave spherical lenses with a focal length of +125 and -100 mm respectively. The beam was passed through light sheet optics from LaVision

Tab. 21: Conditions in lower nozzle featuring hot combustion products.

Parameter	Value	Unit
$\overline{U}_{b,LN}$	3.000	m/s
$T_{b,LN}$	1638	K
$T_{b,LN}^*$	7.124	K
Φ_{LN}	0.600	–
$\chi_{Air,LN}$	90.79	%
$\chi_{H_2,LN}$	4.605	%
$\chi_{CH_4,LN}$	4.605	%

with an adjustable focus between 0.3 – 2 m using a cylindrical lens with a focus length of -20 mm. The light sheet is directed by a third mirror which mounted on a precision linear adjuster onto the vertical central plane between the nozzles. The laser sheet thickness was approximately 0.3 mm in the interrogation region. The optical setup, shown in Fig. 35, allows a high level of flexibility and accurate adjustment of the laser sheet. The flow field was recorded using an interline-transfer CCD-camera (LaVision Intense Camera [57]) with an acquisition size of 1376×1040 pixels. The interrogation region, using a 100 mm Nikon lens, was approximately 40×30 mm. The aperture of the lens was set to $f5.6$, optimising the depth of view and the captured light. In addition, a 99% optical filter plus a 3 nm bandwidth filter for a wavelength of 532 nm were mounted in front of the lens to minimise noise (e.g. from CH-chemiluminescence).

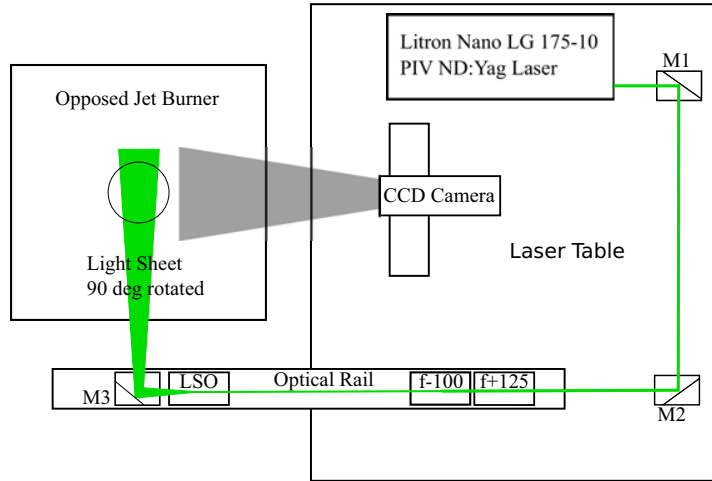


Fig. 35: Optical setup to perform PIV, with M1, M2, M3 indicating mirrors to direct the laser beam while LSO represents the light sheet optics. The light sheet is vertical but is here, for illustration purposes, rotated by 90 degrees.

Tab. 22: Reynolds number and turbulent Reynolds number range, where $Re = (U_{b,UN} \cdot D)/\nu_u$ and $Re_t = (u' \cdot L_I)/\nu_u$ and $U_{b,UN} = 9.0$ m/s.

Mixture	Φ [-]	ν_u [m ² /s]	Re [-]	Re_t [-]
H_2 100% - Air	0.35	$1.776E - 05$	$1.521E + 04$	285.9
H_2 0% - CH_4 100% - Air	0.80	$1.585E - 05$	$1.704E + 04$	320.4

LaVision software (Davis 8.0) was used to control the timing of the laser and the camera. The timing between the double laser pulses was found to be optimum at $\Delta t = 25 \mu s$ for the current flow conditions. Following the data acquisition, a dark image subtraction was performed to enhance the signal to noise ratio and a purpose derived algorithmic mask was applied to segregate the upper stream from the lower stream. The PIV vectors were obtained via a multipass cross-correlation with decreasing interrogation window size starting from 128×128 , via 64×64 down to 32×32 pixels. A 50% overlap of the windows resulted in a vector spacing of 0.45 mm. For each set of conditions, 1000 double frame images were captured to assure statistically independent data. The limiting corresponding Reynolds numbers are given in Table 22.

5.4 Post-processing

The turbulent burning velocity was determined using a purpose written line based flame front detection algorithm applied along the burner centreline. The algorithm involves the following steps:

1. Import instantaneous velocity vector profiles to calculate the mean axial (\bar{U}) and radial (\bar{V}) velocities.
2. Determine the velocity fluctuations $\overline{u'u'}$, $\overline{v'v'}$ and $\overline{u'v'}$ via Eq. (11).
3. Import the instantaneous Mie scattering intensity profiles along the centreline and binarise the occurrence of reactants (1) and products (0).
4. The location of the instantaneous flame front is subsequently found iteratively by applying a moving average filter with a decreasing smoothing span from 64 down to 8 neighbouring pixels.
5. The mean flame front location is determined from the probability of the instantaneous locations.
6. Determine the reaction rate progress (c) variable using the obtained instantaneous flame front location.
7. The calculation of the reaction progress allows the determination of conditional velocities along the centreline with the mean reactant axial U_r and radial velocity V_r profiles obtained along with the conditional velocity fluctuations $\overline{u'_r u'_r}$, $\overline{v'_r v'_r}$, $\overline{u'_r v'_r}$, $\overline{u'_p u'_p}$, $\overline{v'_p v'_p}$ and $\overline{u'_p v'_p}$ (see Eq. (12)).

8. The turbulent burning velocity was determined using the isocontour $c = 0.50$ by mapping the reaction rate progress variable onto the velocity field with the turbulent burning velocity inferred from the matching reactant velocity.

The equations corresponding to the the above procedure as used in the data processing are shown below.

$$\begin{aligned}
 \bar{U} &= \frac{\sum U_i}{N} \\
 \bar{V} &= \frac{\sum V_i}{N} \\
 \overline{u'u'} &= \frac{\sum (U_i - \bar{U})^2}{N} \\
 \overline{v'v'} &= \frac{\sum (V_i - \bar{V})^2}{N} \\
 \overline{u'v'} &= \frac{\sum (U_i - \bar{U}) \cdot (V_i - \bar{V})}{N}
 \end{aligned} \tag{11}$$

The values obtained for the turbulent burning velocity directly provide an indication of the reactivity of the mixture and is also used as basis for the assessment of scaling relationships in the following section.

$$\begin{aligned}
 \bar{U}_r &= \frac{\sum (1-c_i) \cdot U_i}{N} \\
 \bar{U}_p &= \frac{\sum c_i \cdot U_i}{N} \\
 \bar{V}_r &= \frac{\sum (1-c_i) \cdot V_i}{N} \\
 \bar{V}_p &= \frac{\sum c_i \cdot V_i}{N} \\
 \overline{u'_r u'_r} &= \frac{\sum ((1-c_i) \cdot (U_i - \bar{U}_r))^2}{N} \\
 \overline{u'_p u'_p} &= \frac{\sum c_i \cdot (U_i - \bar{U}_p)^2}{N} \\
 \overline{v'_r v'_r} &= \frac{\sum (1-c_i) \cdot (V_i - \bar{V}_r)^2}{N} \\
 \overline{v'_p v'_p} &= \frac{\sum c_i \cdot (V_i - \bar{V}_p)^2}{N} \\
 \overline{u'_r v'_r} &= \frac{\sum (1-c_i) \cdot (U_i - \bar{U}_r) \cdot (1-c_i) \cdot (V_i - \bar{V}_r)}{N} \\
 \overline{u'_p v'_p} &= \frac{\sum c_i \cdot (U_i - \bar{U}_p) \cdot c_i \cdot (V_i - \bar{V}_p)}{N}
 \end{aligned} \tag{12}$$

5.5 Scaling relationships for the turbulent burning velocity

Significant differences in mixture and burning properties, e.g. the unburned gas density (ρ_u), laminar burning velocity, diffusivity, are inherent in the current

investigation due to the wide range of mixture reactivities. A detailed summary of all investigated gas mixtures is presented in Section 5.7.

Classical theories for turbulent combustion resulting in eddy breakup based models for the reaction rate source term (e.g. Spalding [78, 79]) only provide a scaling of the turbulent burning velocity based on the velocity fluctuations. The latter is kept constant in the current set of experiments and hence the current results provide a direct indication of the deviation from the classical limit. It should be pointed out that eddy break up based models are still frequently applied in the context of turbulent combustion and that such models are strictly limited to cases to fuels with similar chemistry.

Multiple definitions of the turbulent burning velocity (e.g. Bray [80]) have been advanced and Driscoll [81] showed that the definitions of Shepherd and Cheng [82] and Lawn and Schefer [83] are not equivalent. Goh et al. [69] determined the local displacement speed of twin premixed opposed jet turbulent flames, from lean methane and propane flame measurements, using velocity-scalar statistics along the burner centreline derived from density segregation technique of Goh et al. [84]. The different definitions introduced by Bray [80], as well as Lawn and Schefer [83], were implemented. Driscoll [81] also proposed using the local minimum in the mean velocity profile in the opposed jet geometry as an indication of the leading edge location. However, local minima tend to be less prominent for lean flames with $\phi \leq 0.8$. Hence, the local minima in the gradient of the axial velocity was used to determine the burning velocity [69]. The resolved values of turbulent burning velocities can normalised with corresponding values of axial velocity fluctuations in accordance with classical theories [78, 79]. All experimental methods of determining turbulent velocities were shown to agree with differences of $\pm 10\%$, which was considered reasonable as the profile of progress variable was asymptotic at the leading edge, and hence relatively difficult to determine [69].

The turbulent burning velocity has also been analysed theoretically using a Kolmogorov, Petrovskii and Piskunov (KPP) type approach [85] and an eigenvalue analysis [86]. The resulting scaling is given in Eq. (13) for the fractal rate expression of Lindstedt and Sakthitharan [87], which introduces the ratio of the laminar burning (S_L) and the Kolmogorov (V_κ) velocities. The following customary constant values [37] are compatible with an eddy viscosity approximation for the flow: $C_\mu = 0.09$, and $C_R \simeq 4$. The customary KPP limit eigenvalue ($\Lambda = 2$) is also applied. σ_{Sc} is the Schmidt number, and u' the turbulent velocity fluctuations. The Kolmogorov velocity can be calculated from the kinematic viscosity (ν) and the dissipation (ϵ) of the turbulent kinetic energy. The dissipation was estimated applying the method developed by George and Hussein [88]. The same method was used by Goh et al. [69], and it was shown that this approximation produced reasonable agreement with experimental values, with maximum differences $\simeq 20\%$.

Tab. 23: Lewis Number Data - H_2/CH_4 Mixtures.

Mixture	Φ	Le_{CH_4}	Le_{H_2}	Le_{CO}
H_2 100% - Air	0.35	1.3261	0.3739	1.4311
H_2 90% - CH_4 10% - Air	0.35	1.2232	0.3506	1.3275
H_2 80% - CH_4 20% - Air	0.35	1.1589	0.3355	1.2622
H_2 80% - CH_4 20% - Air	0.50	1.2235	0.3529	1.3344
H_2 70% - CH_4 30% - Air	0.50	1.1604	0.3381	1.2701
H_2 70% - CH_4 30% - Air	0.60	1.1900	0.3465	1.3045
H_2 60% - CH_4 40% - Air	0.50	1.1129	0.3266	1.2212
H_2 60% - CH_4 40% - Air	0.60	1.1349	0.3333	1.2480
H_2 60% - CH_4 40% - Air	0.70	1.1558	0.3398	1.2736
H_2 50% - CH_4 50% - Air	0.60	1.0918	0.3228	1.2034
H_2 50% - CH_4 50% - Air	0.70	1.1069	0.3279	1.2231
H_2 50% - CH_4 50% - Air	0.80	1.1214	0.3328	1.2420
H_2 40% - CH_4 60% - Air	0.70	1.0674	0.3181	1.1821
H_2 40% - CH_4 60% - Air	0.80	1.0774	0.3219	1.1963
H_2 20% - CH_4 80% - Air	0.80	1.0104	0.3049	1.1262
H_2 0% - CH_4 100% - Air	0.80	0.9624	0.2925	1.0756

$$S_{T,KPP} = \Lambda \sqrt{\frac{C_R C_\mu S_L}{\sigma_{sc} V_\kappa}} u' \quad V_\kappa = (\nu_u \epsilon)^{1/4} \quad (13)$$

Lindstedt et al. [89] also evaluated different correction factors [90, 91] aimed at taking into account transport effects related to the Lewis number and showed that the expression given in Eq. (13) can be modified to account approximately for such effects. The derived correction [91] amounts to a modified value for $C_R = 4.0/e^{\sigma_{Le}-1}$ and the implications for the current hydrogen rich mixtures are evaluated below. The generalisation of the functional dependency of the turbulent burning velocity presents a major challenge. Hence, this aspect is covered extensively below for a substantial range of hydrogen enrichment levels applicable to both CCGT and CCGE operating conditions with stoichiometries from 0.35 to 0.80 and H_2 contents from 100% to 0% (H_2/CH_4) and 100% to 30% (H_2/CO). It is expected that the developed correlation will be applicable with reasonable accuracy to conditions in exhaust systems following further evaluation using data from subsequent larger scale experiments.

Given the predominant scaling of the turbulent burning velocity S_T with the turbulence fluctuations, the current approach of keeping this value approximately constant is of particular importance. However, given the very large range of reactivities considered it can be expected that fuel reactivity effects need to be taken into account. Indeed, if this was not the case, all flames would behave the same in a turbulent flow environment. It is well known in the context of turbulence enhanced DDT that this is not true. For example, Lindstedt and Michels [92, 93] have shown by comparing DDT data for gaseous hydrocarbons obtained in smooth tubes with cases featuring strong turbulence enhancement using Schechtkin spirals, that while the influence of chemistry upon relative detonability is reduced in strongly turbulent environments, the intrinsic reactivity

Tab. 24: Lewis Number Data - H_2/CO Mixtures.

Mixture	Φ	Le_{CH_4}	Le_{H_2}	Le_{CO}
H_2 100% - Air	0.35	1.3260	0.3739	1.4310
H_2 90% - CO 10% - Air	0.35	1.2885	0.3647	1.3910
H_2 80% - CO 20% - Air	0.35	1.2506	0.3553	1.3505
H_2 80% - CO 20% - Air	0.40	1.2823	0.3630	1.3841
H_2 70% - CO 30% - Air	0.35	1.2124	0.3458	1.3096
H_2 70% - CO 30% - Air	0.40	1.2396	0.3525	1.3384
H_2 60% - CO 40% - Air	0.40	1.1967	0.3417	1.2923
H_2 60% - CO 40% - Air	0.45	1.2185	0.3471	1.3154
H_2 50% - CO 50% - Air	0.40	1.1533	0.3307	1.2456
H_2 50% - CO 50% - Air	0.45	1.1708	0.3350	1.2641
H_2 50% - CO 50% - Air	0.50	1.1876	0.3391	1.2818
H_2 40% - CO 60% - Air	0.50	1.1353	0.3258	1.2253
H_2 40% - CO 60% - Air	0.60	1.1590	0.3316	1.2503
H_2 30% - CO 70% - Air	0.50	1.0824	0.3121	1.1681
H_2 30% - CO 70% - Air	0.60	1.0981	0.3160	1.1843

of the fuel remains a factor. Hence, it is likely that the classical scaling of turbulent burning velocities is necessary but not sufficient in the current context. The thermochemical properties related to the laminar flames are determined as outlined in the following section.

5.6 Laminar flame properties

The laminar flame data required for the evaluation of the above scaling relationship were obtained using the chemistry applied by Lindstedt et al. [89] in a study of predictions of turbulent burning velocities of methane and hydrogen mixtures via the application of a transported probability density function method. The chemistry is based on the recommendations of CEC data evaluation group and has been used in a number of studies of laminar [94, 95, 96] and turbulent [9, 97, 98, 99] flames with the transient behaviour of laminar H_2 and CH_4 flames reproduced with good accuracy [96]. Ignition delay times are more sensitive to errors in the chemistry (see Section 2) than the laminar burning velocity with the impact further reduced due to the functional form of Eq. (13).

The laminar burning velocities were calculated with differential diffusion effects included using an in-house FORTRAN code (e.g. [89]). Mixture properties such as kinematic viscosity (ν), density (ρ), Schmidt number (σ_{Sc}) and Lewis number (σ_{Le}) were also extracted from the same simulations. The results of the calculations are summarised in Tables 27 to 30. The corresponding Lewis numbers for the deficient reactants (i.e. the fuel components for lean mixtures and for simplicity denoted Le_{H_2} etc.) are given in Tables 23 to 26. The impact of such corrections are discussed further below. The temperature boundary conditions in the laminar flame calculation was set to room temperature (298 K) and the pressure to 101325 Pa.

Tab. 25: Lewis Number Data - $H_2/CH_4/N_2$ Mixtures.

Mixture	Φ	Le_{CH_4}	Le_{H_2}	Le_{CO}
H_2 100% - N_2 - <i>Air</i>	0.60	1.3189	0.3734	1.4229
H_2 100% - N_2 - <i>Air</i>	0.65	1.3419	0.3789	1.4471
H_2 90% - CH_4 10% - N_2 - <i>Air</i>	0.65	1.2384	0.3555	1.3430
H_2 90% - CH_4 10% - N_2 - <i>Air</i>	0.75	1.2715	0.3640	1.3789
H_2 90% - CH_4 10% - N_2 - <i>Air</i>	0.85	1.3025	0.3718	1.4125
H_2 80% - CH_4 20% - N_2 - <i>Air</i>	0.75	1.1948	0.3462	1.3012
H_2 80% - CH_4 20% - N_2 - <i>Air</i>	0.85	1.2183	0.3525	1.3275
H_2 80% - CH_4 20% - N_2 - <i>Air</i>	0.95	1.2408	0.3586	1.3527
H_2 70% - CH_4 30% - N_2 - <i>Air</i>	0.85	1.1578	0.3381	1.2657
H_2 70% - CH_4 30% - N_2 - <i>Air</i>	0.95	1.1748	0.3430	1.2855
H_2 70% - CH_4 30% - N_2 - <i>Air</i>	1.00	1.1830	0.3454	1.2951
H_2 60% - CH_4 40% - N_2 - <i>Air</i>	0.95	1.1249	0.3309	1.2342
H_2 60% - CH_4 40% - N_2 - <i>Air</i>	1.00	1.1311	0.3328	1.2417
H_2 50% - CH_4 50% - N_2 - <i>Air</i>	1.00	1.0903	0.3228	1.1996
H_2 40% - CH_4 60% - N_2 - <i>Air</i>	1.00	1.0576	0.3146	1.1657
H_2 20% - CH_4 80% - N_2 - <i>Air</i>	1.00	1.0082	0.3020	1.1141
H_2 0% - CH_4 100% - N_2 - <i>Air</i>	1.00	0.9736	0.2931	1.0780

Tab. 26: Lewis Number Data - $H_2/CO/N_2$ Mixtures.

Mixture	Φ	Le_{CH_4}	Le_{H_2}	Le_{CO}
H_2 100% - N_2 - <i>Air</i>	0.60	1.3189	0.3734	1.4229
H_2 100% - N_2 - <i>Air</i>	0.65	1.3419	0.3789	1.4471
H_2 90% - CO 10% - N_2 - <i>Air</i>	0.60	1.2825	0.3644	1.3843
H_2 90% - CO 10% - N_2 - <i>Air</i>	0.65	1.3031	0.3694	1.4060
H_2 90% - CO 10% - N_2 - <i>Air</i>	0.70	1.3231	0.3742	1.4271
H_2 80% - CO 20% - N_2 - <i>Air</i>	0.65	1.2641	0.3598	1.3647
H_2 80% - CO 20% - N_2 - <i>Air</i>	0.70	1.2816	0.3640	1.3833
H_2 70% - CO 30% - N_2 - <i>Air</i>	0.65	1.2245	0.3499	1.3226
H_2 70% - CO 30% - N_2 - <i>Air</i>	0.70	1.2397	0.3536	1.3386
H_2 70% - CO 30% - N_2 - <i>Air</i>	0.75	1.2545	0.3572	1.3543
H_2 60% - CO 40% - N_2 - <i>Air</i>	0.70	1.1974	0.3429	1.2935
H_2 60% - CO 40% - N_2 - <i>Air</i>	0.75	1.2098	0.3460	1.3066
H_2 60% - CO 40% - N_2 - <i>Air</i>	0.85	1.2336	0.3518	1.3320
H_2 50% - CO 50% - N_2 - <i>Air</i>	0.75	1.1647	0.3345	1.2583
H_2 50% - CO 50% - N_2 - <i>Air</i>	0.85	1.1838	0.3392	1.2786
H_2 50% - CO 50% - N_2 - <i>Air</i>	0.95	1.2021	0.3437	1.2981
H_2 40% - CO 60% - N_2 - <i>Air</i>	0.85	1.1335	0.3263	1.2245
H_2 40% - CO 60% - N_2 - <i>Air</i>	0.95	1.1472	0.3297	1.2391
H_2 40% - CO 60% - N_2 - <i>Air</i>	1.00	1.1537	0.3313	1.2461
H_2 30% - CO 70% - N_2 - <i>Air</i>	0.85	1.0827	0.3131	1.1697
H_2 30% - CO 70% - N_2 - <i>Air</i>	0.95	1.0917	0.3153	1.1792
H_2 30% - CO 70% - N_2 - <i>Air</i>	1.00	1.0960	0.3164	1.1838

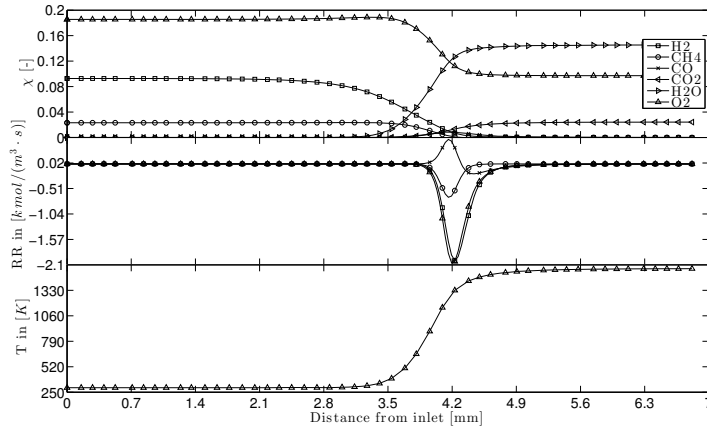


Fig. 36: Laminar flame calculation for the mixture 80% H_2 – 20% CH_4 at an equivalence ratio $\Phi = 0.50$. Top: Species concentrations; Middle: The corresponding reaction rates; Bottom: Temperature profile.

A sample computation is shown in Fig. 36 to provide an illustration of the applied numerical resolution. The markers are used just for illustration purposes as the computational domain was much better resolved using 550 nodes featuring a mesh size of $\sim 10 \mu m$. The results of the laminar burning velocity are discussed in Section 5.7. The illustrative species profiles shown in Fig. 36 include H_2 , CH_4 and CO as well as O_2 which are consumed in the oxidation process. Carbon monoxide is formed during the combustion process and subsequently further oxidized to CO_2 . Hence, the CO profile shows a peak within the reaction zone. For cases where CO is included as a fuel in place of CH_4 , the time scale for the formation of CO_2 in the final oxidation step is correspondingly reduced with a direct impact on the reactivity of the mixture. The final products (e.g. H_2O and CO_2) show a steady increase throughout the domain. The middle row has been included to show the formation (positive) and consumption (negative) rates of selected species. The net rate of CO illustrates both formation and consumption and it is evident that the temperature continues to rise during the further oxidation of CO as shown in the bottom row.

The primary objective of the laminar flame calculations is to determine burning velocities and other thermo-physical properties using the scaling of the turbulent burning velocities for the investigated mixtures. Stable flames were established for all mixtures. The computed laminar burning velocities are shown in Fig. 37 and it is evident that the values are highly dependent on the fuel blending component and the equivalence ratio. The effect of fuel blending is also obvious. While the addition of CH_4 to H_2 results in a rather steep decrease in lami-

Tab. 27: Summary results for H_2/CH_4 mixtures, where Φ is the equivalence ratio and u indicates reactants, ρ_u the density, ν_u the kinematic viscosity, $\sigma_{Sc,u}$ the Schmidt number, T_{ad} the adiabatic flame temperature and S_L the laminar burning velocity

Mixture	Φ [-]	ρ_u [kg/m ³]	ν_u [m ² /s]	$\sigma_{Sc,u}$ [-]	T_{ad} [K]	S_L [m/s]
H_2 100% - Air	0.35	1.0396	$1.7758E-05$	0.8319	1291	0.0768
H_2 90% - CH_4 10% - Air	0.35	1.0756	$1.7127E-05$	0.8256	1258	0.0323
H_2 80% - CH_4 20% - Air	0.35	1.0977	$1.6757E-05$	0.8218	1230	0.0165
H_2 80% - CH_4 20% - Air	0.50	1.0661	$1.7194E-05$	0.8270	1519	0.1641
H_2 70% - CH_4 30% - Air	0.50	1.0880	$1.6824E-05$	0.8232	1501	0.1214
H_2 70% - CH_4 30% - Air	0.60	1.0717	$1.7037E-05$	0.8258	1655	0.2402
H_2 60% - CH_4 40% - Air	0.50	1.1044	$1.6557E-05$	0.8205	1487	0.0961
H_2 60% - CH_4 40% - Air	0.60	1.0911	$1.6711E-05$	0.8226	1644	0.1943
H_2 60% - CH_4 40% - Air	0.70	1.0777	$1.6876E-05$	0.8246	1768	0.3084
H_2 50% - CH_4 50% - Air	0.60	1.1058	$1.6475E-05$	0.8201	1635	0.1645
H_2 50% - CH_4 50% - Air	0.70	1.0947	$1.6595E-05$	0.8217	1761	0.2631
H_2 50% - CH_4 50% - Air	0.80	1.0841	$1.6709E-05$	0.8233	1859	0.3649
H_2 40% - CH_4 60% - Air	0.70	1.1084	$1.6375E-05$	0.8195	1755	0.2314
H_2 40% - CH_4 60% - Air	0.80	1.0994	$1.6461E-05$	0.8208	1854	0.3222
H_2 20% - CH_4 80% - Air	0.80	1.1227	$1.6093E-05$	0.8170	1846	0.2672
H_2 0% - CH_4 100% - Air	0.80	1.1391	$1.5847E-05$	0.8143	1816	0.2280

nar burning velocity, blending with an equal amount of CO leads to only a moderate change. The determined adiabatic flame temperatures are shown in Tables 27 to 30 and further illustrated in Fig. 38. It is obvious that a reduction in equivalence ratio results in a significant decrease in the combustion product temperature. In the case of CH_4 blending, a slight decrease in temperature is notable with increasing CH_4 fraction. The heat of combustion of the pure fuel components is 241.8 [kJ/kmol], 802.4 [kJ/kmol] and 283.0 [kJ/kmol] for H_2 , CH_4 and CO respectively. At a constant equivalence ratio, the energy content of the fuel is affected as indicated by the adiabatic flame temperature.

5.7 Results and Discussion

The flow field conditions are maintained constant in order to separate out the effect of mixture reactivity on the turbulent burning velocity. The example shown in Fig. 39 corresponds to the mean velocity field for mixture of 80% H_2 - 20% CO at an equivalence ratio of $\Phi = 0.4$. The horizontal red and blue lines illustrate the locations of the upper and lower nozzle respectively. The vertical green line depicts the location of the centre axis. A sample Mie scattering image for same mixture is depicted in Fig. 40. The region with high seeding density, on the centre line above the red circle, shows the location of the reactants. The area with the lower seeding density, on the centre line below the red circle, specifies the location of products. The red circle depicts the detected flame front on the centre axis of this instantaneous image. The corresponding instantaneous vector field is shown in Fig. 41.

Tab. 28: Summary results for H_2/CO mixtures, nomenclature as for Table 27.

Mixture	Φ [-]	ρ_u [kg/m ³]	ν_u [m ² /s]	$\sigma_{Sc,u}$ [-]	T_{ad} [K]	S_L [m/s]
H_2 100% - Air	0.35	1.0396	$1.7759E-05$	0.8319	1292	0.0770
H_2 90% - CO 10% - Air	0.35	1.0532	$1.7528E-05$	0.8294	1301	0.0727
H_2 80% - CO 20% - Air	0.35	1.0670	$1.7297E-05$	0.8270	1312	0.0690
H_2 80% - CO 20% - Air	0.40	1.0528	$1.7521E-05$	0.8293	1418	0.1420
H_2 70% - CO 30% - Air	0.35	1.0806	$1.7077E-05$	0.8246	1322	0.0657
H_2 70% - CO 30% - Air	0.40	1.0683	$1.7263E-05$	0.8266	1429	0.1304
H_2 60% - CO 40% - Air	0.40	1.0836	$1.7016E-05$	0.8239	1439	0.1201
H_2 60% - CO 40% - Air	0.45	1.0734	$1.7167E-05$	0.8255	1536	0.1917
H_2 50% - CO 50% - Air	0.40	1.0986	$1.6784E-05$	0.8213	1450	0.1105
H_2 50% - CO 50% - Air	0.45	1.0903	$1.6898E-05$	0.8226	1547	0.1733
H_2 50% - CO 50% - Air	0.50	1.0819	$1.7019E-05$	0.8238	1632	0.2465
H_2 40% - CO 60% - Air	0.50	1.1004	$1.6730E-05$	0.8207	1642	0.2194
H_2 40% - CO 60% - Air	0.60	1.0878	$1.6900E-05$	0.8226	1779	0.3668
H_2 30% - CO 70% - Air	0.50	1.1181	$1.6470E-05$	0.8176	1652	0.1930
H_2 30% - CO 70% - Air	0.60	1.1092	$1.6571E-05$	0.8190	1789	0.3191

Tab. 29: Summary results for $H_2/CH_4/N_2$ mixtures, nomenclature as for Table 27.

Mixture	Φ [-]	ρ_u [kg/m ³]	ν_u [m ² /s]	$\sigma_{Sc,u}$ [-]	T_{ad} [K]	S_L [m/s]
H_2 100% - N_2 - Air	0.60	1.0311	$1.7684E-05$	0.8323	1266	0.0681
H_2 100% - N_2 - Air	0.65	1.0213	$1.7846E-05$	0.8341	1328	0.1102
H_2 90% - CH_4 10% - N_2 - Air	0.65	1.0572	$1.7201E-05$	0.8273	1290	0.0462
H_2 90% - CH_4 10% - N_2 - Air	0.75	1.0423	$1.7429E-05$	0.8301	1405	0.0979
H_2 90% - CH_4 10% - N_2 - Air	0.85	1.0282	$1.7647E-05$	0.8327	1508	0.1599
H_2 80% - CH_4 20% - N_2 - Air	0.75	1.0688	$1.6967E-05$	0.8252	1379	0.0574
H_2 80% - CH_4 20% - N_2 - Air	0.85	1.0573	$1.7130E-05$	0.8273	1484	0.0953
H_2 80% - CH_4 20% - N_2 - Air	0.95	1.0462	$1.7290E-05$	0.8293	1575	0.1349
H_2 70% - CH_4 30% - N_2 - Air	0.85	1.0782	$1.6776E-05$	0.8235	1465	0.0659
H_2 70% - CH_4 30% - N_2 - Air	0.95	1.0690	$1.6896E-05$	0.8251	1559	0.0919
H_2 70% - CH_4 30% - N_2 - Air	1.00	1.0646	$1.6954E-05$	0.8259	1592	0.1041
H_2 60% - CH_4 40% - N_2 - Air	0.95	1.0863	$1.6608E-05$	0.8220	1546	0.0696
H_2 60% - CH_4 40% - N_2 - Air	1.00	1.0825	$1.6654E-05$	0.8227	1580	0.0781
H_2 50% - CH_4 50% - N_2 - Air	1.00	1.0965	$1.6427E-05$	0.8202	1570	0.0628
H_2 40% - CH_4 60% - N_2 - Air	1.00	1.1078	$1.6247E-05$	0.8182	1561	0.0528
H_2 20% - CH_4 80% - N_2 - Air	1.00	1.1245	$1.5988E-05$	0.8154	1548	0.0403
H_2 0% - CH_4 100% - N_2 - Air	1.00	1.1351	$1.5838E-05$	0.8133	1531	0.0335

Tab. 30: Summary results for $H_2/CO/N_2$ mixtures, nomenclature as for Table 27.

Mixture	Φ [-]	ρ_u [kg/m ³]	ν_u [m ² /s]	$\sigma_{Sc,u}$ [-]	T_{ad} [K]	S_L [m/s]
H_2 100% - N_2 - <i>Air</i>	0.60	1.0311	$1.7684E-05$	0.8323	1266	0.0681
H_2 100% - N_2 - <i>Air</i>	0.65	1.0213	$1.7846E-05$	0.8341	1328	0.1102
H_2 90% - CO 10% - N_2 - <i>Air</i>	0.60	1.0443	$1.7461E-05$	0.8296	1276	0.0650
H_2 90% - CO 10% - N_2 - <i>Air</i>	0.65	1.0355	$1.7603E-05$	0.8312	1338	0.1028
H_2 90% - CO 10% - N_2 - <i>Air</i>	0.70	1.0269	$1.7743E-05$	0.8328	1397	0.1478
H_2 80% - CO 20% - N_2 - <i>Air</i>	0.65	1.0495	$1.7370E-05$	0.8284	1349	0.0963
H_2 80% - CO 20% - N_2 - <i>Air</i>	0.70	1.0419	$1.7489E-05$	0.8297	1408	0.1365
H_2 70% - CO 30% - N_2 - <i>Air</i>	0.65	1.0636	$1.7141E-05$	0.8256	1359	0.0904
H_2 70% - CO 30% - N_2 - <i>Air</i>	0.70	1.0571	$1.7238E-05$	0.8268	1418	0.1264
H_2 70% - CO 30% - N_2 - <i>Air</i>	0.75	1.0504	$1.7344E-05$	0.8279	1474	0.1671
H_2 60% - CO 40% - N_2 - <i>Air</i>	0.70	1.0720	$1.6999E-05$	0.8240	1429	0.1172
H_2 60% - CO 40% - N_2 - <i>Air</i>	0.75	1.0662	$1.7089E-05$	0.8249	1484	0.1534
H_2 60% - CO 40% - N_2 - <i>Air</i>	0.85	1.0555	$1.7247E-05$	0.8268	1582	0.2370
H_2 50% - CO 50% - N_2 - <i>Air</i>	0.75	1.0824	$1.6830E-05$	0.8220	1494	0.1406
H_2 50% - CO 50% - N_2 - <i>Air</i>	0.85	1.0732	$1.6965E-05$	0.8235	1592	0.2143
H_2 50% - CO 50% - N_2 - <i>Air</i>	0.95	1.0643	$1.7097E-05$	0.8249	1666	0.2973
H_2 40% - CO 60% - N_2 - <i>Air</i>	0.85	1.0906	$1.6697E-05$	0.8204	1601	0.1928
H_2 40% - CO 60% - N_2 - <i>Air</i>	0.95	1.0838	$1.6789E-05$	0.8215	1674	0.2651
H_2 40% - CO 60% - N_2 - <i>Air</i>	1.00	1.0799	$1.6849E-05$	0.8220	1695	0.3025
H_2 30% - CO 70% - N_2 - <i>Air</i>	0.85	1.1082	$1.6433E-05$	0.8173	1610	0.1710
H_2 30% - CO 70% - N_2 - <i>Air</i>	0.95	1.1028	$1.6503E-05$	0.8181	1682	0.2336
H_2 30% - CO 70% - N_2 - <i>Air</i>	1.00	1.1008	$1.6522E-05$	0.8185	1703	0.2657

An example of velocity statistics along the centreline is shown in Fig. 42 for a mixture of 60% H_2 - 40% CH_4 . An increased equivalence ratio results in a faster propagating flame which stabilises further upstream leading to a thickened product zone. Furthermore, a higher equivalence ratio leads to an increase in heat release which also contributes to an earlier acceleration of the flow due to combustion. The influence of the reaction zone on the flow field is also reflected by the axial velocity fluctuations as shown in Fig. 43. The heat release within the reaction zone results in an acceleration of the flow due to the difference in density between reactants and products. This instantaneous acceleration of the flow leads to an increased axial velocity fluctuations within the flame brush. As a consequence, the location of the mean reaction zone is indicated by the peak in the axial velocity fluctuations as shown in Fig. 43.

Further information regarding the flame brush thickness and the mean flame front location can be inferred from conditional velocities obtained via Eq. (12). The conditional axial velocity along the burner centreline shown in Fig. 44 and a significant increase for the higher equivalence ratio is readily apparent.

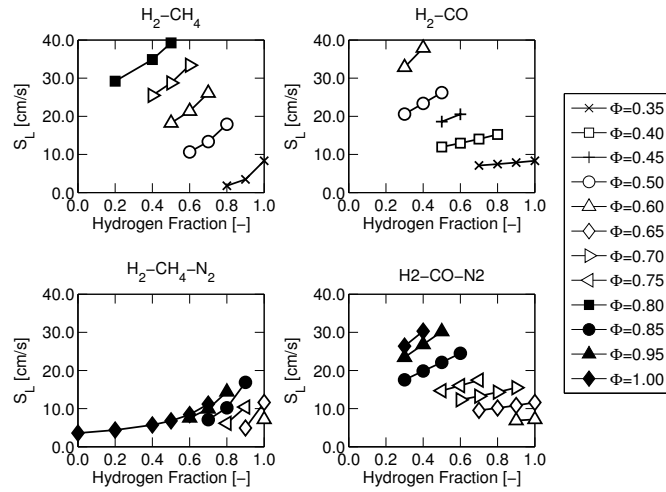


Fig. 37: Laminar burning velocities for all mixtures.

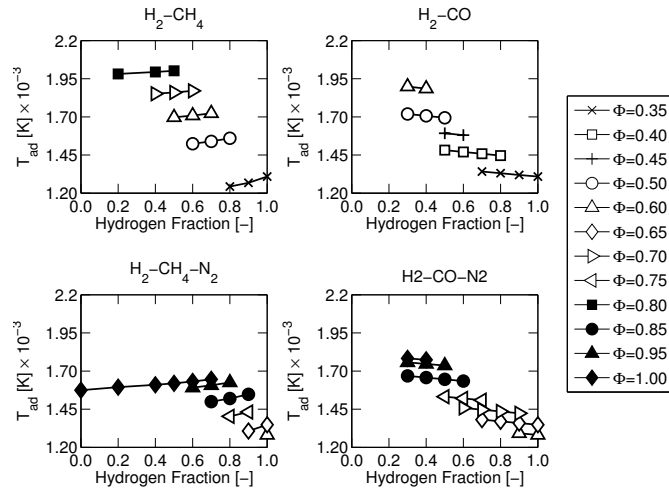


Fig. 38: Adiabatic flame temperatures for all mixtures.

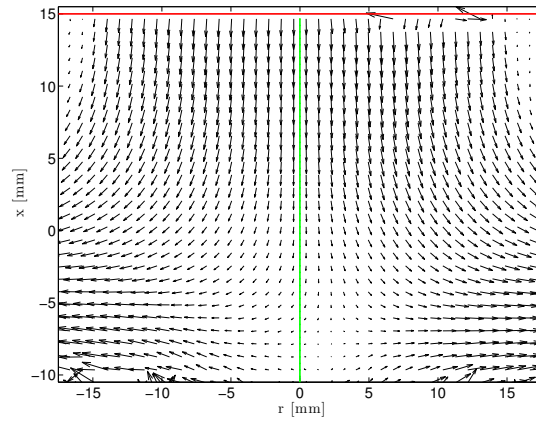


Fig. 39: Mean velocity vectors for the mixture of 80% H_2 – 20% CO at an equivalence ratio of $\Phi = 0.40$. The red and green line illustrate the location of the upper nozzle and centre axis, respectively.

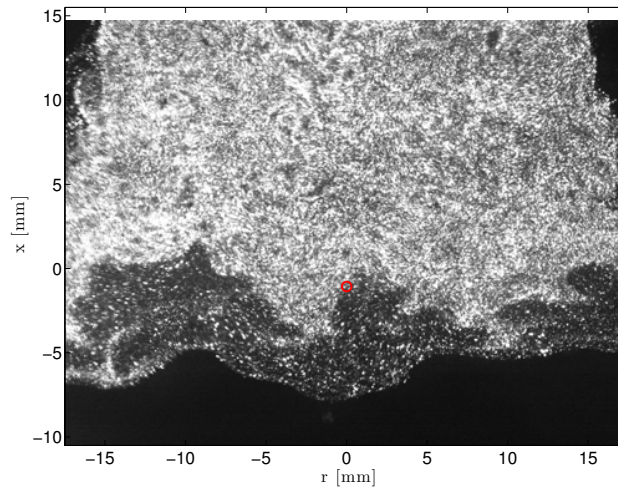


Fig. 40: Instantaneous Mie scattering image for the mixture of 80% H_2 – 20% CO at $\Phi = 0.40$. The red circle illustration the flame front on the centre axis, separating reactants above from products below.

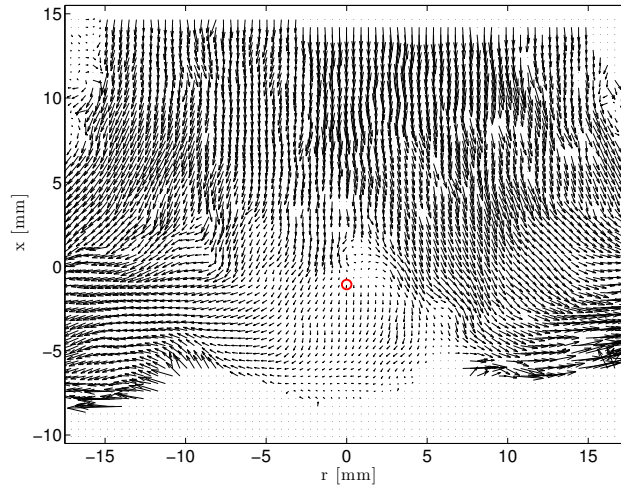


Fig. 41: Instantaneous velocity vector field for the mixture of 80% H_2 – 20% CO at $\Phi = 0.40$. The red circle illustration the flame front on the centre axis, separating reactants above from products below.

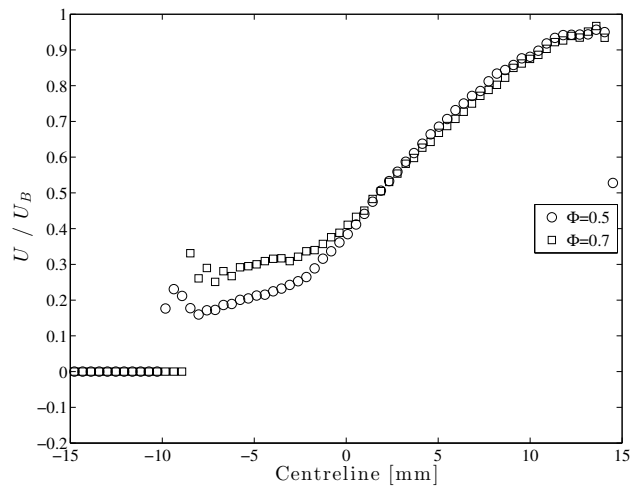


Fig. 42: Normalised axial velocity along the centreline for the mixture 60% H_2 – 40% CH_4 for different equivalence ratios.

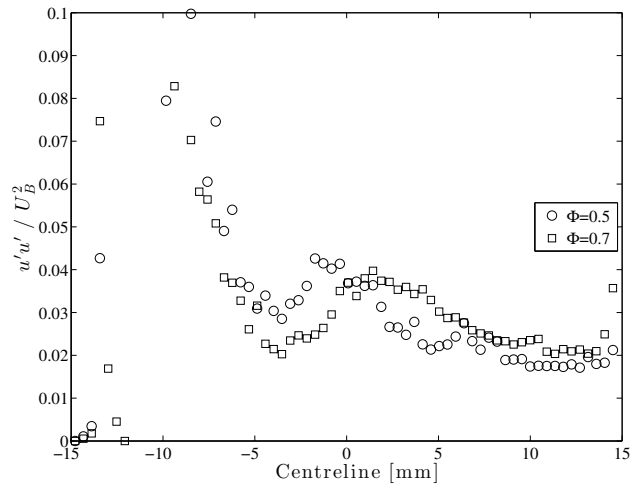


Fig. 43: Normalised axial velocity fluctuations along the centreline for the mixture 60% H_2 – 40% CH_4 for different equivalence ratios.

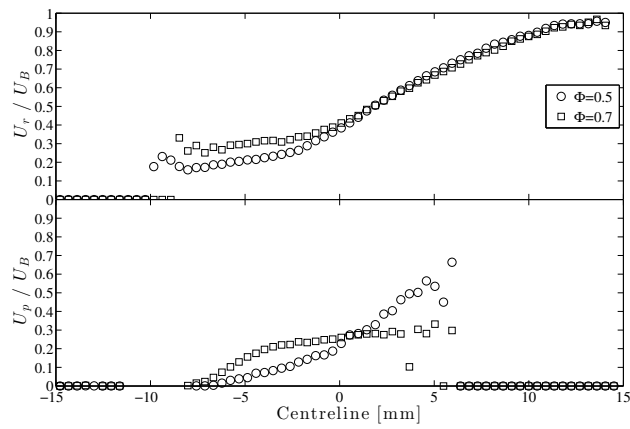


Fig. 44: Conditional normalised axial velocity along the centreline for the mixture 60% H_2 – 40% CH_4 for different equivalence ratios. Top: Reactant velocity U_r ; Bottom: Product velocity U_p .

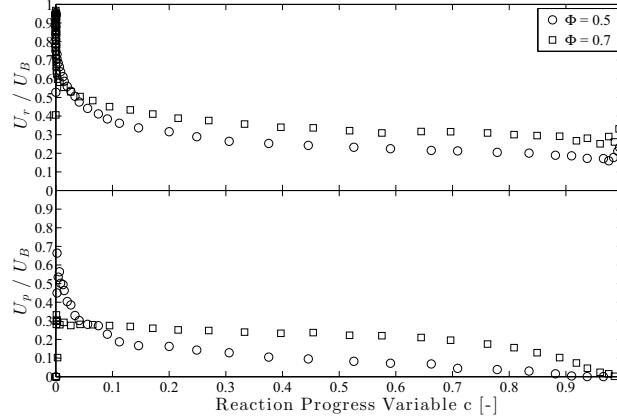


Fig. 45: Conditional normalised axial velocity as a function of reaction progress variable for the mixture 60% H_2 – 40% CH_4 for different equivalence ratios. Top: Reactant velocity U_r ; Bottom: Product velocity U_p .

In Section 3.4, the propensity to auto-ignition was evaluated for H_2 fuel blends using CH_4 and CO as fuel blending components. The lifted flame results suggest that a significant reduction in reactivity of the mixture for CH_4 blending and a modest reduction in reactivity when CO is used as fuel blending component. The observed differences in reactivity suggest the definition of a variable parameter. In contrast to the shock tube and lifted flame experiments, where the temperature was adjusted to quantify the differences in reactivity, the equivalence ratio of the gas mixture of the upper nozzle is varied in the present case. Varying the equivalence ratio has the advantage of maintaining constant flow field conditions and consequently turbulence levels for all mixtures. The equivalence ratio is accordingly adjusted between the lower limit of flame extinction and the upper limit flashback.

5.7.1 Hydrogen Blending with Methane

The principal scaling of the turbulent burning velocity rests with the velocity fluctuations, as discussed above, and not with the chemical time scale represented by the laminar burning velocity and associated transport parameters. However, results can be expected to be influenced by such parameters. The tested H_2 mixtures with increasing amounts of CH_4 are shown in Table 31. The laminar flame data for H_2/CH_4 mixtures, see Table 32, show the strong influence of CH_4 on the laminar burning velocity (S_L). At higher equivalence ratios (e.g. $\Phi = 0.8$), S_L reduces by approximately 50% for the tested mixtures. By comparison, a 10% CH_4 addition to a H_2 mixture with $\Phi = 0.35$ reduces the laminar burning velocity by $\sim 140\%$. In order to estimate the impact on turbulent deflagrations, the normalised turbulent burning velocity (S_T^*)

Tab. 31: Fuel mixtures investigated for H_2/CH_4 blends.

Mixture	Φ_{UN}	χ_{H_2}	χ_{CH_4}	χ_{CO}	χ_{N_2}	χ_{Air}
H_2 100% – <i>Air</i>	0.3500	0.1282	0.0000	0.0000	0.0000	0.8718
H_2 90% – CH_4 10%	0.3500	0.0915	0.0102	0.0000	0.0000	0.8984
H_2 80% – CH_4 20%	0.3500	0.0673	0.0168	0.0000	0.0000	0.9158
H_2 80% – CH_4 20%	0.5000	0.0929	0.0232	0.0000	0.0000	0.8839
H_2 70% – CH_4 30%	0.5000	0.0697	0.0299	0.0000	0.0000	0.9004
H_2 70% – CH_4 30%	0.6000	0.0820	0.0351	0.0000	0.0000	0.8829
H_2 60% – CH_4 40%	0.5000	0.0523	0.0349	0.0000	0.0000	0.9128
H_2 60% – CH_4 40%	0.6000	0.0617	0.0411	0.0000	0.0000	0.8972
H_2 60% – CH_4 40%	0.7000	0.0708	0.0472	0.0000	0.0000	0.8821
H_2 50% – CH_4 50%	0.6000	0.0458	0.0458	0.0000	0.0000	0.9084
H_2 50% – CH_4 50%	0.7000	0.0526	0.0526	0.0000	0.0000	0.8947
H_2 50% – CH_4 50%	0.8000	0.0593	0.0593	0.0000	0.0000	0.8815
H_2 40% – CH_4 60%	0.7000	0.0380	0.0570	0.0000	0.0000	0.9049
H_2 40% – CH_4 60%	0.8000	0.0429	0.0643	0.0000	0.0000	0.8928
H_2 20% – CH_4 80%	0.8000	0.0180	0.0720	0.0000	0.0000	0.9100
H_2 0% – CH_4 100%	0.8000	0.0000	0.0775	0.0000	0.0000	0.9225

was obtained using Eq. (14) with the Le number evaluated as shown in Eq. (15).

$$S_T^* = \frac{S_T}{S_{T,KPP}}, \text{ where } S_{T,KPP} \simeq 1.2 \sqrt{\frac{1}{e^{\sigma_{Le}-1}} \frac{1}{\sigma_{Sc}} \frac{S_L}{V_\kappa}} \cdot u' \quad (14)$$

The evaluation of the Le number in Eq. (14) is not trivial. Law et al. [100] suggested a complex formula based on the Zel'dovich number and a weighted average featuring the heat release associated with each fuel component. Subsequent work [101] showed that such correlations are not yet fully accurate. For example, hydrocarbons tend to show a linear dependency as a function of hydrogen addition, while the impact of CO is anomalous due to the strong catalytic effect on its oxidation. Hence, the simplified version given in Eq. (15) is used to estimate the impact for mixtures with CH_4 .

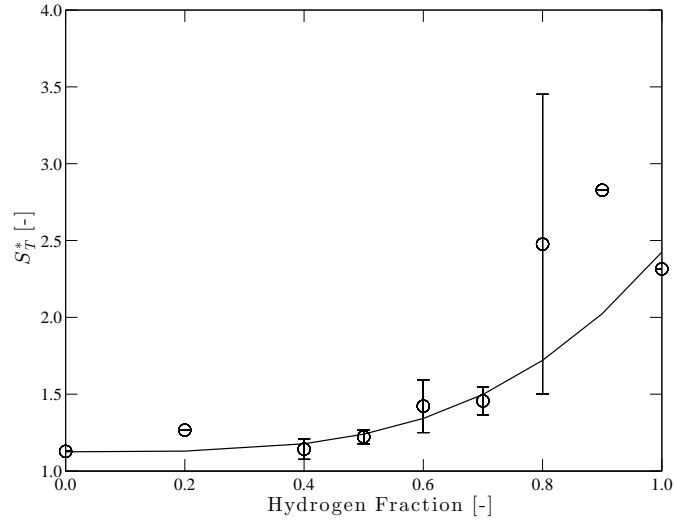
$$\sigma_{Le} = \frac{\chi_{H_2}}{\chi_{H_2} + \chi_{CH_4}} Le_{H_2} + \frac{\chi_{CH_4}}{\chi_{H_2} + \chi_{CH_4}} Le_{CH_4} \quad (15)$$

The expression assumes that the deficient reactant is formed by the dominant fuel component. The results are given in Table 32 and in Fig. 46 for the H_2/CH_4 fuel blends. As the amount of CH_4 is increased, a higher equivalence ratio is required to stabilise a self propagating flame. For the pure $H_2 - Air$ mixture, a flame was stabilised at an equivalence ratio of $\Phi = 0.35$ with the upper limit determined such as to avoid flashback. A CH_4 blending of merely 20% resulted in a significant decrease in reactivity, which is reflected by the increase the equivalence ratio to $\Phi = 0.50$. A 50% blending with CH_4 allowed an increase in equivalence ratio up to $\Phi = 0.80$ demonstrating the strong impact of CH_4 addition on the mixture reactivity. It is evident that the addition of small quantities of CH_4 , i.e. 10 – 20% CH_4 , have a strong impact on the mixture reactivity. However, some caution is required as the current scaling departs appreciably

Tab. 32: Results obtained for H_2/CH_4 fuel mixtures where S_T^* is the scaled value given by Eq. (14).

Mixture	Φ_{UN} [-]	S_L [m/s]	σ_{Le} [-]	u' [m/s]	S_T [m/s]	S_T^* [-]
H_2 100% – Air	0.35	0.0832	0.3739	1.5527	3.3320	2.3150
H_2 90% – CH_4 10% – Air	0.35	0.0346	0.4379	1.5281	2.6376	2.8274
H_2 80% – CH_4 20% – Air	0.35	0.0177	0.5002	1.7264	2.3289	3.4510
H_2 80% – CH_4 20% – Air	0.50	0.2341	0.5271	1.6830	3.3583	1.5017
H_2 70% – CH_4 30% – Air	0.50	0.1336	0.5848	1.6173	2.7990	1.5453
H_2 70% – CH_4 30% – Air	0.60	0.2611	0.5996	1.6105	3.2696	1.3663
H_2 60% – CH_4 40% – Air	0.50	0.1065	0.6411	1.6680	2.5009	1.6562
H_2 60% – CH_4 40% – Air	0.60	0.2135	0.6540	1.6882	2.7389	1.3656
H_2 60% – CH_4 40% – Air	0.70	0.3340	0.6662	1.8025	3.5850	1.2460
H_2 50% – CH_4 50% – Air	0.60	0.1823	0.7073	1.6684	2.4098	1.2557
H_2 50% – CH_4 50% – Air	0.70	0.2875	0.7174	1.6615	3.0387	1.2509
H_2 50% – CH_4 50% – Air	0.80	0.3925	0.7271	1.6473	3.2926	1.1593
H_2 40% – CH_4 60% – Air	0.70	0.2548	0.7677	1.7107	2.7997	1.2089
H_2 40% – CH_4 60% – Air	0.80	0.3488	0.7752	1.7376	3.0310	1.0756
H_2 20% – CH_4 80% – Air	0.80	0.2921	0.8693	1.7348	2.8165	1.2662
H_2 0% – CH_4 100% – Air	0.80	0.2578	0.9624	1.6873	2.3406	1.1276

from a linear relationship for H_2 contents $\geq 60\%$. The use of such H_2 contents is not recommended in the current context in light of the increased propensity to auto-ignition and the corresponding reduction in the ignition delay time as discussed above. It should also be noted that the derivation of the expression given in Eq. (14) assumes the existence of a "flamelet related" burning mode. For very lean cases it can be expected this assumption becomes less reliable.

Fig. 46: Normalised turbulent burning velocity for H_2/CH_4 mixtures.

Tab. 33: Fuel mixtures investigated for H_2/CO blends.

Mixture	Φ_{UN}	χ_{H_2}	χ_{CH_4}	χ_{CO}	χ_{N_2}	χ_{Air}
H_2 100% – Air	0.3500	0.1282	0.0000	0.0000	0.0000	0.8718
H_2 90% – CO 10% – Air	0.3500	0.1154	0.0000	0.0128	0.0000	0.8718
H_2 80% – CO 20% – Air	0.3500	0.1026	0.0000	0.0256	0.0000	0.8718
H_2 80% – CO 20% – Air	0.4000	0.1151	0.0000	0.0288	0.0000	0.8561
H_2 70% – CO 30% – Air	0.3500	0.0897	0.0000	0.0385	0.0000	0.8718
H_2 70% – CO 30% – Air	0.4000	0.1007	0.0000	0.0432	0.0000	0.8561
H_2 60% – CO 40% – Air	0.4000	0.0863	0.0000	0.0576	0.0000	0.8561
H_2 60% – CO 40% – Air	0.4500	0.0954	0.0000	0.0636	0.0000	0.8410
H_2 50% – CO 50% – Air	0.4000	0.0719	0.0000	0.0719	0.0000	0.8561
H_2 50% – CO 50% – Air	0.4500	0.0795	0.0000	0.0795	0.0000	0.8410
H_2 50% – CO 50% – Air	0.5000	0.0868	0.0000	0.0868	0.0000	0.8264
H_2 40% – CO 60% – Air	0.5000	0.0694	0.0000	0.1042	0.0000	0.8264
H_2 40% – CO 60% – Air	0.6000	0.0805	0.0000	0.1208	0.0000	0.7987
H_2 30% – CO 70% – Air	0.5000	0.0521	0.0000	0.1215	0.0000	0.8264
H_2 30% – CO 70% – Air	0.6000	0.0604	0.0000	0.1409	0.0000	0.7987

5.7.2 Hydrogen Blending with Carbon Monoxide

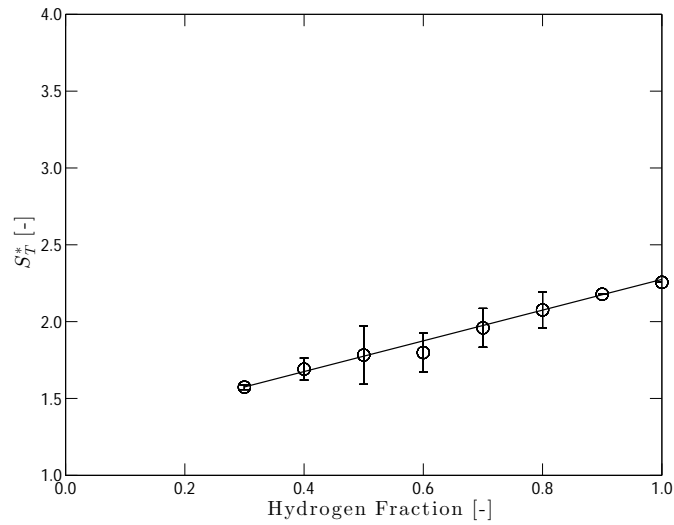
The mixtures featuring H_2 and CO include hydrogen concentrations down to a mixture of 30% H_2 – 70% CO as listed in Table 33. Experimental results for the turbulent burning velocities and velocity fluctuations are given in Table 34 along with results obtained from laminar flame calculations and the normalised turbulent burning velocity S_T^* . The expression used to derive the Le number for CO blends follows directly by replacing the CH_4 parameters in Eq. (15).

$$\sigma_{Le} = \frac{\chi_{H_2}}{\chi_{H_2} + \chi_{CO}} Le_{H_2} + \frac{\chi_{CO}}{\chi_{H_2} + \chi_{CO}} Le_{CO} \quad (16)$$

The determined values for the laminar burning velocity (S_L) suggest that the effect of CO blending is much less pronounced than for CH_4 addition. An substitution of 10% and 20% of H_2 with CO reduces the laminar burning velocity by $\sim 6\%$ and $\sim 10\%$, while same CH_4 blending factor lead to a reduction of $\sim 59\%$ and $\sim 79\%$. At higher blending fractions, i.e. $CO \geq 50\%$, the effect of CO addition causes a moderate change as S_L decreases by $\sim 11\%$ and $\sim 21\%$ from the case 50% H_2 – 50% CO , via 40% H_2 – 60% CO and 30% H_2 – 70% CO at $\Phi = 0.50$. The results for S_T^* are shown in Fig. 47. As shown in the auto-ignition experiments, see Section 3, and as is evident from Fig. 47, the blending with CO exhibits a significantly different effect on the mixture reactivity as compared to CH_4 addition. While the substitution of small quantities H_2 with CH_4 has a strong effect on the mixture reactivity, the influence of CO blending is much less profound. This is also readily apparent by a comparison of Figs. 46 and 47. While the addition of CH_4 exhibits a good correlation for H_2 contents $\leq 60\%$, blending with CO shows an offset followed by an approximately linear deviation from the theoretical value ($S_{T,KPP}$).

Tab. 34: Results obtained for H_2/CO fuel mixtures where S_T^* is the scaled value given by Eq. (14).

Mixture	Φ_{UN} [-]	S_L [m/s]	σ_{Le} [-]	u' [m/s]	S_T [m/s]	S_T^* [-]
H_2 100% – Air	0.35	0.0834	0.3739	1.5997	3.1171	2.2558
H_2 90% – CO 10% – Air	0.35	0.0786	0.4674	1.5549	3.0283	2.1786
H_2 80% – CO 20% – Air	0.35	0.0747	0.5544	1.5929	2.8417	2.1926
H_2 80% – CO 20% – Air	0.40	0.1525	0.5673	1.5086	3.4774	1.9594
H_2 70% – CO 30% – Air	0.35	0.0711	0.6349	1.6013	2.6486	2.0857
H_2 70% – CO 30% – Air	0.40	0.1404	0.6483	1.7200	3.1389	1.8332
H_2 60% – CO 40% – Air	0.40	0.1296	0.7219	1.6095	2.9213	1.9248
H_2 60% – CO 40% – Air	0.45	0.2052	0.7344	1.6443	3.2652	1.6724
H_2 50% – CO 50% – Air	0.40	0.1194	0.7881	1.8083	3.1261	2.0379
H_2 50% – CO 50% – Air	0.45	0.1861	0.7995	1.8262	3.4345	1.7291
H_2 50% – CO 50% – Air	0.50	0.2619	0.8105	1.7347	3.4894	1.5804
H_2 40% – CO 60% – Air	0.50	0.2337	0.8655	1.5848	3.4615	1.7630
H_2 40% – CO 60% – Air	0.60	0.3790	0.8828	1.5299	3.8388	1.6197
H_2 30% – CO 70% – Air	0.50	0.2059	0.9113	1.7794	3.0418	1.5897
H_2 30% – CO 70% – Air	0.60	0.3286	0.9238	1.5343	3.1376	1.5580

Fig. 47: Normalised turbulent burning velocity for H_2/CO mixtures.

5.7.3 Hydrogen Blending with Methane and Nitrogen Dilution

The effect of N_2 dilution on $H_2 - CH_4$ mixtures was also investigated following the same detailed operation procedure as described in Section 3. The mixtures tested are listed in Table 35 and Table 36 summarises the results obtained from laminar flame calculations and the experimental study. As shown in Table 36,

Tab. 35: Fuel mixtures investigated for H_2/CH_4 blends with N_2 dilution.

Mixture	Φ_{UN}	χ_{H_2}	χ_{CH_4}	χ_{CO}	χ_{N_2}	χ_{Air}
H_2 100% - N_2 - <i>Air</i>	0.6000	0.1235	0.0000	0.0000	0.3868	0.4897
H_2 100% - N_2 - <i>Air</i>	0.6500	0.1324	0.0000	0.0000	0.3829	0.4847
H_2 90% - CH_4 10% - N_2 - <i>Air</i>	0.6500	0.0945	0.0105	0.0000	0.3950	0.5000
H_2 90% - CH_4 10% - N_2 - <i>Air</i>	0.7500	0.1073	0.0119	0.0000	0.3887	0.4920
H_2 90% - CH_4 10% - N_2 - <i>Air</i>	0.8500	0.1198	0.0133	0.0000	0.3826	0.4843
H_2 80% - CH_4 20% - N_2 - <i>Air</i>	0.7500	0.0793	0.0198	0.0000	0.3976	0.5033
H_2 80% - CH_4 20% - N_2 - <i>Air</i>	0.8500	0.0887	0.0222	0.0000	0.3924	0.4967
H_2 80% - CH_4 20% - N_2 - <i>Air</i>	0.9500	0.0979	0.0245	0.0000	0.3873	0.4903
H_2 70% - CH_4 30% - N_2 - <i>Air</i>	0.8500	0.0665	0.0285	0.0000	0.3994	0.5056
H_2 70% - CH_4 30% - N_2 - <i>Air</i>	0.9500	0.0735	0.0315	0.0000	0.3950	0.5000
H_2 70% - CH_4 30% - N_2 - <i>Air</i>	1.0000	0.0770	0.0330	0.0000	0.3928	0.4973
H_2 60% - CH_4 40% - N_2 - <i>Air</i>	0.9500	0.0552	0.0368	0.0000	0.4007	0.5073
H_2 60% - CH_4 40% - N_2 - <i>Air</i>	1.0000	0.0578	0.0386	0.0000	0.3988	0.5048
H_2 50% - CH_4 50% - N_2 - <i>Air</i>	1.0000	0.0429	0.0429	0.0000	0.4034	0.5107

Tab. 36: Results obtained for $H_2/CH_4/N_2$ fuel mixtures where S_T^* is the scaled value given by Eq. (14).

Mixture	Φ_{UN} [-]	S_L [m/s]	σ_{Le} [-]	w' [m/s]	S_T [m/s]	S_T^* [-]
H_2 100% - N_2 - <i>Air</i>	0.60	0.0719	0.3734	1.5850	2.7978	1.9927
H_2 100% - N_2 - <i>Air</i>	0.65	0.1161	0.3789	1.5424	3.0307	1.7828
H_2 90% - CH_4 10% - N_2 - <i>Air</i>	0.65	0.0491	0.4438	1.6317	2.0931	1.8574
H_2 90% - CH_4 10% - N_2 - <i>Air</i>	0.75	0.1040	0.4547	1.6003	2.4682	1.4769
H_2 90% - CH_4 10% - N_2 - <i>Air</i>	0.85	0.1688	0.4649	1.6073	2.6139	1.2617
H_2 80% - CH_4 20% - N_2 - <i>Air</i>	0.75	0.0614	0.5159	1.6605	2.1120	1.6079
H_2 80% - CH_4 20% - N_2 - <i>Air</i>	0.85	0.1020	0.5257	1.5897	2.0784	1.3449
H_2 80% - CH_4 20% - N_2 - <i>Air</i>	0.95	0.1439	0.5350	1.6376	2.2298	1.1478
H_2 70% - CH_4 30% - N_2 - <i>Air</i>	0.85	0.0710	0.5840	1.8270	1.7691	1.2955
H_2 70% - CH_4 30% - N_2 - <i>Air</i>	0.95	0.0992	0.5926	1.7162	2.0870	1.3379
H_2 70% - CH_4 30% - N_2 - <i>Air</i>	1.00	0.1118	0.5967	1.6747	2.1875	1.3717
H_2 60% - CH_4 40% - N_2 - <i>Air</i>	0.95	0.0756	0.6485	1.7237	1.8820	1.3750
H_2 60% - CH_4 40% - N_2 - <i>Air</i>	1.00	0.0843	0.6521	1.6907	2.0362	1.4774
H_2 50% - CH_4 50% - N_2 - <i>Air</i>	1.00	0.0680	0.7066	1.9137	2.0572	1.5750

the dilution with N_2 necessitates a significant increase in equivalence ratio to achieve flame stabilisation. For H_2 concentrations below 50% flames appeared to be on the borderline of a flameless combustion mode and results are hence excluded. For the case of a pure H_2 -air mixture, the N_2 dilution requires an increase in equivalence ratio from $\Phi = 0.35$ to $\Phi = 0.65$. The N_2 dilution effect is significant throughout the entire mixture matrix. Stoichiometric conditions could be achieved for the mixture of 70% H_2 - 30% CH_4 while the highest realisable equivalence ratio without N_2 was found to be $\Phi = 0.60$ prior to flashback.

The determined values for the laminar burning velocity also reveal, despite the increase in equivalence ratio, the significant reduction in mixture reactivity when N_2 added. The normalised turbulent burning velocities for this data set are shown in Fig. 48. Low H_2 concentrations, i.e. H_2 fuel fraction smaller

than 50%, show acceptable agreement with the theoretical correlation for the mixture reactivity under the evaluated conditions. Furthermore, it is evident that the addition of small quantities of CH_4 again has a strong impact on the reduction in mixture reactivity. For H_2 fuel fractions $\geq 80\%$ the mixture reactivity shows a similar behaviour to that observed in the non-diluted case. Overall, it is evident that there is a significant impact of dilution on the strength of the turbulent deflagration. It is also of relevance to note that the theoretical correlation appears to work well for a significant range of H_2/CH_4 mixtures.

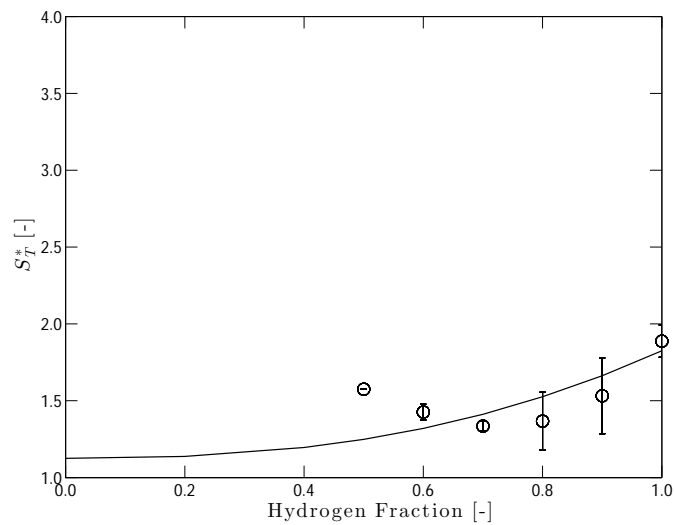


Fig. 48: Normalised turbulent burning velocity for $H_2/CH_4/N_2$ mixtures.

5.7.4 Hydrogen Blending with Carbon Monoxide and Nitrogen Dilution

The impact of N_2 dilution on the reactivity of H_2/CO fuel blends was also investigated using the same methodology as for the $H_2/CH_4/N_2$ case. The investigated mixture compositions are listed in Table 37 and the results obtained from the corresponding laminar flame calculations, the raw experimental data and the normalised turbulent burning velocity are summarised in Table 38. As the equivalence ratio was varied to obtain a self propagating flame for each mixture, it was found that the stoichiometric range varies from $\Phi = 0.6 \dots 1.0$ as was the case of $H_2/CH_4/N_2$ blends. However, while in the case of $H_2/CH_4/N_2$ stoichiometric conditions could be used at a blending fraction of 70% H_2 , the corresponding H_2 content with a CO blend was reduced to 40%. Again, the higher reactivity of CO mixtures is readily evident.

The normalised burning velocities for the diluted $H_2/CO/N_2$ mixtures are

Tab. 37: Fuel mixtures investigated for H_2/CO blends with N_2 dilution.

Mixture	Φ_{UN}	χ_{H_2}	χ_{CH_4}	χ_{CO}	χ_{N_2}	χ_{Air}
H_2 100% - N_2 - <i>Air</i>	0.6000	0.1235	0.0000	0.0000	0.3868	0.4897
H_2 100% - N_2 - <i>Air</i>	0.6500	0.1324	0.0000	0.0000	0.3829	0.4847
H_2 90% - CO 10% - N_2 - <i>Air</i>	0.6000	0.1111	0.0000	0.0123	0.3868	0.4897
H_2 90% - CO 10% - N_2 - <i>Air</i>	0.6500	0.1191	0.0000	0.0132	0.3829	0.4847
H_2 90% - CO 10% - N_2 - <i>Air</i>	0.7000	0.1270	0.0000	0.0141	0.3790	0.4798
H_2 80% - CO 20% - N_2 - <i>Air</i>	0.6500	0.1059	0.0000	0.0265	0.3829	0.4847
H_2 80% - CO 20% - N_2 - <i>Air</i>	0.7000	0.1129	0.0000	0.0282	0.3790	0.4798
H_2 70% - CO 30% - N_2 - <i>Air</i>	0.6500	0.0927	0.0000	0.0397	0.3829	0.4847
H_2 70% - CO 30% - N_2 - <i>Air</i>	0.7000	0.0988	0.0000	0.0423	0.3790	0.4798
H_2 70% - CO 30% - N_2 - <i>Air</i>	0.7500	0.1048	0.0000	0.0449	0.3752	0.4750
H_2 60% - CO 40% - N_2 - <i>Air</i>	0.7000	0.0847	0.0000	0.0565	0.3790	0.4798
H_2 60% - CO 40% - N_2 - <i>Air</i>	0.7500	0.0898	0.0000	0.0599	0.3752	0.4750
H_2 60% - CO 40% - N_2 - <i>Air</i>	0.8500	0.0998	0.0000	0.0665	0.3679	0.4658
H_2 50% - CO 50% - N_2 - <i>Air</i>	0.7500	0.0749	0.0000	0.0749	0.3752	0.4750
H_2 50% - CO 50% - N_2 - <i>Air</i>	0.8500	0.0832	0.0000	0.0832	0.3679	0.4658
H_2 50% - CO 50% - N_2 - <i>Air</i>	0.9500	0.0912	0.0000	0.0912	0.3608	0.4568
H_2 40% - CO 60% - N_2 - <i>Air</i>	0.8500	0.0665	0.0000	0.0998	0.3679	0.4658
H_2 40% - CO 60% - N_2 - <i>Air</i>	0.9500	0.0729	0.0000	0.1094	0.3608	0.4568
H_2 40% - CO 60% - N_2 - <i>Air</i>	1.0000	0.0760	0.0000	0.1141	0.3574	0.4525
H_2 30% - CO 70% - N_2 - <i>Air</i>	0.8500	0.0499	0.0000	0.1164	0.3679	0.4658
H_2 30% - CO 70% - N_2 - <i>Air</i>	0.9500	0.0547	0.0000	0.1276	0.3608	0.4568
H_2 30% - CO 70% - N_2 - <i>Air</i>	1.0000	0.0570	0.0000	0.1331	0.3574	0.4525

Tab. 38: Results obtained for $H_2/CO/N_2$ fuel mixtures where S_T^* is the scaled value given by Eq. (14).

Mixture	Φ_{UN} [-]	S_L [m/s]	σ_{Le} [-]	u' [m/s]	S_T [m/s]	S_T^* [-]
H_2 100% - N_2 - <i>Air</i>	0.60	0.0719	0.3734	1.5850	2.7978	1.9927
H_2 100% - N_2 - <i>Air</i>	0.65	0.1161	0.3789	1.5424	3.0307	1.7828
H_2 90% - CO 10% - N_2 - <i>Air</i>	0.60	0.0686	0.4664	1.5470	2.3424	1.9404
H_2 90% - CO 10% - N_2 - <i>Air</i>	0.65	0.1083	0.4731	1.5140	2.8632	1.9301
H_2 90% - CO 10% - N_2 - <i>Air</i>	0.70	0.1549	0.4795	1.6592	3.1326	1.6244
H_2 80% - CO 20% - N_2 - <i>Air</i>	0.65	0.1015	0.5608	1.6855	2.6695	1.8961
H_2 80% - CO 20% - N_2 - <i>Air</i>	0.70	0.1431	0.5679	1.6133	3.0965	1.8565
H_2 70% - CO 30% - N_2 - <i>Air</i>	0.65	0.0953	0.6417	1.6718	2.9054	2.0199
H_2 70% - CO 30% - N_2 - <i>Air</i>	0.70	0.1327	0.6491	1.6291	2.9956	1.7219
H_2 70% - CO 30% - N_2 - <i>Air</i>	0.75	0.1747	0.6563	1.6409	3.2496	1.6479
H_2 60% - CO 40% - N_2 - <i>Air</i>	0.70	0.1230	0.7231	1.7401	2.7054	1.6557
H_2 60% - CO 40% - N_2 - <i>Air</i>	0.75	0.1604	0.7302	1.6944	2.4990	1.2960
H_2 60% - CO 40% - N_2 - <i>Air</i>	0.85	0.2450	0.7439	1.5659	2.6554	1.2652
H_2 50% - CO 50% - N_2 - <i>Air</i>	0.75	0.1470	0.7964	1.5847	2.3589	1.4858
H_2 50% - CO 50% - N_2 - <i>Air</i>	0.85	0.2213	0.8089	1.6007	2.6552	1.3654
H_2 50% - CO 50% - N_2 - <i>Air</i>	0.95	0.3021	0.8209	1.4754	2.9236	1.3245
H_2 40% - CO 60% - N_2 - <i>Air</i>	0.85	0.1986	0.8652	1.5518	2.4051	1.3765
H_2 40% - CO 60% - N_2 - <i>Air</i>	0.95	0.2682	0.8753	1.5405	2.6204	1.2799
H_2 40% - CO 60% - N_2 - <i>Air</i>	1.00	0.3031	0.8802	1.3149	2.5808	1.3402
H_2 30% - CO 70% - N_2 - <i>Air</i>	0.85	0.1756	0.9127	1.5956	2.2729	1.3002
H_2 30% - CO 70% - N_2 - <i>Air</i>	0.95	0.2345	0.9200	1.5329	2.3325	1.1943
H_2 30% - CO 70% - N_2 - <i>Air</i>	1.00	0.2639	0.9236	1.5296	2.5388	1.2345

shown in Fig. 49. It can again be observed that the normalised values (S_T^*) imply an approximately linear deviation from the theoretical values as a function of the hydrogen fuel blending fraction as also observed for the non-diluted counterpart. The absolute value of the normalised turbulent burning velocity is also slightly reduced throughout the whole range. It is again apparent that the CO system shows an anomaly that can possibly be related to the catalytic effect [101] of hydrogen on blends with carbon monoxide. Such a conclusion can also be drawn from the purely kinetic shock tube experiments used to determine ignition delay times by Stanford University as reported in Section 2.

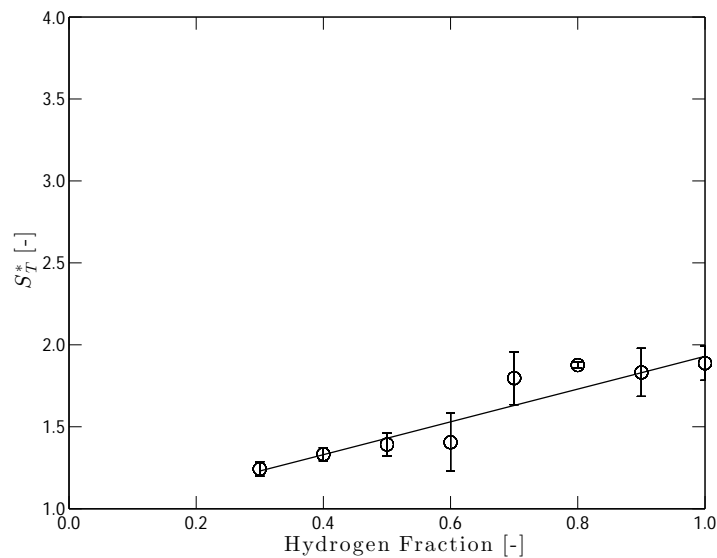


Fig. 49: Normalised turbulent burning velocity for $H_2/CO/N_2$ mixtures.

6 The Potential of DDT via Turbulence Induced Confined Explosions

The objective of the experimental flame tube investigation is to measure the propensity to deflagration to detonation transition (DDT) as characterised by over-pressures and flame speeds for binary fuel blends of H_2/CH_4 and H_2/CO . The findings are also related to the strengths of the turbulent deflagrations as characterised by the turbulent burning velocity discussed in Section 5 and the ignition propensity determined in Sections 2 and 3. The data is reported in absolute terms as well as relative to the case of methane-air mixtures in the absence of hydrogen addition. The latter was added to the study to provide a reference point to the common operation of CCGT and CCGE plant.

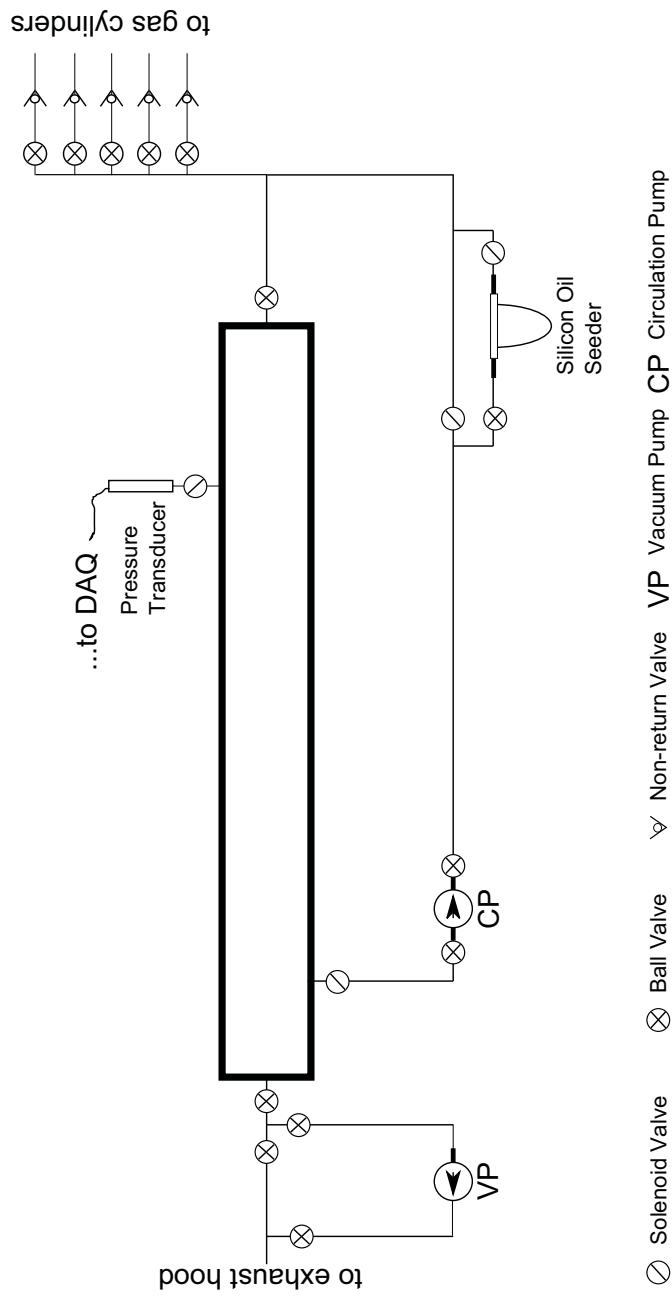


Fig. 50: Schematic of experimental facility

6.1 Experimental Setup

The section below describes the instrumentation and experimental procedure used for the determination of flame induced pressures and flow velocities in an investigation of confined explosions in binary H_2/CH_4 and H_2/CO fuel blends.

6.1.1 The Flame Tube

The present study is focussed on flame-obstacle interactions in an initially quiescent medium with turbulence developing as the result of advancing flame fronts interacting with obstacles. The obstacle configuration was chosen on the basis of earlier studies [48, 50] considering single and multiple obstacles in order to ensure significant (≥ 150 kPa) over-pressures and flame speeds (≥ 200 m/s) for the least reactive cases. A schematic of the experimental facility is shown in Figure 50. The setup consist of a closed flame tube made of two interchangeable rectangular sections (72 mm x 34 mm) of length 1.825 m and two optical sections 0.385 m in length. The flame tube is equipped with four solenoid valves, an absolute pressure transducer, vacuum and recirculation pumps and five mass flow controllers that allow remote operation. The flame tube has ports along the top and bottom of the first window section and along the sides of the longer flame tube sections. The ports can be used for either flame speed measurements, using ionisation probes, or pressure transducer measurements. The applied locations and corresponding measurement taken from each port are shown in Table 39, while the port positions together with the position of the two baffle configuration used in the current study can be seen in Fig. 51. The first obstacle was mounted on the top of the tube at a distance of 120 mm from the closed ignition end, while the second was mounted on the bottom of the tube 402.5 mm from the same end. The current staggered obstacle arrangement was used to encourage flow curvature. Each obstacle provides 50 % blockage ratio, i.e. reducing the tube height from 72 mm down to 36 mm. The width of each obstacle was 5 mm. The large length/height ratio (= 60) of the flame tube allows the investigation of flame-obstacle interactions without the interference of acoustic waves reflected off the non-ignition end plate.

6.1.2 Gas Preparation and Mixing Procedure

The nature of the present investigation required the preparation of homogeneous gas mixtures of known composition to generate reproducible data. The method of partial pressure mixing provides high accuracy and has been used in the past (e.g. Lindstedt and Sakthitharan [50]) for the current flame tube. Hence, this method was used in the current work to prepare gas mixture of various equivalence ratios using the flame tube as the mixing chamber.

For each experiment the flame tube was evacuated to a pressure below 0.5 kPa using a vacuum pump (RZ6, Vacuubrand) and the required proportions of fuel(-s) and air for the desired target pressure were calculated using the partial pressure method. The pressure was monitored by a pressure transducer (model

UNIK 5000, GE Measurement & Control) interfaced to a computer via a 16-bit data acquisition card (PCIe-7842R, National Instruments) and LABVIEW software. Starting with the fuel(-s) and with air the final component, the reactants were fed into the flame tube using a purpose written LABVIEW routine that controls each fuel/gas mass flow controller individually.

The fuel-air mixture was subsequently circulated in a closed loop using an explosion proof pump (MD 4C EX, Vacuubrand) for 5 min - the equivalent of 28 flame tube volumes to ensure mixture homogeneity. The circulation time adopted in this study was based on the investigation of Sakthitharan [48] which showed that the displacement of 25 flow tube volumes produced consistently repeatable results. Moreover, both the accuracy in the equivalence ratio, as well as the mixture homogeneity, were validated by means of comparing the over-pressure and pressure rise times observed for a stoichiometric methane-air mixture with previous studies concerned with similar obstacle configurations [48, 49, 50].

Tab. 39: Ports Locations and Fitted Devices

Probe	Distance (m)	Position	Type
<i>P1</i>	0.03	Top	–
<i>P2</i>	0.03	Bottom	–
<i>P3</i>	0.12	Top	–
<i>P4</i>	0.12	Bottom	–
<i>P5</i>	0.23	Top	–
<i>P6</i>	0.23	Bottom	–
<i>P7</i>	0.885	Side	Pressure Transducer
<i>P8</i>	0.885	Side	Ionisation Probe
<i>P9</i>	1.115	Side	–
<i>P10</i>	1.115	Side	Ionisation Probe
<i>P11</i>	1.345	Side	Pressure Transducer
<i>P12</i>	1.345	Side	Ionisation Probe
<i>P13</i>	1.575	Side	–
<i>P14</i>	1.575	Side	Ionisation Probe
<i>P15</i>	1.805	Side	–
<i>P16</i>	1.805	Side	Ionisation Probe
<i>P17</i>	2.035	Side	–
<i>P18</i>	2.035	Side	Ionisation Probe
<i>P19</i>	2.035	Side	–
<i>P20</i>	2.035	Side	–
<i>P21</i>	2.265	Side	Pressure Transducer
<i>P22</i>	2.265	Side	–
<i>P23</i>	3.180	Side	Pressure Transducer

6.1.3 The Ignition System

The ignition system used in the current work consisted of a 12V power supply; an inductance coil (Lucas coil); a purpose build capacitive ignition device; a custom made spark plug and electrode arrangement (spark gap distance 10 mm). The ignition was initiated by a TTL pulse, sent from the PC via a selected counter output port of the data acquisition card (PCI-6115, National Instruments). It

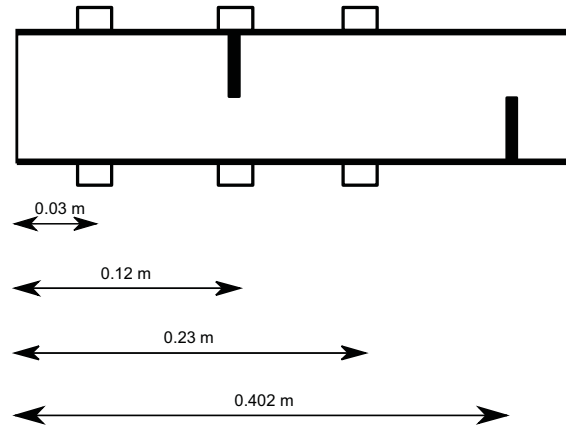


Fig. 51: Schematic of the ignition end of the flame tube showing the applied obstacle configuration and positions of ports.

should also be noted that before ignition, the fuel-air mixture was left to settle for two minutes to achieve quiescent condition.

6.2 Basic Instrumentation

The basic instrumentation included 4 piezo electric pressure transducers and six coaxial ionisation probes located at various ports along the flame tube, as shown in Table 39, in order to record the propagation wave. The piezo-electric pressure transducers (3xPCB-113B21 and 1xPCB-113A21; PCB Piezotronics Inc.) were used due to their proven durability under highly reactive conditions as shown in previous investigations (e.g. [50]). The transducers have a sensitivity of 3.6 mV/kPa (113B21) and 2.9 mV/kPa (113A21), a resonant frequency of 500 kHz and a rise time of 1 ns. A silicone rubber insulating coating was applied on the surface of the transducer to protect it from thermal variations during the combustion event [48]. The pressure records were interfaced to the PC via a 12-bit simultaneous sampling data acquisition card (PCI-6115, National Instruments) at a rate of 1 MHz after conditioning using a four-channel signal conditioner (PCB 482C05; PCB Piezotronics Inc).

The ionisation probes serve as flame detection devices providing information on the combustion wave propagation process. The probes were made of coaxial stainless steel and connected in parallel with an oscilloscope and a 9V alkaline battery. The positive ions in the reaction region induce a current flow between the core and the sheath of the probe triggering a fall of the open circuit voltage. The design has been used extensively in the past and found to operate reliably [50, 92, 93].

The data acquisition devices, as well as ignition, were triggered using TTL pulses generated from the PCI-6115 counters ensuring the synchronisation of events - the time delay between each pulse is less than 100 ns. A diagram of the routine used for the synchronisation of the different diagnostic systems can be seen in Fig. 52.

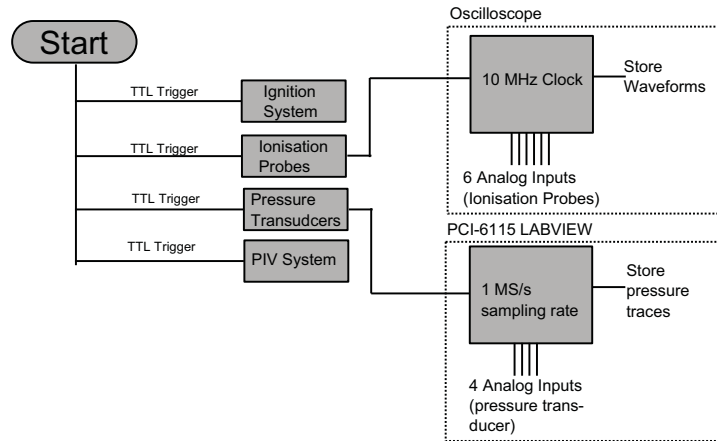


Fig. 52: Diagram of the routine used for the synchronisation of different diagnostic systems.

6.2.1 High Speed Particle Image Velocimetry

A high speed PIV setup controlled using LaVision software Davis High Speed 8.0 was used to obtain flow velocities. An external high speed programmable timing unit (PTU) from LaVision was used to control the timing and synchronisation of the high speed laser and camera. An Edgewave INNOSLAB Nd:YAG laser with a wavelength of 532 nm, pulse length of 10 ns and a pulse energy of 4 mJ at a maximum repetition rate of 10 kHz was used. The high speed camera, Photron Fastcam SA3, features a maximum repetition rate of 1000 double frame images per second at full resolution of 1024×1024 pixels with an increased rate at lower resolution. A 105 mm Nikkor camera lens was used with a 3 nm narrow bandwidth filter for a wavelength 532 nm installed to increase the signal to noise ratio and filter out any other sources of light (e.g. chemiluminescence). The optical setup consist of:

- Four mirrors to direct and make the laser beam parallel.
- A set of convex and concave spherical lenses with a focal length of +200 and -100 mm to reduce the beam diameter.
- Light sheet forming optics from LaVision. The light sheet optics features

an adjustable focus from 0.3 m to 2 m using a cylindrical lens with a focus length of -20 mm.

Part of optical setup, as well as the optical section, is shown in Fig. 53. The field of view was set to 65.85 mm \times 65.85 mm. The light sheet was directed vertically from the top into the optical section of the flame tube. The light sheet illuminates the particle laden flow and a silicon oil seeder from Palas was installed. The seeding was introduced along with the flow through the inlet pipe. The flow field is viewed through a quartz glass window using the high speed camera which is installed at a 90 degree angle to the light sheet. The glass window was mounted shortly after the second obstacle.



Fig. 53: Optical section of the flame tube along with the optical setup (final three mirrors, telescope and light sheet optics).

The recording rate was set to 3 kHz featuring a resolution of 512×512 pixels. Hence, the timing between two double frame is fixed to 0.33 ms. The timing between the double laser pulses was found to be optimum at $\Delta t = 20$ μ s. Subsequent to the data acquisition, a dark image subtraction was performed to enhance the signal to noise ratio.

The PIV vectors were calculated using a multipass cross-correlation with decreasing interrogation window size starting from 128×128 , via 64×64 down to 32×32 pixels. A 50% overlap of the interrogation windows lead to a vector spacing of 2.06 mm.

6.3 Operational Procedure

A flow control system, detailed in Section 6.3.1, feeds each gas separately into the tube. Solenoid valves were installed to facilitate remote control if required. A purpose written LABVIEW interface was used to control the mass flow controllers and to drive the solenoid valves as also outlined in detail in Section 6.3.1. Each mixture is created using a partial pressure method, starting with fuel components and filled up to atmospheric pressure with air. The same procedure was used if lower final pressures were required. Once the separate mixture components are injected into the tube, the tube and circulation loop is isolated from the environment. The circulation loop is connecting the following:

- Circulation connection to inlet circulation pump
- Circulation pump
- Outlet circulation pump to the inlet of the tube
- The tube volume

Solid stainless steel pipes were used throughout with stainless steel flexible hoses connecting vibrating equipment such as the two pumps and the tube inlet and outlet. The flexible hoses remove any stresses from the piping system which may be introduced from pump vibrations or other sources. Moreover, the flame tube is fixed onto optical tables which feature vibration isolation therefore protecting the optical setup from the combustion processes. The tube outlet is connected to the vacuum pump as well as the exhaust. Depending on the state of the experiment, Swagelok ball valves connect either to the exhaust or the vacuum pump. All connection to the vacuum pump are made of stainless steel with one stainless steel flexible hose installed to assure required flexibility.

6.3.1 Flow Control System

A purpose written LABVIEW interface was used to control and operate the experiment with the interface featuring the following functionalities:

- Control Bronkhorst mass flow controllers.
- Define mixture components, monitor component flow rates and partial pressures.
- Control venting of the flame tube to eject combustion product gases into the laboratory extraction system.
- Activate and deactivate the solenoid valves.
- Monitor the pressure within the flame tube.
- Send trigger signal to the ignition system.

The full operational procedure is available upon request.

6.3.2 Mixture Preparation

The operational procedure is detailed below:

1. Flushing of the flame tube: Before the start of an experiment, the flame tube is flushed with 10 times the tube volume using air.
2. Flushing of the circulation loop: Subsequently the circulation loop is flushed for same amount of time. This cleaning procedure assures the removal of remaining fuel and combustion product gases from the entire system.
3. Evacuation: The flame tube is evacuated including pipes, except the pipes connected to the circulation pump. A vacuum pressure of ~ 5 mbar is obtained. Leak rate measurement revealed a leakage of ~ 3.5 mbar/min.
4. Mixture creation: The mixture is created using a partial pressure method. First, the required fuel blending fractions, dilution and equivalence ratio are specified in the Labview interface. The required partial pressures are calculated based on the specified values. An automated filling procedure activates the corresponding mass flow controller, feeding first the separate fuel components, then diluent and followed by air. The flow rates are set dynamically, depending on the difference between measured pressure and required partial pressure. The flow rate of the mixture component stops automatically when the calculated partial pressure is obtained. Subsequently, the filling of the next mixture component is initialised using same procedure. Once all mixture components are injected into the tube, the inlet valves of the supply lines are closed to isolate the pure gases from the mixture.
5. Mixing: The mixing of the gas mixture is performed by circulating the gases through the circulation loop for 5 min. This corresponds to a flow through of approximately 30 times the tube volume and was found to be sufficient to create a homogeneous mixture. For further increase in repeatability, the mixture is subsequently allowed to settle for 2 min before the ignition.
6. Ignition: A custom build capacitive ignition circuit is triggered via a TTL pulse from the Labview interface. This circuit initiates a single spark at the rising edge of the TTL signal. The ignition circuit is connected to a Lukas ignition coil which is further connected to the electrode. The spark gap is modified to ~ 10 mm.
7. Experiment: Detailed below.
8. Venting: After successful ignition, first the exhaust is opened to release the combustion products into the exhaust tract. Subsequently, the flame tube and the circulation loop is flushed again with ~ 20 times the tube volume using air.

The actual experiments, e.g. the activation of the dynamic pressure transducers, starts by sending a trigger pulse to the ignition circuit. The experimental run is detailed below:

1. Sending the TTL ignition signal starts the internal clock and defines therefore the reference time.
2. The flame front, initiated by the spark, deflagrates along the tube. When it passes the obstacles, the flame front is accelerated due to the turbulence generation.
3. The pressure wave, generated by the flame, is detected by the dynamic pressure transducers which are installed along the tube and the flame speed is measured using the ionisation probes.

A minimum of three runs per mixture was used in order to assess the reproducibility.

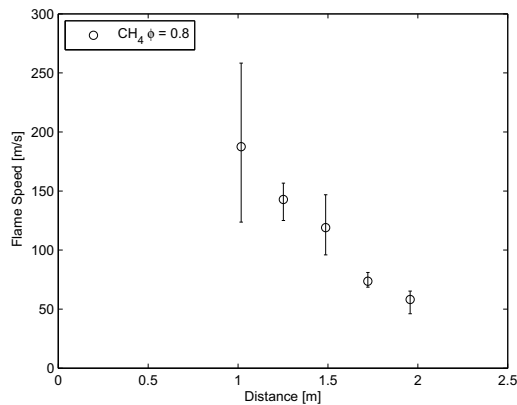


Fig. 54: Flame speed for CH_4 mixtures without H_2 addition.

6.4 Results

6.4.1 Initial Conditions

Experience of previous work using CH_4 -air mixtures (e.g. [50]) as well as the data obtained on the strength of the turbulent deflagrations outlined in Section 5 was taken into account when formulating the initial matrix of test conditions. As a reference experiment, stoichiometric CH_4 -air mixtures at an equivalence ratio $\Phi = 1.0$ were used and over-pressure traces compared with previous work [48]. The comparison was made to ensure the accuracy of the measuring equipment and the updated operation methodology. The results of the comparisons were very satisfactory with only a marginal changes observed.

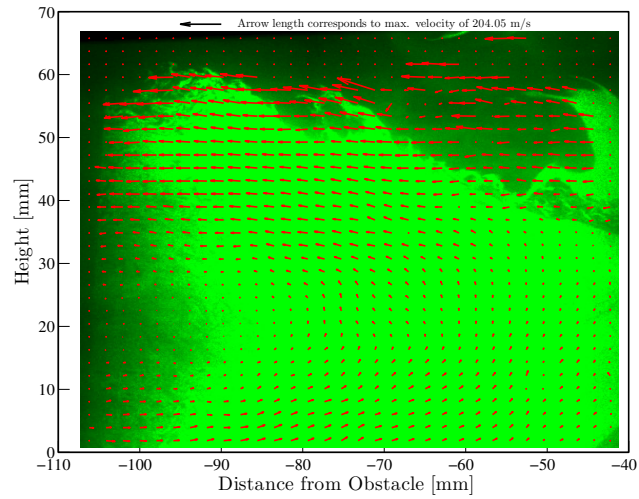


Fig. 55: Flame image obtained using high speed PIV for a CH_4 mixture without H_2 addition. The image shows the flame (top) moving over the second obstacle.

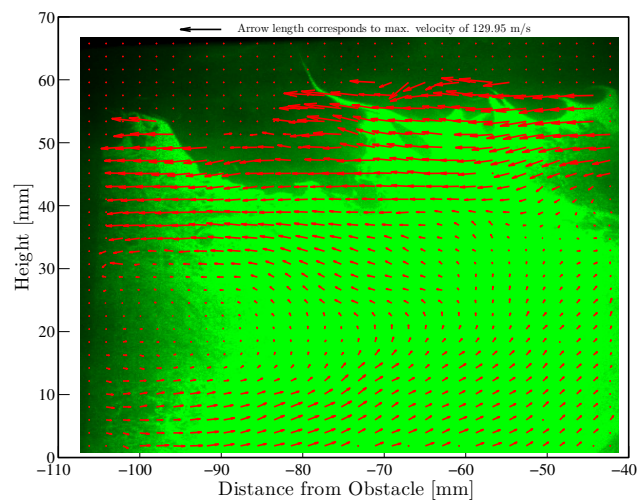


Fig. 56: Flame image obtained using high speed PIV for a CH_4 mixture without H_2 addition. The image shows the further breakup of the flame in the shear layer formed by the second obstacle and starting to engulf the re-circulation zone. The image is taken 0.33 ms later than that shown in Fig. 55.

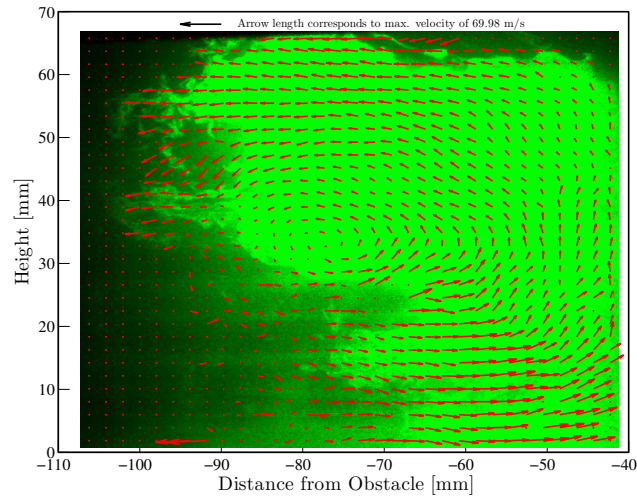


Fig. 57: Flame image obtained using high speed PIV for a CH_4 mixture without H_2 addition. The image shows a point close to the middle point of the explosion in the re-circulation zone behind the second obstacle. The extreme contortion of the flame is readily apparent

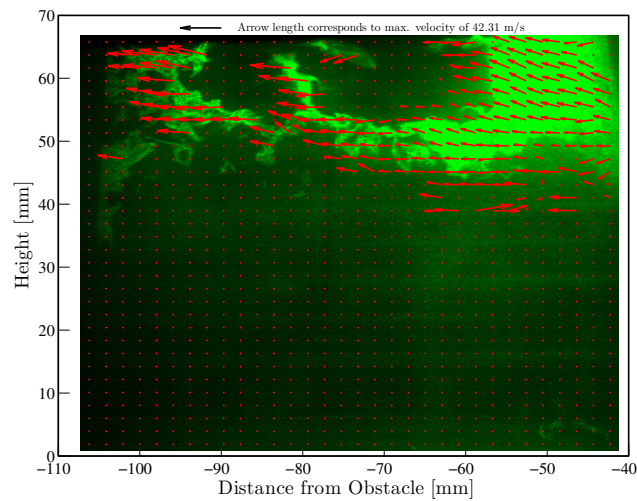


Fig. 58: Flame image obtained using high speed PIV for a CH_4 mixture without H_2 addition. The image shows the final stage of the explosion behind the second obstacle.

The experimental conditions for all mixtures features an equivalence ratio of

0.80, temperature of 298 K and an initial pressure of 1.0 atm. Starting from the least reactive case of each mixture, e.g. pure CH_4 -air in the instance of H_2/CH_4 mixtures, H_2 was gradually added to the fuel mixture. An example of the measured flame speed for the least reactive mixture of CH_4 without H_2 addition is shown in Fig. 54. The large variation close to the obstacle at the first measuring point is due to the stochastic nature of the turbulent explosion. High speed PIV images obtained at the reduced initial pressure of 0.475 atm, due to the high over-pressures discussed below, are shown in Figs. 55 to 58. The data presented is quantitative with the magnitude of the velocity vectors indicated at the top of each figure. The same applies for all PIV data. The light parts of the images are reactants and the dark parts the products. The images belong to the same experiment with the first two separated by 0.33 ms in time and the final two by 2 ms. The applied time resolution was 1 ms and the breakup of the flame front along with the violent distortion of the flame is readily visible.

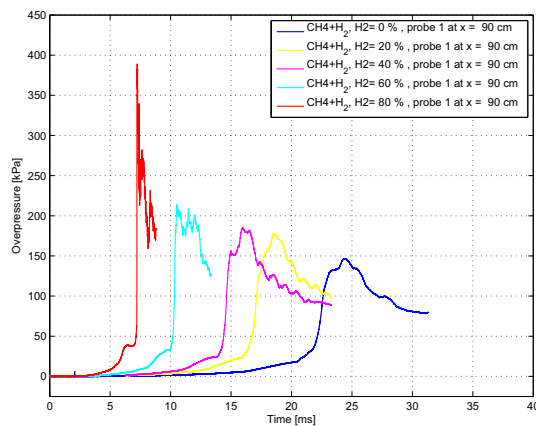


Fig. 59: Maximum over-pressures for turbulent explosions in stoichiometric H_2/CH_4 mixtures at 1 atm initial pressure.

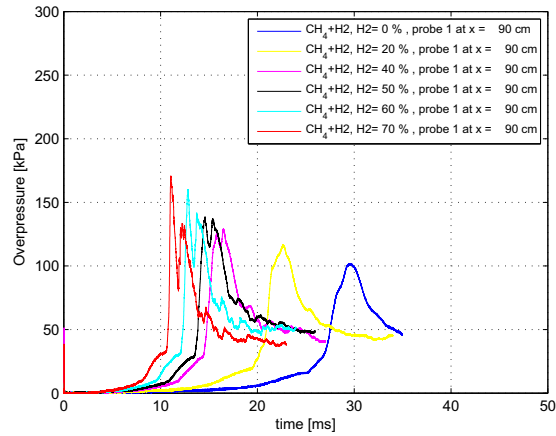
Throughout the experimental series, the maximum overpressure and minimum pressure rise time Δt (0.9 m from ignition end) was monitored and defined the cut-off point for the mixture with highest reactivity to be investigated. The maximum required overpressure was defined to 200 kPa and the minimum Δt between the ignition on the pressure rise on the first pressure transducer was defined to be $\Delta t = 10$ ms. The sharp onset of further increases in peak pressures is illustrated for stoichiometric H_2/CH_4 mixtures in Fig. 59, which shows that over-pressures around 400 kPa can readily be generated for hydrogen rich mixtures. Such reactivity is unlikely to be compatible with the safe operation of CCGT and CCGE engine based installations.

Tab. 40: Fuel mixtures investigated for H_2/CH_4 blends.

Mixture	Φ	P_{init} [kPa]	Composition
1	0.80	101.3	0% H_2 /100% CH_4
2	0.80	101.3	20% H_2 /80% CH_4
3	0.80	101.3	40% H_2 /60% CH_4
4	0.80	101.3	50% H_2 /50% CH_4
5	0.80	101.3	60% H_2 /40% CH_4
6	0.80	101.3	70% H_2 /30% CH_4

Tab. 41: Summary velocity data obtain from high speed PIV for three selected mixtures.

Mixture	Φ [-]	P_{init} [kPa]	U_{peak} [m/s]	U_{mean} [m/s]	U_{std} [m/s]
H_2 40% – CH_4 60% – Air	0.80	47.5	218.7	179.8	39.41
H_2 20% – CH_4 80% – Air	0.80	47.5	234.5	210.0	21.46
H_2 0% – CH_4 100% – Air	0.80	47.5	276.1	227.6	46.07

Fig. 60: Maximum over-pressures for fuel lean ($\Phi = 0.80$) H_2/CH_4 mixtures at 1 atm initial pressure.

6.4.2 Hydrogen-Methane Fuel Blends

The investigated fuel blends for the H_2/CH_4 system ranges from 100% H_2 to 100% CH_4 with incremental steps of 10% on the high reactivity side and 20% on the low reactivity side. The highest reactivity mixture investigated was a mixture of 70% H_2 – 30% CH_4 . A list of the investigated H_2/CH_4 blends is shown in Table 40 and pressure traces at a selected measuring station in Fig. 60.

The pressure data obtained at a distance of 90 cm corresponds to a turbulent explosion (not DDT) and was selected as representative of peak pressures with only modest reductions observed at other locations.

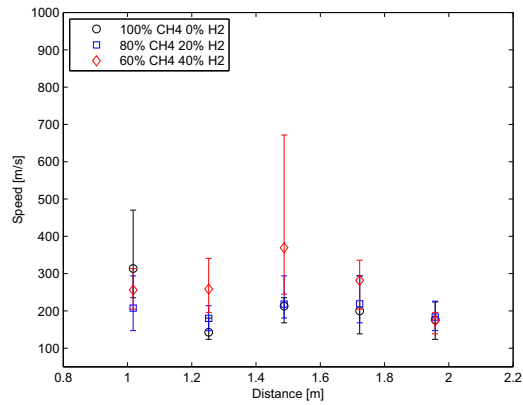


Fig. 61: Flame speeds for CH_4 mixtures with H_2 addition at conditions corresponding to Table 41.

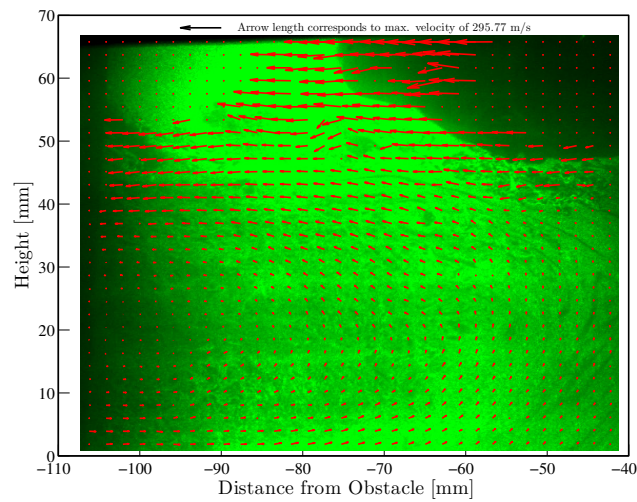


Fig. 62: Flame image obtained using high speed PIV for a CH_4 mixture with 40% H_2 addition. The image shows the flame (top) moving over the second obstacle after around 15.5 ms.

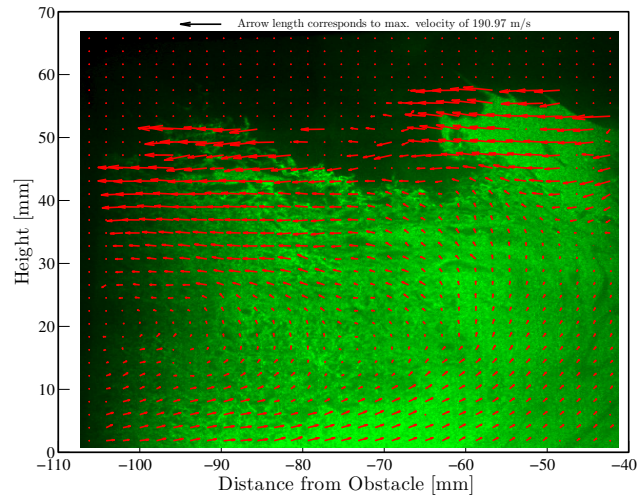


Fig. 63: Flame image obtained using high speed PIV for a CH_4 mixture with 40% H_2 addition. The image shows the flame breakup over the second obstacle 0.33 ms later than shown in Fig. 62.

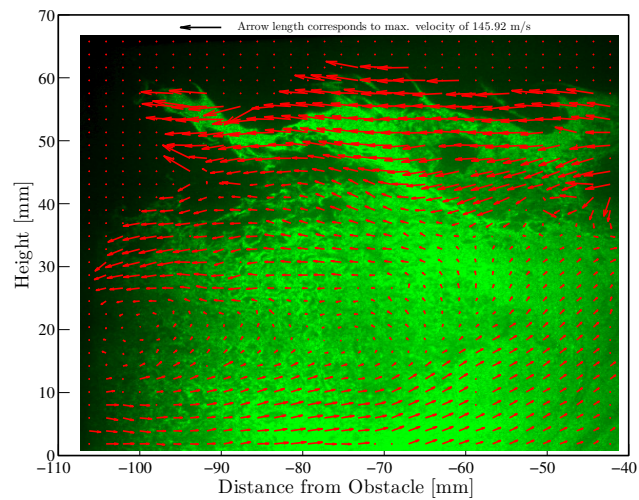


Fig. 64: Flame image obtained using high speed PIV for a CH_4 mixture with 40% H_2 addition. The image shows the flame breakup over the second obstacle 0.33 ms later than shown in Fig. 63.

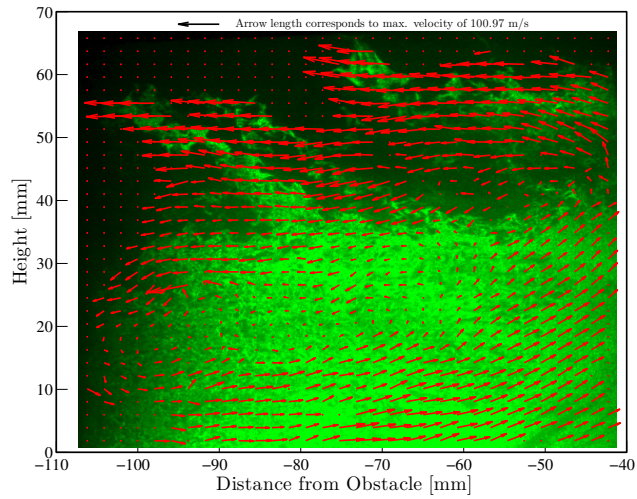


Fig. 65: Flame image obtained using high speed PIV for a CH_4 mixture with 40% H_2 addition. The image shows the flame breakup over the second obstacle 0.33 ms later than shown in Fig. 64.

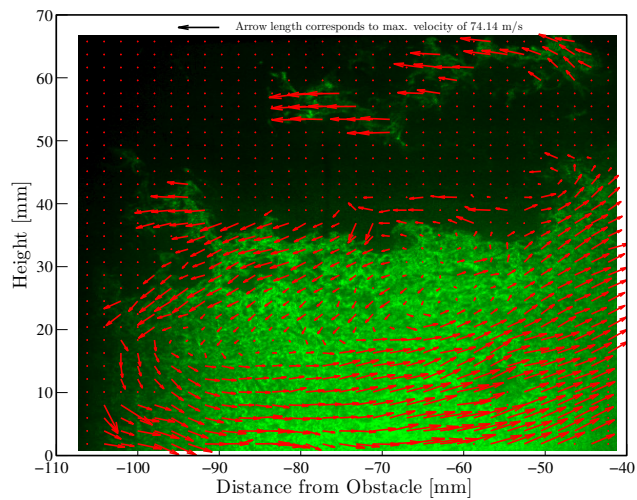


Fig. 66: Flame image obtained using high speed PIV for a CH_4 mixture with 40% H_2 addition. The image shows the explosion in the re-circulation zone behind the second obstacle 0.33 ms later than shown in Fig. 65.

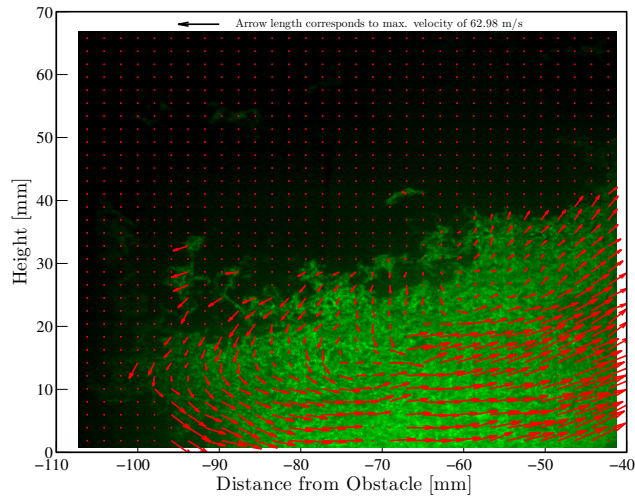


Fig. 67: Flame image obtained using high speed PIV for a CH_4 mixture with 40% H_2 addition. The image shows the explosion in the re-circulation zone behind the second obstacle 0.33 ms later than shown in Fig. 66.

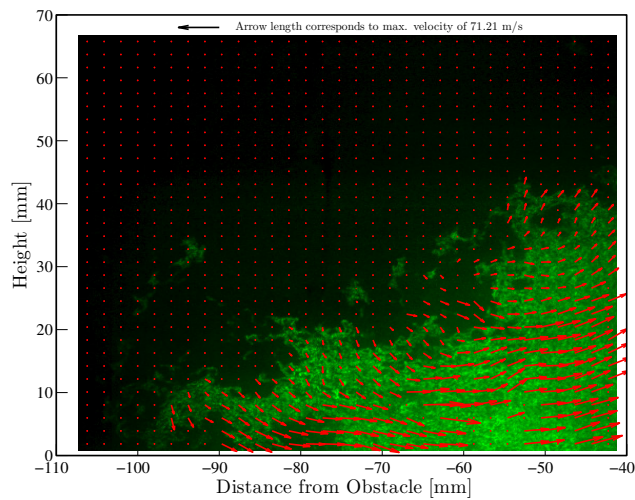


Fig. 68: Flame image obtained using high speed PIV for a CH_4 mixture with 40% H_2 addition. The image shows the explosion in the re-circulation zone behind the second obstacle 0.33 ms later than shown in Fig. 67.

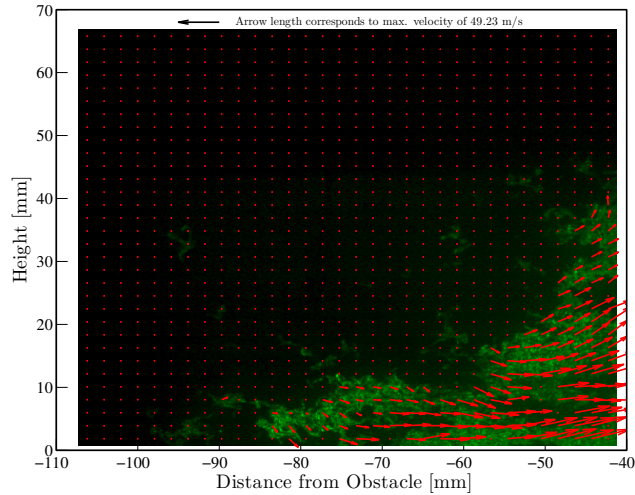


Fig. 69: Flame image obtained using high speed PIV for a CH_4 mixture with 40% H_2 addition. The image shows the final stages of the explosion in the re-circulation zone behind second obstacle 0.33 ms later than shown in Fig. 68.

Table 41 shows the peak mean velocities measured using high speed PIV for selected mixtures. The mean is built from the three peak values of three runs for each mixture, U_{std} is the standard deviation and U_{peak} is the absolute peak value from the three runs. The pressure was reduced to 0.475 atm in these cases in order to reduce the strain on the optical sections. The recorded flame speeds are shown in Fig. 61 at the same conditions as for the high speed PIV measurements. It is evident that the wide flame brush does influence the determined flame speed through reduced triggering times at some measurement locations.

6.4.3 Hydrogen-Carbon Monoxide Fuel Blends

The mixture matrix for the H_2/CO fuel blends includes mixtures up 70% H_2 – 30% CO with incremental steps of 10%. The experience gained for the H_2/CH_4 blends and the corresponding H_2/CO auto-ignition experiments outlined in Sections 2 and 3 along with the strength of the turbulent deflagration studies outlined in Section 5 suggest the need to significantly modify the experimental conditions as much higher over-pressures can be expected. Hence, a blend of moderate reactivity 30% H_2 – 70% CO was initially investigated at the lower initial pressure of 50 kPa using further diluted mixtures. The stoichiometry was subsequently gradually increased to the target of $\Phi = 0.80$ and subsequently the mixture was varied from 30% H_2 – 70% CO to 70% H_2 – 30% CO at sub-atmospheric initial pressures. Finally, three H_2/CO fuel blends were in-

investigated at an initial pressure of 101.3 kPa with compositions ranging from 10% H_2 –90% CO to 30% H_2 –70% CO . The fuel blends and initial conditions can be found in Table 42. Pressure traces at a selected measuring station are shown in Fig. 71.

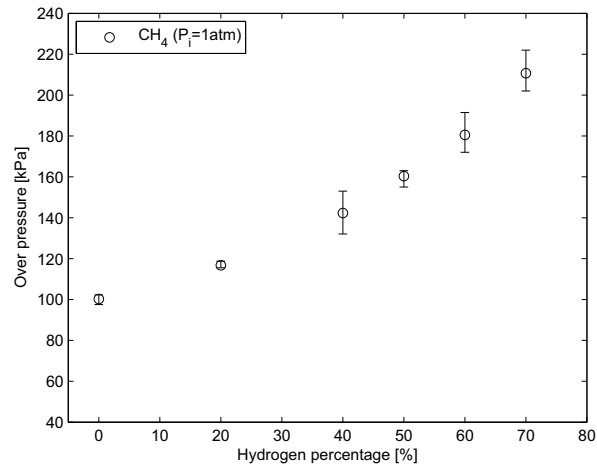


Fig. 70: Maximum over-pressures for H_2/CH_4 mixtures.

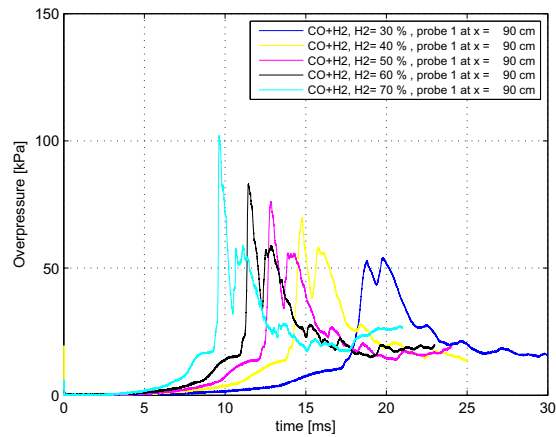


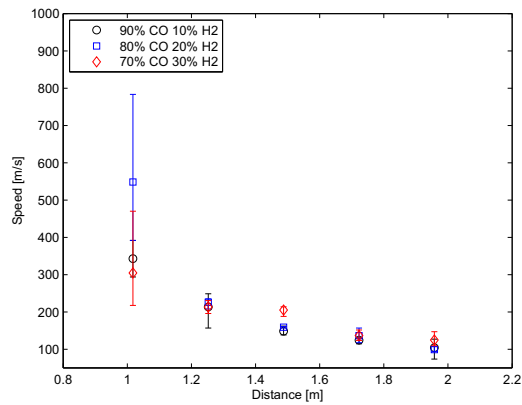
Fig. 71: Maximum over-pressures for fuel lean ($\Phi = 0.80$) H_2/CO mixtures at 0.5 atm initial pressure.

Tab. 42: Fuel mixtures investigated for H_2/CO blends.

Mixture	Φ	P_{init} [kPa]	Composition
1	0.50	50.0	30% H_2 /70% CO
2	0.60	50.0	30% H_2 /70% CO
3	0.70	50.0	30% H_2 /70% CO
4	0.80	50.0	30% H_2 /70% CO
5	0.80	50.0	40% H_2 /60% CO
6	0.80	50.0	50% H_2 /50% CO
7	0.80	50.0	60% H_2 /40% CO
8	0.80	50.0	70% H_2 /30% CO
9	0.80	101.3	10% H_2 /90% CO
10	0.80	101.3	20% H_2 /80% CO
11	0.80	101.3	30% H_2 /70% CO

6.4.4 Recorded Peak Pressures

Methane-hydrogen fuel blends with up to 70% hydrogen were used for a full testing cycle. The equivalence ratio was set to 0.80 and atmospheric pressure used for all mixtures. Carbon monoxide-hydrogen fuel blends were used at the same conditions, but with the hydrogen content reduced to between 10% and 30% as outlined above. Carbon monoxide-hydrogen fuel blends were also investigated for the full range of hydrogen contents from 30% to 70% at the reduced initial pressure of 0.5 atm.

Fig. 72: Flame speeds for CO mixtures with H_2 addition at 1 atm pressure.

Peak over-pressures for the H_2/CH_4 mixtures are shown in Fig. 70 and for the H_2/CO mixtures in Fig. 73. The flame speeds corresponding to the CO mixtures are shown in Fig 72. The stochastic nature of the explosion in the recirculation zone is apparent by the large variations at the first measuring station.

Methane-hydrogen fuel mixtures produced maximum over-pressures ranging from around 100 kPa for pure methane to about 210 kPa for fuels containing 70% hydrogen. The normalised values for carbon monoxide-hydrogen fuel mixtures were higher at 1 atm compared to equivalent mixtures at 0.5 atm suggesting that the absolute value of pressure plays a role in determining the explosion strength. It can also be observed that the normalised maximum pressures for carbon monoxide-hydrogen fuel blends at 0.5 atm were up to around 10% higher than equivalent methane-hydrogen fuel mixtures at 1 atm. Also, the effects of hydrogen addition are more pronounced for carbon monoxide mixtures, which correlates well with the trends in the turbulent burning velocities discussed in Section 5. Overall, the results obtained on explosion trends for the two binary systems confirm the findings outlined using the other three methodologies.

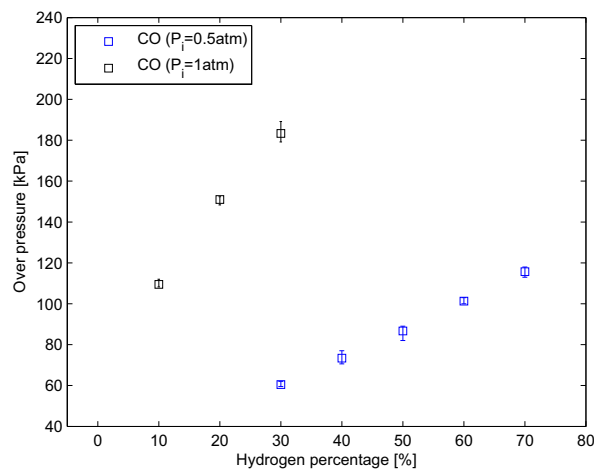


Fig. 73: Maximum over-pressures for H_2/CO mixtures.

The DDT studies discussed above were selected to cover the upper reactivity band of relevance to CCGE applications and show a good correlation with the corresponding turbulent burning velocity data. Data relating to the CCGE and CCGT applications is already available for the latter as outlined above. It is, however, recognised that verification using DDT studies for the lower stoichiometric band relating to CCGT applications is desirable. Such experiments have been included in the medium scale programme for the next phase and could also be included in an extended laboratory program.

7 Findings and Recommendations

The current report details all aspects of the work performed. Thus the objectives have been set out, the methods and experimental facilities described and illustrated, the results quantified with the recognition of clear trends in the behaviour of characteristic flame development, intensity and propagation parameters for the fuel mixtures to be investigated. Modelling techniques for turbulent burning velocity predictions have been assessed and consequences of the findings for the testing and use of the fuel mixtures in large CCGT/CCGE models and practical systems have been identified. Furthermore, a good correlation was observed between the pressure rise/flame speed in the confined experiments and the turbulent burning velocity measured in the opposed jet configuration. For example, unacceptable over-pressures were obtained with 70/30 (H_2/CH_4) and 30/70 (H_2/CO) mixtures in the DDT studies with both points corresponding to a normalised turbulent burning velocity (S_T^*) of 1.5.

As in the context of the whole project, the purpose of the Work Package 2 (Task 1) was to obtain primary information for the execution of Tasks 2 and 3 such that findings and recommendations may appropriately be mentioned together. The investigation found generally parallel trends for each of the four assessment methodologies. The main observations are:

1. Enriching high methane concentration in binary systems with hydrogen will proportionally enhance reactivity. For industrial scale installations it is not recommended to use more than 40% hydrogen in the fuel mixture unless accompanied with significant inert dilution.
2. The enhancement of the explosivity of carbon monoxide with hydrogen is more than twice that of comparable H_2/CH_4 mixtures and carbon monoxide enriched with only some 30% (i.e. 1/3rd) hydrogen will ignite as readily with air as 100% hydrogen. There is also a substantial difference in the over-pressures generated by the two types of mixtures. For practical systems extreme caution and reservation towards hydrogen enrichment is therefore imperative in the context of CO blends.
3. Where moderation by dilution with inert is employed, there is always a high chance that any premixed fuel mixture ejected unburned will ignite on the hot exhaust surfaces. Assurance must therefore be incorporated in designs that the flow will be fully mixed and/or combusted before it meets major turbulence generating obstructions, such as at the entry into heat exchangers. The current study has shown that significant over-pressures can be generated by explosion kernels using very simple obstacle configurations.
4. Within the range of fuel mixture compositions deemed appropriate for large scale experimentation and/or practical use, in-house modelling based on the parameters obtained from this work support the experimental findings and conclusions.

The work has identified scope for important further investigations.

1. The first is an extension of the experimental programme at Imperial College to ternary mixtures of hydrogen, carbon monoxide and methane, from which it is expected that the potential for moderation (or otherwise) by CH_4 of the aggressive influence of CO will be identified. In particular, it is expected to confirm that reactivity will not be proportional to composition, which would have important consequences for large scale experiments and/or industrial operations.
2. A second objective would be to obtain a better understanding and thereby control of the carbon monoxide behaviour by a more thorough study of the chemistry of pure and diluted H_2/CO blends. Each and both of these two recommended options for further work will increase the scope and clarify further the boundaries for expansion of hydrogen enrichment of COG and/or bio-syngas systems.
3. It has additionally become evident from the work that for the critical aspect of carbon monoxide/hydrogen composition a much better distinction and understanding must be obtained between its influence on ignitability and on subsequent explosion strength. These are distinctive differences in reactivity and energetics that have important implications for the design and local temperature control of different power generation applications.
4. From a rather fundamental chemical, but also industrially important aspect, it is evident that hydrogen catalyses the reactivity/combustion of carbon monoxide. The natural question arises as to if this will apply equally (or even more) for larger and more reactive hydrocarbons such as ethylene and propane.
5. It has also been shown that inconsistencies in the treatment of the chemistry of pure hydrogen and mixtures with methane and carbon monoxide prevail and that it would be strongly beneficial to resolve such issues in order to extrapolate the ignition delay time data obtained by Stanford University to atmospheric pressure with increased confidence.

While a priority of such options would have to be debated, their recognition is a direct result of the work of Work Package 2, Task 1 and they are all relevant to the main objective of the current contract.

References

- [1] H. Michels, R. P. Lindstedt, K. Moodie, R. Santon, B. Ewan, S. Hawksworth, R. Gibson, Literature review of CCGT/CCGE/CHP systems operating on high hydrogen content gases, Tech. Rep. 1, ETI Project no. PE02162 (February 2012).
- [2] B. Choi, S. Chung, Autoignited laminar lifted flames of methane/hydrogen mixtures in heated coflow air, *Combust. Flame* 159 (1) (2012) 1481–1488.

- [3] R. Cabra, T. Myhrvold, J. Chen, R. Dibble, A. Karpetis, R. Barlow, Simultaneous laser Raman-Rayleigh-LIF measurements and numerical modeling results of a lifted turbulent H₂/N₂ jet flame in a vitiated coflow, *Proc. Combust. Inst.* 29 (2) (2002) 1881–1888.
- [4] R. Cabra, Turbulent jet flames in a vitiated coflow, Tech. rep., CR-2004-212887, NASA (2000).
- [5] R. Cabra, J. Chen, R. W. Dibble, A. N. Karpetis, R. S. Barlow, Lifted methane–air jet flames in a vitiated coflow, *Combust. Flame* 143 (4) (2005) 491–506.
- [6] R. Cabra, R. Dibble, available online at <http://www.me.berkeley.edu/cal/index.htm> (2002).
- [7] A. R. Masri, R. W. Bilger, available online at <http://www.aeromech.usyd.edu.au/thermofluids> (2003).
- [8] K. Gkagkas, R. P. Lindstedt, Transported pdf modelling with detailed chemistry of pre-and auto-ignition in CH₄/air mixtures, *Proc. Combust. Inst.* 31 (1) (2007) 1559–1566.
- [9] K. Gkagkas, R. P. Lindstedt, The impact of reduced chemistry on auto-ignition of H₂ in turbulent flows, *Combust. Theor. Model.* 13 (4) (2009) 607–643.
- [10] A. R. Masri, R. Cao, S. B. Pope, G. M. Goldin, PDF calculations of turbulent lifted flames of H₂/N₂ fuel issuing into a vitiated co-flow, *Combust. Theor. Model.* 8 (1) (2003) 1–22.
- [11] Q. Tang, J. Xu, S. B. Pope, Probability density function calculations of local extinction and NO production in piloted-jet turbulent methane/air flames, *Proc. Combust. Inst.* 28 (1) (2000) 133–139.
- [12] R. P. Lindstedt, S. A. Louloudi, E. M. Vaos, Joint scalar probability density function modeling of pollutant formation in piloted turbulent jet diffusion flames with comprehensive chemistry, *Proc. Combust. Inst.* 28 (1) (2000) 149–156.
- [13] R. P. Lindstedt, S. A. Louloudi, Joint scalar transported probability density function modeling of turbulent methanol jet diffusion flames, *Proc. Combust. Inst.* 29 (2) (2002) 2147–2154.
- [14] H. Wang, S. B. Pope, Comparisons of detailed reaction mechanisms in non-premixed combustion, 5th US Combustion Meeting Paper 55 (2007).
- [15] A. E. Potter, J. N. Butler, A novel combustion measurement based on the extinguishment of diffusion flames, *ARS Journal* 29 (1959) 54–56.

-
- [16] A. E. Potter, S. HeimeI, J. N. Butler, Apparent flame strength: A measure of maximum reaction rate in diffusion flames, *Proc. Combust. Inst.* 8 (1) (1961) 1027–1034.
- [17] E. Anagnostou, A. E. Potter, Flame strength of propane-oxygen flames at low pressures in turbulent flow, *Proc. Combust. Inst.* 9 (1) (1963) 1–6.
- [18] T. P. Pandya, F. J. Weinberg, The study of the structure of laminar diffusion flames by optical methods, *Proc. Combust. Inst.* 9 (1) (1963) 587–596.
- [19] T. P. Pandya, F. J. Weinberg, The structure of flat, counter-flow diffusion flames, *P. Roy. Soc. A-Math Phy.* (1964) 544–561.
- [20] H. Tsuji, I. Yamaoka, The counterflow diffusion flame in the forward stagnation region of a porous cylinder, *Proc. Combust. Inst.* 11 (1) (1967) 979–984.
- [21] H. Tsuji, I. Yamaoka, The structure of counterflow diffusion flames in the forward stagnation region of a porous cylinder, *Proc. Combust. Inst.* 12 (1) (1969) 997–1005.
- [22] H. Tsuji, I. Yamaoka, Structure analysis of counterflow diffusion flames in the forward stagnation region of a porous cylinder, *Proc. Combust. Inst.* 13 (1) (1971) 723–731.
- [23] I. G. Shepherd, R. K. Cheng, P. J. Goix, The spatial scalar structure of premixed turbulent stagnation point flames, *Proc. Combust. Inst.* 23 (1) (1990) 781–787.
- [24] J. C. Rolon, D. Veynante, J. P. Martin, F. Durst, Counter jet stagnation flows, *Exp. Fluids* 11 (5) (1991) 313–324.
- [25] E. Mastorakos, A. Taylor, J. H. Whitelaw, Scalar dissipation rate at the extinction of turbulent counterflow nonpremixed flames, *Combust. Flame* 91 (1) (1992) 55–64.
- [26] L. W. Kostiuk, Premixed turbulent combustion in counterflowing streams, Ph.D. thesis, Churchill College, University of Cambridge (1991).
- [27] L. W. Kostiuk, K. N. C. Bray, R. K. Cheng, Experimental study of premixed turbulent combustion in opposed streams. part ii—reacting flow field and extinction, *Combust. Flame* 92 (4) (1993) 396–409.
- [28] L. W. Kostiuk, I. G. Shepherd, K. N. C. Bray, Experimental study of premixed turbulent combustion in opposed streams. part iii—spatial structure of flames, *Combust. Flame* 118 (1-2) (1999) 129–139.
- [29] C. Mounaïm-Rousselle, I. Gökalp, Strain effects on the structure of counterflowing turbulent premixed flames, *Proc. Combust. Inst.* 25 (1) (1994) 1199–1205.

-
- [30] K. Sardi, A. Taylor, J. H. Whitelaw, Conditional scalar dissipation statistics in a turbulent counterflow, *J. Fluid Mech.* 361 (1998) 1–24.
- [31] K. Sardi, J. H. Whitelaw, Extinction timescales of periodically strained, lean counterflow flames, *Exp. Fluids* 27 (3) (1999) 199–209.
- [32] K. Sardi, A. Taylor, J. H. Whitelaw, Extinction of turbulent counterflow flames under periodic strain, *Combust. Flame* 120 (3) (2000) 265–284.
- [33] G. Stan, D. A. Johnson, Experimental and numerical analysis of turbulent opposed impinging jets, *AIAA J.* 39 (10) (2001) 1901–1908.
- [34] D. Geyer, S. Omar, A. Nauert, A. Ludwig, A. Dreizler, J. Janicka, A comprehensive characterisation of a turbulent opposed jet flame by 1D-Raman/Rayleigh, 2D-LIF and 2D-LDV, *VDI Berichte* 1750 (2003) 435–440.
- [35] P. Geipel, K. H. H. Goh, R. P. Lindstedt, Fractal-generated turbulence in opposed jet flows, *Flow Turbul. Combust.* 85 (2010) 397–419.
- [36] R. P. Lindstedt, E. M. Váos, Second moment modeling of premixed turbulent flames stabilized in impinging jet geometries, *Proc. Combust. Inst.* 27 (1) (1998) 957–962.
- [37] R. P. Lindstedt, E. M. Váos, Modeling of premixed turbulent flames with second moment methods, *Combust. Flame* 116 (4) (1999) 461–485.
- [38] V. Yakhot, S. Orszag, S. Thangam, T. Gatski, C. Speziale, Development of turbulence models for shear flows by a double expansion technique, *Phys. Fluids A-Fluid* 4 (1992) 1510–1520.
- [39] D. C. Haworth, S. B. Pope, A generalized langevin model for turbulent flows, *Phys. Fluids* 29 (1986) 387–405.
- [40] D. C. Haworth, S. B. Pope, A pdf modeling study of self-similar turbulent free shear flows, *Phys. Fluids* 30 (1987) 1026–1044.
- [41] D. Geyer, A. Kempf, A. Dreizler, J. Janicka, Turbulent opposed-jet flames: a critical benchmark experiment for combustion les, *Combust. Flame* 143 (4) (2005) 524–548.
- [42] D. Geyer, A. Kempf, A. Dreizler, J. Janicka, Scalar dissipation rates in isothermal and reactive turbulent opposed-jets: 1-d-raman/rayleigh experiments supported by les, *Proc. Combust. Inst.* 30 (1) (2005) 681–689.
- [43] G. Coppola, B. Coriton, A. Gomez, Highly turbulent counterflow flames: A laboratory scale benchmark for practical systems, *Combust. Flame* 156 (9) (2009) 1834–1843.

- [44] J. C. Vassilicos, J. C. R. Hunt, Fractal dimensions and spectra of interfaces with application to turbulence, *P. Roy. Soc. A-Math Phys.* 435 (1895) (1991) 505–534.
- [45] R. E. Seoud, J. C. Vassilicos, Dissipation and decay of fractal-generated turbulence, *Phys. Fluids* 19 (10) (2007) 1–11.
- [46] D. Hurst, J. C. Vassilicos, Scalings and decay of fractal-generated turbulence, *Phys. Fluids* 19 (2007) 1–31.
- [47] K. H. H. Goh, P. Geipel, F. Hampf, R. P. Lindstedt, Regime transition from premixed to flameless oxidation in turbulent JP-10 flames, *Proc. Combust. Inst.* (2012) 34.
- [48] V. Sakthitharan, Time-resolved measurements of flame propagation over baffle-type obstacles, PhD-thesis, Imperial College, London (1995).
- [49] H. A. McCann, Time-resolved measurements of freely propagating turbulent flames, PhD-thesis, Imperial College, London (1997).
- [50] R. P. Lindstedt, V. Sakthitharan, Time resolved velocity and turbulence measurements in turbulent gaseous explosions, *Combust. Flame* 114 (1998) 469–483.
- [51] T. S. Kuan, R. P. Lindstedt, E. M. Váos, Higher moment based modeling of turbulence enhanced explosion kernels in confined fuel-air mixtures, in: G. Roy, S. Frolov, R. Santoro, S. Tsyganov (Eds.), *Advances in Confined Detonations and Pulse Detonation Engines*, Torus Press, 2003, pp. 17–40.
- [52] D. F. Davidson, R. K. Hanson, Interpreting shock tube ignition data, *Int. J. Chem. Kinet.* 36 (2004) 510–523.
- [53] Z. Hong, D. F. Davidson, R. K. Hanson, An improved H_2/O_2 mechanism based on recent shock tube/laser absorption measurements, *Combust. Flame* 158 (2011) 633–644.
- [54] H. Wang, E. Dames, B. Sirjean, D. A. Sheen, R. Tangko, A. Violi, J. Y. W. Lai, F. N. Egolfopoulos, D. F. Davidson, R. K. Hanson, C. T. Bowman, C. K. Law, W. Tsang, N. P. Cernansky, D. L. Miller, R. P. Lindstedt, A high-temperature chemical kinetic model of n-alkane (up to n-dodecane), cyclohexane, and methyl-, ethyl-, n-propyl and n-butyl-cyclohexane oxidation at high temperatures, *JetSurF* version 2.0 September 19 (2010) <http://melchior.usc.edu/JetSurF/JetSurF2.0>.
- [55] TRIDELTA GmbH, available online at <http://www.tridelta.de/tridelta-gruppe-unternehmensgruppe-en.html>.
- [56] Omega Engineering Inc., available online at <http://www.omega.com/>.
- [57] LaVision GmbH, available online at <http://www.lavision.de/en/>.

- [58] National Instruments Corporation, available online at <http://www.ni.com/3/>.
- [59] Bronkhorst High-Tech B.V., available online at <http://www.bronkhorst.com/>.
- [60] R. K. Cheng, A. K. Oppenheim, Autoignition in methane–hydrogen mixtures, *Combust. Flame* 58 (2) (1984) 125–139.
- [61] S. Gersen, N. B. Anikin, A. V. Mokhov, H. B. Levinsky, Ignition properties of methane/hydrogen mixtures in a rapid compression machine, *Int. J. Hydrogen Energ.* 33 (7) (2008) 1957–1964.
- [62] M. Ilbas, A. Crayford, I. Yilmaz, P. Bowen, N. Syred, Laminar-burning velocities of hydrogen-air and hydrogen-methane-air mixtures: An experimental study, *Int. J. Hydrogen Energ.* 31 (12) (2006) 1768–1779.
- [63] T. G. Scholte, P. B. Vaags, Burning velocities of mixtures of hydrogen, carbon monoxide and methane with air, *Combust. Flame* 3 (1959) 511–524.
- [64] V. Di Sarli, A. D. Benedetto, Laminar burning velocity of hydrogen–methane/air premixed flames, *Int. J. Hydrogen Energ.* 32 (5) (2007) 637–646.
- [65] C. Sung, C. Law, Fundamental combustion properties of H₂/CO mixtures: ignition and flame propagation at elevated pressures, *Combust. Sci. Technol.* 180 (6) (2008) 1097–1116.
- [66] T. Lieuwen, V. McDonell, E. Petersen, D. Santavicca, Fuel flexibility influences on premixed combustor blowout, flashback, autoignition, and stability, *J. Eng. Gas Turb. Power* 130 (2008) 011506.
- [67] C. G. Fotache, Y. Tan, C. J. Sung, C. K. Law, Ignition of CO/H₂/N₂ versus heated air in counterflow: experimental and modeling results, *Combust. Flame* 120 (4) (2000) 417 – 426.
- [68] L. J. Spadaccini, M. B. Colket III, Ignition delay characteristics of methane fuels, *Prog. Energ. Combust.* 20 (5) (1994) 431–460.
- [69] K. H. H. Goh, P. Geipel, F. Hampp, R. P. Lindstedt, Flames in fractal grid generated turbulence, submitted to *Fluid Dyn. Res.* (2012).
- [70] R. P. Lindstedt, D. S. Luff, J. H. Whitelaw, Velocity fields of fuel lean premixed turbulent opposed jet flames, *Proc. Combust. Inst.* 31 (1) (2007) 1459 – 1466.
- [71] R. P. Lindstedt, D. S. Luff, J. H. Whitelaw, Velocity and strain-rate characteristics of opposed isothermal flows, *Flow Turbul. Combust.* 74 (2) (2005) 169–194.

- [72] D. S. Luff, Experiments and calculations of opposed and ducted flows, PhD-thesis, Imperial College, London (2005).
- [73] P. Geipel, K. H. H. Goh, R. P. Lindstedt, The stability of flames burning against hot exhaust products in fractal generated turbulence, in: Proceedings of the European Combustion Meeting, 2011.
- [74] E. Mastorakos, A. Taylor, J. H. Whitelaw, Extinction and temperature characteristics of turbulent counterflow diffusion flames with partial pre-mixing, *Combust. Flame* 91 (1) (1992) 40–54.
- [75] F. Hampp, K. H. H. Goh, H. J. Michels, R. P. Lindstedt, Auto-ignition of hydrogen rich mixtures in hot combustion products, Tech. Rep. 2, ETI Project no. PE02162 (April 2012).
- [76] Swagelok, available online at <http://www.swagelok.com/>.
- [77] Litron Lasers, available online at <http://www.litron.co.uk/>.
- [78] D. B. Spalding, Mixing and chemical reaction in steady confined turbulent flames, *Proc. Combust. Inst.* 13 (1) (1971) 649–657.
- [79] D. B. Spalding, Development of the eddy-break-up model of turbulent combustion, *Proc. Combust. Inst.* 16 (1) (1977) 1657–1663.
- [80] K. N. C. Bray, Studies of the turbulent burning velocity, *P. Roy. Soc. A-Math Phy.* 431 (1882) (1990) 315–335.
- [81] J. F. Driscoll, Turbulent premixed combustion: Flamelet structure and its effect on turbulent burning velocities, *Prog. Energ. Combust.* 34 (1) (2008) 91–134.
- [82] I. G. Shepherd, R. K. Cheng, The burning rate of premixed flames in moderate and intense turbulence, *Combust. Flame* 127 (3) (2001) 2066–2075.
- [83] C. J. Lawn, R. W. Schefer, Scaling of premixed turbulent flames in the corrugated regime, *Combust. Flame* 146 (1) (2006) 180–199.
- [84] K. H. H. Goh, P. Geipel, R. P. Lindstedt, Conditional statistics of lean premixed turbulent opposed jet flames using particle image velocimetry and density segregation, in: Proceedings of the European Combustion Meeting, 2011.
- [85] B. Hakberg, A. D. Gosman, Analytical determination of turbulent flame speed from combustion models, *Proc. Combust. Inst.* 20 (1) (1985) 225–232.
- [86] C. A. Catlin, R. P. Lindstedt, Premixed turbulent burning velocities derived from mixing controlled reaction models with cold front quenching, *Combust. Flame* 85 (3-4) (1991) 427–439.

- [87] R. P. Lindstedt, V. Sakthitharan, Modelling of transient compressible turbulent reacting flows, in: 8th Symposium on Turbulent Shear Flows, 1991.
- [88] W. K. George, H. J. Hussein, Locally axisymmetric turbulence, *J. Fluid Mech.* 233 (1) (1991) 1–23.
- [89] R. P. Lindstedt, V. D. Milosavljevic, M. Persson, Turbulent burning velocity predictions using transported pdf methods, *Proc. Combust. Inst.* 33 (1) (2011) 1277–1284.
- [90] N. K. Aluri, P. K. G. Pantangi, S. P. R. Muppala, F. Dinkelacker, A numerical study promoting algebraic models for the Lewis number effect in atmospheric turbulent premixed bunsen flames, *Flow Turbul. Combust.* 75 (1) (2005) 149–172.
- [91] N. K. Aluri, S. P. Reddy Muppala, F. Dinkelacker, Substantiating a fractal-based algebraic reaction closure of premixed turbulent combustion for high pressure and the Lewis number effects, *Combust. Flame* 145 (4) (2006) 663–674.
- [92] R. P. Lindstedt, H. J. Michels, Deflagration to detonation transition in mixtures of alkane LNG/LPG constituents with O₂N₂, *Combust. Flame* 72 (1) (1988) 63–72.
- [93] R. P. Lindstedt, H. J. Michels, Deflagration to detonation transitions and strong deflagrations in alkane and alkene air mixtures, *Combust. Flame* 76 (2) (1989) 169–181.
- [94] W. Juchmann, H. Latzel, D. I. Shin, G. Peiter, T. Drier, H. R. Volpp, J. Wolfrum, R. P. Lindstedt, K. M. Leung, Absolute radical concentration measurements and modelling of low-pressure CH₄/O₂/NO flames, in: *Proc. Combust. Inst.*, Vol. 27, 1998, pp. 469–476.
- [95] V. Sick, F. Hildenbrand, R. P. Lindstedt, Quantitative laser based measurements and detailed chemical kinetic modelling of the nitric oxide concentrations in methane-air counterflow diffusion flames, in: *Proc. Combust. Inst.*, Vol. 27, 1998, pp. 1401–1409.
- [96] M. P. Meyer, The application of detailed and systematically reduced chemistry to transient laminar flames, PhD-thesis, Imperial College, London (2001).
- [97] R. P. Lindstedt, S. A. Louloudi, E. M. Váos, Joint scalar probability density function modeling of pollutant formation in piloted turbulent jet diffusion flames with comprehensive chemistry, in: *Proc. Combust. Inst.*, Vol. 28, 2000, pp. 149–156.

-
- [98] R. P. Lindstedt, S. A. Louloudi, J. J. Driscoll, V. Sick, Finite rate chemistry effects in turbulent reacting flows, *Flow Turbul. Combust.* 72 (2004) 407–426.
 - [99] R. P. Lindstedt, E. M. Város, Transported pdf modeling of high-reynolds-number premixed turbulent flames, *Combust. Flame* 145 (2006) 495–511.
 - [100] C. Law, G. Jomaas, J. Bechtold, Cellular instabilities of expanding hydrogen/propane spherical flames at elevated pressures: Theory and experiment., *Proc. Combust. Inst.* 30 (1) (2005) 159–167.
 - [101] F. Wu, A. Kelley, D. Zhu, C. Law, Further study of effects of hydrogen addition on laminar flame speeds of fuel–air mixtures, *Proc. US Nat. Combust. Meeting 7 (LE10)* (2011) 1–17.

A Supplementary Tables

Tab. 43: Summary of projected Syngas Mixtures

Mixture	u_j [m/s]	Re	H_2 slpm	CH_4 slpm	CO slpm	N_2 slpm	Air slpm
H_2 100% - Air	100.1	2.049E + 04	20.94	0.000	0.000	0.000	62.28
H_2 90% - CH_4 10% - Air	96.82	2.127E + 04	14.88	1.650	0.000	0.000	63.95
H_2 80% - CH_4 20% - Air	94.74	2.180E + 04	10.94	2.733	0.000	0.000	65.08
H_2 70% - CH_4 30% - Air	93.29	2.218E + 04	8.158	3.497	0.000	0.000	65.89
H_2 60% - CH_4 40% - Air	92.23	2.247E + 04	6.095	4.063	0.000	0.000	66.51
H_2 50% - CH_4 50% - Air	91.42	2.270E + 04	4.506	4.506	0.000	0.000	66.99
H_2 40% - CH_4 60% - Air	90.78	2.288E + 04	3.237	4.852	0.000	0.000	67.37
H_2 20% - CH_4 80% - Air	89.83	2.316E + 04	1.344	5.377	0.000	0.000	67.96
H_2 0% - CH_4 100% - Air	89.17	2.299E + 04	0.000	5.746	0.000	0.000	68.38
H_2 100% - Air	100.1	2.049E + 04	20.94	0.000	0.000	0.000	62.28
H_2 90% - CO 10% - Air	98.66	2.078E + 04	18.57	0.000	2.067	0.000	61.38
H_2 80% - CO 20% - Air	97.28	2.107E + 04	16.28	0.000	4.068	0.000	60.52
H_2 70% - CO 30% - Air	95.95	2.136E + 04	14.05	0.000	6.022	0.000	59.69
H_2 60% - CO 40% - Air	94.68	2.165E + 04	11.88	0.000	7.918	0.000	58.90
H_2 50% - CO 50% - Air	93.45	2.193E + 04	9.773	0.000	9.773	0.000	58.14
H_2 40% - CO 60% - Air	92.28	2.222E + 04	7.717	0.000	11.58	0.000	57.42
H_2 30% - CO 70% - Air	91.14	2.250E + 04	5.720	0.000	13.34	0.000	56.70
H_2 100% - N_2 - Air	95.54	2.164E + 04	12.56	0.000	0.000	29.51	37.36
H_2 90% - CH_4 10% - N_2 - Air	93.60	2.215E + 04	8.839	0.9803	0.000	30.00	37.98
H_2 80% - CH_4 20% - N_2 - Air	92.37	2.249E + 04	6.450	1.612	0.000	30.33	38.39
H_2 70% - CH_4 30% - N_2 - Air	91.52	2.272E + 04	4.793	2.054	0.000	30.55	38.68
H_2 60% - CH_4 40% - N_2 - Air	90.90	2.291E + 04	3.552	2.380	0.000	30.73	38.89
H_2 50% - CH_4 50% - N_2 - Air	90.43	2.296E + 04	2.623	2.623	0.000	30.86	39.07
H_2 40% - CH_4 60% - N_2 - Air	90.06	2.315E + 04	1.879	2.822	0.000	30.96	39.20
H_2 0% - CH_4 100% - N_2 - Air	89.13	2.321E + 04	0.000	3.319	0.000	31.23	39.53
H_2 100% - N_2 - Air	95.54	2.164E + 04	12.56	0.000	0.000	29.51	37.36
H_2 90% - CO 10% - N_2 - Air	94.75	2.182E + 04	11.21	0.000	1.244	29.26	37.05
H_2 80% - CO 20% - N_2 - Air	93.97	2.199E + 04	9.881	0.000	2.468	29.02	36.74
H_2 70% - CO 30% - N_2 - Air	93.21	2.217E + 04	8.577	0.000	3.673	28.79	36.45
H_2 60% - CO 40% - N_2 - Air	92.47	2.235E + 04	7.295	0.000	4.858	28.56	36.16
H_2 50% - CO 50% - N_2 - Air	91.74	2.253E + 04	6.032	0.000	6.032	28.33	35.87
H_2 40% - CO 60% - N_2 - Air	91.04	2.271E + 04	4.783	0.000	7.182	28.11	35.60
H_2 30% - CO 70% - N_2 - Air	90.35	2.288E + 04	3.560	0.000	8.314	27.90	35.33

Tab. 44: Experimental conditions for the mixture $H_2 - Air$ for varying pilot conditions, where subindices j and p refer to the jet and pilot, respectively

$\chi_{H_2,j}$ [-]	$\chi_{GH_4,j}$ [-]	$\chi_{CO,j}$ [-]	$\chi_{N_2,j}$ [-]	$\chi_{Air,j}$ [-]	MW_j [kg/kmol]	$\rho_{u,j}$ [kg/m ³]	$\mu_{u,j}$ [μ Pa·s]	u_j [m/s]	Re_j [-]	$\chi_{H_2,p}$ [-]	$\chi_{GH_4,p}$ [-]	$\chi_{Air,p}$ [-]	Φ_p [-]	u_p [m/s]	T_p [K]
0.2516	0.0000	0.0000	0.0000	0.7484	22.16	0.8977	18.42	100.1	2.049E+04	0.1041	0.0000	0.8959	0.277	0.994	1041
0.2516	0.0000	0.0000	0.0000	0.7484	22.16	0.8977	18.42	100.1	2.049E+04	0.1084	0.0000	0.8916	0.289	0.998	1069
0.2516	0.0000	0.0000	0.0000	0.7484	22.16	0.8977	18.42	100.1	2.049E+04	0.1127	0.0000	0.8873	0.302	1.003	1092

Tab. 45: Experimental conditions for the mixture H_2 90% – CH_4 10% – Air for varying pilot conditions

$\chi_{H_2,j}$ [-]	$\chi_{GH_4,j}$ [-]	$\chi_{CO_2,j}$ [-]	$\chi_{N_2,j}$ [-]	$\chi_{Air,j}$ [-]	MW_j [kg/kmol]	$\rho_{u,j}$ [kg/m ³]	$\mu_{u,j}$ [μ Pa·s]	u_j [m/s]	Re_j [-]	$\chi_{H_2,p}$ [-]	$\chi_{GH_4,p}$ [-]	$\chi_{Air,p}$ [-]	Φ_p [-]	u_p [m/s]	T_p [K]
0.1849	0.0205	0.0000	0.0000	0.7946	23.69	0.9597	18.35	96.82	2.127E+04	0.1041	0.0000	0.8959	0.277	0.994	1043
0.1849	0.0205	0.0000	0.0000	0.7946	23.69	0.9597	18.35	96.82	2.127E+04	0.1084	0.0000	0.8916	0.289	0.998	1070
0.1849	0.0205	0.0000	0.0000	0.7946	23.69	0.9597	18.35	96.82	2.127E+04	0.1127	0.0000	0.8873	0.302	1.003	1098

Tab. 46: Experimental conditions for the mixture H_2 80% – CH_4 20% – Air for varying pilot conditions

$\chi_{H_2,j}$ [-]	$\chi_{CH_4,j}$ [-]	$\chi_{CO_2,j}$ [-]	$\chi_{N_2,j}$ [-]	$\chi_{Air,j}$ [-]	MW_j [kg/kmol]	$\rho_{u,j}$ [kg/m ³]	$\mu_{u,j}$ [μ Pa·s]	u_j [m/s]	Re_j [-]	$\chi_{H_2,p}$ [-]	$\chi_{CH_4,p}$ [-]	$\chi_{Air,p}$ [-]	Φ_p [-]	u_p [m/s]	T_p [K]
0.1389	0.0347	0.0000	0.0000	0.8264	24.75	1.0025	18.30	94.74	2.180E+04	0.1041	0.0000	0.8959	0.277	0.994	1042
0.1389	0.0347	0.0000	0.0000	0.8264	24.75	1.0025	18.30	94.74	2.180E+04	0.1084	0.0000	0.8916	0.289	0.998	1070
0.1389	0.0347	0.0000	0.0000	0.8264	24.75	1.0025	18.30	94.74	2.180E+04	0.1127	0.0000	0.8873	0.302	1.003	1099
0.1389	0.0347	0.0000	0.0000	0.8264	24.75	1.0025	18.30	94.74	2.180E+04	0.1126	0.0010	0.8864	0.313	1.004	1119
0.1389	0.0347	0.0000	0.0000	0.8264	24.75	1.0025	18.30	94.74	2.180E+04	0.1225	0.0022	0.8854	0.353	1.005	1141
0.1389	0.0347	0.0000	0.0000	0.8264	24.75	1.0025	18.30	94.74	2.180E+04	0.1124	0.0031	0.8845	0.336	1.006	1160

Tab. 47: Experimental conditions for the mixture H_2 70% – CH_4 30% – Air for varying pilot conditions

$\chi_{H_2,j}$ [-]	$\chi_{CH_4,j}$ [-]	$\chi_{CO,j}$ [-]	$\chi_{N_2,j}$ [-]	$\chi_{Air,j}$ [-]	MW_j [kg/kmol]	$\rho_{u,j}$ [kg/m ³]	$\mu_{u,j}$ [μ Pa·s]	u_j [m/s]	Re_j [-]	$\chi_{H_2,p}$ [-]	$\chi_{CH_4,p}$ [-]	$\chi_{Air,p}$ [-]	Φ_p [-]	u_p [m/s]	T_p [K]
0.1052	0.0451	0.0000	0.0000	0.8497	25.52	1.0338	18.26	93.29	2.218E+04	0.1063	0.0000	0.8937	0.283	0.9961	1042
0.1052	0.0451	0.0000	0.0000	0.8497	25.52	1.0338	18.26	93.29	2.218E+04	0.1125	0.0000	0.8875	0.302	1.003	1068
0.1052	0.0451	0.0000	0.0000	0.8497	25.52	1.0338	18.26	93.29	2.218E+04	0.1084	0.0000	0.8916	0.289	0.9985	1067
0.1052	0.0451	0.0000	0.0000	0.8497	25.52	1.0338	18.26	93.29	2.218E+04	0.1127	0.0000	0.8873	0.302	1.003	1090
0.1052	0.0451	0.0000	0.0000	0.8497	25.52	1.0338	18.26	93.29	2.218E+04	0.1126	0.0010	0.8928	0.311	1.004	1095
0.1052	0.0451	0.0000	0.0000	0.8497	25.52	1.0338	18.26	93.29	2.218E+04	0.1125	0.0017	0.8858	0.321	1.005	1115
0.1052	0.0451	0.0000	0.0000	0.8497	25.52	1.0338	18.26	93.29	2.218E+04	0.1124	0.0024	0.8862	0.328	1.006	1145
0.1052	0.0451	0.0000	0.0000	0.8497	25.52	1.0338	18.26	93.29	2.218E+04	0.1124	0.0031	0.8845	0.336	1.006	1158
0.1052	0.0451	0.0000	0.0000	0.8497	25.52	1.0338	18.26	93.29	2.218E+04	0.1123	0.0041	0.8837	0.347	1.007	1177
0.1052	0.0451	0.0000	0.0000	0.8497	25.52	1.0338	18.26	93.29	2.218E+04	0.1122	0.0048	0.8831	0.354	1.008	1192

Tab. 48: Experimental conditions for the mixture H_2 60% – CH_4 40% – Air for varying pilot conditions

$\chi_{H_2,j}$ [-]	$\chi_{CH_4,j}$ [-]	$\chi_{CO_2,j}$ [-]	$\chi_{N_2,j}$ [-]	$\chi_{Air,j}$ [-]	MW_j [kg/kmol]	$\rho_{u,j}$ [kg/m ³]	$\mu_{u,j}$ [μ Pa·s]	u_j [m/s]	$Re_{e,j}$ [-]	$\chi_{H_2,p}$ [-]	$\chi_{CH_4,p}$ [-]	$\chi_{Air,p}$ [-]	Φ_p [-]	u_p [m/s]	T_p [K]
0.0795	0.0530	0.0000	0.0000	0.8675	26.11	1.0577	18.23	92.23	2.247E+04	0.1127	0.0000	0.8873	0.302	1.003	1115
0.0795	0.0530	0.0000	0.0000	0.8675	26.11	1.0577	18.23	92.23	2.247E+04	0.1126	0.0010	0.8864	0.313	1.004	1140
0.0795	0.0530	0.0000	0.0000	0.8675	26.11	1.0577	18.23	92.23	2.247E+04	0.1125	0.0022	0.8854	0.326	1.005	1156
0.0795	0.0530	0.0000	0.0000	0.8675	26.11	1.0577	18.23	92.23	2.247E+04	0.1124	0.0031	0.8845	0.336	1.006	1176
0.0795	0.0530	0.0000	0.0000	0.8675	26.11	1.0577	18.23	92.23	2.247E+04	0.1123	0.0041	0.8837	0.347	1.007	1176
0.0795	0.0530	0.0000	0.0000	0.8675	26.11	1.0577	18.23	92.23	2.247E+04	0.1121	0.0050	0.8828	0.356	1.008	1196
0.0795	0.0530	0.0000	0.0000	0.8675	26.11	1.0577	18.23	92.23	2.247E+04	0.1119	0.0069	0.8812	0.377	1.010	1230

Tab. 49: Experimental conditions for the mixture H_2 50% – CH_4 50% – Air for varying pilot conditions

$\chi_{H_2,j}$ [-]	$\chi_{CH_4,j}$ [-]	$\chi_{CO_2,j}$ [-]	$\chi_{N_2,j}$ [-]	$\chi_{Air,j}$ [-]	MW_j [kg/kmol]	$\rho_{u,j}$ [kg/m ³]	$\mu_{u,j}$ [μ Pa·s]	u_j [m/s]	$Re_{e,j}$ [-]	$\chi_{H_2,p}$ [-]	$\chi_{CH_4,p}$ [-]	$\chi_{Air,p}$ [-]	Φ_p [-]	u_p [m/s]	T_p [K]
0.0593	0.0593	0.0000	0.0000	0.8815	26.58	1.0765	18.21	91.42	2.270E+04	0.1125	0.0022	0.8854	0.326	1.005	1133
0.0593	0.0593	0.0000	0.0000	0.8815	26.58	1.0765	18.21	91.42	2.270E+04	0.1123	0.0033	0.8843	0.338	1.007	1159
0.0593	0.0593	0.0000	0.0000	0.8815	26.58	1.0765	18.21	91.42	2.270E+04	0.1122	0.0045	0.8833	0.351	1.008	1183
0.0593	0.0593	0.0000	0.0000	0.8815	26.58	1.0765	18.21	91.42	2.270E+04	0.1121	0.0052	0.8826	0.358	1.009	1198
0.0593	0.0593	0.0000	0.0000	0.8815	26.58	1.0765	18.21	91.42	2.270E+04	0.1120	0.0064	0.8816	0.371	1.010	1221
0.0593	0.0593	0.0000	0.0000	0.8815	26.58	1.0765	18.21	91.42	2.270E+04	0.1119	0.0071	0.8810	0.379	1.011	1237
0.0593	0.0593	0.0000	0.0000	0.8815	26.58	1.0765	18.21	91.42	2.270E+04	0.1118	0.0081	0.8801	0.390	1.011	1256

Tab. 50: Experimental conditions for the mixture H_2 40% – CH_4 60% – Air for varying pilot conditions

$\chi_{H_2,j}$ [-]	$\chi_{CH_4,j}$ [-]	$\chi_{CO_2,j}$ [-]	$\chi_{N_2,j}$ [-]	$\chi_{Air,j}$ [-]	MW_j [kg/kmol]	$\rho_{u,j}$ [kg/m ³]	$\mu_{u,j}$ [μ Pa·s]	u_j [m/s]	Re_j [-]	$\chi_{H_2,p}$ [-]	$\chi_{CH_4,p}$ [-]	$\chi_{Air,p}$ [-]	Φ_p [-]	u_p [m/s]	T_p [K]
0.0429	0.0643	0.0000	0.0000	0.8928	26.95	1.0918	18.19	90.78	2.288E+04	0.1123	0.0038	0.8839	0.343	1.007	1171
0.0429	0.0643	0.0000	0.0000	0.8928	26.95	1.0918	18.19	90.78	2.288E+04	0.1121	0.0050	0.8828	0.356	1.008	1196
0.0429	0.0643	0.0000	0.0000	0.8928	26.95	1.0918	18.19	90.78	2.288E+04	0.1120	0.0064	0.8816	0.371	1.010	1222
0.0429	0.0643	0.0000	0.0000	0.8928	26.95	1.0918	18.19	90.78	2.288E+04	0.1119	0.0076	0.8805	0.385	1.011	1244
0.0429	0.0643	0.0000	0.0000	0.8928	26.95	1.0918	18.19	90.78	2.288E+04	0.1118	0.0083	0.8799	0.392	1.012	1259
0.0429	0.0643	0.0000	0.0000	0.8928	26.95	1.0918	18.19	90.78	2.288E+04	0.1117	0.0090	0.8793	0.400	1.012	1273

Tab. 51: Experimental conditions for the mixture H_2 25% – CH_4 75% – Air for varying pilot conditions

$\chi_{H_2,j}$ [-]	$\chi_{CH_4,j}$ [-]	$\chi_{CO_2,j}$ [-]	$\chi_{N_2,j}$ [-]	$\chi_{Air,j}$ [-]	MW_j [kg/kmol]	$\rho_{u,j}$ [kg/m ³]	$\mu_{u,j}$ [μ Pa·s]	u_j [m/s]	Re_j [-]	$\chi_{H_2,p}$ [-]	$\chi_{CH_4,p}$ [-]	$\chi_{Air,p}$ [-]	Φ_p [-]	u_p [m/s]	T_p [K]
0.0240	0.0710	0.0000	0.0000	0.9050	27.37	1.1149	18.16	90.08	2.323E+04	0.1121	0.0057	0.8822	0.364	1.009	1209
0.0240	0.0710	0.0000	0.0000	0.9050	27.37	1.1149	18.16	90.08	2.323E+04	0.1119	0.0069	0.8812	0.377	1.010	1236
0.0240	0.0710	0.0000	0.0000	0.9050	27.37	1.1149	18.16	90.08	2.323E+04	0.1119	0.0076	0.8805	0.385	1.011	1249
0.0240	0.0710	0.0000	0.0000	0.9050	27.37	1.1149	18.16	90.08	2.323E+04	0.1117	0.0090	0.8793	0.400	1.012	1277
0.0240	0.0710	0.0000	0.0000	0.9050	27.37	1.1149	18.16	90.08	2.323E+04	0.1116	0.0102	0.8782	0.413	1.014	1300
0.0240	0.0710	0.0000	0.0000	0.9050	27.37	1.1149	18.16	90.08	2.323E+04	0.1114	0.0114	0.8772	0.426	1.015	1323

Tab. 52: Experimental conditions for the mixture H_2 0% – CH_4 100% – Air for varying pilot conditions

$\chi_{H_2,j}$ [-]	$\chi_{CH_4,j}$ [-]	$\chi_{CO_2,j}$ [-]	$\chi_{N_2,j}$ [-]	$\chi_{Air,j}$ [-]	MW_j [kg/kmol]	$\rho_{u,j}$ [kg/m ³]	$\mu_{u,j}$ [μ Pa·s]	u_j [m/s]	Re_j [-]	$\chi_{H_2,p}$ [-]	$\chi_{CH_4,p}$ [-]	$\chi_{Air,p}$ [-]	Φ_p [-]	u_p [m/s]	T_p [K]
0.0000	0.0775	0.0000	0.0000	0.9225	27.94	1.1149	18.16	89.17	2.299E+04	0.1046	0.0155	0.8799	0.451	1.012	1358
0.0000	0.0775	0.0000	0.0000	0.9225	27.94	1.1149	18.16	89.17	2.299E+04	0.1046	0.0162	0.8793	0.459	1.012	1373
0.0000	0.0775	0.0000	0.0000	0.9225	27.94	1.1149	18.16	89.17	2.299E+04	0.1045	0.0171	0.8784	0.468	1.013	1394
0.0000	0.0775	0.0000	0.0000	0.9225	27.94	1.1149	18.16	89.17	2.299E+04	0.1044	0.0180	0.8776	0.478	1.014	1406
0.0000	0.0775	0.0000	0.0000	0.9225	27.94	1.1149	18.16	89.17	2.299E+04	0.1043	0.0190	0.8768	0.489	1.015	1425

Tab. 53: Experimental conditions for the mixture H_2 90% – CO 10% – Air for varying pilot conditions

$\chi_{H_2,j}$ [-]	$\chi_{CH_4,j}$ [-]	$\chi_{CO,j}$ [-]	$\chi_{N_2,j}$ [-]	$\chi_{Air,j}$ [-]	MW_j [kg/kmol]	$\rho_{u,j}$ [kg/m ³]	$\mu_{u,j}$ [μ Pa·s]	u_j [m/s]	Re_j [-]	$\chi_{H_2,p}$ [-]	$\chi_{CH_4,p}$ [-]	$\chi_{Air,p}$ [-]	Φ_p [-]	u_p [m/s]	T_p [K]
0.2264	0.0000	0.0252	0.0000	0.7484	22.82	0.9243	18.43	98.66	2.078E+04	0.1028	0.0000	0.8972	0.273	0.9922	1042
0.2264	0.0000	0.0252	0.0000	0.7484	22.82	0.9243	18.43	98.66	2.078E+04	0.1074	0.0000	0.8926	0.286	0.9973	1071
0.2264	0.0000	0.0252	0.0000	0.7484	22.82	0.9243	18.43	98.66	2.078E+04	0.1073	0.0010	0.8918	0.297	0.9982	1090

Tab. 54: Experimental conditions for the mixture H_2 80% – CO 20% – Air for varying pilot conditions

$\chi_{H_2,j}$ [-]	$\chi_{CH_4,j}$ [-]	$\chi_{CO,j}$ [-]	$\chi_{N_2,j}$ [-]	$\chi_{Air,j}$ [-]	MW_j [kg/kmol]	$\rho^{u,j}$ [kg/m ³]	$\mu^{u,j}$ [μ Pa·s]	u_j [m/s]	Re_j [-]	$\chi_{H_2,p}$ [-]	$\chi_{CH_4,p}$ [-]	$\chi_{Air,p}$ [-]	Φ_p [-]	u_p [m/s]	T_p [K]
0.2013	0.0000	0.0503	0.0000	0.7484	23.47	0.9508	18.44	97.28	2.107E+04	0.1028	0.0000	0.8972	0.273	0.9922	1045
0.2013	0.0000	0.0503	0.0000	0.7484	23.47	0.9508	18.44	97.28	2.107E+04	0.1074	0.0000	0.8926	0.286	0.9973	1075
0.2013	0.0000	0.0503	0.0000	0.7484	23.47	0.9508	18.44	97.28	2.107E+04	0.1073	0.0010	0.8918	0.297	0.9982	1096

Tab. 55: Experimental conditions for the mixture H_2 70% – CO 30% – Air for varying pilot conditions

$\chi_{H_2,j}$ [-]	$\chi_{CH_4,j}$ [-]	$\chi_{CO,j}$ [-]	$\chi_{N_2,j}$ [-]	$\chi_{Air,j}$ [-]	MW_j [kg/kmol]	$\rho_{u,j}$ [kg/m ³]	$\mu_{u,j}$ [μ Pa·s]	u_j [m/s]	Re_j [-]	$\chi_{H_2,p}$ [-]	$\chi_{CH_4,p}$ [-]	$\chi_{Air,p}$ [-]	Φ_p [-]	u_p [m/s]	T_p [K]
0.1761	0.0000	0.0755	0.0000	0.7484	24.12	0.9774	18.44	95.95	2.136E+04	0.1028	0.0000	0.8972	0.273	0.9922	1049
0.1761	0.0000	0.0755	0.0000	0.7484	24.12	0.9774	18.44	95.95	2.136E+04	0.1074	0.0000	0.8926	0.286	0.9973	1076
0.1761	0.0000	0.0755	0.0000	0.7484	24.12	0.9774	18.44	95.95	2.136E+04	0.1073	0.0010	0.8918	0.297	0.9982	1097

Tab. 56: Experimental conditions for the mixture H_2 60% – CO 40% – Air for varying pilot conditions

$\chi_{H_2,j}$ [-]	$\chi_{CH_4,j}$ [-]	$\chi_{CO,j}$ [-]	$\chi_{N_2,j}$ [-]	$\chi_{Air,j}$ [-]	MW_j [kg/kmol]	$\rho^{u,j}$ [kg/m ³]	$\mu^{u,j}$ [μ Pa·s]	u_j [m/s]	Re_j [-]	$\chi_{H_2,p}$ [-]	$\chi_{CH_4,p}$ [-]	$\chi_{Air,p}$ [-]	Φ_p [-]	u_p [m/s]	T_p [K]
0.1509	0.0000	0.1006	0.0000	0.7484	24.78	1.0040	18.44	94.68	2.165E+04	0.1028	0.0000	0.8972	0.273	0.9922	1051
0.1509	0.0000	0.1006	0.0000	0.7484	24.78	1.0040	18.44	94.68	2.165E+04	0.1074	0.0000	0.8926	0.286	0.9973	1078
0.1509	0.0000	0.1006	0.0000	0.7484	24.78	1.0040	18.44	94.68	2.165E+04	0.1073	0.0010	0.8918	0.297	0.9982	1099

Tab. 57: Experimental conditions for the mixture H_2 50% – CO 50% – Air for varying pilot conditions

$\chi_{H_2,j}$ [-]	$\chi_{CH_4,j}$ [-]	$\chi_{CO,j}$ [-]	$\chi_{N_2,j}$ [-]	$\chi_{Air,j}$ [-]	MW_j [kg/kmol]	$\rho_{u,j}$ [kg/m ³]	$\mu_{u,j}$ [μ Pa·s]	u_j [m/s]	Re_j [-]	$\chi_{H_2,p}$ [-]	$\chi_{CH_4,p}$ [-]	$\chi_{Air,p}$ [-]	Φ_p [-]	u_p [m/s]	T_p [K]
0.1258	0.0000	0.1258	0.0000	0.7484	25.43	1.0305	18.44	93.45	2.193E+04	0.1028	0.0000	0.8972	0.273	0.9922	1051
0.1258	0.0000	0.1258	0.0000	0.7484	25.43	1.0305	18.44	93.45	2.193E+04	0.1062	0.0010	0.8929	0.294	0.9970	1075
0.1258	0.0000	0.1258	0.0000	0.7484	25.43	1.0305	18.44	93.45	2.193E+04	0.1061	0.0019	0.8920	0.303	0.9980	1096
0.1258	0.0000	0.1258	0.0000	0.7484	25.43	1.0305	18.44	93.45	2.193E+04	0.1060	0.0029	0.8911	0.314	0.9990	1115

Tab. 58: Experimental conditions for the mixture H_2 40% – CO 60% – Air for varying pilot conditions

$\chi_{H_2,j}$ [-]	$\chi_{CH_4,j}$ [-]	$\chi_{CO,j}$ [-]	$\chi_{N_2,j}$ [-]	$\chi_{Air,j}$ [-]	MW_j [kg/kmol]	$\rho_{u,j}$ [kg/m ³]	$\mu_{u,j}$ [μ Pa·s]	u_j [m/s]	Re_j [-]	$\chi_{H_2,p}$ [-]	$\chi_{CH_4,p}$ [-]	$\chi_{Air,p}$ [-]	Φ_p [-]	u_p [m/s]	T_p [K]
0.1006	0.0000	0.1509	0.0000	0.7484	26.08	1.0571	18.44	92.28	2.222E+04	0.1028	0.0000	0.8972	0.273	0.9922	1044
0.1006	0.0000	0.1509	0.0000	0.7484	26.08	1.0571	18.44	92.28	2.222E+04	0.1074	0.0000	0.8926	0.286	0.9973	1071
0.1006	0.0000	0.1509	0.0000	0.7484	26.08	1.0571	18.44	92.28	2.222E+04	0.1073	0.0010	0.8918	0.297	0.9982	1092
0.1006	0.0000	0.1509	0.0000	0.7484	26.08	1.0571	18.44	92.28	2.222E+04	0.1072	0.0019	0.8909	0.307	0.9992	1111
0.1006	0.0000	0.1509	0.0000	0.7484	26.08	1.0571	18.44	92.28	2.222E+04	0.1070	0.0029	0.8901	0.317	1.000	1140

Tab. 59: Experimental conditions for the mixture H_2 30% – CO 70% – Air for varying pilot conditions

$\chi_{H_2,j}$ [-]	$\chi_{CH_4,j}$ [-]	$\chi_{CO,j}$ [-]	$\chi_{N_2,j}$ [-]	$\chi_{Air,j}$ [-]	MW_j [kg/kmol]	$\rho_{u,j}$ [kg/m ³]	$\mu_{u,j}$ [μ Pa·s]	u_j [m/s]	Re_j [-]	$\chi_{H_2,p}$ [-]	$\chi_{CH_4,p}$ [-]	$\chi_{Air,p}$ [-]	Φ_p [-]	u_p [m/s]	T_p [K]
0.0755	0.0000	0.1761	0.0000	0.7484	26.74	1.0837	18.44	91.14	2.250E+04	0.1028	0.0000	0.8972	0.273	0.9922	1050
0.0755	0.0000	0.1761	0.0000	0.7484	26.74	1.0837	18.44	91.14	2.250E+04	0.1074	0.0000	0.8926	0.286	0.9973	1075
0.0755	0.0000	0.1761	0.0000	0.7484	26.74	1.0837	18.44	91.14	2.250E+04	0.1073	0.0010	0.8918	0.297	0.9982	1098
0.0755	0.0000	0.1761	0.0000	0.7484	26.74	1.0837	18.44	91.14	2.250E+04	0.1072	0.0019	0.8909	0.307	1.000	1113
0.0755	0.0000	0.1761	0.0000	0.7484	26.74	1.0837	18.44	91.14	2.250E+04	0.1070	0.0031	0.8899	0.319	1.004	1139
0.0755	0.0000	0.1761	0.0000	0.7484	26.74	1.0837	18.44	91.14	2.250E+04	0.1069	0.0038	0.8892	0.327	1.010	1153

Tab. 60: Experimental conditions for the mixture $H_2 - N_2 - Air$ for varying pilot conditions

$\chi_{H_2,j}$ [-]	$\chi_{GH_4,j}$ [-]	$\chi_{CO,j}$ [-]	$\chi_{N_2,j}$ [-]	$\chi_{Air,j}$ [-]	MW_j [kg/kmol]	$\rho_{u,j}$ [kg/m ³]	$\mu_{u,j}$ [μ Pa·s]	u_j [m/s]	Re_j [-]	$\chi_{H_2,p}$ [-]	$\chi_{GH_4,p}$ [-]	$\chi_{Air,p}$ [-]	Φ_p [-]	u_p [m/s]	T_p [K]
0.1581	0.0000	0.0000	0.3715	0.4704	24.33	0.9870	18.31	95.54	2.164E+04	0.1127	0.0000	0.8873	0.302	1.003	1042
0.1581	0.0000	0.0000	0.3715	0.4704	24.33	0.9870	18.31	95.54	2.164E+04	0.1125	0.0014	0.8860	0.317	1.004	1068
0.1581	0.0000	0.0000	0.3715	0.4704	24.33	0.9870	18.31	95.54	2.164E+04	0.1124	0.0026	0.8850	0.330	1.006	1091

Tab. 61: Experimental conditions for the mixture H_2 90% – CH_4 10% – N_2 – Air for varying pilot conditions

$\chi_{H_2,j}$ [-]	$\chi_{CH_4,j}$ [-]	$\chi_{CO_2,j}$ [-]	$\chi_{N_2,j}$ [-]	$\chi_{Air,j}$ [-]	MW_j [kg/kmol]	$\rho_{u,j}$ [kg/m ³]	$\mu_{u,j}$ [μ Pa·s]	u_j [m/s]	Re_j [-]	$\chi_{H_2,p}$ [-]	$\chi_{CH_4,p}$ [-]	$\chi_{Air,p}$ [-]	Φ_p [-]	u_p [m/s]	T_p [K]
0.1136	0.0126	0.0000	0.3856	0.4882	25.35	1.0285	18.25	93.60	2.215E+04	0.1127	0.0000	0.8873	0.302	1.003	1048
0.1136	0.0126	0.0000	0.3856	0.4882	25.35	1.0285	18.25	93.60	2.215E+04	0.1125	0.0014	0.8860	0.317	1.004	1074
0.1136	0.0126	0.0000	0.3856	0.4882	25.35	1.0285	18.25	93.60	2.215E+04	0.1124	0.0026	0.8850	0.330	1.006	1084
0.1136	0.0126	0.0000	0.3856	0.4882	25.35	1.0285	18.25	93.60	2.215E+04	0.1124	0.0026	0.8850	0.330	1.006	1106
0.1136	0.0126	0.0000	0.3856	0.4882	25.35	1.0285	18.25	93.60	2.215E+04	0.1123	0.0036	0.8841	0.341	1.007	1123

Tab. 62: Experimental conditions for the mixture H_2 80% – CH_4 20% – N_2 – Air for varying pilot conditions

$\chi_{H_2,j}$ [-]	$\chi_{CH_4,j}$ [-]	$\chi_{CO_2,j}$ [-]	$\chi_{N_2,j}$ [-]	$\chi_{Air,j}$ [-]	MW_j [kg/kmol]	$\rho_{u,j}$ [kg/m ³]	$\mu_{u,j}$ [μ Pa·s]	u_j [m/s]	Re_j [-]	$\chi_{H_2,p}$ [-]	$\chi_{CH_4,p}$ [-]	$\chi_{Air,p}$ [-]	Φ_p [-]	u_p [m/s]	T_p [K]
0.0840	0.0210	0.0000	0.3950	0.5000	26.03	1.0560	18.22	92.37	2.249E+04	0.1074	0.0000	0.8926	0.286	0.9973	1078
0.0840	0.0210	0.0000	0.3950	0.5000	26.03	1.0560	18.22	92.37	2.249E+04	0.1072	0.0013	0.8914	0.300	0.9986	1099
0.0840	0.0210	0.0000	0.3950	0.5000	26.03	1.0560	18.22	92.37	2.249E+04	0.1060	0.0022	0.8918	0.306	0.9982	1107
0.0840	0.0210	0.0000	0.3950	0.5000	26.03	1.0560	18.22	92.37	2.249E+04	0.1060	0.0029	0.8911	0.314	0.9990	1125
0.0840	0.0210	0.0000	0.3950	0.5000	26.03	1.0560	18.22	92.37	2.249E+04	0.1059	0.0038	0.8903	0.324	0.9999	1130
0.0840	0.0210	0.0000	0.3950	0.5000	26.03	1.0560	18.22	92.37	2.249E+04	0.1058	0.0048	0.8894	0.334	1.0009	1157
0.0840	0.0210	0.0000	0.3950	0.5000	26.03	1.0560	18.22	92.37	2.249E+04	0.1057	0.0058	0.8875	0.346	1.0019	1185

Tab. 63: Experimental conditions for the mixture H_2 70% – CH_4 30% – N_2 – Air for varying pilot conditions

$\chi_{H_2,j}$ [-]	$\chi_{CH_4,j}$ [-]	$\chi_{CO_2,j}$ [-]	$\chi_{N_2,j}$ [-]	$\chi_{Air,j}$ [-]	MW_j [kg/kmol]	$\rho_{u,j}$ [kg/m ³]	$\mu_{u,j}$ [μ Pa·s]	u_j [m/s]	Re_j [-]	$\chi_{H_2,p}$ [-]	$\chi_{CH_4,p}$ [-]	$\chi_{Air,p}$ [-]	Φ_p [-]	u_p [m/s]	T_p [K]
0.0630	0.0270	0.0000	0.4016	0.5084	26.52	1.0756	18.20	91.52	2.272E+04	0.1062	0.0012	0.8926	0.296	0.9973	1101
0.0630	0.0270	0.0000	0.4016	0.5084	26.52	1.0756	18.20	91.52	2.272E+04	0.1060	0.0026	0.8914	0.311	0.9987	1123
0.0630	0.0270	0.0000	0.4016	0.5084	26.52	1.0756	18.20	91.52	2.272E+04	0.1059	0.0036	0.8905	0.322	0.9997	1142
0.0630	0.0270	0.0000	0.4016	0.5084	26.52	1.0756	18.20	91.52	2.272E+04	0.1058	0.0046	0.8896	0.332	1.001	1160
0.0630	0.0270	0.0000	0.4016	0.5084	26.52	1.0756	18.20	91.52	2.272E+04	0.1057	0.0058	0.8886	0.345	1.002	1186
0.0630	0.0270	0.0000	0.4016	0.5084	26.52	1.0756	18.20	91.52	2.272E+04	0.1055	0.0070	0.8875	0.358	1.003	1211

Tab. 64: Experimental conditions for the mixture H_2 60% – CH_4 40% – N_2 – Air for varying pilot conditions

$\chi_{H_2,j}$ [-]	$\chi_{CH_4,j}$ [-]	$\chi_{CO_2,j}$ [-]	$\chi_{N_2,j}$ [-]	$\chi_{Air,j}$ [-]	MW_j [kg/kmol]	$\rho_{u,j}$ [kg/m ³]	$\mu_{u,j}$ [μ Pa·s]	u_j [m/s]	Re_j [-]	$\chi_{H_2,p}$ [-]	$\chi_{CH_4,p}$ [-]	$\chi_{Air,p}$ [-]	Φ_p [-]	u_p [m/s]	T_p [K]
0.0630	0.0270	0.0000	0.4016	0.5084	26.52	1.0756	18.20	91.52	2.272E+04	0.1058	0.0048	0.8894	0.334	1.001	1147
0.0630	0.0270	0.0000	0.4016	0.5084	26.52	1.0756	18.20	91.52	2.272E+04	0.1057	0.0055	0.8888	0.342	1.002	1169
0.0630	0.0270	0.0000	0.4016	0.5084	26.52	1.0756	18.20	91.52	2.272E+04	0.1056	0.0065	0.8879	0.353	1.003	1190
0.0630	0.0270	0.0000	0.4016	0.5084	26.52	1.0756	18.20	91.52	2.272E+04	0.1055	0.0074	0.8871	0.362	1.004	1212
0.0630	0.0270	0.0000	0.4016	0.5084	26.52	1.0756	18.20	91.52	2.272E+04	0.1054	0.0084	0.8862	0.373	1.004	1234
0.0630	0.0270	0.0000	0.4016	0.5084	26.52	1.0756	18.20	91.52	2.272E+04	0.1053	0.0091	0.8856	0.381	1.005	1249

Tab. 65: Experimental conditions for the mixture H_2 50% – CH_4 50% – N_2 – Air for varying pilot conditions

$\chi_{H_2,j}$ [-]	$\chi_{CH_4,j}$ [-]	$\chi_{CO_2,j}$ [-]	$\chi_{N_2,j}$ [-]	$\chi_{Air,j}$ [-]	MW_j [kg/kmol]	$\rho_{u,j}$ [kg/m ³]	$\mu_{u,j}$ [μ Pa·s]	u_j [m/s]	Re_j [-]	$\chi_{H_2,p}$ [-]	$\chi_{CH_4,p}$ [-]	$\chi_{Air,p}$ [-]	Φ_p [-]	u_p [m/s]	T_p [K]
0.0349	0.0349	0.0000	0.4105	0.5197	27.16	1.0985	18.17	90.43	2.296E+04	0.1056	0.0068	0.8876	0.356	1.003	1211
0.0349	0.0349	0.0000	0.4105	0.5197	27.16	1.0985	18.17	90.43	2.296E+04	0.1055	0.0077	0.8869	0.366	1.004	1229
0.0349	0.0349	0.0000	0.4105	0.5197	27.16	1.0985	18.17	90.43	2.296E+04	0.1053	0.0089	0.8858	0.379	1.005	1253
0.0349	0.0349	0.0000	0.4105	0.5197	27.16	1.0985	18.17	90.43	2.296E+04	0.1053	0.0097	0.8851	0.387	1.006	1268
0.0349	0.0349	0.0000	0.4105	0.5197	27.16	1.0985	18.17	90.43	2.296E+04	0.1051	0.0108	0.8841	0.399	1.007	1296
0.0349	0.0349	0.0000	0.4105	0.5197	27.16	1.0985	18.17	90.43	2.296E+04	0.1050	0.0117	0.8833	0.409	1.008	1309

Tab. 66: Experimental conditions for the mixture H_2 40% – CH_4 60% – N_2 – Air for varying pilot conditions

$\chi_{H_2,j}$ [-]	$\chi_{CH_4,j}$ [-]	$\chi_{CO_2,j}$ [-]	$\chi_{N_2,j}$ [-]	$\chi_{Air,j}$ [-]	MW_j [kg/kmol]	$\rho_{u,j}$ [kg/m ³]	$\mu_{u,j}$ [μ Pa·s]	u_j [m/s]	Re_j [-]	$\chi_{H_2,p}$ [-]	$\chi_{CH_4,p}$ [-]	$\chi_{Air,p}$ [-]	Φ_p [-]	u_p [m/s]	T_p [K]
0.0251	0.0377	0.0000	0.4136	0.5236	27.39	1.1109	18.15	90.06	2.315E+04	0.1054	0.0079	0.8867	0.368	1.004	1230
0.0251	0.0377	0.0000	0.4136	0.5236	27.39	1.1109	18.15	90.06	2.315E+04	0.1054	0.0086	0.8860	0.376	1.005	1254
0.0251	0.0377	0.0000	0.4136	0.5236	27.39	1.1109	18.15	90.06	2.315E+04	0.1052	0.0100	0.8847	0.391	1.006	1276
0.0251	0.0377	0.0000	0.4136	0.5236	27.39	1.1109	18.15	90.06	2.315E+04	0.1051	0.0110	0.8839	0.401	1.007	1293
0.0251	0.0377	0.0000	0.4136	0.5236	27.39	1.1109	18.15	90.06	2.315E+04	0.1050	0.0122	0.8828	0.415	1.008	1311
0.0251	0.0377	0.0000	0.4136	0.5236	27.39	1.1109	18.15	90.06	2.315E+04	0.1049	0.0133	0.8818	0.427	1.010	1331

Tab. 67: Experimental conditions for the mixture H_2 0% – CH_4 0% – N_2 – Air for varying pilot conditions

$\chi_{H_2,j}$ [-]	$\chi_{CH_4,j}$ [-]	$\chi_{CO_2,j}$ [-]	$\chi_{N_2,j}$ [-]	$\chi_{Air,j}$ [-]	MW_j [kg/kmol]	$\rho_{u,j}$ [kg/m ³]	$\mu_{u,j}$ [μ Pa·s]	u_j [m/s]	Re_j [-]	$\chi_{H_2,p}$ [-]	$\chi_{CH_4,p}$ [-]	$\chi_{Air,p}$ [-]	Φ_p [-]	u_p [m/s]	T_p [K]
0.0000	0.0448	0.0000	0.4215	0.5336	27.96	1.1245	18.13	89.13	2.321E+04	0.1045	0.0171	0.8784	0.468	1.013	1381
0.0000	0.0448	0.0000	0.4215	0.5336	27.96	1.1245	18.13	89.13	2.321E+04	0.1044	0.0180	0.8776	0.478	1.014	1398
0.0000	0.0448	0.0000	0.4215	0.5336	27.96	1.1245	18.13	89.13	2.321E+04	0.1042	0.0199	0.8759	0.499	1.016	1314
0.0000	0.0448	0.0000	0.4215	0.5336	27.96	1.1245	18.13	89.13	2.321E+04	0.1041	0.0208	0.8751	0.509	1.017	1451
0.0000	0.0448	0.0000	0.4215	0.5336	27.96	1.1245	18.13	89.13	2.321E+04	0.1040	0.0217	0.8743	0.519	1.018	1469
0.0000	0.0448	0.0000	0.4215	0.5336	27.96	1.1245	18.13	89.13	2.321E+04	0.1038	0.0231	0.8731	0.535	1.020	1487

Tab. 68: Experimental conditions for the mixture H_2 90% – CO 10% – N_2 – Air for varying pilot conditions

$\chi_{H_2,j}$ [-]	$\chi_{CH_4,j}$ [-]	$\chi_{CO,j}$ [-]	$\chi_{N_2,j}$ [-]	$\chi_{Air,j}$ [-]	MW_j [kg/kmol]	$\rho^{u,j}$ [kg/m ³]	$\mu^{u,j}$ [μ Pa·s]	u_j [m/s]	Re_j [-]	$\chi_{H_2,p}$ [-]	$\chi_{CH_4,p}$ [-]	$\chi_{Air,p}$ [-]	Φ_p [-]	u_p [m/s]	T_p [K]
0.1423	0.0000	0.0158	0.3715	0.4704	24.74	1.0037	18.31	94.75	2.182E+04	0.1063	0.0000	0.8937	0.283	0.9961	1049
0.1423	0.0000	0.0158	0.3715	0.4704	24.74	1.0037	18.31	94.75	2.182E+04	0.1062	0.0007	0.8931	0.290	0.9968	1072
0.1423	0.0000	0.0158	0.3715	0.4704	24.74	1.0037	18.31	94.75	2.182E+04	0.1061	0.0014	0.8924	0.298	0.9975	1086

Tab. 69: Experimental conditions for the mixture H_2 80% – CO 20% – N_2 – Air for varying pilot conditions

$\chi_{H_2,j}$ [-]	$\chi_{CH_4,j}$ [-]	$\chi_{CO,j}$ [-]	$\chi_{N_2,j}$ [-]	$\chi_{Air,j}$ [-]	MW_j [kg/kmol]	$\rho_{u,j}$ [kg/m ³]	$\mu_{u,j}$ [μ Pa·s]	u_j [m/s]	Re_j [-]	$\chi_{H_2,p}$ [-]	$\chi_{CH_4,p}$ [-]	$\chi_{Air,p}$ [-]	Φ_p [-]	u_p [m/s]	T_p [K]
0.1265	0.0000	0.0316	0.3715	0.4704	25.15	1.0204	18.31	93.97	2.199E+04	0.1037	0.0000	0.8963	0.275	0.9932	1052
0.1265	0.0000	0.0316	0.3715	0.4704	25.15	1.0204	18.31	93.97	2.199E+04	0.1054	0.0000	0.8946	0.280	0.9951	1066
0.1265	0.0000	0.0316	0.3715	0.4704	25.15	1.0204	18.31	93.97	2.199E+04	0.1062	0.0007	0.8931	0.290	0.9968	1082
0.1265	0.0000	0.0316	0.3715	0.4704	25.15	1.0204	18.31	93.97	2.199E+04	0.1060	0.0022	0.8918	0.306	0.9982	1109
0.1265	0.0000	0.0316	0.3715	0.4704	25.15	1.0204	18.31	93.97	2.199E+04	0.1059	0.0031	0.8909	0.316	0.9992	1124

Tab. 70: Experimental conditions for the mixture H_2 70% – CO 30% – N_2 – Air for varying pilot conditions

$\chi_{H_2,j}$ [-]	$\chi_{CH_4,j}$ [-]	$\chi_{CO,j}$ [-]	$\chi_{N_2,j}$ [-]	$\chi_{Air,j}$ [-]	MW_j [kg/kmol]	$\rho_{u,j}$ [kg/m ³]	$\mu_{u,j}$ [μ Pa·s]	u_j [m/s]	Re_j [-]	$\chi_{H_2,p}$ [-]	$\chi_{CH_4,p}$ [-]	$\chi_{Air,p}$ [-]	Φ_p [-]	u_p [m/s]	T_p [K]
0.1107	0.0000	0.0474	0.3715	0.4704	25.56	1.0370	18.31	93.21	2.217E+04	0.1037	0.0000	0.8963	0.275	0.9932	1052
0.1107	0.0000	0.0474	0.3715	0.4704	25.56	1.0370	18.31	93.21	2.217E+04	0.1063	0.0000	0.8937	0.283	0.9961	1069
0.1107	0.0000	0.0474	0.3715	0.4704	25.56	1.0370	18.31	93.21	2.217E+04	0.1062	0.0010	0.8929	0.294	0.9970	1090
0.1107	0.0000	0.0474	0.3715	0.4704	25.56	1.0370	18.31	93.21	2.217E+04	0.1060	0.0022	0.8918	0.306	0.9982	1112
0.1107	0.0000	0.0474	0.3715	0.4704	25.56	1.0370	18.31	93.21	2.217E+04	0.1059	0.0031	0.8909	0.316	0.9992	1130
0.1107	0.0000	0.0474	0.3715	0.4704	25.56	1.0370	18.31	93.21	2.217E+04	0.1058	0.0041	0.8901	0.327	1.000	1151

Tab. 71: Experimental conditions for the mixture H_2 60% – CO 40% – N_2 – Air for varying pilot conditions

$\chi_{H_2,j}$ [-]	$\chi_{CH_4,j}$ [-]	$\chi_{CO,j}$ [-]	$\chi_{N_2,j}$ [-]	$\chi_{Air,j}$ [-]	MW_j [kg/kmol]	$\rho_{u,j}$ [kg/m ³]	$\mu_{u,j}$ [μ Pa·s]	u_j [m/s]	Re_j [-]	$\chi_{H_2,p}$ [-]	$\chi_{CH_4,p}$ [-]	$\chi_{Air,p}$ [-]	Φ_p [-]	u_p [m/s]	T_p [K]
0.0949	0.0000	0.0632	0.3715	0.4704	25.97	1.0537	18.31	92.47	2.235E+04	0.1028	0.0000	0.8972	0.273	0.9922	1053
0.0949	0.0000	0.0632	0.3715	0.4704	25.97	1.0537	18.31	92.47	2.235E+04	0.1063	0.0000	0.8937	0.283	0.9961	1071
0.0949	0.0000	0.0632	0.3715	0.4704	25.97	1.0537	18.31	92.47	2.235E+04	0.1062	0.0010	0.8929	0.294	0.9970	1091
0.0949	0.0000	0.0632	0.3715	0.4704	25.97	1.0537	18.31	92.47	2.235E+04	0.1059	0.0031	0.8909	0.316	0.9992	1108
0.0949	0.0000	0.0632	0.3715	0.4704	25.97	1.0537	18.31	92.47	2.235E+04	0.1058	0.0041	0.8901	0.327	1.000	1133
0.0949	0.0000	0.0632	0.3715	0.4704	25.97	1.0537	18.31	92.47	2.235E+04	0.1057	0.0050	0.8892	0.336	1.001	1148

Tab. 72: Experimental conditions for the mixture H_2 50% – CO 50% – N_2 – Air for varying pilot conditions

$\chi_{H_2,j}$ [-]	$\chi_{CH_4,j}$ [-]	$\chi_{CO,j}$ [-]	$\chi_{N_2,j}$ [-]	$\chi_{Air,j}$ [-]	MW_j [kg/kmol]	$\rho_{u,j}$ [kg/m ³]	$\mu_{u,j}$ [μ Pa·s]	u_j [m/s]	Re_j [-]	$\chi_{H_2,p}$ [-]	$\chi_{CH_4,p}$ [-]	$\chi_{Air,p}$ [-]	Φ_p [-]	u_p [m/s]	T_p [K]
0.0791	0.0000	0.0791	0.3715	0.4704	26.39	1.0704	18.31	91.74	2.253E+04	0.1028	0.0000	0.8972	0.273	0.9922	1043
0.0791	0.0000	0.0791	0.3715	0.4704	26.39	1.0704	18.31	91.74	2.253E+04	0.1063	0.0000	0.8937	0.283	0.9961	1066
0.0791	0.0000	0.0791	0.3715	0.4704	26.39	1.0704	18.31	91.74	2.253E+04	0.1062	0.0012	0.8926	0.296	0.9970	1085
0.0791	0.0000	0.0791	0.3715	0.4704	26.39	1.0704	18.31	91.74	2.253E+04	0.1060	0.0029	0.8911	0.314	0.9992	1119
0.0791	0.0000	0.0791	0.3715	0.4704	26.39	1.0704	18.31	91.74	2.253E+04	0.1059	0.0038	0.8903	0.324	1.000	1135
0.0791	0.0000	0.0791	0.3715	0.4704	26.39	1.0704	18.31	91.74	2.253E+04	0.1058	0.0048	0.8894	0.334	1.001	1159

Tab. 73: Experimental conditions for the mixture H_2 40% – CO 60% – N_2 – Air for varying pilot conditions

$\chi_{H_2,j}$ [-]	$\chi_{CH_4,j}$ [-]	$\chi_{CO,j}$ [-]	$\chi_{N_2,j}$ [-]	$\chi_{Air,j}$ [-]	MW_j [kg/kmol]	$\rho_{u,j}$ [kg/m ³]	$\mu_{u,j}$ [μ Pa·s]	u_j [m/s]	Re_j [-]	$\chi_{H_2,p}$ [-]	$\chi_{CH_4,p}$ [-]	$\chi_{Air,p}$ [-]	Φ_p [-]	u_p [m/s]	T_p [K]
0.0632	0.0000	0.0949	0.3715	0.4704	26.80	1.0872	18.31	91.04	2.271E+04	0.1028	0.0000	0.8972	0.273	0.9922	1050
0.0632	0.0000	0.0949	0.3715	0.4704	26.80	1.0872	18.31	91.04	2.271E+04	0.1063	0.0000	0.8937	0.283	0.9961	1068
0.0632	0.0000	0.0949	0.3715	0.4704	26.80	1.0872	18.31	91.04	2.271E+04	0.1062	0.0010	0.8929	0.294	0.9970	1087
0.0632	0.0000	0.0949	0.3715	0.4704	26.80	1.0872	18.31	91.04	2.271E+04	0.1060	0.0022	0.8918	0.306	0.9982	1110
0.0632	0.0000	0.0949	0.3715	0.4704	26.80	1.0872	18.31	91.04	2.271E+04	0.1059	0.0034	0.8907	0.319	0.9994	1134
0.0632	0.0000	0.0949	0.3715	0.4704	26.80	1.0872	18.31	91.04	2.271E+04	0.1058	0.0046	0.8896	0.332	1.001	1157

Tab. 74: Experimental conditions for the mixture H_2 30% – CO 70% – N_2 – Air for varying pilot conditions

$\chi_{H_2,j}$ [-]	$\chi_{CH_4,j}$ [-]	$\chi_{CO,j}$ [-]	$\chi_{N_2,j}$ [-]	$\chi_{Air,j}$ [-]	MW_j [kg/kmol]	$\rho_{u,j}$ [kg/m ³]	$\mu_{u,j}$ [μ Pa·s]	u_j [m/s]	Re_j [-]	$\chi_{H_2,p}$ [-]	$\chi_{CH_4,p}$ [-]	$\chi_{Air,p}$ [-]	Φ_p [-]	u_p [m/s]	T_p [K]
0.0474	0.0000	0.1107	0.3715	0.4704	27.21	1.1039	18.31	90.35	2.288E+04	0.1028	0.0000	0.8972	0.273	0.9922	1052
0.0474	0.0000	0.1107	0.3715	0.4704	27.21	1.1039	18.31	90.35	2.288E+04	0.1063	0.0000	0.8937	0.283	0.9961	1069
0.0474	0.0000	0.1107	0.3715	0.4704	27.21	1.1039	18.31	90.35	2.288E+04	0.1061	0.0019	0.8920	0.303	0.9980	1085
0.0474	0.0000	0.1107	0.3715	0.4704	27.21	1.1039	18.31	90.35	2.288E+04	0.1059	0.0034	0.8907	0.319	0.9994	1116
0.0474	0.0000	0.1107	0.3715	0.4704	27.21	1.1039	18.31	90.35	2.288E+04	0.1059	0.0038	0.8903	0.324	0.9999	1130
0.0474	0.0000	0.1107	0.3715	0.4704	27.21	1.1039	18.31	90.35	2.288E+04	0.1058	0.0048	0.8894	0.334	1.001	1149

B Supplementary Figures

B.1 Hydrogen Blends with Methane

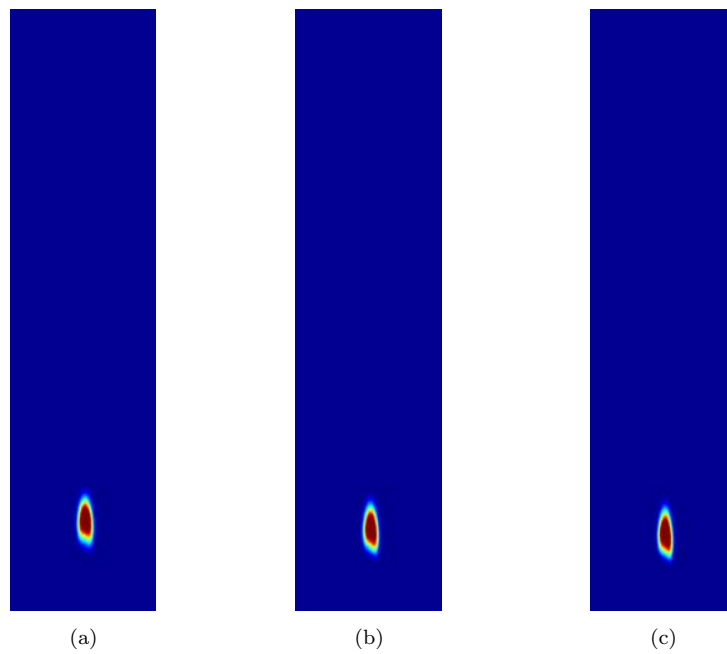


Fig. 74: OH^* Chemiluminescence for H_2 100%: (a) at $T_p \approx 1040$ K; (b) at $T_p \approx 1070$ K; (c) at $T_p \approx 1095$ K;

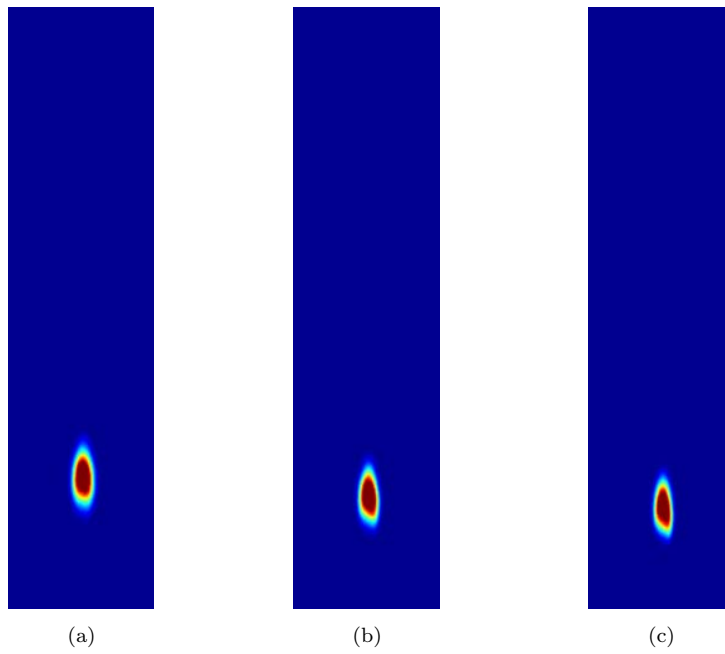


Fig. 75: OH^* Chemiluminescence for H_2 90% – CH_4 10%: (a) at $T_p \approx 1040$ K; (b) at $T_p \approx 1070$ K; (c) at $T_p \approx 1095$ K;

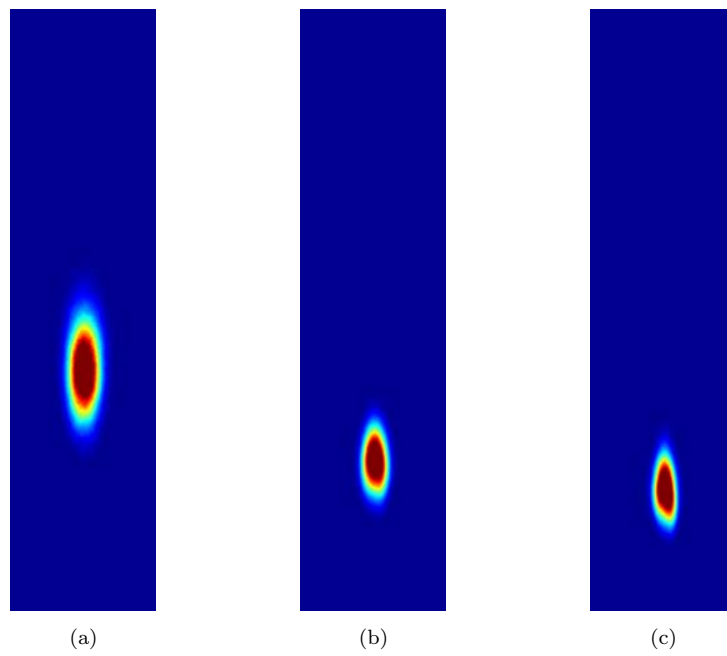


Fig. 76: OH^* Chemiluminescence for H_2 80% – CH_4 20%: (a) at $T_p \approx 1040$ K; (b) at $T_p \approx 1100$ K; (c) at $T_p \approx 1160$ K;

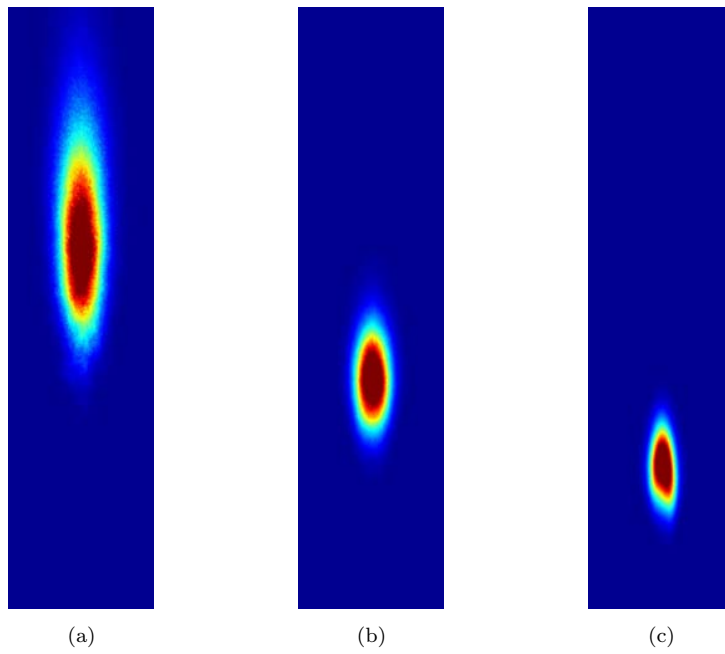


Fig. 77: OH^* Chemiluminescence for H_2 70% – CH_4 30%: (a) at $T_p \approx 1070$ K; (b) at $T_p \approx 1110$ K; (c) at $T_p \approx 1190$ K;

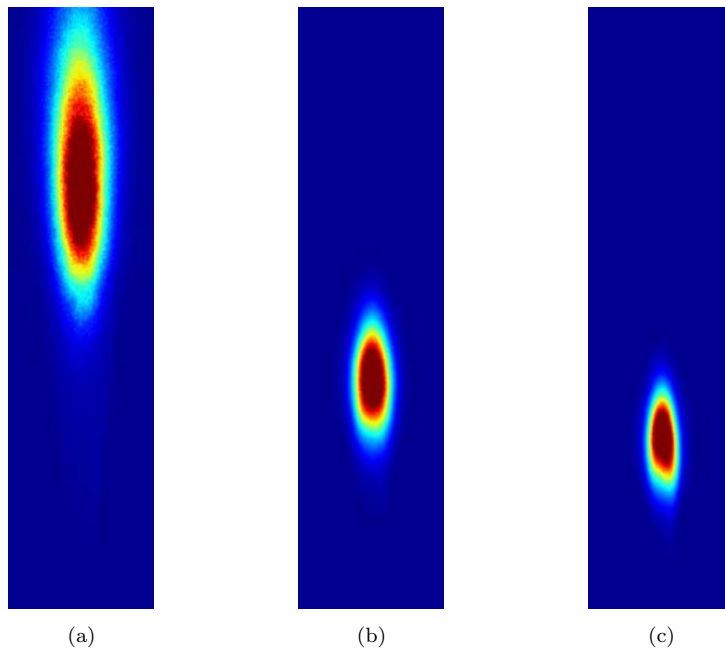


Fig. 78: OH^* Chemiluminescence for H_2 60% - CH_4 40%: (a) at $T_p \approx 1140$ K; (b) at $T_p \approx 1175$ K; (c) at $T_p \approx 1230$ K;

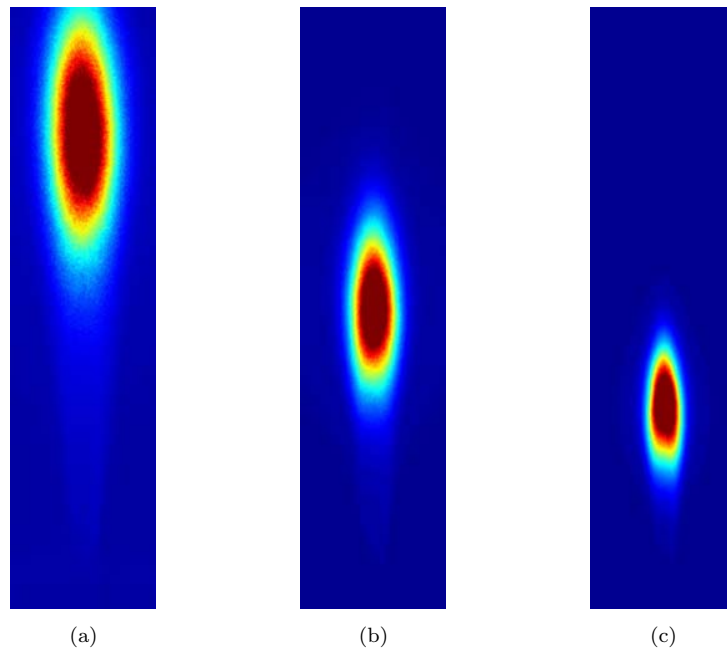


Fig. 79: OH^* Chemiluminescence for H_2 50% – CH_4 50%: (a) at $T_p \approx 1160$ K; (b) at $T_p \approx 1200$ K; (c) at $T_p \approx 1255$ K;

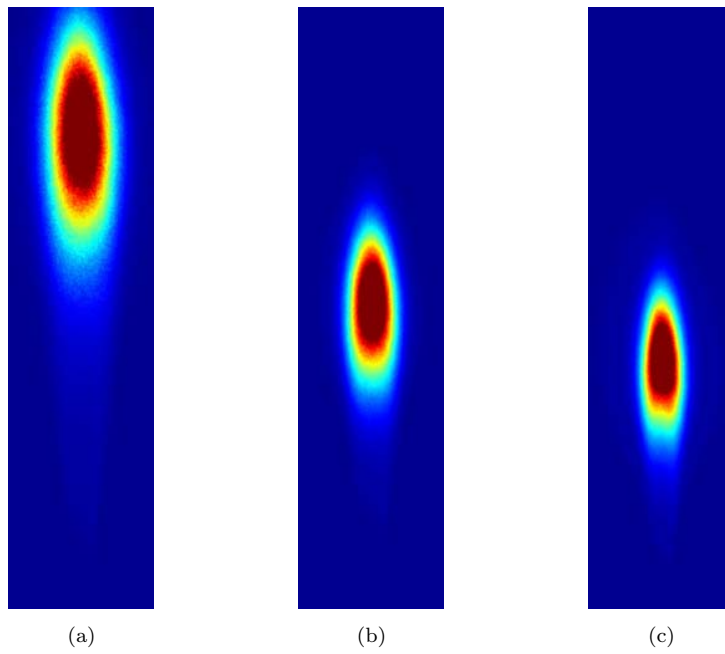


Fig. 80: OH^* Chemiluminescence for H_2 40% – CH_4 60%: (a) at $T_p \approx 1200$ K; (b) at $T_p \approx 1240$ K; (c) at $T_p \approx 1275$ K;

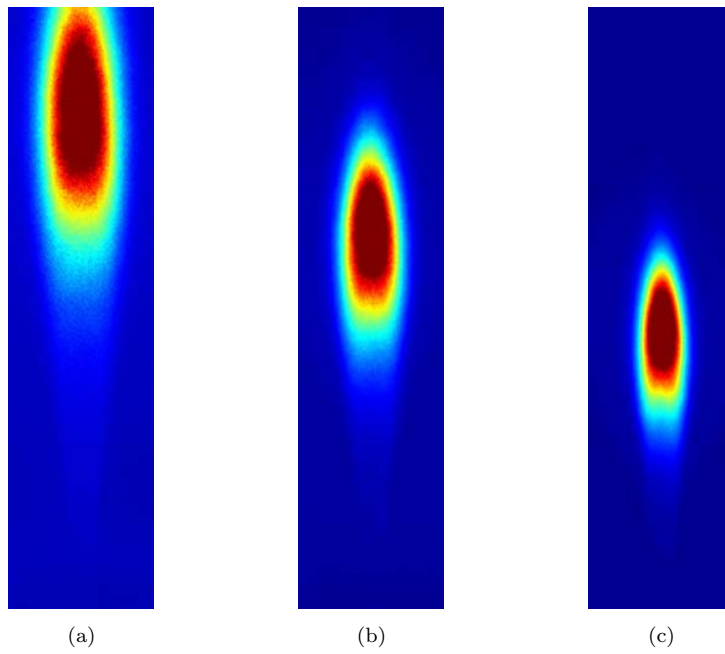


Fig. 81: OH^* Chemiluminescence for H_2 25% – CH_4 75%: (a) at $T_p \approx 1210$ K; (b) at $T_p \approx 1275$ K; (c) at $T_p \approx 1320$ K;

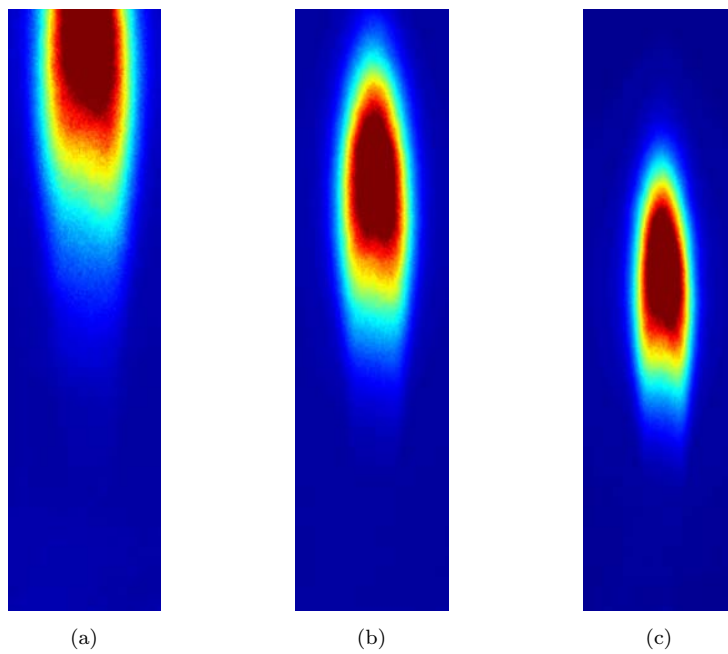


Fig. 82: OH^* Chemiluminescence for H_2 0% – CH_4 100%: (a) at $T_p \approx 1355$ K; (b) at $T_p \approx 1395$ K; (c) at $T_p \approx 1425$ K;

B.2 Hydrogen Blends with Carbon Monoxide

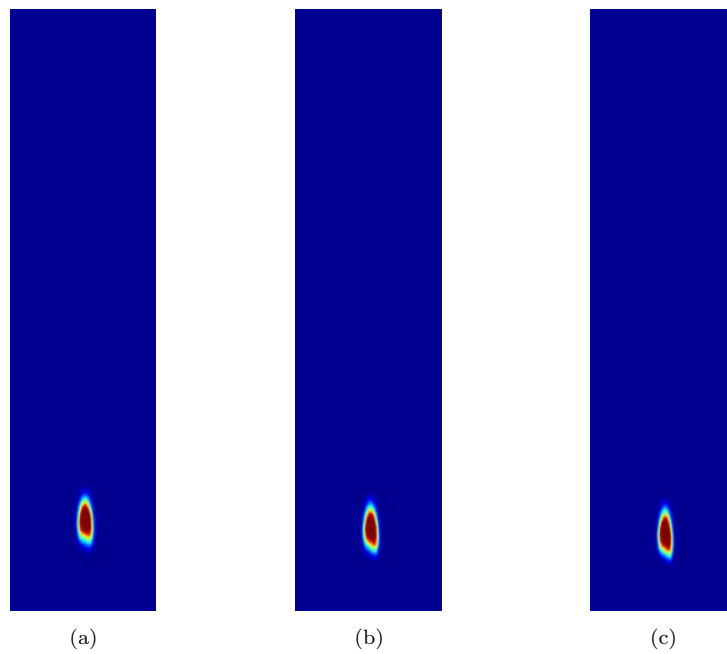


Fig. 83: OH^* Chemiluminescence for H_2 100%: (a) at $T_p \approx 1040$ K; (b) at $T_p \approx 1070$ K; (c) at $T_p \approx 1095$ K;

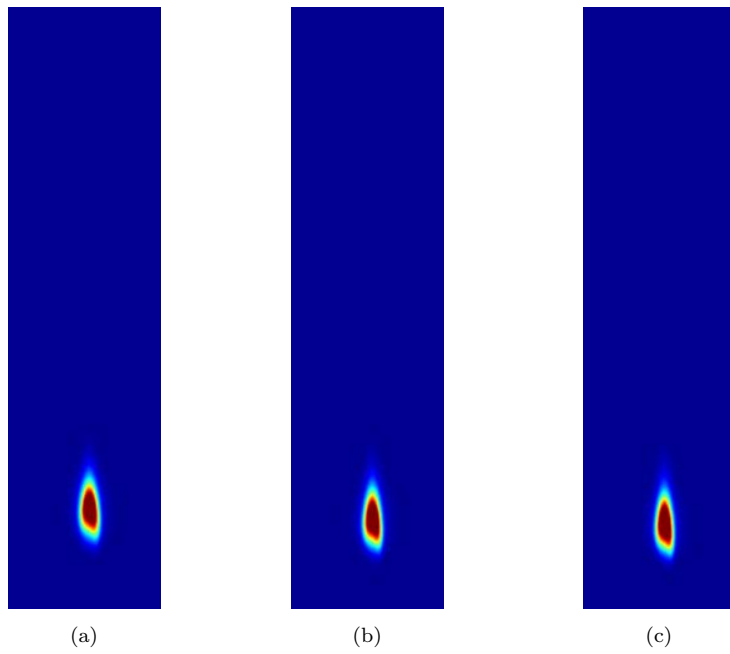


Fig. 84: OH^* Chemiluminescence for H_2 90% – CO 10%: (a) at $T_p \approx 1040$ K; (b) at $T_p \approx 1070$ K; (c) at $T_p \approx 1095$ K;

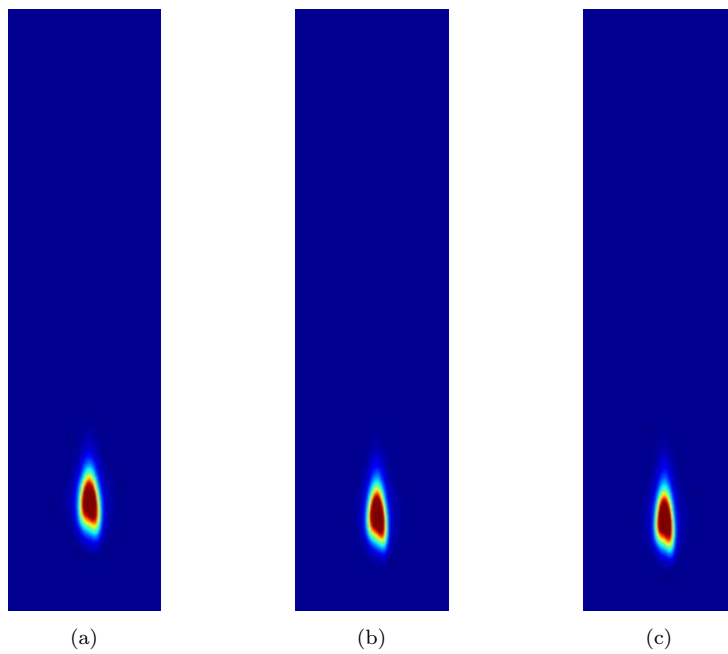


Fig. 85: OH^* Chemiluminescence for H_2 80% – CO 20%: (a) at $T_p \approx 1040$ K; (b) at $T_p \approx 1075$ K; (c) at $T_p \approx 1095$ K;

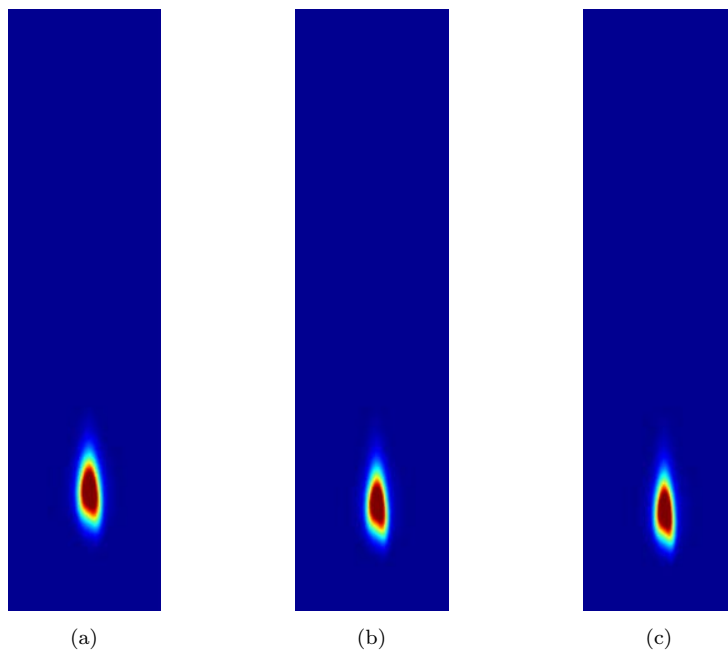


Fig. 86: OH^* Chemiluminescence for H_2 70% – CO 30%: (a) at $T_p \approx 1050$ K; (b) at $T_p \approx 1075$ K; (c) at $T_p \approx 1095$ K;

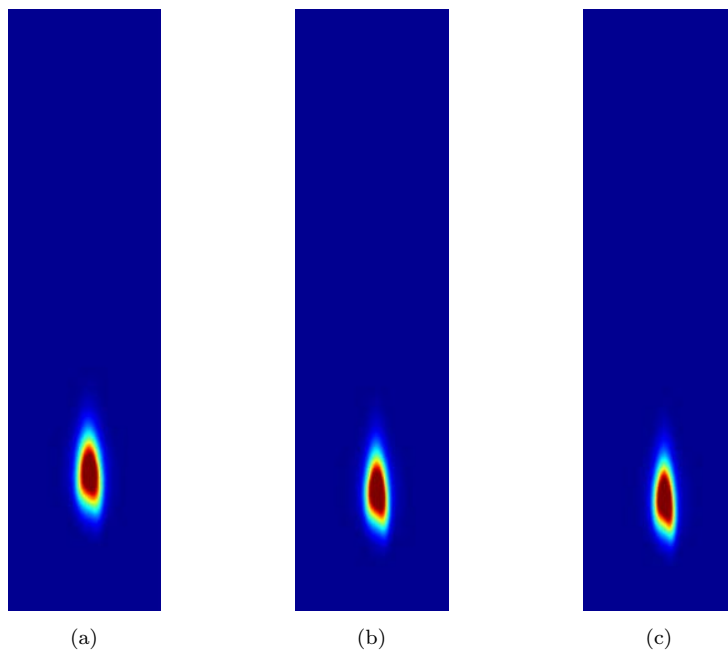


Fig. 87: OH^* Chemiluminescence for H_2 60% – CO 40%: (a) at $T_p \approx 1050$ K; (b) at $T_p \approx 1075$ K; (c) at $T_p \approx 1100$ K;

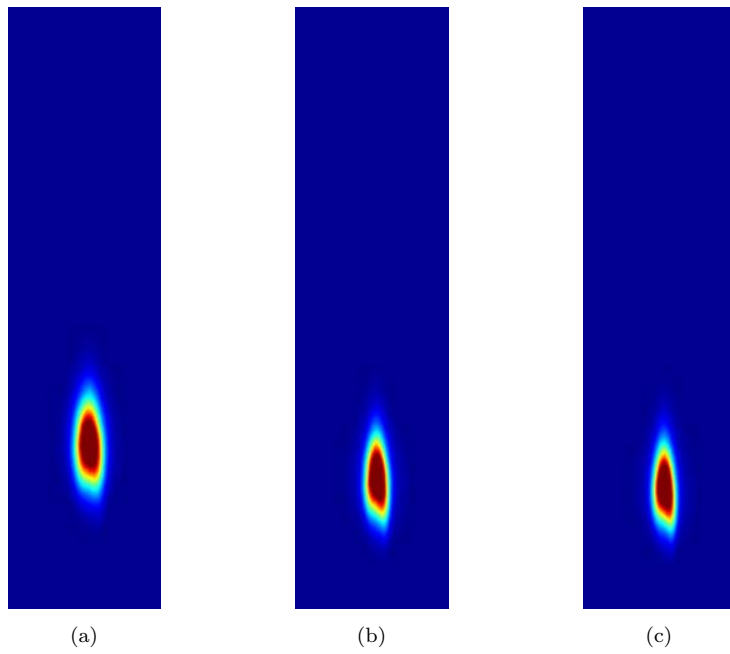


Fig. 88: OH^* Chemiluminescence for H_2 50% – CO 50%: (a) at $T_p \approx 1050$ K; (b) at $T_p \approx 1095$ K; (c) at $T_p \approx 1115$ K;

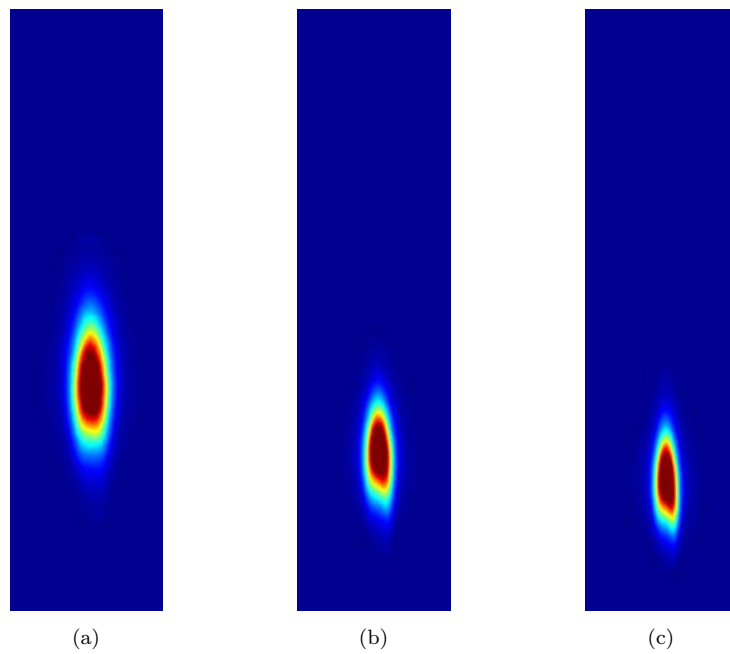


Fig. 89: OH^* Chemiluminescence for H_2 40% – CO 60%: (a) at $T_p \approx 1045$ K; (b) at $T_p \approx 1090$ K; (c) at $T_p \approx 1140$ K;

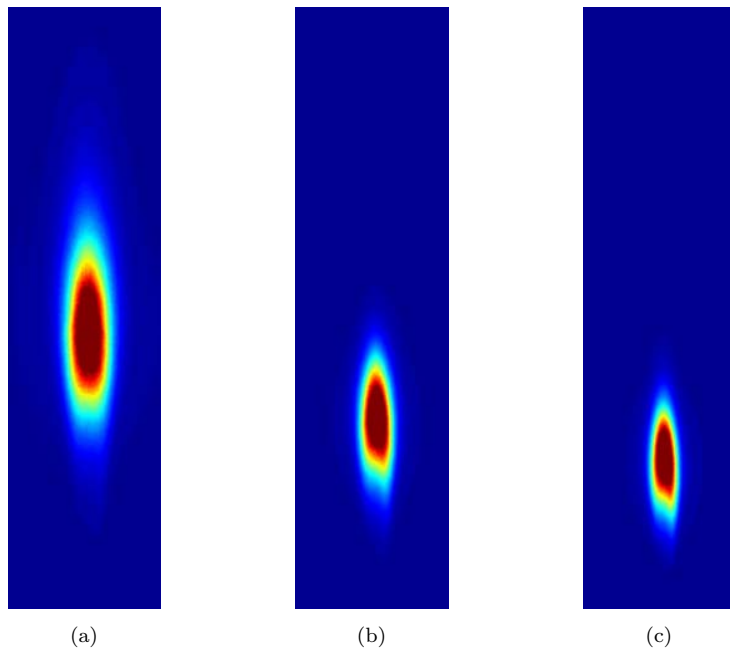


Fig. 90: OH^* Chemiluminescence for H_2 30% – CO 70%: (a) at $T_p \approx 1050$ K; (b) at $T_p \approx 1100$ K; (c) at $T_p \approx 1150$ K;

B.3 Hydrogen Blends with Methane and Nitrogen Dilution

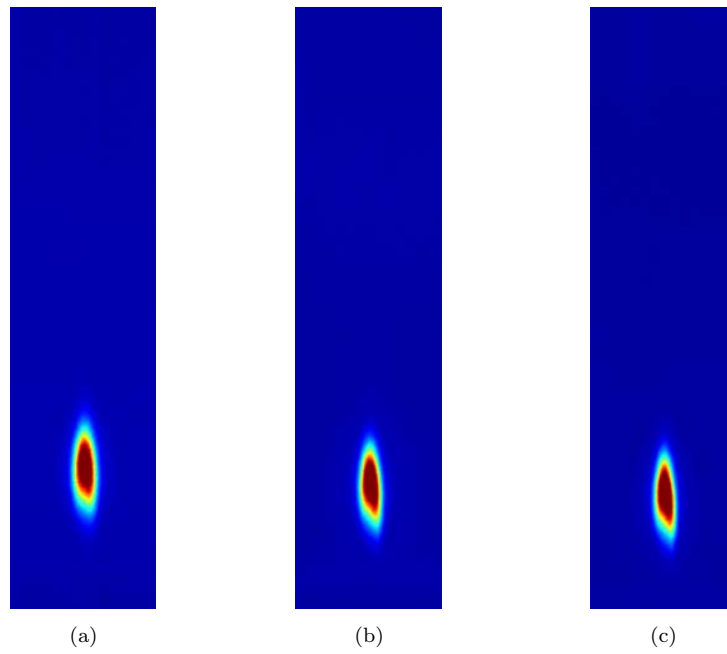


Fig. 91: OH^* Chemiluminescence for H_2 100% - N_2 : (a) at $T_p \approx 1040$ K; (b) at $T_p \approx 1070$ K; (c) at $T_p \approx 1090$ K;

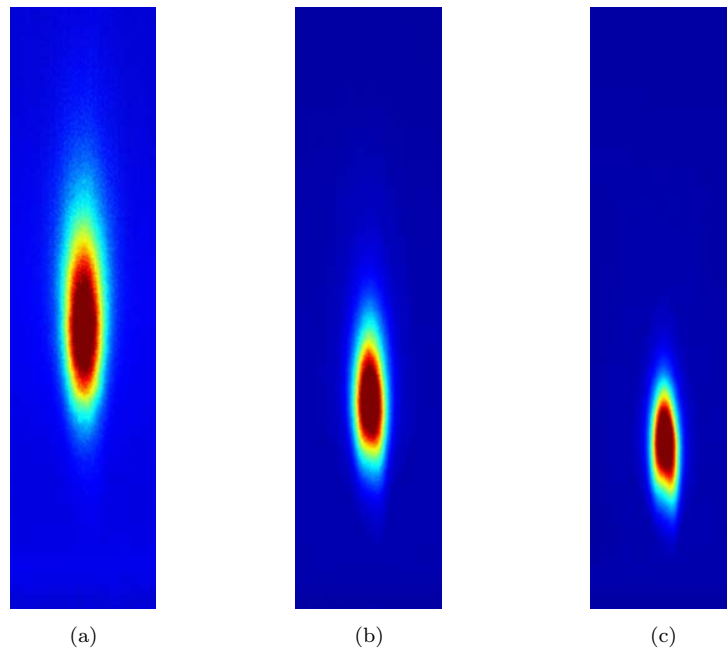


Fig. 92: OH^* Chemiluminescence for H_2 90% – CH_4 10% – N_2 : (a) at $T_p \approx 1045$ K; (b) at $T_p \approx 1075$ K; (c) at $T_p \approx 1125$ K;

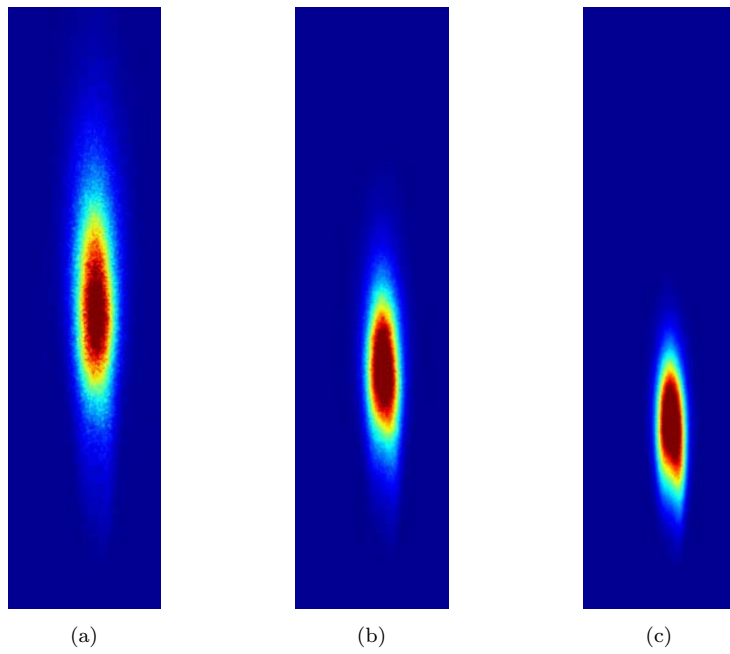


Fig. 93: OH^* Chemiluminescence for H_2 80% – CH_4 20% – N_2 : (a) at $T_p \approx 1100$ K; (b) at $T_p \approx 1140$ K; (c) at $T_p \approx 1185$ K;

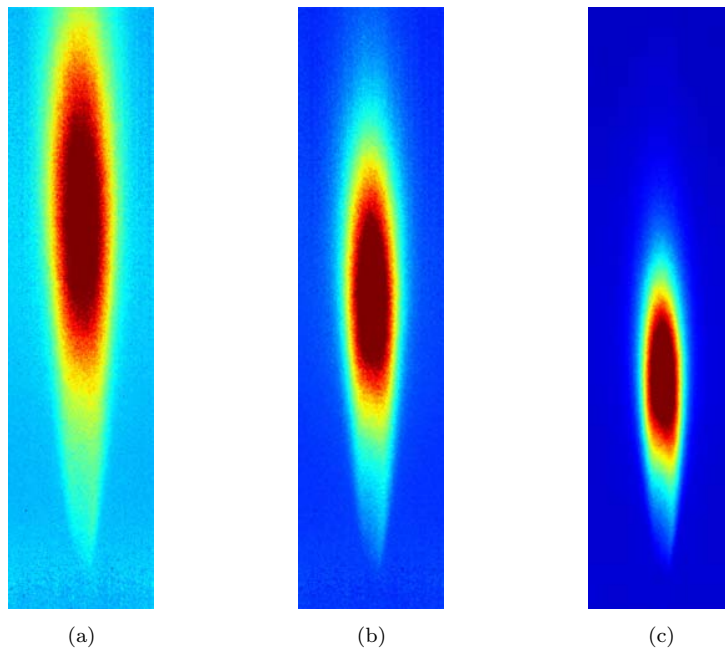


Fig. 94: OH^* Chemiluminescence for H_2 70% – CH_4 30% – N_2 : (a) at $T_p \approx 1140$ K; (b) at $T_p \approx 1160$ K; (c) at $T_p \approx 1210$ K;

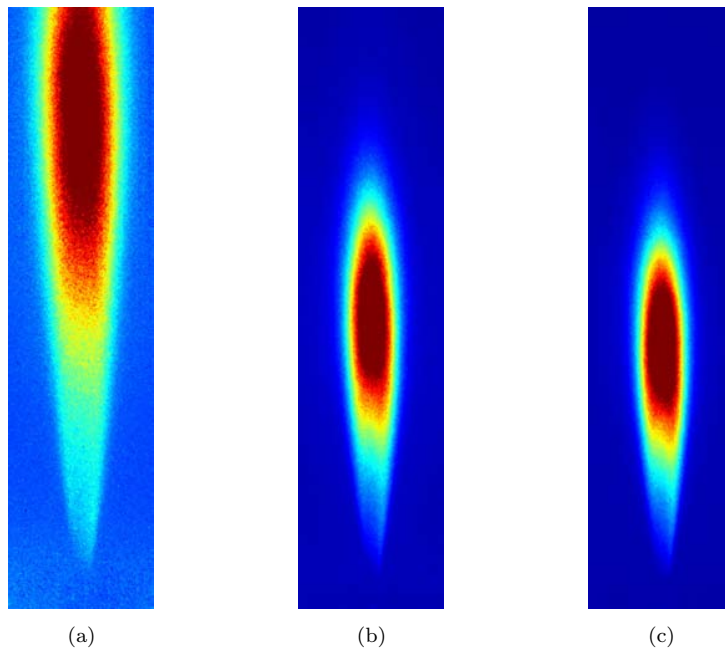


Fig. 95: OH^* Chemiluminescence for H_2 60% – CH_4 40% – N_2 : (a) at $T_p \approx 1170$ K; (b) at $T_p \approx 1210$ K; (c) at $T_p \approx 1250$ K;

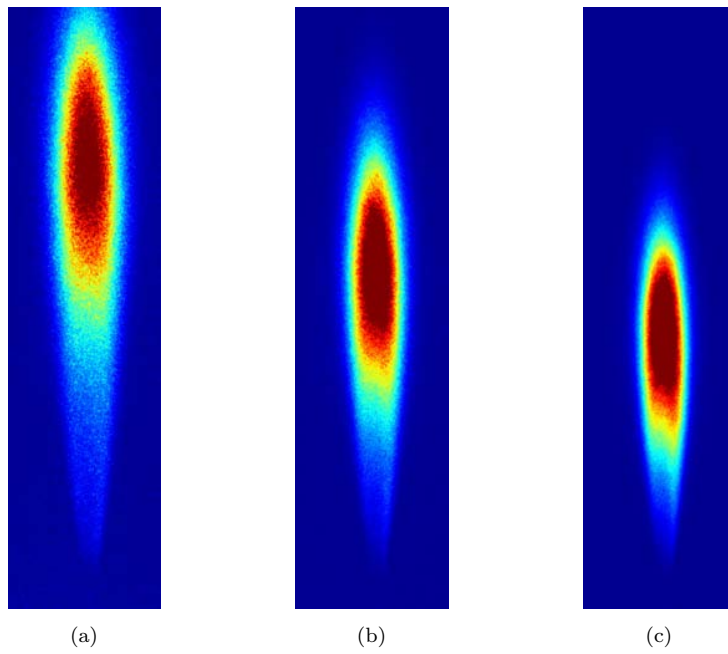


Fig. 96: OH^* Chemiluminescence for H_2 50% – CH_4 50% – N_2 : (a) at $T_p \approx 1230$ K; (b) at $T_p \approx 1270$ K; (c) at $T_p \approx 1310$ K;

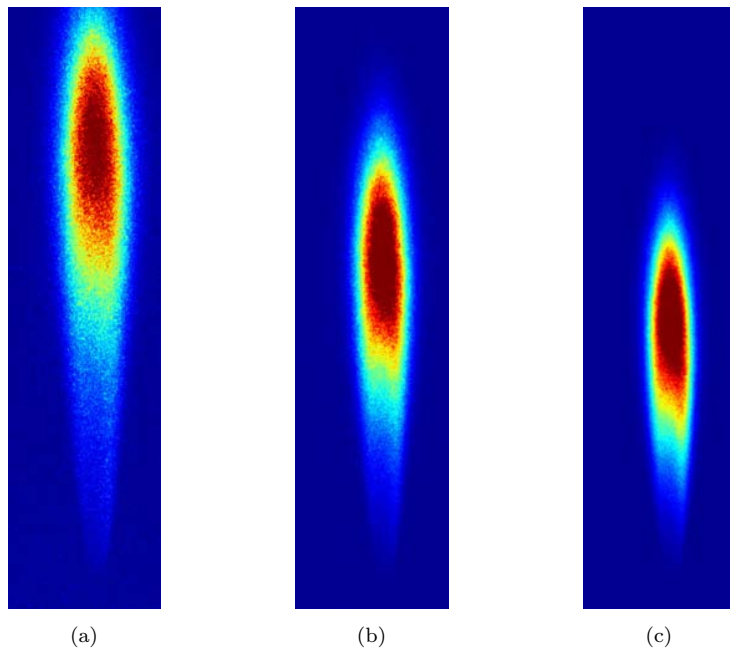


Fig. 97: OH^* Chemiluminescence for H_2 40% – CH_4 60% – N_2 : (a) at $T_p \approx 1250$ K; (b) at $T_p \approx 1290$ K; (c) at $T_p \approx 1330$ K;

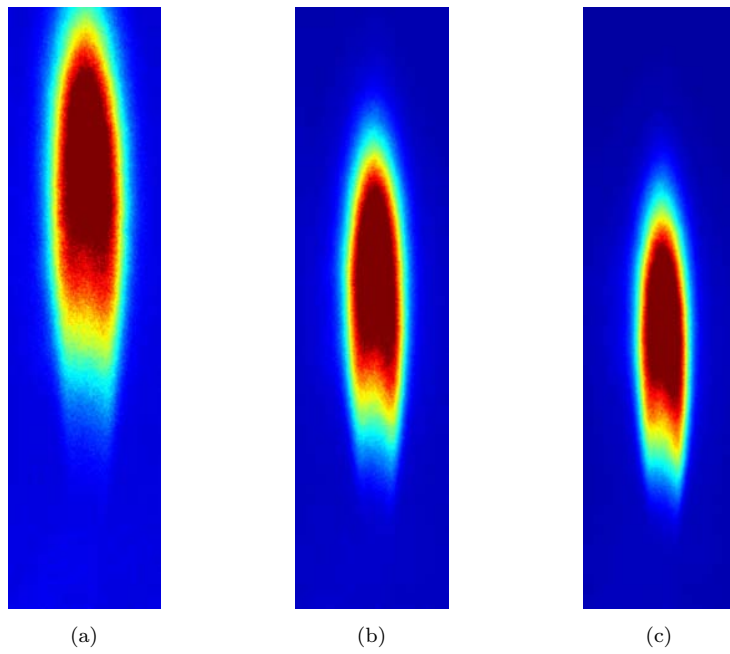


Fig. 98: OH^* Chemiluminescence for H_2 0% – CH_4 100% – N_2 : (a) at $T_p \approx 1400$ K; (b) at $T_p \approx 1450$ K; (c) at $T_p \approx 1485$ K;

B.4 Hydrogen Blends with Carbon Monoxide and Nitrogen Dilution

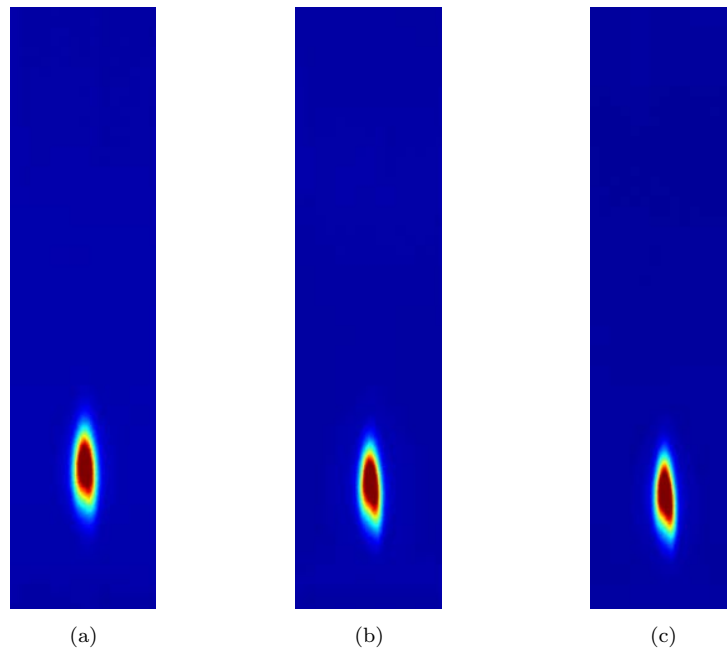


Fig. 99: OH^* Chemiluminescence for H_2 100%: (a) at $T_p \approx 1040$ K; (b) at $T_p \approx 1070$ K; (c) at $T_p \approx 1090$ K;

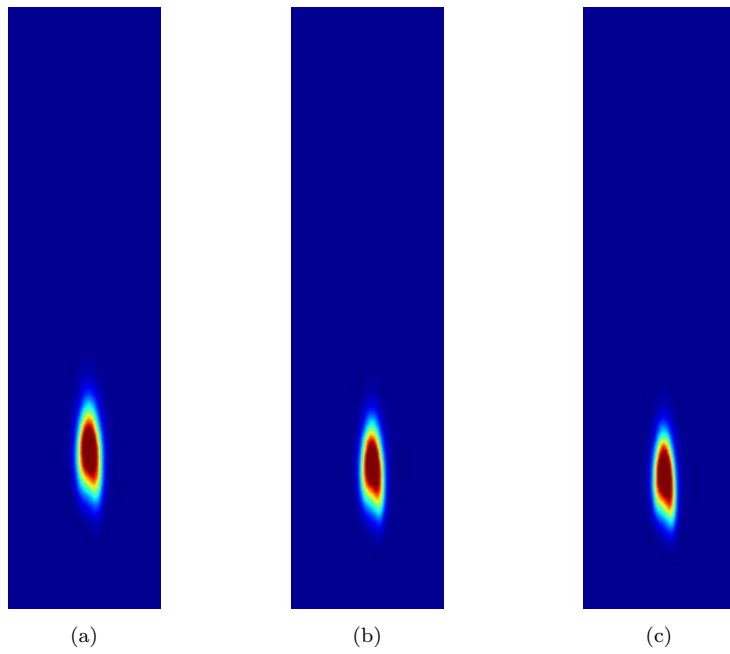


Fig. 100: OH^* Chemiluminescence for H_2 90% – CO 10%: (a) at $T_p \approx 1050$ K; (b) at $T_p \approx 1070$ K; (c) at $T_p \approx 1085$ K;

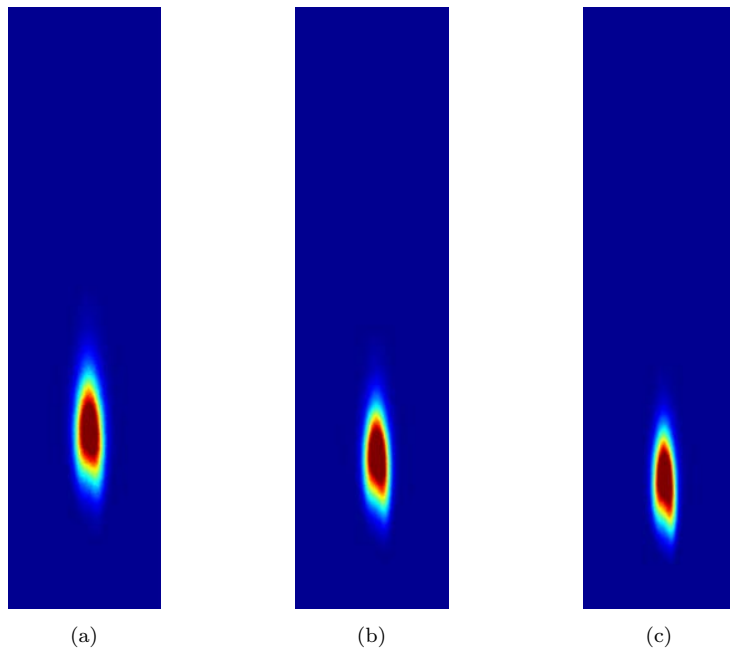


Fig. 101: OH^* Chemiluminescence for H_2 80% – CO 20%: (a) at $T_p \approx 1050$ K; (b) at $T_p \approx 1080$ K; (c) at $T_p \approx 1125$ K;

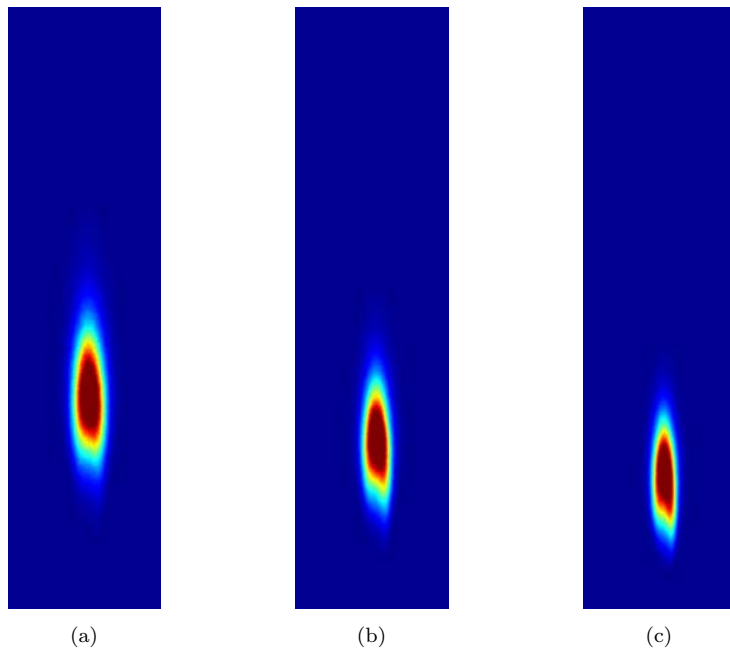


Fig. 102: OH^* Chemiluminescence for H_2 70% – CO 30%: (a) at $T_p \approx 1050$ K; (b) at $T_p \approx 1090$ K; (c) at $T_p \approx 1150$ K;

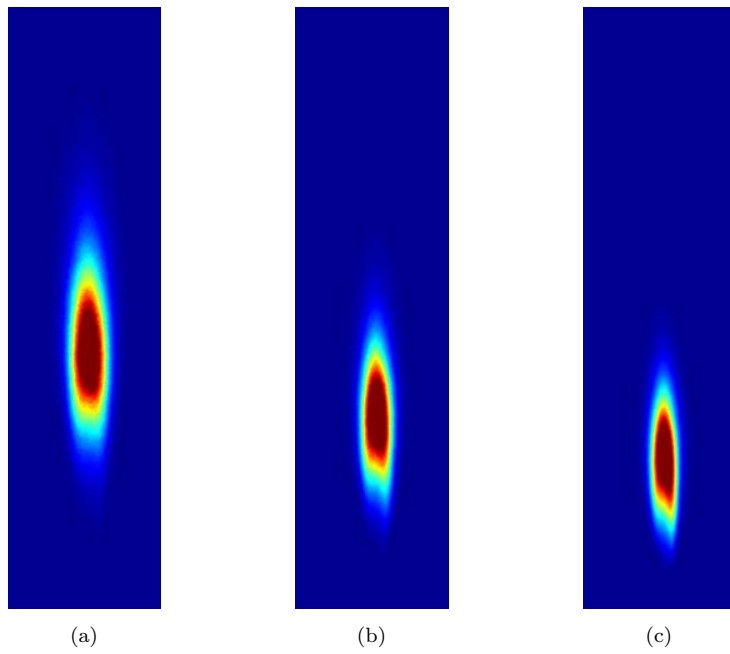


Fig. 103: OH^* Chemiluminescence for H_2 60% – CO 40%: (a) at $T_p \approx 1050$ K; (b) at $T_p \approx 1090$ K; (c) at $T_p \approx 1150$ K;

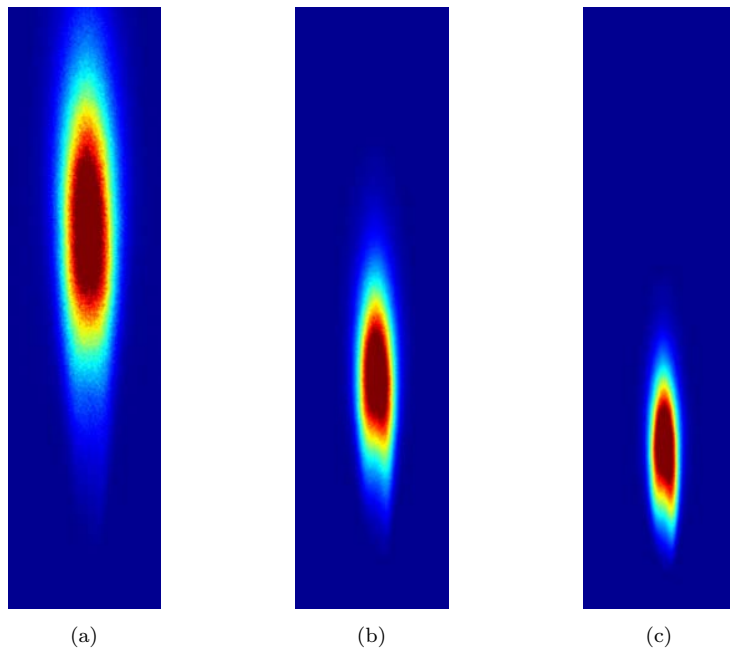


Fig. 104: OH^* Chemiluminescence for H_2 50% – CO 50%: (a) at $T_p \approx 1045$ K; (b) at $T_p \approx 1085$ K; (c) at $T_p \approx 1160$ K;

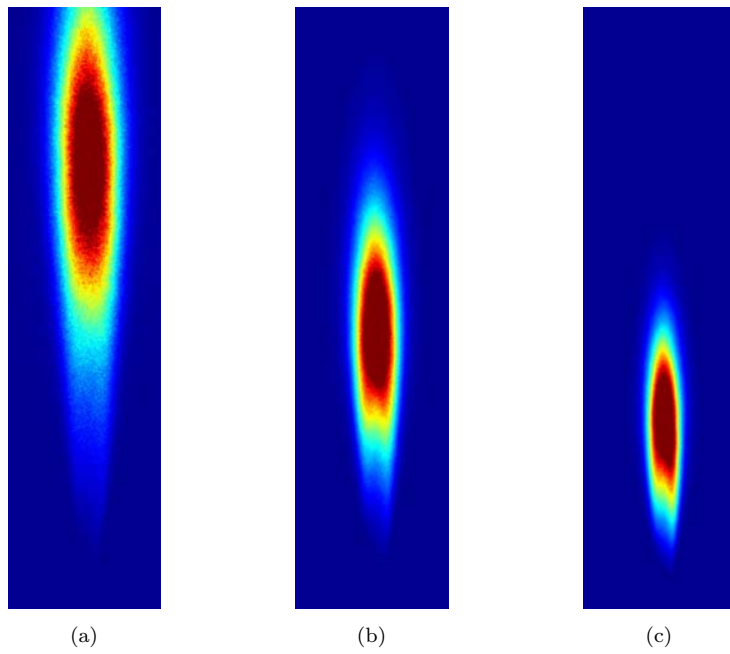


Fig. 105: OH^* Chemiluminescence for H_2 40% – CO 60%: (a) at $T_p \approx 1050$ K; (b) at $T_p \approx 1085$ K; (c) at $T_p \approx 1155$ K;

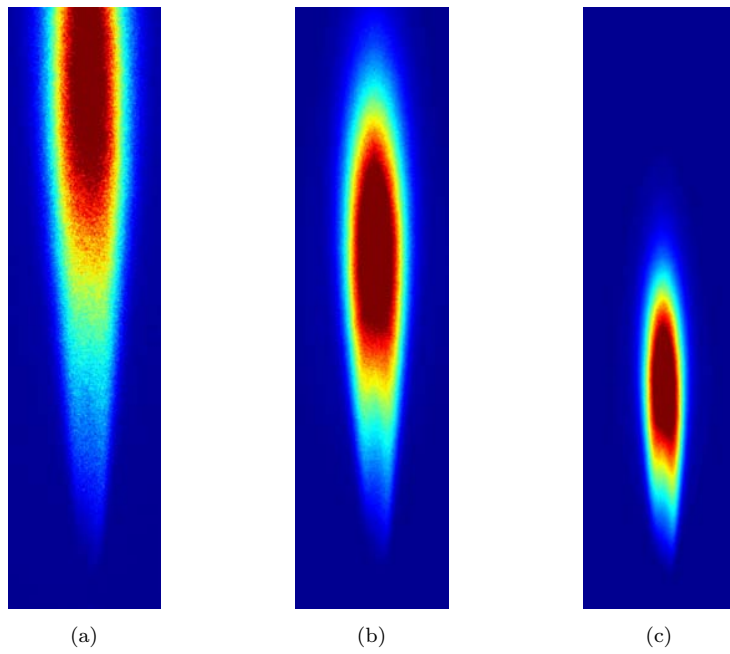


Fig. 106: OH^* Chemiluminescence for H_2 30% – CO 70%: (a) at $T_p \approx 1050$ K; (b) at $T_p \approx 1085$ K; (c) at $T_p \approx 1150$ K;

Final Technical Report

For

IC Consultants Limited

Sherfield Building

Exhibition Road

London SW7 2QA

United Kingdom

Technical Contact: Professor Peter Lindstedt

Shock Tube Studies of the Ignition Delay Times of Syn-Gases

Prof. R. K. Hanson, Dr. D. F. Davidson

Mechanical Engineering Department

418 Panama Street, Room 104

Stanford University, Stanford CA

Sept 7, 2012

Contents

Summary	3
Methodology.....	3
Results and Conclusions.....	4
Table 1: Ignition Delay Time Measurements	7

Summary

Ignition properties of syngas fuel mixtures have been measured using shock tube methodologies at the Mechanical Engineering Department at Stanford University. In particular ignition delay times were measured behind reflected shock waves using endwall emission (OH*) and sidewall pressure signals. Data is presented graphically and tabular format.

Conditions of interest are covered by the temperature range of 950 to 1200 K, near 1 atm, with fuel mixtures of H₂/CH₄, (80/20, 60/40, 40/60, 20/80) H₂/CO (80/20, 60/40, 40/60) and neat H₂ at a single stoichiometry of 0.8 in oxidizer mixtures up to 21% O₂/79% argon.

Methodology

Ignition delay times were measured using emission at both a sidewall (2 cm from end wall) and end wall locations from the OH band near 306 nm, and using side wall pressure at the same location. Ignition delay times from all methods were nearly identical and end wall emission values are reported. The shock emission diagnostic setup is shown in Figure 1. Further details on shock tube ignition delay times can be found in D. F. Davidson, R. K. Hanson, "Interpreting Shock Tube Ignition Data," in the International Journal of Chemical Kinetics, Volume 36, pp. 510-523, (2004).

The ignition delay time was defined as the time interval between the arrival of the reflected shock at the observation point and the extrapolation of the most rapid signal rise to the pre-ignition baseline. Representative data are shown in Figure 2.

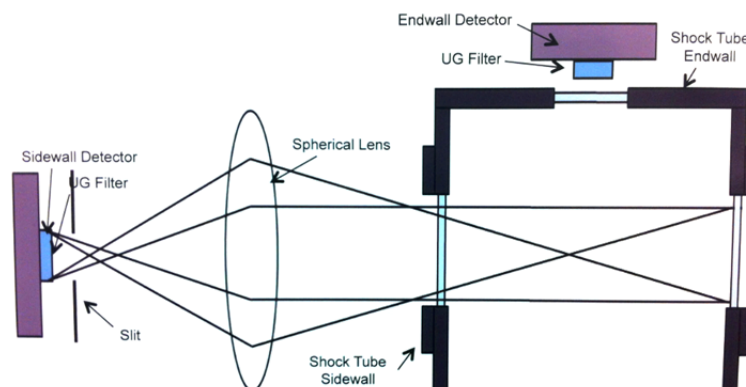


Figure 1. Shock tube emission diagnostic setup.

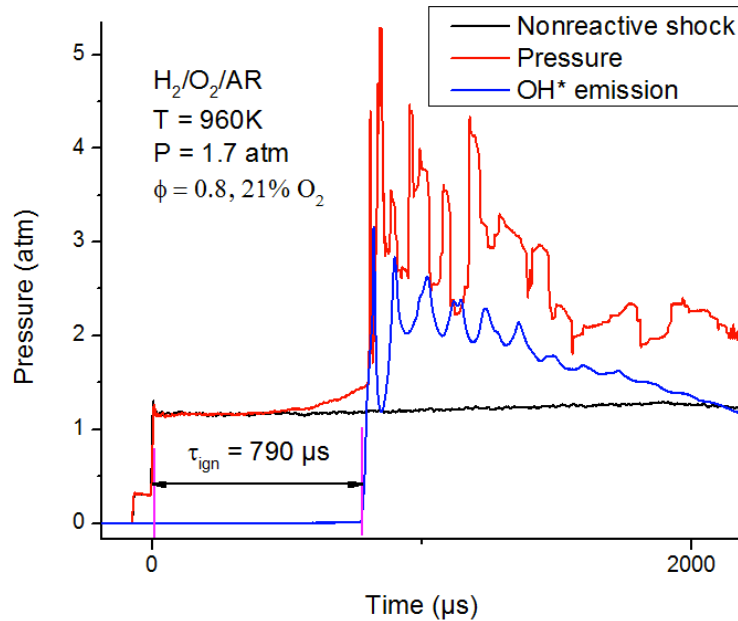


Figure 2. Example shock tube emission and pressure data.

Results and Conclusions.

The ignition delay times are shown in final form in Figures 3-5 and in Table 1. Figures 3-5 also show simulations of measurements using constant volume simulations and the JetSurF 2.0 mechanism of Wang et al. or the Hydrogen mechanism of Hong et al. Excellent agreement is seen with the Hong et al. mechanism for the neat Hydrogen results and good agreement with the JetSurF 2.0 mechanism for the H_2/CO and H_2/CH_4 mixture results.

H. Wang, E. Dames, B. Sirjean, D. A. Sheen, R. Tangko, A. Violi, J. Y. W. Lai, F. N. Egolfopoulos, D. F. Davidson, R. K. Hanson, C. T. Bowman, C. K. Law, W. Tsang, N. P. Cernansky, D. L. Miller, R. P. Lindstedt, A high-temperature chemical kinetic model of *n*-alkane (up to *n*-dodecane), cyclohexane, and methyl-, ethyl-, *n*-propyl and *n*-butyl-cyclohexane oxidation at high temperatures, JetSurF version 2.0, September 19, 2010 (<http://melchior.usc.edu/JetSurF/JetSurF2.0>).

Z. Hong, D. F. Davidson, R. K. Hanson, "An improved H_2/O_2 mechanism based on recent shock tube/laser absorption measurements," in *Combustion and Flame* volume 158 pp. 633–644 (2011).

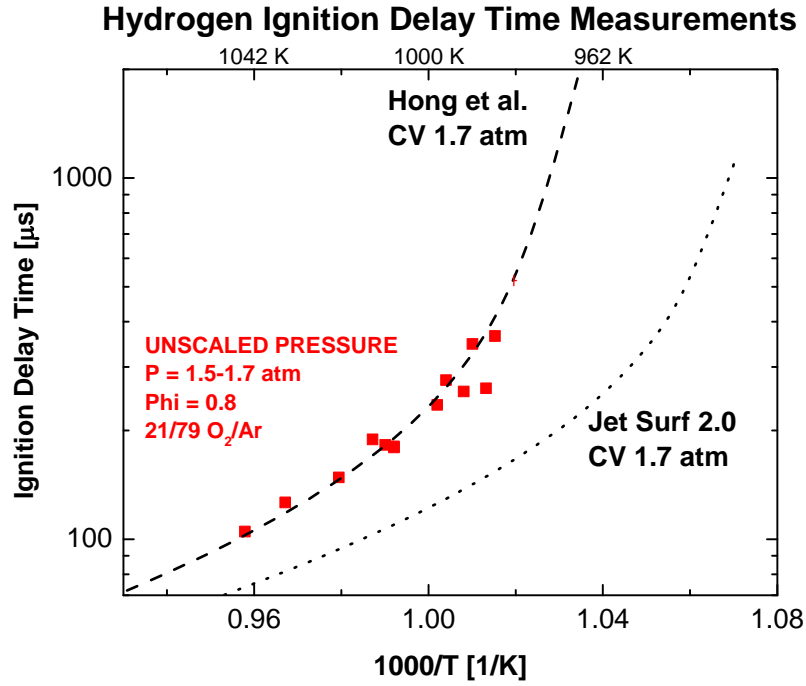


Figure 3. Neat Hydrogen Ignition Delay Time Measurements.

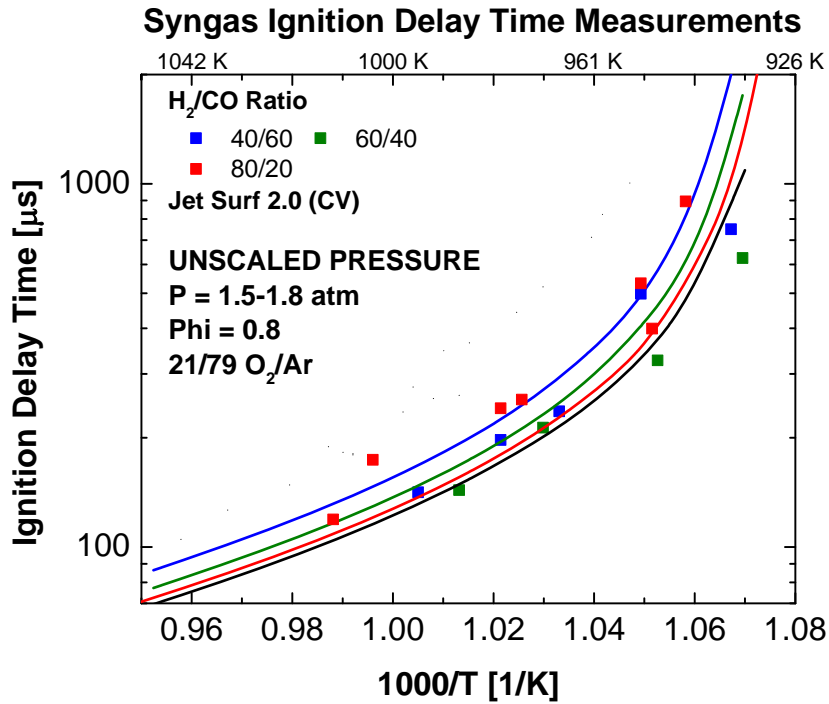


Figure 4. Hydrogen/Carbon Monoxide Mixture Ignition Delay Time Measurements.

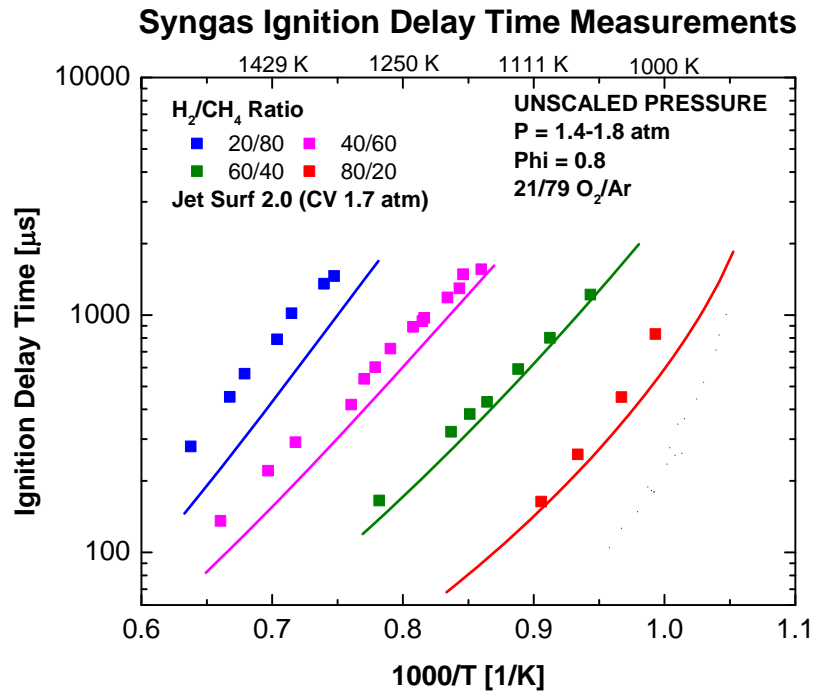


Figure 4. Hydrogen/Methane Mixture Ignition Delay Time Measurements.

Table 1: Ignition Delay Time Measurements

Neat H2 in O2/Argon, (O2/Argon = 21/79), phi = 0.8

T5 [K]	P5 [atm]	tau (us)
985	1.68	365.1
1008	1.66	179.6
1010	1.66	182.3
996	1.70	275.9
990	1.77	347.2
1021	1.59	148.3
1013	1.67	188.9
992	1.72	256.4
1008	1.62	180.6
1044	1.57	105.0
1034	1.59	126.4
998	1.65	235.6
987	1.74	261.7

H2/CO 40/60 in AR Phi = 0.8 (O2/AR = 21/79)

968	1.87	236.6
953	1.95	498.2
995	1.90	141.6
979	1.87	197.2
937	1.93	749.9

H2/CO 60/40 in AR Phi = 0.8 (O2/AR = 21/79)

987	1.81	143.5
971	1.87	213.2
935	1.85	624.8
950	1.85	326.6

H2/CO 80/20 in AR Phi = 0.8 (O2/AR = 21/79)

975	1.76	254.8
1012	1.76	119.2
1004	1.76	174.0
979	1.72	241.0
953	1.80	532.4
951	1.86	399.3
945	1.89	894.4

H2/CH4 20/80 in AR Phi = 0.8 (O2/AR = 21/79)

1399	1.58	1017.0
1421	1.45	789.9
1338	1.56	1457.9
1473	1.40	565.6
1568	1.39	279.4
1352	1.53	1354.1
1498	1.47	451.9

H2/CH4 40/60 in AR Phi = 0.8 (O2/AR = 21/79)

1163	1.68	1558.1
1186	1.60	1294.9
1238	1.55	891.2
1298	1.54	538.4
1182	1.65	1483.4
1227	1.59	942.0
1225	1.64	972.7
1199	1.64	1185.3
1284	1.56	602.9
1265	1.56	722.1
1315	1.52	419.1
1435	1.45	220.8
1514	1.43	135.8
1393	1.53	291.0

H2/CH4 60/40 in AR Phi = 0.8 (O2/AR = 21/79)

1096	1.78	801.0
1126	1.71	591.5
1157	1.70	430.2
1175	1.63	382.4
1195	1.55	322.2
1279	1.52	165.5
1060	1.83	1218.4

H2/CH4 80/20 in AR Phi = 0.8 (O2/AR = 21/79)

1071	1.69	258.7
1034	1.78	451.0
1007	1.77	831.5
1104	1.63	163.7

Appendix to “Modelling of blast in hydrogen power generation systems.”
HSL/BAES response to Deliverable review feedback

Issued 11/12/2012

Comment: The propagation of a detonation wave in a circular pipe is modeled using three different approaches. Of particular interest is the reflection of the detonation wave off the turbine located at one end of the tube. The purpose of this simulation is not clear, is it to be used for design purposes? The commercial CFD code LS DYNA, versions 971 R5 and 980 are used, and the third approach is to use the open source code Open Foam. The main problem with all three calculations is they do not model the initial flame acceleration and the elevated pressure generated at the DDT location. There is no discussion on the selection of the mesh size and testing for solution mesh independence.

Response: *The rationale for carrying out the simulations was two-fold: 1) It is of importance for the design process, and 2) A safety case for the experiment must be provided before the experiments can be performed. Objective 1): Is the current proposed design fit for purpose. Objective 2): Modelling of the pressure dynamics in the tube can show that the experiments are safe to be conducted in the proposed manner.*

The DDT has not been modelled, as we do not believe that the current mathematical models are capable of being predictive tools when it comes to DDT. If the model does not predict DDT or detonation, but DDT or detonation does occur, then what value has the modelling provided if the pressures are lower than actually experienced in the experiments? This would then not have been taken into account during the design phase.

In respect of the mesh resolution, a limited number of mesh resolution tests, we understand, were undertaken by BAES before running the models described in the report. These were limited and we accept that this is a potential weakness with the modelling.

Comment: There are very little details provided concerning the calculation using LS DYNA 971 code, it is not clear to me how the detonation propagates as there is no mention of any reaction rate model. It appears that a large amount of energy is applied at a point in the duct creating a blast wave that propagates in either direction. The pressure profiles provided show significant pressure oscillations behind the front that do not appear to decay in magnitude. The detailed shock dynamics of the reflection process appear to be physical possible.

Response: *No combustion model was used in the LS-DYNA v751 simulations. Hence the simulations are just looking at the behaviour of the pressure, temperature and velocity in the tube. We agree that the finite rate combustion model implemented in LS-DYNA v980 is more appropriate, see below.*

Comment: The LS DYNA 980 appears to be more appropriate for this simulation. The report clearly states that a reaction model is used, however which one is not specified. The calculation is initiated by the deposit of energy at a point. The energy is not sufficient to directly initiate detonation; instead a shock wave is produced that eventually results in detonation initiation. For initiation 0.5 meters from the turbine a detonation does not form fast enough, however for initiation at 6 m a detonation wave

does form before the turbine. The pressure profile obtained near the turbine exit in Figure 27 and 28 shows a small precursor shock wave. This is not consistent with Figure 23 that does not show a precursor shock wave at the pressure transducer locations. In order to validate the code the detonation propagation velocity and peak pressure should be compared with the theoretical CJ value.

Response: *The pressures were compared to the theoretical CJ value, Table 4 in the report provides the pressure and velocity associated with a detonation of a stoichiometric hydrogen-air mixture. The values listed in Table 4 have not been explicitly compared to the LS-DYNA predictions, though a comparison between the predicted and theoretical values can be made.*

Regarding the pressure profiles, the first precursor pressure peak is shown at location p.p. 24 which is located at $y = 629.4$ mm. This is less than 0.3 m from the ignition point. The first precursor pressure peak occurs after $169 \mu\text{s}$. In Figure 23, the plots at 70 ms and 290 ms indicate that the pressure has travelled some way from the ignition location. It is not clear what the predicted velocity would be at that stage of the simulation, but it does not seem unreasonable that the initial pressure wave has gone past the location of p.p. 24 in that time. It would have been easier if the locations of some of the pressure gauges had been indicated in a figure showing the whole model, but this would have made it quite hard to decipher, given the physical dimension of the rig (however, indicating p.p. 24 would have helped). We have not pursued all the precursor pressure traces, but the pressure traces for gauges 6, 21, 24 and 27 were extracted from the pressure trace data. The first pressure peak at gauge 24 occurs after $169 \mu\text{s}$. The pressure traces at locations 21 and 27 are nearly identical as they are roughly the same distance from the ignition location and the flow is expected to be (nearly) symmetrical in the early stages of the simulation. At location 6, the location nearest the combustor exit shown in Figures 27 and 28, the precursor pressure peak occurs after approximately $2270 \mu\text{s}$, It is not possible to say with accuracy if the pressure peaks occurs at the same time in the colour contour plots (Figure 23) and the pressure traces shown in Figures 27 and 28, but we are content that the simulation (CESE, ignition at 6.0 m) appears to be self-consistent having gone back to the raw data supplied by Ricardo Rosario and Chris Constantinou from BAES.

Furthermore, in the colour contour plots in Figure 23 the colour scale goes from 0.1 MPa to 2 MPa so a pressure of less than 0.4 MPa makes it difficult to say exactly what level pressure is predicted.

Comment: Open Foam is an open source code, the pedigree of the version used is not given in the report. It is not clear if the code has gone through proper validation procedures. A simulation is provided at 773K where auto-ignition occurs. Pressure profiles with a lot of noise are all superimposed such that nothing can be seen.

Response: *We agree with this comment, as the version of OpenFOAM used has not been specified. The code has been used to model other detonation/DDT scenarios. Additional information from BAES (University of Kingston) has not given any further clarification of the version of OpenFOAM used. However, this aspect of the modelling was incidental to the detonation predictions from LS-DYNA as these formed the basis of the design studies.*

The autoignition temperature of a hydrogen-air mixture is not very clearly defined, but is sometimes quoted to be as high as 585°C or 858 K . A review by Gummer and

Hawksworth¹ suggests that the autoignition temperature could be in the range 773-850 K (500-577 °C). The variation in autoignition temperature can in part be attributed to the means of measuring the AIT. Hence the temperature in the OpenFOAM simulation is at the lower end of the range, but is still feasible.

The question asked by the experiment design team was not whether the mixture can be ignited and run up to DDT and subsequent detonation, but rather what would be the overpressure and the duration of the pressure spikes were the hydrogen-air mixture to detonate.

In conclusion: The reviewer raises a number of valid points. However, we believe that the results obtained by BAES are valid in providing guidance to the design of the experimental rig and in writing the safety case.

¹ Gummer, J., and Hawksworth, S. (2008). *Spontaneous ignition of hydrogen: Literature Review*. Health and Safety Executive Research Report No. **RR-615**.

Modelling of Blast in Hydrogen Power Generation Systems

Ricardo Rosário

TES109464 / September 2012

Modelling of Blast in Hydrogen Power Generation Systems

TES109464 – 2
September 2012

Prepared by
Ricardo Rosário

SIGNATURES

Author:



Ricardo Rosário

Project Manager

Approved by:



Andrew Press

Group Leader

Authorised by:



Robert Banim

Computational Engineering
Capability Leader

BAE SYSTEMS Advanced Technology Centre
P.O. Box 5, Filton, Bristol BS34 7QW

This is an unpublished work created in 201212, any copyright in which vests in BAE SYSTEMS. All rights reserved.

The information contained in this document/record is proprietary to BAE SYSTEMS unless stated otherwise and is made available in confidence; it must not be used or disclosed without the express written permission of BAE SYSTEMS. This document/record may not be copied in whole or in part in any form without the express written consent of BAE SYSTEMS which may be given by contract.

DOCUMENT INFORMATION:

Project No: 117337	Local Document Ref.:
Project Title: HSL Hydrogen Blast Modelling	

CHANGES SINCE LAST ISSUE:

Tables of the pressure peak duration over 20bar were added to the report.

ABSTRACT

An HSL led consortium has been contracted by the Energies Technology Institute (ETI) to define the safe operating conditions for power generation systems running on high hydrogen fuel compositions. One of the hazards that was been identified, is the detonation of flammable fuel mixtures as they enter the hot exhaust system. Such events may arise as a result of flameout, valve or engine management failures, or in-duct burner flameout. This programme of work researches the effects of a detonation wave propagating through the hydrogen - air mixture to enable the prediction of pressure loadings on critical components.

DISTRIBUTION**Full**

Copy No	Name	Company
1	Keith Moodie	HSL
2	Library	Baddow/Filton

Abstract only

A1	Technical Director	TES (electronic format)
A2	Head of Business Stream	TES (electronic format)

SUMMARY

This report describes a programme of work to simulate the effects of a detonation wave propagating through a hydrogen - air mixture to enable the prediction of pressures loadings on critical system components which was undertaken for the Health & Safety Laboratory, HSL.

Three different modelling approaches were used to predict the dynamic and static pressures at the exhaust face and throughout the duct. The multi-physics version of LS-DYNA software, 980, and finite element version of the LS-DYNA software, 971 R5 were used in this program of work to determine the pressures in the worst case scenario, i.e. the detonation of a stoichiometric mixture of hydrogen and air in the duct. OpenFOAM software was used to predict whether H₂-O₂-N₂-CO₂ mixture (Mole fraction: hydrogen 0.122, nitrogen 0.656, oxygen 0.183 and carbon dioxide 0.039) with the total mass flow 16.1kg/s, initial temperature 500° and at ambient pressure would detonate.

The Arbitrary-Lagrangian-Eulerian approach (ALE) used in the FE version of LS-DYNA predicted a maximum peak pressure for the two detonation scenarios considered in the study of 104bar at the duct centre line. The high peak pressure is due to the shock wave reflection in the duct. The peak pressure predicted at the exhaust face reached 32bar for the case where the detonation point was located at 6.0m from the origin and up to 25bar for the detonation point located at 0.5m. The static pressure at the exhaust face reached 3.6bar. The peak pressure near the wall reached a peak value of 29bar near the detonation point and the static pressure was approximately 6bar for both scenarios.

Similar peak and static pressure values to those observed with the ALE approach were predicted with the multi-physics version of the LS-DYNA finite element software for the majority of pressure points. The peak pressure at the exhaust face reached a value of 17bar for the detonation point located at 0.5m and up to 35bar for the detonation point located at 6.0m. The static pressures predicted for the both scenarios reached 6bar and 3bar respectively.

In the presence of a sufficiently strong ignition source the H₂-O₂-N₂-CO₂ mixture is able to detonate. The simulation showed that the peak pressure at the exhaust face reaches 5bar, 8bar along the length of the duct centre line, and up to 4bar near the wall. The static pressure in all the locations reached a 2.5bar average. Also, there is evidence of combustion and a pressure wave in the downstream region prior to the arrival of the detonation wave. Without an ignition source the gas mixture is seen to auto-ignite. The maximum pressure predicted is less than 3bar and the maximum temperature is nearly 1800K.

TABLE OF CONTENTS

List of Figures v

List of Tables vii

1 Introduction 1

2 Modelling Approach 2

 2.1 LS-DYNA – ALE Approach 4

 2.1.1 Numerical Methods 4

 2.1.2 Detonation point at 0.5m 6

 2.1.3 Detonation point at 6.0m 13

 2.2 LS-DYNA – CESE Approach 19

 2.2.1 Numerical Methods 19

 2.2.1.1 Limitation of LS-DYNA 980 code: 19

 2.2.2 Detonation point at 0.5m 20

 2.2.3 Detonation point at 6.0m 26

 2.3 Comparison between the ALE and CESE modelling approaches 32

 2.4 OpenFOAM Approach 34

 2.4.1 Numerical Methods 34

 2.4.2 CJ Detonation parameters 34

 2.4.3 Initiation case study 34

 2.4.3.1 Wave evolution 35

 2.4.3.2 Pressure profiles 36

 2.4.4 No ignition source 40

 2.4.4.1 Constant combustion 40

 2.4.4.2 No initiation case 40

3 Conclusions 42

4 References 44

LIST OF FIGURES

Figure 1 – Schematic representation of the Exhaust System []	2
Figure 2 – Schematic representation of the pressure points location	3
Figure 3 – Sequence of images showing the expansion of the detonation wave when initiated at 0.5m – ALE	7
Figure 4 – Sequence of images showing the reflection of the pressure wave near the exhaust system exit – ALE	7
Figure 5 – Pressure plot for the points 1, 46 and 47 - Detonation point at 0.5m – ALE	10
Figure 6 – Pressure plot for the points 2, 48 and 49 - Detonation point at 0.5m – ALE	10
Figure 7 – Pressure plot for the points 3, 50 and 51 - Detonation point at 0.5m – ALE	11
Figure 8 – Pressure plot for the points along the centre line - Detonation point at 0.5m – ALE	11
Figure 9 – Pressure plot for the points at 5mm from the wall - Detonation point at 0.5m – ALE	12
Figure 10 – Sequence of images showing the expansion of the detonation wave when initiated at 6.0m – ALE	13
Figure 11 – Reflection of the pressure wave near the exhaust system exit – ALE	13
Figure 12 – Pressure plot for the points 1, 46 and 47 - Detonation point at 6.0m – ALE	16
Figure 13 – Pressure plot for the points 2, 48 and 49 - Detonation point at 6.0m – ALE	16
Figure 14 – Pressure plot for the points 3, 50 and 51 - Detonation point at 6.0m – ALE	17
Figure 15 – Pressure plot for the points along the centre line - Detonation point at 6.0m – ALE	17
Figure 16 – Pressure plot for the points at 5mm from the wall - Detonation point at 6.0m – ALE	18
Figure 17 – Sequence of images showing the expansion of the detonation wave when initiated at 0.5m – CESE	20
Figure 18 – Pressure plot for the points 1, 46 and 47 - Detonation point at 0.5m – CESE	23
Figure 19 – Pressure plot for the points 2, 48 and 49 - Detonation point at 0.5m – CESE	23
Figure 20 – Pressure plot for the points 3, 50 and 51 - Detonation point at 0.5m – CESE	24
Figure 21 – Pressure plot for the points along the centre line - Detonation point at 0.5m – CESE	24
Figure 22 – Pressure plot for the points at 5mm from the wall - Detonation point at 0.5m – CESE	25
Figure 23 – Sequence of images showing the expansion of the detonation wave when initiated at 6.0m – CESE	26
Figure 24 – Pressure plot for the points 1, 46 and 47 - Detonation point at 6.0m – CESE	29
Figure 25 – Pressure plot for the points 2, 48 and 49 - Detonation point at 6.0m – CESE	30
Figure 26 – Pressure plot for the points 3, 50 and 51 - Detonation point at 6.0m – CESE	30

Figure 27 – Pressure plot for the points along the centre line - Detonation point at 6.0m – CESE. 31

Figure 28 – Pressure plot for the points at 5mm from the wall - Detonation point at 6.0m – CESE. 31

Figure 29 – Comparison between ALE and CESE approach for the peak pressure - Detonation at 0.5m. 32

Figure 30 – Comparison between ALE and CESE approach for the peak pressure - Detonation at 6.0m. 32

Figure 31 – Comparison between ALE and CESE approach for the static pressure - Detonation at 0.5m. 33

Figure 32 – Comparison between ALE and CESE approach for the static pressure - Detonation at 6.0m. 33

Figure 33 – Sequence of images showing the evolution of the pressure wave in the tube. 35

Figure 34 – Sequence of images showing the evolution of the H₂O concentration in the tube. . 36

Figure 35 – Pressure plot for the points 1, 2, 3, 4, and 5 - Detonation point at 0.5m – OpenFOAM. 37

Figure 36 – Pressure plot for the points 6, 7, 8, 9, and 10 - Detonation point at 0.5m – OpenFOAM. 37

Figure 37 – Pressure plot for the points 11, 12, 13, 14, and 15 - Detonation point at 0.5m – OpenFOAM. 38

Figure 38 – Pressure plot for the points 16, 17, 18, 19, and 20 - Detonation point at 0.5m – OpenFOAM. 38

Figure 39 – Pressure plot for the points 21, 22, 23, 24, and 25 - Detonation point at 0.5m – OpenFOAM. 39

Figure 40 – Pressure plot for the points 26, 27, 28, 29, and 30 - Detonation point at 0.5m – OpenFOAM. 39

Figure 41 – The predicted temperature vs time for 0-dimensional constant-pressure adiabatic combustion simulation. 40

Figure 42 – The predicted pressure, temperature and H₂O concentration in the case without an ignition source. 41

LIST OF TABLES

Table 1 – Coordinates of the pressure points.....	2
Table 2 – Truncation error Lagrangian vs ALE.....	5
Table 3 – JWL Equation of State parameters.....	6
Table 4 – Detonation properties of the gas mixture.....	6
Table 5 – Summary of the peak and static pressure - Detonation point at 0.5m – ALE.	8
Table 6 – Summary of the pressure peaks duration over 20bar - Detonation point at 0.5m – ALE.	9
Table 7 – Summary of the peak and static pressure - Detonation point at 6.0m – ALE.	14
Table 8 – Summary of the pressure peaks duration over 20bar - Detonation point at 6.0m – ALE.	15
Table 9 – Summary of the peak and static pressure - Detonation point at 0.5m – CESE.	21
Table 10 – Summary of the pressure peaks duration over 20bar - Detonation point at 0.5m – CESE.....	22
Table 11 – Summary of the peak and static pressure - Detonation point at 6.0m – CESE.	27
Table 12 – Summary of the pressure peaks duration over 20bar - Detonation point at 6.0m – CESE.....	28
Table 13 – Detonation parameter.....	34

1 INTRODUCTION

This report describes a programme of work to simulate the effects of a detonation wave propagating through a hydrogen - air mixture to enable the prediction of pressures loadings on critical components which was undertaken for the Health & Safety Laboratory, HSL.

To define the safe operating conditions for power generation systems running on high hydrogen fuel compositions, it's necessary to understand the possible hazards that could occur. One of the hazards that was identified is the detonation of flammable fuel mixtures as they enter the hot exhaust system. In the case of ignition of the gas mixture, the flame would propagate towards the unburned gas mixture. The fluid motion acts like a hot-gas piston and generates a compression wave, which imparts a downstream velocity to the unburned gases ahead of the flame. Under suitable conditions, these travelling compression waves will produce a shock wave ahead of the flame. With enough transition distance, the accelerating flame will strengthen and catch up the shock. As a result, a detonation is initiated. Two mechanisms are responsible for flame acceleration: (i) an increasing flame area that increases heat release rate, and (ii) induced turbulence in the moving unburned mixture ahead of the flame which allows the flame to leap ahead. This process is referred to as deflagration to detonation transition (DDT) or self-initiation because the detonation is initiated solely by the energy release from the combustion of the mixture itself [1]. Such events may arise as a result of flameout, valve or engine management failures, or in-duct burner flameout.

The main objective of work package 1 within the overall programme was to predict the pressures on the internal surfaces of the cylindrical duct and at the engine exhaust as the result of an ignition in the duct. The gases were ignited at two locations along the length of the duct to assess the effect of position on pressure levels.

2 MODELLING APPROACH

Different modelling techniques were used to simulate the detonation of the hydrogen-air mixture exiting the exhaust system presented in Figure 1 to provide confidence in the results and modelling approach. Pressure points were positioned along the duct centre line and at 5mm from the wall to measure the pressure generated by the detonation or the combustion of the gas mixture. The following sections describe the different modelling approaches used in work package 1 and the pressures predicted by the different methodologies.

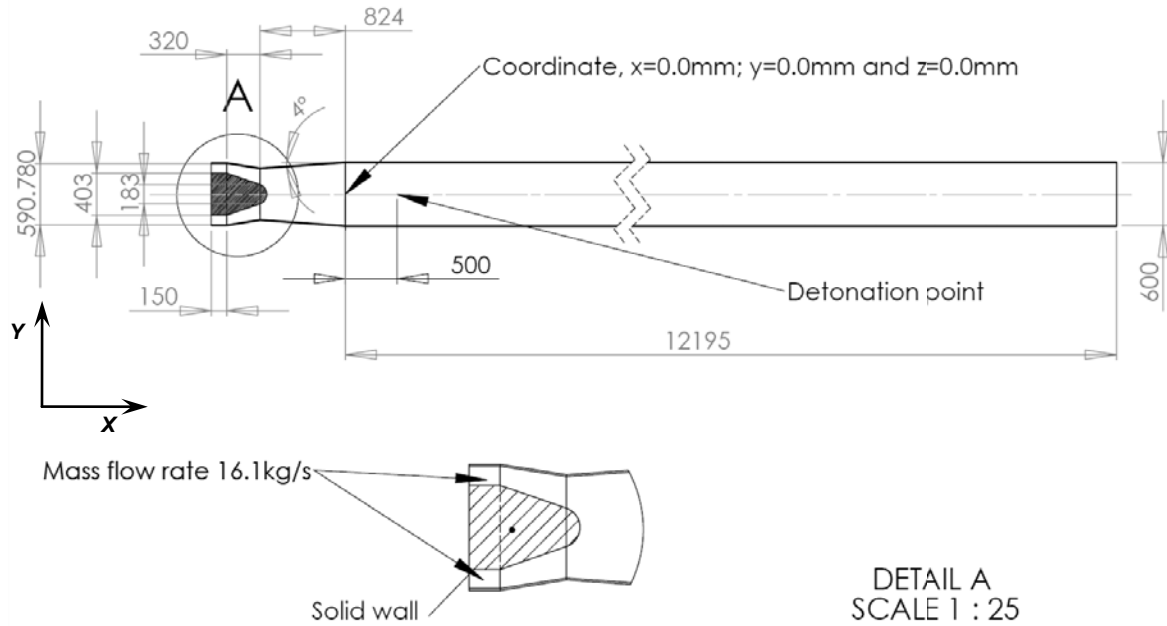


Figure 1 – Schematic representation of the Exhaust System [ii].

The locations of the pressure points in the flow field are presented in Table 1 and schematic represented in Figure 2.

	Y [cm]	X [cm]		Y [cm]	X [cm]		Y [cm]	X [cm]
P.P. - 1	24.70	15.00	P.P. - 18	0.00	1329.40	P.P. - 35	15.00	329.40
P.P. - 2	16.70	47.00	P.P. - 19	29.50	179.40	P.P. - 36	15.00	429.40
P.P. - 3	26.40	88.20	P.P. - 20	29.50	229.40	P.P. - 37	15.00	529.40
P.P. - 4	24.70	129.40	P.P. - 21	29.50	329.40	P.P. - 38	15.00	629.40
P.P. - 5	0.00	129.40	P.P. - 22	29.50	429.40	P.P. - 39	15.00	729.40
P.P. - 6	29.50	129.40	P.P. - 23	29.50	529.40	P.P. - 40	15.00	829.40
P.P. - 7	0.00	229.40	P.P. - 24	29.50	629.40	P.P. - 41	15.00	929.40
P.P. - 8	0.00	329.40	P.P. - 25	29.50	729.40	P.P. - 42	15.00	1029.40
P.P. - 9	0.00	429.40	P.P. - 26	29.50	829.40	P.P. - 43	15.00	1129.40
P.P. - 10	0.00	529.40	P.P. - 27	29.50	929.40	P.P. - 44	15.00	1229.40
P.P. - 11	0.00	629.40	P.P. - 28	29.50	1029.40	P.P. - 45	15.00	1329.40
P.P. - 12	0.00	729.40	P.P. - 29	29.50	1129.40	P.P. - 46	28.80	15.00
P.P. - 13	0.00	829.40	P.P. - 30	29.50	1229.40	P.P. - 47	20.65	15.00
P.P. - 14	0.00	929.40	P.P. - 31	29.50	1329.40	P.P. - 48	9.65	47.00
P.P. - 15	0.00	1029.40	P.P. - 32	0.00	179.40	P.P. - 49	23.70	47.00
P.P. - 16	0.00	1129.40	P.P. - 33	15.00	179.40	P.P. - 50	0.00	88.20
P.P. - 17	0.00	1229.40	P.P. - 34	15.00	229.40	P.P. - 51	13.20	88.20

Table 1 – Coordinates of the pressure points.

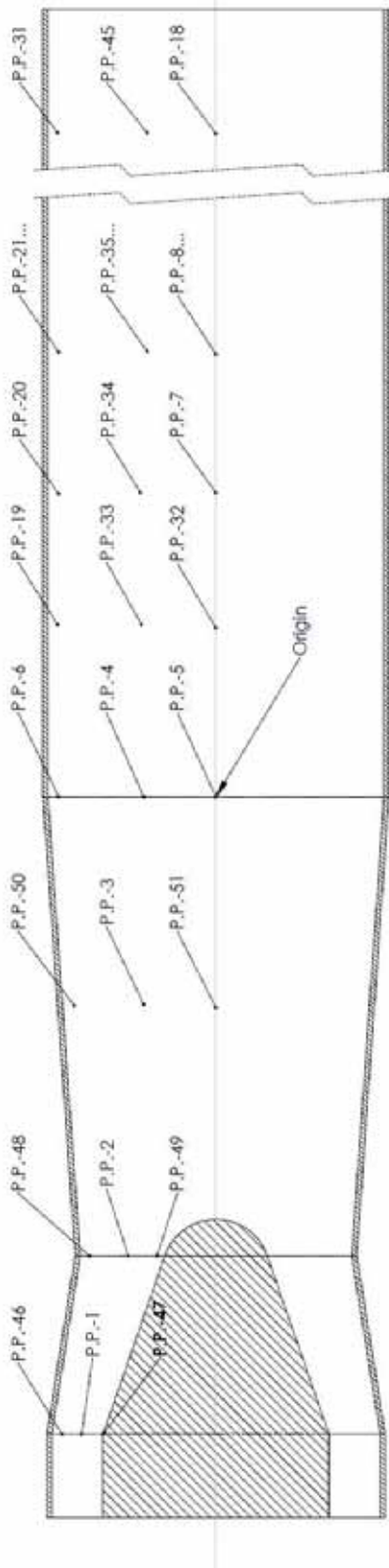


Figure 2 – Schematic representation of the pressure points location.

2.1 LS-DYNA – ALE Approach

The Arbitrary-Lagrangian-Eulerian formulation implemented in the version 971 R5 of the LS-DYNA finite element software was used to predict the dynamic and static pressure generated inside the exhaust systems when stoichiometric hydrogen – air mixture detonates at two positions in the duct. Various blast empirical models have been developed and implemented along the years to simulate the blast of energetic materials. In this specific case, the Jones-Wilkins-Lee equation of state was used for determining the pressure of the detonation products of the gas mixture. The equation of state assumes a stoichiometric mixture and OpenFOAM has been used in section 2.4 to model a non-stoichiometric mixture. However, the LS-DYNA code has some limitations and for some of the cases analysed numerical instabilities were observed. In this particular case, it was not possible fully to stabilise the flow field inside the duct before the detonation of the gas mixture without causing numerical instabilities at the duct exit. This instability influenced the pressure predicted inside the duct. Therefore, the calculations and the pressures presented in this section are without the mass flow rate of 16.1kg/s. The boundaries at exhaust exit and the duct exit were defined as being open.

A brief description of the formulations implemented in LS-DYNA V971 R5 code is presented in the next section, followed by two sections that describe the detonation of a stoichiometric mix of hydrogen-air at two locations in the duct. In section 2.1.2, the detonation point or the high activation energy was positioned at 0.5m from the origin with the objective of assessing the pressure levels at the exit of the exhaust system in case of a detonation. In section 2.1.3, the detonation point was located at 6.0m from the origin. In this case the pressure wave has enough time to develop and reach to it full strength before arrives at the exhaust exit.

2.1.1 Numerical Methods

The LS-DYNA Version 971 R5 finite element software provides formulations for the three basic finite element formulations:

- Lagrangian,
- Eulerian,
- Arbitrary-Lagrangian-Eulerian (ALE).

The software enables each of the methodologies to be coupled in a single model by means of Fluid-Structure-Interaction (FSI) algorithms.

In the traditional Lagrangian finite element formulation the mesh moves with the material. The acceleration of a material point is calculated as the centred finite difference approximation,

$$\ddot{x}_n = \frac{\dot{x}_{n+1/2} - \dot{x}_{n-1/2}}{\Delta t} = \frac{\partial \dot{x}}{\partial t} \quad (1)$$

Wherever possible, the Lagrangian formulation should be used. It is simple, efficient and second order accurate. However, for problems where the material undergoes extreme deformation, elements of the mesh become highly distorted causing degenerate elements leading to reduced accuracy and stability. This is a particular problem for high velocity impact and penetration problems and for blast simulations.

In the Eulerian approach the material flows through the finite element mesh whilst the mesh remains fixed in space. The material derivative is then the rate of change of a variable at a point moving through the domain and consists of a partial time derivative term and a convective term. The acceleration is given as,

$$\ddot{x} = \frac{\partial \dot{x}}{\partial t} + \dot{x} \frac{\partial \dot{x}}{\partial x} \tag{2}$$

Numerical stability in solving this equation requires the time step to be such that the material does not move further than one element size in one time step.

$$\dot{x}_{n-1/2} > 0, \quad \dot{x}_{n-1/2} < \frac{\Delta x}{\Delta t} \Rightarrow \Delta t < \frac{\Delta x}{\dot{x}_{n-1/2}} \tag{3}$$

This is often more restrictive than the CFL condition.

	<i>Lagrangian</i>	<i>ALE</i>
Material derivative	$\dot{f} = \frac{\partial f}{\partial t}$	$\dot{f} = \frac{\partial f}{\partial t} + \dot{x} \frac{\partial f}{\partial x}$
Time step	$\Delta t \leq \frac{l}{c}$	$\Delta t \leq \frac{l}{c + \dot{x}}$
Momentum conservation	$error \approx \Delta t^3$	$error \approx \Delta t^3 \rightarrow \Delta t^2$
Mass & energy conservation	$error = 0$	$error \approx \Delta t^3 \rightarrow \Delta t^2$

Table 2 – Truncation error Lagrangian vs ALE

The Arbitrary Lagrangian Eulerian (ALE) approach allows the background mesh to be controlled by the user. This enables the mesh to follow or scale according to the material deformation of the problem. In this case the convective velocity also depends on the mesh velocity, \dot{x}_m

$$\ddot{x} = \frac{\partial \dot{x}}{\partial t} + (\dot{x} - \dot{x}_m) \frac{\partial \dot{x}}{\partial x} \tag{4}$$

When $\dot{x}_m = 0$ the formulation is purely Eulerian and when $\dot{x}_m = \dot{x}$ the formulation is purely Lagrangian. The main properties of the Lagrangian and ALE formulations are compared in Table 2.

The Jones-Wilkins-Lee equation of state, JWL, defines pressure as a function of relative volume, V , and internal energy per initial volume, E , as

$$p = A \left(1 - \frac{\omega}{R_1 V} \right) e^{-R_1 V} + B \left(1 - \frac{\omega}{R_2 V} \right) e^{-R_2 V} + \frac{\omega E}{V} \quad (5)$$

Where w , A , B , R_1 , and R_2 are user defined input parameters. The JWL equation of state is used for determining the pressure of the detonation products of high explosives in applications involving metal accelerations and Stoichiometric gas mixtures [iii].

The parameters used in the equation of state used for the ALE simulation presented in the following section are:

ω	A	B	R_1	R_2	$E \text{ (J/m}^3\text{)}$
0.218	0.0	0.0	1.0	1.0	4.05×10^6

Table 3 – JWL Equation of State parameters.

The parameters presented above are valid only for a stoichiometric mixture of hydrogen and air initially at a pressure of 1 bar, and equation of state assumes that there is a perfect mixture, that there is a strong enough energy source to give prompt ignition and that the dimensions of the system are such that they allow detonation propagation. The detonation properties of the gas mixture are:

$\rho_o \text{ (kg/m}^3\text{)}$	$V_{det} \text{ (m/s)}$	$P_{CJ} \text{ (bar)}$	γ
0.4879	2843.16	18.01	1.218

Table 4 – Detonation properties of the gas mixture.

2.1.2 Detonation point at 0.5m

The detonation point was located at 0.5m from the origin as shown in Figure 1. The blast wave grows and develops towards both ends of the duct as shown in the sequence of images in Figure 3. The reflection on the duct wall created regions of high pressure near the wall, and at the centre line. After the blast wave has developed and expanded, the major pressure regions dissipate, leaving a single high pressure region developing and expanding towards the duct exit.

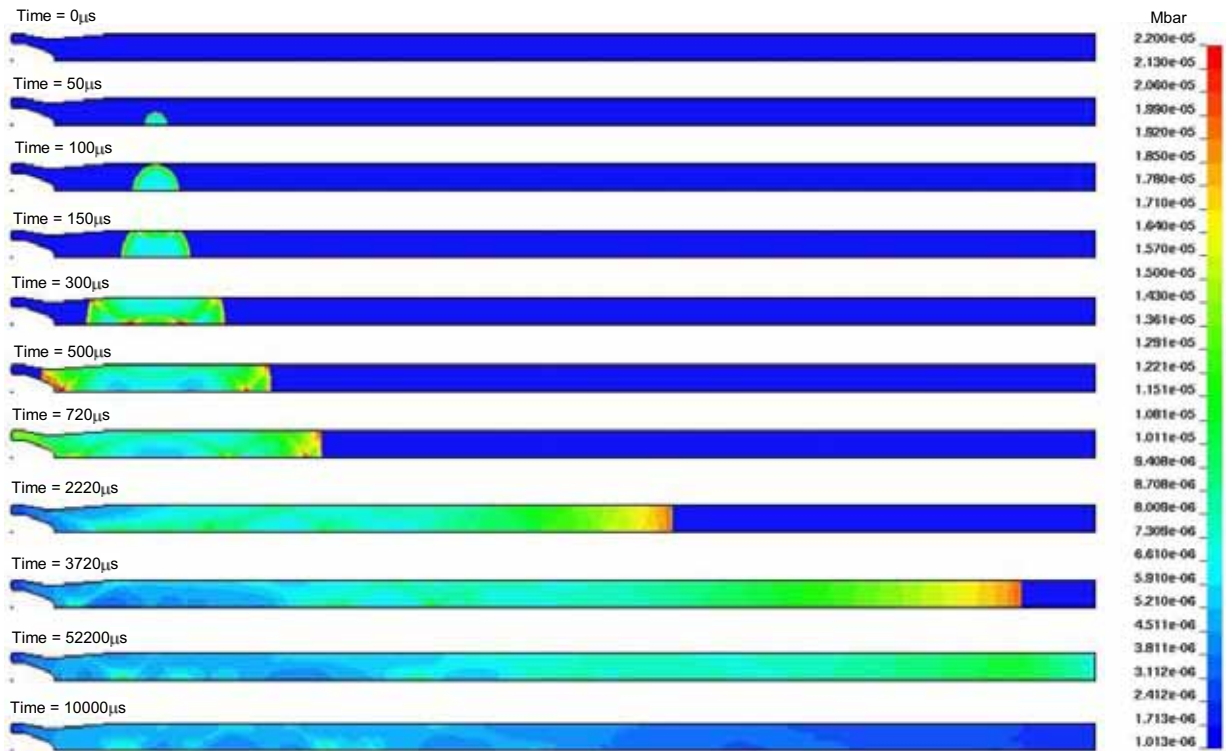


Figure 3 – Sequence of images showing the expansion of the detonation wave when initiated at 0.5m – ALE.

Figure 4 shows a sequence of images highlighting the development and reflection of the pressure wave near the exhaust exit. The reflection of the pressure wave increases the maximum pressure predicted at point 1 located at the exhaust exit, and at the pressure points near the wall. The peak pressure at the point 1 reached a maximum of 20bar and 25bar near the wall as shown in Figure 5.

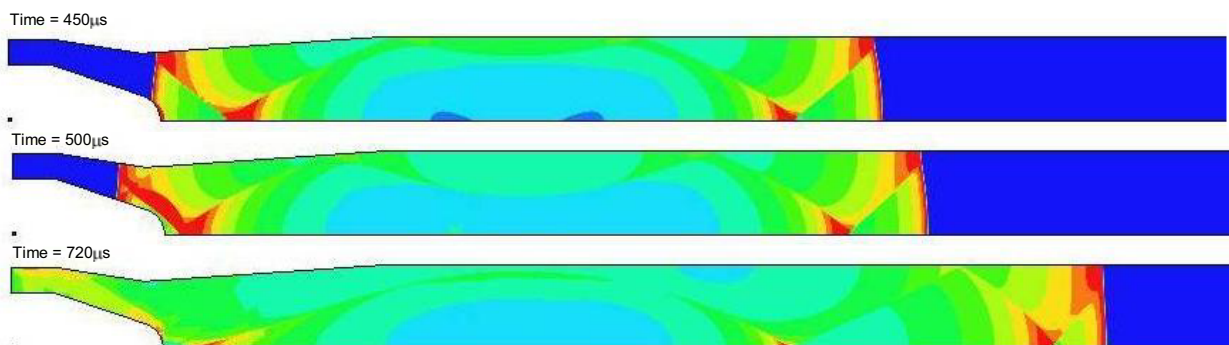


Figure 4 – Sequence of images showing the reflection of the pressure wave near the exhaust system exit – ALE.

Figure 5 to Figure 9 present the pressure profiles at given points. The pressure profile at exhaust face is shown in Figure 5. The pressure near the wall at this location reached a maximum of 26bar and 3bar static pressure. The peak pressure at all three pressure points was of a very short duration.

The pressure profile at points 2, 48 and 49 located at the end of the flow straightener are presented in Figure 6. Figure 7 shows the pressure profiles measured at ¾ of the nozzle length, i.e. pressure points 3, 50 and 51. Pressure point 50 which was located at the centre line of the duct measured periodic peak pressures that weakened in time. These peaks are related to the shock wave reflections with the duct, nozzle and flow straightener walls.

Figure 8 shows the evolution of the detonation pressure wave along the duct. The pressures recorded between points 7 and 18 and showed that the pressure wave front maintained an approximately constant pressure which is a characteristic of a self-sustaining detonation wave. This behaviour is evident in Figure 9 which shows the pressure profile near the wall and along the duct.

The following table summarises the peak and static pressures predicted for the pressure points 1 to 51.

	Peak Pressure	Static Pressure		Peak Pressure	Static Pressure		Peak Pressure	Static Pressure
	[bar]	[bar]		[bar]	[bar]		[bar]	[bar]
P.P. - 1	20.493	3.20	P.P. - 18	19.481	2.66	P.P. - 35	19.180	5.44
P.P. - 2	20.272	4.21	P.P. - 19	29.428	5.44	P.P. - 36	19.480	5.41
P.P. - 3	27.905	5.00	P.P. - 20	29.964	5.48	P.P. - 37	19.445	5.36
P.P. - 4	19.292	5.30	P.P. - 21	24.252	5.45	P.P. - 38	19.474	5.30
P.P. - 5	60.505	5.06	P.P. - 22	22.712	5.41	P.P. - 39	19.453	5.18
P.P. - 6	30.410	5.31	P.P. - 23	22.064	5.36	P.P. - 40	19.444	5.02
P.P. - 7	60.215	5.36	P.P. - 24	22.031	5.27	P.P. - 41	19.503	4.79
P.P. - 8	31.457	5.41	P.P. - 25	21.922	5.17	P.P. - 42	19.503	4.42
P.P. - 9	27.603	5.37	P.P. - 26	21.875	5.02	P.P. - 43	19.511	3.85
P.P. - 10	24.136	5.38	P.P. - 27	22.426	4.80	P.P. - 44	19.461	3.05
P.P. - 11	19.441	5.31	P.P. - 28	21.981	4.43	P.P. - 45	19.458	2.66
P.P. - 12	19.510	5.17	P.P. - 29	22.507	3.88	P.P. - 46	22.251	3.64
P.P. - 13	19.447	5.02	P.P. - 30	22.478	3.09	P.P. - 47	25.642	2.79
P.P. - 14	19.450	4.78	P.P. - 31	21.984	2.68	P.P. - 48	27.546	4.26
P.P. - 15	19.455	4.38	P.P. - 32	104.368	5.36	P.P. - 49	25.569	3.72
P.P. - 16	19.453	3.83	P.P. - 33	16.969	5.45	P.P. - 50	55.200	4.85
P.P. - 17	19.481	3.04	P.P. - 34	19.173	5.47	P.P. - 51	19.089	4.98

Table 5 – Summary of the peak and static pressure - Detonation point at 0.5m – ALE.

The duration of the pressure peaks over 20bar are summarised in Table 6.

	P.P. - 1		P.P. - 2		P.P. - 3		P.P. - 4		P.P. - 5		P.P. - 6		P.P. - 7		P.P. - 8		P.P. - 9		P.P. - 10			
	ΔT [μs]	P[bar]	ΔT [μs]	P[bar]	ΔT [μs]	P[bar]	ΔT [μs]	P[bar]	ΔT [μs]	P[bar]	ΔT [μs]	P[bar]	ΔT [μs]	P[bar]	ΔT [μs]	P[bar]	ΔT [μs]	P[bar]	ΔT [μs]	P[bar]		
P. Peak 1	3	21	-	-	11	28	-	-	17	61	10	30	17	60	10	31	5	24	2	23		
P. Peak 2	-	-	-	-	-	-	-	-	9	45	-	-	7	43	1	31	2	28	-	-		
P. Peak 3	-	-	-	-	-	-	-	-	6	38	-	-	3	31	1	25	-	-	-	-		
P. Peak 4	-	-	-	-	-	-	-	-	10	36	-	-	-	-	1	23	-	-	-	-		
	P.P. - 11		P.P. - 12		P.P. - 13		P.P. - 14		P.P. - 15		P.P. - 16		P.P. - 17		P.P. - 18		P.P. - 19		P.P. - 20			
	ΔT [μs]	P[bar]	ΔT [μs]	P[bar]	ΔT [μs]	P[bar]	ΔT [μs]	P[bar]	ΔT [μs]	P[bar]	ΔT [μs]	P[bar]	ΔT [μs]	P[bar]	ΔT [μs]	P[bar]	ΔT [μs]	P[bar]	ΔT [μs]	P[bar]		
P. Peak 1	-	-	-	-	-	-	-	-	-	-	-	-	-	-	-	-	-	8	30	9	30	
	P.P. - 21		P.P. - 22		P.P. - 23		P.P. - 24		P.P. - 25		P.P. - 26		P.P. - 27		P.P. - 28		P.P. - 29		P.P. - 30			
	ΔT [μs]	P[bar]	ΔT [μs]	P[bar]	ΔT [μs]	P[bar]	ΔT [μs]	P[bar]	ΔT [μs]	P[bar]	ΔT [μs]	P[bar]	ΔT [μs]	P[bar]	ΔT [μs]	P[bar]	ΔT [μs]	P[bar]	ΔT [μs]	P[bar]		
P. Peak 1	7	24	6	23	3	22	2	22	2	22	2	22	2	22	2	22	2	22	1	20	2	22
P. Peak 2	-	-	-	-	1	20	1	20	1	20	1	20	1	21	1	20	-	-	-	-	2	21
	P.P. - 31		P.P. - 32		P.P. - 33		P.P. - 34		P.P. - 35		P.P. - 36		P.P. - 37		P.P. - 38		P.P. - 39		P.P. - 40			
	ΔT [μs]	P[bar]	ΔT [μs]	P[bar]	ΔT [μs]	P[bar]	ΔT [μs]	P[bar]	ΔT [μs]	P[bar]	ΔT [μs]	P[bar]	ΔT [μs]	P[bar]	ΔT [μs]	P[bar]	ΔT [μs]	P[bar]	ΔT [μs]	P[bar]		
P. Peak 1	2	22	22	104	-	-	-	-	-	-	-	-	-	-	-	-	-	-	-	-	-	
P. Peak 2	1	20	8	45	-	-	-	-	-	-	-	-	-	-	-	-	-	-	-	-	-	
P. Peak 3	-	-	3	28	-	-	-	-	-	-	-	-	-	-	-	-	-	-	-	-	-	
	P.P. - 41		P.P. - 42		P.P. - 43		P.P. - 44		P.P. - 45		P.P. - 46		P.P. - 47		P.P. - 48		P.P. - 49		P.P. - 50			
	ΔT [μs]	P[bar]	ΔT [μs]	P[bar]	ΔT [μs]	P[bar]	ΔT [μs]	P[bar]	ΔT [μs]	P[bar]	ΔT [μs]	P[bar]	ΔT [μs]	P[bar]	ΔT [μs]	P[bar]	ΔT [μs]	P[bar]	ΔT [μs]	P[bar]		
P. Peak 1	-	-	-	-	-	-	-	-	-	-	1	20	6	26	4	28	8	26	18	52		
P. Peak 2	-	-	-	-	-	-	-	-	-	-	30	22	-	-	17	24	-	-	9	49		
P. Peak 3	-	-	-	-	-	-	-	-	-	-	-	-	-	-	-	-	-	-	5	39		
P. Peak 4	-	-	-	-	-	-	-	-	-	-	-	-	-	-	-	-	-	-	9	55		

Table 6 – Summary of the pressure peaks duration over 20bar - Detonation point at 0.5m – ALE.

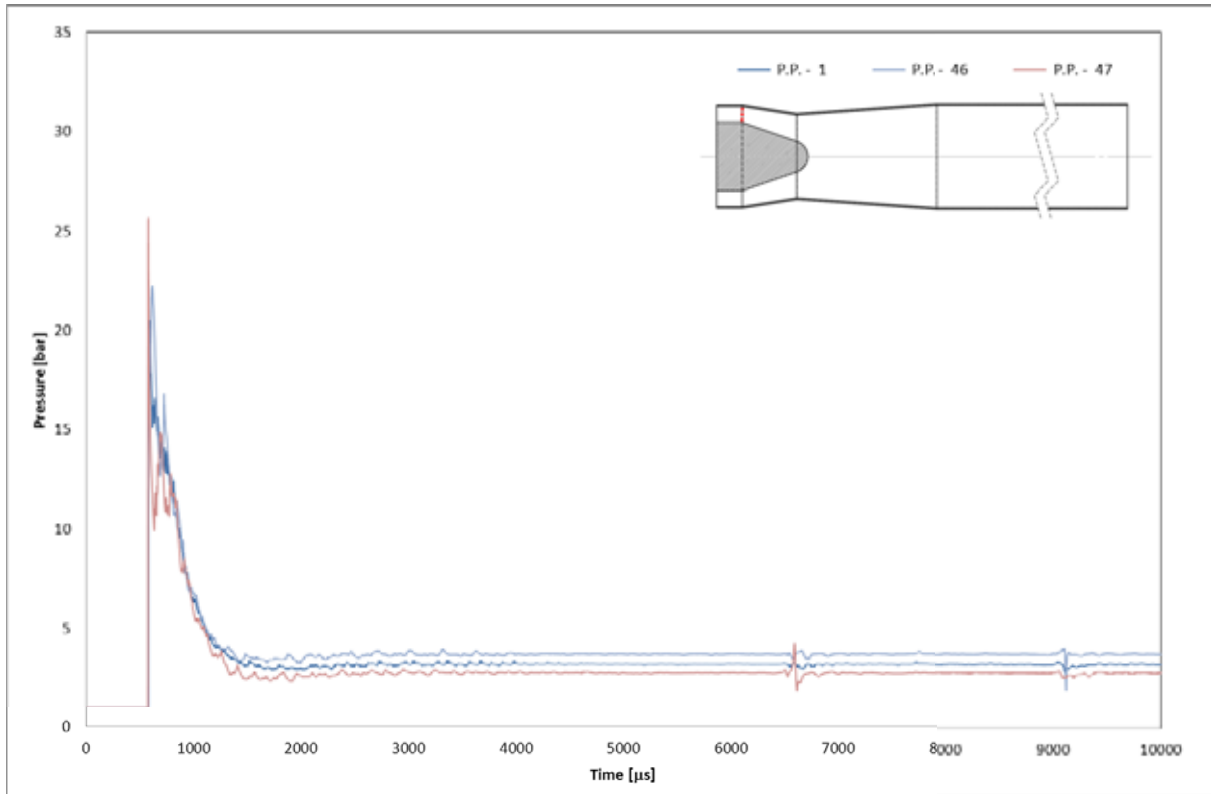


Figure 5 – Pressure plot for the points 1, 46 and 47 - Detonation point at 0.5m – ALE.

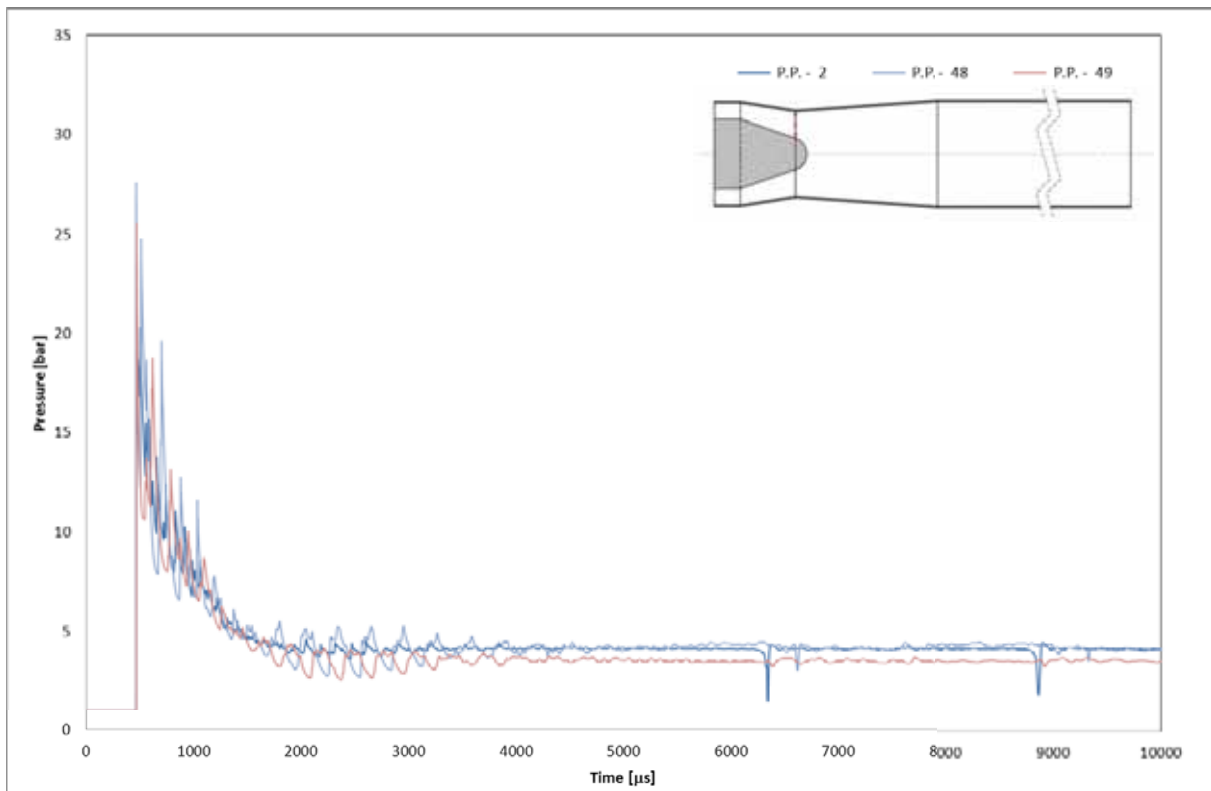


Figure 6 – Pressure plot for the points 2, 48 and 49 - Detonation point at 0.5m – ALE.

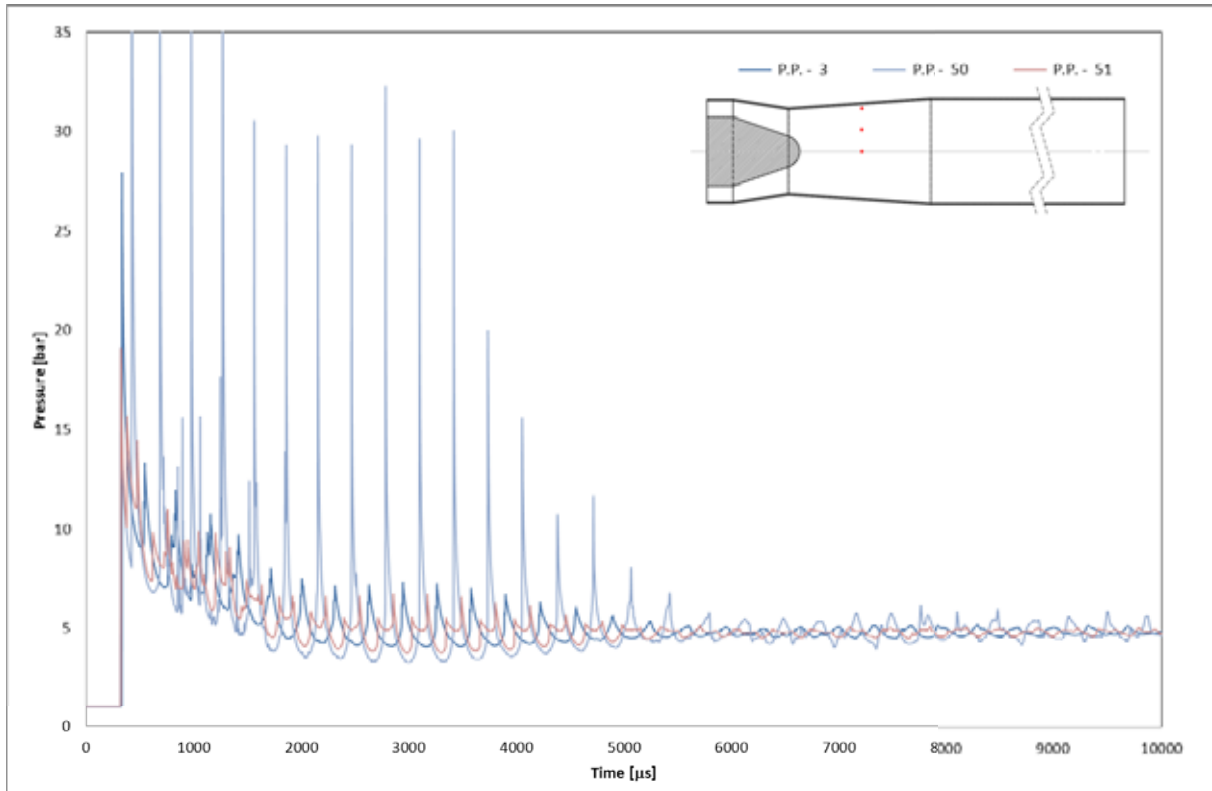


Figure 7 – Pressure plot for the points 3, 50 and 51 - Detonation point at 0.5m – ALE.

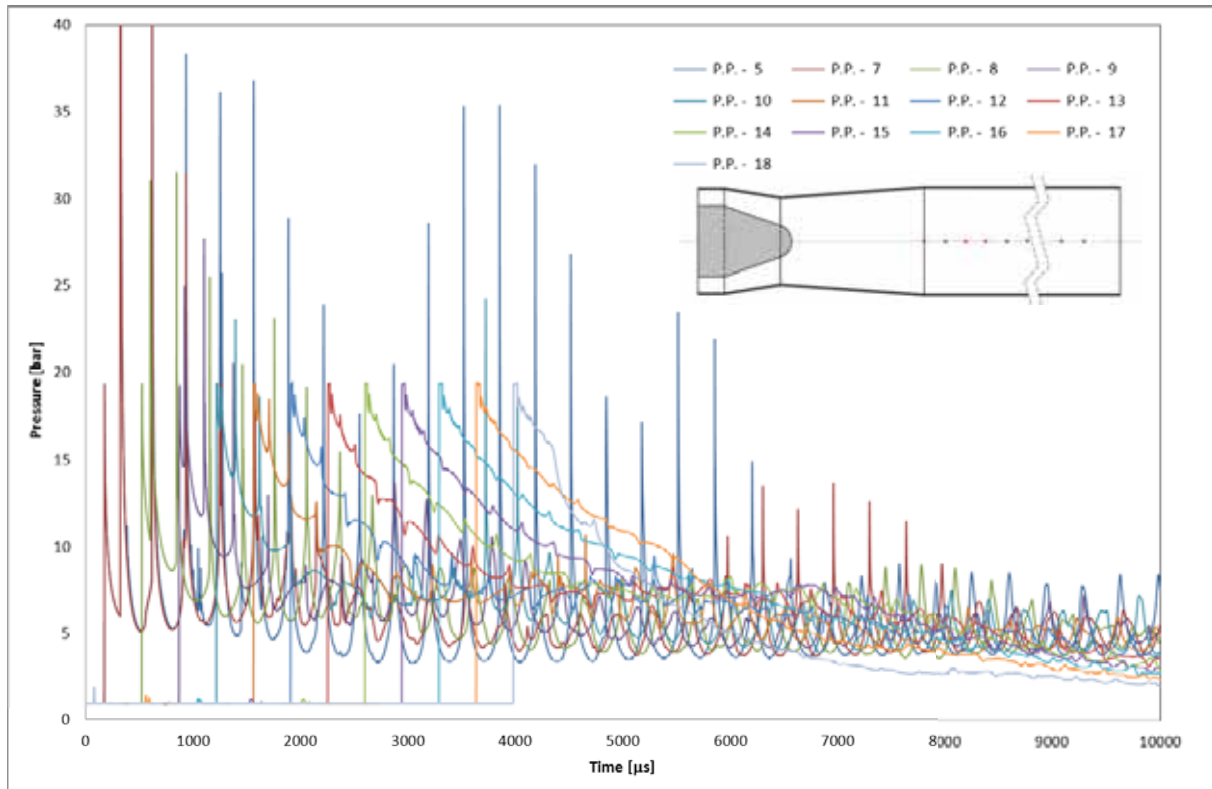


Figure 8 – Pressure plot for the points along the centre line - Detonation point at 0.5m – ALE.

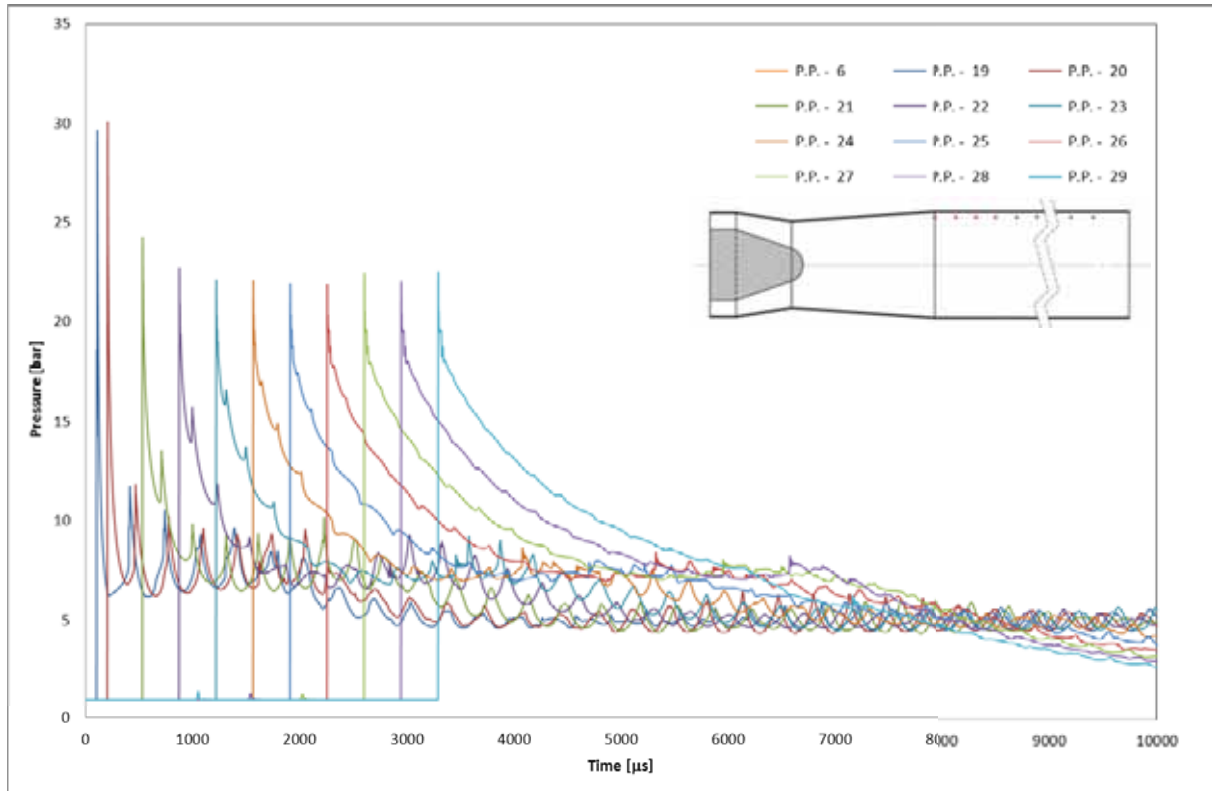


Figure 9 – Pressure plot for the points at 5mm from the wall - Detonation point at 0.5m – ALE.

2.1.3 Detonation point at 6.0m

In this case the detonation point was positioned at 6.0m from the origin. As shown in Figure 10 the blast wave expands towards both ends of the duct. High pressures are generated near the wall also along the centre line of the duct.

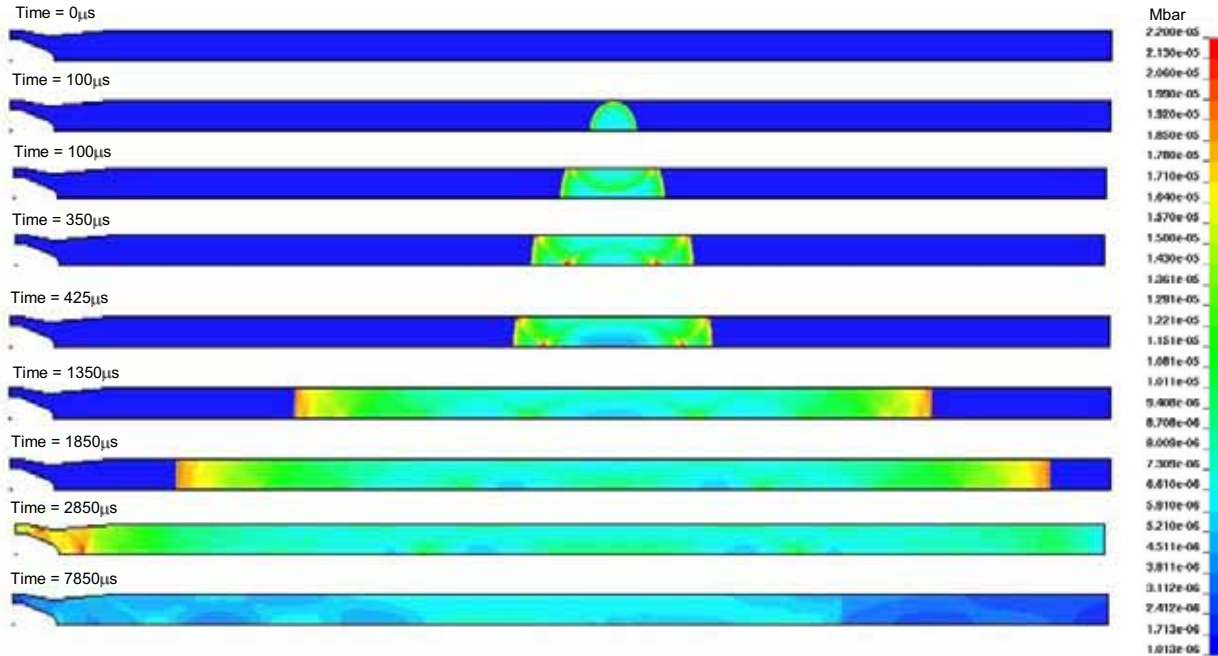


Figure 10 – Sequence of images showing the expansion of the detonation wave when initiated at 6.0m – ALE.

Numerous shock wave reflections occurred when the pressure front reached the engine exhaust and diffuser as shown in Figure 11. The reflection caused a rise in the pressure values between 10 and 15bar at the exhaust face.

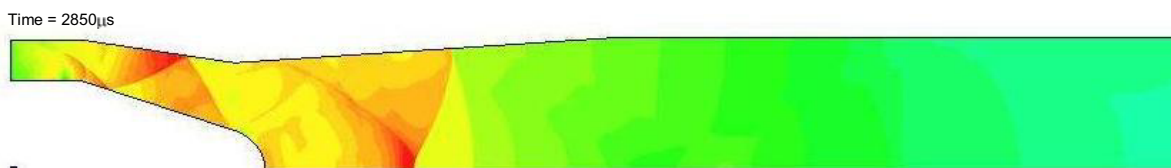


Figure 11 – Reflection of the pressure wave near the exhaust system exit – ALE.

The pressure profiles at the 51 pressure points are presented in Figure 12 to Figure 15.

The maximum peak pressures and their duration, predicted in the nozzle section are higher and longer than the previous scenario, where the detonation point was located at 0.5m. Also, fewer peak pressure periodic fluctuations occurred in this scenario at pressure point 50 as shown in Figure 14.

Figure 15 and Figure 16 show the pressure profile measured along the duct line and at 5mm from the duct wall. Similar pressure profiles, for both maximum peak pressure and static pressure, to those observed with the detonation point at 0.5m were predicted.

The following table summarises the peak and static pressures predicted for the pressure points 1 to 51.

	Peak Pressure	Static Pressure		Peak Pressure	Static Pressure		Peak Pressure	Static Pressure
	[bar]	[bar]		[bar]	[bar]		[bar]	[bar]
P.P. - 1	25.315	3.05	P.P. - 18	20.110	2.65	P.P. - 35	19.435	5.70
P.P. - 2	26.413	3.69	P.P. - 19	22.069	4.76	P.P. - 36	19.440	6.01
P.P. - 3	23.354	4.15	P.P. - 20	22.069	5.28	P.P. - 37	19.325	6.32
P.P. - 4	19.555	4.37	P.P. - 21	22.113	5.69	P.P. - 38	19.065	6.55
P.P. - 5	19.454	4.38	P.P. - 22	22.266	6.02	P.P. - 39	17.008	6.61
P.P. - 6	22.418	4.40	P.P. - 23	22.972	6.32	P.P. - 40	18.997	6.21
P.P. - 7	19.439	5.32	P.P. - 24	25.830	6.55	P.P. - 41	19.256	5.69
P.P. - 8	19.693	5.68	P.P. - 25	29.692	6.60	P.P. - 42	19.440	5.10
P.P. - 9	25.934	5.84	P.P. - 26	26.884	6.25	P.P. - 43	19.466	4.39
P.P. - 10	27.847	6.20	P.P. - 27	23.792	5.74	P.P. - 44	19.439	3.52
P.P. - 11	36.050	6.42	P.P. - 28	22.273	5.13	P.P. - 45	19.420	2.61
P.P. - 12	103.078	6.50	P.P. - 29	22.567	4.42	P.P. - 46	32.441	3.35
P.P. - 13	38.825	6.17	P.P. - 30	22.553	3.57	P.P. - 47	25.580	2.74
P.P. - 14	30.332	5.67	P.P. - 31	22.179	2.61	P.P. - 48	30.956	3.66
P.P. - 15	26.415	5.06	P.P. - 32	19.444	4.80	P.P. - 49	24.077	3.35
P.P. - 16	20.406	4.40	P.P. - 33	19.521	4.79	P.P. - 50	25.881	4.17
P.P. - 17	19.449	3.52	P.P. - 34	19.443	5.30	P.P. - 51	20.075	4.16

Table 7 – Summary of the peak and static pressure - Detonation point at 6.0m – ALE.

The duration of the pressure peaks over 20bar are summarised in Table 8.

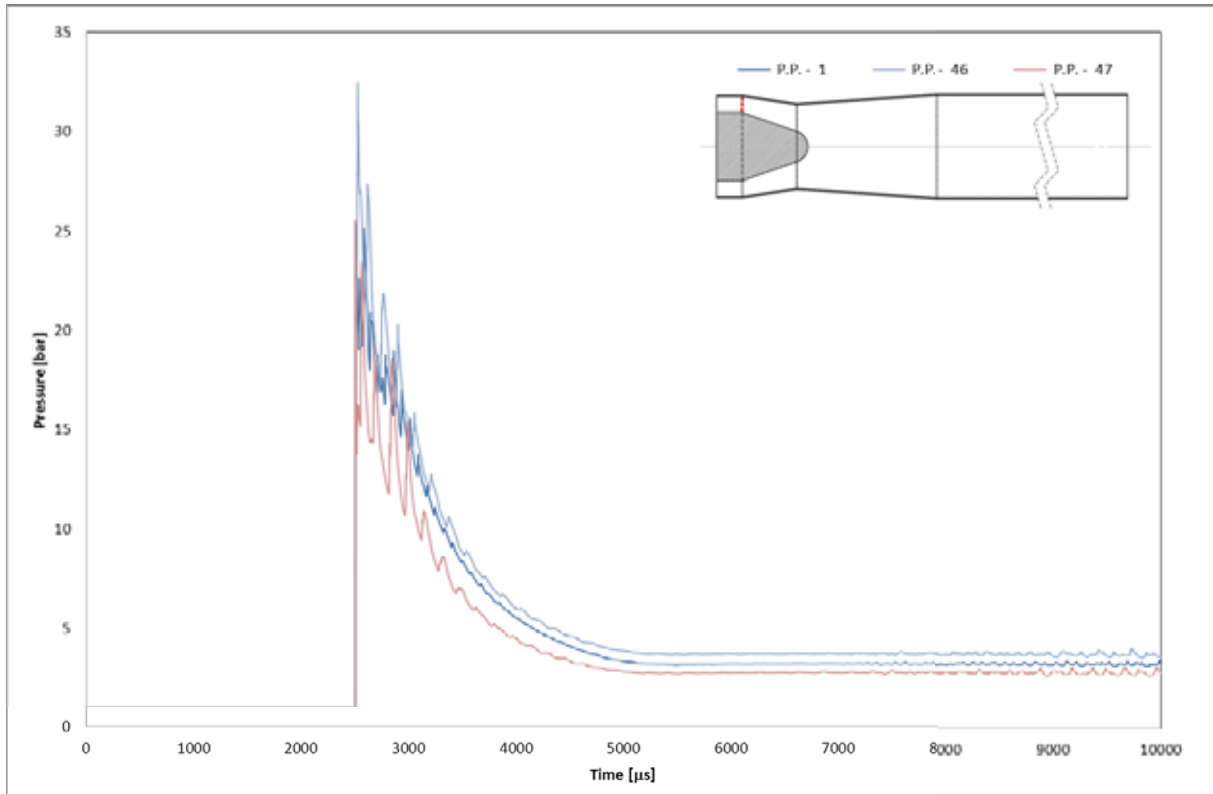


Figure 12 – Pressure plot for the points 1, 46 and 47 - Detonation point at 6.0m – ALE.

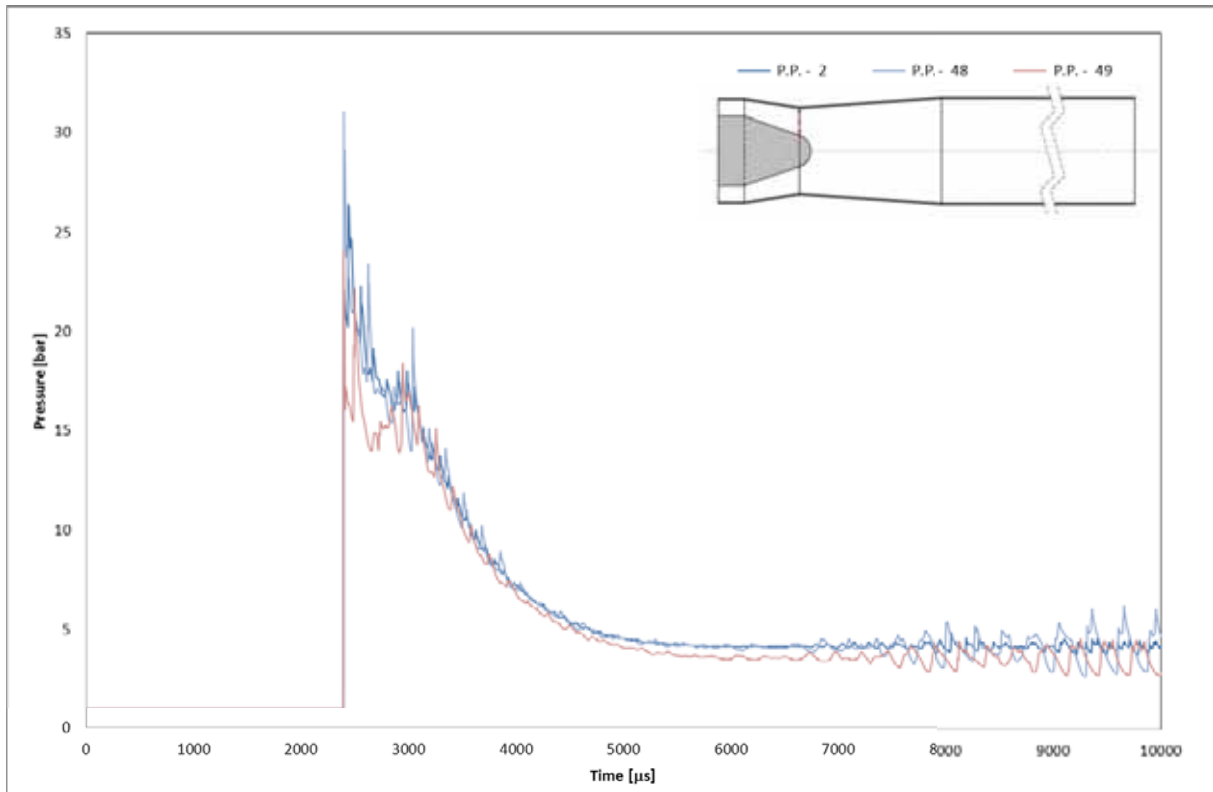


Figure 13 – Pressure plot for the points 2, 48 and 49 - Detonation point at 6.0m – ALE.

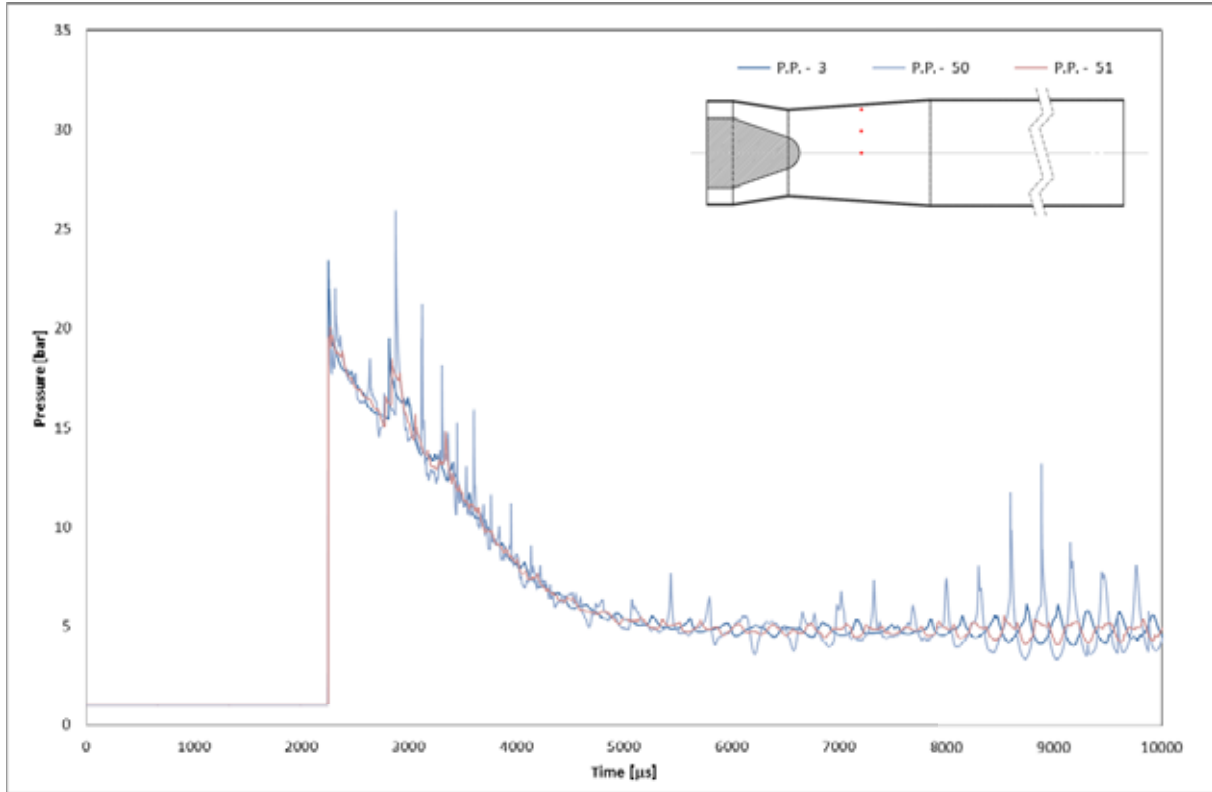


Figure 14 – Pressure plot for the points 3, 50 and 51 - Detonation point at 6.0m – ALE.

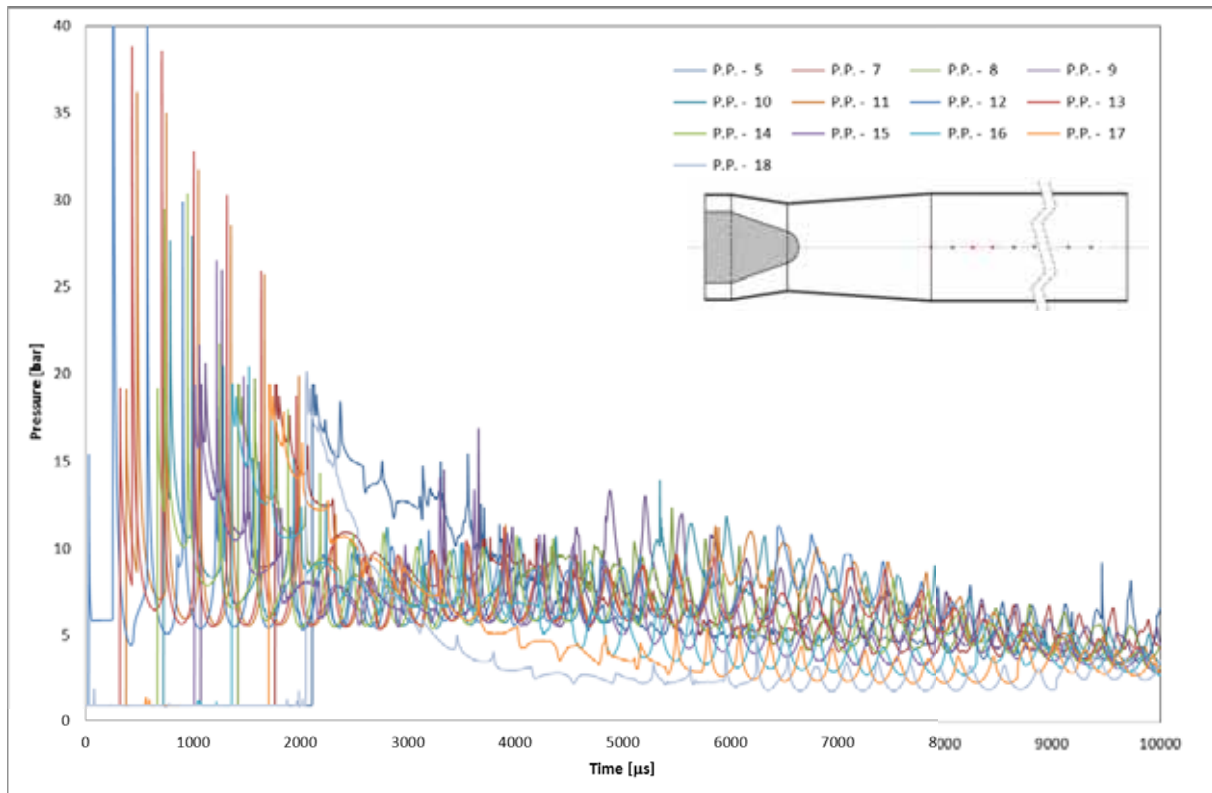


Figure 15 – Pressure plot for the points along the centre line - Detonation point at 6.0m – ALE.

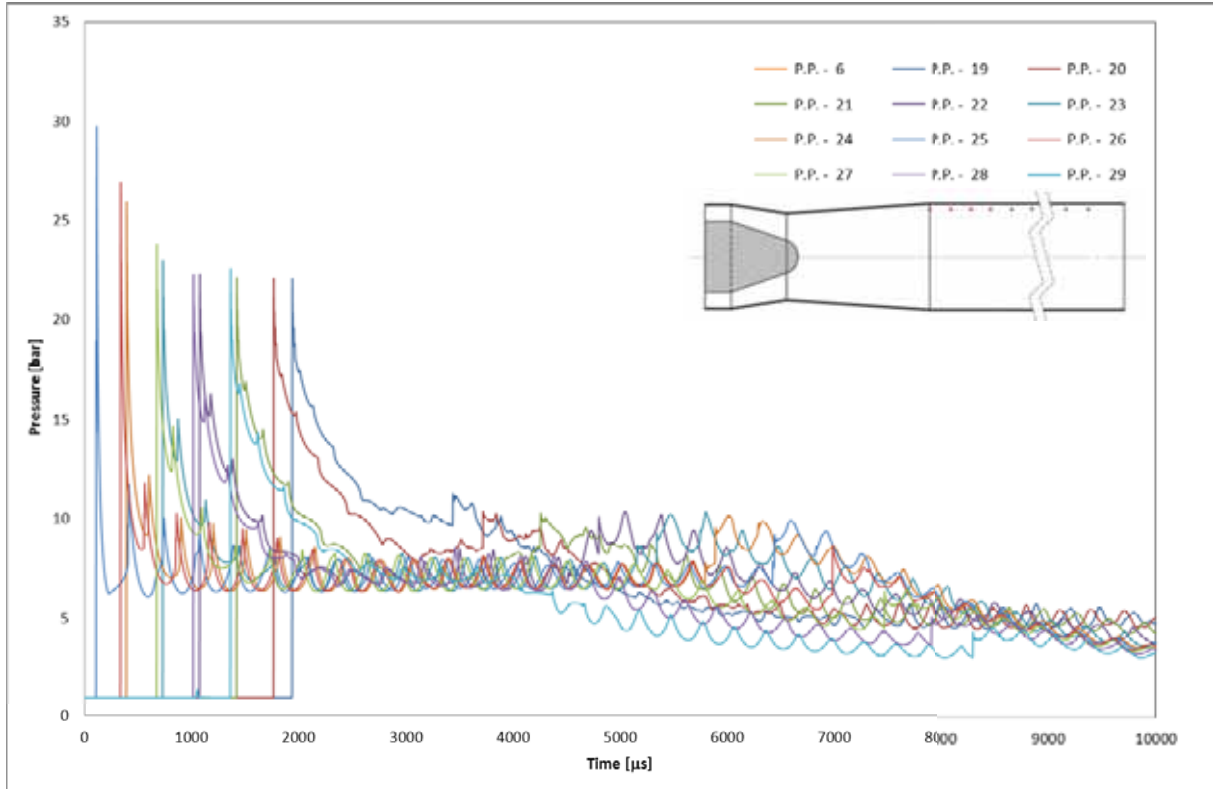


Figure 16 – Pressure plot for the points at 5mm from the wall - Detonation point at 6.0m – ALE.

2.2 LS-DYNA – CESE Approach

The latest version of the LS-DYNA finite element software, 980, includes a multi-physics capability, i.e. electromagnetics, chemistry, incompressible fluid solver and compressible fluid solver based on Conservation Element and Solution Element Method, CESE. The CESE solver can be used for different applications such as: compressible flows across a range of Mach numbers; low and high speed flows (subsonic, supersonic); acoustic flows and flows with complex shock patterns. The advantage of the CESE method for compressible flows is its capability to solve compressible inviscid and viscous flows. Strong shocks and small disturbances can be computed very well and the flux conservation in space and time is 2nd order accurate [iv,v].

Unlike version 971 where the JWL equation of state assumes a stoichiometric mixture, here a detailed chemistry was used to model the detonation of the gas mixtures. The detailed reaction mechanism in a detonating flow simulation is typically made via a chemistry input file compatible with the CHEMKIN code [vi,vii]. The file includes information about the elements, species, thermodynamics data, and elementary chemical reaction mechanisms. In this particular project the direct initiation method was used to initiate a detonation of stoichiometric hydrogen-air mixture at two locations along the duct. The following sections present a brief description of the numerical methods, and the results of the detonation of the gas mixture at two locations along the duct.

2.2.1 Numerical Methods

The governing equations are solved by the Space-Time CESE method, including realistic finite rate models of multiple species and multiple reactions steps, correctly derived Jacobian matrices of convection terms and source terms, and comprehensive thermodynamics relations. In the setting of the CESE method, stiff source terms in species equations due to chemical reactions are solved using a unique space-time volumetric integration with sub-time-step integrations for high resolution. A finite-rate model of twenty one reaction steps and three species is adopted in the present work. More information about the governing equations is provided in the LS-DYNA CESE theory manual [iv].

2.2.1.1 Limitation of LS-DYNA 980 code:

The multi-physics version of LS-DYNA code is at a beta release stage and consequently some features of the code are not linked or fully implemented. However, the code is capable of simulating the detonation of gas mixtures accurate with the modelling approach implemented. Momently it is not possible to simulate an aerodynamic flow followed by a detonation. It is possible to simulate the two cases separately, but no connection between the mathematical models. Once this connection is made the code will be able to fully solve the detonation problem with a superimposed flow field.

2.2.2 Detonation point at 0.5m

A direct initiation mode was used to initiate the detonation of the gas mixture at 0.5m from the origin. A large amount of energy was instantaneously deposited to a small region of unconfined combustible mixture. Immediately, a strong blast wave was generated. This spherical shock wave expands and decays while it continues heating the gas mixture as shown in the sequence of images in Figure 17 and the pressure plot in Figure 21. Due to shock heating, chemical reactions occur and chemical energy was released. Under these conditions, detonation was initiated.

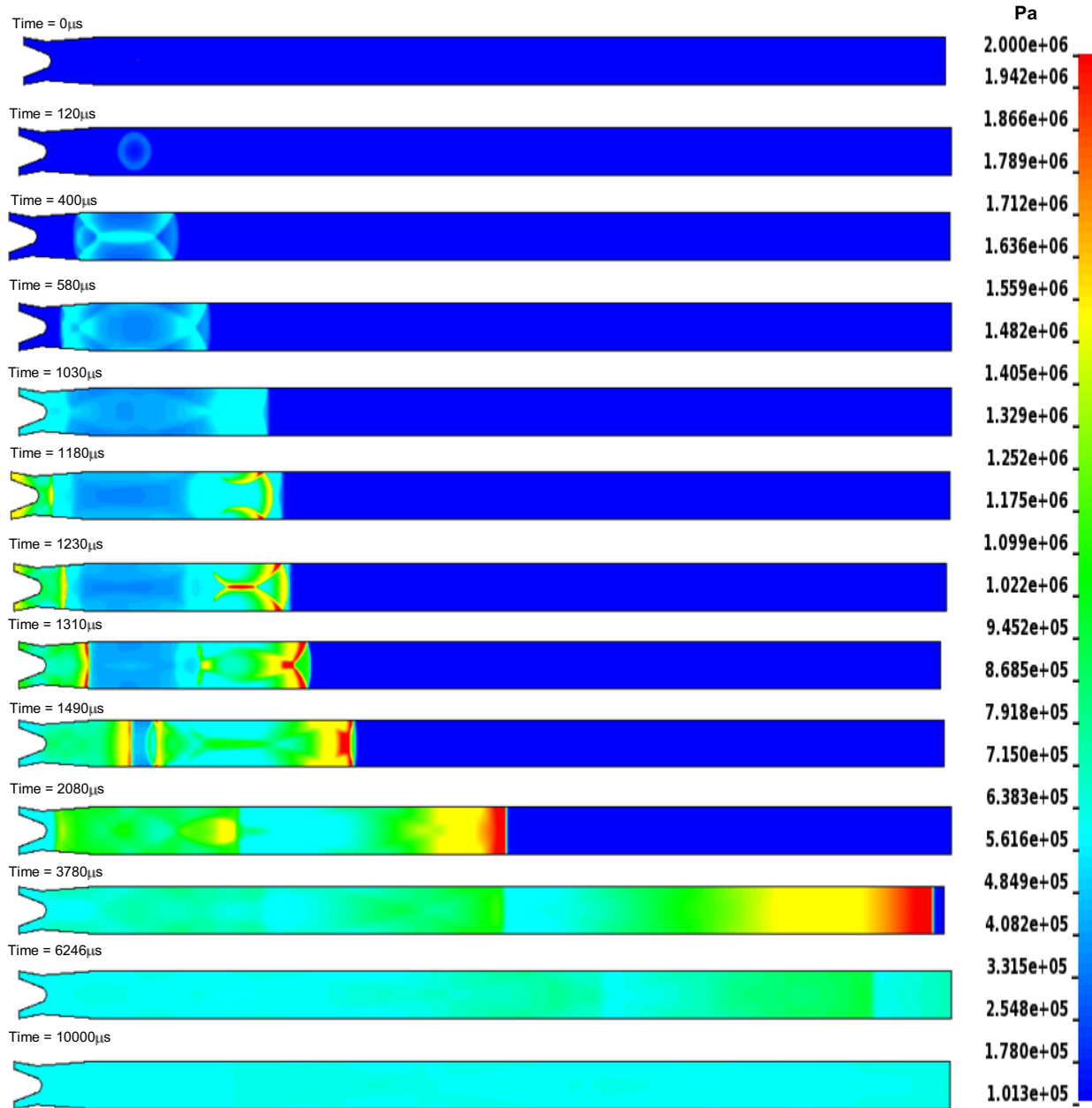


Figure 17 – Sequence of images showing the expansion of the detonation wave when initiated at 0.5m – CESE.

The pressure profiles at given points are presented in Figure 18 to Figure 22.

The CESE approach predicted that a second pressure wave with a maximum peak pressure of 15bar occurred in the nozzle section, after the detonation wave passed through. This shock wave may be generated by the reflection of secondary shock waves that occurred in the duct behind the main pressure shock front. This behaviour is shown in Figure 18, Figure 19, and Figure 20.

Figure 21 and Figure 22 show the evolving pressure profiles of the detonation process with the direct initiation mode. The initial blast wave developed into a stable detonation wave as shown at the pressures points along the duct that predicted an approximately constant pressure front.

The following table summarises the peak and static pressures predicted for the pressure points 1 to 51. No data were available for the pressure points 31 to 45.

	Peak Pressure	Static Pressure		Peak Pressure	Static Pressure		Peak Pressure	Static Pressure
	[bar]	[bar]		[bar]	[bar]		[bar]	[bar]
P.P. - 1	17.214	6.052	P.P. - 18	22.120	2.235	P.P. - 35	n.a.	n.a.
P.P. - 2	13.346	6.620	P.P. - 19	20.159	6.488	P.P. - 36	n.a.	n.a.
P.P. - 3	18.549	6.653	P.P. - 20	13.638	6.464	P.P. - 37	n.a.	n.a.
P.P. - 4	1.000	1.000	P.P. - 21	20.581	5.992	P.P. - 38	n.a.	n.a.
P.P. - 5	16.377	6.411	P.P. - 22	20.818	5.592	P.P. - 39	n.a.	n.a.
P.P. - 6	18.481	6.558	P.P. - 23	22.097	5.112	P.P. - 40	n.a.	n.a.
P.P. - 7	17.887	6.270	P.P. - 24	22.052	4.518	P.P. - 41	n.a.	n.a.
P.P. - 8	22.165	6.232	P.P. - 25	21.908	4.062	P.P. - 42	n.a.	n.a.
P.P. - 9	25.308	5.791	P.P. - 26	21.883	3.476	P.P. - 43	n.a.	n.a.
P.P. - 10	24.656	5.455	P.P. - 27	22.168	2.850	P.P. - 44	n.a.	n.a.
P.P. - 11	22.244	5.043	P.P. - 28	21.980	2.610	P.P. - 45	n.a.	n.a.
P.P. - 12	22.096	4.522	P.P. - 29	22.131	2.414	P.P. - 46	19.421	6.050
P.P. - 13	21.948	3.954	P.P. - 30	22.124	2.235	P.P. - 47	17.332	6.035
P.P. - 14	21.870	3.387	P.P. - 31	n.a.	n.a.	P.P. - 48	12.737	6.600
P.P. - 15	22.146	2.852	P.P. - 32	n.a.	n.a.	P.P. - 49	13.066	6.672
P.P. - 16	21.969	2.592	P.P. - 33	n.a.	n.a.	P.P. - 50	18.392	6.596
P.P. - 17	22.135	2.414	P.P. - 34	n.a.	n.a.	P.P. - 51	18.791	6.519

Table 9 – Summary of the peak and static pressure - Detonation point at 0.5m – CESE.

The duration of the pressure peaks over 20bar are summarised in Table 10. The values presented in table below were measured at a different frequency to those presented for the ALE simulations. Therefore, it's difficult to provide an accurate duration of the pressure peaks.

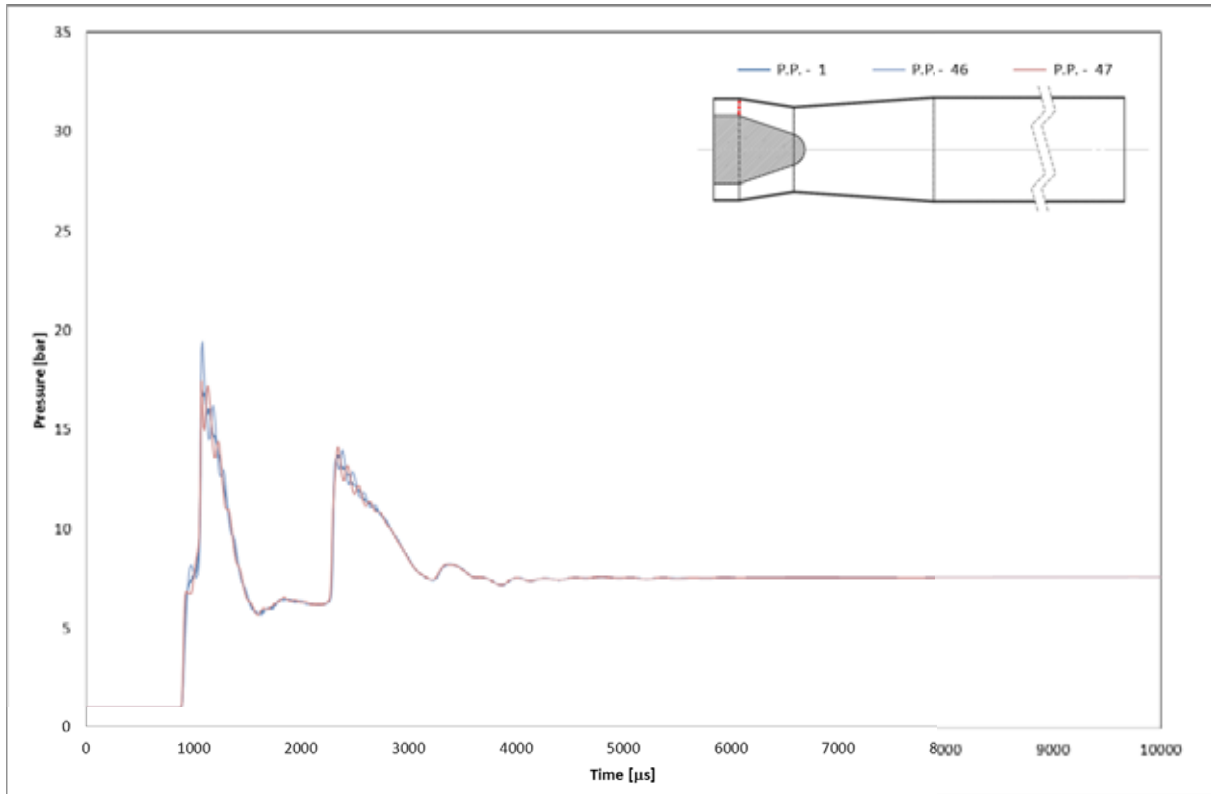


Figure 18 – Pressure plot for the points 1, 46 and 47 - Detonation point at 0.5m – CESE.

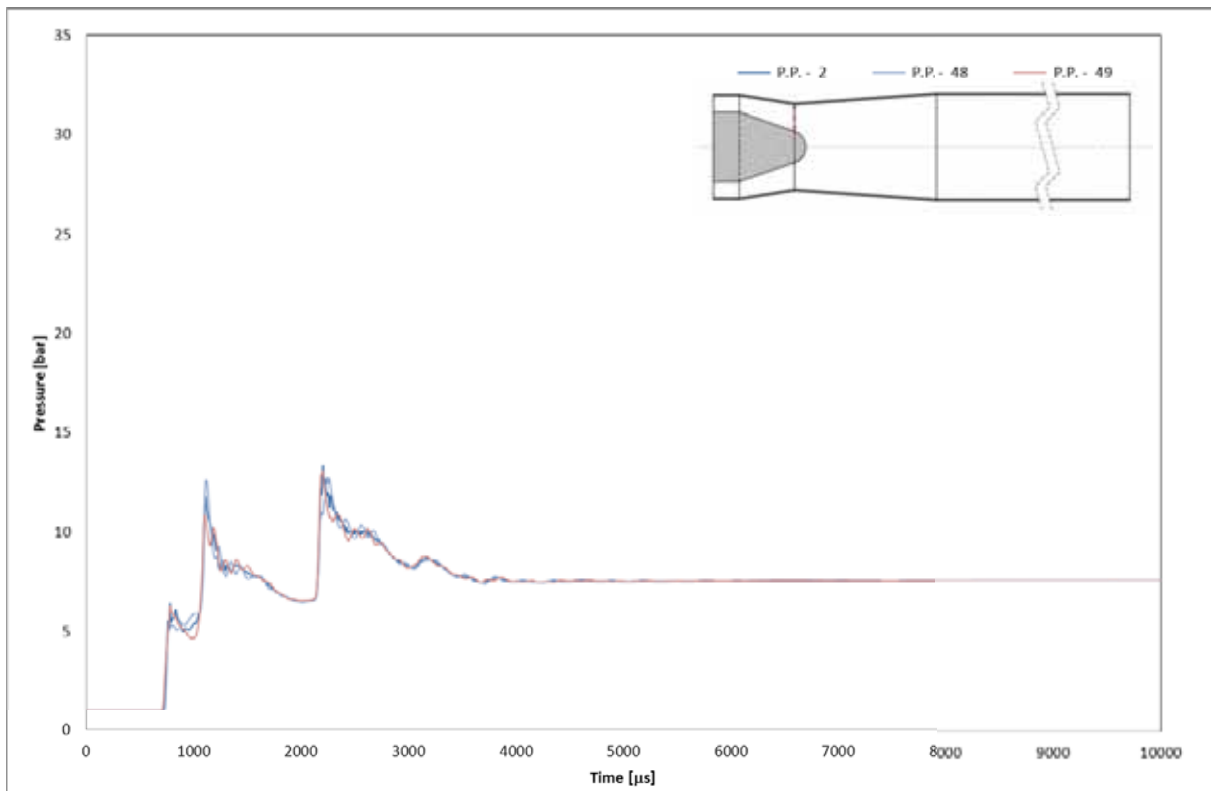


Figure 19 – Pressure plot for the points 2, 48 and 49 - Detonation point at 0.5m – CESE.

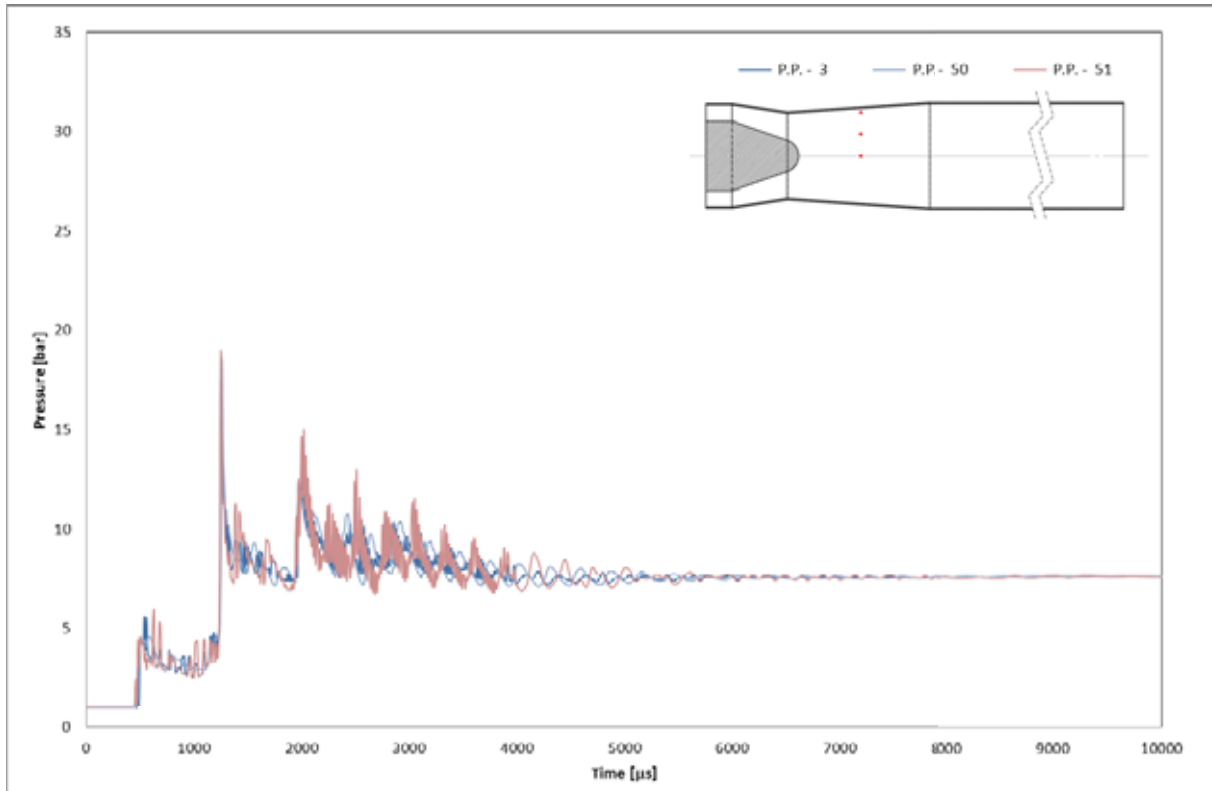


Figure 20 – Pressure plot for the points 3, 50 and 51 - Detonation point at 0.5m – CESE.

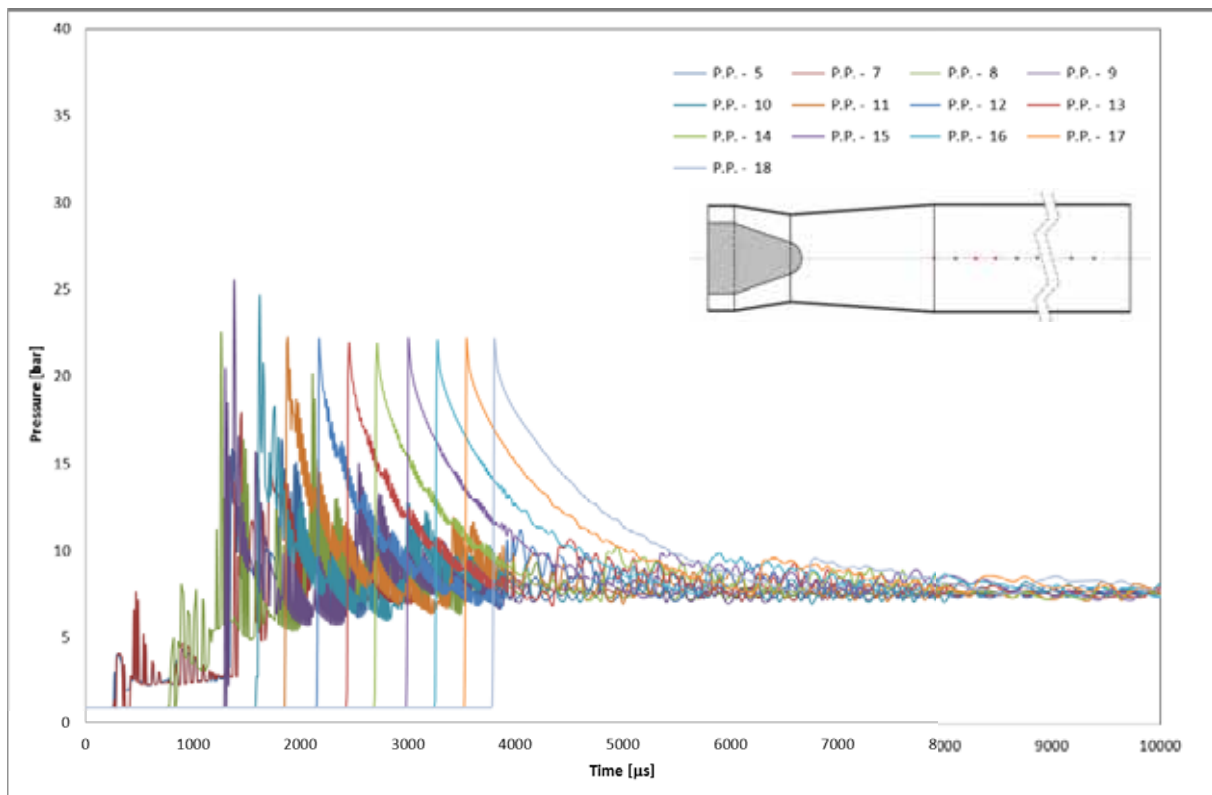


Figure 21 – Pressure plot for the points along the centre line - Detonation point at 0.5m – CESE.

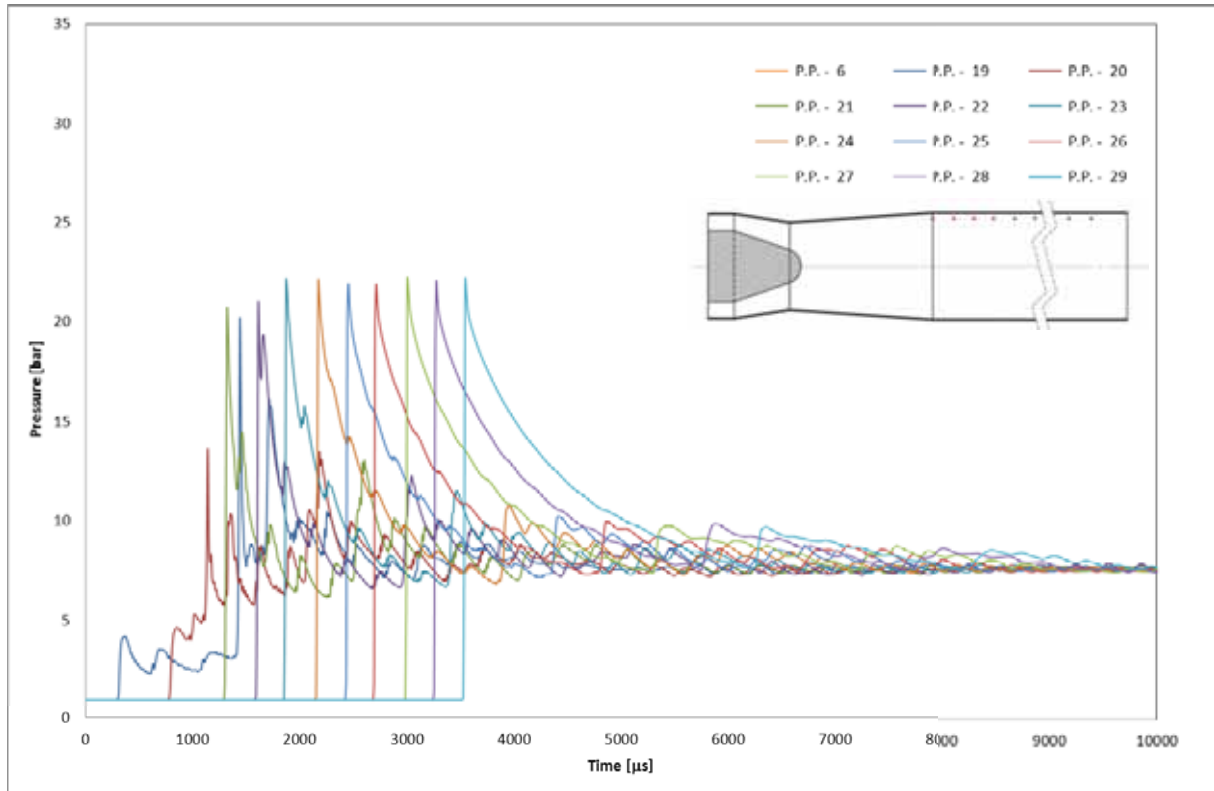


Figure 22 – Pressure plot for the points at 5mm from the wall - Detonation point at 0.5m – CESE.

2.2.3 Detonation point at 6.0m

The intention of this simulation was to model the impingement of a fully developed detonation by positioning the detonation point at centre of the duct so that the pressure wave has enough time to evolve and become a self-sustaining detonation wave as shown in Figure 23.

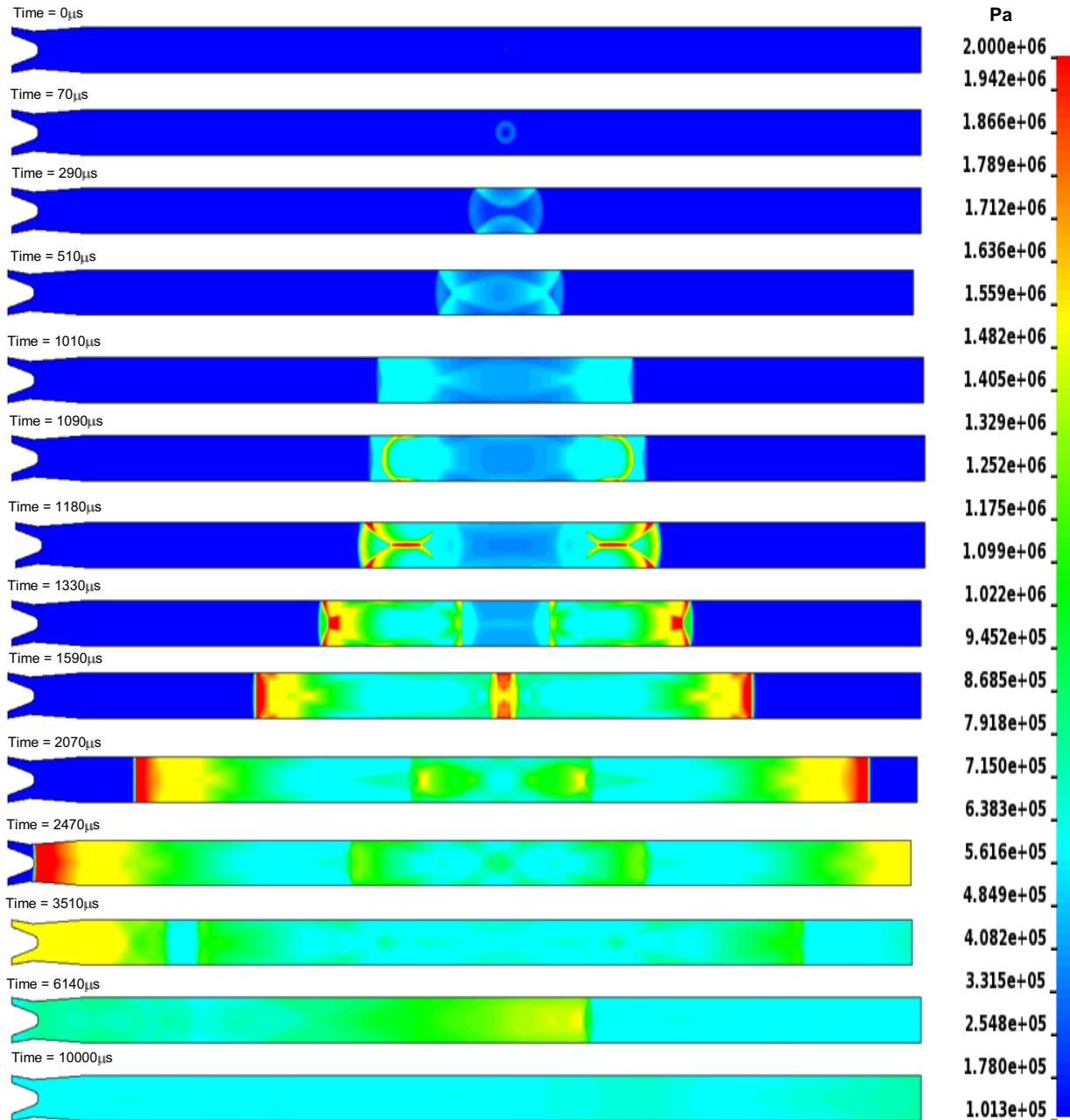


Figure 23 – Sequence of images showing the expansion of the detonation wave when initiated at 6.0m – CESE.

In this scenario where the detonation point was located at 6.0m, the maximum peak pressures reached 35bar at the exhaust face, i.e. 15bar higher than the previous detonation case, see Figure 18 and Figure 24. Similar increases in the maximum peak pressures and duration were predicted in the nozzle section as shown in Figure 25 and Figure 26.

Figure 27 and Figure 28 present the evolution of the pressure profiles along the duct. As shown in the figures, secondary shock waves occurred after the detonation wave passed through. The magnitude of the secondary shock waves reached a maximum value of between 12-15bar.

The following table summarises the peak and static pressures predicted for the pressure points 1 to 51. No data were available for the pressure points 31 to 45.

	Peak Pressure	Static Pressure		Peak Pressure	Static Pressure		Peak Pressure	Static Pressure
	[bar]	[bar]		[bar]	[bar]		[bar]	[bar]
P.P. - 1	32.062	2.771	P.P. - 18	22.030	4.265	P.P. - 35	n.a.	n.a.
P.P. - 2	28.922	3.006	P.P. - 19	21.792	4.281	P.P. - 36	n.a.	n.a.
P.P. - 3	22.357	3.132	P.P. - 20	21.653	5.102	P.P. - 37	n.a.	n.a.
P.P. - 4	1.000	1.000	P.P. - 21	20.132	5.668	P.P. - 38	n.a.	n.a.
P.P. - 5	21.835	3.098	P.P. - 22	24.243	6.075	P.P. - 39	n.a.	n.a.
P.P. - 6	22.028	3.134	P.P. - 23	12.908	6.346	P.P. - 40	n.a.	n.a.
P.P. - 7	21.782	4.321	P.P. - 24	39.614	6.058	P.P. - 41	n.a.	n.a.
P.P. - 8	22.338	5.008	P.P. - 25	12.357	6.299	P.P. - 42	n.a.	n.a.
P.P. - 9	26.556	5.598	P.P. - 26	24.037	6.120	P.P. - 43	n.a.	n.a.
P.P. - 10	37.160	5.875	P.P. - 27	19.438	5.647	P.P. - 44	n.a.	n.a.
P.P. - 11	26.678	6.171	P.P. - 28	21.786	5.177	P.P. - 45	n.a.	n.a.
P.P. - 12	39.929	5.936	P.P. - 29	22.005	4.622	P.P. - 46	35.769	2.764
P.P. - 13	30.215	6.133	P.P. - 30	21.966	4.149	P.P. - 47	35.176	2.787
P.P. - 14	32.137	5.863	P.P. - 31	n.a.	n.a.	P.P. - 48	29.720	3.026
P.P. - 15	26.911	5.600	P.P. - 32	n.a.	n.a.	P.P. - 49	30.436	3.008
P.P. - 16	22.909	5.131	P.P. - 33	n.a.	n.a.	P.P. - 50	23.542	3.109
P.P. - 17	21.946	4.555	P.P. - 34	n.a.	n.a.	P.P. - 51	22.872	3.134

Table 11 – Summary of the peak and static pressure - Detonation point at 6.0m – CESE.

The duration of the pressure peaks over 20bar are summarised in Table 12. The values presented in Table 12 were measured at a frequency of 10µs which is a different frequency to those presented for the ALE simulations. Therefore, it's difficult to provide an accurate duration of the pressure peaks.

	P.P.- 1	P.P.- 2	P.P.- 3	P.P.- 4	P.P.- 5	P.P.- 6	P.P.- 7	P.P.- 8	P.P.- 9	P.P.- 10
	$\Delta T[\mu s]$									
	P[bar]									
P. Peak 1	<750	<730	<50	<20	<40	<50	<30	<40	<10	<20
P. Peak 2	-	-	-	-	-	-	-	-	<50	<10
P. Peak 3	-	-	-	-	-	-	-	-	-	<10
	P.P.- 11	P.P.- 12	P.P.- 13	P.P.- 14	P.P.- 15	P.P.- 16	P.P.- 17	P.P.- 18	P.P.- 19	P.P.- 20
	$\Delta T[\mu s]$									
	P[bar]									
P. Peak 1	<10	<30	<20	<20	<50	<20	<20	<30	<30	<30
P. Peak 2	<10	<10	<10	<10	-	<10	-	-	-	-
P. Peak 3	-	<40	-	-	-	-	-	-	-	-
	P.P.- 21	P.P.- 22	P.P.- 23	P.P.- 24	P.P.- 25	P.P.- 26	P.P.- 27	P.P.- 28	P.P.- 29	P.P.- 30
	$\Delta T[\mu s]$									
	P[bar]									
P. Peak 1	<10	<20	-	<70	-	<20	-	<30	<30	<30
	P.P.- 31	P.P.- 32	P.P.- 33	P.P.- 34	P.P.- 35	P.P.- 36	P.P.- 37	P.P.- 38	P.P.- 39	P.P.- 40
	$\Delta T[\mu s]$									
	P[bar]									
P. Peak 1	-	-	-	-	-	-	-	-	-	-
	P.P.- 41	P.P.- 42	P.P.- 43	P.P.- 44	P.P.- 45	P.P.- 46	P.P.- 47	P.P.- 48	P.P.- 49	P.P.- 50
	$\Delta T[\mu s]$									
	P[bar]									
P. Peak 1	-	-	-	-	-	<740	<740	<730	<730	<50
P. Peak 2	-	-	-	-	-	-	-	-	-	<50

Table 12 – Summary of the pressure peaks duration over 20bar - Detonation point at 6.0m – CESE.

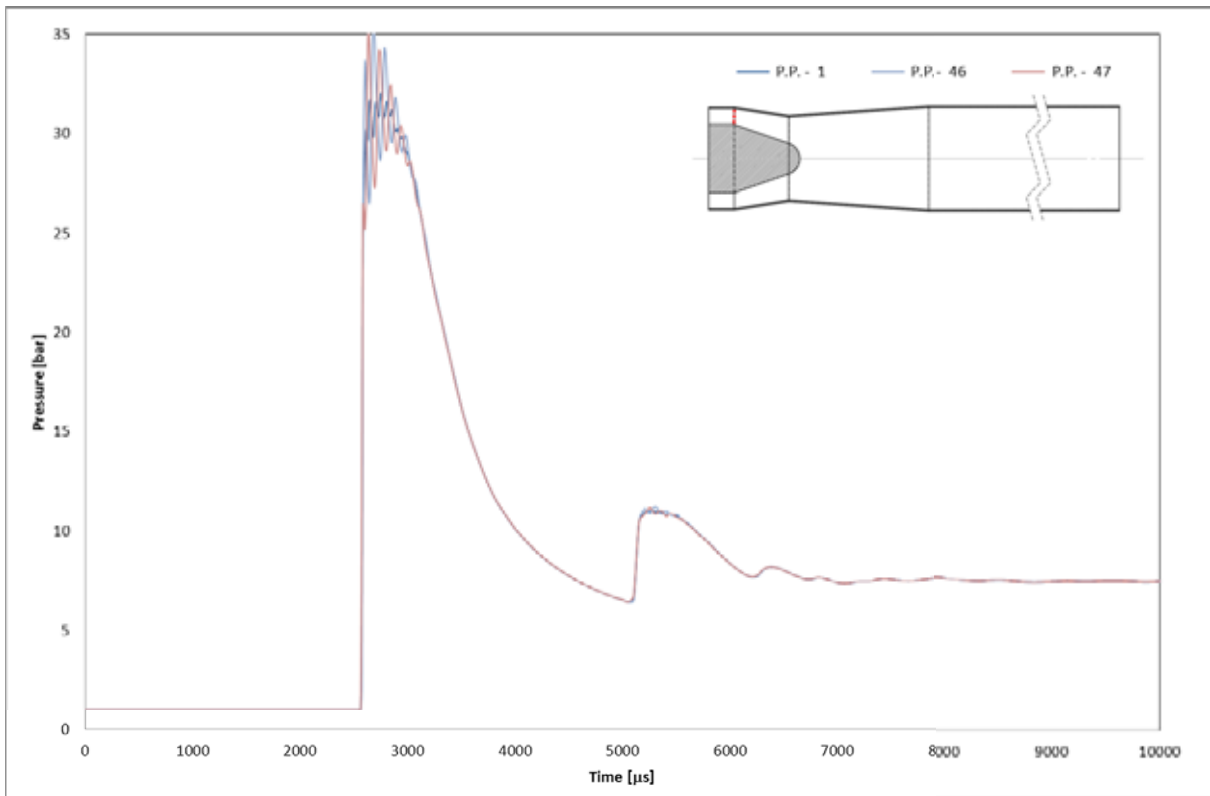


Figure 24 – Pressure plot for the points 1, 46 and 47 - Detonation point at 6.0m – CESE.

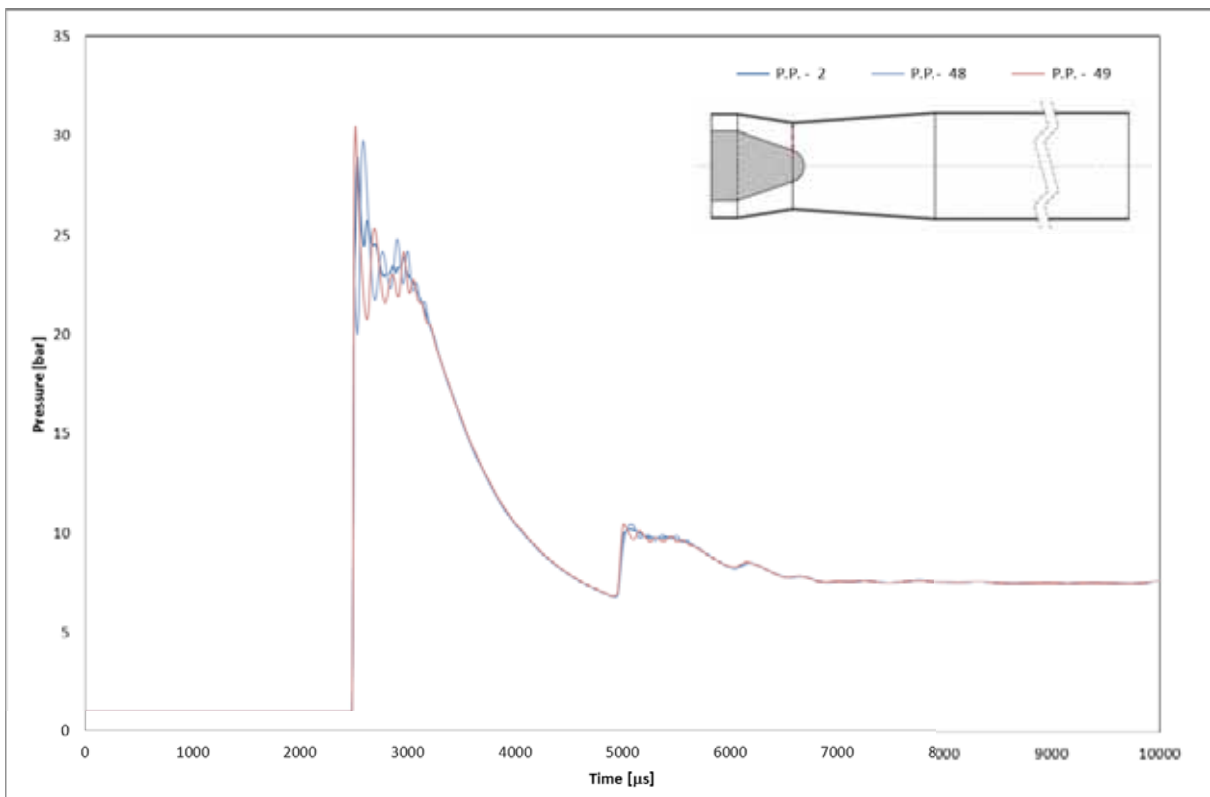


Figure 25 – Pressure plot for the points 2, 48 and 49 - Detonation point at 6.0m – CESE.

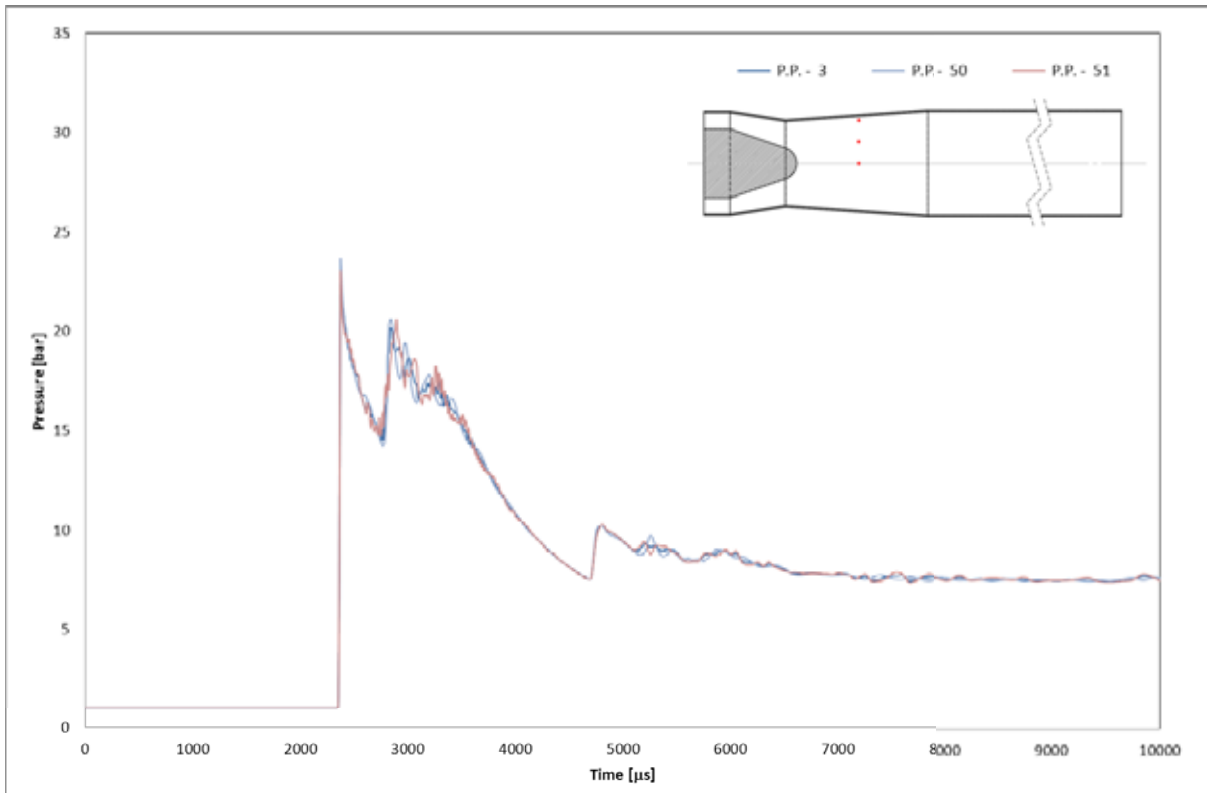


Figure 26 – Pressure plot for the points 3, 50 and 51 - Detonation point at 6.0m – CESE.

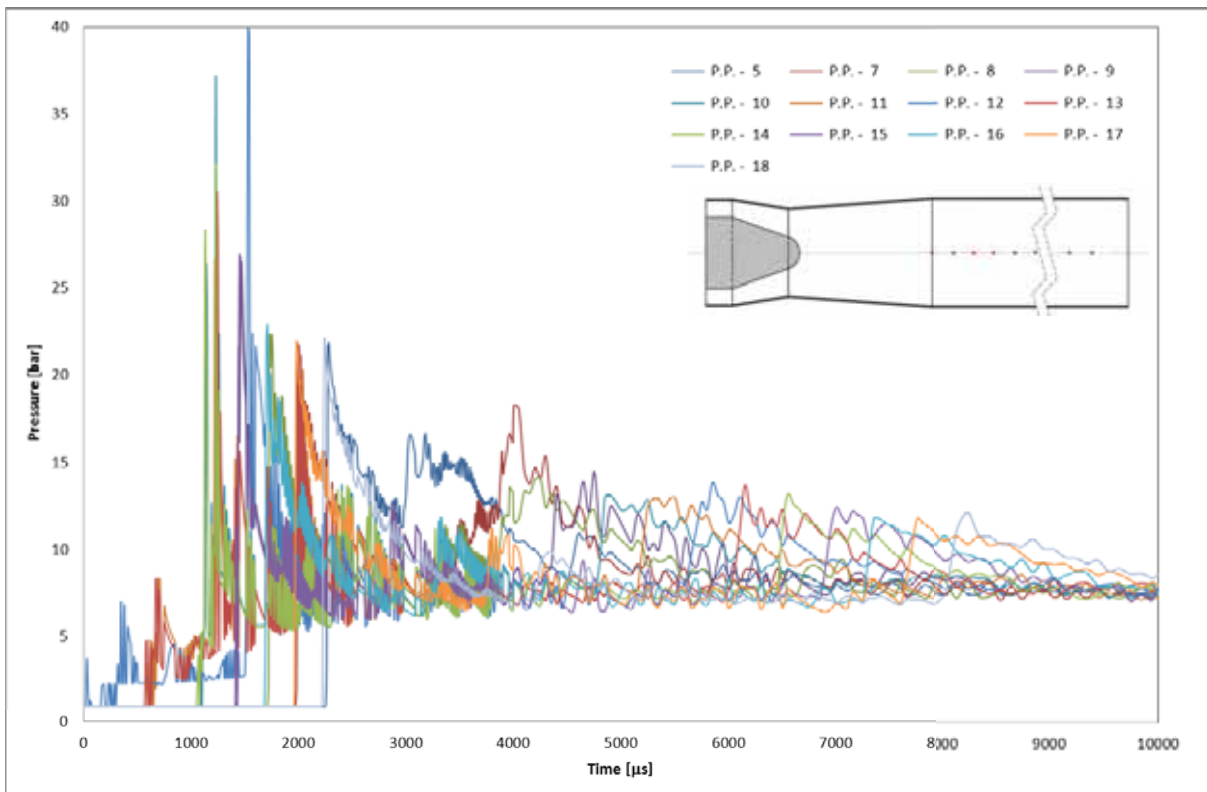


Figure 27 – Pressure plot for the points along the centre line - Detonation point at 6.0m – CESE.

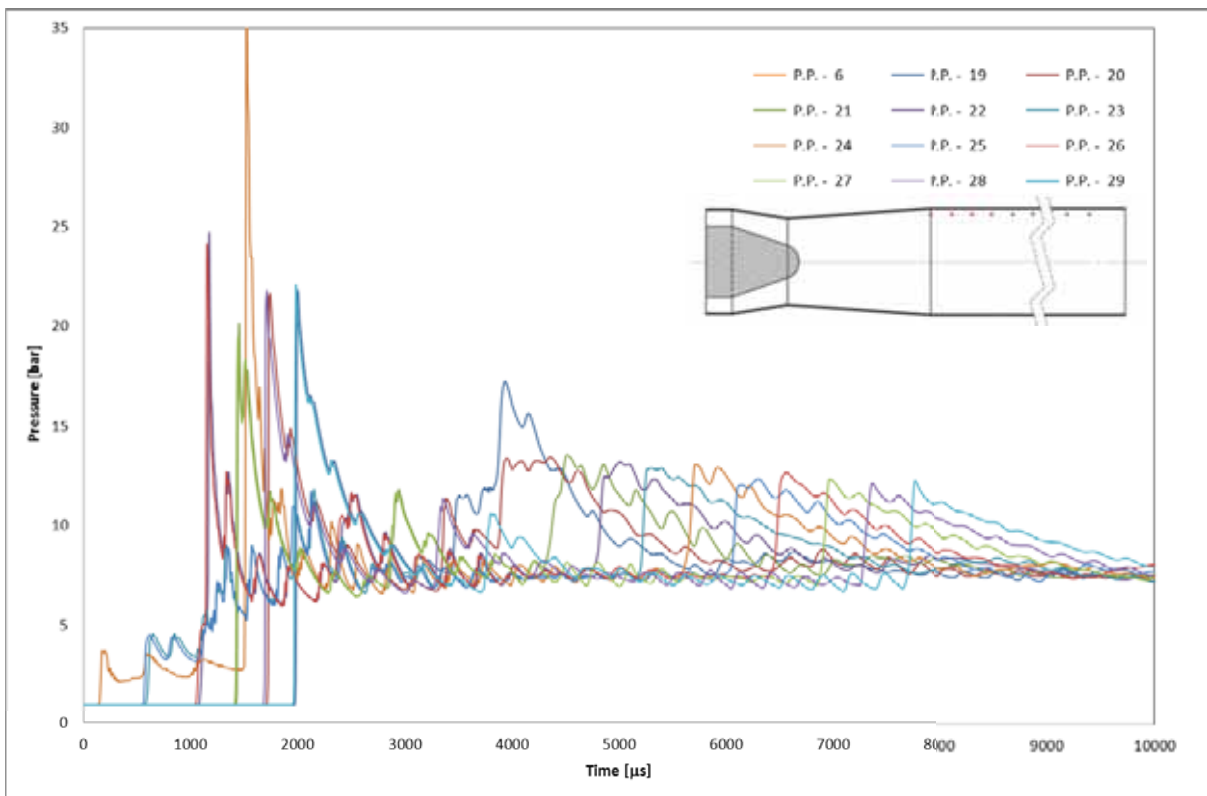


Figure 28 – Pressure plot for the points at 5mm from the wall - Detonation point at 6.0m – CESE.

2.3 Comparison between the ALE and CESE modelling approaches

Figure 29, Figure 30, Figure 31 and Figure 32 show the comparison between the ALE and CESE approach for the peak and static pressures predicted in the duct. This comparison was made to verify whether the beta release of LS-DYNA code predicted the pressure levels and behaviour accurately. Both approaches predicted similar peak and static pressures for all the 51 pressure points located in the duct. The major difference between the two approaches was the static pressure predicted near the exhaust exit and the duct exit for the detonation at 0.5m. The difference in the results might be related to the boundary condition methodology implemented in both versions of the code and the mesh resolution. This variance was not explored. No data were available for the pressure points 31 to 45 for the CESE approach.

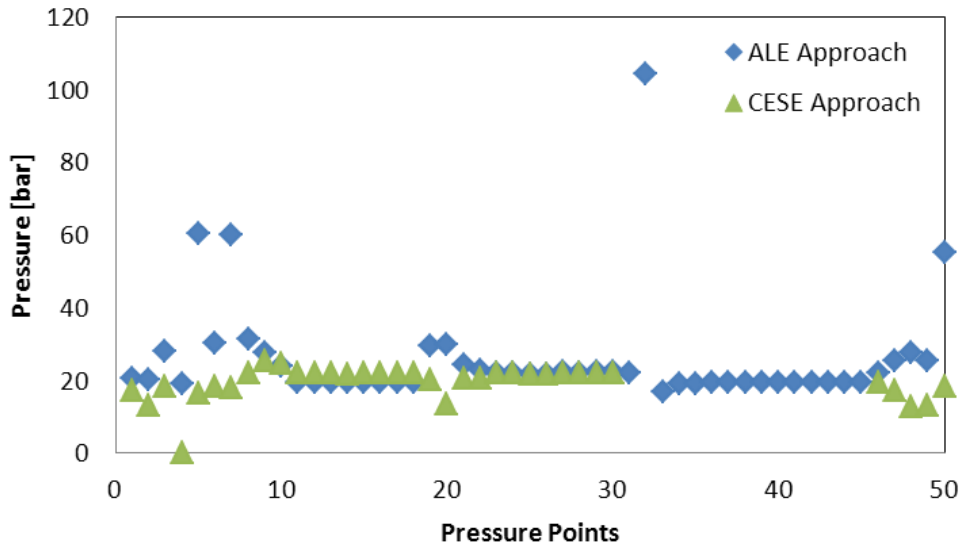


Figure 29 – Comparison between ALE and CESE approach for the peak pressure - Detonation at 0.5m.

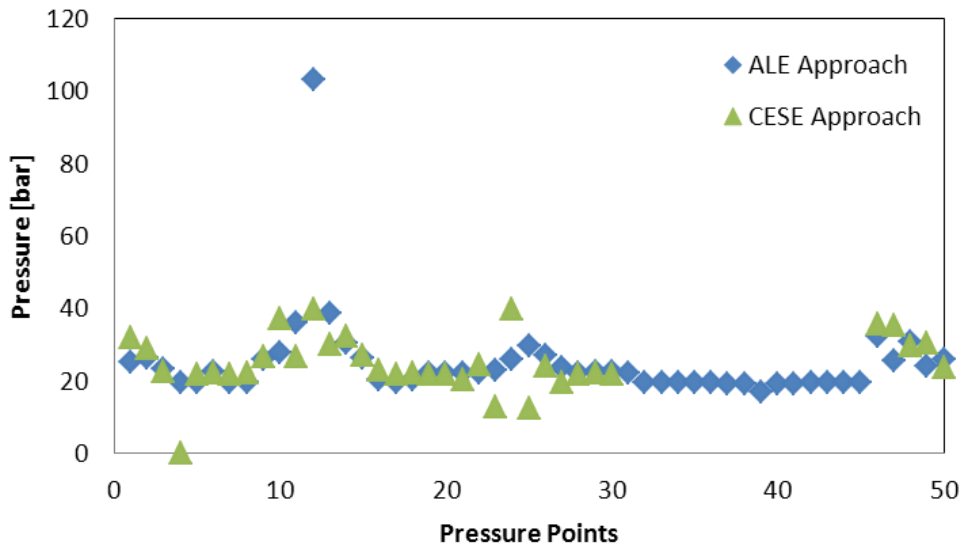


Figure 30 – Comparison between ALE and CESE approach for the peak pressure - Detonation at 6.0m.

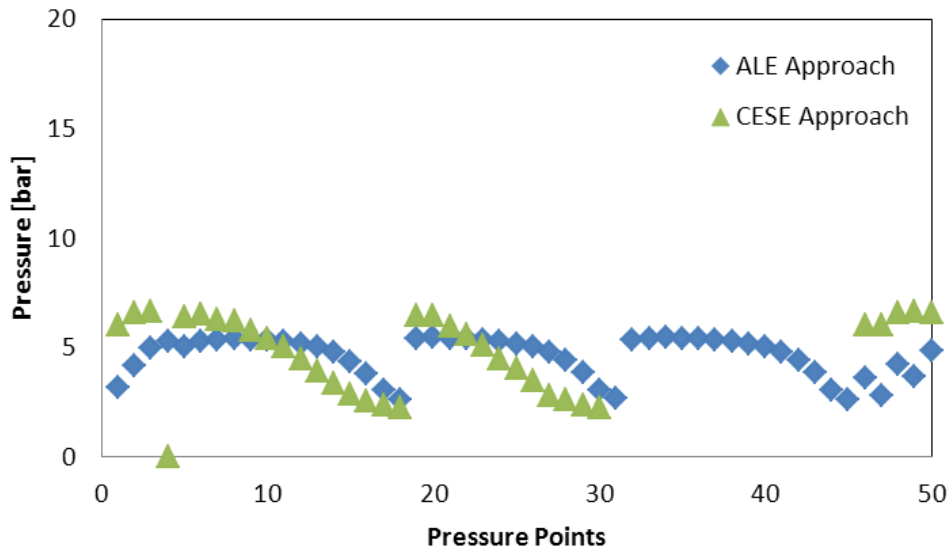


Figure 31 – Comparison between ALE and CESE approach for the static pressure - Detonation at 0.5m.

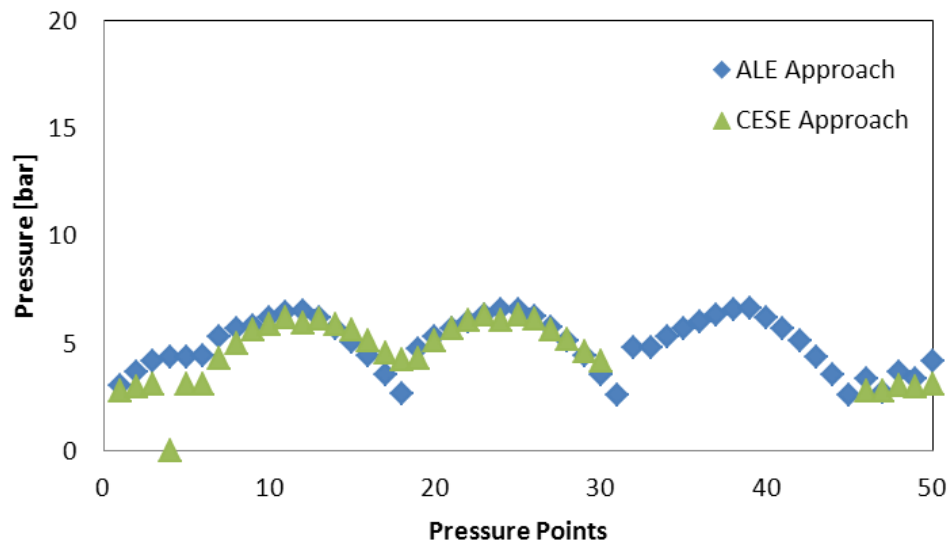


Figure 32 – Comparison between ALE and CESE approach for the static pressure - Detonation at 6.0m.

2.4 OpenFOAM Approach

The open source code "OpenFOAM" was used to determine whether the H₂-O₂-N₂-CO₂ mixture (Mole fraction: hydrogen 0.122, nitrogen 0.656, oxygen 0.183 and carbon dioxide 0.039) with the total mass flow 16.1kg/s, initial temperature 500° and at ambient pressure would detonate when the mixture is ignited and to determine the pressures that are generated inside the duct. The OpenFOAM code used in this program of work has been modified and new mathematical models have been implemented to simulate the deflagration, detonation and combustion of stoichiometric and non-stoichiometric gas mixtures. The following sections describe the governing equations, numerical methods, and the results for the case where there is direct ignition of the gas mixture and for a case without any ignition source.

2.4.1 Numerical Methods

The governing equations for the detonation propagation problem are the three-dimensional Navier-Stokes equations for a chemically reacting gas mixture. The equations are discretized using the finite volume method and a Crank-Nicholson discretization was employed for time integration. The convective terms are calculated by the Monotone Upstream-centred Scheme for Conservation Laws (MUSCL) scheme. The diffusion terms are evaluated by a Gauss linear corrected method.

2.4.2 CJ Detonation parameters

A Gordon-McBride computer program has been employed to treat the complex chemical equilibrium compositions in Chapman-Jouguet (CJ) detonations and to compute the CJ detonation speed. As shown below, for the specified mixture composition, the CJ pressure and temperature are 4.0297bar and 2065.83K, respectively.

Items	Unburned gas	Burned gas	ratio
Pressure	1.0bar	4.0297bar	4.0297
Temperature	773.15°K	2065.83°K	2.672
Density	0.41289 kg/m ³	0.66269 kg/m ³	1.605
Velocity	0 m/s	1404.4 m/s	-

Table 13 – Detonation parameter.

2.4.3 Initiation case study

Firstly, without considering the chemical reaction, the quasi-steady flow field was obtained by axi-symmetric simulation and was used to set up the initial flow field. The detonation was then initiated by imposing high pressure and temperature in a small region. The detonation then propagates through the tube. Dynamic and stagnation pressures at given points as well as other parameters such as H₂O mass fraction, temperature were monitored.

2.4.3.1 Wave evolution

Figure 33 and Figure 34 present the pressure contours and H₂O mass fraction in the tube at the same instances of time. The H₂O mass fraction is indicative of the reaction zone, which is coupled with the precursor shock wave. The predictions show that a self-propagating detonation wave can be generated in the presence of a sufficiently strong ignition source. The detonation wave undergoes outward-propagation, normal reflection and Mach reflection when travelling along the tube. It is noted that, in Figure 33 (c) and Figure 34 (b), there is evidence of combustion and there is a pressure wave in the downstream region prior to the arrival of the detonation wave. The implication is that if such a mixture with the initial conditions prescribed here enters the long tube, auto-ignition could occur in the downstream region even if there is no ignition source. To further investigate, another computation has been carried out and described in the next section.

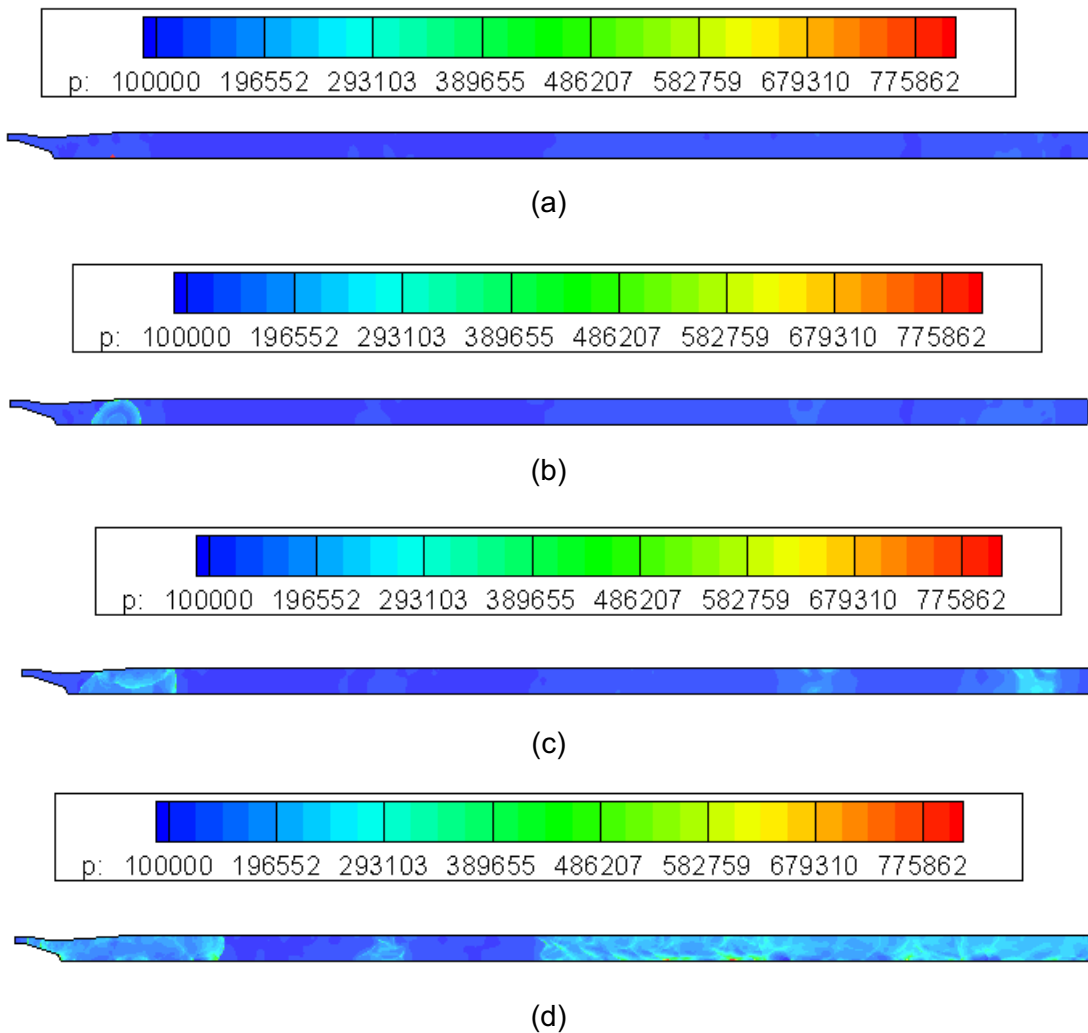


Figure 33 – Sequence of images showing the evolution of the pressure wave in the tube.

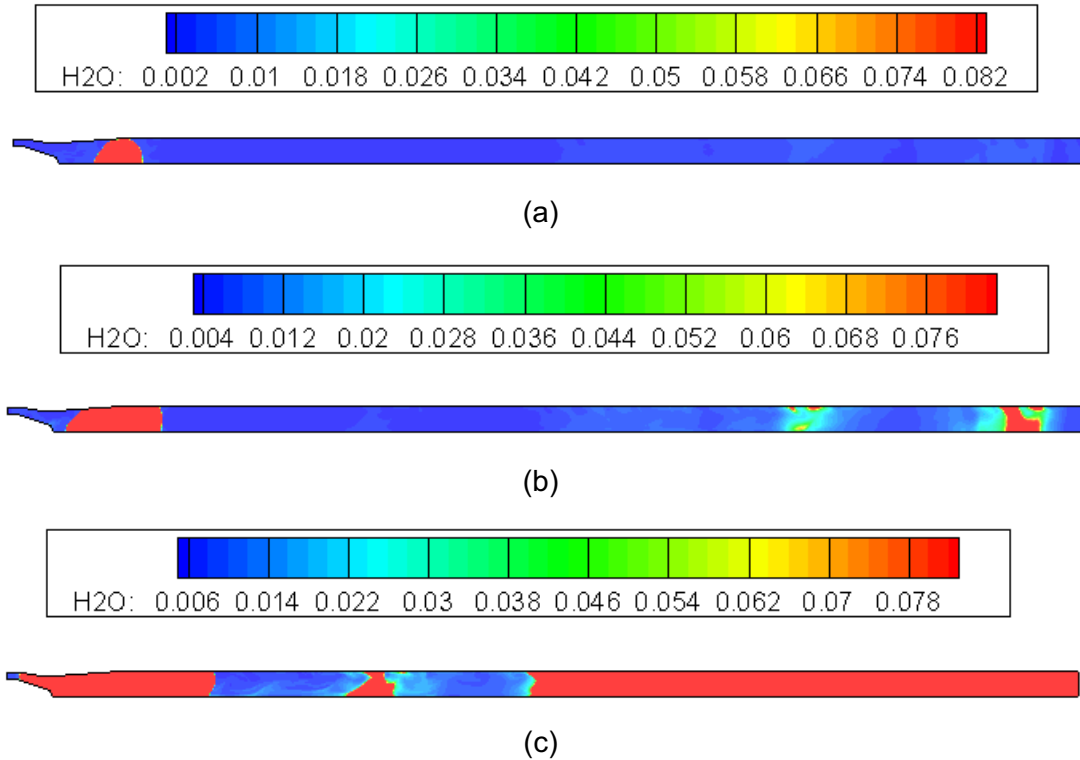


Figure 34 – Sequence of images showing the evolution of the H₂O concentration in the tube.

2.4.3.2 Pressure profiles

Figure 35 to Figure 40 show the pressure profiles at the specified points. The pressure in the upstream region is influenced by the detonation wave whereas the pressure in the downstream region is affected by the combustion following auto-ignition. At some upstream points, the maximum pressure induced by the detonation wave is 4-5bar, and this is consistent with CJ pressure in Table 13. At other points, the maximum pressure can reach 8bar due to the reflected pressure wave. In the downstream region, the pressure induced by auto-ignition is less than 3bar.

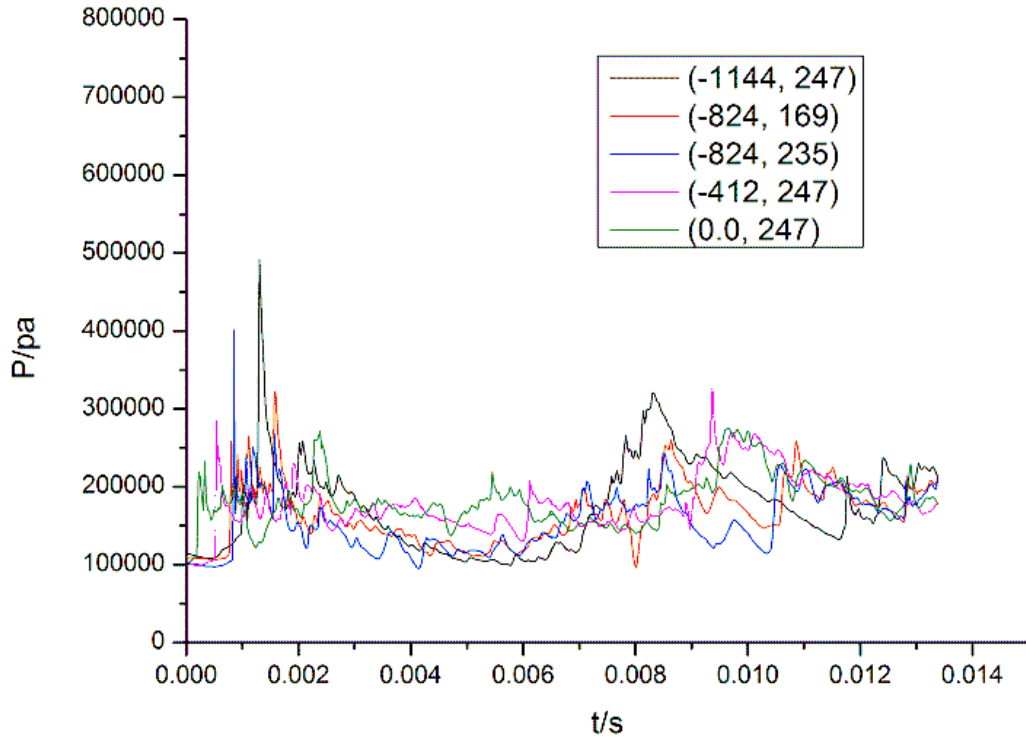


Figure 35 – Pressure plot for the points 1, 2, 3, 4, and 5 - Detonation point at 0.5m – OpenFOAM.

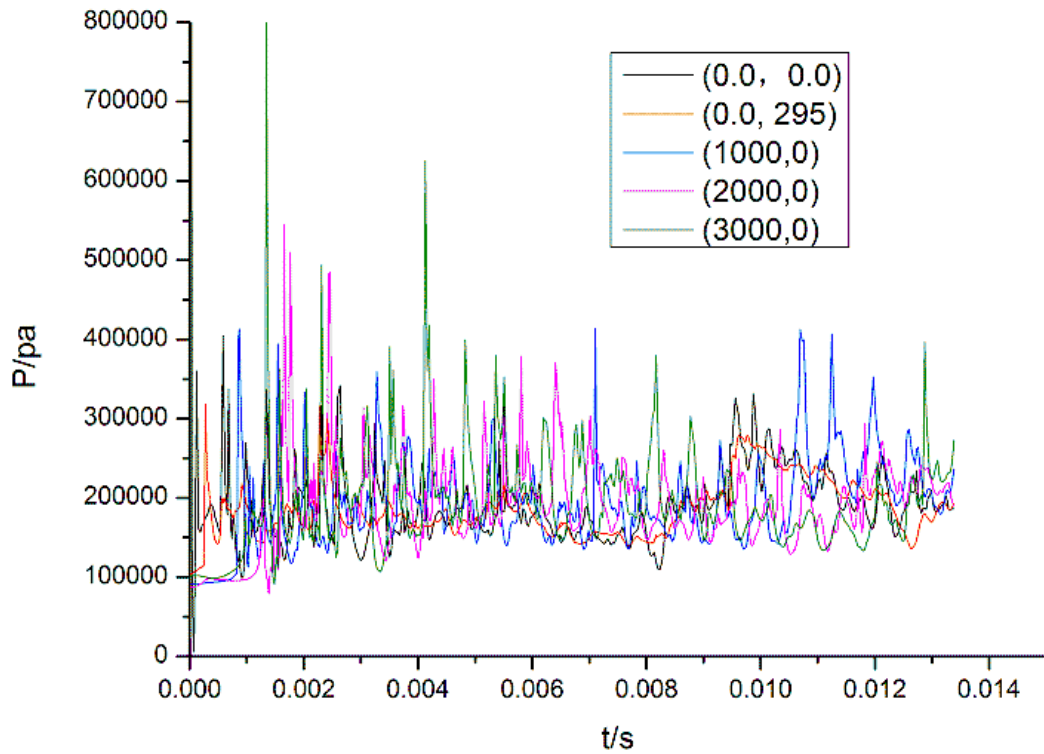


Figure 36 – Pressure plot for the points 6, 7, 8, 9, and 10 - Detonation point at 0.5m – OpenFOAM.

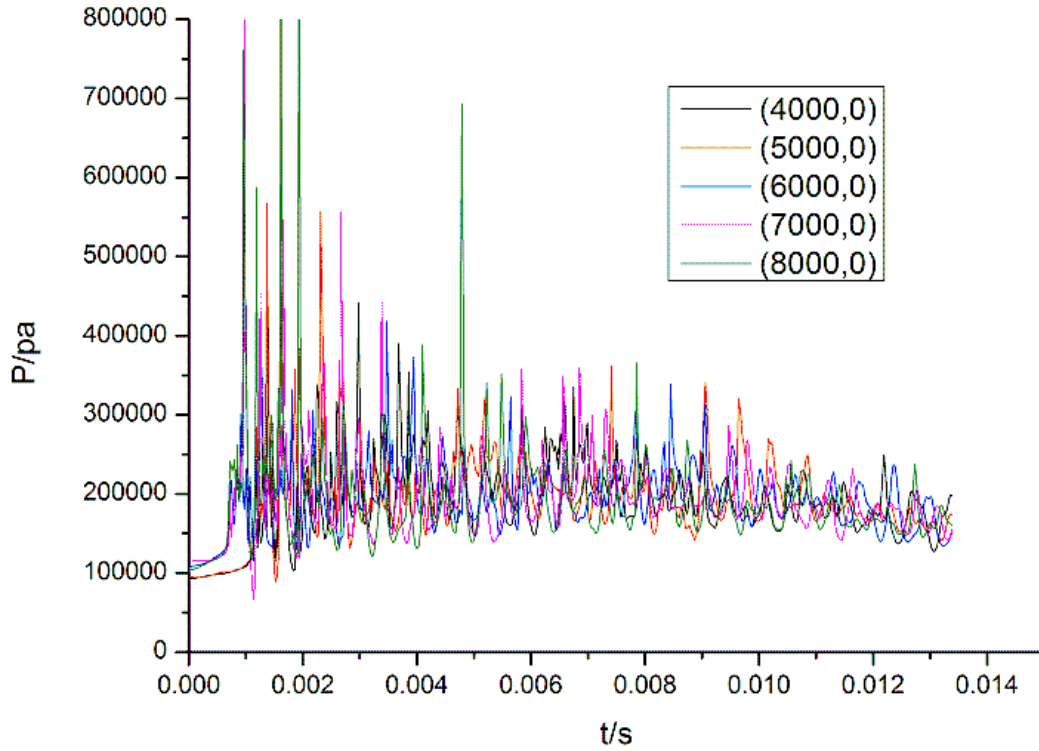


Figure 37 – Pressure plot for the points 11, 12, 13, 14, and 15 - Detonation point at 0.5m – OpenFOAM.

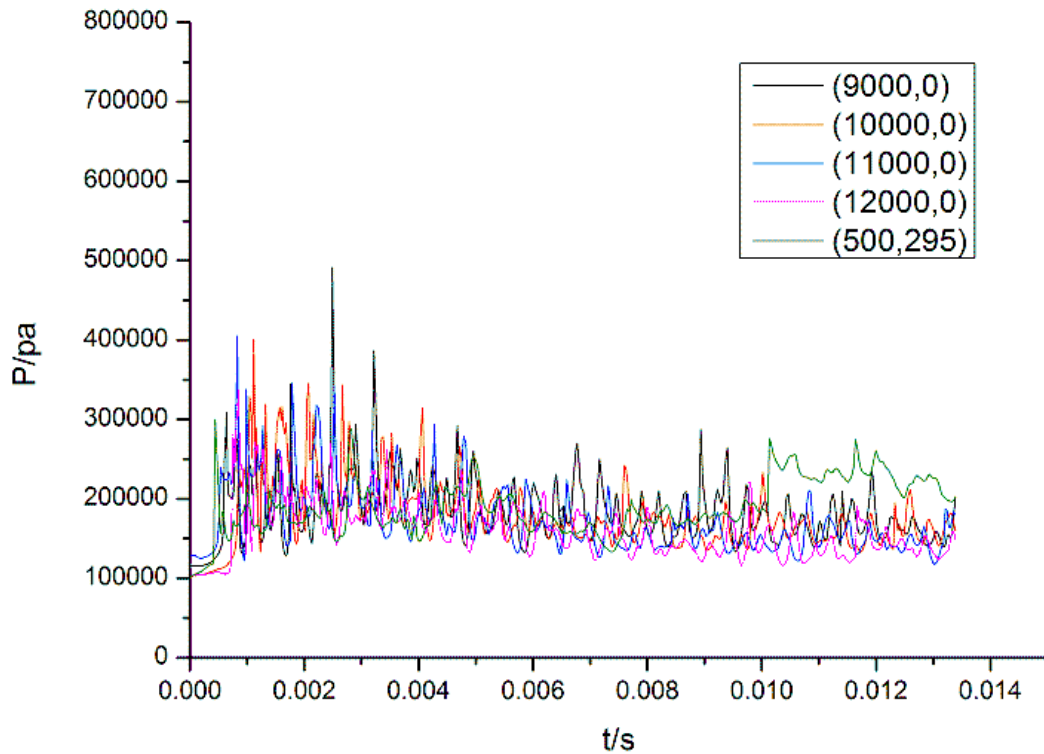


Figure 38 – Pressure plot for the points 16, 17, 18, 19, and 20 - Detonation point at 0.5m – OpenFOAM.

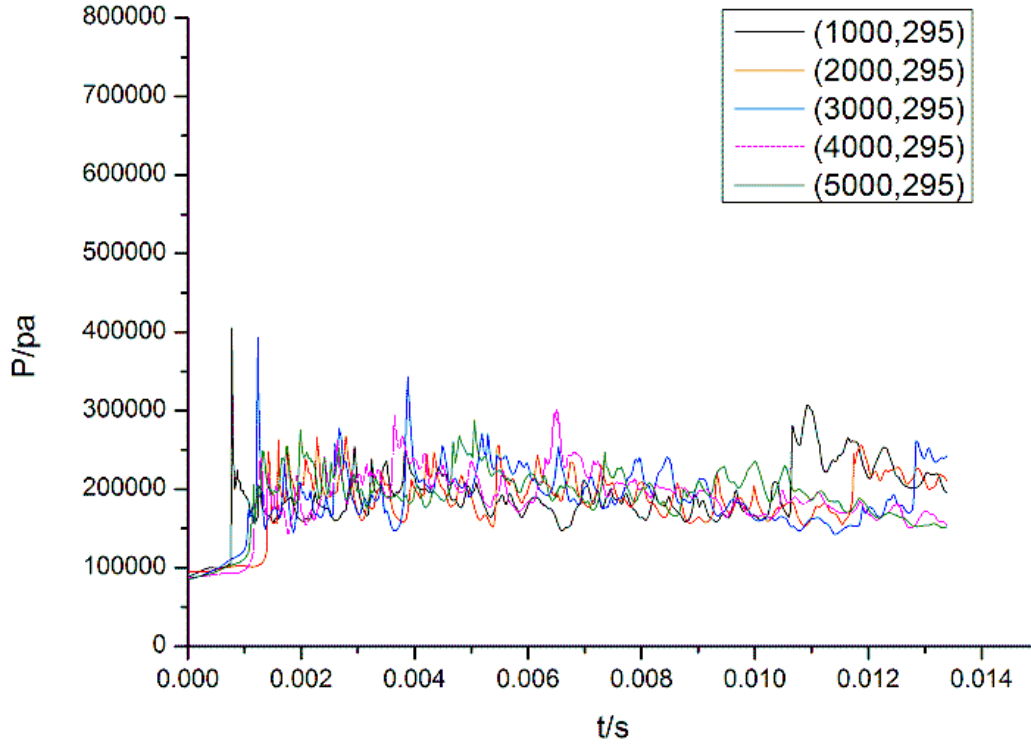


Figure 39 – Pressure plot for the points 21, 22, 23, 24, and 25 - Detonation point at 0.5m – OpenFOAM.

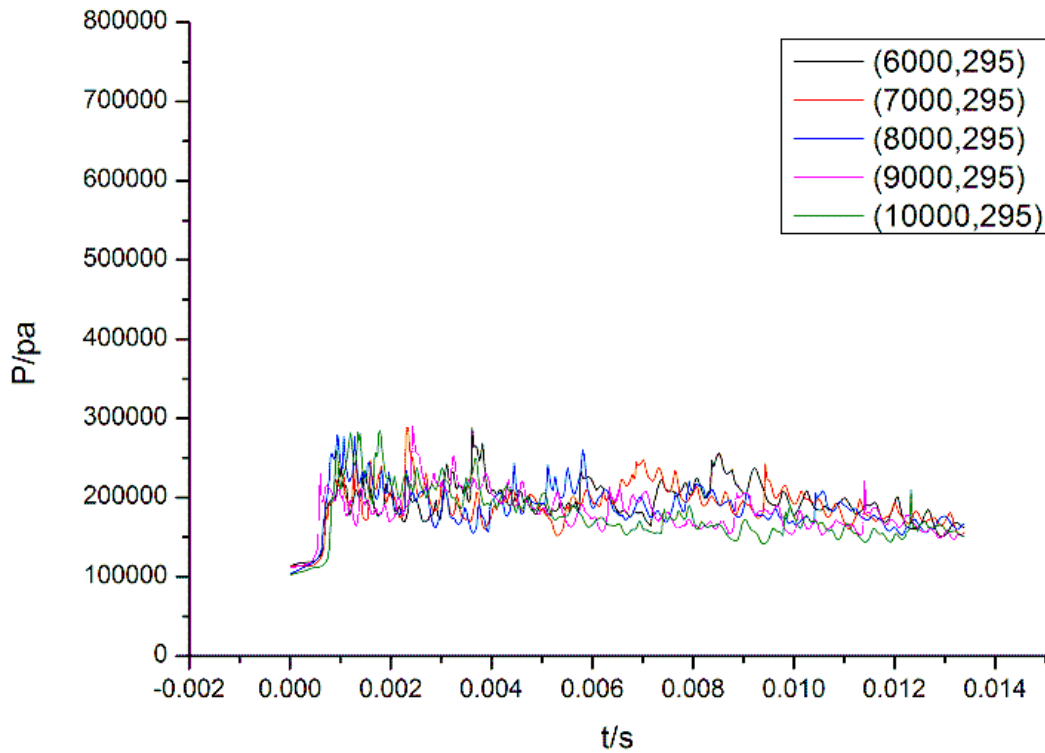


Figure 40 – Pressure plot for the points 26, 27, 28, 29, and 30 - Detonation point at 0.5m – OpenFOAM.

2.4.4 No ignition source

As discussed earlier, it is possible that the initial temperature of 500°C could lead to auto-ignition in the downstream section. Numerical simulations have therefore been carried out firstly for zero-dimension constant pressure to investigate auto-ignition and secondly for the same tube configuration but without the ignition source to further clarify this.

2.4.4.1 Constant combustion

Figure 41 presents the predicted temperature profile from the zero-dimension constant-pressure adiabatic combustion simulation. It shows that auto-ignition could occur in the current mixture at 500°C, resulting in a maximum temperature of more than 2500 K. That indicates that the critical self-ignition temperature for the current mixture is less than 500°C.

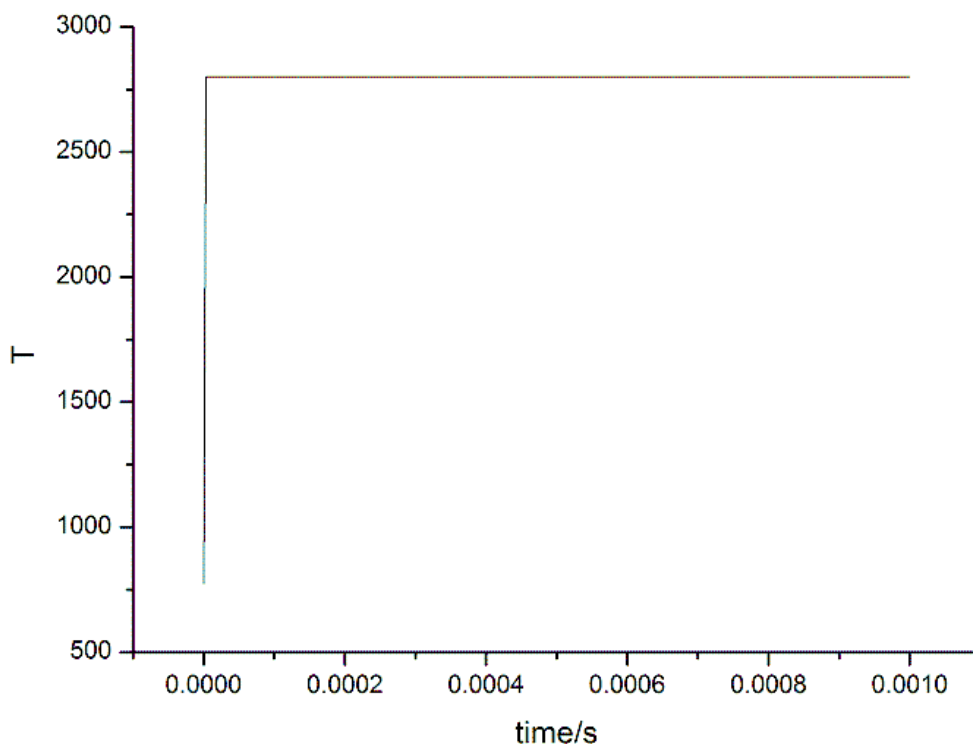


Figure 41 – The predicted temperature vs time for 0-dimensional constant-pressure adiabatic combustion simulation.

2.4.4.2 No initiation case

Since the current mixture is prone to auto-ignition, another simulation was carried out without imposing an ignition source.

Figure 42 presents the predicted contours of the predicted pressure, temperature and H₂O. It is seen that the mixture auto-ignited. The maximum pressure is less than 3bar and the maximum temperature is nearly 1800K.

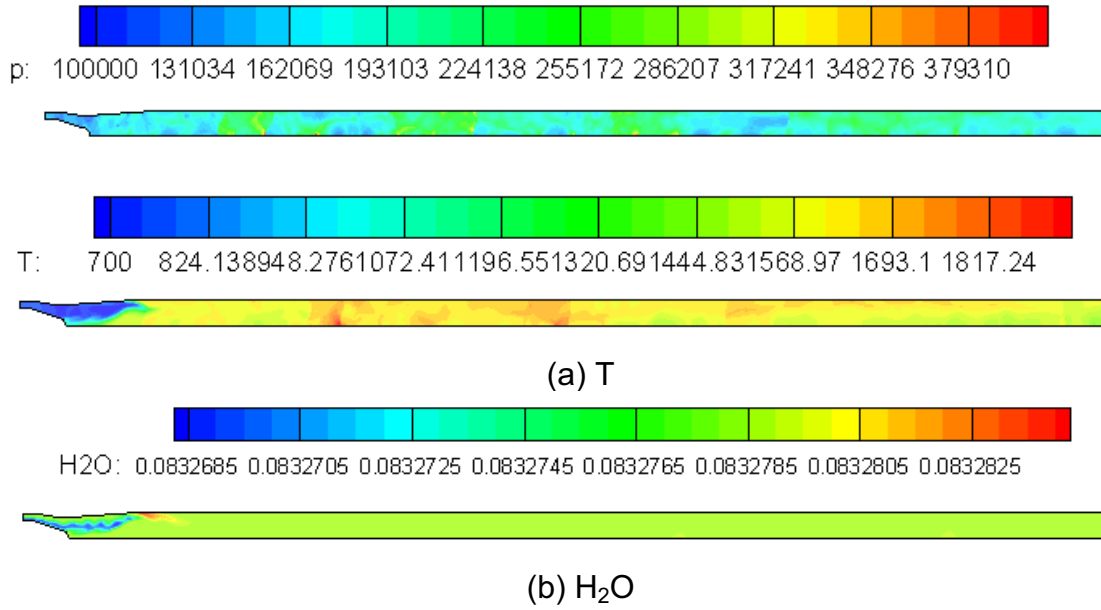


Figure 42 – The predicted pressure, temperature and H₂O concentration in the case without an ignition source.

3 CONCLUSIONS

The following conclusions can be drawn from the three modelling approaches used in this programme of work.

ALE modelling:

- In the worst case scenario, i.e. the detonation of a stoichiometric mixture of hydrogen air in the duct, the ALE approach predicted a maximum peak pressure for the two detonation scenarios of 104bar at the duct centre line. The high peak pressure is due to the shock wave reflection in the duct, and is of very short duration.
- The peak pressure predicted at the exhaust face reached a maximum value of 32bar in the case where the detonation point was located 6.0m from the origin and a peak value of 25bar for the detonation point located at 0.5m. The static pressure at exhaust face reached a maximum value of 3.6bar.
- The peak pressure near the wall reached 29bar and the static pressure reached 6bar for both scenarios near the detonation point.
- ALE – Established capability but limited to Equation of State assuming stoichiometric mixture.

CESE modelling:

- Similar peak and static pressure values to those observed with the ALE approach were predicted with the multi-physics version of the LS-DYNA finite element software for the majority of pressure points.
- The peak pressure at the exhaust face reached a value of 17bar for the detonation point located at 0.5m and 35bar for the detonation point located at 6.0m. The static pressures predicted for the both scenarios are approximately 6bar and 3bar respectively.
- CESE – Improved functionality over the ALE approach through the use of CESE chemistry, but code is comparatively immature and coupling of chemistry and flow field still required. Is also currently mesh sensitive and requires Cartesian mesh making it very hard to use for complex geometries.

OpenFOAM:

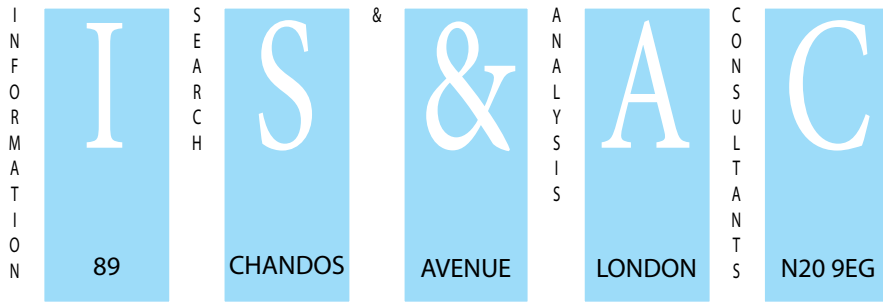
- The H₂-O₂-N₂-CO₂ mixture (Mole fraction: hydrogen 0.122, nitrogen 0.656, oxygen 0.183 and carbon dioxide 0.039) with the total mass flow 16.1kg/s, initial temperature 500° and at ambient pressure is able to detonate in the presence of a sufficiently strong ignition source.
- The predictions show that the peak pressure at the exhaust faces reaches 5bar for a short duration. The maximum peak pressure predicted in the duct was 8bar throughout the duct centre line, and up to 4bar near the wall. The static pressure in both locations reached 2.5bar. These values are lower than pressures predicted for the detonation of a stoichiometric mixture of hydrogen air, as expected.
- There is evidence of combustion and a pressure wave was observed in the downstream region prior to the arrival of the detonation wave.

- Without an ignition source the gas mixture is seen to auto-ignite. The maximum pressure is less than 3bar and the maximum temperature is nearly 1800K.
- OpenFOAM – Most mature approach for including full chemistry and DDT.

4 REFERENCES

- [i] - Kyoung-Su Im, S.-T. John Yu, Simulation of Direct Initiation of Detonation Using Realistic Finite-Rate Models, 38th AIAA /ASME/SAE/ASEE Joint Propulsion Conference & Exhibit, July 2002.
- [ii] - K. Moodie, to R. Rosario and J. Gummer, "ETI Test Rig -600 dia Tube Sections, e-mail on 17.05.2012.
- [iii] - LS-DYNA, Keyword User's Manual, Version 971, LSTC 2012.
- [iv] - LS-DYNA CESE Theory Manual, LSTC 2012.
- [v] - LS-DYNA Keyword User's Manual, Volume III, Multi-Physics Solvers, 09.12.2011.
- [vi] - Private communication, Reacting Flow: Examples, LSTC 2012.
- [vii] - Private communication, Chemistry Input File, LSTC 2012.

END OF DOCUMENT



TELEPHONE N° 44 (0)20 8446 2776
FACSIMILE N° 44 (0)20 8343 9471
MOBILE N° 0973 214 720
email gmunday@compuserve.com

DELIVERABLE ONE
ETH HIGH HYDROGEN PROJECT
RE IMPERIAL COLLEGE
MAY 31ST 2012
EUR ING DR GEORGE MUNDAY
BSc PhD DIC CEng

Contents

	SUMMARY	
1.	1-D Constant Velocity Calculations - Analytical	1
1.1	Introduction	1
1.2	Test Samples	1
1.2	Steady-State Detonation Overpressures	2
1.3	DDT overpressures	3
2.	1-D Constant Velocity Calculations - MOC	5
3.	NEXT PHASE - Deliverable Two	8
	REPORT	
1	Introduction	10
1.1	Background	10
1.2	PROPOSAL AND CONTRACT	10
1.3	SCOPE OF THE REPORT	12
2	CONSTANT VELOCITY MODEL	13
2.1	Introduction	13
2.2	Running the Programme	14
3	VARIABLE VELOCITY MODEL	20
3.1	Introduction	20
3.2	FORTRAN Language Version	20
3.3	C++ Language Version	21
3.4	Conclusions	25
1.	Completed tasks.	25
2.	Enhancements.	26

SUMMARY

The Report for Deliverable One commences with summaries of the achievements of the objectives set out in the proposal. The Summaries are followed by the full report which provides the necessary detail to back up the results and provide explanations for the methodologies.

There are three Summaries in Deliverable One.

- 1 1-D Constant Velocity Calculations - Analytical
- 2 1-D Constant Velocity Calculations - Method of Characteristics
- 3 Preliminary Summary for Deliverable Two

1. SUMMARY FOR 1-D CONSTANT VELOCITY CALCULATIONS - ANALYTICAL

1.1 INTRODUCTION

Deliverable One provides the results of the calculations for pressure loadings on the test-rig walls for the one dimensional case and for a matrix of fuels involving binary mixtures of hydrogen and carbon monoxide and hydrogen and methane. The oxidant is air with a 0.8 stoichiometry (also known as the 'equivalence ratio' which is the ratio of the mixture fuel-to-oxidant-ratio and the stoichiometric fuel-to-oxidant-ratio for the binary fuel components). The calculations are based on a detonation rig having a length of 9000mm and a rectangular cross-section of 36 by 72mm. Operating conditions are ambient pressure and temperature and zero gas movement. The results reported here have been based on an idealized rig configuration to match the calculation procedure in which the cross-section has been assumed to be circular with a diameter giving the same area as the 36 by 72mm rectangular rig. Furthermore, for reasons which are discussed in the final chapter of this report, the results do not include reflections from the end of the rig.

1.2 TEST SAMPLES

The matrix of mixture compositions considered in these calculations are set out in the table below. Each calculation is identified by a code $HnnnFFmmm$ where nn is the percentage hydrogen (H) in the binary FF is either CO or CH to identify the fuel component and mmm is the percentage of that component. The numbers

in the tables are the mol gas compositions.

Mole gas compositions for test matrix

SPECIFICATION		CALCULATION DATA				
H2/CO	H2	CO	O2	N2	CODE	
100#0	1	0	0.125	0.306	<i>H100CO000</i>	
80#20	1	0.25	0.156	0.383	<i>H080CO020</i>	
60#40	1	0.667	0.208	0.510	<i>H060CO040</i>	
40#60	1	1.5	0.313	0.765	<i>H040CO060</i>	
H2/CH4	H2	CH4	O2	N2		
80#20	1	0.25	0.125	0.306	<i>H080CH020</i>	
60#40	1	0.667	0.333	0.816	<i>H060CH040</i>	
50#50	1	1	0.5	1.224	<i>H050CH050</i>	

1.2 STEADY-STATE DETONATION OVERPRESSURES

The following values for over pressures for CJ steady-state condition and at the shock front of the Von Neumann spike have been calculated employing standard steady-state detonation wave procedures.

Detonation Calculation Results

CODE	Overpressure		Mach No	Shock Velocity	Mol Wt	Gamma	Sound Velocity
	VN	CJ					
H100CO000	22.94	12.496	4.448	2553.68	10.181	1.403	574.55
H080CO020	22.51	12.227	4.407	2175.13	13.822	1.403	493.03
H060CO040	22.75	12.421	4.43	1942.94	17.448	1.403	438.77
H040CO060	22.80	12.461	4.435	1769.20	21.082	1.402	399.12
H080CH020	12.78	6.992	3.334	1826.96	11.046	1.394	549.73
H060CH040	15.20	8.188	3.635	1629.85	16.400	1.388	450.11
H050CH050	16.05	8.607	3.736	1582.62	18.333	1.385	425.36
	Atmos			m/s			m/s

The overpressures associated with the von Neumann spike are of very short duration and hence they would be absorbed by the inertia of most solid bodies

before stresses have had a chance to grow to any significant levels in terms of the strength of the containment. In contrast, the CJ overpressures apply decaying pressure loads on the surrounding containment over much larger time periods which are not easily calculated since they depend upon cooling processes and the propagation of refraction waves which are very test specific. A rough estimate for the period required for a significant fall in such overpressure is the time taken for the rarefaction wave to propagate twice the length of the detonation test rig - in the above examples for the 9m test rig a duration of some 25msec. More detailed assessments would be required if a more reliable figure is required.

1.3 DEFLAGRATION TO DETONATION TRANSITION (DDT) OVERPRESSURES

A deflagration to detonation transition (DDT) phase produces a transient pressure pulse whose pressure can be calculated as a range of values which depend upon the precise nature of the transition process which to date cannot be predicted on a fundamental basis. However, the calculation method adopted in the present study does allow for the pressure levels in the selected range to be linked with an excess overpressure duration. The data pairs (excess overpressure level and duration) derived in these calculations are also dependent upon the location of the deflagration to transition but in a very simple way.

Experience suggests that this DDT pressure pulse often occurs at the same location in the test-rig for all the tests in a series. At the present time however the location cannot be established by calculation and could well depend upon the design and physical construction of the detonation channel so that it is necessary to perform a limited number of calculations for different locations or provide a metric which provides the necessary excess-overpressure/duration worst case loadings. It is possible to define quite clearly the calculation which provides the highest excess-overpressure. The magnitude and duration for this overpressure transient can be determined as well as a measure of the constant flame burning velocity leading to this extreme condition. The magnitude of the excess-pressure is measured by the CJ steady-state pressure of a detonation propagating through the gas compressed by the high velocity flame and has the same value irrespective of where the source of detonation promotion is located in the detonation channel. The duration of the excess-pressure is given as n milliseconds for a 1metre DDT promotion location from the ignition source. Its value for other locations is directly proportional to this length.

The data on durations provides data for a specific distance along the detonation channel. However, the transient behaves as a moving wave of disturbance and therefore affects a limited length of the channel at the chosen distance. The calculation procedure can also be employed to determine the length of the detonation channel to which this impulse is subjected. The length of this channel element, like the excess-pressure duration is a linear function of the DDT promotion location selected and in the table this has a value of 1 metre.

The columns in the table give the calculated values for the following properties of DDT behaviour for the four mixtures under consideration.

The first two columns after the mixture code contain two pressure levels for DDT excess-pressures the first for the calculation using the highest 'flame velocity'. In the next column, to provide a measure of the range of pressures which are possible with calculations at other 'flame velocities', the DDT excess-pressure for a 'flame velocity' of half the maximum value is added.

The next two columns provide the values for the maximum 'flame velocity' and the shock front velocity (calculated with half maximum 'flame velocity', both in m/s. The last column gives figures in milliseconds for the duration of the DDT excess-pressure transient for calculations employing a 'flame velocity' of half the maximum value.

Deflagration to Detonation Transition Calculation Results

CODE	Excess-pressure		Sf	Ss	$\Delta t(1)$
	max	half-Sf			
H100CO000	31.89	28.44	351.7	945	0.138
H060CO040	31.34	27.98	357.2	945.2	0.137
H040CO060	28.93	26.43	255.5	649	0.200
H060CH040	17.847	16.20	300.7	663	0.233
			Atmos	m/s	milliseconds

The full results are not given in this Table but are available as Microsoft Excel files for each composition and will be provided when requested.

2. SUMMARY FOR 1-D CONSTANT VELOCITY CALCULATIONS - MOC (METHOD OF CHARACTERISTICS)

The 1-D constant velocity calculation employing the method of characteristics is a relatively simple exercise in computing. The computer programme used by a research student JC Gibbs who was supervised by the author of this report in the early 1970s has been used for the basis of the calculations in this study involving a simple rewriting of the code in C++. The results agree with those obtained from the analytically based calculations.

All the cases evaluated in the previous part of the work do not need to be calculated again. This part of Deliverable One therefore does not present any new data but confirms that the calculation by the method of characteristics produces results which are consistent with those obtained by the programme which uses the equations presented in the paper by Khul, Kemal and Oppenheim.

The present report, however, does include, in a later Chapter, a description of the C++ programme which has been designed and coded to perform the method of characteristics numerical operations using the basic steps described in some detail by a mathematician who developed and exploited this method (MOC) for simulating explosive effects in the gas phase. This chapter also describes in some detail the approach which has been adopted in the design of the structure and appearance of the programme so that the computing manipulations are easily understood and the physical and mathematical principles involved have maximum clarity.

The C++ code is ready for use. It has been compiled with Borland C++Builder 4 which is an old but well established Rapid Application Development (RAD) product for Windows platforms. As will become apparent in Deliverable Two further development of the programme which relate to the accommodation of 2-D effects will necessitate discussions with the users of the programme to determine both the choice of platforms and the development tools needed for its extensions as planned in this project. Only a description of the programme and a examples of its application are supplied in the later sections this report.

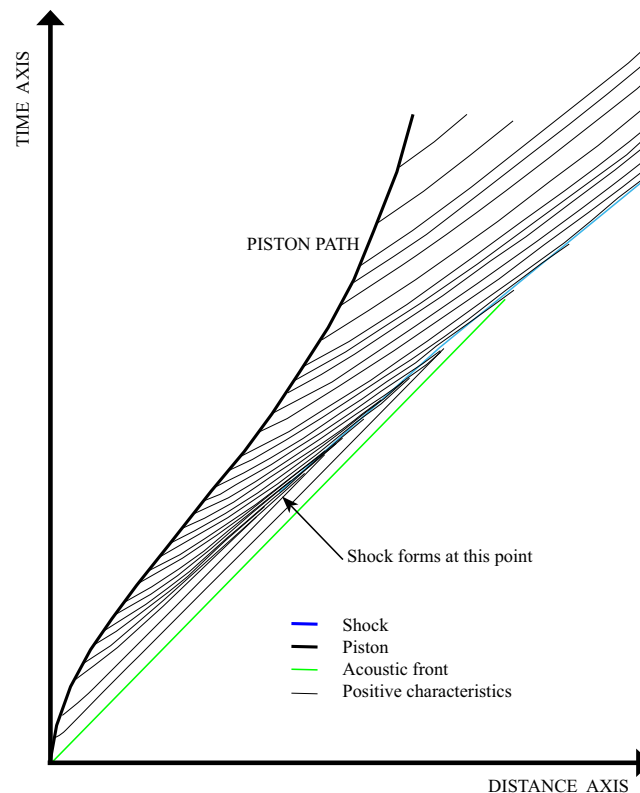
Some examples of output from the Gibbs based programme are reproduced on the next page. The presentation demonstrates the similarity between the method of characteristics results and those from the analytical approach. It also highlights two

differences. The first is the movement of the piston path no longer produces an instant shock front. The growth of this front is a function of the trajectory. The question arises as to which figures should be used to describe the trajectory. Experimental results are required to determine the answer.

The second problem is the presence of the shock front behind the leading disturbance. This complication adds to the complexity of any solution produced. There is the possibility that a solution for both these differences is available if one of the restrictions on the model involves a limitation to those cases in which the choice of piston trajectory always leads to the shock front starting on the leading acoustic disturbance.

It is noted here in this report that the results from the C++ programme are more relevant to the 2-D configurations and a more detailed description of it will be found in Deliverable Two. Additional information, however, is to be found in the report section of Deliverable One.

The diagram depicts a plot of some of the output from the programme PISTON which is a one-dimensional analysis by the method of characteristics.



The X-axis in the diagram above represents the locations along the detonation rig of the features of the piston-shock interaction as they traverse the rig at various time located on the vertical, time, axis. The trajectories of shock and piston are clearly marked. All the other trajectories represent the positive characteristic curves which form one half of the network which propagates the calculation procedure. The other half of the network construction, not shown consists of the negative characteristics which have been omitted in the interests of diagram clarity. A more detailed exposition of the method of characteristics is given in the body of the report.

The programme which has been adapted for inclusion in Deliverable One has a number of disadvantages from the point of view of the final objectives of the contract which will be achieved with Deliverable Two. At the time of writing, an alternative computer programme is being developed which uses a different computer language, C++ instead of Fortran, and a programme structure which contains features which allow for the adaption of the basic one-dimensional limitation of these calculations to the two-dimensional problem. The new programme also includes the identification of the 'flame' trajectory and properties. This last named feature has not been included in the Fortran version of the programme since the author of this report does not have the familiarity with Fortran programming to warrant such additional effort.

3. PRELIMINARY SUMMARY FOR NEXT PHASE OF PROJECT - DELIVERABLE TWO

The theme behind the whole approach to the development of a tool to provide numerical results relevant to safe design and operation of exhaust systems which might be subject to deflagration to detonation transitions is the usefulness of the simple concept of self-similarity specifically in applications to all compressible flow phenomena associated with explosive events from military explosives through gas explosions and bursting vessels to detonations. Many research workers involved in numerous studies, both experimental and theoretical support this view. Just one of many comments from a review of deflagration to detonation transition research is quoted below.

“ *In detonative flows the acoustic Reynolds number is so large that it would be unreasonable to try to model the flow using the Navier-Stokes equations. The Euler equations provide an effective model for these kinds of flows. However, the Euler equations are hyperbolic in nature and require the addition of special hyperbolic shock capturing techniques.*”

Numerical Modeling of Acoustic Timescale Detonation Initiation Using the Adaptive Wavelet-Collocation Method (Jonathan D. Regele University of California, 2001)

A classical way of dealing with solutions to partial differential equations is to adjust the form of the equations so that exact differentials replace the partial differentials by the introduction of a suitable but acceptable modification such as the restrictions pertaining to self-similarity. Self-similarity achieves the transformation by accepting the limitation that the solution will always have the same form as it progresses. As a result the solution is restricted to constant rates of change. Thus the rate of change of distances with time (velocities) will always be constant. In the present study this limitation has an advantage since constant velocities can be described with just a single number. Characterising a solution for a system in which velocities are not restricted in this way would involve additional parameters such as acceleration if that were to be constant and further numbers if not. As can be seen from the summary for Deliverable One even the limitation of constant velocity has not allowed for a completely comprehensive presentation of the potential range of results

Thus, it has been quite difficult to envisage how the development of the two-dimensional tool can be satisfactorily presented in Deliverable Two. At the time of drafting of the present report the difficulty can be described as follows, The constant velocity one-dimensional version of the calculation tool based on the

method of characteristics has been completed. The design of the programme and its implementation in code is described in the present report. As reported here results obtained using this version of the tool duplicate those obtained employing the analytical version for the constant velocity case.

The design of the method of characteristics version of the tool allows for calculations in which the velocity is not constant by giving the user the facility for providing Coefficients of a power series which describes the charging velocity. The programme has been tested with arbitrary coefficients. However, no useful results relating to the DDT safety issues relevant to the present studies have been reported in Deliverable One since meaningful velocity profiles are not presently available.

A similar approach for the presentation of the two-dimensional tool in Deliverable Two would be unsatisfactory since this would be the final report in the contract. At the present time, Deliverable Two will deal with this problem by giving a detailed explanation of the work reported in Deliverable One as it is assembled in the two-dimensional version of the calculation tool to determine the safety performance of the scale model exhaust system under investigation.

It is intended that Deliverable Two will contain a description of the design and implementation of an application which employs the developments undertaken and reported upon in the tasks defined by Deliverable One to implement a calculation tool applicable to two-dimensional configurations. This presentation will provide an explanation for the choice of this approach rather than one involving the full method of characteristics for time dependant two-dimensional flows. Programme code which compiles the one-dimensional tool into a scheme enabling two-dimensioned configurations relevant to the turbine exhaust system under consideration in the safety studies will be set out in detail although actual results will not be included.

REPORT

1 INTRODUCTION

1.1 BACKGROUND

A test programme involving the ignition of flammable mixtures of air and hydrogen enriched fuels requires the evaluation of the pressures which might develop in the test rigs. The tests are required to investigate safety issues relating to the potential for explosions involving detonation waves. Hence, the designs of the test rigs will be based on calculations of the pressure loads on the walls of the test equipment developed in the explosion processes which include deflagration-to-detonation-transition as well as steady-state detonation.

Values for these pressure transients have to be obtained by procedures which are clearly defined with regard to their origin and methodology so that their use in the design has the confidence of the users.

1.2 PROPOSAL AND CONTRACT

Calculation of pressure transients for steady-state detonations involve quite standard procedures well established over many years. The choice of procedure is a matter of personal preference although procedures are quite complex and involve computer programmes of some complexity. The results from such procedures are generally accepted as being reliable.

In contrast, the phenomenon of deflagration to detonation transition is almost devoid of consistent interpretation of its behaviour and no accepted procedure for its prediction has been generally accepted. In fact, the behaviour of this phenomenon varies to such an extent from one fuel to another that no single theory fitting all situations has been devised so far.

Explosions start at a centre and expand outwards. Flames in premixed fuel-air clouds behave in a similar fashion as do detonation waves. This similarity in behaviour provides a useful starting point for the development of the calculation procedure. The premise is that an accelerating flame, expanding outwards from the ignition centre, sets up gas movement ahead of it causing the gas to move outward accompanied by compression and adiabatic heating. These processes can be represented by mathematical

equations which may be solved analytically or by numerical methods employing approximations. The simplest solutions using either method are those which deal with one-dimensional flow (flows which “start at a centre and expand outwards”) and rapidly increase in complexity for the two-dimensional and three-dimensional flows. Simplicity can also be bought at the cost of flexibility of the solution. One constraint, which is not only acceptable for the present objective of examining ‘worst case’ conditions but also has the advantage of restricting the number of variables required to define initial conditions, is that of constant velocity.

The proposal for this work was therefore formulated as follows:

- i Combustion pressures for one-dimensional constant velocity simulation
- ii Detonation pressures for one-dimensional constant velocity simulation with superimposed constant velocity stable detonation scenarios
- iii Combustion pressures for one-dimensional increasing velocity numerical simulation by method of characteristics
- iv Detonation pressures for one-dimensional increasing velocity simulation with superimposed constant velocity stable detonation scenarios by method of characteristics
- v Combustion pressures for two-dimensional increasing velocity numerical simulation by method of characteristics
- vi Detonation pressures two-dimensional increasing velocity simulation with superimposed constant velocity stable detonation scenarios by method of characteristics

Items (i) to (iv) are included in Deliverable One and items (v) and (vi) in Deliverable Two

The behaviour of the DDT transient is to be modelled on the supposition that two constant velocity detonation waves are propagated in either direction in the flow-field, one with the flow and one against. The latter detonation will end when it reaches the flame front and the fuel is no longer present and in the former case the transient constant velocity detonation wave will, upon reaching the shock front, instantaneously degrade to a constant velocity detonation in the undisturbed fuel-air mixture ahead of the shock front. Account will be taken of the moving gases behind the shock front and the direction of travel of the detonation wave.

A complication arises because of the unknown location of the detonation initiation between the flame and the leading flame-driven shock front. It could be at the flame or at the shock or somewhere in between. It is suspected that for the higher velocity flames this effect is quite small but for the lower velocity flames the largest duration from the DDT transient will be associated with the case in which the secondary detonation starts at the flame front.

1.3 SCOPE OF THE REPORT

Following the introduction above two separate Chapters will deal with pairs of items in turn. Chapter 2 will report on items (i) and (ii) for the constant velocity case and Chapter 3 will deal with items (iii) and (iv). Each Chapter will have an introduction.

This will be followed by a description of the calculation method employed to model the DDT phenomenon. A comprehensive description will not be provided as decisions still need to be taken as to what end product is required. However, sufficient information will be provided to give the reader an understanding of the way in which the results are achieved and the constraints on, and difficulties with interpretation of results from, the calculation procedure. The scientific sources for the methods on which the calculation procedures are based are to be found in appendices to this document since direct reference to their contents is involved in all the programmes under development in this project.

A final section will examine how this work impacts on the development of the project and what joint decisions need to be discussed to produce the desired product.

2 ONE-DIMENSIONAL, CONSTANT VELOCITY MODEL

2.1 INTRODUCTION

Development of analytical and numerical techniques for obtaining answers to the behaviour of a variety of explosive processes arising from wartime experiences and a number of industrial incidents took place over the 1950s and 1960s. The Detonation Laboratories in the Department of Chemical Engineering & Chemical Technology were active in this field at that time and the author of the present report developed a number of models which also formed the basis of lectures on combustion given to postgraduate research students. This background has been influential in the choice of approach reported here as part of Deliverable One.

To maintain a neutral stance on the choice of method, an almost identical approach was described in a paper by the authors A.L.Kuhl, M.M.Kamel and A.K.Oppenheim entitled "Pressure Waves Generated by Steady Flames". The paper describes an analytical method for the solution of the appropriate equations obtaining simplifications by assuming self-similarity for the time-space variable and which then imposes constant velocity on the movements within solution domain. The boundaries to this domain are an artificial expanding piston moving at constant velocity and a shock front which precedes it a higher velocity governed by the processes in between. The self-similarity assumption rules that the distribution of flow properties either at a fixed time or at a fixed distance are identical in shape but not in scale. The solution of these equations can be obtained for plane symmetry when the piston is planar and there is a single direction of motion, cylindrical symmetry when the piston expands as a cylinder and the flow field expands as a series of cylinders extending indefinitely in their length or spherical symmetry when the piston expands in all directions at the same speed and the flow is outwards in an identical way in all directions.

The paper sets out the differential equations which take the form of a set of exact differential equations. These equations are solved by assuming a value for the shock strength and integrating all the equations simultaneously back towards the piston where the solution is complete. The authors have employed a variable transformation to ease the solution of these particular equations in which logarithmic expressions of the variables are employed. The improved performance of the solution routines justifies this change but it leads to considerable confusion as to the significance of the solutions obtained. The confusion arises from the need to transform back to the actual form of the variable when it is required in other aspects of the solution.

A copy of this paper is reproduced in an appendix. It is noted here that this copy contains corrections made by the author of this report. The need for these corrections has been identified as a result of the requirement that the values calculated by the procedure used in Deliverable One should match those presented in the graphs in the paper.

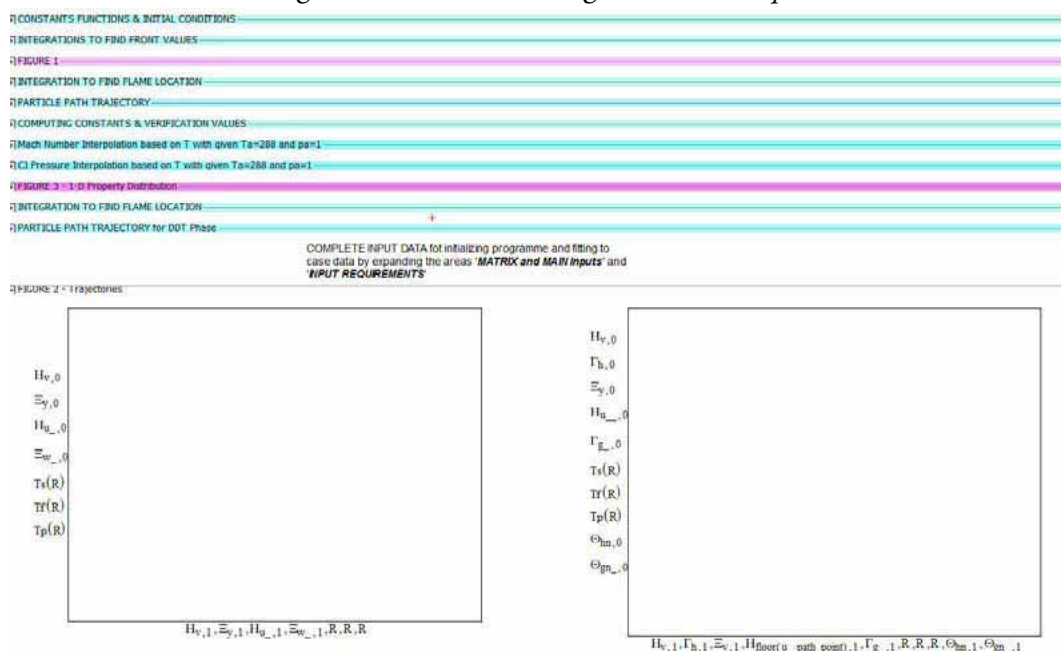
The solution is implemented on a commercial mathematical application known as MathCAD. The file to which this solution has been saved is available but a user would require access to the application on a computer. A print out of the programme is also available but is not included as its interpretation requires a thorough knowledge of the MathCAD application and is not easy to interpret without this knowledge.

2.2 RUNNING THE PROGRAMME

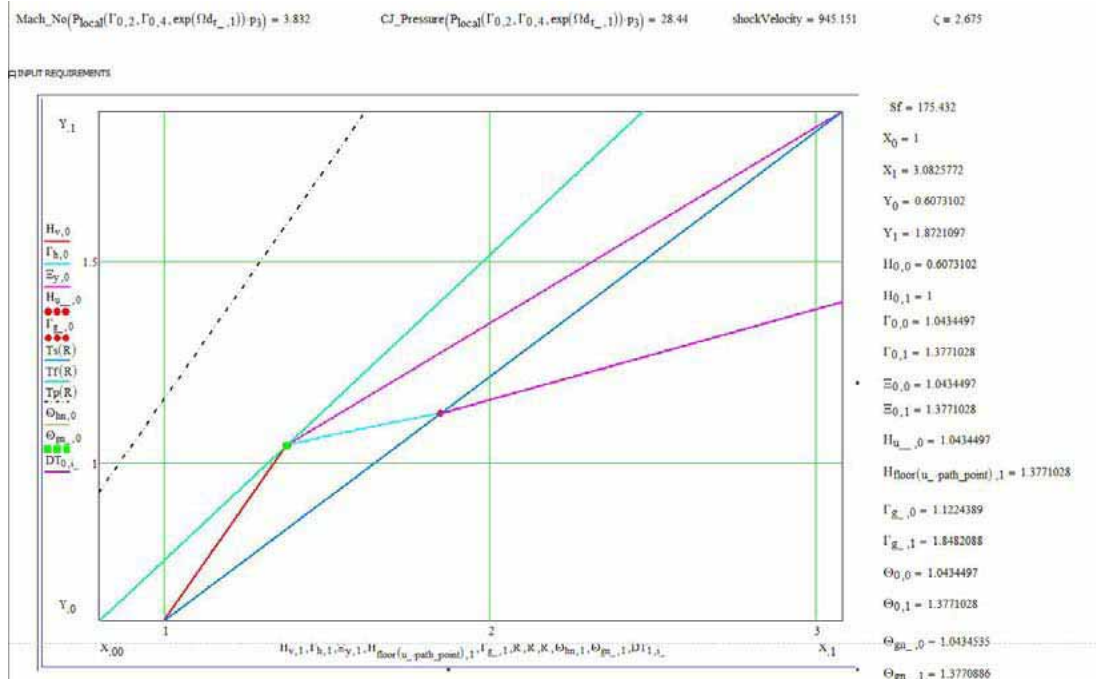
2.2.1 WHAT YOU SEE.

Once the programme is loaded using MathCAD the monitor will present the application as shown in the illustration below.

The horizontal bars are each associated with a part of the calculation located in the named area and identified by the title on the bar. The mauve bars contain graphics and the blue ones sections of code. The bars are opened by right clicking on the bar and left clicking on *Expand*. They are closed by right clicking on one of the two bands bordering the area and clicking on the *Collapse*



If the programme code is scrolled down so that the large graphic appears the screen will depict what is shown in the figure below.



The figures down the right hand side of the graph are all outputs from the programme. Likewise the figures along the top and bottom of the diagram are the values of various variables. Some of the figures can be identified as CJ Detonation Pressure of 21.44 atmospheres, shock velocity of 945 m/s and flame speed of 175.432 m/s.

2.2.2 WHAT YOU DO.

Data relating to the properties of the fuel-air mixture is entered into the code for the programme specific to that fuel-air mixture. A single variable locates the position of the detonation ignition between the flame and the shock wave The best choice for this location is at the flame front Sub-section 2.2.3 sets out the details for these data entries.

At the present time a very large amount of information is available on screen and more can be added with ease. Most of the most useful information is to be found on the screen as the name of a variable followed by its value. There are also a number of graphical outputs which depict, on a distance/time diagram various aspects of the DDT process by way of trajectories. Sub-section 2.2.5 defines some of the numerical outputs which are available and describes the graphic items.

The piston velocity input variable is the last item to be entered and by using a series of values to repeat the calculation variations in the results can be examined in terms of some chosen key variable such as the 'flame speed'. There are also a couple of control variables which have default values. It may be necessary to alter these to obtain convergence for the many integration and path tracing routines in the programme Sub-section 2.2.4 provides some preliminary advice regarding the way to chose the best values for these last named three variables.

2.2.3 DATA ENTRY FOR FUEL-AIR MIXTURE PROPERTIES

There are two matrices and a set of initial conditions to be determined before the programme can be run for a particular fuel/oxidant mixture. The matrices are of the same dimensions and contain the precalculated information for the thermodynamic and detonation properties of the mixture.

The two matrices contain the CJ pressures and detonation Mach Numbers over a range of initial pressures and temperatures. The two matrices are of a similar form and an example of the one containing values of Mach Numbers, as it appears in the programme is shown in the illustrations below.

4.448	4.45	4.452	4.455	4.456	4.457	288
4.361	4.363	4.366	4.368	4.369	4.37	300
4.05	4.051	4.055	4.058	4.059	4.06	350
3.798	3.8	3.804	3.807	3.809	3.81	400
3.589	3.591	3.596	3.599	3.601	3.603	450
3.411	3.414	3.419	3.423	3.425	3.427	500
1	1.25	2	3	4	5	1

The last column contains the temperatures in K and the last row the pressures in atmospheres. The entry in the extreme right and bottom location is a dummy 1. The two matrices are the same with values for CJ pressure and detonation velocity in the body entries. The illustration above contains the detonation Mach Numbers. The units for CJ pressure are atmospheres. Different units can be used as long as they are consistent throughout the data input.

The initial conditions for the calculation and the velocity of sound for the mixture are also required as are the ratio of specific heats for the burnt and unburnt gases in the model. These figures need to be calculated by an appropriate gas equilibrium routine for the combustion reactions appropriate to the fuel-air mixture.

Two additional properties relating to the flame are required and involve the same gas equilibrium calculation. The first is the volume ratio occurring in the equilibrium reaction and the second is represented by the ratio of molecular weight of the burnt gases to the unburnt gases in the same calculation.

The location of these data entries are as follows;

- i. The matrices and the initial condition entries are accessed in the programme by expanding the blue bar titled "*MATRICES AND MAIN INPUTS*" just below the two smaller graph areas. The existing numbers in the entries are replaced with the new values. The identities of the specific variables should be quite clear.
- ii. The remaining variables for the gas properties are to be found in the "*INPUT REQUIREMENTS*" area which is the last blue bar in the programme. The first two specific heat ratio entries, shown as γ and γ_{30} , both represent specific heat ratio for the unburnt gas and the third value designated γ_{40} is that of the burnt gas. M_{ratio} and V_{ratio} are the molecular weight and volume ratios respectively.

2.2.4 ADDITIONAL ENTRY VARIABLES

The remaining entries are in the same area and fall into two categories - three items requiring user input and the remaining default items which assist with the smooth running of the programme.

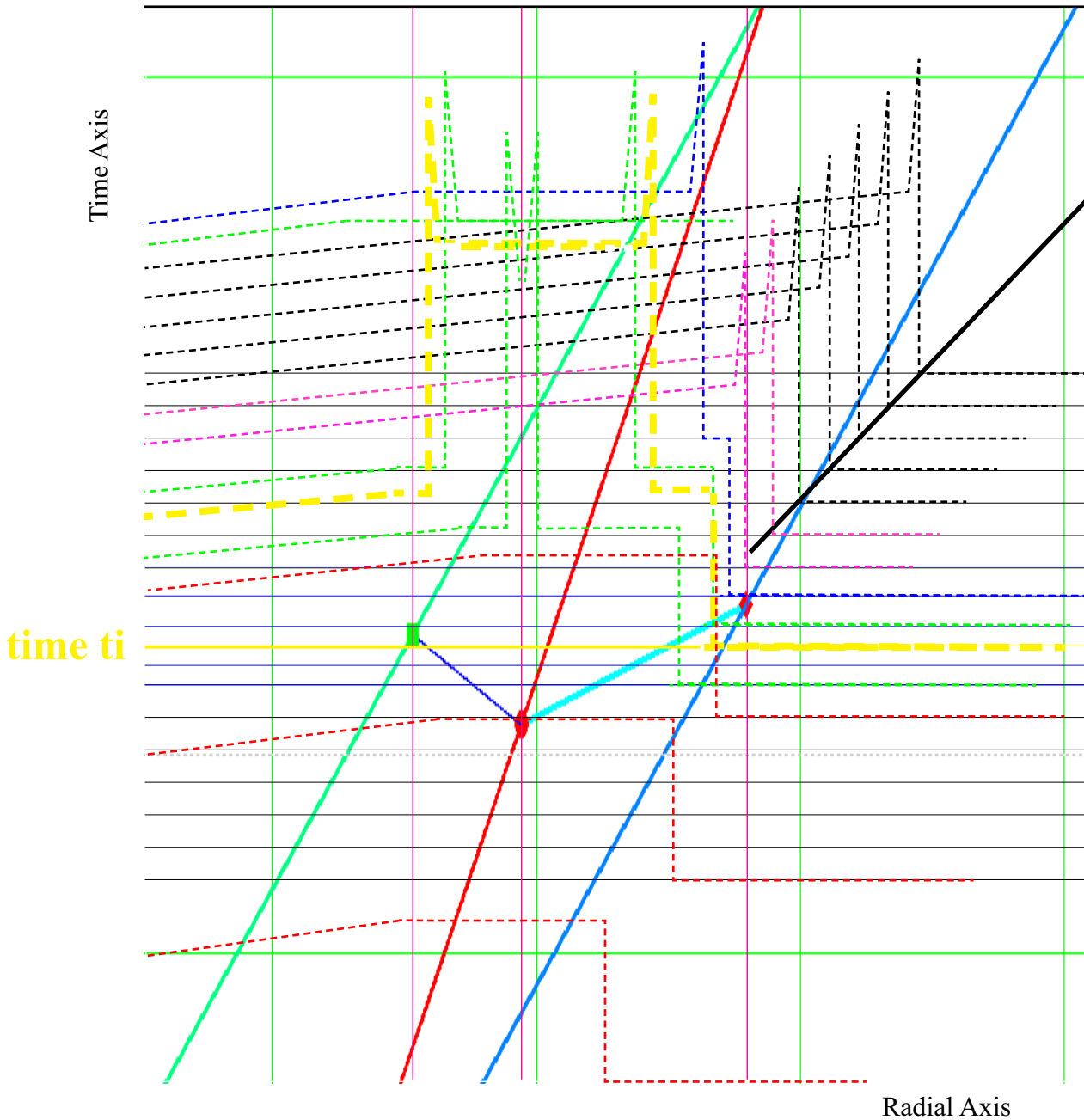
The first two user variables are the piston speed parameter ζ and the ignition location parameter "path_point" and they have already been described. The additional user variable "ignitionLength" is used to identify the location in the detonation channel where DDT is promoted. The value is normally left at 1.

The remaining variables ($\tau_{2_}$, $\tau_{2___}$, s and δ) should be left unchanged.

2.2.5 GRAPHICAL OUTPUT

The two smaller graphs show the trajectories for two successive stages in the calculation and are included to assist an expert in the programme to adjust the default variable values to obtain the correct answer.

The large graph which is the last item in the program shows how the figures are obtained for the two properties of DDT excess-pressure magnitude and duration.



The trajectories on the distance/time diagram are shown as thick unbroken lines colour coded as follows. Green for the flame, blue for the shock front and red for the path a particle would follow between entry at the shock front to combustion at the flame. The cyan and dark blue trajectories in the centre of the diagram are associated with the DDT detonation wave and retonation wave and the black trajectory is that of the steady state detonation wave propagating into undisturbed and unburnt gases.

One of the dotted line transients at time t_s has been emphasized to provide an illustration of the way the shape of the DDT excess-pressure transient has been defined by the various trajectories. Moving towards the centre of the expansion process from undisturbed fuel-air mixture ahead of the shock front the first disturbance encountered is the jump in pressure at the shock front. This is followed by a short period of constant pressure until we meet the detonation wave travelling forward through the compressed gas between flame and shock when the pressures and temperatures rise to the peak von Neumann spike values before falling rapidly to the CJ values. The conditions probably remain relatively constant until we catch up with the detonation wave moving in the other direction where the changes are reversed, pressures and temperatures rising the von Neumann spike values and then falling sharply to values a little below the shock front levels. Thereafter pressures and temperatures decline as cooling of the burnt gases takes place.

3 ONE-DIMENSIONAL, VARIABLE VELOCITY MODEL

3.1 INTRODUCTION

In the results section the one-dimensional variable velocity model obtained by the employment of the numerical method known as Method of Characteristics (MOC) was presented with a brief reference to its testing. This model was abandoned at a very early stage because of some limitations of the way in which the formation of the shock front was identified and its subsequent development with time was tracked. There were also some very difficult issues with the language employed, for two reasons. Firstly, the code from which the programme was re-written would need very extensive modifications for implementation with a modern FORTRAN language Compiler and the employment of earlier compiler versions had already proved difficult. Secondly, the skills base for writing code in FORTRAN would need to reach much higher levels if the programme was to be redesigned.

Nevertheless, the time spent in reviving this old programme provided an understanding of the basics of good programme design for MOC programmes. For this reason the programme code has been recorded in section 3.2 but without any new material describing the source equations, construction and logic. These topics are of more importance to the MOC application which has now been coded in the new language.

Section 3.2 therefore refers the reader to the appendices which contain a selection of extracts from the thesis which describes the programme as well as the computer programme code for the original.

There are additional reasons why a different approach to the production of a MOC application was recommenced with a new language, C++, and a new approach. Some of these reasons are set out in the later part of section 3.3 after a brief introduction of the main issues.

3.2 FORTRAN LANGUAGE VERSION

The code, definitions of the variables and its structure are reproduced from the thesis in various appendices. The Fortran language version is F90 and various free compilers were tried with most success coming from G95. The relevant pages of explanation from the thesis are also reproduced in an appendix. A very clear description of the approach employed to trace the shock front is provided.

3.3 C++ LANGUAGE VERSION

3.3.1 INTRODUCTION

The C++ computer language gives the designer a much greater scope for a structured development of a calculation procedure. Several pages have been taken with the Fortran Version and the effort involved in converting the 1970's code was quite considerable. Their inclusion in this report is intended to show that there will be added value to the resulting calculation tool as a result. It should be noted that, on its own, the development of the one-dimensional variable velocity model is of little value compared to the analytical model for the constant velocity case. The real value for a successful completion of this task is the role this model will play in attempting to tackle more realistic circumstances not restricted by the single space dimension. Hence a comparatively short Chapter 3 will describe the main objectives underpinning the design of the programme together with some results which show that the programme produces reliable results for all three cases of symmetry, namely planar symmetry, cylindrical symmetry and spherical symmetry.

This Chapter therefore devotes the first few sections to these objectives. This is followed by a brief description of how these objectives have been implemented in the design of the programme code. Then, after a brief description of how the application is used and how the raw output is converted to meaningful results, three examples of calculations will be reported, one for each case of symmetry.

In a final section three outstanding problems requiring client/user input for their resolution will be presented.

3.3.2 CLARITY IN THE CODING.

The computer code should show quite clearly in form and in content that they match the equations provided by mathematicians which represent the physics of the processes under study. The reader of the code should also be given an indication that consistency of dimensions (and units when they are involved) exists throughout.

The way in which the solution is achieved should also be quite carefully organised so that the reader can have an understanding how the calculation propagates through the structure and how the programme controls work. Many of the programming features of C++ can be used to give the code this form of clarity.

It is not always sufficient to employ programme language comments to identify and explain how the programme works. Many code writers will produce a short note to help them define an approach to they need to perform quite simple repetitive or multi-branching computing tasks. Such notes can be imbedded in the code using the multi-layer approach to document preparation found in many modern applications.

An appendix at the end of this report provides a number of instances of how these features have been included in the design of the new programme code.

3.3.3 PROGRAMME USER INTERFACE.

Input and output of data is implemented by the reading and writing of text files. The input data has been kept as simple as possible and separate files for different categories of data make the data entry task quite simple and not too burdensome.

On the other hand, the volume of output data can be quite large. The solution to this problem involves the design of spreadsheet templates into which a complete file figures can be copied. This approach has been used to produce the distance/time diagrams to be found in the examples at the end of this chapter.

An additional problem which has arisen in this part of the development which requires to be resolved with assistance from the client/user is that of the definition of the piston path. In the constant velocity case only one variable, the velocity needs to be considered but with more complex piston trajectories several variables are need to describe how the piston moves with time. Of course once the calculation has been successfully completed the flame velocity can be derived but the criteria for accepting that flame velocity profile as representative of conditions for the occurrence of DDT has not be established to date.

3.3.4 SHOCK FRONT TRAJECTORY DETERMINATION.

Another issue requiring resolution concerns the development of the shock wave in a dynamic way as the calculation proceeds. The piston trajectory selected for a test on the Fortran programme calculated a shock front appearance not at the forward most part of the compression process but behind the acoustic wave. Such behaviour would prove difficult to accommodate in the chosen DDT model. Since the location of the start point of the shock depends upon the piston trajectory selected and, as discussed above, this selection is quite arbitrary, one solution would to perform these

calculations only in cases where the shock is first formed on the acoustic. Subsequent movement of the shock front will always be located as the leading disturbance in the undisturbed gases.

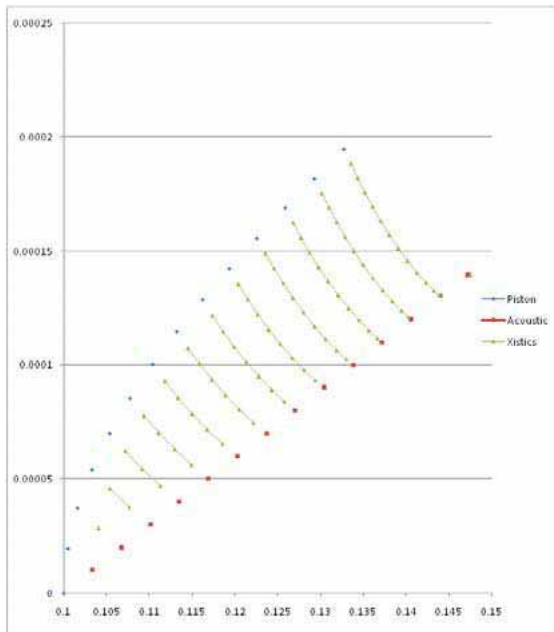
Since it is not possible without input from the client/user to make a unilateral decision on this issue no decision has been taken on its solution.

3.3.5 BEYOND ONE-DIMENSIONAL SOLUTIONS.

The schedule of work specifically entitles the last stage as “Detonation pressures two-dimensional increasing velocity simulation with superimposed constant velocity stable detonation scenarios by method of characteristics”. The progression through the increasing levels of complexity provides the picture of a learning curve dealing in every case with solutions based on self-similarity. Progress through this learning curve has clarified the decision to employ self-similar solutions throughout. The reasons supporting this decision have become more apparent as the work has progressed and they will be presented in Deliverable Two. However, it is noted here near the end of Deliverable One that the C++ version of the method of characteristics programme developed so far will have its main use in the next stage.

3.3.6 THREE TEST CASES.

Three test cases are presented below. As a demonstration of the way in which the programme is used, the data input files for the first case will be described and detailed. In addition one of the output files produced by the calculation procedure will be described and the first few rows of values will be detailed. The full file will not be detailed since there a very large number of rows in the completed run. The results from these tests have been graphed using Microsoft Excel and these graphs will be presented for all three cases. The only differences between the three cases are the form of symmetry tackled, planar, cylindrical and spherical. Hence, only one variable is changed between runs - alpha in the **File** gasProps.txt (see below)



TEST ONE - PLANAR SYMMETRY

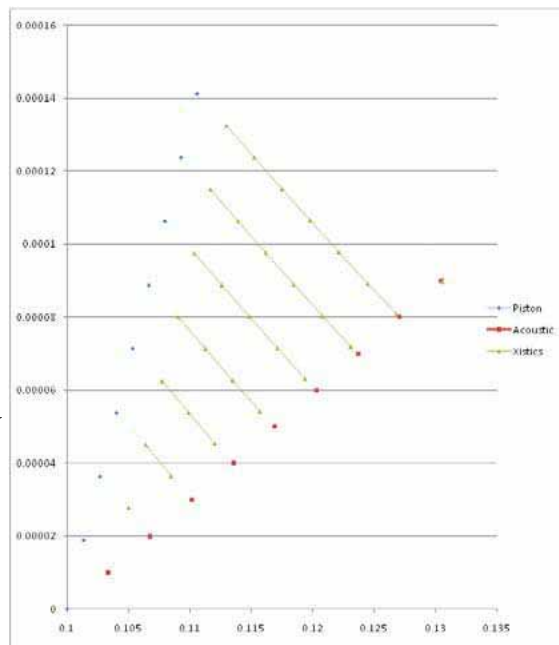
File controlParameters.txt
0.00001 1000 32
baseDelta & total number of
nodes & path number to print

File pistonCoeffs.txt
0.1 75.0 0.0 0.0 0.0
A0 A1 A2 A3 A4 Piston path
coefficients

File gasProps.txt
0 1.4 1.24 355.513
alpha gamma rho0 Gas-constant
per unit volume

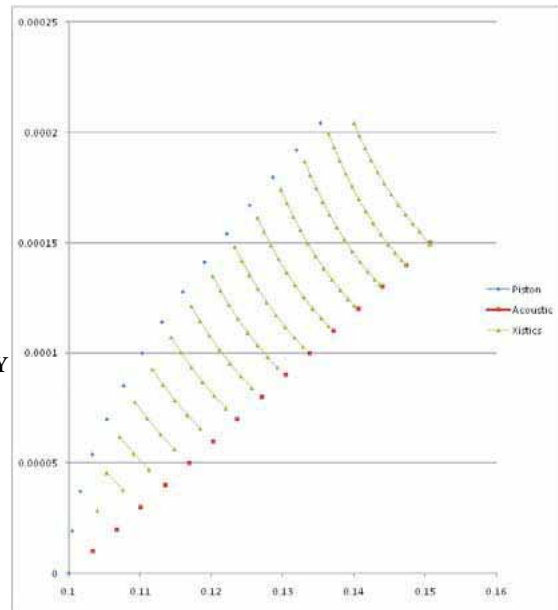
TEST TWO - CYLINDRICAL SYMMETRY

File gasProps.txt
1 1.4 1.24 355.513
alpha gamma rho0 Gas-constant
per unit volume



TEST THREE - CYLINDRICAL SYMMETRY

File gasProps.txt
2 1.4 1.24 355.513
alpha gamma rho0 Gas-constant
per unit volume



3.4 CONCLUSIONS

1. DELIVERABLE ONE HAS COMPLETED THE FOLLOWING TASKS.

- 1.1. A one-dimensional constant velocity analytical tool for calculating various critical parameters relating to safety issues for experimental work on DDT (deflagration to detonation transition) has been devised, constructed and tested.
- 1.2 Criteria for giving numerical values to the safety related aspects of DDT properties have been defined
- 1.3 A matrix of four fuel-air mixtures have been evaluated with numerical values for critical conditions employing these criteria in test calculations for which steady-state detonation properties have been calculated.
- 1.4 Microsoft Excel files containing input and output formation have been provided for the four test fuel-air mixtures'
- 1.5 The tool in the form of MathCAD programmes, one for each fuel-air mixture are available for use.
- 1.6 Two ways of developing a one-dimensional variable velocity numerical tool for calculating the same critical parameters have been developed and the best of these has been selected and developed with additional functions.

- 1.7 The tool in the form of an executable file with accompanying data handling facilities developed to a level which allows for calculations on a limited basis restricted by questions of an appropriate way in which to define non-constant velocity cases.
 - 1.8 An abbreviated description of the way in which the tool might be employed at this stage of its development.
- 2. DELIVERABLE ONE ACHIEVEMENTS CAN BE ENHANCED BY ADDITIONAL IMPROVEMENTS.**
- 2.1 Calculations for the outstanding fuel-air mixtures
 - 2.2 Development of a user interface to clients specification
 - 2.3 Recalculation of any results with user provided steady-state detonation data.
 - 2.4 Formulation of criteria for non-constant velocity cases by way of piston trajectory properties and criteria for safety related numerical measures.
 - 2.5 Design of user interface for the numerical method tool based upon the results of 2.4 above.

LIST OF APPENDICES

- I KUHL, KAMEL & OPPENHEIM
“PRESSURE WAVES GENERATED BY STEADY FLAMES”
- II FORTRAN VERSION MOC Programme Variables
- III FORTRAN VERSION MOC Programme Structure
- IV FORTRAN VERSION MOC Computer CODE
- V C++ VERSION MOC Languagr Features
- VI C++ VERSION MOC Programme Code Features

I KUHL, KAMEL & OPPENHEIM
“PRESSURE WAVES GENERATED BY STEADY
FLAMES”

PRESSURE WAVES GENERATED BY STEADY FLAMES*

A. L. KUHL, M. M. KAMEL, AND A. K. OPPENHEIM

University of California, Berkeley, California

The paper is concerned primarily with the analysis of pressure waves that can be generated by clouds of explosive gas mixtures in a free atmosphere which is initially at a uniform state. Since maximum effects are of prime interest, ignition and initial flame acceleration are considered to be out of scope, and the treatment is restricted only to the final stage of constant flame velocity when the flow field is self-similar. By the introduction of reduced blast-wave parameters as phase-plane coordinates, the problem is resolved into the determination of the appropriate integral curves on this plane. Salient properties of such solutions related to deflagrations are worked out in detail for the regimes of blast waves and acoustic fields. Results, including space profiles of gasdynamic parameters, have been computed for a specific case of a hydrocarbon-air mixture that is characterized by a specific heat ratio of 1.3, sound speed at N.T.P. of 345 m/sec, and volumetric expansion ratio corresponding to constant pressure deflagration of 7, covering a complete range of burning speeds from 0.5 m/sec to the Chapman-Jouguet deflagration of about 120 m/sec. Maximum overpressure ratios that can be generated by such flames in point- and line-symmetrical waves range from 0.53×10^{-3} , for the lower bound in the burning speed, up to 6 for the deflagration, while, for the average speeds of 5 to 10 m/sec, they are at a level of 0.05 to 0.10.

Introduction

The ability of flames to generate pressure waves forms one of their most interesting features. In closed vessels, this trait is of fundamental significance to the development of detonation,¹ as well as being one of the primary causes for the onset of instabilities in combustion chambers, especially those associated with high frequency that occur in jet-propulsion systems.² In an unbounded atmosphere, it can manifest itself in the form of destructive explosions. This phenomenon recently became of particular interest as a consequence of environmental hazards associated with the occurrence of explosive clouds, made out of hydrocarbon-air mixtures, in the vicinity of large fuel-storage facilities.³ It is then an estimate of the strength of pressure waves that can be generated by such clouds that forms the primary objective of this paper.

Since, of course, maximum effects are for this purpose of prime importance, the processes of ignition and initial flame acceleration are considered to be out of scope. For the same reason, the decay of the pressure wave after the explosive cloud is consumed by the flame is also excluded. Instead then, our attention is focused upon the steady state which the system attains when the flame propagation velocity acquires a constant value. At the same time, the front of the pressure wave generated by such a flame propagates also at a constant velocity, while the burned gases immediately behind the flame are at rest.

Under such circumstances, the flow field is self-similar, representing a special case of flows studied, in particular, by Taylor,⁴ Sedov,⁵ and Shikin,⁶ and discussed in the text of Courant and Friedrichs.⁷ The analysis presented here follows, in essence, the technique of the above references. The formulation is, however, modified to take advantage of the simplifications that can be obtained as a consequence of our recent studies of the fundamental properties of blast waves.^{8,9}

The results are worked out in detail to yield a full description of the pressure wave that can be formed by the cloud of a hydrocarbon-air mixture. The effects of geometry are taken into

* This work was supported by the United States Air Force through the Air Force Office of Scientific Research under Grant AFOSR-72-2200, by the National Aeronautics and Space Administration under Grant NsG-702/05-003-050, and by the National Science Foundation under Grant NSF GK-22975.

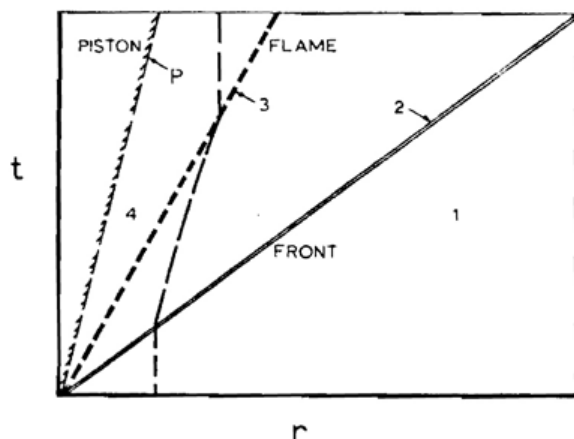


FIG. 1. Wave diagram of the flow field.

account by the consideration of either point-, line-, or plane-symmetrical flow fields. In free space, the most probable shape the flame may take should be encompassed by the point- and line-symmetrical geometry, so that the physically realizable case should be bounded by these two solutions.

Salient Features of the Analysis

The time-space wave diagram of the system is presented in Fig. 1, the coordinates t and r being measured from the origin where all wave fronts intersect. The medium into which the leading wave front propagates, state 1, as well as the products of combustion behind the flame, state 4, are considered to be at rest.

The flame is treated as a steady deflagration so that its trajectory in the time-space domain, as well as that of the front of the pressure wave it generates, are straight lines. The flow field between the two—i.e., the process associated with the change of state from 2 to 3, as shown in Fig. 1—is self-similar so that the gasdynamic parameters are invariant along similarity lines $x \equiv r/r_2 = \text{const}$.

The problem is to determine the space profiles of the gasdynamic parameters, i.e., the pressure p , density ρ , temperature T , and particle velocity u , that would be established at any point in space in a combustible mixture giving rise to a deflagration front propagating into the medium immediately ahead of it at a given burning speed S .

The evaluation of the self-similar flow field between states 2 and 3 presents, of course, the key to the solution. This is, in fact, part of the pressure wave generated by a piston expanding at constant velocity—a problem which for spherical geometry was solved by Taylor,⁴ while

its general properties were presented by Courant and Friedrichs⁷ as a representative case of “progressive waves.” The particular difficulty in the case of flames is due to their relatively low propagation velocity. As a consequence, the flow fields they generate fall within the intersection between the regimes of blast wave and acoustic solutions. However, as pointed out by Taylor in his classical paper,⁴ the two are mutually incompatible.

In what follows we present first the analysis of piston-driven blast waves, and then a corresponding treatment for self-similar acoustic fields. We then introduce the relationships for deflagration that fix the position of its front in the flow field. Since the pressure rises monotonically from the front toward the center, this establishes at the same time its maximum value attained immediately ahead of the flame front.

On this basis, a numerical solution is obtained for a representative case of a hydrocarbon-air mixture, demonstrating in particular that the transition between the blast-wave solution and the acoustic is, in essence, continuous, clarifying thus the Taylor dilemma of incompatibility between these solutions.

Blast Wave

The conservation equations for a self-similar blast wave can be reduced to a single ordinary differential equation⁹ by the introduction of the following reduced parameters:

$$F \equiv (t/r\mu)u \quad \text{and} \quad Z \equiv [(t/r\mu)a]^2, \quad (1)$$

where $\mu \equiv (t_2/r_2)w_2$; and a is the local velocity of sound while, with reference to Fig. 1, $w_2 = dr_2/dt$.

The above parameters represent, in effect, the phase-plane coordinates of the problem, so that its solution is obtained, in essence, by determining the appropriate integral curve which prescribes $Z = Z(F)$, subject to some specific boundary conditions. The latter are given, on one side, by the Rankine-Hugoniot relations across the shock front and, on the other side, by the jump conditions across the deflagration front, associated with zero particle velocity in the burned gas regime immediately behind it. Properties of the phase plane were presented by Sedov⁵ for a variety of self-similar flow fields. The particular features of flows associated with constant velocity deflagrations were treated by Shikin.⁶

For a blast wave whose front propagates at a constant velocity, one has $\mu = 1$. If the state of the undisturbed medium is uniform, while the substance is a perfect gas with constant specific

heats, the differential equation governing the solution can be expressed then as follows⁹:

$$\frac{d \log Z}{d \log F} = \frac{2D + j(\gamma - 1)(1 - F)F}{D + jZ}, \quad (2)$$

where

$$D \equiv Z - (1 - F)^2,$$

while $j=0, 1, 2$ for the plane-, line-, and point-symmetrical geometry, respectively, and γ is the specific heat ratio.

Once the integral curve in the phase plane is known, the solution is completed by the quadrature

$$\begin{aligned} (d \log x)/(d \log F) &= - (d \log r)/(d \log F) \\ &= - D/(D + jZ), \end{aligned} \quad (3)$$

where, as already mentioned, $x \equiv r/r_2$ at a fixed time, $\tau \equiv t/t_2$ at a fixed radius, while the gas dynamic parameters of the flow field are determined from the algebraic relations

$$u = w_2 x^F,$$

and, since the flow is isentropic,

$$\frac{T}{T_2} = \left(\frac{a}{a_2}\right)^2 = \left(\frac{p}{p_2}\right)^{(\gamma-1)/\gamma} = \left(\frac{\rho}{\rho_2}\right)^{\gamma-1} = x^2 \frac{Z}{Z_2}. \quad (5)$$

All the integral curves of Eq. (2) representing the solutions of our problem pass through nodal singularity A located at the point $F=0, Z=1$.⁹ The numerical integration should be, therefore, performed toward A . The line $F=1$ represents the locus of states at the piston face,⁹ and provides the most convenient starting place for the integration. All the parameters of the problem corresponding to this state are here denoted by subscript p , and the solutions are obtained in terms of $\xi \equiv \gamma_1 Z_p$ as the parameter. From Eqs. (2) and (3), it follows that

$$\left. \frac{d \log Z}{d \log F} \right|_{F=1} = \frac{2}{j+1}, \quad (6)$$

while

$$\left. \frac{d \log x}{d \log F} \right|_{F=1} \equiv - \frac{1}{j+1}. \quad (7)$$

In the plane-symmetrical case, $j=0$ and Eqs. (6) and (7) acquire the role of the governing differential equations for the flow field. The solution is then obtained immediately by inte-

gration, giving

$$Z = Z_p F^2 \quad (8)$$

and

$$x = x_p F^{-1}. \quad (9)$$

The parameters of the state at the piston face can be then related directly to the boundary conditions at the front $Z=Z_2$ and $F=F_2$ at $x=1$, so that

$$Z_p = Z_2 F_2^{-2} \quad \text{for } j=0, \quad (10)$$

while

$$x_p = F_2 \quad \text{for } j=0. \quad (11)$$

Equations (4) and (5) yield, for the profiles of the gasdynamic parameters, simple conditions:

$$u/a_1 = F_2 M = \text{const} \quad \text{for } j=0, \quad (12)$$

where $M \equiv w_2/a_1$, and

$$T/T_1 = (a/a_1)^2 = Z_2/Z_1 = \text{const} \quad \text{for } j=0, \quad (13)$$

while the corresponding pressure and density ratios are given by the Rankine-Hugoniot relations, Eqs. (18) and (19).

For the line- and point-symmetrical cases ($j=1$ and $j=2$), the solution is obtained by numerical integration of Eqs. (2) and (3). As indicated by the form of these equations, best computational stability has been obtained by the use of the logarithmic coordinates $\log F$, $\log Z$ and $\log x$ as the primary variables in the computer code.

Integration is terminated at the shock front whose phase-plane coordinates are given by^{7,8}

$$F_2 = [2/(\gamma+1)](1-y) \quad (14)$$

and

$$\begin{aligned} Z_2 &= [2(\gamma-1)/(\gamma+1)^2] \{ [2\gamma/(\gamma-1)] - y \} \\ &\quad \times [\frac{1}{2}(\gamma-1) + y], \end{aligned} \quad (15)$$

where $y \equiv a_1^2/w_2^2 = 1/M^2$. Eliminating the latter from Eqs. (14) and (15), one obtains, for the locus of the end points, the following relation

$$Z_2 = [(\gamma-1)/2\gamma](1-F_2) \{ [2/(\gamma-1)] + F_2 \}, \quad (16)$$

omit

representing the equation of the Rankine-Hugoniot curve in the phase plane. The corresponding initial condition is that of a quiescent

atmosphere ahead of the wave, that is,

$$\begin{aligned} F_1 &= 0 \\ Z_1 &= a_1^2/w_2^2 = y, \end{aligned} \quad (17)$$

while the change of the gasdynamic parameters across the front is specified by

$$\frac{p_2}{p_1} = \frac{\gamma-1}{\gamma+1} \left(\frac{2\gamma}{\gamma-1} - y \right) \quad (18)$$

$$\frac{\rho_2}{\rho_1} = \frac{\gamma+1}{\gamma-1+2y} \quad (19)$$

$$\begin{aligned} \frac{T_2}{T_1} = \frac{Z_2}{Z_1} &= \frac{2(\gamma-1)}{(\gamma+1)^2} \left(\frac{2\gamma}{\gamma-1} - y \right) \\ &\times \left[\frac{1}{2}(\gamma-1)y^{-1} + 1 \right]. \end{aligned} \quad (20)$$

For weak waves, the Mach number of the front approaches unity and there arises a basic difficulty in the integration of the differential equation governing the structure of the blast wave. This is due to the particular property of singularity *A* at point $F=0$, $Z=1$ which lies at the intersection of the Rankine-Hugoniot curve with the $F=0$ axis and corresponds to the condition of $M=1$ at the front.⁹ The problem is caused by the fact that the integral curves, representing the blast-wave structure, intersect the Rankine-Hugoniot curve at a positive slope that becomes larger for weaker waves, while they have to approach singularity *A* at $F=0$ with an infinitely negative slope. The consequent rapid change in the derivatives produces strange numerical results which led Taylor⁴ initially to the belief that there may be a lower bound to the solution corresponding to the condition that x_p cannot be smaller than a certain value, somewhere between 0.4 and 0.5.

Actually, as it has been observed by Taylor,⁴ when the front Mach number approaches unity, the problem is governed by the acoustic wave equation and, as it will be demonstrated here, there exists a continuous transition between the acoustic and blast-wave domains, so that, in fact, the weak limit does not exist, and x_p can be as small as one pleases, corresponding to arbitrarily small flame velocities.

Acoustic Wave

The acoustic wave is described in terms of the velocity potential $\phi(r,t)$, which satisfies the

equation:

$$\partial^2\phi/\partial t^2 = (a_1^2/r^j) (\partial/\partial r)[r^j(\partial\phi/\partial r)], \quad (21)$$

and is related to the particle velocity and pressure, respectively, as follows:

$$u = -\partial\phi/\partial r \quad (22)$$

$$p - p_1 = \rho_1 (\partial\phi/\partial t). \quad (23)$$

In the case of a constant-velocity piston, one can obtain a similarity solution by assuming for the potential the functional form

$$\phi(r, t) = tf(r/a_1t) = tf(x), \quad (24)$$

where $x=r/a_1t$ is, as before, the similarity variable. Equation (21) is transformed then into the ordinary differential equation:

$$x(1-x^2)f'' + jf' = 0, \quad (25)$$

while Eqs. (22) and (23) yield, respectively,

$$u = -a_1^{-1}f'(x) \quad (26)$$

and

$$\begin{aligned} (p-p_1)/p_1 &= (\gamma/a_1^2)[f(x) - xf'(x)] \\ &= \gamma\{[f(x)/a_1^2] - [u(x)/a_1]x\}. \end{aligned} \quad (27)$$

Integrating Eq. (25), one obtains

$$f' = (C_j/x^j)(1-x^2)^{j/2}. \quad (28)$$

The constant of integration C_j is determined from the boundary condition at the piston where

$$u = u_p = a_1x_p = -(\partial\phi/\partial r)_{r=x_p} = -a_1^{-1}f'(x_p),$$

so that

$$C_j = -[x_p^{j+1}/(1-x_p^2)^{j/2}]a_1^2,$$

whence, by virtue of Eq. (26), the acoustic velocity profile is given by

$$u(x) = (x_p/x)^j [(1-x^2)/(1-x_p^2)]^{j/2} x_p a_1. \quad (29)$$

Integrating Eq. (28), one gets

$$\begin{aligned} f(x) &= C_1((1-x^2)^{1/2} - \ln\{[1+(1-x^2)^{1/2}/x]\}) + K_1, \\ &\quad \text{for } j=1, \\ &= -C_2[(1+x^2)/x] + K_2 \quad \text{for } j=2. \end{aligned} \quad (30)$$

Substituting the above into Eq. (27) together with Eq. (29), and eliminating the integration constants K_1 and K_2 from the boundary condition at the front, i.e.,

$$p = p_1 \quad \text{at} \quad r_2 = a_1 t,$$

one obtains the following expressions for the pressure profile:

$$\begin{aligned} (p - p_1)/p_1 &= \gamma [x_p^2 / (1 - x_p^2)^{1/2}] \\ &\times \ln \{ [1 + (1 - x^2)^{1/2}] / x \} \quad \text{for } j=1, \\ &= 2\gamma [x_p^3 / (1 - x_p^2)] [(1 - x) / x] \quad \text{for } j=2. \end{aligned} \quad (31)$$

On the basis of Eqs. (1), (29), and (31), the integral curves in the phase plane corresponding to the acoustic solutions can be thus expressed parametrically as follows:

$$F(x) = u(x) / a_1 x = (x_p / x)^{j+1} [(1 - x^2) / (1 - x_p^2)]^{j/2} \quad (32)$$

$$\begin{aligned} Z(x) &= (1/x^2) (p/p_1)^{(\gamma-1)/\gamma} \\ &= (1/x^2) (1 + [\gamma x_p^2 / (1 - x_p^2)]^{1/2}) \\ &\quad \times \ln \{ [1 + (1 - x^2)^{1/2}] / x \}^{(\gamma-1)/\gamma} \quad \text{for } j=1, \\ &= (1/x^2) \{ 1 + 2[\gamma x_p^3 / (1 - x_p^2)] \\ &\quad \times [(1 - x) / x] \}^{(\gamma-1)/\gamma} \quad \text{for } j=2. \end{aligned} \quad (33)$$

For the plane-symmetrical case ($j=0$), the acoustic wave is identical to the blast wave corresponding to $M=1$, one being just a simple limit of the other without any anomaly.

The case of the spherical piston-driven acoustic wave was solved by Taylor,⁴ while that of the cylindrical wave was treated more recently by Zeldovich¹¹ in a somewhat circuitous way by regarding it as a limit of a system of plane waves whose envelope forms the cylindrical front.

Flame

For the steady-state solution that is sought here, the flame is considered to act as a constant-velocity deflagration which, as indicated in Fig. 1, establishes state 3 under the condition that state 4, in the region immediately behind it, is at rest. The corresponding pressure-specific volume diagram for all the processes undergone by a particle of the flow field is presented in Fig. 2. After compression by the shock front

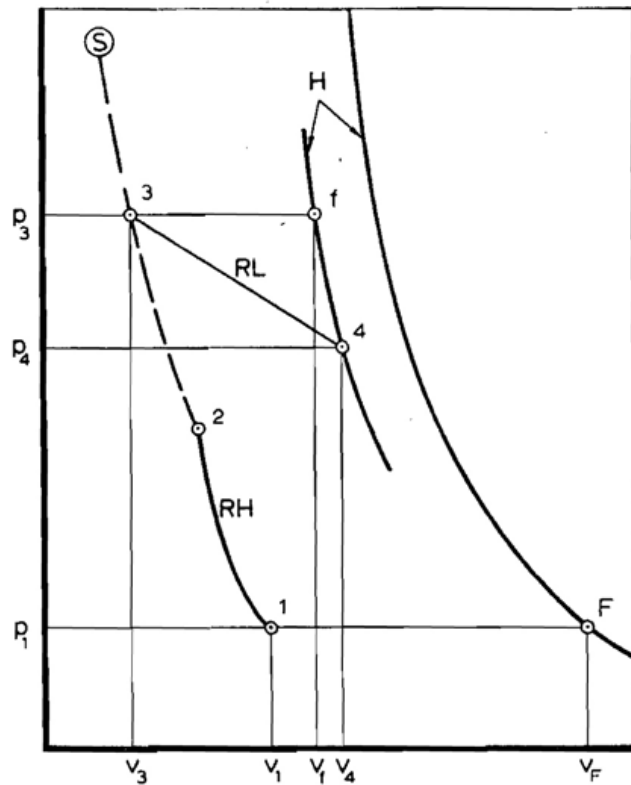


FIG. 2. Description of the thermodynamic processes on the pressure-specific volume plane.

from state 1 to state 2 represented by a point lying on the Rankine-Hugoniot curve (RH), the particle undergoes an isentropic compression in the blast wave to state 3 immediately ahead of the deflagration which, in turn, yields state 4 specified by a point lying on the appropriate Hugoniot curve (H). The transition from state 3 to state 4 takes place along the Rayleigh line (RL).

Thus, under the condition of $u_4=0$, the continuity equation for the deflagration gives

$$v_d = v_4 / v_3 = w_3 / S, \quad (34)$$

where v is the specific volume, $w_3 = dr_3/dt$, and S is the burning speed.

The corresponding Rayleigh relation can be written as follows:

$$P_d \equiv p_4 / p_3 = 1 + \gamma_3 (S^2 / a_3^2) (1 - v_d),$$

and, since from the definition of Eq. (1), $Z_3 = a_3^2 / w_3^2$, while $(S/a_3)^2 = (S/w_3)^2 (w_3/a_3)^2 = 1/v_d^2 Z_3$, one gets

$$P_d = 1 + (\gamma_3 / Z_3) [(1 - v_d) / v_d^2]. \quad (35)$$

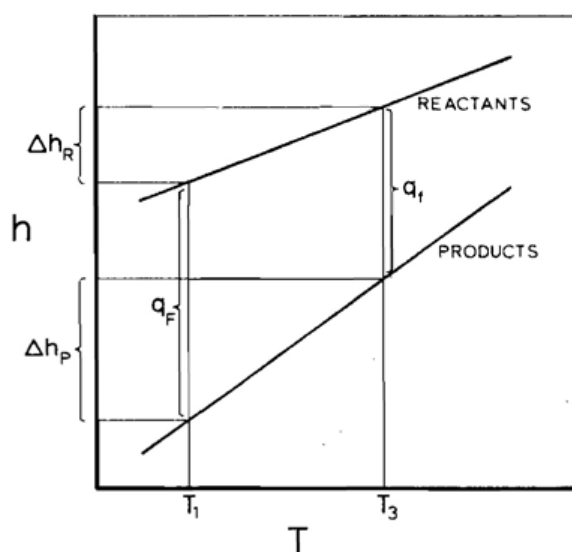


FIG. 3. The enthalpy-temperature diagram, demonstrating the effect of heating on heat released per unit mass.

The Hugoniot condition can be expressed in terms of the hyperbolic relation¹⁰

$$(P_d + \beta)(v_d - \beta) = (1 + \beta)(v_f - \beta)$$

where $\beta \equiv \gamma_4 - 1/\gamma_4 + 1$, while $v_f \equiv v_f/v_3$, state f , as shown in Fig. 2, corresponding to the specific volume ratio at constant pressure. This yields, with the use of Eq. (35), the following relationship between v_d and v_f :

$$v_f = v_d + (\gamma_3/Z_3)[(1 - v_d)(v_d - \beta)/(1 + \beta)v_d^2]. \quad (36)$$

In order to relate this to the heat of reaction, proper account has to be taken of the effect of heating that occurs in the blast wave ahead of the flame. For the present purpose, the most convenient way to express the heat of reaction is in terms of the specific volume ratio $v_F \equiv v_F/v_1$ (see Fig. 2). The relationship between v_f and v_F reflects the change in the amount of heat released due to the temperature increase between state 1 of the undisturbed medium and state 3 of the gas compressed by the blast wave, as described schematically by Fig. 3. It follows then that, taking into account the perfect-gas behavior of the reactants R and products P , one has

$$\begin{aligned} q_f &= q_F + \Delta h_R(1 - \Delta h_P/\Delta h_R) \\ &= q_F + (\gamma_3 - 1)^{-1}(a_3^2 - a_1^2) \\ &\quad \times [1 - (\gamma_4/\gamma_3)(\gamma_3 - 1)/(\gamma_4 - 1)\mathfrak{N}], \quad (37) \end{aligned}$$

where $\mathfrak{N} \equiv \mathfrak{N}_3/\mathfrak{N}_4$ is the molecular weight ratio.

On the basis of the Hugoniot relation,¹⁰ one has

$$v_k = [(\gamma_4 - 1)/\gamma_4]\{[\gamma_3/(\gamma_3 - 1)] + \gamma_3(q_k/a_1^2)\}, \quad (38)$$

where, with reference to Figs. 2 and 3, $k=f$ or F .

With the use of Eq. (37), Eq. (38) yields the required relationship between v_f and v_F , namely

$$\begin{aligned} v_f &= (a_1/a_3)^2 v_F + [1 - (a_1^2/a_3^2)] \\ &\quad \times [2(\gamma_3/\gamma_4)(\gamma_4 - 1)/(\gamma_3 - 1) - \mathfrak{N}]. \quad (39) \end{aligned}$$

Now, from the definitions of Eq. (1), noting that $x_1 = 1$,

$$(a_1/a_3)^2 = (1/x_3^2)(Z_1/Z_3), \quad (40)$$

while $F_3 = u_3/w_3$, so that as a consequence of Eq. (34),

$$v_d = 1/(1 - F_3). \quad (41)$$

Substituting Eqs. (39), (40), and (41) into Eq. (36), one obtains finally

$$\begin{aligned} v_F &= x_3^2(Z_3/Z_1)\{(1 - F_3)^{-1} + (\gamma_3/\gamma_4)(F_3/Z_3) \\ &\quad \times [1 + \frac{1}{2}(\gamma_4 - 1)F_3]\} \\ &\quad - [2(\gamma_3/\gamma_4)(\gamma_4 - 1)/(\gamma_3 - 1) - \mathfrak{N}] \\ &\quad \times [x_3^2(Z_3/Z_1) - 1]. \quad (42) \end{aligned}$$

In the course of computations, the parameters Z_3 , F_3 , and x_3 are evaluated point by point, starting from the piston face. The corresponding value of v_F can be therefore determined from Eq. (42), and the position of the flame front is thus established when it attains the appropriate magnitude, as demanded by this equation, for a given combustible mixture.

The quantity in the curly brackets represents the expression for v_f given by Eq. (36), the two terms in each corresponding respectively to each other. For a constant-pressure deflagration, $v_f = v_d$ and, consequently, the second term in the brackets vanishes. If, moreover, the influence of heating in the blast wave is negligible, $x_3^2(Z_3/Z_1) = (a_3/a_1)^2 \cong 1$, and Eq. (42) is reduced to the asymptotic form

$$v_F \cong v_d = (1 - F_3)^{-1}. \quad (43)$$

The value of the parameter $F = F_3$ at the flame front is, under such circumstances, established solely on the basis of the value of v_F as specified by the above relation.

Finally, it should be noted that, to each point

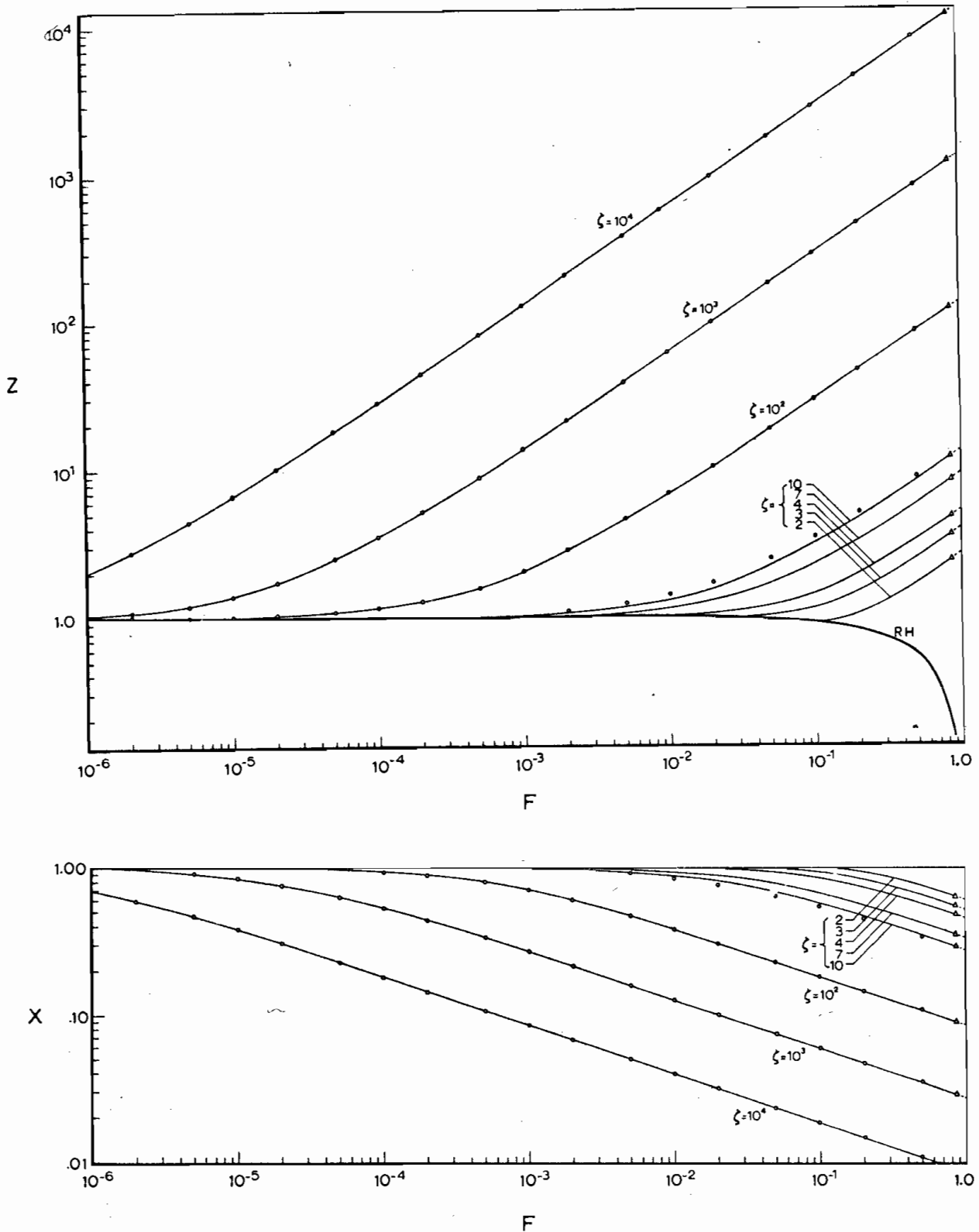


FIG. 4. Integral curves in the phase plane for point-symmetrical waves and the auxiliary plot of the self-similarity coordinate x , as a function of the phase-plane coordinate F . Triangles denote positions of the flame fronts: $\gamma = 1.3$, $\gamma_4 = 1.2$, $\nu_F = 7$.

of the integral curve, there corresponds a certain value of the burning speed which, on the basis of Eqs. (34), (41), and (14), can be expressed as

$$S = x_3 w_2 (1 - F_3). \quad (44)$$

One should also observe that, in an earlier treatment of the problem,^{5,6} the position of the flame front was established by the use of the locus of constant values of the nondimensional parameter q/S^2 in the phase plane. This ap-

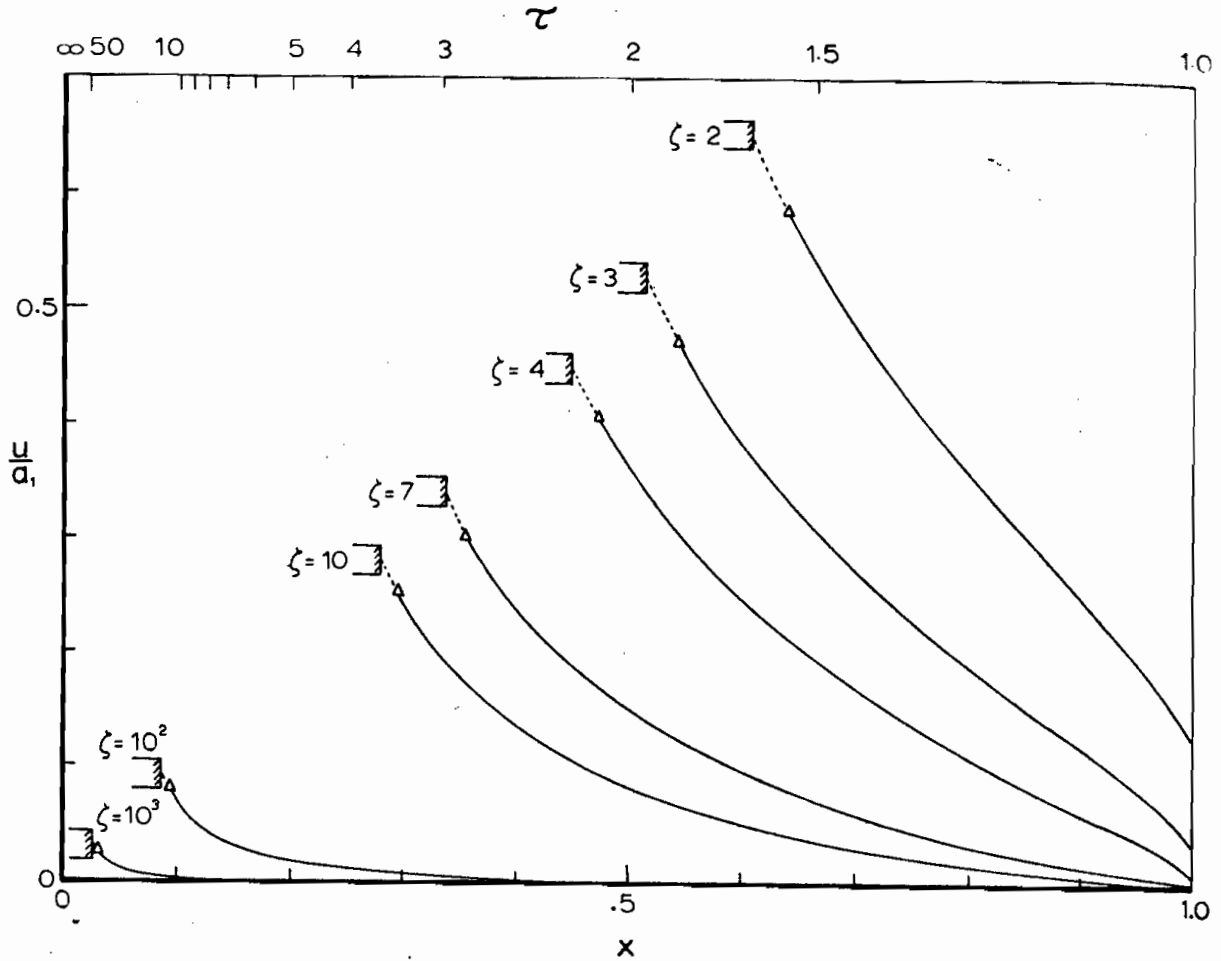


FIG. 5. Particle-velocity profiles for point-symmetrical waves. Position of the piston face is indicated by the appropriate symbol; triangles denote positions of the flame fronts: $\gamma = 1.3$, $\gamma_4 = 1.2$, $\nu_F = 7$.

proach has not been used here, however, since our computational technique based on the use of Eq. (42) is more straightforward, its application in the algorithm involving just the evaluation of the algebraic expression it specifies.

The burning speed cannot exceed the value corresponding to the Chapman-Jouguet deflagration. For the case considered throughout this study of $u_4 = 0$, or $F_4 = 0$, this theoretical limit of S corresponds to $Z_4 = 1$. Since, according to the definition of Eq. (1),

$$Z_4 = (\gamma_4/\gamma_3)(P_d \nu_d/Z_3), \tag{45}$$

one obtains, by involving this condition for Z_4 in the above equation and combining it with Eqs. (35) and (41), a quadratic expression

$$Z_3 = (\gamma_3/\gamma_4)(1 - F_3)(1 + \gamma_4 F_3) \tag{46}$$

for the locus of states immediately ahead of such deflagrations.

Equation (46), in turn, together with Eqs.

(42) and (44), yields the following unique relation between ν_F , S_{CJ} , and F_3

$$\begin{aligned} \nu_F = & (\gamma_3/\gamma_4)[S_{CJ}^2/a_1^2(1 - F_3)^2] \\ & \times [1 + \frac{1}{2}(\gamma_4 - 1)(2 - F_3)F_3] \\ & - [2(\gamma_3/\gamma_4)(\gamma_4 - 1)/(\gamma_3 - 1) - \mathfrak{M}] \\ & \times \left\{ \frac{\gamma_3}{\gamma_4} \frac{S_{CJ}^2}{a_1^2} \frac{1 + \gamma_4 F_3}{1 - F_3} - 1 \right\}. \tag{47} \end{aligned}$$

Results

Numerical solutions based on the theory presented here were obtained for the particular case of hydrocarbon-air mixture initially at N.T.P. conditions. Its thermodynamic properties were expressed in terms of the following parameters:

$$\nu_F = 7; a_1 = 345 \text{ m/sec}; p_1 = 1 \text{ atm};$$

$$\gamma_1 = \gamma_2 = \gamma_3 = 1.3; \gamma_4 = 1.2; \mathfrak{M} = 1.$$

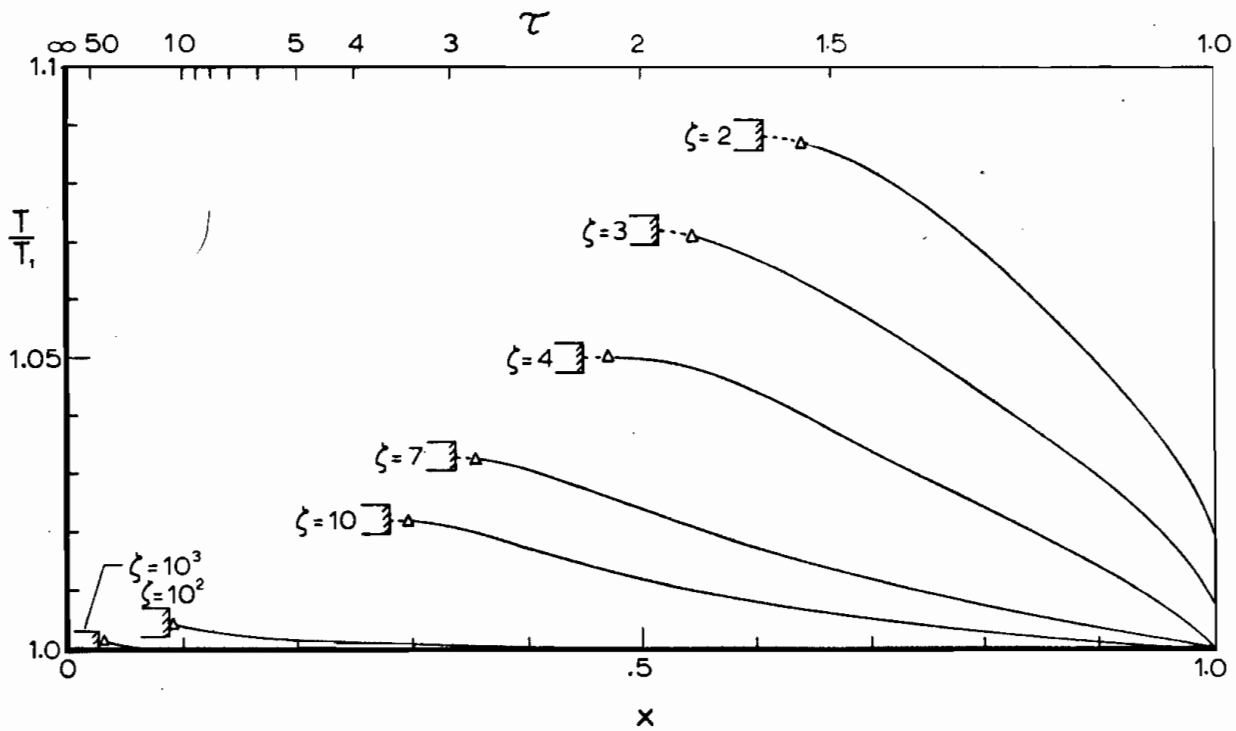


FIG. 6. Temperature profiles for point symmetrical waves. Position of the piston face is indicated by the appropriate symbol; triangles denote positions of the flame fronts: $\gamma = 1.3$, $\gamma_4 = 1.2$, $\nu_F = 7$.

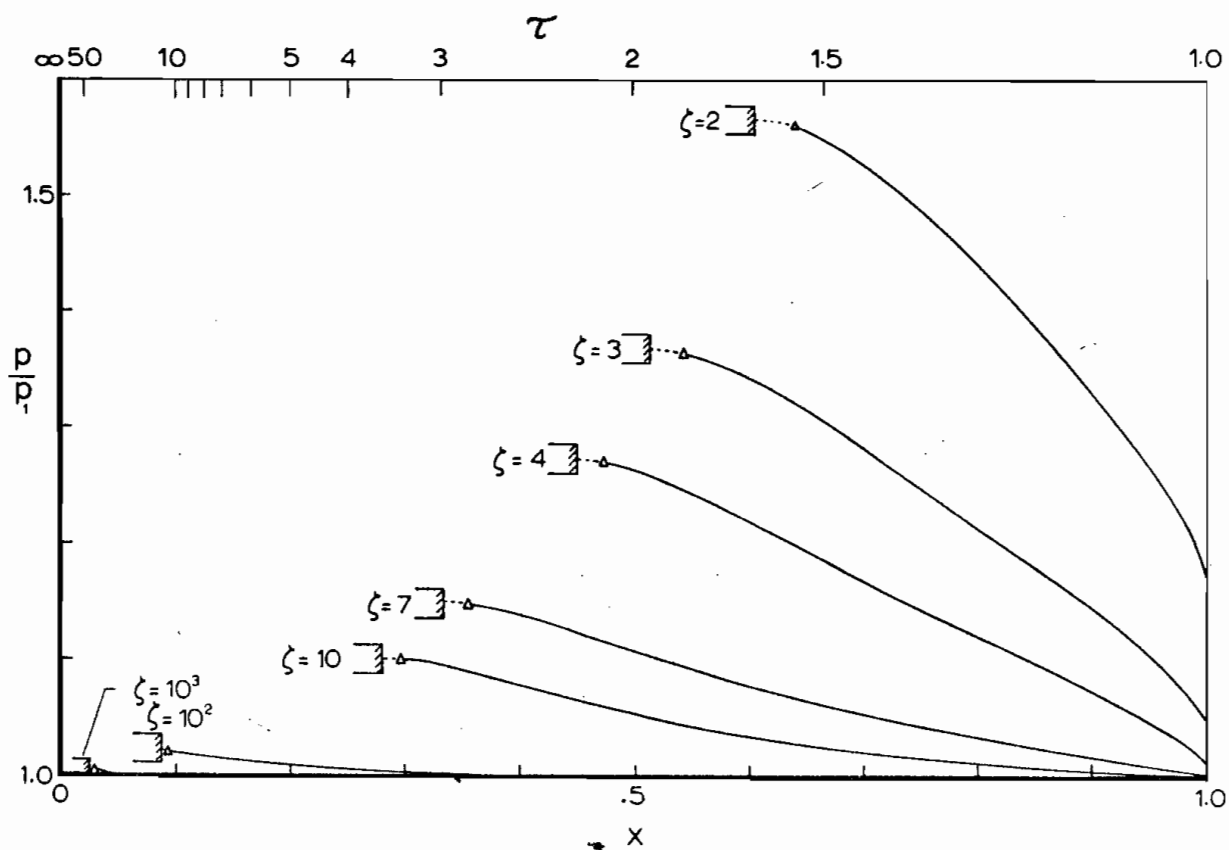


FIG. 7. Pressure profiles for point symmetrical waves. Position of the piston face is indicated by the appropriate symbol; triangles denote positions of the flame fronts: $\gamma = 1.3$, $\gamma_4 = 1.2$, $\nu_F = 7$.

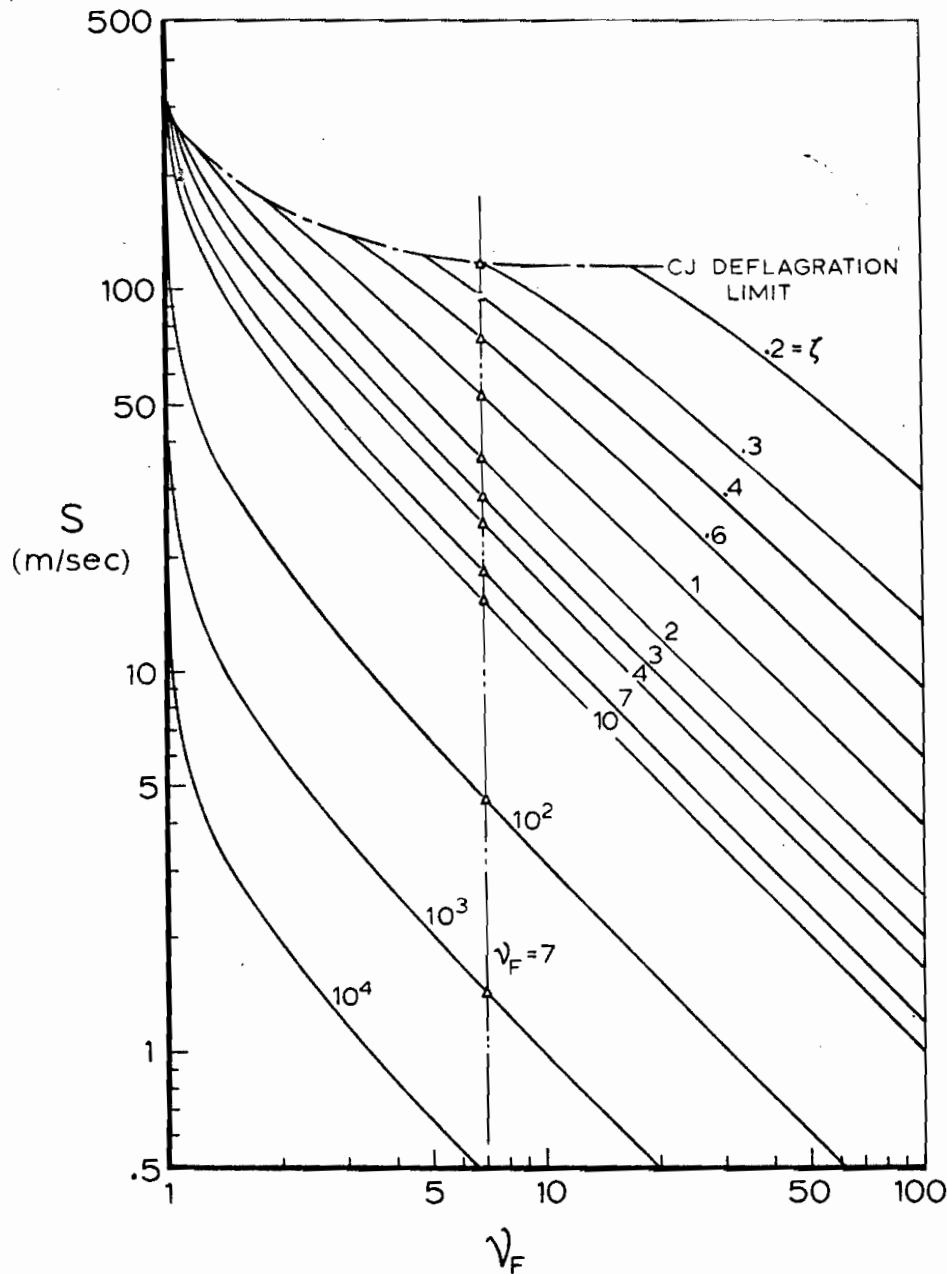


FIG. 8. Graphic representation of the interrelationship between the burning speed S and the specific volume ratio ν_F , for point-symmetrical waves: $\gamma = 1.3$, $\gamma_1 = 1.2$, $a_1 = 345$ m/sec.

Integral curves in the phase plane for a point-symmetrical flow field ($j=2$) are shown in Fig. 4, together with the corresponding plot of $x=x(F)$. Each is labeled with the appropriate value of $\zeta = \gamma Z_p$. For the blast wave, they represent the solutions of Eqs. (2) and (3), respectively. The computations for each integral curve were started at the point $F=1$, $Z=Z_p = \zeta/\gamma$, while the coordinate x was expressed initially in terms of x/x_p . The latter was then determined at the shock front where, by definition, $x=1$, yielding thus the value of x_p . In our algorithm this was obtained when the integral curve satisfied the

$Z=Z(F)$ functional relationship specified by the Rankine-Hugoniot relation, Eq. (16).

Points corresponding to flame fronts are indicated by triangles. In the domain of relatively weak waves covered by the diagram, they are practically at their asymptotic value expressed by Eq. (43), annihilating concomitantly any noticeable difference between the constant-pressure deflagration and one associated with pressure drop.

The open dots denote the acoustic solutions. For $\zeta=10^2$ and above, they lie exactly on the continuous lines representing the integral curves

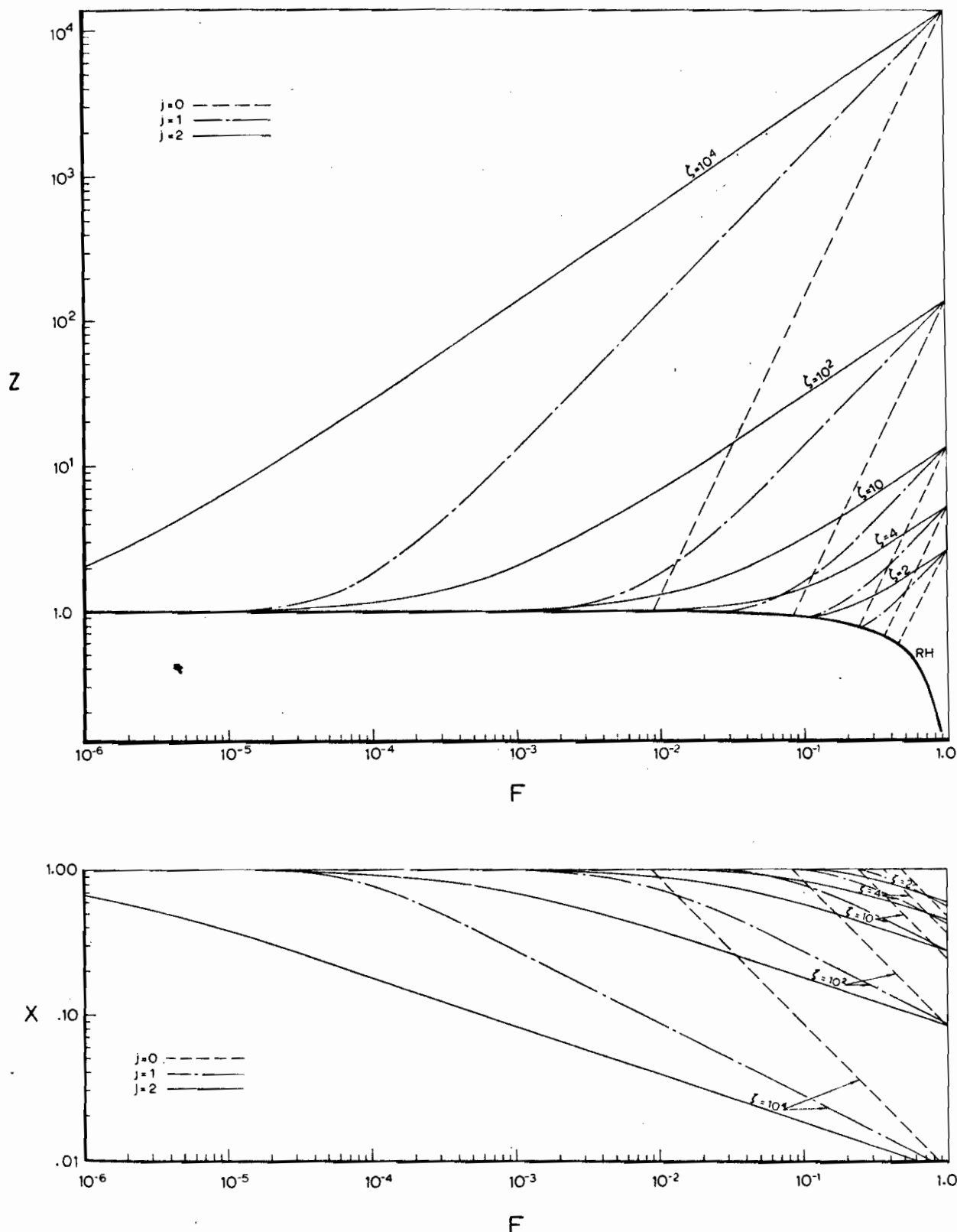


Fig. 9. Integral curves in the phase plane for point-, line-, and plane-symmetrical waves and the corresponding plots of the self-similarity coordinate x , as functions of the phase-plane coordinate F ($\gamma=1.3$).

of the blast-wave equations, while for $\zeta=10$ the deviation between the two solutions is quite small. Thus, one can conclude that the domains governed by the nonlinear blast waves and linear acoustic waves have an appreciable

overlap, so that the transition from one to the other is quite smooth. Evidently, then, the problem of an inherent incompatibility between the two at the piston face, that has been pointed out by Taylor,⁴ does not involve any difficulty,

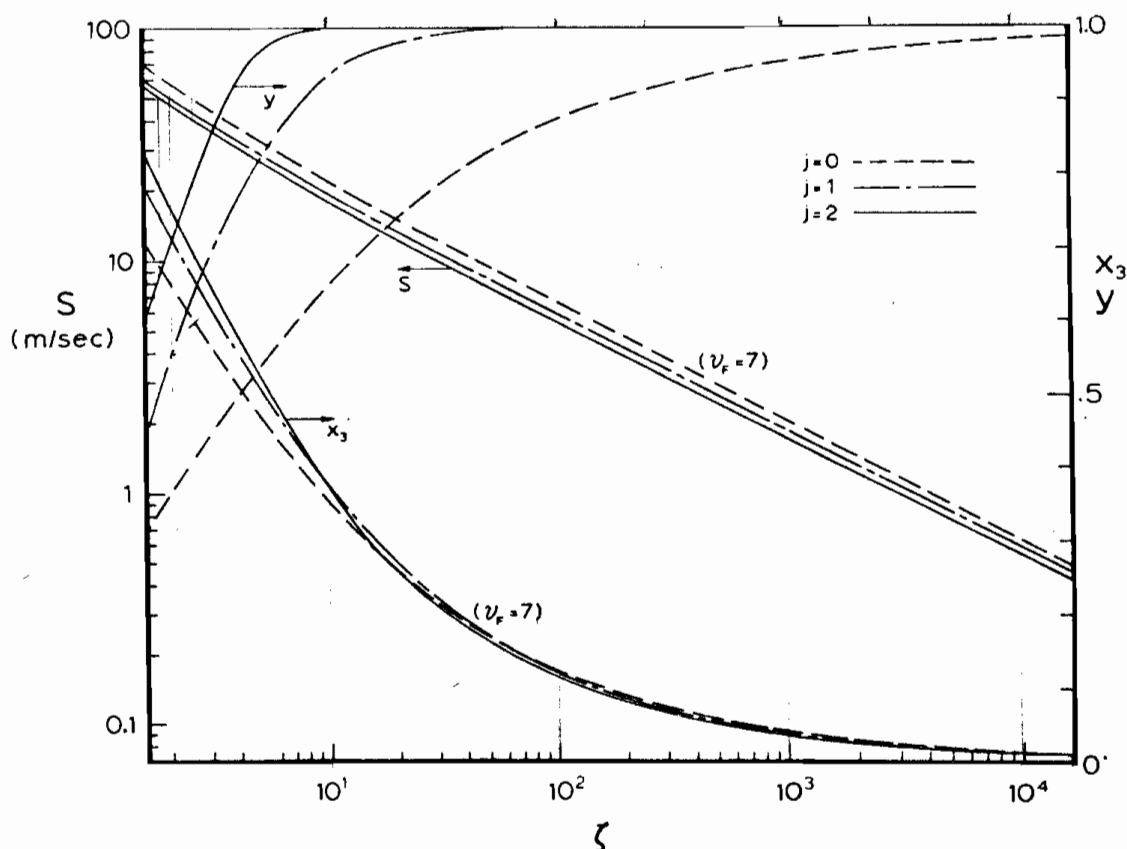


Fig. 10. Plot of the primary parameters of the problem as a function of the integral curve parameter ζ , for point-, line-, and plane-symmetrical waves ($\gamma = 1.3$, $\gamma_1 = 1.2$, $a_1 = 345$ m/sec, $\nu_F = 7$).

provided that proper care is exercised in the numerical integration procedure.

To give a complete physical description of the flow fields thus evaluated, the corresponding particle velocity, temperature, and pressure profiles are presented in Fig. 5, 6, and 7, respectively, as functions of both space at a fixed instant of time and time at a fixed position in space.

Figure 8 gives the burning speed S , evaluated from Eq. (44), as a function of ν_F determined by the use of Eq. (42) for the spherically symmetric case, with ζ as the parameter. The graph is quite general in that it is applicable to any value of the heat of reaction that may be ascribed to the combustible mixture. As on the other diagrams, points corresponding to the given substance for which $\nu_F = 7$ are denoted by triangles. The family of curves presented in Fig. 8 is bounded by the Chapman-Jouguet deflagration limit. This was obtained by the intersection of each integral curve with the locus of states specified by Eq. (46), the equation of the line being then given by Eq. (47) for the appropriate values of F_3 .

Using the same algorithm, numerical solutions

for the line-symmetrical case ($j=1$) were also obtained. The integral curves in the phase plane and the auxiliary $x=x(F)$ plot are shown in Fig. 9, compared to the point- and plane-symmetrical cases, the latter being simply a plot of Eqs. (10) and (11).

The most significant physical parameters for all the geometries are shown in Fig. 10, plotted as a function of ζ , the parameter identifying specific solutions. This includes the burning speed S and the flame position x_3 , both referring to a typical hydrocarbon-air mixture that corresponds to $\nu_F = 7$, as well as the front parameter $y = 1/M^2$. The latter exhibits most distinctly the effect of the geometry on the strength of the wave generated by the flame—the Mach Number increasing considerably from a point- to a plane-symmetrical case for the same value of S , while the corresponding change in x_3 is quite insignificant.

Since the space profiles of the gasdynamic parameters are, for the point- and line-symmetrical geometries, quite similar in character, while, for the plane-symmetrical case, they are reduced to the trivial case of plateaus of constant values, graphic displays for cylin-

is the molecular weight of burnt gas at point 4 figure 2 where conditions are known but not the chemistry. Hence this molecular weight cannot be calculated.

drical and planar waves are relatively uninformative and they are, therefore, not presented. In any case, the velocity, temperature, and pressure profiles can be easily derived from Figs. 9 and 10 and Eqs. (4) and (5).

Instead then, presented here finally in Fig. 11 are the significant pressure levels as a function of the burning speed S attained in a combustible medium corresponding to $\nu_F=7$. For the same burning speeds, the differences between the three geometries are quite significant, the plateau of $p_3=p_2$ for the plane-symmetrical wave being appreciably higher than the pressure

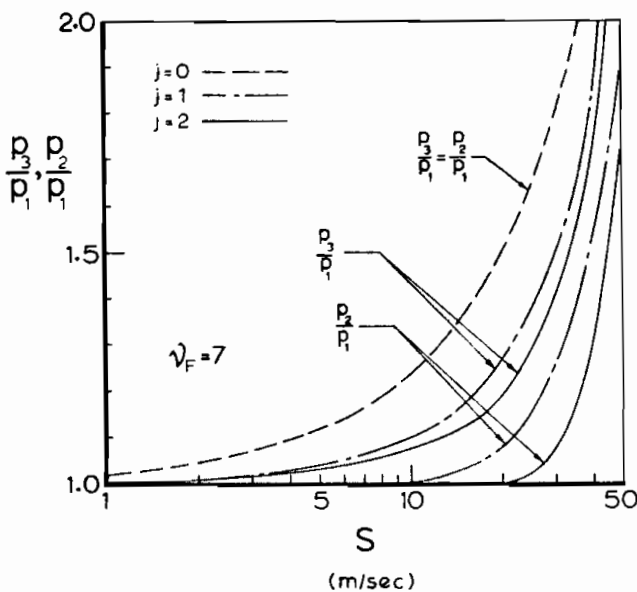


FIG. 11. Significant pressure levels as a function of the burning speed S for point-, line-, and plane-symmetrical waves ($\gamma=1.3$, $\gamma_4=1.2$, $a_1=345$ m/sec, $\nu_F=7$).

levels in the other two cases. In practice, one can expect such high pressures to be attained whenever the flame front is well confined, as in corridors or tunnels. The solution for the spherically-symmetric case gives, of course, the lower bound. In safety codes for buildings, an overpressure level of 0.3 atm is considered to be definitely destructive. This limit is attained at the flame front for burning speeds of 12, 21, and 25 m/sec for plane-, line-, and point-symmetrical cases, respectively. This, however, does not include the dynamic effects of wall reflections, which should make the situation considerably worse. Taking proper account of such effects is, however, left outside the scope of this publication.

Nomenclature

a	sound speed
F	$\equiv (t/r\mu)u$, reduced blast-wave parameter
h	enthalpy
j	geometric factor ($=0, 1, 2$, for plane, line, or point symmetry, respectively)
\mathfrak{M}	molecular weight (with subscript denoting state) or molecular weight ratio (without subscript) see comment in top margin
M	Mach Number of shock front
p	pressure
P	pressure ratio
q	heat released per unit mass
r	radius
S	local flame propagation or burning speed
t	time
T	absolute temperature
u	particle velocity
v	specific volume
w	wave-front velocity
x	$\equiv r/r_2$, nondimensional radius; similarity variable
y	$\equiv 1/M^2$, front parameter
Z	$\equiv [(t/r\mu)a^2]$, reduced blast-wave parameter
β	$\equiv (\gamma_4-1)/(\gamma_4+1)$
γ	specific heat ratio
ζ	$=\gamma Z_p$, modified reduced blast-wave parameter
μ	$=t_2w_2/r_2$, blast front velocity modulus
ν	specific volume ratio
ρ	density
τ	nondimensional time; similarity variable
ϕ	velocity potential

Subscripts

1	state ahead of shock front
2	state immediately behind shock front
3	state immediately ahead of deflagration
4	state behind deflagration
d	denotes deflagration
p	denotes piston
F	end state for a constant-pressure deflagration from state 1; relative change of a parameter between 1 and F
f	end state for a constant-pressure deflagration from state 3; relative change of a parameter between 3 and f
P	denotes products
R	denotes reactants
CJ	denotes Chapman-Jouquet deflagration

Acknowledgment

The authors express their appreciation to Professor Heinz Wagner who suggested the problem and

provided them with the background information, including the specification of conditions for numerical solutions presented in the paper.

REFERENCES

1. URTIEW, P. A. AND OPPENHEIM, A. K.: Proc. Roy. Soc. *A295*, 13 (1966).
2. OPPENHEIM, A. K.: Significance of Blast Wave Studies to Propulsion, Proceedings of the XXI International Astronautical Congress (in press), 1970.
3. STREHLOW, R. A.: Preceding paper, This Symposium.
4. TAYLOR, G. I.: Proc. Roy. Soc. *A186*, 273 (1946).
5. SEDOV, L. I.: Similarity and Dimensional Methods in Mechanics, Moscow, Gostekhizdat, 4th ed., 1957; English translation: M. Holt, Ed., Academic Press, 1959, (especially Chap. 4, Sec. 9, pp. 200-206).
6. SHIKIN, I. S.: Investigation of Some Problems of Detonations and Combustion in Media of Variable Density, (Issledovanie Nekotorykh Zadach o Detonakii i Gorenii w Sredakch z Peremennoi Plotnostiu), *News of Moscow University* (Viestnik Moskovskovo Universyteta), Series on Math., Mech. Astron. Phys. Chem. *12*, 49 (1957).
7. COURANT, R. AND FRIEDRICHS, K. O.: *Supersonic Flow and Shock Waves*, especially Chap. VI, Sec. 162, pp. 424-429. Wiley 1948.
8. OPPENHEIM, A. K., LUNDSTROM, E. A., KUHL, A. L., AND KAMEL, M. M.: *J. Appl. Mech.* *38*, E4, 783 (1971).
9. OPPENHEIM, A. K., KUHL, A. L., LUNDSTROM, E. A., AND KAMEL, M. M.: *J. Fluid Mech.* *52*, 657 (1972).
10. ZAJAC, L. J. AND OPPENHEIM, A. K.: *Combust. Flame* *13*, 537 (1969).
11. ZELDOVICH, YA. B.: *Sov. Phys.* (English translation) *6*, 537 (1958).

COMMENTS

H. - Gg. Wagner, University of Gottingen, Gottingen, W. Germany. The paper is, in my opinion, of great importance to the subject of pressure waves that can be generated by unconfined clouds of explosive air-fuel mixtures. In particular, the pressure profiles are completely different from those of classical blast waves of point explosions, in that the pressure increases with time behind the shock front, rather than decreasing. One should expect, therefore, that since their positive action persists over a much longer period of time, the effect of such waves on buildings should be considerably more destructive.

In this connection, I have the following questions: (1) Since pressure waves that can cause real damage are associated with turbulent flame velocities, while the most likely start of combustion should be in the form of laminar flame, how is the pressure wave affected by flame acceleration, and how soon can one expect steady flame conditions, treated in the paper, to be established? (2) How is the pressure profile modified after the explosive cloud is burned? I would expect that its decay should be significantly slower than that of a blast wave caused by point explosion and, hence, its effects should extend over appreciably longer distances from the source; (3) How is the pressure wave

affected by reflections from the ground or a wall, and from a corner between the ground and the wall?

Such information should be quite valuable, since it would allow us to set more realistic upper bounds on stress resistance of buildings which are to be, for some special reason, protected from destruction by explosive clouds, than is possible at present.

Authors' Reply. The questions posed are well taken, in that they extend well beyond the scope of our paper. Specific answers to them can be found only by numerical computations.

We considered the problem of acceleration, and prepared a few slides demonstrating a typical solution obtained by the method of characteristics. Although they are qualitatively correct, their quantitative value is questionable, due to the inappropriateness of the Hartree method we used for this purpose, and the unrealistic assumption concerning the flame acceleration. We intend to carry out such computations by the use of a Lagrangian code especially suited for this purpose.

We also considered the problem of reflection from a wall or the ground. The solution involves the use of a two-dimensional code for nonsteady flow analysis, and we had the good fortune of

II FORTRAN VERSION MOC Programme Variables

would prove difficult to accommodate in the chosen DDT model. Since the location

- 136 -

Principle Names used by Program PISTON

(in order of appearance)

MAIN ROUTINE

I, J	refers to the point of intersection of the I th positive and the J th negative characteristic
XX	distance)
TT	time)
UU	particle velocity) used in the graph plotting routine
CC	sonic velocity)
PP	gas pressure)
X	distance at a point on the characteristic network
T	time at a point on the characteristic network
U	particle velocity at a point on the characteristic network
C	Sonic velocity at a point on the characteristic network
S	entropy at a point on the characteristic network
XS	distance co-ordinate of the shock wave
TS	time co-ordinate of the shock wave
US1	particle velocity behind the shock wave
US0	particle velocity in front of the shock wave
CS1	sonic velocity behind the shock wave
CS0	sonic velocity in front of the shock wave
SS1	entropy behind the shock wave
SS0	entropy in front of the shock wave
GAMMA	ratio of the gas specific heats
CO	sound speed in air at 20°C
XO	scaling length (set to unity in this work)
VELSH	shock wave velocity
WORKT	total work done by the piston (Ft. lbs F)
TSTOP	time at which the computation is terminated

PIST starting distance co-ordinate of the piston
JSE number of negative characteristics that are computed
XSTEP integration step length
IU number of positive characteristics ahead of the shock wave
IOST number of positive characteristics behind the shock wave
J END(I) negative characteristic at which the positive characteristic (I) terminates on the shock path

SUBROUTINE PT3

R1, R2, R3, R4, dependent variables at points 1,2,3 and 4
S1, S2, S3, S4 dependent variables at points 1,2,3 and 4
SS4 entropy at point 4

SUBROUTINE PATH

A0, A1, A2, A3 coefficients of the polynomial representing the piston path
WORK work increment done by the piston during a single integration step

SUBROUTINE SHOCK

SHMACH Shock wave Mach number

III FORTRAN VERSION MOC Programme Structure

THE FORMATION OF A SPHERICAL SHOCK WAVE BY AN ACCELERATING CONTACT SURFACE

Extracts from the PhD Thesis
by JC Gibbs

LONDON October 1973

2.1 External Gas Movements and The Method of Characteristics

The unsteady one-dimensional flow of an ideal gas is governed by a set of quasilinear partial differential equations of the hyperbolic type.

$$\frac{\partial \rho}{\partial t} + u \frac{\partial \rho}{\partial x} + \rho \frac{\partial u}{\partial x} + (\eta - 1) \frac{\rho u}{x} = 0 \quad (2.1)$$

$$\frac{\partial u}{\partial t} + u \frac{\partial u}{\partial x} + \frac{1}{\rho} \frac{\partial P}{\partial x} = 0 \quad (2.2)$$

$$\frac{\partial S}{\partial t} + u \frac{\partial S}{\partial x} = 0 \quad (2.3)$$

$$P = P_0 \left[\frac{\rho}{\rho_0} \right]^\eta \exp \left[\frac{S - S_0}{C_v} \right] \quad (2.4)$$

where $\eta = 1, 2$ or 3 for planar, cylindrical or spherical flow. The first two equations express the conservation of mass and momentum respectively, the third is the necessary condition for isentropic flow and the fourth is the equation of state for an ideal gas.

The sound speed c is given by the relation:

$$c^2 = \left[\frac{\partial P}{\partial \rho} \right]_S = \text{const.} \quad (2.5)$$

Using equations (2.5) and (2.3) the derivatives of the ... (2.1) can be eliminated to give:

$$\frac{\partial P}{\partial t} + u \frac{\partial P}{\partial x} + \rho c^2 \frac{\partial u}{\partial x} + (\eta - 1) \rho \frac{u c^2}{x} = 0 \quad (2.6)$$

In these equations the direction of differentiation of each dependant variable is different. However a linear combination of equations (2.2) and (2.6) can be formed such that each variable is differentiated in the same direction. These are known as the characteristic directions and along them the partial derivatives become total.

Multiplying equation (2.2) by λ and adding to equation (2.6) gives:

$$\frac{\partial P}{\partial t} + \frac{\partial P}{\partial x} \left[u + \frac{\lambda}{\rho} \right] + \lambda \frac{\partial u}{\partial t} + \frac{\partial u}{\partial x} \left[\lambda u + \rho c^2 \right] + (\eta - 1) \rho \frac{u c^2}{x} = 0 \quad (2.7)$$

The condition that P and u are differentiated in the same direction is then:

$$u + \frac{\lambda}{\rho} = u + \frac{\rho c^2}{\lambda}$$

from which:

$$\lambda = \pm \rho c$$

Each value of λ gives a characteristic direction whose path becomes:

$$(\lambda_1) \quad \frac{dx}{dt} = u + c, \quad (\lambda_2) \quad \frac{dx}{dt} = u - c$$

Along each of these directions equation (2.7) reduces to:

$$(\lambda_1) \quad \frac{dP}{dt} + \rho^c \frac{du}{dt} + (\eta - 1) \frac{\rho u c^2}{x} = 0 \quad (2.8)$$

$$(\lambda_2) \quad \frac{dP}{dt} - \rho^c \frac{du}{dt} + (\eta - 1) \frac{\rho u c^2}{x} = 0 \quad (2.9)$$

Also along a third direction $(\lambda_3) \quad \frac{dx}{dt} = u$, the entropy equation (2.3) becomes:

$$(\lambda_3) \quad \frac{dS}{dt} = 0 \quad (2.10)$$

The form of the characteristic equations (2.8), (2.9) and (2.10) are ideal for numerical solution by finite difference techniques along a network of characteristic directions. It is convenient to replace u and c by a new set of dependent variables which have a special significance for one-dimensional planar flow that will be explained shortly.

$$r = \frac{u}{2} + \frac{c}{\gamma - 1} \quad (2.11)$$

$$s = \frac{u}{2} - \frac{c}{\gamma - 1} \quad (2.12)$$

The characteristic directions now become:

$$(\lambda_1) \quad \frac{dx}{dt} = \frac{(\gamma + 1)}{2} r - \frac{(\gamma - 3)}{2} s \quad (2.13)$$

$$(\lambda_2) \quad \frac{dx}{dt} = \frac{(3 - \gamma)}{2} r + \frac{(\gamma + 1)}{2} s \quad (2.14)$$

$$(\lambda_3) \quad \frac{dx}{dt} = r + s \quad (2.15)$$

Also from the equation of state (equation 2.4) and the use of the definition of the sound speed (equation 2.5) the following relationship is derived.

$$\frac{dP}{\rho c} = \frac{2}{\gamma - 1} dc - \frac{c}{c_p (\gamma - 1)} dS \quad (2.16)$$

and hence the characteristic equations become.

$$(\lambda_1) \quad \frac{dr}{dt} = \frac{1}{4C_p} (r - s) \frac{dS}{dt} - \frac{(\gamma - 1)}{4} (r^2 - s^2) \frac{(\eta - 1)}{x} \quad (2.17)$$

$$(\lambda_2) \quad \frac{ds}{dt} = \frac{1}{4C_p} (s - r) \frac{dS}{dt} - \frac{(\gamma - 1)}{4} (s^2 - r^2) \frac{(\eta - 1)}{x} \quad (2.18)$$

$$(\lambda_3) \quad \frac{dS}{dt} = 0 \quad (2.19)$$

It can be seen that for one-dimensional planar homentropic flow, as distinct from isentropic flow, that the new dependant variables are constant along their respective characteristics and are generally referred to as the Riemann invariants. This considerably simplifies the calculations and leads to analytic solutions for some special cases.

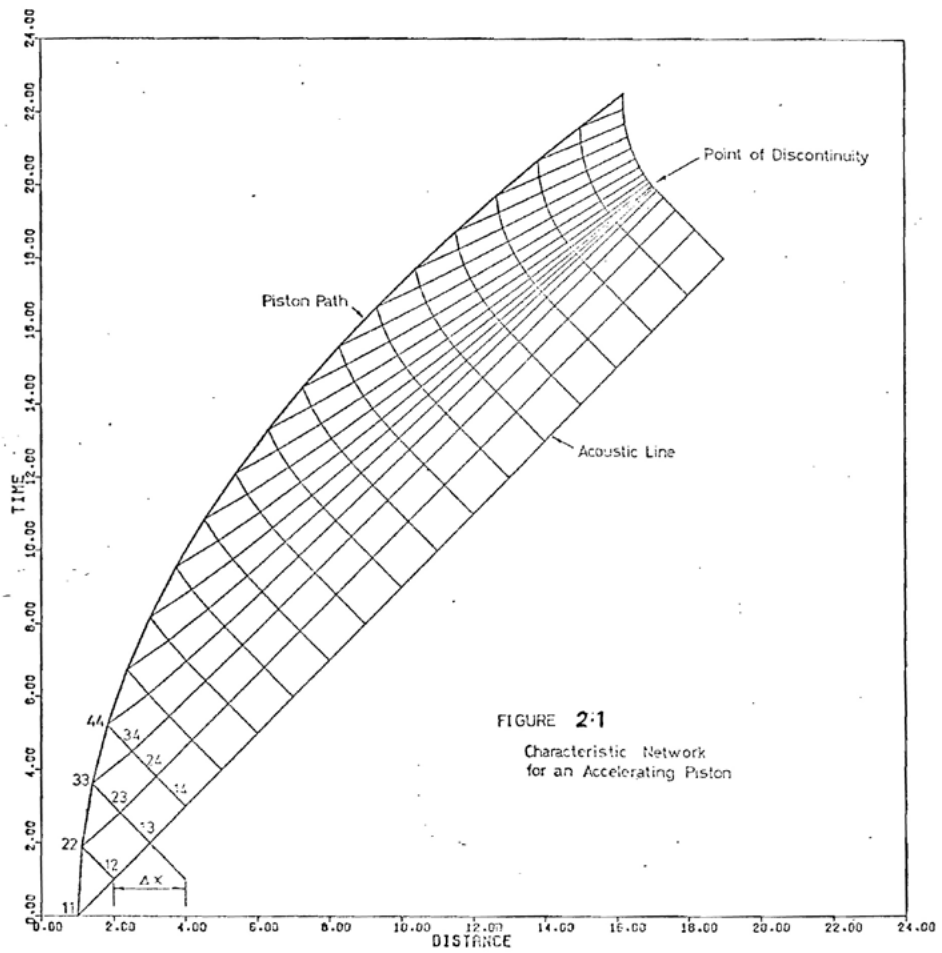
The normal solution of equations (2.17), (2.18) and (2.19) is obtained by replacing the differentials by finite difference relations and assuming the variable coefficients are constant over the step length. The correct value for the coefficient is obtained by iteration procedures.

The method adopted in this work for the solution of these equations makes use of a C.D.C. 6400 computer and the programing methods described below are based on the techniques presented by Courant and Friedrichs (1948), Ferri (1961), Glass (1959), and Hartree (1953).

2.2 A Computer Program To Determine The Motion of a Gas Ahead of an Expanding Spherical Piston

A computer program has been written which solves the flow equations, using the method of characteristics, for a gas moving in front of an expanding spherical piston. It deals with both compression and rarefaction waves and can introduce a single discontinuity into the flow at the appropriate time and position. Use of the program is limited to a continuous piston motion and is easily adapted to deal with one-dimensional cylindrical and planar flows. The program, for which a listing and flow diagram appears in Appendix B, consists of the main routine, PISTON, which sets the boundary and initial conditions, controls the integration steps and builds up the characteristic network and shock profile. Three subroutines, PT3, PATH and SHOCK are called during the integration to determine the gas properties throughout the required distance-time domain.

In the early stages of the integration the execution of the main program is straight forward and it is only when discontinuities have to be introduced into the flow that more complex procedures are adopted. Initially integration is performed over a network of characteristics as in Figure 2.1, the upper left hand boundary representing the path of an accelerating piston and the lower right hand boundary the path of the first disturbance caused by the piston motion which travels at the speed of sound. The conditions at the starting point (1,1) are known, since there is no motion at $t = 0$. The step length Δx determines the starting point (1,2) of the next negative characteristic. The conditions at this point, which is on the acoustic line, are again those of the undisturbed gas and they determine the gradient of the characteristic drawn to intersect the piston path at point (2,2). From this point a new positive characteristic is introduced and its first intersection is with the third negative one at point (2,3). The procedure is continued by integrating up each negative



characteristic to the piston and thus building up the network. It can be seen that there are three types of intersection, (i) at the acoustic line, (ii) in between each of the boundaries, and (iii) at the piston path. The co-ordinates and gas properties at intersections of type (i) are easily determined due to the undisturbed conditions along the acoustic line, those of type (ii) and (iii) are determined by calling the subroutines PT3 and PATH respectively.

SUBROUTINE PT3

In general subroutine PT3 is called from the main program to determine any point on the network (i, j) where $i \neq 1$ or $i \neq j$. It is supplied with the co-ordinates of and the values of gas velocity, ^{sonic velocity} and entropy at the points (i-1, j) and (i, j-1) and it returns the respective values for point (i, j). The method is described below with the use of Figure 2.2

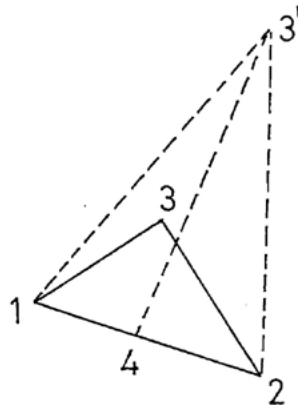


Figure 2.2 Part of the characteristic network

If all the flow parameters and the co-ordinates are known at points 1 and 2 on part of the network and provided the points are sufficiently close

together the assumption that the characteristic directions are straight and the dependant variables change linearly between any two points is quite acceptable. The co-ordinates of point 3, to a first approximation, are those of point 3' and are determined from the solution of equations (2.13) and (2.14) using the values of r and s for points 1 and 2. The entropy at point 3' is found by projecting a path line from point 4 suitably chosen to intersect 3'. Along a path line entropy is conserved and therefore the value of S_3 , is found by linear interpolation between S_1 and S_2 . A similar procedure for determining the values of r_3 , and s_3 , is adopted, this time using equations (2.17) and (2.18). A second approximation to the co-ordinates and the values of r_3 , s_3 and S_3 can be made by repeating the calculations using the mean values for the quantities on the right hand side of the equations instead of the initial values.

The error incurred by approximating the differential equations in this way is of the order $(\Delta t)^3$ for each integration step; it is cumulative and may lead to instabilities of the solution if the integration step is too large or if the calculations are extended over too great a domain.

SUBROUTINE PATH

Subroutine PATH is called from the main program to determine the profile of the piston path together with the co-ordinates and gas properties at the points where the characteristics intersect. It is supplied with these values for the point $(j-1, j)$ and imposes the necessary boundary conditions that exist at the piston. At this surface the gas velocity is equal to that of the piston due to there being zero mass flux across the boundary. The movement of the piston is determined by the values of the co-efficients of a polynomial which are chosen either to fit experimental data or are suitable alternatives. The method used in this subroutine is described below using Figure 2.3.

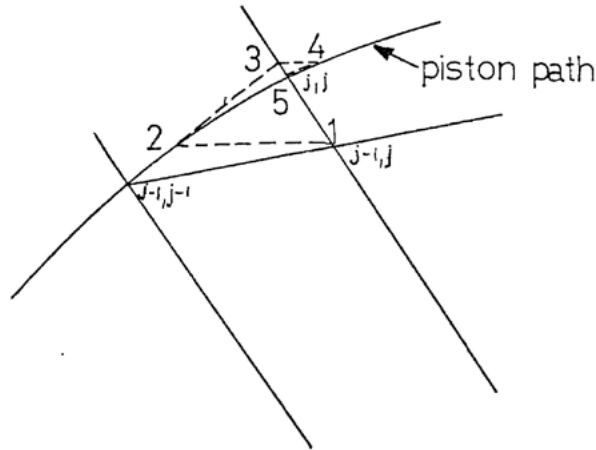


Figure 2.3 Intersection of a characteristic and the piston path

Knowing $x = f(t)$ for the piston path an initial estimate is made of $t_{j,j}$ by setting $t_{j,j} = t_{j-1,j}$. The value of x at point 2 is now given by $x = f(t_{j,j})$ and the corresponding value of gas velocity or piston speed is $\frac{dx}{dt} = f'(t_{j,j})$. A line is now drawn with this gradient to intersect the negative characteristic projected from point $(j-1,j)$ at point 3. The value of the time co-ordinate at point 3 gives an improved estimate of $t_{j,j}$. An iteration procedure is now implemented, calculating points 4, 5, etc., until convergence is complete. The value of s at the point of intersection is found from equation (2.18) and knowing the gas velocity the sonic velocity can be determined. The entropy, S , is taken as being equal to that of the undisturbed gas because, the piston motion being continuous, the gas at its surface undergoes no irreversible processes. The subroutine also calculates the amount of work done by the expanding piston on the gas that is driven ahead of it.

As the characteristic network is built up a point will be reached at

which two positive characteristics intersect. The values of r and s on each characteristic at this point will differ and lead to a discontinuity in the solution with which the procedure used up to now will not deal. To overcome this problem a shock wave is introduced into the flow and the integration is performed as before on either side with the Rankine-Hugoniot relations used to take the solution from one side to the other. It is at this point that the main program revises its method for fixing the starting co-ordinates of all negative characteristics. The positive characteristics will initially intersect the shock path from both behind and ahead and determine its profile by the values of r and s they carry. It is convenient to start the new negative characteristics at such a position on the acoustic line that they meet the shock and the positive characteristics at their intersection points (figure 2.4).

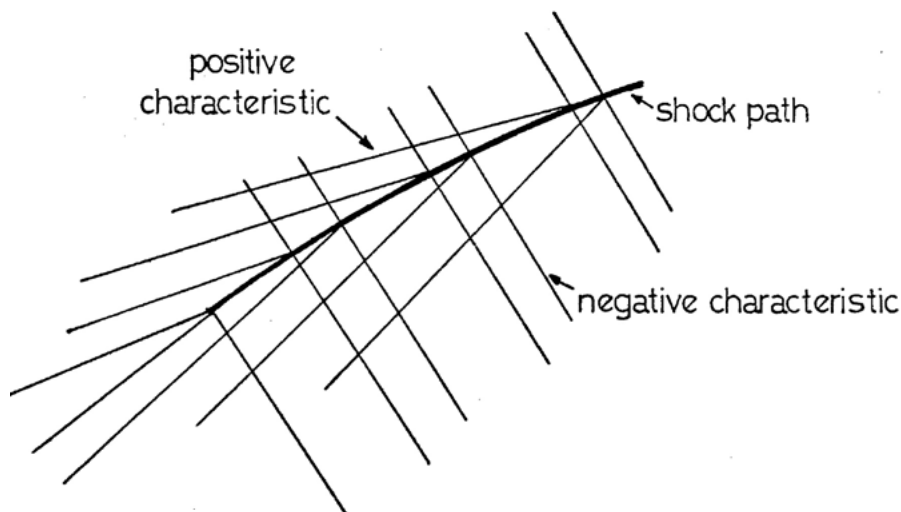


Figure 2.4 Positioning of new negative characteristics

An iterative procedure is adopted for choosing the starting point. There are two types of shock intersection points which have to be dealt with in slightly different ways, (i) the point where the positive characteristic

intersects the shock from ahead and (ii) the point where the positive characteristic intersects the shock from behind. In the first case normal integration is made upto the shock front at point (i,j) (figure 2.5).

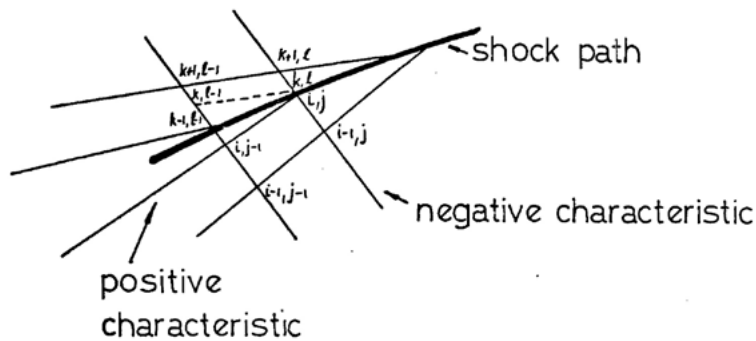


Figure 2.5 Positive characteristic intersection ahead of the shock wave

The shock velocity is chosen such that its transition is compatible with the conditions of flow already existing behind it. The program initially sets the shock velocity equal to $(u + c)_{k+1;l-1}$ and then by calling subroutine SHOCK with the gas properties at point (i,j) , the Rankine-Hugoniot conditions are used to determine the appropriate values at point (k,l) behind the shock. The approximate values of these properties can be determined by introducing a further positive characteristic between points $(k,l-1)$ and (k,l) and using equation (2.17). The flow properties at point $(k,l-1)$ and the gradient of this characteristic are found by interpolation between points $(k+1, l-1)$ and $(k-1, l-1)$. The shock velocity is adjusted and the procedure repeated until the solution for the conditions at point k,l converges. The integration is now continued to the piston path as before.

For the second case integration proceeds upto point $(i-1, j)$ (figure 2.6) and then a new positive characteristic is introduced between points $(i, j-1)$

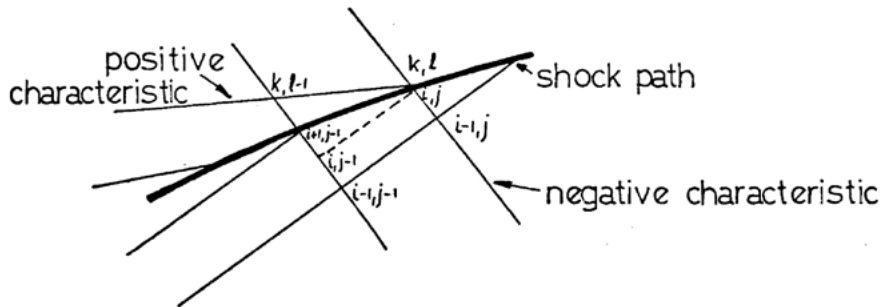


Figure 2.6 Positive characteristic intersection behind
the shock wave

and (i, j) . The flow properties at point $(i, j-1)$ and the gradient of this characteristic are found by interpolation between points $(i+1, j-1)$ and $(i-1, j-1)$. Subroutine PT3 is called to determine the appropriate values at point (i, j) immediately in front of the shock. An initial guess of the shock velocity is made and subroutine SHOCK called for the conditions behind the wave at point (k, l) . As in the previous case the conditions at point (k, l) are also determined from point $(k, l-1)$ using equation (2.17) and an identical procedure is used to find the correct shock velocity. Eventually the shock wave will be intersected from ahead by the final positive characteristic whereupon it emerges into the undisturbed gas. The integration is now solely performed behind the shock wave and is started by calling subroutine SHOCK and continuing as in case one.

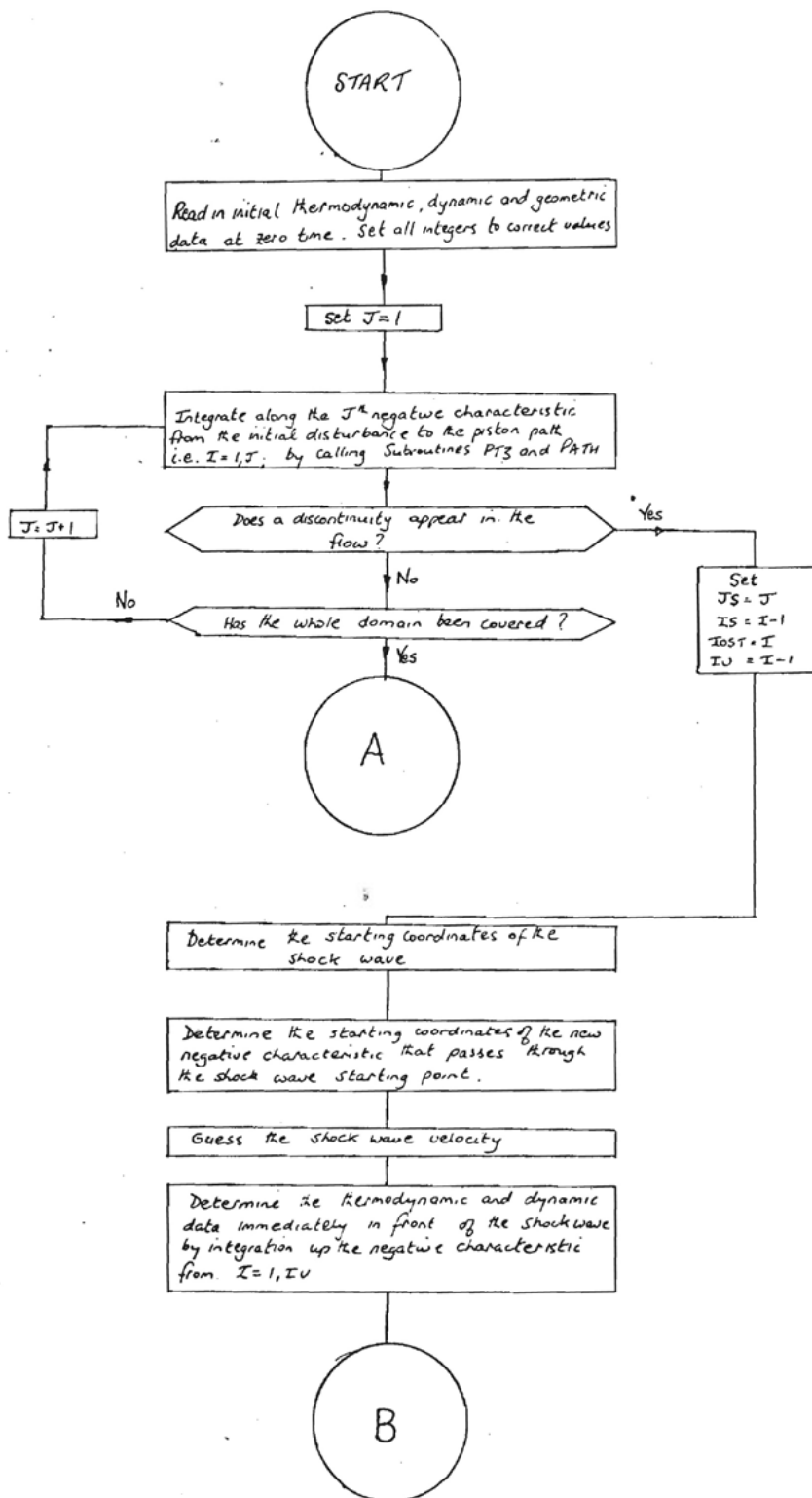
The main program ends by making use of the computer graph plotting

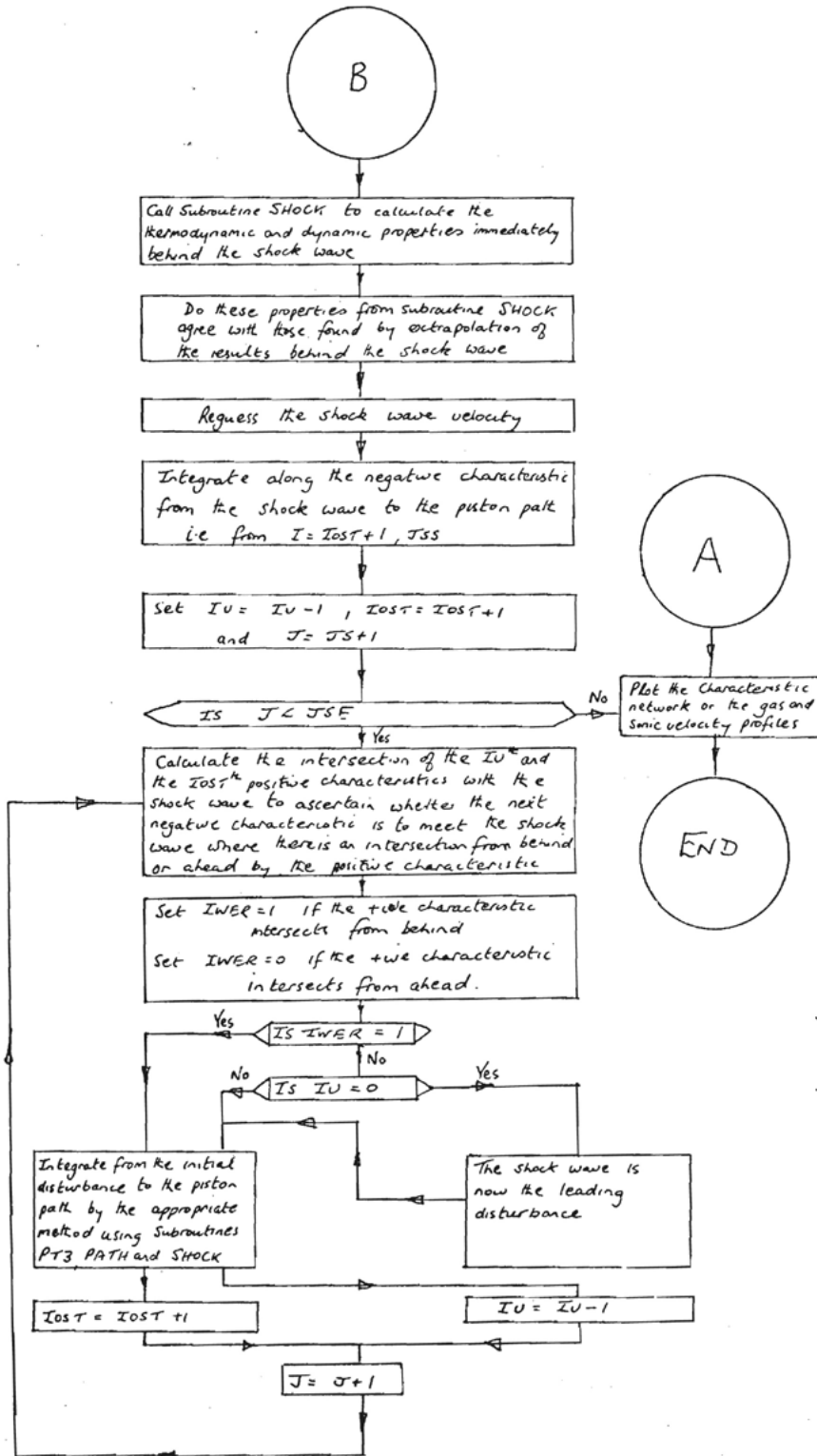
facilities. The entire characteristic network can be drawn together with the piston and shock paths. Alternatively, gas velocity and sonic velocity profiles can be plotted for a series of six constant time lines between the piston path and the outermost disturbance.

2.3 Gas Movements Inside the Vessel During Discharge

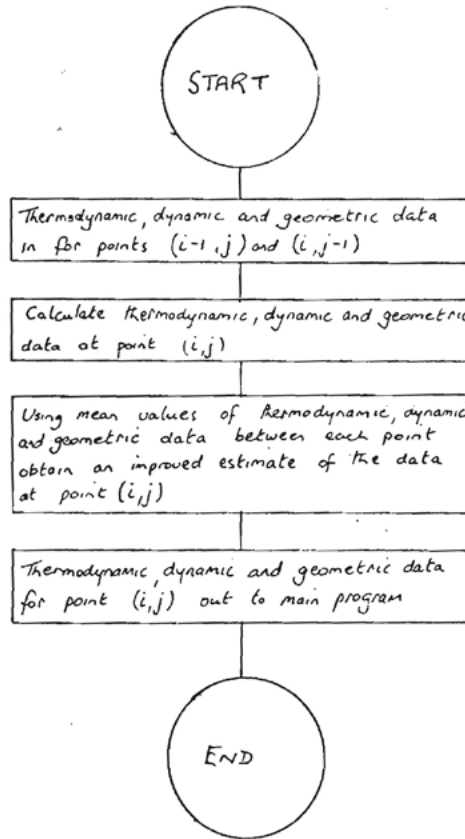
Giffen (1940) discusses the theory of the rapid discharge of a gas from a vessel which had at the time an important part to play in the exhaust process of an internal-combustion engine. The implications of the term "rapid discharge" are considered and it is pointed out that the rate of release of a gas determines the criterion used for developing the associated theory. One method uses the theory of propagation of waves within the vessel and allows for internal pressure gradients. A second uses a quasi-steady state theory which, being an approximation, considers the gas pressure in the vessel to be uniform and the gas velocity as being negligible. The former theory has obvious advantages when the area, A_2 , of the orifice formed after the rupture of a bursting disc is not small compared with the cross-sectional area of the vessel, A_1 . In this case the rate of fall of pressure at the orifice end of the vessel will be significant before the disturbance can be transmitted throughout the whole volume giving rise to internal pressure gradients. For a relatively small orifice area the pressure drop is considerably less and the disturbance is transmitted throughout the vessel before any further significant pressure drop can take place and therefore the approximation of a uniform vessel pressure is valid. Kestin and Glass (1951) examined the rate of discharge of gas using Giffen's wave theory and compared it with the values obtained from the quasi-steady state theory. It was shown that the latter method gave mass flow rates which were considerably less than those predicted by the wave theory and from experimental data. The discrepancy between the two theories was most apparent

FLOWCHART FOR PROGRAM PISTON

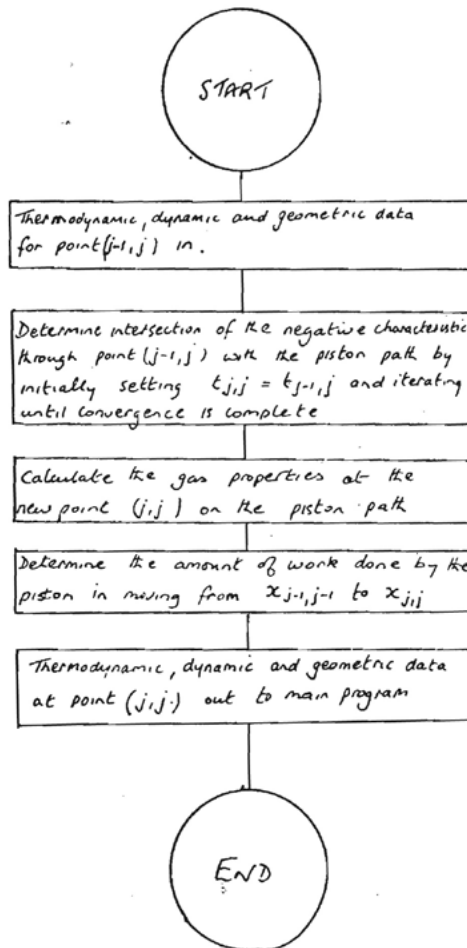




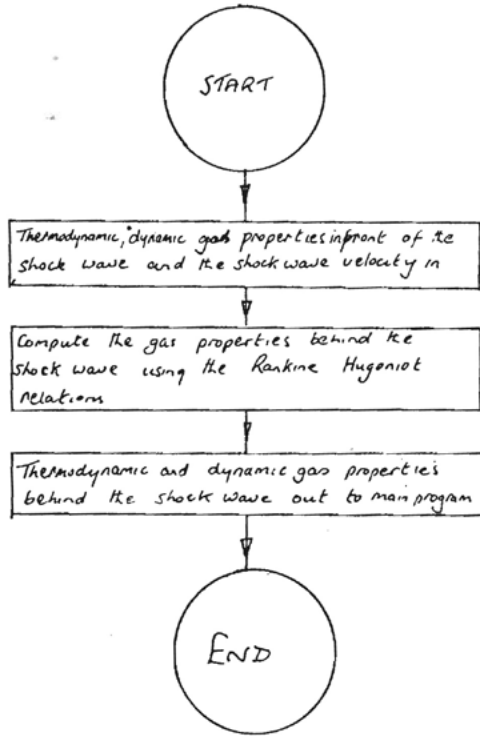
FLOWCHART FOR SUBROUTINE PT3



FLOWCHART FOR SUBROUTINE PATH



FLOWCHART FOR SUBROUTINE SHOCK



**DDT Excess PressureModels
ETH High Hydrogen Project
DELIVERABLE ONE**

DELIVERABLE ONE

Appendices

IV FORTRAN VERSION MOC Computer CODE

3.2.1 FORTRAN LANGUAGE CODE

```
PROGRAM PISTON(INPUT,OUTPUT,TAPE5=INPUT,TAPE6=OUTPUT,TAPE62)
DIMENSION XX(100),TT(100)
COMMON X(50,50),T(50,50),U(50,50),C(50,50),S(50,50),XS(50),TS(50),
JEND(50),US1(50),US0(50),CS1(50),CS0(50),SS1(50),SS0(50)
COMMON/ONE/GAMMA,C0,X0,ETA,I,J,VELSH,IP,WORKT
WRITE(6,597)
597 FORMAT(/1X,'.....OUTPUT FROM DECK NUMBER1,.....')
IP=0
WORKT=0.0
X0=1.0
C0=1126.0
ISTOP=20.0
TSTOP=TSTOP*C0/(X0*10.0**3)
GAMMA=1.4
ETA=2.0
ETA=0.0
PIST=1.0
PIST=PIST/12.0
XSTEP=0.1
JSE=49
JSTOP=JSE
DO 400 I=1,JSE
JEND(I)=JSE
400 CONTINUE
DO 20 J=1,JSE
JS=J
XSTART=PIST+FLOAT(J-1)*XSTEP
DO 21 I=1,J
IS=I-1
IF(I-1) 25,25,26
25 X(I,J)=(XSTART+PIST)/2.0
T(I,J)=X(I,J)-PIST
U(I,J)=0.0
C(I,J)=1.0
S(I,J)=1.0
GO TO 27
26 IF(I-J)23,22,22
22 CALL PATH
GOTO 24
23 CALL PT3
IF (T(I,1)-T(I-1,J)) 28,28,29
29 CONTINUE
24 CONTINUE
27 CONTINUE
WRITE(6,31)I,J,X(I,J),T(I,J),U(I,J),C(I,J),S(I,J)
31 FORMAT(1X,2I5,5(4X,F12.6))
21 CONTINUE
20 CONTINUE
WRITE(6,33)
33 FORMAT(1X,'NO SHOCK FORMATION IN THE REGION OF INTEGRATION')
GOTO 32
```

```

28 I=IS+1
J=JS
XT1=(X(I,J)-X(I,J-1))/(T(I,J)-T(I,J-1))
XT2=(X(I-1,J)-X(I-1,J-1))/(T(I-1,J)-T(I-1,J-1))
TS(JS)=(X(I-1,J-1)-X(I,J-1)+XT1*T(I,J-1)-XT2*T(I-1,J-1))/(XT1-XT2)
XS(JS)=X(I-1,J-1)+XT2*(TS(JS)-T(I-1,J-1))
WRITE(6,30)TS,JS,XS(JS),TS(JS)
30 FORMAT(1X,2(5X,I3),5X,'THE SHOCK REGION TO FORMAT X=';F5.3;'AND A
TIME OF';F6.3)
32 CONTINUE
J=JS
JSS=JS
IU=IS
JEND(IS)=JS
JEND(IS+1)=JS
I0=JSS-IS
IOST=IS+1
VELSH=U(IOST,JSS-1)+S(IOST,JSS-1)
XSTART=PIST+FLOAT(JSS-1)*XSTEP+XS(JSS)-X(IOST,JSS-1)
34 CONTINUE
DO 131 I=1,IU
IF(I-1) 35,35,36
35 X(I,J)=(XSTART+PIST)/2.0
T(I,J)=X(I,J)-PIST
U(I,J)=0.0
C(I,J)=1.0
S(I,J)=1.0
GO TO 37
36 CALL PT3
37 CONTINUE
131 CONTINUE
XERR=XS(JSS)-X(IU,JSS)
IF(ABS(XERR)-0.00001) 38,38,39
39 XSTART=XSTART+XERR
GOTO 34
38 CONTINUE
DO 601 I=1,IU
WRITE(6,120)I,J,X(I,J),T(I,J),U(I,J),C(I,J),S(I,J)
120 FORMAT(1X,2I3,6X,5F10.5)
601 CONTINUE
US0(JSS)=U(IU,JSS)
CS0(JSS)=C(IU,JSS)
SS0(JSS)=S(IU,JSS)
42 CALL SHOCK
U(IOST,JSS)=US1(JSS)
C(IOST,JSS)=CS1(JSS)
S(IOST,JSS)=SS1(JSS)
X(IOST,JSS)=XS1(JSS)
T(IOST,JSS)=TS1(JSS)
C CHECK THE SHOCK VELOCITY HAS BEEN CHOSEN CORRECTLY
R1=(U(IOST,JSS-1)/2.0)+C(IOST,JSS-1)/(GAMMA-1.0)
S1=(U(IOST,JSS-1)/2.0)-C(IOST,JSS-1)/(GAMMA-1.0)

```

```

RSH1=(U(IOST,JSS)/2.0)+C(IOST,JSS)/(GAMMA-1.0)
SSH1=(U(IOST,JSS)/2.0)-C(IOST,JSS)/(GAMMA-1.0)
SR1=(R1-S1+RSH1-SSH1)/2.0
SR2=(R1**2-S1**2+RSH1**2-SSH1**2)/2.0
X1=(X(IOST,JSS)+X(IOST,JSS-1))/2.0
R3=R1+SR1*(S(IOST,JSS)-S(IOST,JSS-1))/4.0-((GAMMA-
1.0)/4.0)*SR2*ETA/X1*(T(IOST,JSS)-I(IOST,J-1))
RERR=R3-RSH1
IF(ABS(RERR)-0.00001) 40,40,41
41 VELSH=VELSH+RERR
GOTO 42
40 CONTINUE
WRITE(6,117)VELSH,J,RERR
117 FORMAT(1X,'A SHOCK VELOCITY OF',F10.5,'ON J=',I3,'GIVES A RERR
OF',F10.5)
WRITE(6,700)J,VELSH
700 FORMAT(/1X,I5,4X,F6.4,'USCSSS')
WRITE(6,701)USC(J),CS0(J)SS0(J)
701 FORMAT(1X,'0',3(4X,F8.5))
WRITE(6,702)US1(J),CS1(J),SS1(J)
702 FORMAT(1X,'1',3(4X,F8.5))
C PROCEED FROM THE SHOCK TO THE PISTON PATH
IOST1=IOST+1
DO 43 I=IOST1,JSS
IS=I-1
JS=J
IF(I-J)44,45,45
45 CALL PATH
GO TO 46
44 CALL PT3
IF(T(I,J)-T(I-1,J)) 47,48,48
48 CONTINUE
46 CONTINUE
WRITE(6,121)I,J,X(I,J),T(1,J),U(I,J),C(I,J),S(I,J)
121 FORMAT(1X,2I3,5X,5F10.5)
43 CONTINUE
GO TO 99
47 WRITE(6,49)I,J
49 FORMAT(1X,'SORRY CHOSEN INCORRECT SHOCK STARTING POINT',2I4
GO TO 29
99 CONTINUE
IU=IU-1
IOST=IOST+1
JS1=JS+1
DO 55 J=JS1,JSE
C CALCULATE INTERSECTION OF SHOCK WITH CHARACTERISTIC BEHIND
UC=U(IOST,J-1)+C(IOST,J-1)
TINT1=(X(IOST,J-1)-XS(J-1)+VELSH*TS(J-1)-US*T(IOST,J-1))/(VELSHUC)
XINT1=X(IOST,J-1)+UC*(TINT1-T(IOST,J-1))
IF(IU-1) 52,64,64
C CALCULATE INTERSECTION OF SHOCK WITH CHARACTERISTIC IN FRONT
64 UC=U(IU,J-1)+C(IU,J-1)

```

```

TINT0=(X(IU,J-1)-XS(J-1)+VELSH*TS(J-1)-UC*T(IU,J-1))/(VELSH-UC)
XINT0=X(IU,J-1)+UC*(TINT0-T(IU,J-1))
IF(XINT0-XINT1) 51,51,52
51 IWEP=0
XS(J)=XINT0
TS(J)=TINT0
GO TO 53
52 INER=1
XS(J)=XINT1
TS(J)=TINT1
53 CONTINUE
DXS=XS(J)-XS(J-1)
IF(DXS-0.5) 980,981,981
981 JSE=J-1
IF(JSTOP,EQ,JSE+1) JSTOP=JSE
GO TO 100
980 CONTINUE
IF(JSTOP-JSE) 997,996,996
996 IF(TSTOP-T(J-1,J-1)) 999,999,995
999 JSTOP=J-1
997 ISTOP=JSTOP
GO TO 995
998 ISTOP=J
995 CONTINUE
WRITE(6,107)J,XS(J),TS(J),IWEP
107 FORMAT(/1X,I3,'XS=',F10.5,'TS=',F10.5,'IWEP=',I3)
IF(IU-1) 180,181,181
181 CONTINUE
XSTART=PIST+FLOAT(J-1)*XSTEP+XS(J)-XS(J-1)
54 CONTINUE
DO 55 I=1,IU
IF(I-1) 56,56,57
56 X(I,J)=(XSTART+PIST)/2.0
T(I,J)=X(I,J)-PIST
U(I,J)=0.0
C(I,J)=1.0
S(I,J)=1.0
GO TO 58
57 CALL PT3
58 CONTINUE
55 CONTINUE
IF(IWER) 59,59,60
60 IU=IU+1
UC=U(I-1,J)-C(I-1,J)
VUC=VELSH-UC
TX=(Y(I-1,J)-XS(J-1)+TS(J-1)*VELSH-(T(I-1,J)*UC))/VUC
XX=X(I-1,J)+UC*(TX-T(I-1,J))
XERR=XS(J)-XX
IF(ABS(XERR)-0.00001) 65,65,66
66 XSTART=XSTART+XERR
GO TO 54
65 CONTINUE

```

```

DO 602 I=1,IU
WRITE(6,122)I,J,K(I,J),T(I,J),U(I,J),C(I,J),S(I,J)
122 FORMAT(1X,2I3,5X,5F10.5)
602 CONTINUE
I=IU+1
XWAIT=X(I,J-1)
TWAIT=T(I,J-1)
UWAIT=U(I,J-1)
CWAIT=C(I,J-1)
SWAIT=S(I,J-1)
C CALCULATE THE CONDITIONS AT THE SHOCK BOUNDARY BY PROJECTING A
NEXT
C +IVE CHARACTERISTIC BACKTO J-1
TBACK=TS(J)-T(I-1,J)+T(I-1,J-1)
63 UC=(UWAIT+U(I-1,J-1)-CWAIT-C(I-1,J-1))/2.0
XBACK=X(I-1,J-1)+UC(TBACK-T(I-1,J-1))
CBACK=C(I-1,J-1)+((CWAIT-C(I-1,J-1))*(TBACK-T(I-1,J-1)))/(TWAIT(
I-1,J-1))
UBACK=U(I-1,J-1)+((UWAIT-U(I-1,J-1))*(TBACK-T(I-1,J-1)))/(TWAIT(
I-1,J-1))
SBACK=S(I-1,J-1)+((SWAIT-S(I-1,J-1))*(TBACK-T(I-1,J-1)))/(TWAIT(
I-1,J-1))
X(I,J-1)=XBACK
T(I,J-1)=TBACKCALLPT3
XERR=XS(J)-X(I,J)
IF(ABS(XERR)-0.00001) 61,61,62
62 TBACK=TBACK-XERR
GOTO 63
61 CONTINUE
X(I,J-1)=XWAIT
T(I,J-1)=TWAIT
U(I,J-1)=UWAIT
C(I,J-1)=CWAIT
S(I,J-1)=SWAIT
US0(J)=U(I,J)
CS0(J)=C(I,J)
SS0(J)=S(I,J)
GO TO 182
180 CONTINUE
US0(J)=0.0
CS0(J)=1.0
SS0(J)=1.0
182 CONTINUE
JEND(IOST)=J
VELSH=U(IOST,J-1)+C(IOST,J-1)
69 CALL SHOCK
U(IOST,J)=USI(J)
C(IOST,J)=CSI(J)
S(IOST,J)=SSI(J)
X(IOST,J)=XSI(J)
T(IOST,J)=TSI(J)
R1=(U(IOST,J-1)/2.0)+C(IOST,J-1)/(GAMMA-1.0)

```

```

S1=(U(IOST,J-1)/2.0)-C(IOST,J-I)/(GAMMA-1.0)
RSH1=(U(IOST,J)/2.0)+C(IOST,J)/(GAMMA-1.0)
SSH1=(U(IOST,J)/2.0)-C(IOST,J)/(GAMMA-1.0)
SR1=(R1-S1+RSH1-SSH1)/2.0
SR2=(R1**2-S1**2+RSH1**2-SSH1**2)/2.0
X1=(X(IOST,J)+X(IOST,J-1))/2.0
R3=R1+SR1*(S(IOST,J-1))/4.0-((GAMMA-1.0)/4.0)*SR2*(ETA/
X1)*(T(IOST,J)-T(IOST,J-1))
RERR=R3-RSH1
IF(ABS(RERR)-0.00001) 67,67,68
68 VELSH=VELSH+RERR
IF(VELSH.LT.1.0) VELSH=1.0
GO TO 69
67 CONTINUE
WRITE(6,110)VELSH,J,RERR
110 FORMAT(1X,'A SHOCK VELOCITY OF',F10.5,'ON J=',I3,'GIVES A RERR
OF',510.5)
WRITE(6,800)J,VELSH
800 FORMAT(/1X,I5,4X,F6.4,'USCSSS')
WRITE(6,801)US0(J),CS0(J),SS0(J)
801 FORMAT(1X,*0*,3(4X,F8.5))
WRITE(6,802)US1(J),CS1(J),SS1(J)
802 FORMAT(1X,'1',3(4X,F8.5))
IOST=IOST+1
DO 70 I=IOST,ISTOP
IF(I-J) 71,72,72
72 CALL PATH
GO TO 73
71 CALL PT3
IF(T(I,J)-T(I-1,J)) 74,74,75
75 CONTINUE
73 CONTINUE
WRITE(6,123)I,J,X(I,J),T(I,J),U(I,J),C(I,J),S(I,J)
123 FORMAT(1X,2I3,5X,5F10.5)
70 CONTINUE
GO TO 77
74 WRITE(6,76)
76 FORMAT(1X,'SECOND SHOCK FORMATION')
77 CONTINUE
GO TO 50
59 XERR=XS(J)-X(IU,J)
IF(ABS(XERR)-0.00001)80,80,81
61 XSTART=XSTART+XERR
GO TO5 4
60 CONTINUE
DO 603 I=1,IU
WRITE(6,111)I,J,X(I,J),T(I,J),U(I,J),C(I,J),S(I,J)
111 FORMAT(1X,2I3,5X,5F10.5)
603 CONTINUE
JEND(IU)=J
US0(J)=U(IU,J)
CS0(J)=C(IU,J)

```

```

SS0(J)=S(IU,J)
84 CALLSHOCK
I=IOST-1
X(I,J)=XS(J)
T(I,J)=TS(J)
U(I,J)=US(J)
C(I,J)=CS(J)
S(I,J)=SS(J)
C CALCULATE THE INTERSECTION OF THE CHARACTERISTIC BEHIND THE SHOCK
WITH J-1
UC1=U(I,J)+C(I,J)
UC2=(JS1(J-1)+U(IOST,J-1))/2.0-(CS1(J-1)+C(IOST,J-1))/2.0
UC3=UC1-UC2
TX=(XS(J-1)-X(I,J)-UC2*TS(J-1)+UC1*T(I,J))/UC3
XX=XS(J-1)+UC2*(TX-TS(J-1))
UX=US1(J-1)+((U(IOST,J-1)-US1(J-1))*(TX-TS(J-1)))/(T(IOST,J-1)-
TS(J-1))
CX=CS1(J-1)+((C(IOST,J-1)-CS1(J-1))*(TX-TS(J-1)))/(T(IOST,J-1)-
TS(J-1))
SX=SS1(J-1)+((S(IOST,J-1)-SS1(J-1))*(TX-TS(J-1)))/(T(IOST,J-1)-
TS(J-1))
R1=UX/2.0+CX/(GAMMA-1.0)
S1=UX/2.0-CX/(GAMMA-1.0)
RSH1=US1(J)/2.0+CS1(J)/(GAMMA-1.0)
SSH1=US1(J)/2.0-CS1(J)/(GAMMA-1.0)
SR1=(R1-S1+RSH1-SSH1)/2.0
SR2=(R1**2-S1**2+RSH1**2-SSH1**2)/2.0
X1=(XX+XS(J))/2.0
R3=R1+SR1*(SS1(J)-SX)/4.0-((GAMMA-1.0)/4.0)+SR2*(ETA/X1)*(TS(J)-
TX1)
RERR=R3-RSH1
IF(ABS(RERR)-0.00001) 82,82,83
83 VELSH=VELSH+RERR
IF(VELSH.LT.1.0) VELSH=1.0
GO TO 84
82 CONTINUE
WRITE(6,112)VELSH,J,RERR
112 FORMAT(1X,'SHOCK VELOCITY OF',F10.5,'ON J=',I3,'GIVES A RERR
OF',F10.5)
WRITE(6,900)J,VELSH
900 FORMAT(/1X,I5,4X,F6.4,'USCSSS')
WRITE(6,901)US0(J),CS0(J),SS0(J)
901 FORMAT(1X,'0',3(4X,F8.5))
WRITE(6,902)US1(J),CS1(J),SS1(J)
902 FORMAT(1X,'1',3(4X,F8.5))
DO 85 I=IOST,ISTOP
IF(I-J) 86,87,87
87 CALL PATH
GO TO 88
CALL PT3
IF(T(I,J)-T(I-1,J)) 89,89,90
90 CONTINUE

```

```

88 CONTINUE
WRITE(6,124)I,J,X(I,J),T(I,J),U(I,J),C(I,J),S(I,J)
124 FORMAT(1X,2I3,5X,5F10.5)
85 CONTINUE
IU=IU-1
GO TO 92
59 WRITE(6,91
91 FORMAT(1X,'SECOND SHOCK FORMATION')
92 CONTINUE
50 CONTINUE
80 CONTINUE
C PLOT THE CHARACTERISTIC NETWORK
CALL START(2)
XX(1)=0.0
XX(2)=XS(JSE)
TT(1)=0.0
TT(2)=T(ISTOP,JSE)
CALL SCALE(XX,12.0,2,1)
CAL LSCALE(TT,12.0,2,1)
FIRSTX=XX(3)
DELTX=0.25
DELTX=XX(4)
RIRSTT=TT(3)
DELTT=0.25
DELTT=TT(4)
CALL AXIS(0.0,0.0,22H RADIAL DISTANCE (FEET),-
22,12.0,0.0,FIRSTX,DELTX)
CALL AXIS(0.0,0.0,22H RADIAL TIMET*CO (FEET),-
23,12.0,9.0,FIRSTT,DELTT)
CALL PLOT(0.0,12.0,3)
CALL PLOT(0.0,12.0,2)
CALL PLOT(0.0,0.0,3)
C PLOT THE PISTON PATH
JP=JSTOP
DO 101 J=1,JP
XX(J)=X(J,J)-PIST
TT(J)=T(J,J)
101 CONTINUE
XX(JP+1)=FIRSTX
TT(JP+1)=FIRSTT
TT(JP+2)=DELTT
CALL LINE(XX,TT,JP,1,0,1)
C PLOT THE +IVE CHARACTERISTICS
JS1=1
JS1=JSTOP
DO 102 I=1,JS2
IF(JEND(I).GT.JSE) JEND(I)=JSE
JS2=JEND(I)
DO 103 J=I,JS2
JP=J-1+I
XX(JP)=X(I,J)-PIST
TT(JP)=T(I,J)

```

```

103 CONTINUE
XX(JP+1)=FIRSTX
XX(JP+2)=DELTX
TT(JP+1)=FIRSTT
TT(JP+2)=DELT
CALLLINE(XX,TT,JP,1,0,1)
102 CONTINUE
C PLOT THE SHOCK PROFILE
DO 106 J=JS,JSE
JP=J+1-JS
XX(JP)=XS(J)-PIST
TT(JP)=TS(J)
106 CONTINUE
XX(JP+1)=FIRSTX
XX(JP+2)=DELTX
TT(JP+1)=FIRSTT
TT(JP+2)=DELTT
CALL LINE(XX,TT,JP,1,0,1)
CALL ENPLOT
JS=JS+1
STOP
END
SUBROUTINE PT3
DIMENSION XX(100),TT(100)
COMMON X(50,50),T(50,50),U(50,50),C(50,50),S(50,50),XS(50),TS
(50),JEND(50),US1(50),US0(50),CS1(50),CS0(50),SS1(50),SS0(50)
COMMON/ONE/GAMMA,C0,X0,ETA,I,J,VELSH,IP,WORKT
IT=-1
ITT=-1
ITT=1
R1=(U(I,J-1)/2.0+C(I,J-1))/(GAMMA-1.0)
S1=(U(I,J-1)/2.0-C(I,J-1))/(GAMMA-1.0)
R2=(U(I-1,J)/2.0+C(I-1,J))/(GAMMA-1.0)
S2=(U(I-1,J)/2.0-C(I-1,J))/(GAMMA-1.0)
RS1=(GAMMA+1.0)*R1/2.0-(GAMMA-3.0)*S1/2.0
RS2=(3.0-GAMMA)*R2/2.0+(GAMMA+1.0)*S2/2.0
T(I,J)=(X(I-1,J)-X(I,J-1)+RS1*T(I,J-1)-RS2*T(I-1,J))/(RS1-
RS2)
X(I,J)=X(I,J-1)+RS1*(T(I,J)-T(I,J-1))
IF(IT) 11,12,12
11 CONTINUE
R4=(R1+R2)/2.0
S4=(RS1+S2)/2.0
RS4=R4+S4
XT2=(X(I,J)-X(I-1,J))/(T(I,J)-T(I-1,J))
12 T4=(X(I,J)-X(I-1,J)-T(I,J)+RS4+T(I-1,J)*XT2)/((XT2-RS4)
x4=X(I,J)-RS4*(T(I,J)-T4)
SS4=S(I-1,J)+(S(I,J-1)-S(I-1,J))*(X4-X(I-1,J))/(X(I,J-1)-X(I-
1,J))
S(I,J)=SS4
IF(IT) 13,14,14
13 CONTINUE

```

```

SR1=R1-S1
SR2=R1**2-S1**2
X1=(X(I,J-1)+X(I,J))/2.0
14 R3=R1+SR1*(S(I,J)-S(I,J-1))/4.0-((GAMMA-1.0)/4.0)*SR2*(ETA/
X1)+(T(I,J)-T(I,J-1))
IF(IT) 15,16,16
15 CONTINUE
SR3=S2-R2
SR4=S2**2-R2**2
X2=(X(I-1,J)+X(I,J))/2.0
16 S3=S2+SR3*(S(I,J)-S(I-1,J))/4.0-((GAMMA-1.0)/4.0)*SR4*(ETA/
X2)*T(I,J)-T(I,J-1))
U(I,J)=R3+S3
C(I,J)=(R3-S3)*(GAMMA-1.0)/2.0
IF(IT)17,18,18
17 CONTINUE
IF(ITT)18,21,21
21 CONTINUE
RS11=(GAMMA+1.0)*R1/2.0-(GAMMA-3.0)*S1/2.0
RS11=(GAMMA+1.0)*R1/2.0-(GAMMA-3.0)*S1/2.0
RS12=(GAMMA+1.0)*R3/2.0-(GAMMA-3.0)*S3/2.0
RS1=(RS11+RS12)/2.0
RS21=(3.0-GAMMA)*R2/2.0-(GAMMA-3.0)*S1/2.0
RS22=(3.0-GAMMA)*R3/2.0-(GAMMA-3.0)*S3/2.0
RS2=(RS21+RS22)/2.0
RS4=(R4+S4+r3+S3)/2.0
SR1=(R1-S1+R3-S3)/2.0
SR2=(R1**2-S1**2+R3**2-S3**2)
SR3=(S2-R2+S3-R3)/2.0
SR4=(S2**2-R2**2+S3**2-R3**2)/2.0
X1=(X(I,J-1)+X(I,J))/2.0
X2=(X(I-1,J)+X(I,J))/2.0
IT=1
GO TO 10
13 RETURN
END
SUBROUTINE PATH
DIMENSION XX(100),TT(100)
COMMON X(50,50),T(50,50),U(50,50),C(50,50),S(50,50),XS(50),TS(50),
JEND(50),US1(50,US0(50)),CS1(50),CS0(50),SS1(50),SS0(50)
COMMON/ONE/GAMMA,C0,X0,ETA,I,J,VELSH,IP,WORKT
A0=0.0
A1=1.0
A2=0.0
A4=1.0
A4=A4/12.0
IF(IP) 1,1,2
1 WRITE(6,3)A0,A1,A2
3 FORMAT(/1X,*A0=*,E11.5,*A1=*,E5,11,A2=*,E11.5)
TRET=0
2 CONTINUE
IP=1

```

```

T(I,J)=T(I-1,J)
11 TREAL=T(I,J)*X0*10.03/C0
XREAL=(TREAL**2)*(A0+A1*TREAL+A2*TREAL**2)+A4
UREAL=2.0*A0*TREAL+3.0*A1*TREAL**2+4.0*A2*TREAL**3
X(I,J)=XREAL/X0
U(I,J)=(UREAL/C0)*10.0**3
TNEW=((X(I-1,J)-X(I,J))+T(I,J)*U(I,J)-(U(I-1,J)-C(I-1,J))*T(I-
1,J))/(U(I,J)-(U(I-1,J)-C(I-1,J)))
TOLD=T(I,J)
T(I,J)=TNEW
TDIFF=ABS(TNEW-TOLD)
IF(TDIFF-0.00001) 10,10,11
10 CONTINUE
S2=(U(I-1,J)/2.0)-C(I-1,J)/(GAMMA-1.0)
R2=(U(I-1,J)/2.0)+C(I-1,J)/(GAMMA-1.0)
SR4=S2**2-R2**2
X2=(X(I-1,J)+X(I,J))/2.0
S3=S2-((GAMMA-1.0)/4.0)*SR4*(ETA/X2)*(T(I,J)-T(I-1,J))
C(I,J)=((U(I,J)/2.0)-S3)*(GAMMA-1.0)
S(I,J)=S(I-1,,J)
IF(U(J,J)-U(J-1,J-1)) 22,22,13
22 IRET=1
13 IF(IRRET)15,15,16
16 IF(U(J,J)-U(J-1,J-1))17,18,18
18 U(J,J)=U(J-1,J-1)
C(J,J)=C(J-1,J-1)
S(J,J)=S(J-1,J-1)
15 CONTINUE
17 CONTINUE
P0=14.7
PP1=C(I-1,J-1)**((2.0*GAMMA)/(GAMMA-1.0))
PP2=C(I,J)**((2.0*GAMMA)/(GAMMA-1.0))
WORK=(PP1+PP2)*3.14159*(X(I,J)**3-X(I-1,J-1)**3)/3.0
WORK=WORK*P0*144.0
WORKT=WORKT+WORK
WR=PP2*P0*144.0*2.0*3.14159*X(I,J)**2*U(I,J)*C0
WRITE(6,12)I,WORK,WORKT,WR
12 FORMAT(1/X,I5,5X,'INCREMENTANDTOTALWORK';2F15.6,'FTLBF, RATE OF
WORK';F13.5,'FTLBF/SEC')
RETURN
END
SUBROUTINE SHOCK
COMMON X(50,50),T(50,50),U(50,50),C(50,50),S(50,50),XS(50),TS(50),
JEND(50),US1(50),US0(50),CS1(50),CS0(50),SS1(50),SS0(50)
COMMON/ONE/GAMMA,C0,X0,ETA,I,J,VELSH,IP,WORKT
SHMACH=(VELSH-US0(J))/CS0(J)
SHMAC2=SHMACH**(-2)
US1(J)=US0(J)+2.0*SHMACH*(1.0-SHMAC2)/(GAMMA+1.0)
PS0=CS0(J)**((2.0*GAMMA)/(GAMMA-1.0))
PS1=PS0*(1.0+2.0*GAMMA*(SHMACH**2-1.0)/GAMMA+1.0)
RHOS0=PS0**{1.0/GAMMA)
RHOS1=RHOS0/(1.0-2.0*(1.0-SHMAC2)/(GAMMA+1.0)

```

```
ENT1=(1.0/GAMMA)*ALOG(1.0+2.0*GAMMA*(SHMACH**2-1.0)/(GAMMA+1))
ENT2=ALOG(SHMAC2*(1.0+(GAMMA-1.0)*(SHMACH**2-1.0)/(GAMMA+1)))
SS1(J)=SS0(J)+ENT1+ENT2
GM1=GAMMA*SHMACH**2-SHMAC2-(GAMMA-1.0)
GM1=GM1*2.0*(GAMMA-1.0)/((GAMMA+1.0)**2)
CS1(J)=CS0(J)*SQRT(1.0+GM1)
RETURN
END
```

**DDT Excess PressureModels
ETH High Hydrogen Project
DELIVERABLE ONE**

DELIVERABLE ONE

Appendices

V C++ VERSION MOC Language Features

Appendix 2. Programme Code Features Promoting Clarity

Programme languages are designed with features that arise from the basic philosophy on which their inventors and promoters approached their evolution into their present day manifestation. However, in the search for an approach which might provide a clarity to obscure pathway to the implementation of physical and mathematical concepts as programme code, it was decided that these features might form a way to make the link between the various disciplines less obscure.

Programme languages are designed with features that arise from the basic philosophy on which their inventors and promoters approached their evolution into their present day manifestation. However, in the search for an approach which might provide a clarity to confusing pathway from physical and mathematical concepts to implementation as programme code, it was decided that these features might form a way to make the link between the various disciplines less obscure.

The chosen computer language is C++. The following commentary is very largely based on the introduction from "C++ Primer Plus 5th Edition" by Stephen Prara (SAMS, Indianapolis, 2005)

In general, computer languages deal with two concepts — data and algorithms. The data constitutes the information a program uses and processes. The algorithms are the methods the program uses in those processes. Like most mainstream languages, C (the forerunner of C++) is a procedural language. That means it emphasizes the algorithm side of programming. Conceptually, procedural programming consists of figuring out the actions a computer should take and then using the programming language to implement those actions. A program asks for a set of procedures for the computer to follow to reach a particular outcome. In response, computer scientists developed in C a style of programming called structured programming which overcame the difficulties revealed as the complexities of applications due to the attempts using earlier languages such as FORTRAN to solve larger problems. C includes features to facilitate this approach. For example, structured programming limits branching (choosing which instruction to do next) to a small set of well-behaved constructions into its vocabulary.

Top-down design was another of the new principles. With C, the idea is to break a large program into smaller, more manageable tasks. C's design facilitates this approach, encouraging the use of program units called functions to represent individual task modules. The structured programming techniques involves thinking of a program in terms of the actions it performs.

C++ introduced Object Orientated Programming (OOP). Unlike procedural programming, which emphasizes algorithms, OOP emphasizes the data. Rather than try to fit a problem to the procedural approach of a language, OOP attempts to fit the language to the problem. The idea is to design data forms that correspond to the essential features of a problem.

In C++, this idea is implemented in the two concepts of: (i) a **class**, which is a specification describing a

Modelling of Infrastructure Protection – From Materials to Devices

"With the support of the Prevention, Preparedness and Consequence Management of Terrorism and other Security-related Risks Programme" European Commission - Directorate-General Justice, Freedom and Security

new data form and; (ii) an **object** which is a particular data structure constructed according to that form. For example, in a computer drawing program capable of drawing geometric shapes. one aim would be to draw a rectangle. You could define a class to describe a rectangle. The definition of the class in the code would require a data part of the specification which could include such things as the location of the corners, the height and width, the colour and style of the boundary line etc. The the definition might also have an operations part which might include methods for moving the rectangle, resizing it, rotating it, changing colours and patterns, and copying the rectangle to another location. Using the program to draw a rectangle, would create an object according to this class specification. That object would hold all the data values describing the rectangle, and you could use the class methods to modify that rectangle. If you drew two rectangles, the program would create two objects, one for each rectangle. The OOP approach to program design is to first design classes that accurately represent those things with which the program deals. The process of going from this lower level of organization, such as classes, to the next level, such as program design, is called bottom-up programming.

OOP brings a new approach to that challenge. Unlike procedural programming, which emphasizes algorithms, OOP emphasizes the data. Rather than try to fit a problem to the procedural approach of a language, OOP attempts to fit the language to the problem. The idea is to design data forms that correspond to the essential features of a problem.

The short commentary above is the briefest of views of the basic structures of the computer language C++. Other features not described will be referred to in this appendix including inheritance, polymorphism and the file types which are assembled in the completed programme design. These terms will be explained in tge narrative which follows.

The features of the language chosen to represent the approach in this appendix are as follows:

- 2.1 Classes and objects
- 2.2 Inheritance
- 2.3 Polymorphism
- 2.4 Inline functions
- 2.5 Source Code, Headers and Libraries
- 2.6 Comments

2.1 Classes and Objects

The numerical procedure in the Method of Characteristics (MOC) like many solutions for of partial differential equations is based upon a network created in a space-time domain. In the case of MOC the network expands into the space-time domain as the calculation proceeds by determining both the location and the variable values of new nodes in the network from the position and variable values at existing nodes (either the nodes representing initial conditions at the start of the procedure or previously established nodes once the calculations have commenced). Hence, **nodes** are the first choice for the first C++ class.

In principle and in terms of the numerical solution results, the nodes are the only relevant parts of the network. However, there two aspects of the MOC approach which take value from the curves which link the nodes.

First, in relation to the numerical method, the determination of the new node location coordinates and variable values is based upon the equations defining changes of these along these curves and the procedure requires interpolation of values between the nodes. Second, the trajectories described by these curves represent physical processes associated with the phenomenon (blast-wave behaviour) under investigation. Hence, **paths** are the next choice for a C++ class.

Other C++ classes might be required but these two important ones provide sufficient examples of the way in which the programme code may be clarified. The sections of programme code defining these two classes developed in this project for the software tool are briefly described below. Note that some lines of code which are required for the correct definition of a class are in faint print in these examples so that the emphasis can be placed on those features relevant to the clarity of the physical aspects. Bold font is employed to identify language features.

nodes

```
1  class nodes {
2      public:
3          nodes ();
4          nodes (double _r, double _R, double _t, double _p,
5                  double _u, double _c, double _v, double _e,
6                  double _T, double _eta);
7
8          int nodeType, xisticPlus, xisticMinus;
9          double radius, Radius, time, pressure,
10             velocity, soundSpeed, specificVolume,
11             entropy, absoluteTemperature;
12         int _3rdPoint (int , int , int , int , int);
13         int _piston (int , int , int , int , int);
14     private:
15         double radiusF, RadiusF, tF, pF, uF, cF, vF, eF, TF;
16         double RadiusDA, RadiusDB, RadiusPA, RadiusPB;
17             // A == 0 and B == 1
18         double betaAD, betaAP, phiAD, phiAP, psiAD, psiAP;
19             // A == 0 and B == 1
20         double betaBD, betaBP, phiBD, phiBP, psiBD, psiBP;
21         double velocityPluscAD, velocityMinuscBD;
22             // D == 0 and P == 1
23         double velocityPluscAP, velocityMinuscBP;
24     };
25
26     nodes* Xnodes [MAXI*MAXJ + 1];
```

The first line declares the **class** of `nodes` and the definition then follows within the two parenthesis { and } in two parts, **public** and **private**.

Lines 5 and 6 of the code declare the variables associated with a node and these are all given names which, wherever possible, are clearly related to the physical properties they represent. Thus the variable `time` is the time coordinate and `radius` is the radial coordinate. The names `Radius` and `radius` are used to differentiate between the Eulerian and Lagrangian radii respectively but could have been named as `radiusEulerian` and `radiusLagrangian` instead for added clarity. (Data content of the class).

Lines 7 and 8 declare functions employed in the determination of these variables' values from the properties of two other nodes. (Algorithm content of the class). The existence of the two functions is required to allow for the very different calculation procedures between the majority of the nodes within the atmosphere and those at the piston surface.

Line 20 declares the objects which will provide the array of `Xnodes` in the calculation procedure limited to a total number of $(MAXI * MAXJ + 1)$ where `MAXI` and `MAXJ` are user defined numbers. (The upper case letter X is a commonly used substitution for 'character' or 'characteristic').

Lines 10 to 18 form the private part of the class and in the present example declare data consisting of values, or mathematical combinations of values, of the variables which are more conveniently (with regard to mathematical and computational aspects) calculated as intermediates. Their relation to the mathematical aspects of the programme have been dealt with in the first appendix.

paths

```
1  class paths {
2      public:
3          paths(int, int, int, int, int);
4          paths();
5          ~paths();
6          int pathsType, pathNumber, pathI, pathJ;
7          int currentNodeCount;
8          int trajectoryNodes[MAXI + MAXJ + 1];
9
10         void _savePathsNode(int, int);
11         void _printPathDetail();
12     };
13
14     paths* Xpaths[MAXJ + MAXI + 1];
```

The first line declares the **class** of `paths` and the definition then follows within the two parenthesis { and } in one part only in this case, **public**.

The `paths` **class** does not contain data or algorithms directly associated with the variables which determine the process (blast wave behaviour) so that the convention of requiring the separation of these variables from others is not called for. The class involves these variables indirectly by identifying all the **nodes** which trace out the individual paths. An alternative convention is required to distinguish classes which explicitly use the physically related variables to obtain solutions and therefore should be subject to our concerns about clarity.

2.2 Inheritance

All the **nodes** in the calculation procedures involved in MOC involve (in the case of one-dimensional) transient compressible flow) two characteristic paths. Hence, all nodes will have the properties associated with objects `Xnodes`. However, certain groups of **nodes** are also associated with specific time-distance related phenomena in the flow processes which require alternative calculation procedures and the definition of other variables. One such class of nodes relates to those falling on the surface of the piston. These, however, can be treated in a similar way to the `Xnodes` because the piston movement is prescribed by the user and its behaviour is not determined any response to the neighbouring nodes.

One of the advantages of the C++ language is its ability to define classes of objects which have many of the attributes of an existing class but with various changes to their algorithm and data parts. This attribute is known as **inheritance** and allows the programmer to use an existing class and add and/or subtract data and algorithms to suit the particular requirements of the new class. Subsequently objects of this new class can be declared and then employed in the numerical manipulations.

No examples are available from the software tool under development in the MIPMaDe project since the initial trials of the programme all involved coding which did not take advantage of **inheritance** because the full advantages of this higher level of sophistication had not been appreciated. Inherited **Classes** from the **class nodes** such as `shockNodes`, `contactSurfaceNodes` and `obstacleNodes` are involved. Similarly for the class paths there would be `shockPaths`, `contactSurfacePaths` and `obstacPaths` and `streamLinePaths`. (There is no equivalent `streamLineNode` since streamlines do not form part of the network structure defined by the node network.

Further sophistication, for instance polymorphic inheritance may yield equally fruitful approaches to providing clarity to s software tool.

2.3 Inline functions and Function Overloading

Inline functions are small algorithms which are not coded as separate blocks of code. They appear within a component of a software program as part of the body of the programme code and is executed in the same way as a line of code at that location. Its existence is largely an issue of programming efficiency. However, its existence could also provide a useful way of incorporating clarity into the software.

Inline functions can be declared in either of two ways and this provides the key to an approach to higher levels of clarity. A convention can be defied which reserves one of these ways to functions which perform tasks related to pure mathematical algorithms associated with computing objectives such as interpolation or equation solving. The other way would then be reserved for functions in which values of physical variables are used to determine the corresponding values of another physical variable.

However, inline functions should be used in cases where the function is very small – only a very few lines of code. Another form of function variation is to be found in function overloading. An example of this is to be found in the first sample of code in this appendix. Lines 3 and 4 which were intentionally faded in this sample of code form the constructors in the class `nodes`. This feature is available for functions in general. Function overloading is having two or more functions of the same name but with different parameter lists. The compiler will recognise the different function calls by the change in parameters.

Here again, functions could be defined by a convention based on an additional dummy parameter which would identify whether the function was involved in computing issues or mathematical issues or physical issues. The convention would be of the type: “All function overloads must comply with convention that the first parameter to be passed is a dummy having a data type **int** for computing issues, a data type **double** for mathematical issues and a data type **void** for physical issues. These data types would be coded employing the `#define` convention’.

```

#define DUMMY_CODE int
#define DUMMY_MATH double
#define DUMMY_PHYS void
.....
Void callMe(DUMMY_CODE, int double); // function callMe for
// computing matters
Void callMe(DUMMY_MATH, int double); // function callMe for
// mathematical matters
Void callMe(DUMMY_PHYS, int double); // function callMe for
// physical matters

```

2.4 Source Code, Headers and Libraries

The *source file* is a text file that contains the program's source code. The compiler takes the source code file, parses it, and produces machine language that the computer can execute.

In practice, a program of any consequence has several source files. A program's code is divided up into different source files for a number of reasons. One of the primary reasons is that of organization. By keeping related chunks of code together, you can more easily find a certain section of code when needed.

The compiler compiles each source file (.cpp) into an object file (.obj). After each module has been compiled, the linker links all the object files together to make a single executable file (. exe). The linker also can link in other needed files such as resource files { . res) and library files (.lib).

The declarations for classes and structures are often kept in a separate file called a *header file*. Headers have a filename extension of (.h) or (. Hpp).

In ways similar to those in 2.1 to 2.3 conventions could be defined to separate the computing, mathematical and physical parts of the code. Such organisation would considerably improve the understanding of programme codes especially a logical design can be determined at the start of coding and both file naming conventions and file type conventions organised with the cooperation of non-programmers. However, some consideration has to be given to the effect of such a plan would have on the traditional practices of seasoned code writers.

2.5 Comments

Comments are a traditional way for a code writer to communicate his intentions and methods for achieving the efficient and reliable computational procedures set out in the objectives he has been given. It would be a mistake to suggest any changes or complementary uses for comments which are permitted and encouraged for inclusion in source files. This section of the appendix contains two suggestions which experience in the MIPMaDe project software tool development has suggested.

One of these has already been suggested in the first appendix. It is suggested there that all equations which are implemented in the source code should be checked for consistency in scientific and engineering unit. The code for each equation should be followed by a series of standard comment lines (each prefixed by //). On the first comment line, each variable in the equation on both sides of the equality would be represented by its Derived SI Unit as a fraction showing each of the component Standard SI Units. On the second and subsequent comment lines the fractions would be simplified by cancellations above and below and the third comment line would need to show consistency in units for the whole equation.

In the course of the development of the source codes it was found that many of the computing tasks were made simpler when a detailed narrative of the mathematical solution methodology was provided. In such instances when the code was written in accordance with

the narrative the final programme was considerable easier to appreciate in terms of both the computing logic and the mathematics.

2.6 Conclusions

This appendix has attempted to bring together the experience gained in the development of a software tool. The term software tool has been used to imply a computer programme which

- (a) performs a task which has been sought by a user,
- (b) will be employed by the user to obtain solutions to problems of which the user has a great deal of experience and knowledge and
- (c) provide the user with results he has confidence in and whose derivation he understands.

This appendix deals specifically with the ways in which the construction of the source code is attempted may help to give the user a tool which achieves all three objectives.

Some of the methods suggested have been used in the present project but in other instances the absence of a professional programmer has limited the extent to which the more sophisticated suggestions have been tried.

Appendix 3. User Interfaces

As with all real applications, this software tool will be implemented as a computer based application. As such it will require an user interface which provides the means whereby necessary input data can be communicated to the programme and by which results of the calculation can be provided to those seeking technical assistance by way of e software tool the most useful data for its intended purpose.

In practical terms the design of such an interface would require a trial-and-error approach involving the programme designers and the programme users. This development was not feasible in this project but some thought has been given to a selection of methods which might be employed. However, the usual approach via Operating System GUIs (Graphical Unit Interfaces) has implications beyond the scope of this appendix so that only a brief discussion of the problems associated with the use of GUIs is present..

The three techniques illustrated in this appendix are all based on the data handling features of C++ related to input and output files. The techniques fall under the titles:

- 1) Input and output text files.
- 2) Input text files and output spreadsheet
- 3) Spreadsheet input and output.
- 4) The use of GUIs.

3.1 Input and output text files.

This is the simplest of the methods for entering data and recovering results from the software tool. Being the simplest it is also the most suitable for the early stages of a development program.

The programme language used in the development of the software tool, C++, provides functions for input and output of data either to the computer terminal or to files. The former functions provide a facility to prompt the user on the terminal for input data which can then be entered via the keyboard. The use of these functions provides a very flexible way of running software during the early stages since the choice of different solutions can be controlled by appropriate input prompts. The disadvantage of this approach is the absence of an easy way of dealing with output since it only appears on the screen of the terminal and is not recorded. The use of file input and output is an equivalent approach with the data for input provided in text files written and saved prior to the running of the programme. Output data is written to text files in a selected location in storage on the computer. The disadvantage of the use of files is the loss of flexibility but this loss is less serious in the later stages of development.

The output file can be opened by computer applications other than text editors. For instance the data from the file can be inserted-into a spreadsheet. (Office Excel will open a text file into the spreadsheet if the data is correctly formatted). Also, other computer applications can read text files and many of them provide sophisticated graphical functions which can be employed as postprocessors.

The approach involving spreadsheets is discussed in the next two sections. The use of the other applications is effectively a graphical solution to the provision of a user interface relating to output data and is dealt with as part of the final section of this appendix

3.2 Input text files and output spreadsheet

This approach has been used in the development of the software tool and has been found to provide a very useful way of dealing with the input/output issues. It has been found particularly useful with respect to the insight it has provided into the learning process involved in designing a user interface for a software tool.

The original choice of the specific model used for the simulation of the physical processes which take place in the propagation of blast waves was made in response to the objective of simple but effective user intervention and interpretation. As a result the input data requirements for the running of the programme are minimal and can be provided by the user as a single text line of numeric characters with white spaces for separation of the individual items. Input from the user would involve the entry of this data in a text file template in a form clearly defined in the instructions which are included in the template.

In the simplest form of the software tool, the executable file is opened and the input files (including the one provided by the user) are read, the programme performs its designed calculations with the results being written to output files. A message on the terminal identifies the end of the calculation and offers a number of options so that the user can select the nature of the information he desires. These options will provide the name of the output file to be loaded into the spreadsheet application. The formatting of these output files is carefully designed to provide the maximum information concerning the original input and the contents of the tables. The formatting is also designed to ensure that the template file requirements for implementation of the its graphics features are matched.

An example of this approach is illustrated in the following diagram. The figure shows a section of an Excel spreadsheet with the data area on the left of the diagram and the graphical representation on the right.

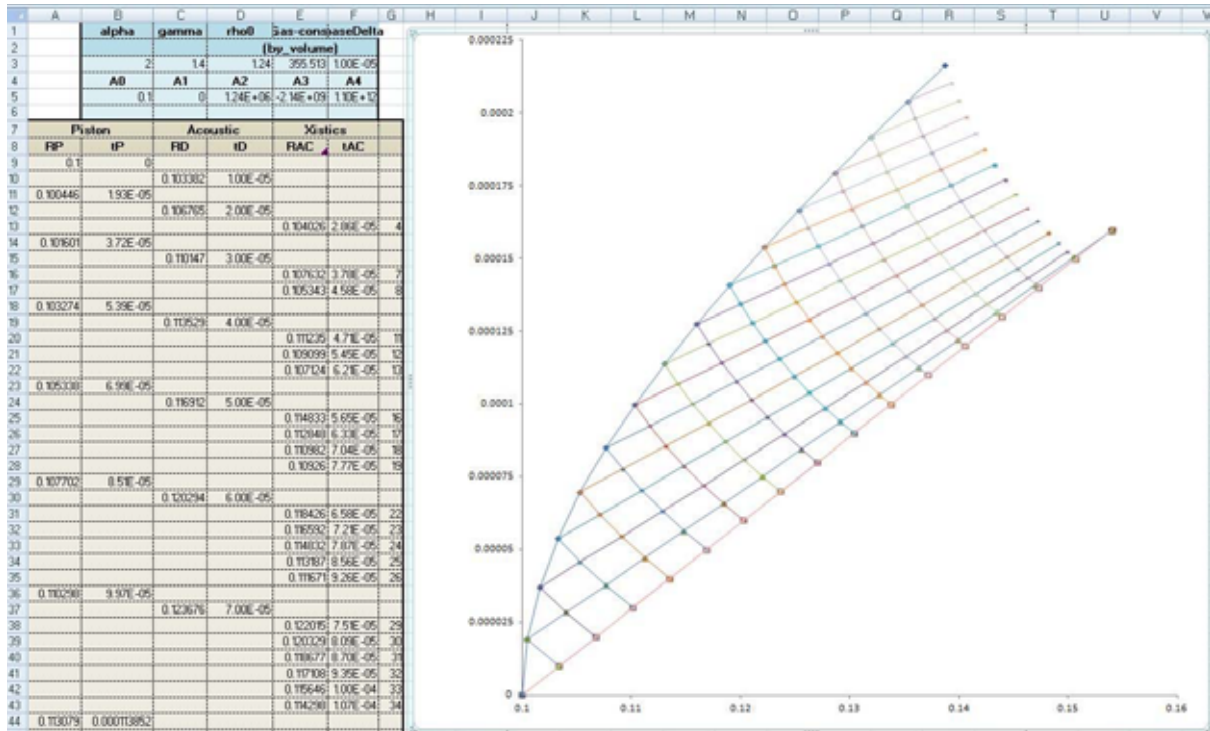


Figure 3.2.1 Spreadsheet demonstration of output file graphics

There are two sections of data one blue and the other beige. The output file reproduces the input data in the blue section with appropriate headings to the columns. In this example the selection has been made to plot the trajectories of the main features of the explosive processes of the explosion at its early stage before the shock front has been formed. The figures for space coordinates for these trajectories at small intervals of time form the data set in the beige coloured section. There are six columns for this data two each for the piston trajectory, the trajectory of the acoustic line and all the characteristics which fill the time-space domain in between.

The graph of this domain has been constructed by inserting a graphic chart in one of the cells and selecting the appropriate cells to represent the curves in the graph.

Initially, the construction of the graphic was achieved manually. However, once the formatting of the data had been standardised it was possible to save this Excel spreadsheet as a template so that the output file automatically produced the scatter chart once it was loaded into Excel.

3.3 Spreadsheet input and output.

Spreadsheets can be programmed so as to allow their plotting features to be used for the presentation of the results from a software tool. It is then also possible to employ the spreadsheet for information input to the tool. In the present case the basic task is to interface the C++ programme with the Office Excel spreadsheet application. The following brief discussion is based upon an article entitled "A brief introduction to C++ and Interfacing with Exce" by AL. Hazel (School of Mathematics, The University of Manchester, Oxford Road, Manchester, M13 9PL, UK)

Communication between C++ and Excel is a complex There are two distinct choices:

- Call a C++ Add-in from Excel,
- Call Excel functions from within a C++ program.

The first option means that the C++ "backend" can be used from within as a function like any other standard function available to the spreadsheet

The second option is more useful for this software tool to enable the plotting and data analysis capabilities of Excel to be used from within the C++ programme.

The first method would not be suitable since it would require a very complicated spreadsheet template to accommodate the large arrays of cell locations for the complex data representation upon which a graphic could be constructed.

The second method appears to be ideal for using the plotting and data analysis capabilities of Excel from within the software tool programme for displaying real-time graphs of simulation results.

Importation is achieved with standard C++ functions and then the following code (for example) will enable Excel functionality from within the programme by making use of the Microsoft Component Object Model (COM) Programme comments (lines starting with //) indicate the functions of lines of code

```
1   int main()
2   {
3
4       Excel::_ApplicationPtr XL;
5       {
6//   Initialise COM interface
7           CoInitialize(NULL);
8//   Start the Excel Application
9           XL.CreateInstance(L"Excel.Application");
10//  Make the Excel Application visible
11           XL->Visible = true;
12;
13       }
14
15 }
```

The result of the program is that an Excel window is created and displayed on the screen. The important feature is that a pointer to the Excel application has been created which can be used to communicate between Excel and the C++ program. In fact, the program is merely a fancy "wrapper" that starts Excel. The inclusion of additional commands would allow the start of Excel with some custom defaults.

A pointer to an Excel Application Object is the only thing that is required to communicate with Excel from a C++, or any other, program. The use any of the Excel objects and functions, however, will require a knowledge of their names and the arguments that they take. The information is known as the Excel Object Model and is documented in the on-line help provided with the VBA editor

This second approach provides the means whereby the software tool can obtain input data from an Excel spreadsheet and supply output data to construct graphic representations using the Excel graphis capabilities.

3.4 The use of GUIs.

It is possible to write Windows Programmes in C++. These are constructed using utilities which ensure that an application built from codes compliant with the rules will allow the designer to incorporate features of the Microsoft Windows operating system related to graphic functions linking computer screen, mouse and keyboard to controls data handling, graphic facilities on a standard computer. The interface described above is known as a Graphics User Interface (GUI) and these are the interfaces which are most commonly used for running applications.

Logically, user interfaces are designed and constructed after the basic programme which provides the calculation machine has been put together and tested. The starting point for the GUI design for a particular application is best done with close cooperation of the intended user and with backup from both the “engineering expert” and thw “mathematics” expert. The collaboration follows the agreement between the user and the producer of the calculation machine part of the tool that the software tool performs the functions required.

The effort required to produce a reliable and effective GUI for a particular application is a matter for computing experts with plenty of experience of the operating system under consideration. Hence,

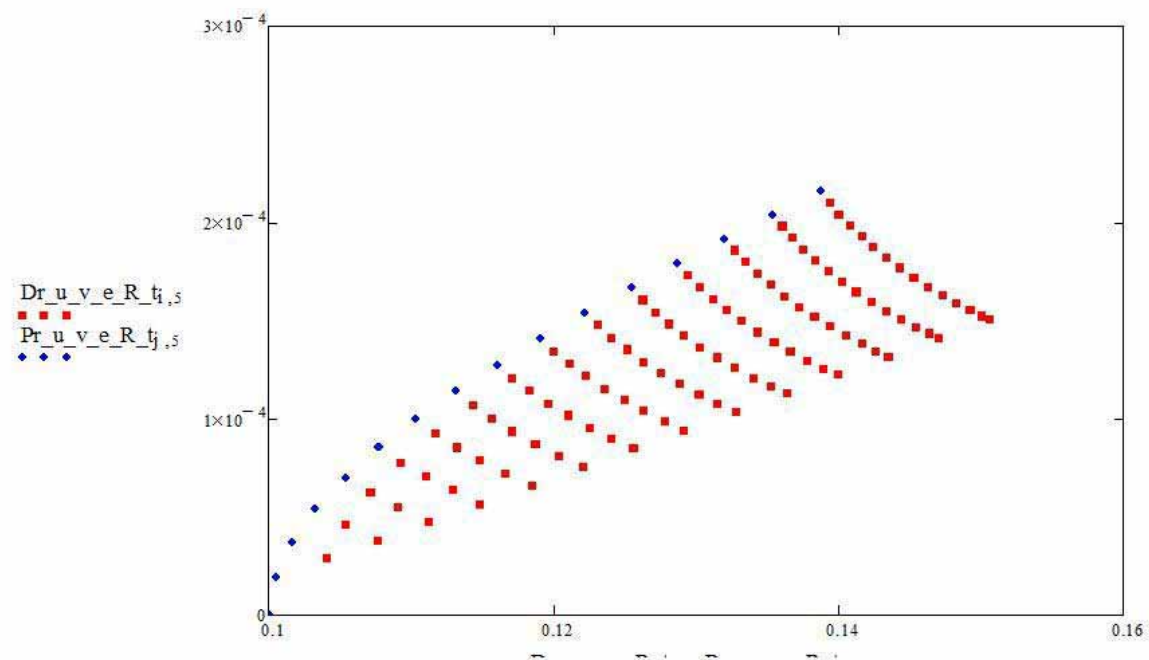
In consequence of the above reasoning no attempt has been made to design and construct a GUI for this software tool. The reader should however know that, with sufficient skill and ingenuity, professional programme writers can provide the software tool with as many of the very large library of GUI functions which cme with a given operating system as a user desires. The main problem is the choice of the best of these for the particular application.

Finally, it has been mentioned earlier in this appendix that many applications which are available from the computer software market provide file reading capabilities which can be used to produce many different sophisticated graphical presentations. Many mathematical applications provide these capabilities and as an example an output file from the software tool under development has been used to produce a graph.

```

Dr_u_v_e_R_t:= READPRN("D_out2.txt")      Pr_u_v_e_R_t:= READPRN("P_out2.txt")
Dr_u_v_e_R_tRows:= rows(Dr_u_v_e_R_t)    Pr_u_v_e_R_tRows:= rows(Pr_u_v_e_R_t)
i:= 0..Dr_u_v_e_R_tRows-1                j:= 0..Pr_u_v_e_R_tRows-1

```



The diagram shows a simpler form of the graphic set out by the spreadsheet but a more complicated arrangement would be quite easily accommodated by this method.

The lines of text in the diagram are the MathCAD instructions required to produce this plot from two output files, D_out2.txt and P_out2.txt which recorded characteristic nodes and piston nodes respectively.

Appendix 4. Reference Publications

A list of references follows which includes those publications on which the software tool has been based. The list is not comprehensive but it includes all the essential items which are those actually employed in the research and development work involving the numerical modelling for the software tool..

- Hoskin, N.E., "Solution by characteristics of the one-dimensional equations of unsteady flow.",
Methods in Computational Physics, Volume 3: Fundamental Methods in Hydrodynamics,
Academic Press, New York, 1964
- Butler, D.S. "The Numerical Solution of Hyperbolic Systems of Partial Differential Equations in Three Independent Variables",
Proc. R. Soc. London, Series A 255, 232-252 (1960).
- Richardson, D.J. "Solutions of Two-Dimensional Hydrodynamic Equations by the Method of Characteristics"
Methods of Computational Physics. Alder, B. Fernback, S. and Rotenberg, M. eds.,
Academic Press, New York, pp. 295-318 (1964).
- Hartree, D.R., "Some Practical Methods of Using Characteristics In the Calculation of Non-Steady Compressible Flow"
Report AECU-2713, US Atomic Energy Commission, September 1953
- Sauerwin, H. "Numerical Calculations of Multidimensional and Unsteady Flows by the Method of Characteristics"
Journal of Computational Physics vol 1, pp 406-432, (1967)

VI C++ VERSION MOC Programme Code Features

PART 1

This appendix is in 4 parts which show four stages of transition from the technical paper which describes the numerical procedure through to the computer code. Appendix II contains the technical paper used as the basis for the code.

The first part of this appendix which follows this page provides a mathematical development of the equations which are employed in the method of characteristics numerical method for solving partial differential equations. It starts with the basic conservation equations for unsteady compressible gas flow and manipulates these equations to produce a set of difference equations capable of developing a network of characteristics in the time-distance domain.

Parts 2 and 3 use the starting point of the difference equations to develop the equivalent computer code for the two sets of calculation involving the 3rd-point nodes in part 2 and the piston nodes in part 3.

Part 4 is a copy of the two parts of code within the context of the main programme.

Each part is separated from the previous one by a blank title sheet.

The one-dimensional differential equations of conservation of mass, momentum and energy for an inviscid non-heat-conducting transient gas flow are respectively:

$$\frac{\partial \rho_l}{\partial t} + u_l \frac{\partial \rho_l}{\partial r} + \rho_l \frac{\partial u_l}{\partial r} + (\varepsilon - 1) \frac{u_l \rho_l}{r} = 0$$

$$\frac{\partial u_l}{\partial t} + u_l \frac{\partial u_l}{\partial r} + \frac{1}{\rho_l} \frac{\partial p_l}{\partial r} = 0$$

$$\frac{\partial s_l}{\partial t} + u_l \frac{\partial s_l}{\partial r} = 0$$

Where ρ is gas density, u is gas velocity, p is gas pressure and s is gas entropy. The two independent variables are r for the radial position and t for time. The subscript l designates a local value. ε has the values 0, 1 or 2 for the one-dimensional configurations for planar, cylindrical and spherical symmetry respectively.

The equation of state of the gas in terms of pressure, density and entropy is:

$$\frac{p_l}{p_0} = \left[\frac{\rho_l}{\rho_0} \right]^{\gamma} \exp \left[\frac{S_0 - S_l}{R} \right]$$

Where C_v is the specific heat at constant volume for the gas and the subscript 0 designates some standard condition. γ is the ratio of specific heats for the gas. Finally, the speed of sound in the gas a is given by the expression:

$$a_l^2 = \left[\frac{\partial p_l}{\partial \rho_l} \right]_{s=\text{constant}} = \gamma R T_l$$

Where R is the gas constant for the gas and T is its absolute temperature.

New dependent variables are defined as follows:

$$u = \frac{u_l}{u_0}, \quad \rho = \frac{\rho_l}{\rho_0}, \quad a = \frac{a_l}{a_0}, \quad p = \frac{p_l}{p_0}, \quad s = \frac{s_l}{R} \quad \text{and} \quad T = \frac{T_l}{T_0}$$

With the corresponding new independent variables taking the form:

$$\tau = \frac{t}{r_0/a_0} \quad \text{and} \quad \eta = \frac{r}{r_0} \quad \text{where} \quad r_0 \text{ is an arbitrary length and} \quad u_0^2 = \frac{p_0}{\rho_0} = R T_0$$

The three original conservation equations are then transformed into:

$$\frac{\partial \rho}{\partial \tau} + u \frac{\partial \rho}{\partial \eta} + \rho \frac{\partial u}{\partial \eta} + (\varepsilon - 1) \frac{\rho u}{\eta} = 0$$

$$\frac{\partial u}{\partial \tau} + u \frac{\partial u}{\partial \eta} + \frac{1}{\rho} \frac{\partial p}{\partial \eta} = 0$$

$$\frac{\partial s}{\partial \tau} + u \frac{\partial s}{\partial \eta} = 0$$

The two versions of the equation of state become:

$$p = \rho \exp[s_0 - s]$$

and

$$p = \rho T$$

And the dimensionless speed of sound can be expressed either as

$$a^2 = \left[\frac{\partial p}{\partial \rho} \right]_{s=\text{constant}} = T$$

The first equation in the line above can be used to replace the partial derivative in density $\partial \rho$ in the dimensionless equation of conservation of mass to yield

$$\frac{\partial p}{\partial \tau} + u \frac{\partial p}{\partial \eta} + \rho a^2 \frac{\partial u}{\partial \eta} + (\varepsilon - 1) \frac{\rho u a^2}{\eta} = 0$$

A linear combination of this equation and the dimensionless equation of momentum conservation produces a useful independent equation. This equation is obtained in a revealing form by multiplying all the terms in the equation above by the factor λ and adding the result to the momentum equation followed by minor rearrangement of terms to yield:

$$\left\{ \frac{\partial p}{\partial \tau} + \frac{\partial p}{\partial \eta} \left[u + \frac{\lambda}{\gamma \rho} \right] \right\} + \lambda \left\{ \frac{\partial u}{\partial \tau} + \frac{\partial u}{\partial \eta} \left[u + \frac{\rho a^2}{\lambda} \right] \right\} + (\varepsilon - 1) \frac{\rho u a^2}{\eta} = 0$$

If it is postulated that

$$u + \lambda/\gamma\rho = u + \rho a^2/\lambda \quad \text{so that} \quad \lambda = \pm \rho a$$

Then the differentials of p and u with respect to η and τ are exact along a set of pairs of curves on the η/τ plane defined by:

$$\frac{d\eta}{d\tau} = u + a \quad \text{and} \quad \frac{d\eta}{d\tau} = u - a$$

Accepting this relationship these last three equations can be employed to set up a pair of expressions for, in the first instance, $\lambda = +\rho c$

$$\left\{ \frac{\partial p}{\partial \tau} + \frac{\partial p}{\partial \eta} [u + a] \right\} + \rho a \left\{ \frac{\partial u}{\partial \tau} + \frac{\partial u}{\partial \eta} [u + a] \right\} + (\varepsilon - 1) \frac{\rho u a^2}{\eta} = 0$$

and, in the second, $\lambda = -\rho c$

$$\left\{ \frac{\partial p}{\partial \tau} + \frac{\partial p}{\partial \eta} [u - a] \right\} - \rho a \left\{ \frac{\partial u}{\partial \tau} + \frac{\partial u}{\partial \eta} [u - a] \right\} + (\varepsilon - 1) \frac{\rho u a^2}{\eta} = 0$$

Which reduce to

$$\frac{dp}{d\tau} + \rho a \frac{du}{d\tau} + (\varepsilon - 1) \frac{\rho u a^2}{\eta} = 0$$

$$\frac{dp}{d\tau} - \rho a \frac{du}{d\tau} + (\varepsilon - 1) \frac{\rho u a^2}{\eta} = 0$$

To summarise, two equations have been derived which define the changes in flow variables (p , ρ , a and u) along two curves in the space domain (η by τ) whose paths are defined by the two corresponding exact differential equations set out earlier but reproduced again below for clarity:

$$\frac{d\eta}{d\tau} = u + a \quad \text{and} \quad \frac{d\eta}{d\tau} = u - a.$$

A third equation relating to the isentropic nature of the flows defines constant entropy given by

$$\frac{ds}{d\tau} = 0$$

Along the streamline or particle path defined in the space domain (η by τ) by

$$\frac{d\eta}{d\tau} = u$$

This set of three pairs of differential equations are amenable to numerical solution by a method known as the “method of characteristics” the characteristics being the three curves in the space domain described above. However, there are advantages, which will be explained later, for replacing the variables u and a by the two dependant variables R_+ and R_- defined by:

$$R_+ = \frac{u}{2} + \frac{a}{\gamma - 1}$$

$$R_- = \frac{u}{2} - \frac{a}{\gamma - 1}$$

When the transformed characteristic differentials (direction in the space domain) become

$$\frac{d\eta}{d\tau} = \frac{\gamma + 1}{2} R_+ + \frac{3 - \gamma}{2} R_-$$

$$\frac{d\eta}{d\tau} = \frac{3 - \gamma}{2} R_+ + \frac{\gamma + 1}{2} R_-$$

$$\frac{d\eta}{d\tau} = R_+ + R_-$$

And the corresponding characteristic equations defining changes in R_+ and R_- along the characteristics take the form

$$\frac{dR_+}{d\tau} = \frac{1}{4C_p} (R_+ - R_-) \frac{ds}{d\tau} - \frac{\gamma - 1}{4} (R_+^2 - R_-^2) \frac{\varepsilon - 1}{\eta}$$

$$\frac{dR_-}{d\tau} = \frac{1}{4C_p} (R_- - R_+) \frac{ds}{d\tau} - \frac{\gamma - 1}{4} (R_-^2 - R_+^2) \frac{\varepsilon - 1}{\eta}$$

$$\frac{ds}{d\tau} = 0$$

The initial change to dimensionless variables was introduced to generalise the solution and thus eliminate any potential problems associated with the choice of units in its application in practice. The use of initial conditions to provide the individual scaling variable allows for the use of consistent units for the variables of the users choice. In this case the only exception to this approach is

the velocity scaling factor where the initial conditions are usually zero velocity everywhere.

The more recent transformation to the dimensionless variables R_+ and R_- (usually known as the Riemann invariants) is to reduce the complexity of the numerical solution of the equations by cutting the number of dependent variables from five (p , ρ , u , c and s) to three (R_+ , R_- and s).

PART 2

Part 2 uses the starting point of the difference equations to develop the equivalent computer code for the 3rd-point nodes

Equations in *roman type* transcribed directly from those in the article which are in red:

$$r_D - r_A - \left[\frac{c}{v} \left(\frac{\alpha u c}{R} \right)^\alpha \right]_{AD} (t_D - t_A) = 0$$

$$r_D - r_A - \text{betaAD} * (t_D - t_A) = 0$$

$$r_D - r_B + \left[\frac{c}{v} \left(\frac{\alpha u c}{R} \right)^\alpha \right]_{AB} (t_B - t_B) = 0$$

$$r_D - r_B + \text{betaBD} * (t_D - t_B) = 0$$

$$\left[\frac{1}{\rho \cdot c} \right]_{BD} (p_D - p_B) - (u_D - u_B) + \left[\frac{\alpha u c}{R} \right]_{AB} (t_D - t_B) = 0$$

$$\text{phiBD} * (p_D - p_B) - (u_D - u_B) + \text{psiBD} * (t_D - t_B) = 0$$

$$\left[\frac{1}{\rho \cdot c} \right]_{AD} (p_D - p_A) + u_D - u_A + \left[\frac{\alpha u c}{R} \right]_{AD} (t_D - t_A) = 0$$

$$\text{phiAD} * (p_D - p_A) + u_D - u_A + \text{psiAD} * (t_D - t_A) = 0$$

$$R_D - R_A - [u + c]_{AD} (t_D + t_A) = 0$$

$$R_D - R_A - u\text{PluscAD} * (t_D - t_A) = 0$$

$$R_D - R_B - [u + c]_{BD} (t_D - t_B) = 0$$

$$R_D - R_B - u\text{MinuscBD} * (t_D - t_B) = 0$$

$$E_D - E_F + \frac{1}{2} (p_D + p_F) (v_D - v_F) = 0$$

$$e_D - e_F + 0.5 * (p_D + p_F) * (v_D - v_F) = 0$$

$$E_D - \frac{p_D v_D}{\rho_0 (\gamma - 1)} = 0$$

$$e_D - p_D * v_D / (\rho_0 * (\gamma - 1)) = 0$$

Each pair of equations rearranged in the form: $x + a1 * y - b1 = 0$ and $x + a2 * y - b2 = 0$

$$r_D - \text{betaAD} * t_D - (r_A - \text{betaAD} * t_A) = 0$$

$$r_D + \text{betaBD} * t_D - (r_B + \text{betaBD} * t_B) = 0$$

$$p_D + u_D / \text{phiAD} - (p_A + u_A / \text{phiAD} - \text{psiAD} * (t_D - t_A) / \text{phiAD}) = 0$$

$$p_D - u_D / \text{phiBD} - (p_B - u_B / \text{phiBD} - \text{psiBD} * (t_D - t_B) / \text{phiBD}) = 0$$

$$e_D + 0.5 * (p_D + p_F) * v_D - (e_F + 0.5 * (p_D + p_F) * v_F) = 0$$

$$eD - pD \cdot vD / (\rho_0 \cdot (\gamma - 1)) = 0$$

Equations rearranged to calculate RD

$$RD = RA + u_{\text{PluscAD}} \cdot (tD - tA) = 0$$

$$RD = RB + u_{\text{MinuscAB}} \cdot (tD - tB) = 0$$

*** Solution of pair of equations: $x + a_1 \cdot y - b_1 = 0$ and $x + a_2 \cdot y - b_2 = 0$**

$$y = (b_1 - b_2) / (a_1 - a_2)$$

$$x = b_1 - a_1 \cdot y$$

PART 3

Part 3 uses the starting point of the difference equations to develop the equivalent computer code for the piston nodes.

Equations transformed from those in the 3rd point set by modification for the piston:

$$r_P - r_A = 0$$

$$r_P - r_A = 0$$

$$r_P - r_B + \left[\frac{c}{v} \left(\frac{\alpha u c}{R} \right)^\alpha \right]_{BP} (t_P - t_B) = 0$$

$$r_P - r_B + \text{betaBP} * (t_P - t_B) = 0$$

$$u_P - (a_1 + 2.a_2 t_P + 3.a_3 t_P^2 + 4.a_4 t_P^3) = 0$$

$$u_P - (A1 + 2.A2.TP + 3.A3.TP^2 + 4.A4.TP^3) = 0$$

$$\left[\frac{1}{\rho.c} \right]_{BP} (p_P - p_B) - (u_P - u_B) + \left[\frac{\alpha u c}{R} \right]_{BP} (t_P - t_B) = 0$$

$$\text{phiBP} * (p_P - p_B) - (u_P - u_B) + \text{psiBP} * (t_P - t_B) = 0$$

$$R_P - (a_0 + a_1 t_P + a_2 t_P^2 + a_3 t_P^3 + a_4 t_P^4) = 0$$

$$R_P - (A0 + A1.tP + A2.tP^2 + A3.tP^3 + A4.tP^4) = 0$$

$$R_P - R_B - [u + c]_{BP} (t_P - t_B) = 0$$

$$R_P - R_B - u_{\text{MinuscBP}} * (t_P - t_B) = 0$$

$$E_P - E_A + \frac{1}{2} (p_P + p_A) (v_P - v_A) = 0$$

$$e_P - e_A + 0.5 * (p_P + p_A) * (v_P - v_A) = 0$$

$$E_P - \frac{p_P v_P}{\rho_0 (\gamma - 1)} = 0$$

$$e_P - p_P * v_P / (\rho_0 * (\gamma - 1)) = 0$$

Apart from the green pair, each pair of equations is rearranged in the form:

x +

$$a1 * y - b1 = 0 \text{ with } x + a2 * y - b2 = 0''$$

$$r_P - r_A = 0$$

$$r_P + \text{betaBP} * t_P - (r_B + \text{betaBP} * t_B) = 0$$

$$u_P - (A1 + 2.A2.tP + 3.A3.tP^2 + 4.A4.tP^3) = 0$$

$$p_P - u_P / \text{phiBP} - (p_B - u_B / \text{phiBP} - \text{psiBP} * (t_P - t_B) / \text{phiBP}) = 0$$

$$e_P + 0.5 * (p_P + p_A) * v_P - (e_A + 0.5 * (p_P + p_A) * v_A) = 0$$

$$e_P - p_P * v_P / (\rho_0 * (\gamma - 1)) = 0$$

Equations rearranged to calculate RD

$$RP = A0 + A1.tP + A2.tP^2 + A3.tP^3 + A4.tP^4$$

$$RP = RB + uMinuscBP*(tP - tB) = 0$$

*** Solution of pair of equations: $x + a1*y - b1 = 0$ and $x + a2*y - b2 = 0$**

$$y = (b1 - b2) / (a1 - a2)$$

$$x = b1 - a1*y$$

*** Solution of pair of equations in green:**

Calculate uP from tP using

$$uP = A1 + 2.A2.tP + 3.A3.tP^2 + 4.A4.tP^3$$

Calculate pP from uP and tP using the equation

$$pP = (uP - uB) / \phi_{iBP} + pB - \psi_{iBP}*(tP - tB) / \phi_{iBP}$$

PART 4

Part 4 is a copy of the two parts of code within the context of the main programme.

The following sections of the code provide the subroutines for determining 3RD-POINT node and PISTON node variable values from these values at two earlier computed nodes. Comments are included in the coding and some of these are employed as a check on the code representation of the equations by testing unit consistency. These comments are shown in red in this appendix.

The units for the variable being calculated on the left-hand-side of the equation are compared with the units in each term of the equation (on the right-hand-side) 3RD-POINT CALCULATION

```

int _3rdPoint()
{
    int iCount = 0;
// Calculate values for points A & B from given conditions at A & B
    TA = gammaFn1*eA/gasConstant;           // K == # N m m-3 / ( N m K-1 m-3) == K
    TB = gammaFn1*eB/gasConstant;           // K == # N m m-3 / ( N m K-1 m-3) == K
    pA = (gammaFn1)*eA/vA;                   // n m-2 == # N m m-3 == N m-2
    pB = (gammaFn1)*eB/vB;                   // n m-2 == # N m m-3 == N m-2
    cA = sqrt(gammaFn2*eA/rho0);             // m s-1 == sqrt(# kg m s-2 m m-3 m3 kg-1)
    == m s-1
    cB = sqrt(gammaFn2*eB/rho0);             // m s-1 == sqrt(# kg m s-2 m m-3 m3 kg-1)
    == m s-1
    etaA = pow((RA/rA), alpha);
    etaB = pow((RB/rB), alpha);

    do {

        if (iCount == 0) {
// Calculate mean values of variables for the first approximation using point A
            eD = eA;
            TD = gammaFn1*eA/gasConstant;     // K == # N m m-3 / ( N m K-1 m-3) == K
            vD = vA;
            pD = (gammaFn1)*eD/vD;             // n m-2 == # N m m-3 == N m-2
            uD = uA;
            cD = sqrt(gammaFn2*eD/rho0);       // m s-1 == sqrt(# kg m s-2 m m-3 m3 kg-1)
            == m s-1
            tD = tA;
            rD = rA;
            RD = RA;
        }
    }
}

```

```
}
```

```
etaD = pow((RD/rD), alpha);  
betaAD = 0.5*(etaA*cA/vA + etaD*cD/vD);  
phiAD = 0.5*(vA/cA+vD/cD)/rho0;  
psiAD = 0.5*alpha*(uA*cA/RA + uD*cD/RD);  
uPluscAD = 0.5*(uA + cA + uD + cD);
```

```
if (iCount == 0) {
```

```
// Calculate mean values of variables for the first approximation using point B
```

```
    eD = eB;  
    TD = gammaFn1*eD/gasConstant;           // K == # N m m-3 / ( N m K-1 m-3) == K  
    vD = vB;  
    pD = (gammaFn1)*eD/vD;                 // n m-2 == # N m m-3 == N m-2  
    uD = uB;  
    cD = sqrt(gammaFn2*eD/rho0);           // m s-1 == sqrt(# kg m s-2 m m-3 m3 kg-1)  
    == m s-1  
    tD = tB;  
    rD = rB;  
    RD = RB;  
    etaD = pow((RB/rB), alpha);  
}
```

```
// Calculate mean values for characteristic slopes etc using points A & B all iterations
```

```
betaBD = 0.5*(etaB*cB/vB + etaD*cD/vD);  
phiBD = 0.5*(vB/cB+vD/cD)/rho0;  
psiBD = 0.5*alpha*(uB*cB/RB + uD*cD/RD);  
uMinuscBD = 0.5*(uB - cB + uD - cD);
```

```
a1 = -betaAD;  
a2 = betaBD;  
b1 = rA - tA*betaAD;  
b2 = rB + tB*betaBD;  
// solveEqun(a1,b1,a2,b2,&rD,&tD);
```

```

y = (b1 - b2) / (a1 - a2);    x = b1 - a1*y;
rD = x;                      tD = y;
//    cout << rA << " " << rB << endl;
//    getch();
if (tB == tA) {
    rF = rD;
    tF = tA;
}
else {
    a1 = 0.0;
    a2 = -(rB - rA) / (tB - tA);
    b1 = rD;
    b2 = rA + tA*a2;
//    solveEqun(a1,b1,a2,b2,&rF,&tF);
    y = (b1 - b2) / (a1 - a2);    x = b1 - a1*y;
    rF = x;                      tF = y;
}
a2 = (rF - rB) / (rA - rB);
eF = eB + a2*(eA - eB);
pF = pB + a2*(pA - pB);
uF = uB + a2*(uA - uB);
RF = RB + a2*(RA - RB);

TF = gammaFn1*eF/gasConstant;           // K == # N m m-3 / ( N m K-1 m-3) == K
vF = eF*gammaFn1 / pF;                 // # == N m m-3 / N m-2 == #
cF = sqrt(gammaFn2*eF/rho0);           // m s-1 == sqrt(# kg m s-2 m m-3 m3 kg-1)
== m s-1

a1 = 1.0 / phiAD;
a2 = -1.0 / phiBD;
b1 = pA + uA / phiAD - psiAD*(tD - tA) / phiAD;
b2 = pB - uB / phiBD - psiBD*(tD - tB) / phiBD;
//    solveEqun(a1,b1,a2,b2,&pD,&uD);
y = (b1 - b2) / (a1 - a2);    x = b1 - a1*y;
pD = x;                      uD = y;

```

```

//      cout << rF << " " << tF << endl;

a1 = 0.5*(pD + pF);
a2 = -pD / (gammaFn1);
b1 = eF + 0.5*(pD + pF)*vF;
b2 = 0.0;
//      solveEqun(a1,b1,a2,b2,&eD,&vD);
y = (b1 - b2) / (a1 - a2);    x = b1 - a1*y;
eD = x;                      vD = y;

TD = gammaFn1*eD/gasConstant;           // K == # N m m-3 / ( N m K-1 m-3) == K
vD = y;
cD = sqrt(gammaFn2*eD/rho0);           // m s-1 == sqrt(# kg m s-2 m m-3 m3 kg-1)
== m s-1

RDA = RA + uPluscAD*(tD - tA);
RDB = RB + uMinuscBD*(tD - tB);
RD = 0.5*(RDA + RDB);
cout << "RDA = " << RDA << " and RDB = " << RDB << " tD = " << tD << " uMinuscBD " <<
uMinuscBD << endl;
}

while(++iCount <= 3);

if (RB < RD) {
    cout << " RB = " << RB << " RD = " << RD << " tB = " << tB << " tD = " << tD << endl
        << "Press any key to continue but press key 'a' to terminate" << endl;
    if (getch() == 'a') return(-1);
}
return(0);
}

```

PISTON CALCULATION

```

int _piston()
{
    int iCount=0;

    // Calculate mean values for characteristic slopes etc
    TA = gammaFn1*eA/gasConstant;           // K == # N m m-3 / ( N m K-1 m-3) == K
    TB = gammaFn1*eB/gasConstant;           // K == # N m m-3 / ( N m K-1 m-3) == K
    pA = (gammaFn1)*eA/vA;                   // n m-2 == # N m m-3 == N m-2
    pB = (gammaFn1)*eB/vB;                   // n m-2 == # N m m-3 == N m-2
    cA = sqrt(gammaFn2*eA/rho0);             // m s-1 == sqrt(# kg m s-2 m m-3 m3 kg-1)
    == m s-1
    cB = sqrt(gammaFn2*eB/rho0);             // m s-1 == sqrt(# kg m s-2 m m-3 m3 kg-1)
    == m s-1
    etaA = pow((RA/rA), alpha);
    etaB = pow((RB/rB), alpha);

    do {

        if (iCount == 0) {
            eP = eA;
            TP = gammaFn1*eA/gasConstant;     // K == # N m m-3 / ( N m K-1 m-3) == K
            vP = vA;
            pP = gammaFn1*eP/vP;               // n m-2 == # N m m-3 == N m-2
            uP = uA;
            cP = sqrt(gammaFn2*eP/rho0);       // m s-1 == sqrt(# kg m s-2 m m-3 m3 kg-1)
            == m s-1
            tP = tA;
            rP = rA;
            RP = RA;
        }

        etaP = pow((RP/rP), alpha);
        betaAP = 0.5*(etaA*cA/vA + etaP*cP/vP);
        phiAP = 0.5*(vA/cA+vP/cP)/rho0;
        psiAP = 0.5*alpha*(uA*cA/RA + uP*cP/RP);
    }
}

```

```

uPluscAP = 0.5*(uA + cA + uP + cP);

if (iCount == 0) {

    eP = eB;
    TP = gammaFn1*eP/gasConstant;           // K == # N m m-3 / ( N m K-1 m-3) == K
    vP = vB;
    pP = (gammaFn1)*eP/vP;                 // n m-2 == # N m m-3 == N m-2
    uP = uB;
    cP = sqrt(gammaFn2*eP/rho0);          // m s-1 == sqrt(# kg m s-2 m m-3 m3 kg-1)
    == m s-1
    tP = tB;
    rP = rB;
    RP = RB;

    etaP = pow((RB/rB), alpha);
}

betaBP = 0.5*(etaB*cB/vB + etaP*cP/vP);
phiBP = 0.5*(vB/cB+vP/cP)/rho0;
psiBP = 0.5*alpha*(uB*cB/RB + uP*cP/RP);
uMinuscBP = 0.5*(uB - cB + uP - cP);

a1 = 0.0;
a2 = betaBP;
b1 = rA;
b2 = rB + tB*betaBP;
y = (b1 - b2) / (a1 - a2);    x = b1 - a1*y;
rP = x;                       tP = y;

uP = A1 + 2.0*A2*tP + 3.0*A3*tP*tP + 4.0*A4*tP*tP*tP;
pP = (uP - uB)/phiBP + pB - psiBP*(tP - tB)/phiBP;

a1 = 0.5*(pP + pA);
a2 = -pP / (gammaFn1);
b1 = eA + 0.5*(pP + pA)*vA;

```

```

b2 = 0.0;

y = (b1 - b2) / (a1 - a2);    x = b1 - a1*y;
eP = x;                       vP = y;
TP = gammaFn1*eP/gasConstant; // K == # N m m-3 / ( N m K-1 m-3) == K
vD = y;
cP = sqrt(gammaFn2*eP/rho0); // m s-1 == sqrt(# kg m s-2 m m-3 m3 kg-1)
== m s-1
RPA = A0 + A1*tP + A2*tP*tP + A3*tP*tP*tP + A4*tP*tP*tP*tP;
RPB = RB + uMinuscBP*(tP - tB);
RP = 0.5*(RPA + RPB);
cout << "RPA = " << RPA << " and RPB = " << RPB << " tP = " << tP << " uMinuscBP " <<
uMinuscBP << endl;
}

while(++iCount <= 3);

return (1);

}

```